

AD-A052 051

NAVAL SURFACE WEAPONS CENTER WHITE OAK LAB SILVER SP--ETC F/G 19/4
STRESS WAVE PROPAGATION IN BARS DUE TO NORMAL IMPACT ON WATER.(U)
AUG 77 W T MESSICK, J M MARSHALL

UNCLASSIFIED

NSWC/WOL/TR-77-128

NL

1 OF 5

AD
A052 051



NSWC/WOL TR 77-128

AD A052051

**STRESS WAVE PROPAGATION IN BARS DUE
TO NORMAL IMPACT ON WATER**

BY WILLIAM T. MESSICK
JOHN M. MARSHALL

ADVANCED WEAPONS DEPARTMENT

AUGUST 1977

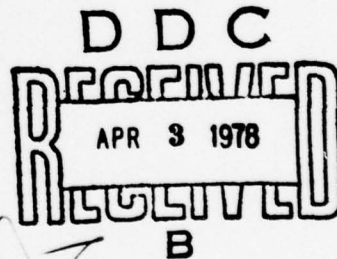
Approved for Public Release; Distribution Unlimited.

JUL FILE COPY



NAVAL SURFACE WEAPONS CENTER

Dahlgren, Virginia 22448 • Silver Spring, Maryland 20910



UNCLASSIFIED

SECURITY CLASSIFICATION OF THIS PAGE (When Data Entered)

REPORT DOCUMENTATION PAGE		READ INSTRUCTIONS BEFORE COMPLETING FORM
1. REPORT NUMBER NSWC/WOL/TR-77-128	2. GOVT ACCESSION NO.	3. RECIPIENT'S CATALOG NUMBER
4. TITLE (and Subtitle) STRESS WAVE PROPAGATION IN BARS DUE TO NORMAL IMPACT ON WATER.		5. TYPE OF REPORT & PERIOD COVERED Final rept.
7. AUTHOR(s) William T./Messick John M./Marshall		8. CONTRACT OR GRANT NUMBER(s)
9. PERFORMING ORGANIZATION NAME AND ADDRESS Naval Surface Weapons Center White Oak Laboratory White Oak, Silver Spring, MD 20910		10. PROGRAM ELEMENT, PROJECT, TASK AREA & WORK UNIT NUMBERS 61153N; SR02303; SR0230300; WA8102;
11. CONTROLLING OFFICE NAME AND ADDRESS		12. REPORT DATE August 1977
14. MONITORING AGENCY NAME & ADDRESS (if different from Controlling Office) 12401p.		13. NUMBER OF PAGES 359
		15. SECURITY CLASS. (of this report) UNCLASSIFIED
16. DISTRIBUTION STATEMENT (of this Report) Approved for public release; distribution unlimited.		
17. DISTRIBUTION STATEMENT (of the abstract entered in Block 20, if different from Report)		
18. SUPPLEMENTARY NOTES		
19. KEY WORDS (Continue on reverse side if necessary and identify by block number) stress waves rigid polyurethane foam water impact magnesium bars method of characteristics strain gages finite differences hydrodynamics		
20. ABSTRACT (Continue on reverse side if necessary and identify by block number) The stress wave response of solid, right circular cylindrical bars due to normal impact on an undisturbed water surface was investigated analytically and experimentally. The analytical problem was formulated as a two dimensional axisymmetrical elastic bar impacting on an initially perfectly flat, compressible water half space. Method of characteristics - finite difference solutions were obtained for the Lagrangian system		

DD FORM 1 JAN 73 1473

EDITION OF 1 NOV 65 IS OBSOLETE
S/N 0102-014-6601

UNCLASSIFIED

SECURITY CLASSIFICATION OF THIS PAGE (When Data Entered)

391 596

LB

UNCLASSIFIED

SECURITY CLASSIFICATION OF THIS PAGE(When Data Entered)

of bar equations and Eulerian water equations, and programmed for computer solution.

Strain-gaged magnesium bars were shot with a 3 inch diameter air gun into a chamber which was evacuated to the vapor pressure of water for preserving an undisturbed water surface prior to impact. Shots were made with a bare magnesium nose (unmitigated) and with rigid polyurethane foam noses of densities 5 and 15 pounds per cubic feet. The use of a foam nose greatly reduces the transmitted stress to the bar.

Agreement of the calculated axial strain on the lateral surface with the experimental data for unmitigated shots is, in general, good. The results of this study demonstrate that a one dimensional stress wave propagation analysis does not accurately predict the response of water impact structures, but that the response is multi-dimensional. The calculated results predict a maximum compressive stress in the bar interior which is approximately 27 percent larger than the impact stress.

UNCLASSIFIED

SECURITY CLASSIFICATION OF THIS PAGE(When Data Entered)

SUMMARY

This report describes the experimental data obtained and the numerical method developed for predicting the stress wave response of solid bars from impact normal to a flat water surface. This work was sponsored by the Naval Sea Systems Command, Mr. Lionel Pasiuk/NAVSEA 03513, under Task Area Number SR02303003, Stress Attenuation.

The results of this investigation have been accepted by the University of Maryland as a thesis in partial fulfillment of the requirements of the Doctor of Philosophy Degree in Mechanical Engineering.

The authors wish to acknowledge the assistance provided by members of the NSWC/WOL staff on the experimental facilities: Dr. Philip Aronson, Mr. Tony Kolodzinski, Mr. Doug Newell, Mr. Howie Steves, and Mr. Robert Waser. Mr. Newell was especially helpful in solving the electronic problems. Thanks is also extended to Mrs. Monica Lloyd for her typing of the manuscript.

C. A. Fisher
C. A. FISHER
By direction

ACCESSION for	
NTIS	White Section <input checked="" type="checkbox"/>
DDC	Buff Section <input type="checkbox"/>
UNANNOUNCED	<input type="checkbox"/>
JUSTIFICATION	
BY	
DISTRIBUTION/AVAILABILITY CODES	
Dist.	AVAIL. and/or SPECIAL
A	

CONTENTS

<u>Chapter</u>		<u>Page</u>
I.	BACKGROUND AND PROBLEM DEFINITION.....	27
II.	TWO SPATIAL DIMENSION METHOD OF CHARACTER- ISTICS SOLUTION TO WATER IMPACT PROBLEMS....	37
	A. Analysis Assumptions.....	37
	B. Equations for the Impact Bar.....	39
	C. Equations for Water Response.....	60
	D. Interface Equations at the Impact Face...	72
	E. Initial Conditions.....	81
III.	FLEBOW COMPUTER PROGRAM.....	84
	A. Discretization and Interpolation Techniques.....	85
	1. Numerical Method for Impact Bar Solution.....	85
	2. Numerical Method for Water Solution.....	89
	B. Philosophy of Computational Method.....	99
	C. Computer Program Elements.....	103

CONTENTS (CONTINUED)

Chapter	Page
IV. WATER-IMPACT EXPERIMENTS.....	116
A. Experimental Facility.....	116
B. Test Models.....	121
C. Recording Equipment.....	125
V. ANALYSIS OF ANALYTICAL AND EXPERI- MENTAL RESULTS.....	129
A. Computer Results.....	129
1. Computer Case No. 1.....	130
2. Computer Case No. 2.....	138
3. Computer Case No. 3.....	141
B. Experimental Results.....	146
1. Foil Gage Model Data.....	147
2. Unmitigated Semiconductor Gage Model Data.....	149
3. Mitigated Shot Data.....	160
C. Comparison of Analytical and Experimental Results.....	169
1. The 2.75-Inch-Diameter Bar...	169
2. The 2.5-Inch-Diameter Bar....	170
D. Comparison with Waser's Data.....	175
VI. CONCLUSIONS AND RECOMMENDATIONS FOR FURTHER WORK.....	177

CONTENTS (CONTINUED)

	Page
REFERENCES.....	357
APPENDIX A. BICHARACTERISTIC EQUATIONS FOR THE LAGRANGIAN FORMULATION OF LINEAR ELASTIC WAVE PROPAGATION.....	A-1
A.1 Governing Equations.....	A-1
A.2 Method of Characteristics Solution.....	A-2
APPENDIX B. BICHARACTERISTIC EQUATIONS FOR THE EULERIAN FORMULATION OF NONLINEAR WAVE PROPAGATION IN WATER.....	B-1
B.1 Governing Equations.....	B-1
B.2 Equations of Bicharacteristic Curves.....	B-3

TABLES

Table		Page
III.1	FLEBOW Computer Program Input.....	105
III.2	Subroutines for Points Along Impact Face Excluding Axis of Symmetry.....	109
III.3	Subroutines for Impact Bar at Points in Between Axial Boundaries.....	111
III.4	Subroutines for Free End of Impact Bar..	113
V.1	Normalized Stress Response at Selected Locations and Times for Computer Cases 1 and 2.....	140
V.2	Ratio of Computer Case 2 Response to Computer Case 1 Response at Selected Locations and Times.....	142
V.3	Maximum Strains and Pulse Rise Times for 5 PCF Foam Nose Shots.....	167

FIGURES

Figure		Page
II.1	Normal Impact of a Finite Length Elastic Bar on a Semi-infinite Smooth Surface.....	183
II.2	Characteristic Cones and Bicharacteristics.....	184
II.3	Characteristic Cones at the Boundaries of the Impact Bar.....	185
II.4	Characteristic Conoid for Hydrodynamic Nonlinear Wave Propagation.....	186
II.5	Planview of RZ Plane Showing Bicharacteristic Scheme at Water Boundary.....	187
II.6	Characteristic Cones in the Impact Bar at the Impact Face.....	188
II.7	Hugoniot Matching for Obtaining Impact Pressure and Particle Velocity.....	189
III.1	Discretized Continuum of the Impact Bar	190
III.2	Interpolation in IJ Grid.....	191
III.3	IJ Grid for Water Points.....	192
III.4	Interpolating Triangles for Water IJ Grid.....	193
III.5	Water Free Surface Tracing Technique...	194
III.6	Point by Point Solution Sequence on IJ Grid.....	195
III.7	Data Flow for Water Impact Problem Solution.....	196
III.8	Flow Chart for FLEBOW Program.....	197
III.9	Subroutine BOUNDARY for Water Equations Near Boundary.....	202
III.10	Subroutine ORIGIN for Axis of Symmetry on Impact Face.....	203

FIGURES (CONTINUED)

Figure		Page
III.11	Subroutines INTEROR and AXIALNB for Water Interior Points and Axis of Symmetry Points, Respectively.....	204
IV.1	Hydroballistics Pilot Tank.....	205
IV.2	Upper Level of Hydroballistics Pilot Facility.....	206
IV.3	Top View of Vacuum Chamber.....	207
IV.4	Side View of Vacuum Chamber Prepared for a Shot.....	208
IV.5	"Foil Gage" Model.....	209
IV.6	Test Models.....	210
IV.7	Strain Gage Circuits for the Two Test Models.....	211
IV.8	Camera and Laser Setups for Experiments.	212
IV.9	Schematic of Data Recording Circuit for Semiconductor Gage Model.....	213
V.1	Axial Stress in a Magnesium Bar at .77 μ sec From a Normal Impact on Water at 96 Ft/Sec (2.5 Inch Diameter).....	214
V.2	Axial Stress in a Magnesium Bar at 3.99 μ sec From a Normal Impact on Water at 96 Ft/Sec (2.5 Inch Diameter).....	215
V.3	Axial Stress in a Magnesium Bar at 5.28 μ sec From a Normal Impact on Water at 96 Ft/Sec (2.5 Inch Diameter).....	216
V.4	Axial Stress in a Magnesium Bar at 6.57 μ sec From a Normal Impact on Water at 96 Ft/Sec (2.5 Inch Diameter).....	217

FIGURES (CONTINUED)

Figure		Page
V.5	Axial Stress in a Magnesium Bar at 9.15 μ sec From a Normal Impact on Water at 96 Ft/Sec (2.5 Inch Diameter).	218
V.6	Axial Stress in a Magnesium Bar at 14.31 μ sec From a Normal Impact on Water at 96 Ft/Sec (2.5 Inch Diameter).....	219
V.7	Axial Stress in a Magnesium Bar at 15.60 μ sec From a Normal Impact on Water at 96 Ft/Sec (2.5 Inch Diameter).	220
V.8	Axial Stress in a Magnesium Bar at 16.89 μ sec From a Normal Impact on Water at 96 Ft/Sec (2.5 Inch Diameter).	221
V.9	Axial Stress in a Magnesium Bar at 18.18 μ sec From a Normal Impact on Water at 96 Ft/Sec (2.5 Inch Diameter).	222
V.10	Axial Stress in a Magnesium Bar at 21.41 μ sec from a Normal Impact on Water at 96 Ft/Sec (2.5 Inch Diameter).	223
V.11	Axial Stress in a Magnesium Bar at 24.63 μ sec From a Normal Impact on Water at 96 Ft/Sec (2.5 Inch Diameter).....	224
V.12	Axial Stress in a Magnesium Bar at 27.21 μ sec From a Normal Impact on Water at 96 Ft/Sec (2.5 Inch Diameter).....	225
V.13	Axial Stress in a Magnesium Bar at 38.82 μ sec From a Normal Impact on Water at 96 Ft/Sec (2.5 Inch Diameter).....	226
V.14	Axial Stress in a Magnesium Bar at 41.40 μ sec From a Normal Impact on Water at 96 Ft/Sec (2.5 Inch Diameter).....	227
V.15	Pressure on the Impact Face of a Magnesium Bar Impacting Water.....	228
V.16	Pressure on the Impact Face of a Magnesium Bar Impacting Water.....	229
V.17	Pressure on the Impact Face of a Magnesium Bar Impacting Water.....	230

FIGURES (CONTINUED)

Figure		Page
V.18	Pressure on the Impact Face of a Magnesium Bar Impacting Water.....	231
V.19	Pressure on the Impact Face of a Magnesium Bar Impacting Water.....	232
V.20	Pressure on the Impact Face of a Magnesium Bar Impacting Water.....	233
V.21	Axial Stress Vs Time (2.500 Inch Diameter Magnesium Bar Impact Velocity = 96.0 Ft/Sec R = 1.250 Inches Z = .625 Inches)....	234
V.22	Axial Stress Vs Time (2.500 Inch Diameter Magnesium Bar Impact Velocity = 96.0 Ft/Sec R = 1.250 Inches Z = 1.250 Inches)...	235
V.23	Axial Stress Vs Time (2.500 Inch Diameter Magnesium Bar Impact Velocity = 96.0 Ft/Sec R = 1.250 Inches Z = 2.500 Inches)...	236
V.24	Axial Stress Vs Time (2.500 Inch Diameter Magnesium Bar Impact Velocity = 96.0 Ft/Sec R = 1.250 Inches Z = 3.750 Inches)...	237
V.25	Axial Stress Vs Time (2.500 Inch Diameter Magnesium Bar Impact Velocity = 96.0 Ft/Sec R = 1.250 Inches Z = 5.0 Inches).....	238
V.26	Axial Stress Vs Time (2.500 Inch Diameter Magnesium Bar Impact Velocity = 96.0 Ft/Sec R = 0.000 Inches Z = 0.000 Inches)...	239
V.27	Axial Stress Vs Time (2.500 Inch Diameter Magnesium Bar Impact Velocity = 96.0 Ft/Sec R = 0.000 Inches Z = 1.250 Inches)...	240
V.28	Axial Stress Vs Time (2.500 Inch Diameter Magnesium Bar Impact Velocity = 96.0 Ft/Sec R = 0.000 Inches Z = 2.500 Inches)...	241
V.29	Axial Stress Vs Time (2.500 Inch Diameter Magnesium Bar Impact Velocity = 96.0 Ft/Sec R = 0.000 Inches Z = 5.000 Inches)...	242

FIGURES (CONTINUED)

Figure		Page
V.30	Axial Stress Vs Time (2.500 Inch Diameter Magnesium Bar Impact Velocity = 96.0 Ft/Sec R = 0.000 Inches Z = 6.250 Inches).....	243
V.31	Radial Stress in a Magnesium Bar at 2.70 μ sec From a Normal Impact on Water at 96 Ft/Sec (2.5 Inch Diameter)	244
V.32	Radial Stress in a Magnesium Bar at 13.02 μ sec From a Normal Impact on Water at 96 Ft/Sec (2.5 Inch Diameter).....	245
V.33	Radial Stress in a Magnesium Bar at 20.12 μ sec From a Normal Impact on Water at 96 Ft/Sec (2.5 Inch Diameter).....	246
V.34	Radial Stress in a Magnesium Bar at 31.72 μ sec From a Normal Impact on Water at 96 Ft/Sec (2.5 Inch Diameter).....	247
V.35	Radial Stress in a Magnesium Bar at 41.40 μ sec From a Normal Impact on Water at 96 Ft/Sec (2.5 Inch Diameter).....	248
V.36	Radial Vel. in a Magnesium Bar at 2.70 μ sec From a Normal Impact on Water at 96 Ft/Sec (2.5 Inch Diameter).....	249
V.37	Radial Vel. in a Magnesium Bar at 5.28 μ sec From a Normal Impact on Water at 96 Ft/Sec (2.5 Inch Diameter).....	250
V.38	Radial Vel. in a Magnesium Bar at 10.44 μ sec From a Normal Impact on Water at 96 Ft/Sec (2.5 Inch Diameter).....	251

FIGURES (CONTINUED)

Figure		Page
V.39	Radial Vel. in a Magnesium Bar at 15.60 μ sec From a Normal Impact on Water at 96 Ft/Sec (2.5 Inch Diameter).....	252
V.40	Radial Vel. in a Magnesium Bar at 20.76 μ sec From a Normal Impact on Water at 96 Ft/Sec (2.5 Inch Diameter).....	253
V.41	Radial Velocity in a Magnesium Bar at 27.21 μ sec From a Normal Impact on Water at 96 Ft/Sec (2.5 Inch Diameter).....	254
V.42	Radial Vel. in a Magnesium Bar at 41.40 μ sec From a Normal Impact on Water at 96 Ft/Sec (2.5 Inch Diameter).....	255
V.43	Shear Stress in a Magnesium Bar at 2.70 μ sec From a Normal Impact on Water at 96 Ft/Sec (2.5 Inch Diameter).....	256
V.44	Shear Stress in a Magnesium Bar at 18.18 μ sec From a Normal Impact on Water at 96 Ft/Sec (2.5 Inch Diameter).....	257
V.45	Shear Stress in a Magnesium Bar at 41.40 μ sec From a Normal Impact on Water at 96 Ft/Sec (2.5 Inch Diameter).....	258
V.46	Velocity Field in Water.....	259
V.47	Velocity Field in Water.....	260
V.48	Axial Stress in a Magnesium Bar at 6.57 μ sec From a Normal Impact on Water at 142 Ft/Sec (2.5 Inch Diameter).....	261
V.49	Axial Stress in a Magnesium Bar at 14.31 μ sec From a Normal Impact on Water at 142 Ft/Sec (2.5 Inch Diameter).....	262
V.50	Pressure on the Impact Face of a Magnesium Bar Impacting Water.....	263

FIGURES (CONTINUED)

Figure		Page
V.51	Pressure on the Impact Face of a Magnesium Bar Impacting Water.....	264
V.52	Axial Stress in a Magnesium Bar at 7.09 μ sec From a Normal Impact on Water at 157 Ft/Sec (2.75 Inch Diameter).....	265
V.53	Axial Stress in a Magnesium Bar at 10.49 μ sec From a Normal Impact on Water at 157 Ft/Sec (2.75 Inch Diameter).....	266
V.54	Axial Stress in a Magnesium Bar at 13.90 μ sec From a Normal Impact on Water at 157 Ft/Sec (2.75 Inch Diameter).....	267
V.55	Axial Stress in a Magnesium Bar at 15.60 μ sec From a Normal Impact on Water at 157 Ft/Sec (2.75 Inch Diameter).....	268
V.56	Axial Stress in a Magnesium Bar at 19.01 μ sec From a Normal Impact on Water at 157 Ft/Sec (2.75 Inch Diameter).....	269
V.57	Axial Stress in a Magnesium Bar at 20.71 μ sec From a Normal Impact on Water at 157 Ft/Sec (2.75 Inch Diameter).....	270
V.58	Axial Stress in a Magnesium Bar at 24.97 μ sec From a Normal Impact on Water at 157 Ft/Sec (2.75 Inch Diameter).....	271
V.59	Axial Stress in a Magnesium Bar at 28.37 μ sec From a Normal Impact on Water at 157 Ft/Sec (2.75 Inch Diameter).....	272
V.60	Axial Stress in a Magnesium Bar at 39.44 μ sec From a Normal Impact on Water at 157 Ft/Sec (2.75 Inch Diameter).....	273
V.61	Axial Stress in a Magnesium Bar at 42.84 μ sec From a Normal Impact on Water at 157 Ft/Sec (2.75 Inch Diameter).....	274

FIGURES (CONTINUED)

Figure		Page
V.62	Axial Stress in a Magnesium Bar at 49.65 μ sec From a Normal Impact on Water at 157 Ft/Sec (2.75 Inch Diameter).....	275
V.63	Pressure on the Impact Face of a Magnesium Bar Impacting Water.....	276
V.64	Pressure on the Impact Face of a Magnesium Bar Impacting Water.....	277
V.65	Axial Stress Vs Time (2.750 Inch Diameter Magnesium Bar Impact Velocity = 157.0 Ft/Sec R = 1.375 Inches Z = .687 Inches)..	278
V.66	Axial Stress Vs Time (2.750 Inch Diameter Magnesium Bar Impact Velocity = 157.0 Ft/Sec R = 1.375 Inches Z = 1.375 Inches)	279
V.67	Axial Stress Vs Time (2.750 Inch Diameter Magnesium Bar Impact Velocity = 157.0 Ft/Sec R = 1.375 Inches Z = 2.750 Inches)	280
V.68	Axial Stress Vs Time (2.750 Inch Diameter Magnesium Bar Impact Velocity = 157.0 Ft/Sec R = 1.375 Inches Z = 3.437 Inches)	281
V.69	Axial Stress Vs Time (2.750 Inch Diameter Magnesium Bar Impact Velocity = 157.0 Ft/Sec R = 1.375 Inches Z = 5.500 Inches)...	282
V.70	Axial Stress Vs Time (2.750 Inch Diameter Magnesium Bar Impact Velocity = 157.0 Ft/Sec R = 1.375 Inches Z = 6.875 Inches)	283
V.71	Axial Stress Vs Time (2.750 Inch Diameter Magnesium Bar Impact Velocity = 157.0 Ft/Sec R = 0.000 Inches Z = 0.000 Inches)...	284
V.72	Axial Stress Vs Time (2.750 Inch Diameter Magnesium Bar Impact Velocity = 157.0 Ft/Sec R = 0.000 Inches Z = 1.375 Inches)...	285

FIGURES (CONTINUED)

Figure		Page
V.73	Axial Stress Vs Time (2.750 Inch Diameter Magnesium Bar Impact Velocity = 157.0 Ft/Sec R = 0.000 Inches Z = 2.750 Inches)...	286
V.74	Radial Stress in a Magnesium Bar at 19.86 μ sec From a Normal Impact on Water at 157 Ft/Sec (2.75 Inch Diameter).....	287
V.75	Radial Stress in a Magnesium Bar at 49.65 μ sec From a Normal Impact on Water at 157 Ft/Sec (2.75 Inch Diameter).....	288
V.76	Radial Stress Vs Time (2.750 Inch Diameter Magnesium Bar Impact Velocity = 157.0 Ft/Sec R = 0.000 Inches Z = .587 Inches)....	289
V.77	Radial Vel. in a Magnesium Bar at 5.39 μ sec From a Normal Impact on Water at 157 Ft/Sec (2.75 Inch Diameter).....	290
V.78	Radial Vel. in a Magnesium Bar at 10.49 μ sec From a Normal Impact on Water at 157 Ft/Sec (2.75 Inch Diameter).....	291
V.79	Radial Vel. in a Magnesium Bar at 28.37 μ sec From a Normal Impact on Water at 157 Ft/Sec (2.75 Inch Diameter).....	292
V.80	Radial Vel. in a Magnesium Bar at 49.65 μ sec From a Normal Impact on Water at 157 Ft/Sec (2.75 Inch Diameter).....	293
V.81	Radial Velocity Vs Time (2.750 Inch Diameter Magnesium Bar Impact Velocity = 157.0 Ft/Sec R = 1.375 Inches Z = 0.000 Inches)...	294
V.82	Shear Stress in a Magnesium Bar at 49.65 μ sec From a Normal Impact on Water at 157 Ft/Sec (2.75 Inch Diameter).....	295
V.83	Stress Versus Time for 2.75 Inch Diameter Bar (Shot Number 31).....	296
V.84	Stress Versus Time for 2.75 Inch Diameter Bar (Shot Number 32).....	297

FIGURES (CONTINUED)

Figure		Page
V.85	Stress Versus Time for 2.75 Inch Diameter Bar (Shot Number 33).....	298
V.86	Shot No. 32 Photograph of Model and Water Surface Prior to Impact.....	299
V.87	Axial Strain Versus Time for Gage Number 1 Shot Number 35.....	300
V.88	Axial Strain Versus Time for Gage Number 2 Shot Number 35.....	301
V.89	Axial Strain Versus Time for Gage Number 3 Shot Number 35.....	302
V.90	Axial Strain Versus Time for Gage Number 1 Shot Number 37.....	303
V.91	Axial Strain Versus Time for Gage Number 2 Shot Number 37.....	304
V.92	Axial Strain Versus Time for Gage Number 3 Shot Number 37.....	305
V.93	Axial Strain Versus Time for Gage Number 4 Shot Number 37.....	306
V.94	Axial Strain Versus Time for Gage Number 5 Shot Number 37.....	307
V.95	Axial Strain Versus Time for Gage Number 6 Shot Number 37.....	308
V.96	Axial Strain Versus Time for Gage Number 1 Shot Number 38.....	309
V.97	Axial Strain Versus Time for Gage Number 2 Shot Number 38.....	310
V.98	Axial Strain Versus Time for Gage Number 3 Shot Number 38.....	311
V.99	Axial Strain Versus Time for Gage Number 4 Shot Number 38.....	312
V.100	Axial Strain Versus Time for Gage Number 5 Shot Number 38.....	313

FIGURES (CONTINUED)

Figure		Page
V.101	Axial Strain Versus Time for Gage Number 6 Shot Number 38.....	314
V.102	Axial Strain Versus Time for Gage Number 2 Shot Number 39.....	315
V.103	Axial Strain Versus Time for Gage Number 3 Shot Number 39.....	316
V.104	Axial Strain Versus Time for Gage Number 4 Shot Number 39.....	317
V.105	Axial Strain Versus Time for Gage Number 5 Shot Number 39.....	318
V.106	Axial Strain Versus Time for Gage Number 6 Shot Number 39.....	319
V.107	Axial Strain Versus Time for Gage Number 2 Shot Number 40.....	320
V.108	Axial Strain Versus Time for Gage Number 4 Shot Number 40.....	321
V.109	Axial Strain Versus Time for Gage Number 5 Shot Number 40.....	322
V.110	Axial Strain Versus Time for Gage Number 6, Shot Number 40.....	323
V.111	Axial Strain Versus Time for Gage Number 1, Shot Number 47.....	324
V.112	Axial Strain Versus Time for Gage Number 3, Shot Number 47.....	325
V.113	Shot 47 Photograph of Foam Nose and Water Prior to Impact.....	326
V.114	Axial Strain Versus Time for Gage Number 4, Shot Number 47.....	327
V.115	Axial Strain Versus Time for Gage Number 5, Shot Number 47.....	328

FIGURES (CONTINUED)

Figure		Page
V.116	Axial Strain Versus Time for Gage Number 6, Shot Number 47.....	329
V.117	Axial Strain Versus Time for Gage Number 5, Shot Number 42.....	330
V.118	Axial Strain Versus Time for Gage Number 6, Shot Number 42.....	331
V.119	Axial Strain Versus Time for Gage Number 1, Shot Number 43.....	332
V.120	Axial Strain Versus Time for Gage Number 2, Shot Number 43.....	333
V.121	Axial Strain Versus Time for Gage Number 3, Shot Number 43.....	334
V.122	Axial Strain Versus Time for Gage Number 5, Shot Number 43.....	335
V.123	Axial Strain Versus Time for Gage Number 6, Shot Number 43.....	336
V.124	Axial Strain Versus Time for Gage Number 1, Shot Number 44.....	337
V.125	Axial Strain Versus Time for Gage Number 2, Shot Number 44.....	338
V.126	Axial Strain Versus Time for Gage Number 3, Shot Number 44.....	339
V.127	Axial Strain Versus Time for Gage Number 5, Shot Number 44.....	340
V.128	Axial Strain Versus Time for Gage Number 6, Shot Number 44.....	341
V.129	Experimental Maximum Axial Strain Values at 7.2 Diameters from Front Face of Bar..	342
V.130	Comparison of Experimental and Analytical Results for Shot Number 31.....	343

FIGURES (CONTINUED)

Figure		Page
V.131	Comparison of Experimental and Analytical Results for Shot Number 32.....	344
V.132	Comparison of Experimental and Analytical Results for Shot Number 33.....	345
V.133	Comparison of Experimental and Analytical Results for Gage Number 1, Shot Number 37.	346
V.134	Comparison of Experimental and Analytical Results for Gage Number 2, Shot Number 37.	347
V.135	Comparison of Experimental and Analytical Results for Gage Number 3, Shot Number 37.	348
V.136	Comparison of Experimental and Analytical Results for Gage Number 1, Shot Number 38.	349
V.137	Comparison of Experimental and Analytical Results for Gage Number 2, Shot Number 38.	350
V.138	Comparison of Experimental and Analytical Results for Gage Number 3, Shot Number 38.	351
V.139	Comparison of Experimental and Analytical Results for Gage Number 2, Shot Number 39.	352
V.140	Comparison of Experimental and Analytical Results for Gage Number 3, Shot Number 39.	353
V.141	Maximum Strain on Radial Surface of Bar Versus Distance From Impact Face.....	354
V.142	Rise Time of Axial Strain Pulse on Radial Surface of Bar Versus Distance from Impact Face.....	355
V.143	Comparison of 2.75 Inch Diameter Bar Data and Reference 10 Data.....	356
A.1	Characteristic Surface and Associated Geometry.....	A-24
A.2	Characteristic Cones and Bicharacteristics for Wave Propagation in Linear Elastic Bar	A-25

SYMBOLS

A, A_{ij}	matrix of elastodynamic coefficients for $U_{j,t}$ terms
a	local sound velocity in water
$a^{(n)}$	constant coefficient for evaluation of water variables in n^{th} interpolation triangle
a_1, a_2, a_3	coefficients for expressing $S_{ij}L_j$ in terms of three orthogonal vectors
B, B_{ij}	matrix of elastodynamic coefficients for $U_{j,r}$ terms
B_{ij}'	$T_{il}B_{lj}$
$b^{(n)}$	coefficient for radial variation of water variables in n^{th} interpolation triangle
C, C_{ij}	matrix of elastodynamic coefficients for $U_{j,z}$ terms
C_{ij}'	$T_{il}C_{lj}$
C_1	reciprocal of Young's modulus
C_2	ratio of Poisson's ratio to Young's modulus
C_3	reciprocal of shear modulus
$c^{(n)}$	coefficient for axial variation of water variables in n^{th} interpolation triangle
c_b	one dimensional stress wave velocity in bar
c_1	dilatational stress wave velocity in bar
c_2	distortional stress wave velocity in bar

SYMBOLS (CONTINUED)

D, D_i	term in elastodynamic equations accounting for cylindrical geometry variations in variables
D_i'	$T_{il} D_l$
D_N	diameter of impacting nose
E	Young's modulus of impact bar material
EPSIL	relative convergence control parameter for water calculations
G	shear modulus of impact bar material
h	discretization mesh dimension
h_1	distance between $J = 1$ and $J = 2$ lines for a particular I line in water
h_2	distance between $J = 2$ and $J = 3$ lines for a particular I line in water
I	radial discretization coordinate
ILINES	maximum number of I lines in computer calculations for water solution at a particular time step
IRAD	number of I lines in impact bar
J	axial discretization coordinate
JBMAX	maximum number of J lines in computer calculations for impact bar solution at a particular time step
JLINES	maximum number J lines in computer calculations for water solution at a particular time step
JMAX	maximum number of J lines in impact bar
J^n	simplification variable for known quantities in water at intersection of n^{th} bicharacteristic with previous time plane, equations (II-35) and (B-43)

SYMBOLS (CONTINUED)

K	time step number in computer calculations
L	length of impact bar
L_i	direction cosines of the normal to the characteristic surface
P_{P_n}	simplification variable for known quantities in water at intersection of n^{th} bicharacteristic with previous time plane, equations (II-35) and (B-43)
p	water pressure
p_o	pressure on impact face at impact
R_o	radius of impact bar
r	radial coordinate
r'	temporary radial coordinate of water free surface point
r_i	radial coordinate for i^{th} point within a water interpolation triangle
S_{ij}	coefficient matrix in characteristic equation
S_i^k	i^{th} component for k^{th} characteristic direction
T_{ij}	characteristic transformation matrix
t	time
Δt	time step
U_{P_n}	"average" water characteristic impedance in radial direction over the time from P to the intersection of the n^{th} bicharacteristic with the old time plane, equations (II-35) and (B-45)
U_j	dependent variables vector

SYMBOLS (CONTINUED)

$(U_j)_i$	value of j^{th} water variable at i^{th} point in interpolation triangle
u	radial velocity of water
V_o	impact velocity
V_{P_n}	"average" water characteristic impedance in axial direction over the time from P to the intersection of the n^{th} bicharacteristic with the old time plane, equations (II-35) and (B-45)
v	axial velocity of water
v_r	radial velocity in impact bar
v_z	axial velocity in impact bar
x_i	coordinate vector; $x_1 = t$, $x_2 = r$, $x_3 = z$
Y	conservatism factor for stability criterion in numerical solution of impact bar equations
z	axial coordinate
z'	temporary axial coordinate of water free surface point
z_i	axial coordinate for i^{th} point within a water interpolation triangle
α_k	coefficient used for evaluating characteristic directions $\phi_{,r}^{(k)} / \phi_{,t}^{(k)}$
β_k	coefficient used for evaluating characteristic directions $\phi_{,z}^{(k)} / \phi_{,t}^{(k)}$

SYMBOLS (CONTINUED)

γ	angle in rz plane measured clockwise with respect to the negative r axis on the backward characteristic cone when looking in the negative t direction
γ_{rz}	engineering shear strain in impact bar
ϵ_r	radial infinitesimal strain in impact bar
ϵ_z	axial infinitesimal strain in impact bar
ϵ_θ	circumferential infinitesimal strain
ζ	coordinate of bicharacteristic curve for a point P at time t, defined by its value γ at P
η	average of the slopes of adjacent water free surface discretization lines
η_1	iteration angle for obtaining water solution at free surface
θ	circumferential angle
λ	Lame's constant
λ_i	coefficient vector for water characteristic equation
μ_i	coefficient vector for water characteristic equation
ν	Poisson's ratio of impact bar material
ν_i	coefficient vector for water characteristic equation
$\xi_i^{(K)}$	i th component of K th eigenvector
ρ	density of water
ρ_b	density of impact bar

SYMBOLS (CONTINUED)

ρ_w	density of water
σ_r	radial stress in impact bar
σ_p	plateau stress of rigid polyurethane foam
σ_y	yield stress of rigid polyurethane foam
σ_z	axial stress in impact bar
σ_θ	circumferential stress in impact bar
τ	bicharacteristic coordinate, $d\tau = dt$
τ_{rz}	shear stress in impact bar
$\phi^{(k)}$	k^{th} characteristic surface
ω	an arbitrary variable used throughout for demonstrating operations

SUPERSCRIPTS

(Superscripts in above list supersede
the following definitions)

n	denotes value of variable at intersection of n^{th} bicharacteristic with previous time plane
P	denotes value of variable at point P in new time plane
$[n]$	n^{th} iteration on water variable at a given time and coordinate
'	normalized impact bar variables for computer results
-	first order variation with respect to τ for water bicharacteristic equations

NSWC/WOL TR 77-128

SYMBOLS (CONTINUED)

SUBSCRIPTS

(subscripts in above list supersede
the following definitions)

b	refers to impact bar
w	refers to water

CHAPTER I

BACKGROUND AND PROBLEM DEFINITION

The design of water-entry structures such as recoverable reentry vehicles, manned spacecraft, missiles, and mines depends on the ability to predict water impact loading and the subsequent dynamic response of the structure. Large impact stresses can cause large plastic deformations in the nose area and in weak sections of the structure, and undesirable accelerations can develop in the area of equipment mounts. These can produce either catastrophic failure of the structure or reduced system performance. The temporal and spatial variations and the amplitude of the loading on the nose of the water entry vehicle are dependent upon the impact velocity, the obliquity of impact, the shape, material and flexibility of the nose, and the water surface condition. The determination of the impact load for various configurations and impact conditions has received considerable attention over the past half century. One of the first major contributions was made by von Karman in Reference 1 for predicting water entry forces on seaplane floats during landing. During

World War II and the post war period, work was done with applications to torpedoes and mines. With the advent of high-velocity missiles in the 1950's and 1960's, investigations were made using shock wave analysis for determining impact stress. In the 1960's, the requirement for safe splashdowns of manned spacecraft spurred some work in the area. Over the past several decades much work has been conducted on the impact of flat plates on water with applications to ship hull slamming. In this later category, the layer of air trapped between the plate and the water surface prior to impact, and the flexibility of the plate have a cushioning effect on the impact, causing loads of reduced amplitude and millisecond or longer duration.

Blunt nose water entry missile structures are desirable for stable vehicle performance after water impact. For blunt nose vehicles, the loading from water impact is predominantly axial, even at low angles of obliquity. For normal impacts on an undisturbed water surface, the loading on the impact face is a large amplitude pulse of microseconds duration which causes stress waves to propagate into the structure. Disturbances on the water surface prior to impact cause a random, but generally large reduction in the peak impact pressure, with the average value being dependent on the ratio of model dimension to wave length. Design philosophy will dictate the level of impact loading to be used for the design

load. On one hand, a statistical approach may be taken in which an expected impact load with an assigned confidence level is used to determine structural response. On the other hand, a worst condition philosophy can be used in which the loading from the normal impact of the vehicle on a flat, undisturbed water surface is used as a design load. The response of a right circular cylindrical solid bar to normal impact on a flat, undisturbed water surface is the configuration of interest in this study. At subsonic velocities, the presence of air above the water surface causes an acoustic wave to propagate in air ahead of the projectile, causing a disturbance of the water surface prior to impact. The presence of the air in flexible flat plate normal impacts reduces the impact pressure and is thought to have a small mitigating effect on the water impact of more rigid, solid nose structures. Except for flat plate impact studies, theoretical predictions for normal impacts of solid blunt nose vehicles have neglected the air above the water surface and have assumed a flat-nose-on-flat-surface impact. Early theoretical predictions and even some recent publications on flat plate impacts without air cushioning have neglected the elasticity of the nose material, using an impact pressure p_0 of

$$p_0 = \rho_w a V_0 \quad (I-1)$$

where ρ_w is the water density, a is the local sound velocity and V_0 is the impact velocity. Seigel (Reference 2) included the elasticity of the nose material of the impacting vehicle and used a one dimensional impact analysis. He calculated

the impact pressure as

$$p_o = \frac{\rho_w a V_o}{1 + \frac{\rho_w a}{\rho_b c_b}} \quad (I-2)$$

where ρ_b and c_b are the density and elastic one dimensional stress wave velocity in the bar, respectively. Including the impact nose elasticity reduces the calculated impact stress. He also stated that the time duration of the pressure amplitude is

$$t = \frac{D_N}{2a} \quad (I-3)$$

where D_N is the diameter of the impacting nose. The time in equation (I-3) is the time that it takes a relief wave in water to travel from the periphery of the impact face to the centerline. Seigel stated that the impact pressure calculated from equation (I-2) is valid up to a velocity where water compressibility from the impact is not excessive. He suggested that the upper limit velocity is 600 feet per second (ft/sec). Laumbach in Reference 3 extended Seigel's prediction to supersonic velocities by a one dimensional strain analysis of the nose of the impact vehicle. He also generalized the impact nose to an ogival shape. The equation he derived for the impact pressure for a right circular cylindrical nose is the same as equation (I-2)

but with the sonic velocities a and c_b replaced by the shock velocities of the respective materials. Plots of impact pressure versus impact velocity using equation (I-2) and Laumbach's equation indicated little difference below the velocity limit imposed by Seigel. Equation (I-2) yielded only half the value from Laumbach's calculated impact pressure at 3500 ft/sec. Laumbach also derived a relationship between impact force and time which accounts for the reduction in area of application of the impact pressure due to the water relief wave.

The pressure loading on the impact face of a blunt nose vehicle from a normal impact on a flat, semi-infinite surface is a function of the radial location on the impact face and time. This spatial and time varying loading on the impact face induces two dimensional stress wave propagation into the impacting structure and should be analyzed accordingly. However, there has been no published work on the two dimensional elastic stress wave response of a blunt nose structure to normal water impacts. Two dimensional finite difference computer codes have been used to investigate damage in plates due to hypervelocity impacts of cylinders; e.g., see Reference 4. Gross plate and cylinder deformations are of interest in these types of studies. Madden and Chang (Reference 5) and Madden (Reference 6) investigated the hypervelocity normal impact of a right circular cylindrical bar on a halfspace using a two dimensional method of characteristics solution. However, the bar and

target materials are the same and are assumed to respond hydrodynamically.

The procedure for determining structural response to normal water impact has been to use a uniform loading over the impact face, with an approximate load-versus-time curve as given by Reference 2 or 3. The uniformly applied load over the impact face and a one dimensional stress wave propagation analysis for uniform structures, or a modified one dimensional analysis for changes in cross section, is used for obtaining the response at points in the structure away from the impact face. The rationale behind this one dimensional analysis is that if the maximum impact stress does not cause yielding or structural damage at the nose, then the subsequent radial and time varying loading occurring at the impact face in reality, averages out to a uniform one dimensional loading at axial locations far away from the impact face and the response at these locations will be reasonably predicted by one dimensional analysis. However, from the work done on two dimensional wave propagation in bars, it is known that the effect of relief waves propagating radially inward from the lateral surface of the bar is to cause stress amplification near the impact face. Bertholf (Reference 7), using a finite difference method, investigated the strain response of a bar near an axial face loaded with a spacewise-uniform step change in pressure.

He demonstrated numerical agreement with the experimental data of Miklowitz and Nisewanger (Reference 8). These works showed the errors introduced near the loaded end when a one dimensional stress wave analysis of the bar response is used. Chang and Horie (Reference 9) used finite differencing of a two dimensional method of characteristics solution to analyze the symmetric impact of identical elastic-viscoplastic bars. Their work indicated that for impact velocities high enough to cause yielding and subsequent viscoplastic response, the radial relief waves cause a tensile zone to develop near the impact face long before the arrival of any reflections from the rear axial end of the bar, and separation of the impact faces of the two bars occurs. These two dimensional effects in bars from initially uniform load applications on an axial end emphasize the need for a two dimensional analysis of the water impact problem.

Waser (Reference 10) experimentally obtained the stress on the radial surface of a 36 inch long, 2.75 inch diameter, right circular cylindrical solid bar at 12 inches from the impact face for water impact angles between 88 and 90 degrees to the water surface. The impact velocities were less than 200 feet per second (ft/sec). For the normal impact shots, the measured maximum stress was less than 73 percent of the calculated impact stress. It was believed that the air entrapped between the bar and the water surface contributed

to mitigating the impact stress by a cushioning effect. In an effort to explain the low stress transmitted to the bar, and to gain an accurate predictive method for elastic structural response from normal water impacts, a combined analytical and experimental program was proposed by the authors. A right circular cylindrical, solid bar was chosen as the impact model and the impact velocities under consideration were small enough to preclude plastic structural response. The analytical method models two dimensional elastic bar response and water compressibility. Although the low velocities being investigated do not require the inclusion of water compressibility effects, it was anticipated that subsequent studies would investigate higher impact velocities with this method. An experimental program was undertaken in which the atmosphere above the water surface was evacuated to a pressure slightly greater than the vapor pressure of water, and strain-gage instrumented right circular, cylindrical solid magnesium bars were launched onto it. The facility and the instrumented impact bars are described in Chapter IV. With this experimental arrangement, air cushioning and water disturbance prior to impact can be minimized. Additionally some shots were made with a rigid polyurethane foam mitigator on the nose of the bar to determine the effect of an energy absorbing material on the transmitted stress in the bar. These experimental results are presented in Chapter V.

The axisymmetric response of the elastic impact bar is formulated in Lagrangian coordinates yielding a system of six equations in two unknown velocities and four unknown stresses. The independent variables are two spatial coordinates and time. In order to accurately predict the response from the interactions of the primary axial compressive pulse and the radial relief waves, a second order numerical method is required. The Lax-Wendroff finite difference method (Reference 11) is a second-order scheme. Butler (Reference 12) derived a method based on integration along bicharacteristic curves for solving a system of symmetric hyperbolic equations when the characteristic equation for the system can be factored into a quadratic factor and a repeated linear factor. He used this method for obtaining solutions to plane, unsteady and steady, three dimensional flow problems. Clifton (Reference 13) extended Butler's work to the case for which a repeated quadratic factor occurs in the characteristic equation so that the elastodynamic equations in plane strain could be solved. In Reference 13, Clifton showed that for proper differencing of the spatial derivatives in the bicharacteristic relations, his method is exactly the same as the Lax-Wendroff scheme for interior points. At boundary points, the extension of Butler's method is more straightforward. Recker (Reference 14) used Clifton's scheme to formulate the equations for axisymmetric elastodynamic problems and applied the method to two shell problems. Chang and Horie (Reference 9) used a

similar method for symmetric bar impacts. This latter work was used for interior points, radial boundary, and the axial free end of the impact bar in the present study.

The time-dependent, axisymmetric, hydrodynamic equations for the response of the water are formulated in Eulerian coordinates. Richardson (Reference 15) and Elliott (Reference 16) used Butler's method to formulate a solution technique for the axisymmetric hydrodynamic problem with shocks and Elliott (Reference 16) applied it to the solution of the detonation of an explosive. Richardson's formulation is used in the present study to obtain the response at interior points in the water. For free surface points, a different scheme of bicharacteristic equations than Richardson's is used. At the impact face, the water equations are coupled to the elastodynamic equations for the impact bar. The method of characteristics formulation for the water and bar response from normal water impact is given in Chapter II. The discretization and interpolation schemes which are applied to the equations of Chapter II for obtaining a numerical solution are described in Chapter III.

A computer program was written to solve the water impact problem described above. A description of the program is given in Chapter III. Three computer cases were run to simulate the conditions of three of the experimental data shots. The two dimensional elastic response of the impact bar in the area of the impact face for the three conditions is presented in Chapter V along with comparisons of computer and experimental strain gage data.

CHAPTER II

TWO SPATIAL DIMENSION METHOD OF CHARACTERISTICS
SOLUTION TO WATER IMPACT PROBLEMS

A. Analysis Assumptions

The problem analyzed is the constant velocity normal impact of a solid finite-length right circular cylindrical bar on a semi-infinite, smooth, perfectly flat water surface. The geometry is depicted in Figure II.1. It will be assumed that there is a vacuum above the water surface. Thus, no disturbances will propagate ahead of the bar in flight to perturb the perfectly flat water surface prior to impact. The "evacuated" impact will cause a step change in the particle velocities of the bar and water at the impact face, forming shock waves in both materials. The impact velocities V_0 considered are sufficiently small so as not to cause material yielding in the bar from the propagated stresses. Furthermore, because of the small impact velocities and corresponding "low" shock pressures generated, the stress waves propagated into each medium will not be considered as strong shocks. Shock physics will be used to calculate initial impact conditions, but it is assumed that these disturbances

then propagate as discontinuities in the first derivatives into each material at the sound velocity of the material. The compressibility of water will be accounted for, so that the water sound velocity will be a function of local density. The material properties of the bar are homogeneous, isotropic, and independent of strain rate.

At the instant of impact (time = 0^+), there is a one dimensional strain state and a corresponding uniform stress loading at the impact face in the bar. Shearing stresses at the bar-water interface are neglected, so the loading at the interface is a uniform pressure and an axial velocity input over a circular area. As time progresses, the stresses propagate outward and release waves propagate inward from the boundary of the circular impact area to reduce the pressure level at the interface. The resulting stress profiles in the bar and in the water are two dimensional and axisymmetric. They are functions of the radial coordinate r from an axis of symmetry and the axial coordinate z along the axis at a given time t .

In the following sections of this chapter, method of characteristics solutions will be obtained for the governing equations of two dimensional axisymmetric

wave propagation in a linear elastic homogeneous isotropic medium subject to the appropriate boundary conditions and for the two dimensional axisymmetric nonlinear wave propagation equations in a compressible hydrodynamic medium. The compatibility conditions at the bar-water interface will then be obtained to ensure a solution to the water impact problem. Finally, the initial conditions will be obtained from shock matching techniques.

B. Equations for the Impact Bar

The equations which govern wave propagation in the impact bar are derived from the equations of motion, the kinematic strain rate-velocity relationships, and the constitutive equations of the propagation medium. Because of the small displacements that occur about the rigid body displacement for the given loading, the Lagrangian formulation will be used to describe the response of the bar; that is, displacements in the bar are measured relative to the undeformed medium. For an axisymmetric body which is loaded independent of circumferential position, to be in dynamic equilibrium, it must satisfy the equations:

$$\sigma_{r,r} + \tau_{rz,z} + \frac{\sigma_r - \sigma_\theta}{r} = \rho_b v_{r,t}$$

$$\tau_{rz,r} + \sigma_{z,z} + \frac{\tau_{rz}}{r} = \rho_b v_{z,t}$$
(II-1)

where ρ_b is the density of the bar, σ_r is the radial stress (in the r direction), σ_θ is the circumferential stress, σ_z is the axial stress (in a direction parallel to the axis), τ_{rz} is the shear stress, v_r is the radial velocity, v_z is the axial velocity, and the comma denotes partial differentiation. For a body which undergoes small displacements due to loading, a linear strain-displacement relation will adequately describe the kinematics of motion. The strain rates are defined as

$$\begin{aligned}\epsilon_{r,t} &= v_{r,r} \\ \epsilon_{\theta,t} &= \frac{v_r}{r} \\ \epsilon_{z,t} &= v_{z,z} \\ \gamma_{rz,t} &= v_{r,z} + v_{z,r}\end{aligned}$$
(II-2)

where ϵ_r , ϵ_θ , and ϵ_z are the material Lagrangian normal strains in the r , θ , and z directions, respectively, and γ_{rz} is the "engineering shear strain". The constitutive equations for a linear elastic isotropic material in strain rate form are:

$$\begin{aligned}
\varepsilon_{r,t} &= C_1 \sigma_{r,t} - C_2 (\sigma_{\theta,t} + \sigma_{z,t}) \\
\varepsilon_{\theta,t} &= C_1 \sigma_{\theta,t} - C_2 (\sigma_{r,t} + \sigma_{z,t}) \\
\varepsilon_{z,t} &= C_1 \sigma_{z,t} - C_2 (\sigma_{r,t} + \sigma_{\theta,t}) \\
\gamma_{rz,t} &= C_3 \tau_{rz,t}
\end{aligned}
\tag{II-3}$$

where the constants C_i are given by

$$C_1 = \frac{1}{E}, \quad C_2 = \frac{\nu}{E}, \quad C_3 = \frac{1}{G} \tag{II-4}$$

The material constants in the relationships (II-4), Young's modulus E , shear modulus G , and Poisson's ratio ν are independent of position in the bar due to the homogeneity assumption.

The strain rates may be eliminated from equations (II-2) and (II-3) to yield stress-particle velocity relationships.

$$\begin{aligned}
C_1 \sigma_{r,t} - C_2 \sigma_{\theta,t} - C_2 \sigma_{z,t} - v_{r,r} &= 0 \\
-C_2 \sigma_{r,t} + C_1 \sigma_{\theta,t} - C_2 \sigma_{z,t} - \frac{v_r}{r} &= 0 \\
-C_2 \sigma_{r,t} - C_2 \sigma_{\theta,t} + C_1 \sigma_{z,t} - v_{z,z} &= 0 \\
C_3 \tau_{rz,t} - v_{r,z} - v_{z,r} &= 0
\end{aligned}
\tag{II-5}$$

Thus the equations of motion (II-1) and the above equations (II-5) represent a system of six first order partial differential equations in six unknowns, which may be cast into matrix form as

$$A_{ij}U_{j,t} + B_{ij}U_{j,r} + C_{ij}U_{j,z} + D_i = 0; \quad i,j = 1,6 \quad (\text{II-6})$$

where

$$U_i = \begin{pmatrix} \sigma_r \\ \sigma_\theta \\ \sigma_z \\ \tau_{rz} \\ v_r \\ v_z \end{pmatrix} \quad (\text{II-7})$$

$$A_{ij} = [A] = \begin{bmatrix} C_1 & -C_2 & -C_2 & 0 & 0 & 0 \\ -C_2 & C_1 & -C_2 & 0 & 0 & 0 \\ -C_2 & -C_2 & C_1 & 0 & 0 & 0 \\ 0 & 0 & 0 & C_3 & 0 & 0 \\ 0 & 0 & 0 & 0 & \rho_b & 0 \\ 0 & 0 & 0 & 0 & 0 & \rho_b \end{bmatrix}$$

$$B_{ij} = [B] = \begin{bmatrix} 0 & 0 & 0 & 0 & -1 & 0 \\ 0 & 0 & 0 & 0 & 0 & 0 \\ 0 & 0 & 0 & 0 & 0 & 0 \\ 0 & 0 & 0 & 0 & 0 & -1 \\ -1 & 0 & 0 & 0 & 0 & 0 \\ 0 & 0 & 0 & -1 & 0 & 0 \end{bmatrix}$$

$$C_{ij} = [C] = \begin{bmatrix} 0 & 0 & 0 & 0 & 0 & 0 \\ 0 & 0 & 0 & 0 & 0 & 0 \\ 0 & 0 & 0 & 0 & 0 & -1 \\ 0 & 0 & 0 & 0 & -1 & 0 \\ 0 & 0 & 0 & -1 & 0 & 0 \\ 0 & 0 & -1 & 0 & 0 & 0 \end{bmatrix}$$

$$D_i = \left\{ D \right\} = \begin{pmatrix} 0 \\ -\frac{v_r}{r} \\ 0 \\ 0 \\ -\frac{(\sigma_r - \sigma_\theta)}{r} \\ -\frac{\tau_{rz}}{r} \end{pmatrix}$$

The system of equations (II-6) does not possess a closed-form solution, but may be simplified by use of the method of characteristics. The method of characteristics seeks to find one or more surfaces, called the characteristic surfaces, within which disturbances propagate. By transforming the rzt coordinates to a new coordinate system with two directions lying in the characteristic surfaces and the other direction normal to the surfaces, the number of partial derivative terms in the system of equations

(II-6) may be reduced by one. The resulting two directional derivatives lie within the characteristic surfaces. The details of the transformation and the derivation of the characteristic surfaces are outlined in Appendix A. The characteristic surfaces for the system of equations (II-6) subject to the particular values (II-7) are two cones given by the equations:

$$(dt)^2 - \frac{(dr)^2 + (dz)^2}{c_\alpha^2} = 0; \quad \alpha = 1, 2 \quad (\text{II-8})$$

where c_α are the wave propagation speeds given by:

$$\begin{aligned} c_1 &= \sqrt{\frac{\lambda + 2G}{\rho_b}} \\ c_2 &= \sqrt{\frac{G}{\rho_b}} \end{aligned} \quad (\text{II-9})$$

$$\lambda = \frac{Ev}{(1+\nu)(1-2\nu)}$$

c_1 is the dilatational wave speed, the speed at which disturbances with no rotational motion travel. c_2 is the distortional wave speed, the speed at which disturbances with no change in volume travel. λ is Lamé's constant.

The generators of the characteristic cones are called the bicharacteristics and it is along the bicharacteristics that disturbances propagate from the old time plane, where all conditions are known, to a point P at the new time. These are shown in Figure II.2. The governing equations along a bicharacteristic located at an angle γ from the negative r axis involve total differentials in the unknown variables at P as well as partial derivatives of the unknown variables. In order to eliminate the unknown partial derivatives and solve for the variables themselves, a scheme is used which involves the bicharacteristics at γ equal to $0, \frac{\pi}{2}, \pi, \frac{3\pi}{2}$ on each of the characteristic cones along with the governing equations along a degenerate surface in the form of a straight line from the point $(t - \Delta t, r_p, z_p)$ in the old time plane to point $P(t, r_p, z_p)$ in the new time plane. These are represented by points 0 through 8 in Figure II.2. The partial differential equations for each characteristic surface are integrated with the following time integration approximations for a variable ω :

$$\int_{P_i} d\omega = \Delta\omega^i = \omega - \omega^i$$

$$\int_{P_i} \omega dt = (\delta\omega^i) \frac{\Delta t}{2} = (\omega + \omega^i) \frac{\Delta t}{2}$$

$$\int_{P_i} \frac{\omega}{r} dt = \frac{\delta\omega^i}{r^i} \cdot \frac{\Delta t}{2} \text{ where } r^i = \frac{r_p + r_i}{2}$$

ω^i represents the value of the variable ω at the bi-characteristic "i" in the old time plane. r_p and r_i denote the radius at the point P and at the intersection of the i^{th} bicharacteristic with the old time plane, respectively. The resulting equations from Appendix A are:

$$\begin{aligned} \underline{c_\alpha = c_1; \gamma = 0:} & \rho_b c_1 \Delta v_r^1 - \Delta\sigma_r^1 + \frac{\Delta t}{2} [\lambda \delta v_{z,z}^1 - c_1 \delta\tau_{rz,z}^1 \\ & - \frac{c_1}{r^1} (\delta\sigma_r^1 - \delta\sigma_\theta^1) + \frac{\lambda}{r^1} \delta v_r^1] = 0 \end{aligned} \quad (\text{II-11a})$$

$$\begin{aligned} \underline{c_\alpha = c_1; \gamma = \frac{3\pi}{2}:} & -\rho_b c_1 \Delta v_z^2 - \Delta\sigma_z^2 + \frac{\Delta t}{2} [\lambda \delta v_{r,r}^2 + c_1 \delta\tau_{rz,r}^2 \\ & + \frac{c_1}{r^2} \delta\tau_{rz}^2 + \frac{\lambda}{r^2} \delta v_r^2] = 0 \end{aligned} \quad (\text{II-11b})$$

$$\begin{aligned} \underline{c_\alpha = c_1; \gamma = \pi:} & -\rho_b c_1 \Delta v_r^3 - \Delta\sigma_r^3 + \frac{\Delta t}{2} [\lambda v_{z,z}^3 + c_1 \delta\tau_{rz,z}^3 \\ & + \frac{c_1}{r^3} (\delta\sigma_r^3 - \delta\sigma_\theta^3) + \frac{\lambda}{r^3} \delta v_r^3] = 0 \end{aligned} \quad (\text{II-11c})$$

$$\begin{aligned} \underline{c_\alpha = c_1; \gamma = \frac{\pi}{2} : \rho_b c_1 \Delta v_z^4 - \Delta \sigma_z^4 + \frac{\Delta t}{2} [\lambda \delta v_{r,r}^4 - c_1 \delta \tau_{rz,r}^4} \\ - \frac{c_1}{r^4} \delta \tau_{rz}^4 + \frac{\lambda}{r^4} \delta v_r^4] = 0 \end{aligned} \quad (\text{II-11d})$$

$$\begin{aligned} \underline{c_\alpha = c_2; \gamma = 0 : -\rho_b c_2 \Delta v_z^5 + \Delta \tau_{rz}^5 + \frac{\Delta t}{2} [-G \delta v_{r,z}^5 + c_2 \delta \sigma_{z,z}^5} \\ + \frac{c_2}{r^5} \delta \tau_{rz}^5] = 0 \end{aligned} \quad (\text{II-11e})$$

$$\begin{aligned} \underline{c_\alpha = c_2; \gamma = \frac{3\pi}{2} : -\rho_b c_2 \Delta v_r^6 - \Delta \tau_{rz}^6 + \frac{\Delta t}{2} [G \delta v_{z,r}^6 + c_2 \delta \sigma_{r,r}^6} \\ + \frac{c_2}{r^6} (\delta \sigma_r^6 - \delta \sigma_\theta^6)] = 0 \end{aligned} \quad (\text{II-11f})$$

$$\begin{aligned} \underline{c_\alpha = c_2; \gamma = \pi : \rho_b c_2 \Delta v_z^7 + \Delta \tau_{rz}^7 + \frac{\Delta t}{2} [-G \delta v_{r,z}^7 - c_2 \delta \sigma_{z,z}^7} \\ - \frac{c_2}{r^7} \delta \tau_{rz}^7] = 0 \end{aligned} \quad (\text{II-11g})$$

$$\begin{aligned} \underline{c_\alpha = c_2; \gamma = \frac{\pi}{2} : \rho_b c_2 \Delta v_r^8 - \Delta \tau_{rz}^8 + \frac{\Delta t}{2} [G \delta v_{z,r}^8 - c_2 \delta \sigma_{r,r}^8} \\ - \frac{c_2}{r^8} (\delta \sigma_r^8 - \delta \sigma_\theta^8)] = 0 \end{aligned} \quad (\text{II-11h})$$

The constitutive equations and the equations of motion are:

$$c_1 \Delta \sigma_r^0 - c_2 \Delta \sigma_\theta^0 - c_2 \Delta \sigma_z^0 - \frac{\Delta t}{2} \delta v_{r,r}^0 = 0 \quad (\text{II-11i})$$

$$-c_2 \Delta \sigma_r^0 + c_1 \Delta \sigma_\theta^0 - c_2 \Delta \sigma_z^0 - \frac{\Delta t}{2r^0} \delta v_r^0 = 0 \quad (\text{II-11j})$$

$$-c_2 \Delta \sigma_r^0 - c_2 \Delta \sigma_\theta^0 + c_1 \Delta \sigma_z^0 - \frac{\Delta t}{2} \delta v_{z,z}^0 = 0 \quad (\text{II-11k})$$

$$C_3 \Delta \tau_{rz}^0 - \frac{\Delta t}{2} (\delta v_{r,z} + \delta v_{z,r}^0) = 0 \quad (\text{II-11l})$$

$$\rho_b \Delta v_r^0 - \frac{\Delta t}{2} [\delta \sigma_{r,r}^0 + \delta \tau_{rz,z}^0 + \frac{(\delta \sigma_r^0 - \delta \sigma_\theta^0)}{r^0}] = 0 \quad (\text{II-11m})$$

$$\rho_b \Delta v_z^0 - \frac{\Delta t}{2} [\delta \sigma_{z,z}^0 + \delta \tau_{rz,r}^0 + \frac{\delta \tau_{rz}^0}{r^0}] = 0 \quad (\text{II-11n})$$

In the fourteen equations (II-11), there are fourteen unknowns: the unknown dependent variables at P: σ_r , σ_θ , σ_z , τ_{rz} , v_r , and v_z , and the unknown partial derivatives: $\sigma_{r,r}$, $\sigma_{z,z}$, $\tau_{rz,r}$, $\tau_{rz,z}$, $v_{r,r}$, $v_{r,z}$, $v_{z,r}$ and $v_{z,z}$. By proper combinations of the equations (II-11), the partial derivatives terms may be eliminated, yielding a system of equations in the unknown dependent variables. Depending on the location of the point P in the medium, whether it lies on a boundary, along the axis, or in the interior, some of the bicharacteristics will not be in the domain of dependence of the point P because material will be physically absent. For example, along the radial boundary of the impact bar, points 3 and 7 of Figure II.2 do not exist and thus equations (II-11c) and (II-11g) do not apply. Furthermore, along the radial boundary, σ_r is zero. Thus different combinations of equations (II-11) will have to be derived.

The equations for a general point in the interior of the impact bar will be derived first. The combinations of equations (II-11) will be referred to by the corresponding (II-11) lower case letters and all of the straightforward algebraic manipulations will be omitted.

-[(a) + (c) + 2λ(k)]:

$$\begin{aligned}
 & [2(1 + \lambda C_2) + \frac{c_1}{2} \Delta t (\frac{1}{r^1} - \frac{1}{r^3})] \sigma_r + [2\lambda C_2 - \frac{c_1}{2} \Delta t (\frac{1}{r^1} - \frac{1}{r^3})] \sigma_\theta \\
 & + [-2\lambda C_1] \sigma_z - \frac{\lambda \Delta t}{2} (\frac{1}{r^1} + \frac{1}{r^3}) v_r = 2\lambda C_2 (\sigma_r^0 + \sigma_z^0) - 2\lambda C_1 \sigma_z^0 \\
 & + \sigma_r^1 + \sigma_z^3 + \rho_b c_1 (v_r^3 - v_r^1) + [\frac{c_1}{r^1} (\sigma_\theta^1 - \sigma_r^1) + \frac{c_1}{r^3} (\sigma_r^3 - \sigma_\theta^3)] \\
 & + \lambda (\frac{v_r^1}{r^1} + \frac{v_r^3}{r^3}) + \lambda (v_{z,z}^1 + v_{z,z}^3 - 2v_{z,z}^0) + c_1 (\tau_{rz,z}^3 - \tau_{rz,z}^1) \frac{\Delta t}{2}
 \end{aligned}$$

(II-12a)

-[(b) + (d) + 2λ(i)]:

$$\begin{aligned}
 & [-2\lambda C_1] \sigma_r + 2\lambda C_2 \sigma_\theta + 2(1 + \lambda C_2) \sigma_z - \frac{\lambda \Delta t}{r^0} v_r = 2\lambda C_2 (\sigma_\theta^0 + \sigma_z^0) \\
 & - 2\lambda C_1 \sigma_r^0 + \sigma_z^2 + \sigma_z^4 + \rho_b c_1 (v_z^2 - v_z^4) + \frac{\Delta t}{2} [\frac{c_1}{r^0} (\tau_{rz}^2 - \tau_{rz}^4) \\
 & + \frac{\lambda}{r^0} (v_r^2 + v_r^4) + c_1 (\tau_{rz,r}^2 - \tau_{rz,r}^4) + \lambda (v_{r,r}^2 + v_{r,r}^4 - 2v_{r,r}^0)]
 \end{aligned}$$

(II-12b)

[-(b) + (d)] - \frac{c_1}{c_2} [(e) - (g)] - 2c_1(n):

$$\begin{aligned}
 & 2\rho_b c_1 v_z - \frac{c_1 \Delta t}{2} (\frac{1}{r^5} + \frac{1}{r^7}) \tau_{rz} = \sigma_z^2 - \sigma_z^4 + \rho_b c_1 (v_z^2 + v_z^4) \\
 & + \rho_b c_1 (v_z^5 + v_z^7 - 2v_z^0) + \frac{c_1}{c_2} (\tau_{rz}^7 - \tau_{rz}^5) + \frac{\Delta t}{2} \cdot \\
 & [c_1 (\frac{\tau_{rz}}{r^5} + \frac{\tau_{rz}}{r^7}) + c_1 (\tau_{rz,r}^2 + \tau_{rz,r}^4 - 2\tau_{rz,r}^0)]
 \end{aligned}$$

$$\begin{aligned}
& + \frac{\lambda}{r^0} (v_r^2 - v_r^4) + \lambda (v_{r,r}^2 - v_{r,r}^4) + \frac{Gc_1}{c_2} (v_{r,z}^7 - v_{r,z}^5) \\
& + c_1 (\sigma_{z,z}^5 + \sigma_{z,z}^7 - 2\sigma_{z,z}^0) + \frac{c_1}{r^0} (\tau_{rz}^2 + \tau_{rz}^4 - 2\tau_{rz}^0)] \\
& \hspace{15em} \text{(II-12c)}
\end{aligned}$$

$$\frac{c_1}{c_2} [2(f) + 2(l) - (g) - (e)] + 2c_1(m) - (a) + (c):$$

$$\begin{aligned}
& \frac{c_1 \Delta t}{2} \left(\frac{1}{r^1} + \frac{1}{r^3} \right) \sigma_r - \frac{c_1 \Delta t}{2} \left(\frac{1}{r^1} + \frac{1}{r^3} \right) \sigma_\theta + \left[-\frac{2c_1}{c_2} - \frac{c_1 \Delta t}{2} \left(\frac{1}{r^5} - \frac{1}{r^7} \right) \right] \tau_{rz} \\
& + [-2\rho_b c_1 - \frac{\lambda \Delta t}{2} \left(\frac{1}{r^1} - \frac{1}{r^3} \right)] v_r = \frac{c_1}{c_2} (2\tau_{rz}^0 - 2\tau_{rz}^6 - \tau_{rz}^5 - \tau_{rz}^7) \\
& + (\sigma_r^1 - \sigma_r^3) - \rho_b c_1 (v_r^1 + v_r^3) + \rho_b c_1 (2v_r^0 - 2v_r^6 + v_z^5 - v_z^7) \\
& + \frac{\Delta t}{2} \left[\frac{c_1}{r^1} (\sigma_\theta^1 - \sigma_r^1) + \frac{c_1}{r^3} (\sigma_\theta^3 - \sigma_r^3) + \frac{2c_1}{r^0} (\sigma_r^0 - \sigma_\theta^0 - \sigma_r^6 + \sigma_\theta^6) \right. \\
& + c_1 \left(\frac{\tau_{rz}^5}{r^5} - \frac{\tau_{rz}^7}{r^7} \right) + \lambda \left(\frac{v_r^1}{r^1} - \frac{v_r^3}{r^3} \right) + 2c_1 (\sigma_{r,r}^0 - \sigma_{r,r}^6) \\
& + c_1 (\sigma_{z,z}^5 - \sigma_{z,z}^7) + \frac{2Gc_1}{c_2} (v_{z,r}^0 - v_{z,r}^6) + \frac{2Gc_1}{c_2} (2v_{r,z}^0 \\
& - v_{r,z}^5 - v_{r,z}^7) + \lambda (v_{z,z}^1 - v_{z,z}^3) + (2\tau_{rz,z}^0 - \tau_{rz,z}^1 \\
& \left. - \tau_{rz,z}^3) c_1 \right] \hspace{15em} \text{(II-12d)}
\end{aligned}$$

(f) + (h) - (g) - (e) + 2(l):

$$\begin{aligned}
 -[2 + \frac{c_2 \Delta t}{2} (\frac{1}{r^5} - \frac{1}{r^7})] \tau_{rz} &= 2\tau_{rz}^0 - \tau_{rz}^5 - \tau_{rz}^6 - \tau_{rz}^7 - \tau_{rz}^8 \\
 + \rho_b c_2 (v_z^5 - v_z^7 + v_r^8 - v_r^6) &+ \frac{\Delta t}{2} [\frac{c_2}{r^0} (\sigma_r^8 - \sigma_r^6 + \sigma_\theta^6 - \sigma_\theta^8) \\
 + c_2 (\frac{\tau_{rz}^5}{r^5} - \frac{\tau_{rz}^7}{r^7}) &+ c_2 (\sigma_{z,z}^5 - \sigma_{z,z}^7 + \sigma_{r,r}^8 - \sigma_{r,r}^6) \\
 + G(2v_{r,z}^0 - v_{r,z}^5 - v_{r,z}^7 &+ 2v_{z,r}^0 - v_{z,r}^6 - v_{z,r}^8)] \\
 &\quad \text{(II-12e)}
 \end{aligned}$$

(j):

$$\begin{aligned}
 -C_2 \sigma_r + C_1 \sigma_\theta - C_2 \sigma_z - \frac{\Delta t}{2r^0} v_r &= -C_2 \sigma_r^0 + C_1 \sigma_\theta^0 \\
 - C_2 \sigma_z^0 + \frac{\Delta t}{2r^0} v_r^0 &\quad \text{(II-12f)}
 \end{aligned}$$

The quantities on the right hand sides of equations (II-12) involve known variables in the old time plane. Therefore, equation (II-12e) may be used to obtain τ_{rz} immediately. Knowing τ_{rz} , equation (II-12c) may be used to obtain v_z . The resulting four unknowns may be solved by using the remaining four equations.

Although the right hand sides of equations (II-12) involve known quantities, these quantities are not explicitly known, for example the partial derivative

terms and the values of the variables at the intersections of the bicharacteristics and the old time plane. A numerical technique must be applied to the equations to obtain a solution. The particular technique will be discussed in Chapter III.

The equations for points on the radial boundary $r = R_0$ of the impact bar given by $P(t, R_0, z)$ are derived by noting that along the radial boundary, the boundary conditions are

$$\begin{aligned}\sigma_r(t, R_0, z) &= 0 \\ \tau_{rz}(t, R_0, z) &= 0 \\ \tau_{rz,z}(t, R_0, z) &= 0\end{aligned}\tag{II-13}$$

Referring to Figure II.2, it may be seen that if P is on the radial boundary, then bicharacteristics P_3 and P_7 do not exist, so equations (II-11c) and (II-11g) do not apply. The intersection of the characteristic cones with the old time plane at the radial surface is shown in Figure II.3(a). The remaining equations (II-11) are combined in the indicated manner:

$$-\frac{[(a) + \lambda(k)] + \frac{1}{2} \frac{c_1}{c_2} [(f) - (h)] + c_1(m)}{2} :$$

$$\begin{aligned} & [\lambda c_2 - \frac{c_1 \Delta t}{2r}] \sigma_\theta - \lambda c_1 \sigma_z - (\rho_b c_1 + \frac{\lambda \Delta t}{2r}) v_r = \lambda c_2 \sigma_\theta^0 \\ & - \lambda c_1 \sigma_z^0 + \sigma_r^1 + \frac{1}{2} \rho_b c_1 (2v_r^0 - 2v_r^1 - v_r^6 - v_r^8) \\ & + \frac{\Delta t}{2} \left[\frac{c_1}{r} (\sigma_\theta^1 - \sigma_r^1) + \frac{\lambda}{r} v_r^1 - c_1 \tau_{rz,z}^1 + \lambda (v_{z,z}^1 - v_{z,z}^0) \right] \\ & + \frac{c_1}{2} (2\sigma_{r,r}^0 - \sigma_{r,r}^6 - \sigma_{r,r}^8) + \frac{c_1}{2r^6} (\sigma_\theta^6 + \sigma_\theta^8 - 2\sigma_\theta^0) \\ & + \frac{Gc_1}{2c_2} (v_{z,r}^8 - v_{z,r}^6) \end{aligned} \quad (II-14a)$$

$$-\frac{[(b) + (d) + 2\lambda(i)]}{2} :$$

$$\begin{aligned} & 2\lambda c_2 \sigma_\theta + 2(1 + \lambda c_2) \sigma_z - \frac{\lambda \Delta t}{r^0} v_r = 2\lambda c_2 (\sigma_\theta^0 + \sigma_z^0) \\ & + \sigma_z^2 + \sigma_z^4 + \rho_b c_1 (v_z^2 - v_z^4) + \frac{\Delta t}{2} \left[\frac{\lambda}{r^0} (v_r^2 + v_r^4) \right. \\ & \left. + c_1 (\tau_{rz,r}^2 - \tau_{rz,r}^4) + \lambda (v_{r,r}^2 + v_{r,r}^4 - 2v_{r,r}^0) \right] \end{aligned} \quad (II-14b)$$

$$\frac{c_1}{c_2} [(f) + (h)] - \frac{2c_1}{c_2} (e) + \frac{2c_1}{c_2} (l) - 2c_1(n) + (d) - (b) :$$

$$\begin{aligned} & 2\rho_b c_1 v_z = \sigma_z^2 - \sigma_z^4 + \rho_b c_1 (2v_z^5 - 2v_z^0 + v_r^8 - v_r^6) - \frac{2c_1}{c_2} \tau_{rz}^5 \\ & + \rho_b c_1 (v_z^2 + v_z^4) + \frac{\Delta t}{2} \left[\frac{2c_1}{r^5} \tau_{rz}^5 + \frac{c_1}{r^0} (\sigma_\theta^6 - \sigma_\theta^8) + \frac{\lambda}{r^0} (v_r^2 - v_r^4) \right. \\ & \left. + c_1 (\sigma_{r,r}^8 - \sigma_{r,r}^6) + 2c_1 (\sigma_{z,z}^5 - \sigma_{z,z}^0) + \frac{2Gc_1}{c_2} (v_{r,z}^0 - v_{r,z}^5) \right. \\ & \left. + \frac{Gc_1}{c_2} (2v_{z,r}^0 - v_{z,r}^6 - v_{z,r}^8) + \lambda (v_{r,r}^2 - v_{r,r}^4) + c_1 (\tau_{rz,r}^2 \right. \\ & \left. + \tau_{rz,r}^4 - 2\tau_{rz,r}^0) \right] \end{aligned} \quad (II-14c)$$

(j):

$$C_1 \sigma_\theta - C_2 \sigma_z - \frac{\Delta t}{2r} v_r = C_1 \sigma_\theta^0 - C_2 \sigma_z^0 + \frac{\Delta t}{2r} v_r^0 \quad (\text{II-14d})$$

Equation (II-14c) yields v_z directly. Equations (II-14a), (II-14b), and (II-14d) are three equations in the remaining three unknowns σ_θ , σ_z , and v_r .

For points being advanced in time on the axis of symmetry but not on an axial boundary, the bicharacteristics P_1 and P_5 do not exist. Therefore, equations (II-11a) and (II-11e) do not apply. The boundary conditions along the axis are

$$\begin{aligned} v_r(t, 0, z) &= 0 \\ v_{r,z}(t, 0, z) &= 0 \\ \tau_{rz}(t, 0, z) &= 0 \\ \tau_{rz,z}(t, 0, z) &= 0 \\ \sigma_r(t, 0, z) &= \sigma_\theta(t, 0, z) \end{aligned} \quad (\text{II-15})$$

From the above conditions and equation (II-11e):

$$v_{z,r}(t, 0, z) = 0 \quad (\text{II-15})$$

Now along the axis, at points 2, 4, 6, and 8 in Figure II.3(b), the terms $\frac{v_r}{r}$ and $\frac{\tau_{rz}}{r}$ appear indeterminate. However, using L'Hospital's rule, for points along the axis:

$$\begin{aligned} \lim_{r \rightarrow 0} \frac{v_r}{r} &= v_{r,r} \\ \lim_{r \rightarrow 0} \frac{\tau_{rz}}{r} &= \tau_{rz,r} \end{aligned} \quad (\text{II-16})$$

Using the boundary conditions and the relations (II-16), the proper combinations of equations (II-11) may be formed to yield a solution for the unknown variables σ_r , σ_z , and v_z at the axis.

$$-[(b) + (d) + 4\lambda(i)]:$$

$$\begin{aligned} -4\lambda(C_1 - C_2)\sigma_r + 2(1 + 2\lambda C_2)\sigma_z &= \sigma_z^2 + \sigma_z^4 + 4\lambda C_2 \sigma_z^0 \\ -4\lambda(C_1 - C_2)\sigma_r^0 + \rho_b C_1(v_z^2 - v_z^4) + \Delta t[C_1(\tau_{rz,r}^2 - \tau_{rz,r}^4) \\ &+ \lambda(v_{r,r}^2 + v_{r,r}^4 - 2v_{r,r}^0)] \end{aligned} \quad (II-17a)$$

$$[-(c) - \lambda(k) - \frac{c_1}{2c_2} [(f) - (h)] - c_1(m)]:$$

$$\begin{aligned} [1 + 2\lambda C_2]\sigma_r - \lambda C_1 \sigma_z &= \sigma_r^3 + 2\lambda C_2 \sigma_r^0 - \lambda C_1 \sigma_z^0 + \rho_b C_1 v_r^3 \\ + \frac{\Delta t}{2} [C_1 \tau_{rz,z}^3 + \frac{c_1}{r^3} (\sigma_r^3 - \sigma_\theta^3) + \frac{\lambda}{r^3} v_r^3 + \lambda(v_{z,z}^3 - v_{z,z}^0)] \\ + \frac{c_1 \Delta t}{2} [\sigma_{r,r}^8 + \sigma_{r,r}^6 - 2\sigma_{r,r}^0 + \frac{1}{2} (2\sigma_{\theta,r}^0 - \sigma_{\theta,r}^6 - \sigma_{\theta,r}^8)] \end{aligned} \quad (II-17b)$$

$$-2c_1(n) + \frac{2c_1}{c_2} (g) + (d) - (b):$$

$$\begin{aligned} 2\rho_b C_1 v_z &= \rho_b C_1 (v_z^2 + v_z^4 + 2v_z^7 - 2v_z^0) + \sigma_z^2 - \sigma_z^4 + \frac{2c_1}{c_2} \tau_{rz}^7 \\ + \frac{c_1 \Delta t}{2} [\frac{2\tau_{rz}^7}{r^7} + \frac{2G}{c_2} v_{r,z}^7 + \frac{2\lambda}{c_1} (v_{r,r}^2 - v_{r,r}^4) + 2(\sigma_{z,z}^7 - \sigma_{z,z}^0) \\ + 2(\tau_{rz,r}^2 + \tau_{rz,r}^4 - 2\tau_{rz,r}^0)] \end{aligned} \quad (II-17c)$$

Equations (II-17c) yields v_z directly and equations (II-17a) and (II-17b) solved simultaneously yield σ_r and σ_z .

At the free axial end of the bar, for points between the axis and the outside corner, the boundary conditions are:

$$\begin{aligned}\sigma_z(t, r, L) &= 0 \\ \tau_{rz}(t, r, L) &= 0 \\ \tau_{rz,r}(t, r, L) &= 0\end{aligned}\tag{II-18}$$

For the free axial end, bicharacteristics P_2 and P_6 do not apply. This implies that equations (II-11b) and (II-11f) are not used. The remaining bicharacteristics are shown in Figure II.3(c). With the remaining equations (II-11), the four unknown variables at the free end: σ_r , σ_θ , v_r , and v_z may be found from the following combinations of equations (II-11):

-(a) - (c) - $2\lambda(k)$:

$$\begin{aligned}& [2(1 + \lambda C_2) + \frac{c_1 \Delta t}{2} (\frac{1}{r^1} - \frac{1}{r^3})] \sigma_r + [2\lambda C_2 - \frac{c_1 \Delta t}{2} (\frac{1}{r^1} - \frac{1}{r^3})] \sigma_\theta \\ & - \frac{\lambda \Delta t}{2} (\frac{1}{r^1} + \frac{1}{r^3}) v_r = 2\lambda C_2 (\sigma_r^0 + \sigma_\theta^0) + \sigma_r^1 + \sigma_r^3 + \rho_b c_1 (v_r^3 - v_r^1) \\ & + \frac{\Delta t}{2} [\frac{c_1}{r^1} (\sigma_\theta^1 - \sigma_r^1) + \frac{c_1}{r^3} (\sigma_r^3 - \sigma_\theta^3) + \lambda (\frac{v_r^1}{r^1} + \frac{v_r^3}{r^3}) + c_1 (\tau_{rz,z}^3 \\ & - \tau_{rz,z}^1) + \lambda (v_{z,z}^1 + v_{z,z}^3 - 2v_{z,z}^0)]\end{aligned}\tag{II-19a}$$

$$(a) - (c) - \frac{2c_1}{c_2} [(g) - (h) - (l)] + 2c_1 [(n) - (m)]:$$

$$\begin{aligned} & \frac{c_1 \Delta t}{2} \left(\frac{1}{r^1} + \frac{1}{r^3} \right) (\sigma_\theta - \sigma_r) + [2\rho_b c_1 + \frac{\lambda \Delta t}{2} \left(\frac{1}{r^1} - \frac{1}{r^3} \right)] v_r = \\ & (\sigma_r^3 - \sigma_r^1) - \frac{2c_1}{c_2} \tau_{rz}^8 + \rho_b c_1 (v_r^1 + v_r^3) + 2\rho_b c_1 (v_z^0 - v_z^7 \\ & + v_r^8 - v_r^0) + \frac{c_1 \Delta t}{2} \left[\frac{1}{r^1} (\sigma_r^1 - \sigma_\theta^1) + \frac{1}{r^3} (\sigma_r^3 - \sigma_\theta^3) + \frac{2}{r^0} \cdot \right. \\ & (\sigma_r^8 - \sigma_r^0 + \sigma_\theta^0 - \sigma_\theta^8) + \frac{\lambda}{c_1} \left(\frac{v_r^3}{r^3} - \frac{v_r^1}{r^1} \right) + \frac{\lambda}{c_1} (v_{z,z}^3 - v_{z,z}^1) \\ & + 2(\sigma_{r,r}^8 - \sigma_{r,r}^0 + \sigma_{z,z}^0 - \sigma_{z,z}^7) + \frac{2G}{c_2} (v_{r,z}^0 - v_{r,z}^7 + v_{z,r}^0 \\ & \left. - v_{z,r}^8) + (\tau_{rz,z}^1 + \tau_{rz,z}^3 - 2\tau_{rz,z}^0) \right] \end{aligned} \quad (II-19b)$$

$$(d) + \lambda(i) - \frac{c_1}{2c_2} [(e) - (g)] - c_1(n):$$

$$\begin{aligned} & \lambda C_1 \sigma_r - \lambda C_2 \sigma_\theta + \frac{\lambda \Delta t}{2r^4} v_r + \rho_b c_1 v_z = \\ & - \sigma_z^4 + \lambda C_1 \sigma_r^0 - \lambda C_2 \sigma_\theta^0 + c_1 \rho_b v_z^4 + \frac{1}{2} c_1 \rho_b (v_z^5 + v_z^7 - 2v_z^0) \\ & + \frac{\Delta t}{2} \left\{ \frac{c_1}{r^4} \tau_{rz}^4 - \frac{\lambda}{r^4} v_r^4 + c_1 \tau_{rz,r}^4 + \lambda (v_{r,r}^0 - v_{r,r}^0) \right. \\ & \left. + \frac{1}{2} c_1 \left[\frac{G}{c_2} (v_{r,z}^7 - v_{r,z}^5) + (\sigma_{z,z}^5 + \sigma_{z,z}^7 - 2\sigma_{z,z}^0) \right] \right\} \end{aligned} \quad (II-19c)$$

(j):

$$-C_2 \sigma_r + C_1 \sigma_\theta - \frac{\Delta t}{2r^0} v_r = C_1 \sigma_\theta^0 - C_2 \sigma_r^0 + \frac{\Delta t}{2r^0} v_r^0 \quad (\text{II-19d})$$

The four equations (II-19) are solved simultaneously for the four variables σ_r , σ_θ , v_r , and v_z .

The boundary conditions for the outer corner of the free axial end must satisfy the boundary conditions for the free end and the radial boundary simultaneously. Thus,

$$\begin{aligned} \sigma_z(t, R_O, L) &= 0 \\ \sigma_r(t, R_O, L) &= 0 \\ \tau_{rz}(t, R_O, L) &= 0 \\ \tau_{rz,r}(t, R_O, L) &= 0 \\ \tau_{rz,z}(t, R_O, L) &= 0 \end{aligned} \quad (\text{II-20})$$

which yields three nonzero variables. The solution equations for the applicable bicharacteristics shown in Figure II.3 (d) are:

$$(a) + \lambda(k) - \frac{c_1}{c_2} [(e) - (h) - (l)] - c_1 [(m) + (n)]:$$

$$\begin{aligned} & \left[-\lambda C_2 + \frac{c_1 \Delta t}{2r^1} \right] \sigma_\theta + \left[\rho_b c_1 + \frac{\lambda \Delta t}{2r^1} \right] v_r = \\ & -\sigma_r^1 - \lambda C_2 \sigma_\theta^0 + c_1 \rho_b v_r^1 + c_1 \rho_b (v_r^8 - v_r^0 + v_z^5 - v_z^0) \\ & + \frac{\Delta t}{2} \left\{ \frac{c_1}{r^1} (\sigma_r^1 - \sigma_\theta^1) - \frac{\lambda}{r^1} v_r^1 + c_1 \tau_{rz,z}^1 + \lambda (v_{z,z}^0 - v_{z,z}^1) \right\} \end{aligned}$$

$$\begin{aligned}
& + c_1 [\sigma_{r,r}^8 - \sigma_{r,r}^0 + \sigma_{z,z}^5 - \sigma_{z,z}^0 + \frac{1}{r^0} (\sigma_\theta^0 - \sigma_\theta^8) \\
& + \frac{G}{c_2} (v_{r,z}^0 - v_{r,z}^5 + v_{z,r}^0 - v_{z,r}^8)] \} \quad (II-21a)
\end{aligned}$$

(d) + λ (i):

$$\begin{aligned}
-\lambda C_2 \sigma_\theta + \frac{\lambda \Delta t}{2r^4} v_r + \rho_b c_1 v_z &= -\lambda C_2 \sigma_\theta^0 - \sigma_z^4 + \rho_b c_1 v_z^4 \\
+ \frac{\Delta t}{2} \left[-\frac{\lambda}{r^4} v_r^4 + c_1 \tau_{rz,r}^4 + \lambda (v_{r,r}^0 - v_{r,r}^4) \right] \quad (II-21b)
\end{aligned}$$

(j):

$$c_1 \sigma_\theta - \frac{\Delta t}{2r^0} v_r = c_1 \sigma_\theta^0 + \frac{\Delta t}{2r^0} v_r^0 \quad (II-21c)$$

For the center of the free axial end, the only nonzero variables are σ_r and v_z . The boundary conditions are:

$$\begin{aligned}
\sigma_z(t, 0, L) &= 0 \\
\sigma_\theta(t, 0, L) &= \sigma_r(t, 0, L) \\
v_r(t, 0, L) &= 0 \\
\tau_{rz}(t, 0, L) &= 0 \\
\tau_{rz,r}(t, 0, L) &= 0 \\
\tau_{rz,z}(t, 0, L) &= 0
\end{aligned} \quad (II-22)$$

Figure II.3(e) shows the applicable bicharacteristics in this case. The two equations for the solution of σ_r and v_z at the free end on the axis are obtained from the indicated combinations:

$$(c) + \lambda(k) + \frac{c_1}{c_2} (h) - c_1(m):$$

$$\begin{aligned} [1 + 2\lambda C_2] \sigma_r = & \sigma_r^3 + 2\lambda C_2 \sigma_r^0 + c_1 \rho_b v_r^3 + \frac{\Delta t}{2} [\lambda (v_{z,z}^3 - v_{z,z}^0) \\ & + c_1 \tau_{rz,z}^3 + \frac{c_1}{r^3} (\sigma_r^3 - \sigma_\theta^3) + \lambda \frac{v_r^3}{r^3} + 2c_1 (\sigma_{r,r}^0 - \sigma_{r,r}^8) \\ & + c_1 (\sigma_{\theta,r}^8 - \sigma_{\theta,r}^0)] \end{aligned} \quad (II-23a)$$

$$(d) + 2\lambda(i) + \frac{c_1}{c_2} (g) - c_1(n):$$

$$\begin{aligned} 2\lambda(C_1 - C_2) \sigma_r + \rho_b c_1 v_z = & 2\lambda(C_1 - C_2) \sigma_r^0 - \sigma_z^4 + c_1 \rho_b (v_z^4 - v_z^0 + v_z^7) \\ & + \frac{\Delta t}{2} [2\lambda (v_{r,r}^0 - v_{r,r}^4) + 2c_1 \tau_{rz,r}^4 + \frac{c_1}{c_2} G v_{r,z}^7 - c_1 (\sigma_{z,z}^0 - \sigma_{z,z}^7)] \end{aligned} \quad (II-23b)$$

C. Equations for Water Response

The impact of the bar on water will theoretically cause a shock to form due to an instantaneous change in velocity of the water surface particles over the impact area. This shock will move into the water at

the shock propagation velocity. For low velocity impacts, in the order of several hundred feet per second, the shock velocity won't be too much different than the compressible sound velocity. Therefore, if the compressibility of water is taken into account, the analysis will yield good results (Reference (3)). The viscous effects will be neglected so that the water behavior will be hydrodynamic. The formulation of the equations will be done in Eulerian coordinates since it offers advantages in hydrodynamic flow problems.

For hydrodynamic flow in two dimensional axisymmetric Eulerian coordinates, the two momentum equations are:

$$\begin{aligned}\rho_w u_{,t} + \rho_w uu_{,r} + \rho_w vu_{,z} + p_{,r} &= 0 \\ \rho_w v_{,t} + \rho_w uv_{,r} + \rho_w vv_{,z} + p_{,z} &= 0\end{aligned}\tag{II-24}$$

where ρ_w is the density of water, u and v are the velocity components in the r and z directions, respectively, and p is the pressure. The continuity equation which ensures conservation of mass is

$$\frac{d\rho_w}{dt} + \rho_w \left(u_{,r} + v_{,z} + \frac{u}{r} \right) = 0\tag{II-25}$$

In this Eulerian formulation, $\frac{d\omega}{dt}$ is the total derivative of the variable ω :

$$\frac{d\omega}{dt} = \omega_{,t} + u\omega_{,r} + v\omega_{,z} \quad (\text{II-26})$$

For conservation of entropy along a particle path in compressible flow

$$\frac{dp}{dt} - a^2 \frac{d\rho_w}{dt} = 0 \quad (\text{II-27})$$

where a is the local sound velocity. The relationship between pressure and density is the low pressure equation of state, given functionally as:

$$p = p(\rho_w) \quad (\text{II-28})$$

Using the relationships (II-26) and (II-27), the continuity equation (II-25) may be rewritten as:

$$p_{,t} + up_{,r} + vp_{,z} + \rho_w a^2 u_{,r} + \rho_w a^2 v_{,z} + \rho_w a^2 \frac{u}{r} = 0 \quad (\text{II-29})$$

Equations (II-24) and (II-29) are the governing equations that are required to determine the behavior of the water, and may be cast into the format of equation (II-6) where

$$U_i = \left\{ U \right\} = \left\{ \begin{matrix} u \\ v \\ p \end{matrix} \right\}$$

$$A_{ij} = [A] = \begin{bmatrix} \rho_w & 0 & 0 \\ 0 & \rho_w & 0 \\ 0 & 0 & 1 \end{bmatrix}$$

$$B_{ij} = [B] = \begin{bmatrix} \rho_w & 0 & 1 \\ 0 & \rho_w u & 0 \\ \rho_w a^2 & 0 & u \end{bmatrix}$$

$$C_{ij} = [C] = \begin{bmatrix} \rho_w v & 0 & 0 \\ 0 & \rho_w v & 1 \\ 0 & \rho_w a^2 & v \end{bmatrix} \quad (\text{II-30})$$

$$D_i = \{D\} = \begin{Bmatrix} 0 \\ 0 \\ \rho_w a^2 \frac{u}{r} \end{Bmatrix}$$

The characteristic surface for the compressible hydrodynamic system of equations has been derived in Appendix B. The surface is a conoid described by the equation

$$(dr - udt)^2 + (dz - vdt)^2 = a^2 dt^2 \quad (\text{II-31})$$

Since the convective terms are present (udt and vdt), and the sound velocity "a" is not constant, this conoid does not have a fixed geometry like the cones in linear elastic homogeneous, isotropic wave propagation, but its shape varies depending on the flow field. Also the bi-characteristics are not straight lines but curves which depend on the varying flow field and therefore, on time.

ζ is the parameter used to identify a particular bi-characteristic curve ($\zeta = \text{constant}$). γ is the angle between the negative r axis and the projection of the tangent to the bicharacteristic curve onto the rz plane. At the point P in Figure II.4, γ is equal to the bicharacteristic parameter ζ . The bicharacteristic coordinates, as derived in Appendix B are:

$$\begin{aligned}\gamma^n &= \zeta^n - \Delta t [\sin \zeta^n \cos \zeta^n u_{,r}^n - (\cos \zeta^n)^2 u_{,z}^n + (\sin \zeta^n)^2 v_{,r}^n \\ &\quad - \sin \zeta^n \cos \zeta^n v_{,z}^n + \sin \zeta^n a_{,r}^n - \cos \zeta^n a_{,z}^n] \\ r^n &= r - \frac{1}{2} \Delta t [u + u^n + a \cos \zeta^n + a^n \cos \gamma^n] \\ z^n &= z - \frac{1}{2} \Delta t [v + v^n + a \sin \zeta^n + a^n \sin \gamma^n] \\ \Delta t &= t - t^n\end{aligned}\tag{II-32}$$

In (II-32), the bicharacteristic $\zeta^n = \text{constant}$ intersects the old time plane at n . The superscript n refers to evaluation of the variable at the intersection of the bicharacteristic ζ^n and the old time plane, which is point n in Figure II.4. The unsubscripted variables refer to evaluation at P in the new time plane. At P , γ^P equals ζ^n . For assumed values of a , u , and v equations (II-32) must be solved by an iteration technique because the value of the velocities u^n and v^n and the sound velocity a^n depend on the coordinates r^n and z^n .

Along the bicharacteristics, compatability equations are derived which contain not only the unknown variables at P but also derivatives of the variables at P. Thus a scheme is used to eliminate the derivatives so that the variables in the new time plane may be obtained as a function of the values in the old time plane. Four bicharacteristics are chosen with respect to the negative r axis.

$$\zeta^n = \frac{(n-1)}{2} \pi ; \quad n = 1, 2, 3, 4 \quad (\text{II-33})$$

The compatability equations are evaluated along the four bicharacteristics (see Appendix B)

$$p + U_{P_1} u + V_{P_1} v + \frac{1}{2} \Delta t \rho (a)^2 [v_{,z} + \frac{u}{r}] = P_{P_1} \quad (\text{II-34a})$$

$$p + U_{P_2} u + V_{P_2} v + \frac{1}{2} \Delta t \rho (a)^2 [u_{,r} + \frac{u}{r}] = P_{P_2} \quad (\text{II-34b})$$

$$p + U_{P_3} u + V_{P_3} v + \frac{1}{2} \Delta t \rho (a)^2 [v_{,z} + \frac{u}{r}] = P_{P_3} \quad (\text{II-34c})$$

$$p + U_{P_4} u + V_{P_4} v + \frac{1}{2} \Delta t \rho (a)^2 [u_{,r} + \frac{u}{r}] = P_{P_4} \quad (\text{II-34d})$$

where

$$\begin{aligned}
 U_{P_n} &= \frac{1}{2} (\rho a \cos \zeta^n + \rho^n a^n \cos \gamma^n) \\
 V_{P_n} &= \frac{1}{2} (\rho a \sin \zeta^n + \rho^n a^n \sin \gamma^n) \\
 P_{P_n} &= p^n + U_{P_n} u^n + V_{P_n} v^n + \frac{1}{2} \rho^n (a^n)^2 \Delta t J^n \\
 J^n &= \sin^2 \gamma^n u_{,r}^n - \sin \gamma^n \cos \gamma^n (u_{,z}^n + v_{,r}^n) \\
 &\quad + \cos^2 \gamma^n v_{,z}^n + \frac{u_n}{r^n}
 \end{aligned} \tag{II-35}$$

Additional equations are obtained along the particle path

$$p + \frac{1}{2} \Delta t \rho (a)^2 [u_{,r} + v_{,z} + \frac{u}{r}] = P_5 \tag{II-36}$$

where

$$P_5 = p^5 + \frac{1}{2} \Delta t \rho^5 (a^5)^2 \left[u_{,r}^5 + v_{,z}^5 + \frac{u^5}{r^5} \right]$$

The particle path from P to the intersection with the old time plane, point 5 in Figure II.4 is given by:

$$\begin{aligned}
 r^5 &= r - \frac{1}{2} \Delta t (u + u^5) \\
 z^5 &= z - \frac{1}{2} \Delta t (v + v^5)
 \end{aligned} \tag{II-37}$$

Using equations (II-34) through (II-37), the variables at points in the new time plane may be obtained. For general interior points in the semi-infinite water space, which are not on the axis of symmetry, the governing equations are chosen by performing the operations on the indicated equations of (II-34)

(a) - (c):

$$(U_{P_1} - U_{P_3})u + (V_{P_1} - V_{P_3})v = P_{P_1} - P_{P_3} \quad (\text{II-38a})$$

(b) - (d):

$$(U_{P_2} - U_{P_4})u + (V_{P_2} - V_{P_4})v = P_{P_2} - P_{P_4} \quad (\text{II-38b})$$

(a) + (b) + (c) + (d) - 2(II-42):

$$2p + (U_{P_1} + U_{P_2} + U_{P_3} + U_{P_4} + \frac{\rho(a)^2 \Delta t}{r})u + \quad (\text{II-38c})$$

$$(V_{P_1} + V_{P_2} + V_{P_3} + V_{P_4})v = P_{P_1} + P_{P_2} + P_{P_3} + P_{P_4} - 2P_5$$

The equations (II-38) cannot be solved explicitly for the three variables p , u , and v because the coefficients U_{P_n} and V_{P_n} are functions of u and v , respectively, and a is a function of p . Thus an iteration technique must be used where values of p , u , and v are assumed, the coefficients of equations (II-38) are evaluated, and a new set of variables p , u , and v are calculated. The iteration procedure continues until the coefficients of equations (II-38) are consistent with the variables themselves to within some numerical criterion. Furthermore, evaluation of variables in the old time plane must be consistent with the above equations (II-38) and the bi-characteristic equations (II-32).

For points on the axis of symmetry within the water volume, the boundary condition

$$u(t, 0, z) = 0 \quad (\text{II-39})$$

must be satisfied for all z . At the axis of symmetry the bicharacteristic P_1 is not applicable. The equations for the variables are derived from equations (II-34) and (II-36) as follows:

(b) - (d):

$$(V_{P_2} - V_{P_4})v = P_{P_2} - P_{P_4} \quad (\text{II-40a})$$

(b) + (d) + 4(c) - 4(II-42):

$$2p + (4V_{P_3} + V_{P_2} + V_{P_4})v = 4P_{P_3} - 4P_{P_5} + P_{P_2} + P_{P_4} \quad (\text{II-40b})$$

Equations (II-40) are solved by an iterative technique just as the interior equations.

The points on the boundary must be handled in a special way because of the irregularity of the surface points at the old time which are propagating disturbances to the point in question, P , at the new time. The points on the free surface near the periphery of the impact bar are especially irregularly shaped because of water splashing after the impact. If the bicharacteristics are chosen at angles of 0 or π at P , then it is possible that as these bicharacteristics are followed down to the previous time plane, they will fall outside of the water space. Thus

provision must be made to handle this potential problem. For an (I,J) discretization grid, where the I axis is parallel to the r axis and the J axis is parallel to the z axis, consider the point (I,1) on the boundary and the surrounding grid points as shown in Figure II.5. In order to eliminate the partial derivative terms in the bicharacteristic compatibility equations by using the fewest number of bicharacteristics, the following scheme is used to determine the variables at the new time for the location (I,1). Take the average of the slopes of the lines from (I-1,1) to (I,1) and (I,1) to (I + 1,1) and call it η . Choose an arbitrary angle η_1 such that the bicharacteristic angles are defined by

$$\begin{aligned}\zeta^1 &= \eta - \eta_1 \\ \zeta^2 &= \pi + \eta + \eta_1\end{aligned}\tag{II-41}$$

Note that

$$\begin{aligned}\tan(\eta - \eta_1) &= \text{slope from (I-1,1) to (I,1)} \\ \tan(\eta + \eta_1) &= \text{slope from (I,1) to (I + 1,1)}\end{aligned}\tag{II-42}$$

Now if values of the field variables are such that these bicharacteristics given by equation (II-41) will intersect the previous time plane outside of the water, then η_1 is increased until both bicharacteristics fall within the surface. Two additional bicharacteristics are used for eliminating unknown partial derivatives in the bicharacteristic compatibility relations. They are

$$\zeta^3 = \frac{3\pi}{2}$$

(II-43)

$$\zeta^4 = \frac{3\pi}{2} + \eta$$

Now the bicharacteristic compatibility equations in Appendix B are evaluated for these four bicharacteristics.

$$p + U_{P_1} u + V_{P_1} v + \frac{1}{2} \Delta t \rho(a)^2 \left[\sin^2(\eta - \eta_1) u_{,r} - \sin(\eta - \eta_1) \cos(\eta - \eta_1) \cdot \right. \\ \left. (u_{,z} + v_{,r}) + \cos^2(\eta - \eta_1) v_{,z} + \frac{u}{r} \right] = P_{P_1} \quad (\text{II-44a})$$

$$p + U_{P_2} u + V_{P_2} v + \frac{1}{2} \Delta t \rho(a)^2 \left[\sin^2(\eta + \eta_1) u_{,r} \right. \\ \left. - \sin(\eta + \eta_1) \cos(\eta + \eta_1) (u_{,z} + v_{,r}) + \cos^2(\eta + \eta_1) v_{,z} \right. \\ \left. + \frac{u}{r} \right] = P_{P_2} \quad (\text{II-44b})$$

$$p + U_{P_3} u + V_{P_2} v + \frac{1}{2} \Delta t \rho(a)^2 \left[u_{,r} + \frac{u}{r} \right] = P_{P_3} \quad (\text{II-44c})$$

$$p + U_{P_4} u + V_{P_4} v + \frac{1}{2} \Delta t \rho(a)^2 \left[\cos^2 \eta u_{,r} + \sin \eta \cos \eta (u_{,z} + v_{,r}) \right. \\ \left. + \sin^2 \eta v_{,z} + \frac{u}{r} \right] = P_{P_4} \quad (\text{II-44d})$$

The equation along a particle path through P is

$$p + \frac{1}{2} \Delta t \rho(a)^2 \left[u_{,r} + v_{,z} + \frac{u}{r} \right] = P_{P_5} \quad (\text{II-44e})$$

Equations (II-44) may be combined to eliminate the unknown partial derivative terms in the following manner:

$$\frac{(a) + (b) + 2(\cos^2 \eta_1 - \sin^2 \eta_1)(d) - 2\cos^2 \eta_1(e)}{2\cos^2 \eta_1 p + (U_{P_1} + U_{P_2} + 2U_{P_4} \cos 2\eta_1 + \frac{\rho(a)^2 \Delta t \cos^2 \eta_1}{r})u} \quad (II-45a)$$

$$+ (V_{P_1} + V_{P_2} + 2V_{P_4} \cos 2\eta_1)v = P_{P_1} + P_{P_2} + 2\cos 2\eta_1 P_{P_4} - 2\cos^2 \eta_1 P_{P_5}$$

$$\frac{(a) - (b) - 2\sin 2\eta_1 \cot 2\eta (d) - \sin 2\eta_1 \tan \eta (e) + \frac{2\sin 2\eta_1}{\sin 2\eta} (c)}{(\sin 2\eta_1 \tan \eta)p + (U_{P_1} - U_{P_2} + \frac{2U_{P_3} \sin 2\eta_1}{\sin 2\eta} - 2U_{P_4} \sin 2\eta_1 \cot 2\eta + \frac{\rho(a)^2 \Delta t \tan \eta \sin 2\eta_1}{2r})u + (V_{P_1} - V_{P_2} + \frac{2V_{P_3} \sin 2\eta_1}{\sin 2\eta} - 2V_{P_4} \sin 2\eta_1 \cot 2\eta)v} \\ = P_{P_1} - P_{P_2} + \sin 2\eta_1 \left(\frac{2}{\sin 2\eta} P_{P_3} - 2P_{P_4} \cot 2\eta - \tan \eta P_{P_5} \right) \quad (II-45b)$$

Equations (II-45) will only apply in the general case of nonzero η and η_1 terms and in the special case of zero η_1 and nonzero η . If both η and η_1 degenerate to zero, then of course the equations (II-34) can be used without equation (II-34b) to obtain a solution. Equation (II-34b) is not applicable for the boundary because the bicharacteristic corresponding to this equation lies outside of the water. The derivation of equations (II-45) involved division by $\sin \eta$ so that terms could be grouped in a manner to minimize numerical inaccuracies. Therefore, if η is zero, equations (II-45) cannot be used. Since η is arbitrary, the problem may be bypassed by assigning a small value to η and using equations (II-44).

For a free surface point, zero pressure is the boundary condition. To obtain the velocities at the free surface, equations (II-45) are used with $p = 0$ and an iteration scheme is implemented to insure satisfaction of the bicharacteristic coordinate equations subject to the constraint that the intersection of the bicharacteristics with the old time plane must lie within the water space bounded by the grid points at the previous time. The governing equations for the free surface will not be written here, because they are merely equations (II-45) with $p = 0$.

D. Interface Equations at the Impact Face

The equations for the impact bar and the water have been derived for grid points located away from the impact face. At the impact face, both the bar and water equations must satisfy contact conditions which ensure displacement and force equilibrium. The specific compatability equations that will be used here apply to a condition of no shear stress capability in water, that is, pure hydrodynamic water response. This uncouples the radial velocities of the bar and water. As long as the two materials are in contact, the axial velocities must be equal

$$v_z(t, r, 0) = -v(t, r, 0) \quad (\text{II-46})$$

The negative sign in equation (II-46) is due to the sign convention. The positive z direction in the bar is away from the water surface and the positive z direction in the water is into the water.

Equality of force over an infinitesimal area of the surface means that:

$$-\sigma_z(t, r, 0) = p(t, r, 0) \quad (\text{II-47})$$

The negative sign is due to the sign convention of water pressure p being positive for (compressive) pressure and stress in the impact bar being positive for tension.

At the axis of symmetry on the impact face the boundary conditions for the impact bar are:

$$\begin{aligned} v_r(t, 0, 0) &= 0 \\ v_{r,z}(t, 0, 0) &= 0 \\ \tau_{rz}(t, 0, 0) &= 0 \\ \tau_{rz,r}(t, 0, 0) &= 0 \\ \tau_{rz,z}(t, 0, 0) &= 0 \\ \sigma_\theta(t, 0, 0) &= \sigma_r(t, 0, 0) \end{aligned} \quad (\text{II-48})$$

From the constitutive equation of the bar material (II-5), the second and third equations of (II-48) yield another condition

$$v_{z,r}(t, 0, 0) = 0 \quad (\text{II-48})$$

At the centerline of the bar, the applicable bicharacteristics in Figure II.6(a) are 2, 3, 6, and 7. Using the applicable bicharacteristic equations, constitutive equations, and equations of motion (II-11), the following combinations of (II-11) yield equations for the unknown variables at the origin of the bar.

$$(b) - 2\lambda(i) + c_1 \left[\frac{1}{c_2} (g) - (n) \right]:$$

$$\begin{aligned} 2\lambda(C_2 - C_1)\sigma_r + [1 + 2\lambda C_2]\sigma_z + \rho_b c_1 v_z = \rho_b c_1 (v_z^2 - v_z^0 + v_z^7) \\ + \sigma_z^2 + 2\lambda C_2 \sigma_z^0 - 2\lambda(C_1 - C_2)\sigma_r^0 + \frac{c_1 \Delta t}{2} (\sigma_{z,z}^7 - \sigma_{z,z}^0) \\ + \lambda \Delta t (v_{r,r}^2 - v_{r,r}^0) + c_1 \Delta t \tau_{rz,r}^2 + \frac{c_1 G \Delta t}{2c_2} v_{r,z}^7 \end{aligned} \quad (II-49a)$$

$$(c) - \lambda(k) - c_1 \Delta t [(f) - (h)]:$$

$$\begin{aligned} (1 + 2\lambda C_2)\sigma_r - \lambda C_1 \sigma_z = (1 + \frac{c_1 \Delta t}{2r^3})\sigma_r^3 - \frac{c_1 \Delta t}{2r^3} \sigma_\theta^3 + 2\lambda C_2 \sigma_r^0 - \lambda C_1 \sigma_z^0 \\ + (\rho_b c_1 + \frac{\lambda \Delta t}{2r^3})v_r^3 + \frac{\lambda \Delta t}{2} (v_{z,z}^3 - v_{z,z}^0) + \frac{c_1 \Delta t}{2} \tau_{rz,z}^3 \\ + c_1 \Delta t [2(\sigma_{r,r}^6 - \sigma_{r,r}^0) + \sigma_{\theta,r}^0 - \sigma_{\theta,r}^6] \end{aligned} \quad (II-49b)$$

At the axis of symmetry on the impact face, the water radial velocity u is zero. The bicharacteristic pattern that is used for the water equations at this particular point is:

$$\begin{aligned} \zeta^2 &= \pi + \eta_1 \\ \zeta^3 &= \frac{5}{4} \pi \\ \zeta^4 &= \frac{3}{2} \pi \end{aligned} \quad (II-50)$$

η is taken to be zero and all variations in slope between points (1,1) and (2,1) on the water IJ grid are accounted for in η_1 . This particular pattern has been chosen because it accounts for a slope at the interface and will yield bicharacteristic compatability equations which may be combined to eliminate the unknown partial derivative terms. The bicharacteristics compatability equations may be obtained from equations (II-44). Equation (II-44b) is used with $\eta = 0$ to obtain the ζ^2 compatability equation, noting that $u = u_{,z} = 0$ and $\frac{u}{r} \rightarrow u_{,r}$.

$$p + v_{p_2} v + \frac{1}{2} \Delta t \rho (a)^2 [(1 + \sin^2 \eta_1) u_{,r} - \sin \eta_1 \cos \eta_1 v_{,r} + \cos^2 \eta_1 v_{,z}] = p_{p_2} \quad (\text{II-51a})$$

The ζ^3 equation may be obtained from equation (II-44b) with $\eta = 0$ and $\eta_1 = \frac{5\pi}{4}$:

$$p + v_{p_3} v + \frac{1}{2} \Delta t \rho (a)^2 [1.5 u_{,r} - 0.5 v_{,r} + 0.5 v_{,z}] = p_{p_3} \quad (\text{II-51b})$$

Equation (II-44c) applied to this case yields:

$$p + v_{p_4} v + \frac{1}{2} \Delta t \rho (a)^2 [2 u_{,r}] = p_{p_4} \quad (\text{II-51c})$$

The equation of the particle path is

$$p + \frac{1}{2} \Delta t \rho (a)^2 [2 u_{,r} + v_{,z}] = p_{p_5} \quad (\text{II-51d})$$

Equations (II-51) may be combined to yield the pressure at the origin as a function of axial particle velocity. Referring to equations (II-51):

$$\frac{2(a) - \sin 2\eta_1 (b) - 2\cos \eta_1 (\cos \eta_1 - \sin \eta_1) (d) - (2\sin \eta_1 + \cos \eta_1) (\sin \eta_1 - \cos \eta_1) (c)}{\cos \eta_1 (\cos \eta_1 - \sin \eta_1) p} = -[2v_{P_2} - 2\sin 2\eta_1 v_{P_3} - (2\sin \eta_1 + \cos \eta_1) (\sin \eta_1 - \cos \eta_1) \cdot v_{P_4}] v_P + 2p_{P_2} - 2\sin 2\eta_1 p_{P_3} - (2\sin \eta_1 + \cos \eta_1) (\sin \eta_1 - \cos \eta_1) p_{P_4} - 2\cos \eta_1 (\cos \eta_1 - \sin \eta_1) p_{P_5} \quad (II-52)$$

Equations (II-46), (II-47), (II-49), and (II-52) are five equations in the five unknowns at the origin σ_z , σ_r , v_z , p , and v , which are solved by iterating on the values of the water variables.

At points on the interface, between the axis of symmetry and the corner of the impact bar, the continuity equations (II-46) and (II-47) apply. All of the water variables are nonzero. The zero-valued bar variables are

$$\begin{aligned} \tau_{rz}(t, r, 0) &= 0 \\ \tau_{rz,r}(t, r, 0) &= 0 \end{aligned} \quad (II-53)$$

For wave propagation in the bar, the applicable bicharacteristics in Figure II.6 are 1, 2, 3, 5, 6, and 7. The following combinations of equations (II-11) are now formed:

$-[(a) + (c) + 2\lambda(k)]:$

$$\begin{aligned} &\left[2(1 + \lambda C_2) + \frac{c_1 \Delta t}{2} \left(\frac{1}{r^1} - \frac{1}{r^3} \right) \right] \sigma_r + \left[2\lambda C_2 + \frac{c_1 \Delta t}{2} \left(\frac{1}{r^3} - \frac{1}{r^1} \right) \right] \sigma_\theta \\ &- 2\lambda C_1 \sigma_z - \frac{\lambda \Delta t}{2} \left(\frac{1}{r^1} + \frac{1}{r^3} \right) v_r = \sigma_r^1 + \sigma_r^3 + \frac{c_1 \Delta t}{2} \left(\frac{\sigma_r^3}{r^3} - \frac{\sigma_r^1}{r^3} \right) \end{aligned}$$

$$\begin{aligned}
& + \frac{c_1 \Delta t}{2} \left(\frac{\sigma_\theta^1}{r^1} - \frac{\sigma_\theta^3}{r^3} \right) + \rho_b c_1 (v_r^3 - v_r^1) + \frac{\lambda \Delta t}{2} \left(\frac{v_r^3}{r^3} + \frac{v_r^1}{r^1} \right) + \frac{\lambda \Delta t}{2} \\
& (v_{z,z}^1 + v_{z,z}^3 - 2v_{z,z}^0) + \frac{c_1 \Delta t}{2} (\tau_{rz,z}^3 - \tau_{rz,z}^1) + 2\lambda c_2 (\sigma_r^0 + \sigma_z^0) \\
& - 2\lambda c_1 \sigma_z^0
\end{aligned} \tag{II-54a}$$

$\lambda(j):$

$$\begin{aligned}
& -\lambda c_2 \sigma_r + \lambda c_1 \sigma_\theta - \lambda c_2 \sigma_z - \frac{\lambda \Delta t}{2r^0} v_r = -\lambda c_2 \sigma_r^0 + \lambda c_1 \sigma_\theta^0 \\
& -\lambda c_2 \sigma_z^0 + \frac{\lambda \Delta t}{2r^0} v_r^0
\end{aligned} \tag{II-54b}$$

$$\begin{aligned}
& -[(b) + \lambda(i)] - \frac{1}{2} c_1 \left\{ 2(n) + \frac{1}{c_2} [(e) - (g)] \right\} : \\
& -\lambda c_1 \sigma_r + \lambda c_2 \sigma_\theta + (1 + \lambda c_2) \sigma_z - \frac{\lambda \Delta t}{2r^2} v_r + \rho_b c_1 v_z = \\
& \frac{\rho_b c_1}{2} (2v_z^2 - 2v_z^0 + v_z^5 + v_z^7) + \sigma_z^2 - \lambda c_1 \sigma_r^0 + \lambda c_2 \sigma_\theta^0 + \lambda c_2 \sigma_z^0 \\
& + \frac{\lambda \Delta t}{2r^0} v_r^2 + \frac{c_1 \Delta t}{2r^2} \tau_{rz}^2 + \frac{\lambda \Delta t}{2} (v_{r,r}^2 - v_{r,r}^0) + \frac{c_1 \Delta t}{2} \tau_{rz,r}^2 \\
& + \frac{c_1 \Delta t}{4} (\sigma_{z,z}^7 + \sigma_{z,z}^5 - 2\sigma_{z,z}^0) + \frac{G c_1 \Delta t}{4c_2} (v_{r,z}^7 - v_{r,z}^5)
\end{aligned} \tag{II-54c}$$

$$\begin{aligned}
& \frac{1}{c_1} [(a) - (c)] - 2(m) + \frac{1}{c_2} [(e) + (g) - 2(f) - 2(l)] : \\
& - \frac{c_1 \Delta t}{2} \left(\frac{1}{r^1} + \frac{1}{r^3} \right) \sigma_r + \frac{c_1 \Delta t}{2} \left(\frac{1}{r^1} + \frac{1}{r^3} \right) \sigma_\theta + c_1 \left[2\rho_b + \frac{\lambda \Delta t}{2c_1} \cdot \right. \\
& \left. \left(\frac{1}{r^1} - \frac{1}{r^3} \right) \right] v_r = \\
& - \frac{c_1 \Delta t}{2} \left(\frac{\sigma_r^1}{r^1} + \frac{\sigma_r^3}{r^3} - \frac{\sigma_\theta^1}{r^1} - \frac{\sigma_\theta^3}{r^3} \right) + \sigma_r^3 - \sigma_r^1 + \rho_b c_1 (v_r^1 + v_r^3 - 2v_r^0 \\
& + 2v_r^6) \\
& + \frac{\lambda \Delta t}{2} \left(\frac{v_r^3}{r^3} - \frac{v_r^1}{r^1} \right) + \frac{\lambda \Delta t}{2} (v_{z,z}^3 - v_{z,z}^1) + \frac{c_1 \Delta t}{2} (\tau_{rz,z}^1 + \tau_{rz,z}^3 \\
& - 2\tau_{rz,z}^0) \\
& + \frac{c_1 \Delta t}{r^0} (\sigma_\theta^0 - \sigma_r^0) + c_1 \Delta t (\sigma_{r,r}^6 - \sigma_{r,r}^0) + \rho_b c_1 (v_z^7 - v_z^5) \\
& + \frac{Gc_1 \Delta t}{2c_2} (v_{r,z}^5 + v_{r,z}^7 - 2v_{r,z}^0) \\
& + \frac{c_1 \Delta t}{2} (\sigma_{z,z}^7 - \sigma_{z,z}^5) + \frac{c_1 \Delta t}{r^6} (\sigma_r^6 - \sigma_\theta^6) + \frac{2c_1}{c_2} \tau_{rz}^6 - \frac{Gc_1 \Delta t}{c_2} \cdot \\
& (v_{z,r}^6 - v_{z,r}^0)
\end{aligned} \tag{II-54d}$$

The bicharacteristic equations in water for points on the interface between the axis of symmetry and the corner of the bar are equations (II-45). Thus eight equations (II-46), (II-47), (II-45), and (II-54) have been obtained to solve for the eight unknowns σ_r , σ_θ , σ_z , v_r , v_z , p , u , and v .

Points at the interface which lie on the corner of the bar, have equations (II-45) as governing equations for the water variables. In the bar, the applicable bi-characteristic compatibility equations of (II-11) are (a), (b), (e), and (f) and these are subject to the boundary conditions

$$\begin{aligned}
 \tau_{rz}(t, R_0, 0) &= 0 \\
 \tau_{rz,r}(t, R_0, 0) &= 0 \\
 \tau_{rz,z}(t, R_0, 0) &= 0 \\
 \sigma_r(t, R_0, 0) &= 0 \\
 \sigma_{r,z}(t, R_0, 0) &= 0
 \end{aligned}
 \tag{II-55}$$

The following combinations of the equations of (II-11) subject to the boundary conditions (II-55) are now formed for the bar equations:

(a) + $\lambda(k)$:

$$\begin{aligned}
 &\left(\frac{c_1 \Delta t}{2r^1} - \lambda C_2 \right) \sigma_\theta + \lambda C_2 \sigma_z + \left(\rho_b c_1 + \frac{\lambda \Delta t}{2r^1} \right) v_r = -\lambda C_2 \sigma_\theta^0 \\
 &+ \lambda C_1 \sigma_z^0 + \frac{\lambda \Delta t}{2} (v_{z,z}^0 - v_{z,z}^1) + \left(\rho_b c_1 - \frac{\lambda \Delta t}{2r^1} \right) v_r^1 + \left(\frac{c_1 \Delta t}{2r^1} - 1 \right) \sigma_r^1 \\
 &- \frac{c_1 \Delta t}{2r^1} \sigma_\theta^1 + \frac{c_1 \Delta t}{2} \tau_{rz,z}^1
 \end{aligned}
 \tag{II-56a}$$

$\lambda(j):$

$$\lambda C_1 \sigma_\theta - \lambda C_2 \sigma_z - \frac{\lambda \Delta t}{2r^0} v_r = \lambda C_1 \sigma_\theta^0 - \lambda C_2 \sigma_z^0 + \frac{\lambda \Delta t}{2r^0} v_r^0 \quad (\text{II-56b})$$

$$(b) + 2(i) + c_1 [(n) - (m)] + \frac{c_1}{c_2} [(e) - (f) - (l)]:$$

$$\begin{aligned} & - (1 + \lambda C_2) \sigma_z - \lambda C_2 \sigma_\theta + \frac{\lambda \Delta t}{2r^2} v_r - \rho_b c_1 v_z = -\sigma_z^2 - \lambda C_2 (\sigma_\theta^0 + \sigma_z^0) \\ & + \rho_b c_1 (v_z^0 - v_z^2 - v_z^5 - v_r^0 - v_r^6) - \frac{\lambda \Delta t}{2r^2} v_r^2 + \frac{\lambda \Delta t}{2} (v_{r,r}^0 - v_{r,r}^2) \\ & - \frac{c_1 \Delta t}{2} \tau_{rz,r}^2 \\ & + \frac{c_1 \Delta t}{2} (\sigma_{z,z}^0 - \sigma_{z,z}^5) + \frac{c_1 \Delta t}{2r^0} \sigma_\theta^0 - \frac{c_1 \Delta t}{2r^6} \sigma_\theta^6 + \frac{c_1 \Delta t}{2} (\sigma_{r,r}^6 - \sigma_{r,r}^0) \\ & + \frac{c_1 G \Delta t}{2c_2} (v_{r,z}^5 - v_{r,z}^0 + v_{z,r}^6 - v_{z,r}^0) \end{aligned} \quad (\text{II-56c})$$

Equations (II-56), (II-45), and the continuity equations (II-46) and (II-47) are a system of seven equations in the seven unknowns, p , u , v , σ_θ , σ_z , v_r , and v_z which are solved by iterating on the water bicharacteristic coordinates and the water variables.

All of the governing equations for each point in the impact bar and water have now been derived to advance the solution vector of the variables at all points in the problem at a given time to the next time. The initial conditions which are used to begin the solution sequence will now be given.

E. Initial Conditions

In this water impact problem, a stress-free circular bar traveling at an initial constant velocity V_0 , impacts the undisturbed surface of a stress-free half space of water. Due to the assumption of an evacuated space above the water surface, the water surface remains perfectly flat until there is contact of the impact bar particles on a circular area of water surface. At this instant of impact, the water particles at the impact face undergo a step change in particle velocity and the impact bar particles at the impact face undergo a step decrease in velocity. From the continuity equations (II-46) and (II-47), the pressure in the water must equal the axial stress in the bar and the axial particle velocities must be equal at the impact face. By using the equations of state, expressing the Hugoniot relations for the impact bar material and water in the form of pressure (or axial stress) versus particle velocity, and simultaneously solving them with the impact bar initial velocity of V_0 , the impact face conditions may be obtained. The Hugoniot matching graphical technique is shown in Figure II.7.

Letting the impact pressure be p_0 and the water particle velocity be v_0 , then the initial conditions for the half space of water are:

$$u(0,r,z) = 0; \text{ for all } r,z$$

$$p(0,r,0) = p_0; v(0,r,0) = v_0; 0 \leq r \leq R_0 \quad (\text{II-57})$$

$$p(0,r,0) = 0; v(0,r,0) = 0; r > R_0$$

$$p(0,r,z) = 0; v(0,r,0) = 0; z > 0$$

At the instant of impact, the particles on the impact face of the bar become compressed in the axial direction. These particles are not free to move transversely because of the constraint of the surrounding material. Therefore, a state of uniaxial strain exists. The constitutive equations in stress-strain form for a linear elastic, isotropic material are

$$\begin{aligned} \epsilon_r &= C_1 \sigma_r - C_2 (\sigma_\theta + \sigma_z) \\ \epsilon_\theta &= C_1 \sigma_\theta - C_2 (\sigma_r + \sigma_z) \\ \epsilon_z &= C_1 \sigma_z - C_2 (\sigma_r + \sigma_\theta) \end{aligned} \quad (\text{II-58})$$

For uniaxial strain in the z direction, and an axial stress of $(-p_0)$, equations (II-58) yield:

$$\sigma_r = \sigma_\theta = \frac{1}{1 - \frac{C_1}{C_2}} p_0 \quad (\text{II-59})$$

At the corner of the impact face, the radial stress is zero and the strain is not uniaxial because of the free radial surface. A relationship can be derived between the axial and circumferential stresses, but neither one can be determined. Numerical results for assumed one dimensional stress and one dimensional strain initial conditions indicated

very little difference in subsequent bar response. The initial stress values were arbitrarily chosen to be the one dimensional strain values. Thus the initial conditions in the bar are given by:

$$\begin{cases} \sigma_z(r, 0, 0) = -P_0 & \text{for } 0 \leq r \leq R_0 \\ \sigma_z(r, z, 0) = 0, & \text{otherwise} \end{cases}$$

$$\begin{cases} \sigma_\theta(r, 0, 0) = -\frac{\nu P_0}{1 - \nu} & \text{for } 0 \leq r \leq R_0 \\ \sigma_\theta(r, z, 0) = 0, & \text{otherwise} \end{cases}$$

$$\begin{cases} \sigma_r(r, 0, 0) = -\frac{\nu}{1 - \nu} P_0 & \text{for } 0 \leq r \leq R_0 \\ \sigma_r(r, z, 0) = 0, & \text{otherwise} \end{cases}$$

$$\tau_{rz}(r, z, 0) = 0 \text{ for all } r \text{ and } z$$

$$v_r(r, z, 0) = 0 \text{ for all } r \text{ and } z$$

$$\begin{cases} v_z(r, 0, 0) = -v_0 & \text{for } 0 \leq r \leq R_0 \\ v_z(r, z, 0) = -v_0, & \text{otherwise} \end{cases}$$

CHAPTER III

FLEBOW COMPUTER PROGRAM

In Chapter II, the axisymmetric field equations for flow in a compressible hydrodynamic medium and for the dynamic response of a linear, elastic, homogeneous, isotropic material were reduced from two systems of partial differential equations in one temporal and two spatial derivatives to two systems of equations involving only two spatial derivatives. However, these new sets of equations along bicharacteristic curves in rzt space are still partial differential equations which must be solved numerically. The bicharacteristic compatibility equations, which are the transformed field equations along the characteristic surface in rzt space, are relationships among the dependent variables along the bicharacteristics. Given the initial conditions as the solution vector at all points in the domain of the problem for time zero, the bicharacteristic compatibility relations may be combined to advance the solution vector forward in time. The combination of bicharacteristic compatibility equations involves the use of a number of bicharacteristics for obtaining the solution vector for one point in the new time plane. This procedure cannot be generalized from a

point-to-point solution to a continuous one, so a discretized field of solution vectors is obtained. In using a discretized field, interpolation must be done for obtaining values of the variables at intermediate coordinate points. This chapter will be used to describe the discretization and interpolation techniques used in the solution of the equations derived in Chapter II. Then the philosophy and programming logic of the computer program that was written to automate the solution will be presented.

A. Discretization and Interpolation Techniques

1. Numerical Method for Impact Bar Solution

The field equations for the bar were formulated in Lagrangian coordinates; that is, displacements are measured relative to the undeformed configuration. For the linear elastic response being considered here, where the deformation displacements are small, the position of a particle after deformation is approximately the same as the position before deformation. The undeformed configuration is discretized into a square I-J grid as shown in Figure III.1. The length of the sides of the squares is h . The radial coordinates which extend from zero to R_0 are divided into discrete I coordinates

which range from 1 to IRAD. The axial coordinates which extend from zero at the impact face to L at the free end of the bar are divided into discrete J values ranging from 1 to JMAX. At the instant of impact, which in this solution scheme is taken to be time equal to zero, conditions are specified at the impact face $J = 1$. For all values of J greater than 1, and for all values of I, all variables have a value of zero except for the constant axial particle velocity which is equal to the impact velocity V_0 . These values at the initial time are advanced to the first time interval or step Δt by using the scheme depicted in the planform view of the rz plane, Figure III.2. The bicharacteristics P_i lie along either an I line or a J line in the old time plane. A linear interpolation scheme along IJ coordinate lines is used to obtain values at the intersections of the bicharacteristics with the old time plane. Points along the outer dilatational cone are located at a distance

$$\overline{P1} = \overline{P2} = \overline{P3} = \overline{P4} = c_1 \Delta t \quad (\text{III-1})$$

from the apex of the cone, and the corresponding distances for the distortional cone is

$$\overline{P5} = \overline{P6} = \overline{P7} = \overline{P8} = c_2 \Delta t \quad (\text{III-2})$$

The linear interpolation formulas for a variable ω at a few representative points are:

$$\begin{aligned}
 \omega^1 &= \frac{c_1 \Delta t}{h} \omega(I-1, J) + \left(1 - \frac{c_1 \Delta t}{h}\right) \omega(I, J) \\
 \omega^3 &= \frac{c_1 \Delta t}{h} \omega(I+1, J) + \left(1 - \frac{c_1 \Delta t}{h}\right) \omega(I, J) \\
 \omega^4 &= \frac{c_1 \Delta t}{h} \omega(I, J-1) + \left(1 - \frac{c_1 \Delta t}{h}\right) \omega(I, J) \\
 \omega^6 &= \frac{c_2 \Delta t}{h} \omega(I, J+1) + \left(1 - \frac{c_2 \Delta t}{h}\right) \omega(I, J)
 \end{aligned}
 \tag{III-3}$$

At boundary points or along the axis of symmetry, the interpolation formulas are the same for the applicable bicharacteristics.

The derivatives at interior points are calculated using a central difference scheme. For a variable ω :

$$\begin{aligned}
 \omega_{,r}^0 &= \omega_{,r}(I, J) = \frac{\omega(I+1, J) - \omega(I-1, J)}{2h} \\
 \omega_{,z}^0 &= \omega_{,z}(I, J) = \frac{\omega(I, J+1) - \omega(I, J-1)}{2h}
 \end{aligned}
 \tag{III-4}$$

Therefore, a derivative at a bicharacteristic intersection with the old time plane, for example at 1 in Figure III.2, would be

$$\begin{aligned}
 \omega_{,z}^1 &= \frac{c_1 \Delta t}{h} \omega_{,z}(I-1, J) + \left(1 - \frac{c_1 \Delta t}{h}\right) \omega_{,z}(I, J) \\
 &= \left(1 - \frac{c_1 \Delta t}{h}\right) \left[\frac{\omega(I, J+1) - \omega(I, J-1)}{2h} \right] + \\
 &\quad \frac{c_1 \Delta t}{h} \left[\frac{\omega(I-1, J+1) - \omega(I-1, J-1)}{2h} \right]
 \end{aligned} \tag{III-5}$$

For points at the boundaries or along the axis of symmetry, the central difference technique cannot be used for numerical approximation of derivatives normal to the boundary or normal to the axis of symmetry. For these derivatives, a second order difference technique is used based on Newton's interpolating polynomials. Terms to the second order in the interpolating polynomial are included and then the polynomial is differentiated to obtain the desired numerical derivative. For derivatives on the minimum coordinate boundaries, that is, on the axis and the impact face, the forward-difference polynomial is used and on the maximum coordinate boundaries, the backward-difference polynomial is used. The following derivatives are used on the indicated boundaries:

On the axis:

$$\omega_{,r}(1, J) = \frac{1}{h} \left[2\omega(2, J) - 1.5\omega(1, J) - 0.5\omega(2, J) \right] \tag{III-6a}$$

On the impact face

$$\omega_{,z}(I,1) = \frac{1}{h} \left[2\omega(I,2) - 1.5\omega(I,1) - 0.5\omega(I,3) \right] \quad (\text{III-6b})$$

On the radial boundary:

$$\omega_{,r}(\text{IRAD},J) = \frac{1}{h} \left[1.5\omega(\text{IRAD},J) - 2\omega(\text{IRAD} - 1,J) + 0.5\omega(\text{IRAD} - 2,J) \right] \quad (\text{III-6c})$$

On the axial free end:

$$\omega_{,z}(I,J\text{MAX}) = \frac{1}{h} \left[1.5\omega(I,J\text{MAX}) - 2\omega(I,J\text{MAX} - 1) + 0.5\omega(I,J\text{MAX} - 2) \right] \quad (\text{III-6d})$$

Thus the interpolating formulas have been developed to obtain the impact bar variables and their derivatives at the intersections of the bicharacteristics with the old time plane from the known variables at the grid points of an IJ network.

2. Numerical Method for Water Solution

The field equations for the compressible, hydrodynamic water response were formulated in an Eulerian coordinate system which is fixed in rzt space. By using the bicharacteristic compatibility equations derived in Chapter II and a numerical solution scheme, the solution vector U_i may be obtained at any selected (r, z) point in the new time plane. However, the numerical technique is not as straightforward as the one used for the impact bar equations because of the Eulerian formulation. The convective terms which are present in the equations for the

characteristic surface cause the bicharacteristic curves along this surface to undergo a change in orientation relative to the r axis in going from a point P in the new time plane to the old time plane. Thus if the orientation of a bicharacteristic is chosen to lie initially along some discretization coordinate line, the intersection of this bicharacteristic with the old time plane will not be on a discretization coordinate line. This necessitates a two dimensional interpolation scheme. Another problem arises because of the deformations that occur on the free surface and at the interface between the impact bar and water. This motion eliminates the use of an IJ grid that remains fixed in the rz plane for all times.

In the selection of a discretization scheme for representing the continuum state of water at a given time, the following was noted. Because the formulation was done in Eulerian coordinates and the bicharacteristic compatibility equations were derived for any selected point in rzt space, there is no requirement to retain an IJ grid that remains fixed in the rz plane at all times. The purpose of the IJ grid is to represent the continuous solution in the rz plane at a given time by a finite number of points.

The only requirements on the discretization grid are that it be sufficiently fine to retain spatial gradients in the variables to some desired degree of accuracy and that it be sufficiently structured to permit an efficient computational technique. For a grid to be efficient for computations, a point in the new time plane at which the solution vector is unknown, should have an a priori knowledge of the (r, z) location of points in the old time plane which are to be used in obtaining the solution. Searching the points in the old time plane for nearest neighbors can be computationally time consuming. Also the nearest neighbors must lie outside of the intersection of the characteristic conoid with the old time plane by at least some distance specified in a stability criterion. Physically this means that if information at a point A in water is used to obtain the solution at another point P at a time Δt later, then the time step Δt must be chosen small enough so that the information from A has not propagated past the point P at the new time. A grid having points with coordinates that change relative to one another, requires a search of all grid points in the previous time plane for determining nearest neighbors. Once the coordinates of the nearest neighbors are known, a time step may be selected. If a grid is chosen so that relative motion between grid points either does not exist or is minimized, then the time step can remain constant.

With the above considerations the IJ discretization grid shown in Figure III.3 was devised. The lines of constant I which are spaced by h_w correspond to constant radial coordinates and remain fixed in the rz plane for all times. A requirement on the I lines is that one of them be located at a radius of R_0 to coincide with the radial surface of the impact bar. If this requirement were not imposed then the combination of the impact bar penetration and the water splash would cause crossing of impact bar and water grid lines and corresponding inaccurate results. The J coordinate lines in Figure III.3 have two regimes. The $J = 1$ line is an interface line. At time equal to zero the $J = 1$ coincides with the $z = 0$ line. The computational method which is to be discussed later, keeps track of the axial movement at the water surface and reassigns the z coordinates for each I coordinate along the $J = 1$ line after each time step. The second regime of J lines includes $J = 2$ and extends to the first J line past the location of the wavefront generated at water impact. This set of J lines has a separation distance of h_w and moves downward at the average velocity of the points on the impact face. With this grid, the $J = 2$ line maintains a relatively constant separation distance from the $J = 1$ line along the impact face. On the

free surface, the water will make a splash so that I points on the $J = 1$ line will move away from the corresponding I points on the $J = 2$ line. This effect contributes to smearing the solution near the free surface. However, for the impact velocities that will be considered in this study and the solution times of interest, the separation distance will not be large enough to introduce large inaccuracies. If higher velocities are to be investigated over longer bar penetration times, it would be advisable to include an intermediate set of points near the free surface.

The IJ grid that has been selected for discretizing the water continuum must have an interpolation scheme for obtaining values at intermediate points that do not lie on the IJ coordinate lines. The values in the area surrounding an IJ grid point are assumed to vary linearly between grid points. For an interior point in the water space, four interpolating triangles are used between the surrounding four grid points as shown in Figure III.4. The n^{th} interpolating triangle corresponds to the n^{th} quadrant. Recalling from Chapter II that the angles are measured positive clockwise from the negative r axis, the quadrant numbers are as shown in Figure III.4.

For linear interpolation, the values of the variable U_j in the n^{th} interpolation triangle is given by:

$$U_j = a^{(n)} + b^{(n)}r + c^{(n)}z \quad (\text{III-7})$$

The coefficients in equation (III-7) may be evaluated by substituting the nodal point values of the triangle into the equation. If point (r_1, z_1) corresponds to the point (I, J) , point (r_2, z_2) corresponds to the nearest grid point in the direction $\gamma = n\left(\frac{\pi}{2}\right)$ for the n^{th} triangle, (r_3, z_3) is the remaining nodal point of the triangle, and $(U_j)_i$ is the value of the variable evaluated at the i^{th} nodal point of the interpolating triangle, then the coefficients of equation (III-7) are:

$$\begin{aligned} b^{(n)} &= \frac{1}{D} \left\{ \left[(U_j)_1 - (U_j)_3 \right] [z_1 - z_2] - \left[(U_j)_1 - (U_j)_2 \right] [z_1 - z_3] \right\} \\ c^{(n)} &= \frac{1}{D} \left\{ \left[(U_j)_1 - (U_j)_2 \right] [r_1 - r_3] - \left[(U_j)_1 - (U_j)_3 \right] [r_1 - r_2] \right\} \\ a^{(n)} &= (U_j)_1 - b^{(n)}r_1 - c^{(n)}z_1 \end{aligned} \quad (\text{III-8})$$

$$D = (z_1 - z_2)(r_1 - r_3) - (z_1 - z_3)(r_1 - r_2)$$

At boundaries or along the axis of symmetry, some of the interpolating triangles do not exist. The following triangles apply for the given locations:

AD-A052 051

NAVAL SURFACE WEAPONS CENTER WHITE OAK LAB SILVER SP--ETC F/G 19/4
STRESS WAVE PROPAGATION IN BARS DUE TO NORMAL IMPACT ON WATER.(U)
AUG 77 W T MESSICK, J M MARSHALL

UNCLASSIFIED

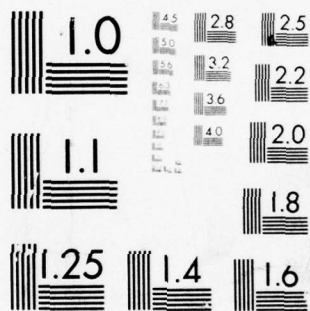
NSWC/WOL/TR-77-128

NL

2 OF 5

AD
A052 051





MICROCOPY RESOLUTION TEST CHART
NATIONAL BUREAU OF STANDARDS-1963-A

axis of symmetry away from impact face: 2, 3

axis of symmetry at impact face: 3

along impact face away from axis and along

free surface: 3, 4

The interpolating triangles are used at interior points for determining derivatives. Since the displacement field within the triangle is linear, the derivative is constant. Examining the bicharacteristic equations in Chapter II, it may be seen that for the bicharacteristics ζ equal to 0 and π , the terms $U_{j,z}$ predominate and for ζ equal to $\frac{\pi}{2}$ and $\frac{3\pi}{2}$, the terms $U_{j,r}$ predominate. At γ equal to 0, there is a discontinuous jump in $U_{j,z}$ when calculated from the linear displacement fields of the adjacent interpolation triangles 1 and 4. Similar discontinuities exist at the angles $\frac{\pi}{2}$, π , and $\frac{3\pi}{2}$. In order to obtain better functional behavior, the value of the derivative $U_{j,z}$ at γ equal to 0 is taken to be the average of the derivatives in the interpolating triangles on either side of the γ equal 0 line; that is

$$U_{j,z}^{(1)} = U_{j,z}^{(4)} = \frac{c^{(1)} + c^{(4)}}{2} \quad (\text{III-9a})$$

where $U_{j,z}^{(n)}$ denotes the derivative for a point located in the n^{th} interpolation triangle. The remaining derivatives are:

$$U_{j,z}^{(2)} = U_{j,z}^{(3)} = \frac{c^{(2)} + c^{(3)}}{2} \quad (\text{III-9b})$$

$$U_{j,r}^{(1)} = U_{j,r}^{(2)} = \frac{b^{(1)} + b^{(2)}}{2} \quad (\text{III-9c})$$

$$U_{j,r}^{(3)} = U_{j,r}^{(4)} = \frac{b^{(3)} + b^{(4)}}{2} \quad (\text{III-9d})$$

For advancing the solution at points along the axis of symmetry (but not on the impact face) forward in time, the z derivative for points in interpolating triangles 2 and 3 are given by equation (III-9b). Derivatives of variables with respect to r at points not on a J line are obtained by linear interpolation of the r derivatives on the two nearest J lines. Derivatives with respect to r on a J line are calculated by the second-order forward difference formula (III-6a).

The derivatives of variables with respect to r at points near the free surface and the impact face are calculated by using equation (III-9d). Derivatives with respect to z are calculated by linear interpolation between the z derivatives along constant I lines, and the z derivatives along these contact I lines are obtained by a second order forward difference method. The forward difference formula (III-6b) cannot be used near the water

boundary because the distance h_1 between the $J = 1$ and $J = 2$ lines at a given I is not necessarily equal to the distance between the $J = 2$ and $J = 3$ lines at this I line, h_2 . Thus a modified formula is used which was derived on heuristic arguments. Rewrite equation (III-6b) as:

$$U_{j,z}(I,1) = \frac{U_j(I,2) - U_j(I,1)}{h} + \frac{U_j(I,2) - U_j(I,3)}{h} + \frac{U_j(I,3) - U_j(I,1)}{2h} \quad (\text{III-20})$$

The first term in equation (III-20) is the slope between the $J = 1$ and $J = 2$ lines, the second term is the negative of the slope between $J = 2$ and $J = 3$, and the third term is a central difference derivative about $J = 2$ spanning the distance from $J = 1$ to $J = 3$. Thus to compensate for the unequal distances h_1 and h_2 , the denominators of the terms in equation (III-20) are replaced by h_1 , h_2 , and $(h_1 + h_2)$ respectively. Combining the resulting formula yields the second order difference formula for the z derivative at a water boundary point

$$U_{j,z}(I,1) = \frac{-h_2(h_2 + 2h_1)U_j(I,1) + (h_1 + h_2)^2 U_j(I,2) - h_1^2 U_j(I,3)}{h_1 h_2 (h_1 + h_2)} \quad (\text{III-21})$$

The free surface of water changes with time and its location must be determined at every time step in the calculation so that the free surface boundary condition may be applied. The procedure that is followed in these calculations is to use the variables and location of the free surface at the $(K-1)$ time step to advance the solution vector forward in time to the K^{th} time step. The radius at the I^{th} grid point on the free surface at the $(K-1)$ time step is denoted by $r[I,1,(K-1)]$ and the axial distance from the free surface at time zero is $z[I,1,(K-1)]$. Once the velocity variables have been obtained at the K^{th} time step, the coordinates of the points on the boundary are advanced by using the trapezoidal integration rule:

$$\begin{aligned} r'[I,1,K] &= r[I,1,(K-1)] + \frac{1}{2} \Delta t \{u[I,1,K] + u[I,1,(K-1)]\} \\ z'[I,1,K] &= z[I,1,(K-1)] + \frac{1}{2} \Delta t \{v[I,1,K] + v[I,1,(K-1)]\} \end{aligned} \quad (\text{III-22})$$

The prime indicates that a temporary computed value is assigned to the variables. The movement of the points at $(I,1)$ as a function of time is shown in Figure III.5. Since it is required that the lines of constant I be lines of constant radius, the coordinates of the surface in equation (III-22) are changed by the linear interpolation formulas:

$$\begin{aligned} r[I,1,K] &= (I-1)h \\ z[I,1,K] &= z'[I,1,K] + \frac{z'[I,1,K] - z'[(I-1),1,K]}{r'[I,1,K] - r'[(I-1),1,K]} \{r[I,1,K] - r'[(I-1),1,K]\} \end{aligned} \quad (\text{III-23})$$

The velocity field at the new coordinates of the free surface is obtained from:

$$u[I,1,K] = u[(I-1),1,K] + \left\{ u' [I,1,K] - u[(I-1),1,K] \right\} \times \left\{ \frac{[z[I,1,K] - z[(I-1),1,K]]^2 + [r[I,1,K] - r[(I-1),1,K]]^2}{[z' [I,1,K] - z[(I-1),1,K]]^2 + [r' [I,1,K] - r[(I-1),1,K]]^2} \right\}^{\frac{1}{2}} \quad (\text{III-24})$$

This equation is just a straight linear interpolation along the surface. The procedure represented by equations (III-22) to (III-24) is carried out along the surface line $J = 1$ from the corner of the impact bar to the location of the pressure wave generated from impact.

B. Philosophy of Computational Method

The equations which govern the solution at interior and boundary points in the domain of the problem have been derived in Chapter II and the numerical techniques that are used to obtain numerical answers have been indicated in the previous section of this Chapter. These methods must be combined into a logical structure for computer programming. Because of the large number of computations involved in this solution of linear and nonlinear sets of equations at numerous time points, the computational method should be as efficient as possible. Also the composition of the program should be modular to permit changes or additions

for analysis of slightly different problems. Of course, writing a generalized, modular program can be very time consuming so the program that was written, is a compromise on development time and generalization. Some other considerations in the program design were simplified input, a restart capability, and plotting capability.

The equations to be solved involve discretization parameters Δt (the time step) and h (mesh size). These parameters can be different for the water equations and the impact bar equations. However, choosing different Δt 's and h 's for the bar and the water complicates and lengthens the solution. For the numerical solution to be stable, a relationship between Δt and h must be satisfied in the water domain and a separate one in the impact bar domain. The stability relationship is a statement which basically ensures that the mesh size in the medium is chosen large enough for a given Δt so that information being propagated by the stress waves does not transverse more than the distance between grid points in the given time Δt . The dilatational stress wave propagation velocity for metallic impact bars is higher than the pressure wave velocity in water so for equal mesh parameters h , the Δt for water may be chosen larger than the Δt for the bar or conversely, for equal Δt 's, a finer mesh size h may be chosen for the water. At the impact face, there must be points of coincidence in the bar and water at

locations in space and time in order that the continuity equations may be applied. Choosing an equal time step but a finer mesh in water involves spacial interpolation between grid points in the bar. Choosing equal meshes but a larger time step in water would involve temporal interpolation and extrapolation along the impact face. At the sacrifice of resolution in the water grid, the time steps and mesh sizes in the bar and water were chosen to be the same. With this choice, no interpolation is necessary at the impact face and the continuity equations may be applied directly. The stability condition for the bar is an approximate relation obtained in reference 13:

$$\left[\frac{c_1 \Delta t}{h} \right]^2 \leq Y \cdot \min \left[\frac{c_1^2}{c_1^2 + c_2^2}, \frac{c_1^2}{2(c_1^2 - c_2^2)} \right] \quad (\text{III-25})$$

where Y is a conservatism factor. By satisfying (III-25) in the bar, the stability of the water solution will automatically be satisfied because of the smaller wave speed.

The solution of the impact problem starts with the calculation of the impact pressure and particle velocity. These values are used as initial conditions at time equal zero. The bicharacteristic relations are then used to advance this impact loading to the next step in time, Δt .

The scheme used to advance the solution is illustrated in Figure III.6. The location of the wave in each medium is estimated by the wave speed times the current time. In the bar, the dilatational wave speed is used and in water, the sound velocity is evaluated at the impact pressure. In advancing the solution forward in time, only the variables for the grid points up to the first grid line past the estimated wave location are obtained. In this way only a minimal amount of calculations are made. The order of the calculations is indicated in Figure III.6. The first point to be advanced in time is the corner of the impact face of the bar where the bicharacteristic equations in the bar and in the water at that point are solved simultaneously. The solution then moves inward along the impact face to the axis of symmetry. Then the sequence goes to the radial boundary of the second J line in the impact bar and moves inward to the axis of symmetry. The equations along this line are linear algebraic systems which are solved directly without iteration. For the first time step, the solution in the bar is complete after this J line. For later times, the procedure would continue J line by J line from the radial boundary inward to the axis of symmetry until the wave location has been bypassed.

After obtaining the solution vector for all perturbed IJ grid points in the bar, the solution for the

free water surface is obtained starting from the first point outside of the corner of the impact bar and moving outward to the first I point past the wave location. The solution of these free surface equations involves iterating on the velocities. Then the $J = 2$ line points are covered beginning with the outermost point and working inward to the axis of symmetry. In the process of solving for the variables along a J line, if the radial velocities at two successive I points are zero, then the calculations for the remaining points are bypassed and the values of the variables at these points are set equal to the values at the zero radial velocity points. These points with zero radial velocity are in a state of "one dimensional" or uniform response. Bypassing the calculations for the one dimensional field saves computer time. After all J lines up to the first one past the wave location have been covered, the entire set of variables for the new time is known. At this time in the solution, the points on the water free surface are moved to the new location corresponding to the new time.

C. Computer Program Elements

The acronym given to the computer program that was developed to solve this water impact problem is FLEBOW, for Finite Length Elastic Bar impacting On Water.

This program was written in FORTRAN IV for a CDC 6500 computer. However, except for changes in format statements, it should be operable on any third generation computer. The solution variables are kept in high-speed storage at all times so a third generation computer storage capacity and operational speed is required to solve any reasonable-sized problem in a reasonable amount of time. The required computer field length for a 21 by 250 IJ grid in the bar and 80 by 60 IJ grid in water is 247000 octal words. Because of the length of the program (approximately 3,500 FORTRAN statements), a listing of it is not included here. However, the subroutines and their functions will be explained and the general flow of the problem using these routines will be outlined.

Included in the capabilities of the program are data dumping on peripheral devices at user-selected frequencies so that post processing plotting may be done or the problem may be restarted from a previously calculated time cycle. A schematic of the data flow is shown in Figure III.7. The required input cards for running the program are explained in Table III.1. The output consists of printed output and data dumping on TAPE10 and TAPE11 if requested by the user. TAPE10 contains

```

*****
*****
*
* F L E B O W (FINITE LENGTH ELASTIC BAR ON WATER) C O D E
*
*****
*****
*
*TWO DIMENSIONAL STRESS WAVE PROPAGATION IN A FINITE LENGTH
*ELASTIC BAR FROM A NORMAL IMPACT ON WATER
*SOLUTION BY THE METHOD OF CHARACTERISTICS WITH FINITE DIFFERENCE*
*APPROXIMATION USING SQUARE MESH WITH EQUAL DIMENSIONS IN BOTH
*BAR AND WATER
*BAR EQUATIONS ARE LAGRANGIAN FORMULATION
*WATER EQUATIONS ARE EULERIAN FORMULATION WITH BOUNDARY TRACING
*
*****
* TAPE9 IS THE RESTART TAPE
* TAPE10 IS THE DUMP TAPE
* TAPE11 IS A PLOT HISTORY TAPE
*****
* READ INPUT
* *****
*
*CARD NO.(FORMAT) VARIABLE=DESCRIPTION
* *****
*
*1.(E15.5) VZERO = IMPACT VELOCITY(FT/SEC)
*2.(4E15.5) E = BAR YOUNGS MODULUS(PSI)
* AMU = BAR SHEAR MODULUS(PSI)
* RHOB = BAR DENSITY(LB-SEC**2/IN**4)
* RA = BAR RADIUS(IN)
*
*3.(5I5) IWMAX = MAX NO OF RADIAL LINES IN WATER
* JWMAX = MAX NO OF AXIAL LINES IN WATER
* IRAD = NO OF RADIAL POINTS IN BAR
* JBMX = MAX NO OF J ZONES IN BAR
* NTS = NO OF TIME STEPS TO BE CALCULATED
*4.(I5) ITERLIM = MAX NO OF ITERATIONS IN WATER ZONES
* (TYPICAL VALUE=5)
*5.(4E15.5) Y = DT/DZ RATIO(DT IN USEC,DZ IN INCHES)
* (TYPICAL VALUE=1.25)
* EPSIL = RELATIVE ERROR CONTROL ON ITERATIONS ON
* WATER ZONES
* EPSIL1 = TRUNCATION CONTROL PARAMETER
* CPU = TIME ON JOB CARD
*

```

TABLE III.1 - FLEBOW COMPUTER PROGRAM INPUT

```

*6.(6I5)      MFREQ1B = PRINT FREQUENCY FOR BAR DATA IF CYCLE LT *
*                                     MCYCL1B *
*      MCYCL1B = CYCLE FOR SWITCH IN PRINT FREQUENCY FOR *
*                                     BAR *
*      MFREQ2B = PRINT FREQUENCY FOR BAR DATA IF CYCLE GE *
*                                     MCYCL1B *
*      MFREQ1W = PRINT FREQUENCY FOR WATER DATA IF CYCLE *
*                                     LT MCYCL1W *
*      MCYCL1W = CYCLE FOR SWITCH IN PRINT FREQUENCY FOR *
*                                     WATER DATA *
*      MFREQ2W = PRINT FREQUENCY FOR WATER DATA IF CYCLE *
*                                     GE MCYCL1W *
*7.(6I5)      IDUMP = 0, IF NO DUMP DESIRED *
*               1, IF DUMP DESIRED *
*      IDMPFRQ = DUMPING FREQUENCY IN CYCLES *
*     IRSTRT = 0, IF NOT RESTARTING *
*               1, IF RESTARTING *
*      IRCYCL = RESTART CYCLE *
*      IPLTHST = 1, SAVE BAR VARIABLES FOR ALL TIME STEPS *
*                                     AT NPLTLOC LOCATIONS *
*      NPLTLOC = NO OF LOCATIONS FOR TIME HISTORY PLOTS *
*      IF IPLTHST EQ 1 NPLTLOC SETS OF CARD NO 8 ARE TO BE INPUT *
*8.(2I5)      IPLTLOC = I LOCATION FOR TIME PLOTS *
*      JPLTLOC = J LOCATION FOR TIME PLOTS *
*****

```

TABLE III.1 (Cont'd)

all the variables at all perturbed grid points at user-selected dumping frequencies and may be used for restarting the problem at any dumped cycle or it may be input to a 3D plot program. TAPE11 contains all bar variables at user-selected locations in the bar and may be input to a time history plot program.

The flow chart for the FLEBOW computer program is Figure III.8. The flow of the solution is basically the same that was outlined in Section B of this Chapter and illustrated in Figure III.6. A minimal amount of input is made by cards and subroutine PRLM is called to generate the required constants and control data. Next, all of the subscripted arrays for the water and bar variables are zeroed out in preparation for the input of initial conditions. If the problem is to be a restart, the TAPE9 file is called to retrieve the data that was stored from a previous run. Otherwise, initial conditions are calculated for the variables on the impact face. Subroutine IMPACT solves for the initial conditions by matching the bar Hugoniot given in IMPACT with the equation of state of water in subroutine WATEREQ. The program is now ready to calculate the variables at the next step in time. The calculations are done J line by J line, replacing the subscripted variable

arrays one J line at a time in order to conserve computer core storage. The first calculations occur at the corner of the impact face of the bar in subroutines CORNIMP and BOUNDRY (see Table III.2 and Figure III.9) where the bar variables and water variables must satisfy the continuity equations (II-46) and (II-47). The nonlinear water equations are solved by an iterative technique requiring an initial guess for the water variables u , v , and p . The values that are used for the first iteration are the values at the same spacial point in the previous time plane. After exiting the subroutine CORNIMP, the input values of $u^{[n]}$, $v^{[n]}$, $p^{[n]}$ are compared to the output values $u^{[n+1]}$, $v^{[n+1]}$, $p^{[n+1]}$, the relative change is calculated, and then a convergence test is applied. In order to satisfy convergence:

$$\frac{u^{[n]} - u^{[n+1]}}{u^{[n]}} < \text{EPSIL} \cap \frac{v^{[n]} - v^{[n+1]}}{v^{[n]}} < \text{EPSIL} \cap \quad (III-26)$$

$$\frac{p^{[n]} - p^{[n+1]}}{p^{[n]}} < \text{EPSIL}$$

If the n^{th} iteration of a variable is a very small number then instead of relative changes, an absolute criterion is used:

$$|u^{[n]} - u^{[n+1]}| < \text{EPSIL} \cap |v^{[n]} - v^{[n+1]}| < \text{EPSIL} \cap |p^{[n]} - p^{[n+1]}| < \text{EPSIL} \quad (III-27)$$

SUBROUTINE CORNIMP

- Impact bar and water variables at corner of impact bar on impact face
- Values assumed for water variables to calculate coefficients in water equations
- Subroutine BOUNDARY called to calculate coefficients of equations (II-45)
- Equations (II-56) for bar variables and (II-45) for water variables cast into form $A X = B$ and solved by inverse multiplication $X = \bar{A}^{-1} B$

SUBROUTINE IMPFACE

- Impact bar and water variables along impact face for points between the corner and the axis of symmetry
- Same solution sequence as followed in CORNIMP except equations for bar variables are equations (II-54)

TABLE III.2 - SUBROUTINES FOR POINTS ALONG IMPACT FACE
EXCLUDING AXIS OF SYMMETRY

If convergence is satisfied for the water variables at the impact corner, then the solution proceeds to points on the impact face between the axis of symmetry and the corner. Subroutines IMPFACE and BOUNDARY are used to find a solution for these points. The solution outline is given in Table III.2 and Figure III.9. An iterative procedure is again used and the convergence criterion, equation (III-26) or equation (III-27) must be satisfied. For the final point on the impact face, the axis of symmetry, subroutine ORIGIN, which is outlined in Figure III.10 is used to obtain a solution by iteration.

After the variables along the impact face have been obtained for the new time, the solution proceeds into the bar, beginning with line $J = 2$. The bar equations are linear algebraic systems which can be solved directly, by elimination, or by matrix inversion and multiplication. The solution proceeds quite rapidly compared to the iterative solutions involving the water equations. Along a J line, the variables at the radial boundary are obtained first, then the variables at the interior points, and finally the variables at the axis of symmetry. The subroutines and pertinent equations for the solution along a J line between axial boundaries are in Table III.3. If the radial

SUBROUTINE BDRY

- Impact bar variables at radial surface points between axial boundaries
- Equations (II-14) expressed in the form $A X = B$ are solved by $X = A^{-1}B$ (inverse multiplication)

SUBROUTINE GNRL

- Impact bar variables at interior points, away from boundaries
- Solution of equations (II-12) by inverse multiplication

SUBROUTINE CNTR

- Impact bar variables on axis of symmetry between axial boundaries
- Solution of equations (II-17) by elimination

TABLE III.3 - SUBROUTINES FOR IMPACT BAR AT POINTS IN BETWEEN AXIAL BOUNDARIES

velocity is zero at two successive I points along the J line, then the stress state between those points and the axis of symmetry is assumed to be one dimensional and all remaining calculations along the present J line are bypassed to conserve computer time.

The J-line-by-J-line solution scheme in the bar continues until the approximated location of the leading stress wave in the bar has been bypassed or until the free end of the bar has been reached. At the free end of the bar, the linear systems of algebraic equations are solved for each type of point by using the equations in Table III.4. This completes the solution for the bar variables at the new time step. At this time in the problem solution the bar variables are printed if the time cycle corresponds to the print cycle selected by the user. The user selects two frequencies of printing of bar variables and a time cycle at which the switch in print frequency occurs.

The variables in the water half space are now advanced in time beginning with those on the free surface. A small sized subroutine FRESURF calls the subroutine BOUNDRY to obtain a solution. As in the case of water variables along the impact face, an iterative solution is used to obtain a solution with the first guess being the values

SUBROUTINE ENFC

- Impact bar variables at outer corner of free end
- Solution of equations (II-21) by elimination

SUBROUTINE ENFF

- Impact bar variables at free end for points between the corner and the free end
- Equations (II-19) expressed in the form $A X = B$ solved by $X = A^{-1}B$

SUBROUTINE ENFZ

- Impact bar variables at axis of symmetry of free end
- Direct solution of equations (II-23)

TABLE III.4 - SUBROUTINES FOR FREE END OF IMPACT BAR

at the same spacial point in the old time plane. The free surface variables solution proceeds outward from the corner of the impact face of the bar to the first I line past the estimated location of the pressure wave.

After the free surface calculations, the solution proceeds into the water space J line by J line starting each J line at the I line just outside the pressure wave location. Subroutines INTEROR and AXIALNB are used for the water interior points. These subroutines are outlined in Figure III.11. Advantage is taken of a uniform pressure state to save on computational time as was done in the bar. After the variables at all points encompassed by the pressure wave have been advanced in time, the points on the water free surface are moved to new axial coordinates by equations (III-23) and then new velocities are calculated for these new boundary points by using equation (III-24). This completes the solution for the new time. The water variables are printed at this time if it is a user selected print cycle.

Before proceeding to the next time step, data dumping is done if the user so desires. If the current time cycle is a dump cycle, all variables for the bar and water plus required control variables are dumped onto

file TAPE10 for three dimensional plots of the variables at this time or for restarting the problem at the current cycle in a later computer run. Next, if the user has selected data dumping at given locations in the bar, the six bar variables at the specified locations will be written on file TAPE11. These data are dumped at every cycle to allow a plot program to plot the value of a variable as a function of time. After this dump, the values of the water variables are shifted from the "new time" array to the "old time" array and then the solution proceeds to the next time step.

CHAPTER IV

WATER IMPACT EXPERIMENTS

An experimental program was conducted with the purpose of measuring the elastic response of a solid right circular cylindrical bar to normal (90 degrees to surface) impacts on water. The impact velocities were sufficiently small to insure elastic response. To minimize water disturbances so that the bar would impact a perfectly flat water surface, the atmosphere above the water surface was evacuated to a pressure slightly greater than the vapor pressure of water. Strain gages were used to obtain the strain response of the bar and the impact velocity was measured both electronically and optically. These strain results provide a means of obtaining a correlation with the analytical model of the phenomenon.

A. Experimental Facility

The facility that was used for the water impact tests is the Hydroballistics Pilot Tank located at the Naval Surface Weapons Center, White Oak Laboratory, in Silver Spring, Maryland. The tank is shown in Figure IV.1. It is 20 feet long, 5 feet wide between glass walls, and 3 feet wide between supporting I beams, which are inside the walls. There are 8 bays of I beams on 26 inch centers. The maximum permissible water depth is about 8.5 feet. The walls are almost entirely glass. The air guns used

to launch models into the tank are fed by a pressure chamber with a differential pressure control valve. The particular gun barrel used for the shots is shown in Figure IV.2. It is a 3.5 inch outside diameter, 3.0 inch inside diameter, 15 feet long unvented, smooth bore stainless steel barrel. A diaphragm holder was designed to attach to the end of the barrel so that the space between the model and the diaphragm, located at the end of the barrel, could be evacuated to pressures much lower than the water vapor pressure.

Much consideration was given to possible methods of reducing the pressure of the atmosphere above the water surface. Provision had to be made for reloading the model into the muzzle end of the gun barrel and lowering of the gun barrel a sufficient distance to pull up the model and stuff the instrumentation wire into the breech of the barrel in preparation for a shot. A design satisfying the above requirements is a cylindrical vacuum chamber that clamps onto the end of the gun barrel and moves with the barrel when reloading. A view of the chamber looking down and along the axis of the tank is shown in Figure IV.3. An elevation view looking through the side wall of the tank is shown in Figure IV.4. The chamber is a plexiglass cylinder with aluminum end plates which is held together with longitudinal tie rods. The outside diameter of the plexiglass cylinder, which is

approximately 36 inches, was made as large as possible to avoid failure from impact shocks, yet small enough to fit between the I-beam walls of the tank. The thickness of 1/2 inch was chosen as optimum for buckling and handling considerations. The initial design of the cylinder was a uniform thickness, unstiffened shell, but it was manufactured one inch out of round necessitating the bonding of axial and circumferential stiffeners to it to avoid a catastrophic buckling failure under vacuum loading. For photographic viewing purposes, two diametrically opposed, 8 inch diameter windows made of optical grade plexiglass were bonded into cutouts in the plexiglass cylinder. These viewing windows are seen in Figure IV.4.

The top plate of the chamber is 40 inches in diameter and 1/2 inch thick. Its edge extends beyond the periphery of the plexiglass cylinder, allowing room for the tie rod holes outside of the seal-line between the cylinder and the end plate. The plate narrowly fits between the I beams in a bay of the tank, and because the gun axis is not exactly in the center of the bay, cutouts were made in the plate as shown in the background of Figure IV.3. The top plate has a hole in the center for the gun barrel and two stainless steel split clamp rings located on the top and underside of the plate clamp onto the gun barrel. An "O" ring groove is machined into the center hole in

the plate to form a vacuum seal around the gun. Two 3 inch diameter holes in the plate allow access into the chamber from above during preparation for a shot. Prior to "pulling" a vacuum on the chamber, these holes are covered with plates having "O" ring seals. These plates are free to blow off if overpressure develops in the chamber due to gun gases. The blowoff plates, the vacuum tubing, and valves are seen in Figure IV.3.

The bottom plate is a 3/8 inch thick, 40 inch diameter aluminum plate with a 10 inch diameter hole in the center to allow passage of the model after water impact. Before every shot, the center hole is fitted with a diaphragm which is clamped against an "O" ring seal. Experimentation was done with the diaphragm thickness and material, and an acetate diaphragm, .030 inches thick was selected as the best performer. The bulged diaphragm under vacuum loading can be seen in Figure IV.4. The bottom plate also has a water inlet hole into which a T'd piping and ball valve arrangement is threaded.

Evacuation of the cylindrical vacuum chamber was done with a two stage Consolidated Vacuum pump and the pressure in the line was measured with a vacuum gage (see Figure IV.2). The large diameter vacuum line shown in Figure IV.3 is the vacuum chamber evacuation line. The small diameter vacuum tubing in this picture is connected to a Duo-seal vacuum pump, feeds through the top plate of

the vacuum chamber and into the diaphragm holder clamped onto the end of the gun barrel, shown in Figure IV.4. This holder was fitted with a .002 inch thick mylar diaphragm and the space between it and the model "0" ring at the top of the barrel was evacuated to pressures in the order of several hundred microns of mercury. This diaphragm prevents the air in the gun barrel ahead of the model, which would be at the pressure of the vacuum chamber without the diaphragm, from forming a high velocity air slug ahead of the model which would perturb the water surface. The pressure in this barrel vacuum line is monitored at the inlet to the vacuum chamber with a Hastings vacuum gage model #DV-6.

The water below the vacuum chamber has to be removed after every shot for model reloading in the gun and diaphragm replacements. For quick turnaround on shots, dumping and refilling the entire tank is time prohibitive. To speed up the removal and refilling of the water, the hydroballistics tank was partitioned into two sections of two and six bays, respectively, by a 1/4 inch thick, 8 feet by 3 1/2 feet retaining wall, and a 65 gallon per minute, 20 feet head water pump was connected to feed lines in each section. The two bay section containing the vacuum chamber is pumped out after every shot and the refill is done slowly by gravity feed to minimize entrapped air in the water. Excessive air in the water contained in the

vacuum chamber precipitates out of the water during evacuation of the chamber, rises in the water column, and disturbs the water surface.

B. Test Models

Two models were used for obtaining data. Each one is a solid, right circular cylindrical bar made of magnesium alloy ZK60A-T5. Magnesium is used because of its relatively low modulus which produces large strains for a given impact stress. The values of the elastic constants are Young's modulus equal to $6.5(10^6)$ pounds per square inch and Poisson's ratio equal to 0.35. One of the models was instrumented with semiconductor strain gages which have a high gage factor, and the other model has foil type strain gages. References 17, 18, and 19 provide a good explanation of the theory and use of semiconductor gages, while Reference 20 contains information on foil strain gages. These two models will be referred to as the semiconductor gage model and the foil gage model, respectively. The output from the strain gages was obtained from a trailing wire which was threaded through the breech of the gun, coiled in the gun barrel behind the model prior to the shot, and then payed out during the shot. The foil gage model is shown in Figure IV.5 with the trailing wire.

The models are subcaliber and fitted with high density polyethylene boreriders which are attached to the model each by three magnesium pins which have a wringing fit with the holes in the model. An obturating cup, made of high density polyethylene, on the back of the model has "O" ring grooves on the outside diameter and at the interface with the magnesium rod to provide a vacuum seal before the shot and to prevent blowby of gun gases during the shot. A ferromagnetic loop of wire on the model is used to generate a voltage in a reluctance gage, housed in the gun near the muzzle, as the model passes by. The electrical pulse is used for instrumentation triggering purposes. The semiconductor gage model was equipped in a similar manner as the foil model in Figure IV.5.

The dimensions of the two models and the strain gage measurement technique on each were slightly different. These models are depicted in Figure IV.6. The foil gage model has four Micro-Measurements #EA-13-125BB-120 foil strain gages arranged in a full bridge circuit (Figure IV.7a) in an axial plane 2.5 inches from the impact face. Two

of the gages are mounted diametrically opposite one another to obtain the axial strain and the other two gages are mounted between the axial gages to obtain the circumferential strain. This configuration subtracts out bending stresses and produces output voltages greater than the output from a single gage. With this strain gage arrangement, only four conductors are required in the trailing wire, making it relatively small in diameter, more flexible, and less prone to damage. This foil gage model was used during the debugging phase of the experimental program because it was less expensive than the semiconductor model and easier to repair. The original length of 36 inches was cut down to 33 inches because of damage sustained by the impact face. The diameter of 2.75 inches doesn't allow sufficient clearance for wires so it was decreased to 2.5 inches for the semiconductor gage model.

SR-4 Type SPB2-06-12 semiconductor gages were used on the second model to gain more output voltage for a given level of strain. This larger output minimizes the effect of electrical noise induced in the circuitry and is especially important for impact shots with low transmitted stresses. There are six gages arranged in 120 degree circumferentially spaced triads at axial locations of one diameter (2.5 inches) and half the bar

length (18 inches) from the impact face. All gages are mounted to sense axial strain. The one diameter location was chosen for obtaining two dimensional response in the bar-water interface area and the half bar-length location was chosen for obtaining the fully developed one dimensional wave characteristics. Each gage is supplied with a constant current (Figure IV.7b) so that independent strains can be measured at each location. By determining the time of arrival of the stress wave at each gage at the forward axial location, the tilt of the model at impact can be determined. Also uniformity of bar response at the axial location can be determined by examining the character of the measured strain pulse at the three circumferential stations.

Both types of gages were bonded onto meticulously cleaned areas of the bars with M-Bond 200 Adhesive which has a fast room temperature cure. After curing, the gages were coated with epoxy for protective purposes. After soldering the conductors of the trailing wire onto the leads of the strain gage wires, the models were calibrated statically in compression in a Tinius-Olsen machine up to 60,000 pounds of applied force. Each calibration on each model was repeated several times to ensure

reproducibility and to test for zero load base shift due to possible viscoelastic effects of gage adhesive. Ambient temperature was recorded and voltages were measured in millivolts with digital voltmeters. The foil gage output was linear with stress and the semiconductor gage output displayed the nonlinear effect so characteristic of these types of gages.

Several shots were made with foam mitigator noses. The material used is rigid polyurethane foam of densities 5 and 15 pounds per cubic foot. The foam material was manufactured in one cubic foot blocks and the noses were made of material from the center of these blocks where the density is uniform. The configuration of the noses is a right circular cylinder, 1.25 inches long and 2.5 inches in diameter. These cylinders were attached to the metal bar with masking tape, allowing relative radial motion between the mitigator and the metal bar at the interface.

C. Recording Equipment

The data to be obtained from a shot consist of strain on the outside diameter of the rod versus time, a double exposure photograph of the model and water surface just prior to water impact which provides impact velocity and water surface condition, and voltage

outputs from the reluctance gage and a laser beam detector providing a backup measurement for impact velocity. Oscilloscopes and transient recorders are the two basic devices used for recording the voltage outputs from the strain gages. The transient recorders are Biomation Model 802 solid state recording devices with rotating memory buffers. When the device is armed for recording, input voltage signals are digitized and fed into the memory buffer one word at a time until the 1024 storage locations of memory are occupied. As the next word is input, the first word that was entered at the time of arming is purged. The sequence continues with the new input word being stored in core after the word that has been in core for the longest time has been purged. The interval between digitized input is controlled by an external switch which permits the user to select the total time interval of the memory. Another switch allows the user to select the percentage of the total memory time that will contain data recorded prior to the trigger pulse. The recording time interval ranges from 500 μ sec to 5 seconds. Therefore, the shortest time between data points is slightly less than 0.5 microsecond. The oscilloscopes that were used are Tektronix models 561A, 531, and 502A.

Photographs of the nose of the model and the water surface just prior to impact are obtained with a 4 x 5 inch Graphic View camera using high speed Type 57 ASA 3000 Polaroid film. Lighting is provided by a strobe unit powered by a high voltage Transmetrics Incorporated flash lamp pulser which has an 8000 volt supply. An oscillator unit controls the frequency of flashing and a counter unit allows a selection of 1 to 512 flashes. Two flashes were used to obtain the velocity of the projectile. The setup of the camera and strobe is shown in Figure IV.8. An additional source of velocity measurement is obtained by recording the voltage output from the reluctance gage and laser beam detector. The primary purpose of the reluctance gage is to provide a trigger to the strobe flashing unit. The laser is a Spectra-Physics Model 155 Helium-Neon Gas Laser with a 0.5 milliwatt output. As the model passes through the beam, a photoelectric sensor outputs a voltage pulse to trigger the strain gage recording equipment. The laser position is shown in Figure IV.8.

The schematic of the data recording circuit for the semiconductor strain gage model is shown in Figure IV.9. The six gages are connected each to separate constant current power supplies one of which is shown in Figure IV.7b.

The transistor and diode combine to maintain a constant current of approximately 40 milliamps through the gage. The output voltage of the front three semiconductor gages were input to three Biomation transient recorders. The output voltage of the gages at the mid-length of the model were input to model 531 and 502A oscilloscopes. The foil gage model is powered by a six volt battery and only one data channel is output. This one output channel is input in parallel to the transient recorders and oscilloscopes. The triggering pulse for the transient recorders and oscilloscopes is initiated by the laser detector output. The voltage from the detector is input to a trigger unit which outputs a "large" voltage step pulse which feeds into a delay unit that outputs a voltage after a preset time delay. The output from the delay unit triggers the recorders. The model 561A scope shown in Figure IV.9 is a "sequence of events" scope which displays output from the various triggering devices and serves as a trigger unit itself to pulse the strobe flashing unit.

CHAPTER V

ANALYSIS OF ANALYTICAL AND EXPERIMENTAL RESULTS

The program that was conducted to obtain an understanding of the water impact phenomenon included three FLEBOW computer runs with detailed post processing of the output, and an extensive experimental program of 47 shots which yielded only 12 sets of good data because of data taking difficulties. The computer results demonstrate the two dimensional and interface effects occurring during water impact. The experimental strain gage results verify the analytical model for elastic structural response and yield additional information about the propagated stress wave. In addition, the mitigation obtained from using rigid polyurethane foam noses is obtained experimentally. The analytical and experimental results are discussed separately and then comparisons are made between the two at the strain gage locations on the bars.

A. Computer Results

The FLEBOW computer program was run for three different input cases corresponding to three different estimated experimental impact velocities. More accurate readings of the data indicated slightly different impact velocities. ZK60A-T5 magnesium impact bars were simulated in all cases. This material has a Young's modulus of

$6.5(10^6)$ pounds per square inch (psi), a Poission's ratio of 0.35, and the density is .066 pounds per cubic inch. For calculation of the initial impact stress in the bar, the shock velocity - particle velocity relationship was obtained from data in Reference 21:

$$\text{Shock velocity} = 183071 + 1.2 \times \text{Particle velocity (in/sec)} \quad (\text{V-1})$$

The water equation of state*in the kilobar range was obtained with pressure expressed as a cubic function for relative change in volume. This equation was truncated to a quadratic equation for ease of solution of the impact pressure. For a ten percent change in volume of the water, which corresponds to approximately 19,000 psi pressure, the error in dropping the cubic term is less than 2 percent. The equation of state is:

$$p = \left[.319 \left(\frac{\rho_w}{\rho_w|_{p=0}} - 1 \right) + 1.13825 \left(\frac{\rho_w}{\rho_w|_{p=0}} - 1 \right)^2 \right] (10^6) \text{ psi} \quad (\text{V-2})$$

1. Computer Case No. 1

The first computer case is the simulation of a 2.5 inch diameter magnesium bar impacting on water at 96 ft/sec (feet per second). Twenty one J lines were chosen to represent the bar continuum from the axis of symmetry to the radial boundary. Thus the mesh dimension h is

* Walker, W., Naval Surface Weapons Center, White Oak Laboratory, private communication

.0625 inches, which is considered to be a relatively fine mesh size. The time step is 0.129 μ sec (microseconds). The computer solution was stopped and restarted twice to check on the progress of the calculations. The run was stopped at cycle 323, which corresponds to a real time of 41.66 μ sec because the run time per cycle was becoming very large. The major portion of the increase in run time per cycle is due to the water calculations because the pressure wave in water travels outward both radially and axially encompassing more grid points and necessitating more calculations per cycle. The movement of the stress waves in the bar requires more calculations per cycle, but are not as time consuming because the calculations do not involve iterative solutions, and the added number of grid points involve only a row of a fixed number of radial points. The 41.66 μ sec of real run time was sufficient to obtain the first pass of the stress pulse over the forward location of the strain gages on the semiconductor rod, and to obtain the changes in wave structure as it moves down the bar. The calculated impact stress is 5787.9 psi compression.

Figure V.1 through V.14 are three dimensional computer plots of computed axial stress versus radial and axial location in the impact bar at various times after impact. The first figure shows a stress state that is

uniform over the radius of the bar at a given axial location except near the radial boundary where a release wave is just starting to propagate inward. Three stress contours are shown for quantitative interpretation of the plots. At 3.99 μ sec (Figure V.2), the release wave has decreased the axial stress level in the bar just behind the impact face over most of the radius, but the stress at the impact face remains essentially uniform over approximately 70 percent of the impact face. The longitudinal wave speed in the magnesium bar is 249,030 in/sec and the sound velocity in water at the impact pressure is 61,950 in/sec. The differences in wave speeds in the two media account for the effect seen in Figure V.2. The greater speed of the release wave in the bar decreases the bar stress in the interior but has little effect on the stress at the impact face because the release wave in water has not arrived. At 5.28 μ sec (Figure V.3), the release wave in the bar has reached the axis of symmetry and about half of the impact face has had a reduction in stress from the water release wave. At 6.57 microseconds (Figure V.4), the stress behind the impact face has been relieved even more. At this time, the "one dimensional" stress at the impact face is reduced slightly below the 5500 psi contour line that existed in the previous figure.

The stress is not uniform over the portion that has not been affected by the water release wave. The axial stress at the axis of symmetry on the impact face at 6.57 μ sec is 5384 psi and the maximum value is 5490 psi at 0.625 inches from the axis. Thus the bar relief wave does reduce the impact face axial stress slightly.

In the next Figure (V.5), one of the interesting phenomena of the two dimensional response is seen developing. Near the impact face, around the axis, the stress is starting to increase. At this time of 9.15 μ sec, the axial stresses in this area are above the 5500 psi compression level. The increase in stress is due to reflection of the relief wave off of the impact face. The relief wave that moves inward from the radial boundary is a tensile wave. Superimposed on the compressive impact stress, it produces a lower total compressive stress. This tensile wave reflects off the impact face as a compressive wave because the characteristic impedance (density times wave speed) of the water is lower than the characteristic impedance of the magnesium impact bar. The reflected wave amplifies the compressive stress that already exists in the bar. At

this time, relief waves which have reflected from the axis of symmetry are traveling radially outward to affect the stress along the radial boundary. Radial relief waves are also reducing the amplitude of the leading wave in the bar. These effects are more apparent in Figure V.6 at a time of 14.31 μ sec, in Figure V.7 at 15.60 μ sec, and Figure V.8 at 16.89 microseconds. The maximum compressive axial stress that occurs in the problem is 7359 psi along the axis at 0.6 diameter from the impact face at 16.89 μ sec. Thus an amplification factor of 1.27 over the impact stress is obtained in the solid bar. The high compressive stress level stays concentrated along the axis and does not propagate outward because of cylindrical attenuation.

As time progresses, the stress at the impact face decreases due to the passage of the relief wave in water. Also the high compressive region around the axis diminishes in amplitude and the leading wave loses its definition and combines with the higher magnitude second wave, causing a longer rise time in the stress pulse at a given location in the bar. Figures V.9, V.10, V.11, and V.12 show this smoothing of the disturbances. At later times of 38.82 and 41.40 μ sec (Figures V.13 and V.14), the leading wave is essentially uniform in the radial coordinate at a given axial location, and possesses a

a long rise time. Some radial disturbances still exist between the peak of the wave and the impact face, but these disturbances are approaching zero at these times.

The water pressure that is acting on the impact face of the bar as it penetrates the water surface is shown in Figures V.15 through V.20. Immediately after impact (2.06 μ sec) the pressure is uniform over most of the impact face (Figure V.15). At a later time of 11.73 μ sec (Figure V.16) the pressure on the impact face is nonuniform. The pressure on the axis has decreased slightly due to the radial relief wave propagation in the bar and a majority of the impact face is under a lower pressure due to the water relief wave. At 15.60 μ sec (Figure V.17) the pressure at the axis has increased slightly over the value at 11.73 μ sec, and the water relief wave is closer to the axis. In Figure V.18, the water relief wave has markedly affected the pressure on the impact face and Figures V.19 and V.20 show the pressure decreasing to a small value.

The axial stress as a function of time at different locations on the outside diameter of the 2.5 inch diameter bar is shown in Figures V.21 through V.25. Near the impact face, the stress pulse has a short rise time to a peak, a dropoff to a lower level, and then eventual decay to zero. At one quarter of a diameter from the impact face, the rise time is 1.7 μ sec and the peak axial

stress is 4385 psi (see Figure V.21). At one half of a diameter from the impact face, the rise time is 3.0 μ sec and the maximum stress is 4337 psi (Figure V.22). The maximum axial stress at one diameter from the impact face, shown in Figure V.23, is even lower than at the two previous locations (3763 psi). Farther down the bar, the stress pulse becomes more of a ramp and the magnitude increases (Figures V.24 and V.25). At one and a half diameters from the impact face the maximum axial stress is 4159 psi and at two diameters away, the maximum value is 4395 psi.

Along the axis of symmetry, the axial stress is greater than at corresponding axial locations on the outside diameter of the bar within two or three diameters of the impact face. The reason for the higher stress is geometrical focusing of radial waves at the axis. The lower stress at the radial boundary is due to a combination of things. The pressure on the corner of the impact face remains low because of the stress-free condition of the water surface in the vicinity of the corner. The axial stress on the radial boundary near the impact face doesn't recover from the low pressure loading at the corner of the impact face because of the stress-free radial boundary which provides relief.

Farther down the bar, where radial waves have been attenuated, the stress becomes uniform over a cross section. Figure V.26 is the axial stress versus time at the axis on the impact face. The dip in the plateau is caused by the radial relief wave discussed above and as seen in the sequence of Figures on the pressure loading on the impact face. Figure V.27 is the axial stress at one half diameter from the impact face on the axis. The pulse exhibits a two wave structure. The first peak in this pulse is due to the initial impact wave propagating down the bar. However, before the magnitude of the impact stress is realized, a radial relief wave mitigates the amplitude. Then the reflection of the relief wave from the impact face strengthens the pulse until a maximum stress of 7265 psi is attained at 16 μ sec. At one diameter from the impact face (Figure V.28) the relief wave affects the axial stress at an earlier time in the initial rise of the pulse. The amplitude of the second peak is lower at this axial location because of attenuation. Moving down the axis of the bar, the axial stress wave is seen to lose more and more of its two wave structure and is smeared into one long rising pulse (Figures V.29 and V.30).

Two good indicators of the two dimensional stress state in a bar are the radial stress and radial velocity. Figures V.31 through V.35 are three dimensional plots of radial stress versus coordinates in the impact bar for various

times, and Figures V.36 through V.42 are three dimensional plots of radial velocity. Figure V.31 is an early time plot of the radial stress which is nearly uniform over a cross section. The radial velocity plot at this time of 2.70 μ sec (Figure V.36) shows the radial surface near the impact face moving outward and relieving the radial stress as it does. As time increases, there are a series of reflections of radial waves which cause alternate tensile and compressive radial stress states producing outward and inward radial velocities, respectively. At later times in the problem, as the disturbances extend several diameters away from impact face, the radial stress and radial velocity become small (see Figures V.35 and V.42). However, near the impact face there are still some radial disturbances at 41.40 μ sec.

Figures V.43 through V.45 are three dimensional plots of shear stress showing the variation of this stress variable with time. Several diameters away from the impact face the shear stress is negligible, but there still are nonzero values near the impact face. Figures V.46 and V.47 show the velocity vectors of the grid points in water at 18.83 μ sec and 41.40 μ sec, respectively, and yield some idea of the flow field that forms from the impact. Also shown in these figures is the splash of the water surface from the impact.

2. Computer Case No. 2

The second case that was run with the FLEBOW computer code is a 142 ft/sec impact of a 2.5 inch diameter

magnesium bar on water. The same mesh size of 0.0625 inches was used as in case no. 1. The problem was stopped at the 117th cycle (15.09 μ sec) to examine the results up to that point. Since the results were in the same ratio to the initial conditions as the case no. 1 results, the problem was not restarted. Rather, the computer time was reserved for running a third case.

The impact stress from a 142 feet per second impact is 8692 psi. Three dimensional plots of axial stress versus bar coordinates for times 6.57 μ sec and 14.31 μ sec are shown in Figures V.48 and V.49. The shapes of the stress profiles are exactly the same as the corresponding profiles in Figures V.4 and V.6 for the 96 ft/sec impact. Likewise, the profiles of the water pressure loading on the impact face at times 2.06 μ sec and 11.73 μ sec are similar for each case (see Figures V.15 and V.50 and Figures V.16 and V.51).

Table V.1 contains a list of normalized stress variables at different locations for the two times 6.58 and 14.32 μ sec. The variables are either relative or absolute maximums at the locations cited for the given time. The normalization is based on values of the variables at time equal zero. As can be seen in the table, the lower velocity case produces a larger normalized response, except for an

Normalized Response for 2.5 Inch
Diameter Magnesium Bar*

	Computer Case No. 1 (96 ft/sec)	Computer Case No. 2 (142 ft/sec)
$\sigma_z'(0,0,6.58)**$.930	.927
$\sigma_z'(0,1.25,6.58)$.827	.823
$\sigma_z'(1.25, 1.00,6.58)$.760	.754
$\sigma_z'(0,0,14.32)$.971	.968
$\sigma_z'(0,1.0,14.32)$	1.199	1.192
$\sigma_z'(0,3.1875,14.32)$.333	.330
$\sigma_z'(1.25,1.9375,14.32)$.633	.628
$\sigma_z'(1.25,2.5,14.32)$.589	.585
$\sigma_r'(0,0,6.58)$	-.501	-.495
$\sigma_r'(0,0,14.32)$.763	.766
$\sigma_r'(0,1.125,14.32)$	-.627	-.624
$\sigma_\theta'(1.25,1.0,14.32)$	-.345	-.342
$\sigma_\theta'(1.25,3.0,14.32)$.192	.190

*normalized to initial (impact) conditions of the variable

**locations given as (r, z, t)

TABLE V.1 - NORMALIZED STRESS RESPONSE AT SELECTED LOCATIONS
AND TIMES FOR COMPUTER CASES 1 AND 2

anomolous behavior of the radial stress on the axis at the impact face for time 14.32 μ sec. Perhaps the lower normalized response for the higher velocity impact case (except for σ_r' (0, 0, 14.32)) is caused by the slightly larger wave propagation velocity in the water due to the higher pressure state. The larger wave propagation velocity causes a faster unloading of the impact face and corresponding lower response. In Table V.2, the ratio of the response for the 142 ft/sec impact to that of the 96 ft/sec impact is given for various variables and locations. Except for the radial stress on the impact face at 14.32 μ sec, all ratios are below the 1.502 ratio of the impact stresses. Thus for the response of a 2.5 inch diameter magnesium bar to a normal impact at a velocity in the range covered here, the response may be approximated by using the ratio of impact stresses.

3. Computer Case No. 3

The third computer case simulated the impact of a 2.75 inch diameter magnesium bar on water at 157 ft/sec. Since the fine mesh of the previous two computer cases caused very long running times, the mesh for this case was made much coarser. Eleven I lines were used between the axis of symmetry and the radial boundary yielding a mesh size h of .1375 inches. A time step of .284 μ sec was used for this material and mesh size. One-hundred seventy-six time cycles were run corresponding to a real time of 49.94 μ sec. The impact stress for 157 ft/sec

Variable and Coordinates*	Ratio (case 2 to case 1)
$\sigma_z(0,0,0)$	1.502
$\sigma_r(0,0,0) = \sigma_\theta(0,0,0)$	1.502
$v_z(0,0,0)$	1.476
$\sigma_z(0,0,6.58)$	1.496
$\sigma_z(0,1.25,6.58)$	1.494
$\sigma_z(1.25,1.00,6.58)$	1.490
$\sigma_z(0,0,14.32)$	1.496
$\sigma_z(0,1.0,14.32)$	1.493
$\sigma_z(0,3.1875,14.32)$	1.492
$\sigma_z(1.25,1.9375,14.32)$	1.490
$\sigma_z(1.25,2.5,14.32)$	1.491
$\sigma_r(0,0,6.58)$	1.482
$\sigma_r(0,0,14.32)$	1.508
$\sigma_r(0,1.125,14.32)$	1.493
$\sigma_\theta(1.25,1.0,14.32)$	1.487
$\sigma_\theta(1.25,3.0,14.32)$	1.492
$\tau_{rz}(.625,.75,6.58)$	1.502
$\tau_{rz}(.75,2.0,14.32)$	1.488
$v_r(1.0,.75,6.58)$	1.495
$v_r(1.0,0.0,14.32)$	1.476
$v_z(0,0,6.58)$	1.476
$v_z(0,0,14.32)$	1.480
* (r,z,t)	

TABLE V.2 - RATIO OF COMPUTER CASE 2 RESPONSE TO COMPUTER CASE 1 RESPONSE AT SELECTED LOCATIONS AND TIMES

impact is 9656 psi compression. The radial and circumferential stresses at impact are 5199 psi compression.

The axial stress is plotted versus coordinates in the bar for different times in Figures V.52 through V.62. The same trends in response occur as in the response of the 2.5 inch diameter bar to water impacts. A profile for the 2.75 inch diameter bar that corresponds to one for the 2.5 inch diameter bar occurs at a later time because of the longer distance for radial relief waves to travel from the radial boundary to the axis. The major difference in the response is that the normalized amplitudes of the axial stress are not as large. This can be seen for the peak compressive wave by comparing Figures V.6 through V.10 for the 2.5 inch diameter bar response to Figures V.55 through V.57 for the 2.75 inch diameter bar. The maximum axial stress for the 2.75 inch diameter bar that occurs during the time of the calculations is 10728 psi compression at a location on the axis, 1.375 inches (or 0.5 diameter) in back of the impact face. This is an amplification of 1.11 times the value of the impact stress. The maximum axial stress level occurs 17.88 μ sec after impact. The amplification factor for the 2.5 inch diameter bar was 1.27 at a location 0.6 diameter behind the impact face and a time of 16.89 μ sec.

The later occurrence of the maximum stress in the 2.75 inch diameter bar is caused by the larger radius. The amplification is lower because of the coarse grid used for this case and particularly, the increase in the grid size in the radial direction. The coarser grid smears the peaks in amplitude that occur in reality, over a wider area and results in lower calculated stress levels. In the radial direction, this smearing is even more detrimental to determining peak response because of the additional attenuation due to the cylindrical geometry.

The peaks of the nearly one dimensional axial stress waves in the case 1 and 3 runs do not exactly coincide in location at a given time. The computer printout for case 1 at time 40.76 μ sec indicates the location of maximum amplitude at 5.6075 inches from the impact face. For case 3 at 41.43 μ sec, slightly later than the case 1 time, the location of maximum stress is 5.5 inches from the impact face. Thus the coarse grid has the effect of delaying the arrival of the nearly one dimensional wave at a given location. At 49.65 μ sec, the wave in Figure V.62 is seen to be essentially one dimensional.

Figures V.63 and V.64 show the pressure loading on the impact face for the 2.75 inch diameter impact. The effect of the larger diameter bar on the time of loading is

seen by comparing Figures V.64 and V.20. At 27.21 μsec , the pressure on the axis is going to zero for the 2.5 inch diameter bar while at a slightly later time of 28.37 μsec , the pressure at the axis of the impact face of the 2.75 inch diameter is at a larger relative value.

The axial stress as a function of time for computer case no. 3 is shown at various locations along the radial boundary in Figures V.65 through V.70. Basically the shape of the stress pulses are the same as those for the 2.5 inch diameter bar at the same relative locations (same location normalized to diameter). The major difference is that the pulses are smoother for the computer case no. 3 results because of the coarser finite-difference grid. As an example, the axial stress pulse at one diameter from the impact face for the 2.5 inch diameter bar (Figure V.23) has distinct oscillations about an average stress level whereas the pulse at one diameter on the 2.75 inch diameter bar is virtually void of oscillations (Figure V.67). The response for locations on the axis of the 2.75 inch diameter bar is shown in Figures V.71 through V.73. The time duration of the pressure loading on the axis of the impact face is 35.7 μsec whereas for the 2.5 inch diameter bar it is 29.5 μsec .

Another point is that the stress pulse in Figure V.26 recovers to 97.5 percent of the impact stress after the slight dip at 6 μ sec due to the radial stress wave in the bar. In Figure V.71, the recovery is only 94.4 percent.

Figures V.74 through V.76 are examples of the radial stress in the 2.75 inch diameter bar. In Figure V.74, the large radial stress at the center of the impact face is shown at 19.86 μ sec. This is similar to Figure V.33. At 49.65 μ sec in Figure V.75, the radial stress is very small throughout the bar indicating a one dimensional stress state. Figures V.77 through V.80 show the radial velocity in the bar. The late time plot at 49.65 μ sec in Figure V.80 shows small radial velocities, less than 36 inches per second. Figure V.81 shows the radial velocity of the corner of the impact face with time, first outward and then oscillating with decreasing amplitude as two dimensional effects are attenuated. Figure V.82 shows the low level of shear stress in the bar at 49.65 μ sec. There is still some shear around the impact face due to residual radial waves from the unloading process.

B. Experimental Results

At the beginning of the program, eleven shots were made to work out mechanical and electronic problems in the setup. The data that were recorded from the strain gages in these shots indicated stress levels that were much lower

than expected for the measured impact velocities. The couple of photographs that were successfully taken of the water surface just prior to impact indicated that the water surface was being disturbed. It was concluded that the original seal design on the model was permitting blowby of gun gases. Another series of twelve tests were conducted during which the seal design was improved, a diaphragm holder was attached to the muzzle of the gun barrel, and a shot preparation sequence developed which yielded a flat water surface prior to impact. The remaining mechanical problem after these shots was model rebounding from the bottom of the tank (see Chapter IV). Subsequently, three shots were made with high-speed camera coverage of the water entry and rebound. From these shots, it was found that a layer of air between the vacuum chamber and the water in the hydroballistics tank solved the rebound problem. Data shots were then begun. These included seven shots with the 2.75 inch diameter foil gage model, six shots with the 2.5 inch diameter semiconductor gage model without a foam mitigator and eight shots of the 2.5 inch diameter model with rigid polyurethane foam noses. Not all shots yielded sufficient data to obtain a strain response or impact velocity.

1. Foil Gage Model Data

Of the seven shots with the 2.75 inch diameter bar with foil gage instrumentation, only three yielded

full sets of data (shots 31, 32, and 33). The strain gage data from shots 31, 32, and 33 having impact velocities of 91.0, 156.2, and 122.5 ft/sec are shown in Figures V.83, V.84, and V.85, respectively. These plots are obtained by multiplying the digitized voltage output from a transient recorder by the calibration factor which converts the output to stress. The data shown represents the difference between the axial and tangential stresses at the axial location of the gage array. The strain gage arrangement and Wheatstone bridge configuration shown in Figure IV.7a were chosen to provide temperature compensation and to increase the voltage output so that the data signal could be distinguished from electrical noise. The output from the Wheatstone bridge is proportional to the difference of the axial and circumferential stresses. For a uniform axial load, a static calibration curve may be used together with the measured voltage from a shot, to obtain the axial stress response as a function of time. However, in the presence of a circumferential stress and without a known relation between axial and circumferential stress, each component of stress may not be identified. The computer results of section A of this Chapter indicate that at the location of the foil gages, there is a considerable amount of circumferential stress present from the impact. If the

gages were placed farther from the impact face, then a uniform axial stress state would exist. The data of Figures V.83 through V.85 will be used in section C of this Chapter for comparison with computer results.

Figure V.86 is a double exposure photograph of the model and water surface just prior to impact on shot number 32. The model traveled 0.93 inches between strobe flashes. The 0.75 inch wide polyethylene bore rider, which is seen in the photograph, is used as a dimension reference. The well-defined reflection of the model on the water surface indicates that the water surface was flat prior to impact. The white spots in the photograph are the primary laser beam and its reflections off the multitude of surfaces in the path of the beam. Also the mylar diaphragm from the gun diaphragm holder can be seen just left of the model above the water surface. On this shot, the gun diaphragm did not hinge and fold out of the way of the model, but rather it was completely sheared off.

2. Unmitigated Semiconductor Gage Model Data

Shots made with the 2.5 inch diameter semiconductor gage model without a mitigator nose yielded data on the tilt of the impact face relative to the water surface at impact. The response at all three circumferential locations

in an axial plane was found not to be uniformly the same. Data was obtained on the magnitude and shape of the strain pulse as it travels from a location near the impact face to an axial location where the stress should be one dimensional. Shot 35 yielded strain gage data on the front three gages but no velocity data were obtained, and an estimated velocity provided inconsistent strain gage data. Other shots made at low chamber pressure also showed inconsistent velocity behavior, and a number of factors can contribute to this. A reasonably good fit was maintained between the bore riders and obturating cup on the model and the inside diameter of the gun barrel, so that excessive model tilt angles could not develop in traveling down the gun barrel. The "O" ring on the obturating cup produced a tight fit with the barrel, even though it was smeared with vacuum grease before every shot and an oil film was put on the bore every five or six shots. Small rust particles from the interior of the pressure chamber of the gun were blown into the gun barrel during every shot and deposited on the inside ~~diameter~~ of the barrel. Although the barrel was dried after every shot by passing dry tissue through it, thorough cleaning with Acetone was done only after five or six shots. Thus the change in coefficient of friction between the parts and the barrel has an effect on the model terminal velocity. Another factor influencing

model terminal velocity is the distance of the backface of the model in the gun barrel from the breech prior to launch. The farther this distance, the more volume the gun gas has to expand, the lower the pressure on the model backface at launch and lower model velocity at impact. A fixed length of nylon string was used to suspend the model at a nominal 18 inches from a tie bar in the gun breech, but doubling the string and tying of knots in the string in the restricted space between the end of the pressure chamber and the gun barrel produced inconsistencies in model location.

The strain gage data is shown in Figures V.87 through V.89 for shot 35 as axial strain versus time. These plots were made by converting the digital voltage output to stress from the calibration curve and dividing by a modulus of $6.5(10^6)$ psi. The tilt angle at impact based on time of arrival of the strain pulses at the three axial locations was at best 0.0 degrees and at worst 0.119 degrees. The wave arrived first at gage 3¹, then at gages 1 and 2 simultaneously. The limiting cases on tilt angle are based on maximum errors introduced by digitizing the data at finite intervals of time, and include not only errors in the recorded

¹See Figure IV.6 for gage locations

data but also in the calibrations of the transient recorders. Using the worst case (lowest) velocity of 90 ft/sec for the gun pressure at launch, the tilt angle of 0.119 degrees yields the lowest rate of closure of the impact face on the water surface as 521,800 inches per second, which is **larger** than the stress wave propagation velocity in the magnesium bar. Thus the impact face senses a flat impact with the associated high level of stress which would be obtained by Hugoniot matching techniques. However, the plane of the leading disturbance in the bar is inclined at an angle with respect to the impact face. The slope of the inclination angle of the leading disturbance is equal to the ratio of the stress propagation velocity in the bar to the closure velocity. For example, if the closure velocity equals the stress propagation velocity, then the angle is 45 degrees. This ~~plane~~ of initial disturbance will cause unequal response at different circumferential angles for a given radial and axial location in the bar. This is one cause for the differences in the response of the front three gages of shot 35. As the disturbance moves down the bar, the effect of radial relief waves should produce a more uniform response at a given axial location.

Another cause of the unequal response characteristics of the three front gages is due to the pins which hold the front bore rider on the bar. They are located one inch ahead of the gages. These 1/4 inch diameter pins are made of the same material as the bar and extend into the bar 3/16 of an inch. The fit between the pin and the hole in the bar is a wringing fit in which nominally the pin and hole are exactly the same diameter. A slight force was required to press these pins in place. The pins were made with a wringing fit to minimize internal stress wave reflections from the free surface created by the pin holes in the bar. Originally two pins were put in the bar and these of course could not be placed symmetrical with the three gages. Just prior to making the series of data shots (shot 27 on) three pins were used to lessen the stress on the holes in the polyethylene bore rider so the two pins already in place were cutoff at the outside diameter of the bar and left in the bar. Reflections of stress waves off these asymmetrically located pins can cause the nonuniform response characteristics of the three front gages.

The axial strain pulses for shot 35 are generally similar but have different rise times, magnitudes, and durations. Rise time is defined here as the time from the

initial arrival of the pulse to a time at which either a decrease or leveling off of stress occurs. Duration of the pulse is defined as the total time of the compressive part of the strain pulse. The response of gage 1 (Figure V.87) has a rise time of 5.4 μsec , a duration of 28.8 μsec and a maximum strain of 661 $\mu\text{in/in}$. The response of gage 2 has a rise time of 2.4 μsec , a duration of 40.1 μsec and a maximum strain of 702 $\mu\text{in/in}$. Gage 3 has a rise time of 5.9 μsec , a duration of 31.3 μsec , and a maximum strain of only 575 $\mu\text{in/in}$. Gages 1 and 3 responses are similar with approximately the same frequency of oscillations about an average, "plateau" strain level, and similar shapes in the unloading phase down to zero strain. The response of gage 2 is quite different from that of 1 and 3, having an initial, very large rise in strain, and then a dropoff to a plateau with higher frequency, lower amplitude oscillations about the plateau than the other two gages. The dropoff in strain from the plateau level at gage 2 is also different from the other two gages. After decreasing from the plateau stress, the strain oscillates about a lower magnitude plateau stress for about 15 μsec before going to zero.

No trigger pulse was received by the strain gage recording devices for shot 36; consequently no data was obtained. The impact velocity for shot 37 was 91.7 ft/sec and data from all six strain gages were obtained (Figures V.90 through V.95). The bounds on the tilt angle are .17 and .30 degrees with the closure velocity of the impact face being approximately equal to the dilatational wave velocity in the bar. The sequence of arrival of the wave at the gage was 1-3-2. The strain pulses at the front three gages were similar to the corresponding gage responses in shot 35. For gages 1, 2, and 3 the rise times were 3.9, 2.0, and 4.4 μ sec respectively, the durations were 43.0, 40.6, and 29.8 μ sec respectively, and the maximum strain values were 602, 815, and 646 μ in/in, respectively. Again, as in shot 35, gages 1 and 3 exhibited lower frequency oscillations about the plateau stress than gage 2. However, the amplitudes of these oscillations were larger for gage 2 in this shot than in shot 35. The average plateau strains are different for each of the three gages, increasing in magnitude in the same order as the arrival of the stress wave: 1-3-2. Also in this shot, gage 1 response has a small duration of low level strain at the tail end of the pulse (from 39 to 53 μ sec in Figure V.90), whereas in shot 35, this behavior was not obtained.

The response of the three gages at the mid-length of the bar for shot 37, shown in Figures V.93 through V.95, are characterized by longer rise times and a more flat-topped pulse than the three forward gages. For gages 4, 5, and 6 the rise times are 22.8, 18.6, and 18.1 μ sec, respectively, the durations are 42.9, 43.0, and greater than 44.9 μ sec, respectively, and the maximum strains are 467, 514, and 461 μ in/in, respectively. Gages 1 and 4 are located at the same circumferential angle on the bar. Gages 2 and 5 also have the same angle, as do 3 and 6. Just as the second gage in the front triad of gages has the maximum strain, so does the second gage in the rear triad. The plateau levels of strain for the rear gages are below the average plateau values for the front gages. Thus in traveling down the bar, the strain pulse is slightly attenuated in magnitude and spreads out into a longer rising pulse.

The calculated axial stress for the impact of a magnesium ZK60A-T5 bar on a flat surface of water at 91.7 ft/sec is 5530 psi. Using equations (II-58) and (II-59), the one dimensional axial strain at the impact face is 530 μ in/in. From Figures V.90 through V.92 it is seen that at one diameter from the impact face the average plateau strain is approximately this value, but there are large oscillatory axial strains superposed on it. At the location of the rear triad of gages, 7.2 diameters from the impact

face, the maximum strain response is lower than the uniaxial impact strain.

The impact velocity for shot 38 was 156 ft/sec. The recorded arrival times of the wave at each of the front gages are exactly the same, indicating a perfectly flat impact. However, due to possible errors from digitizing the data over a finite time interval, the tilt angle could have been a maximum of 0.11 degrees. The calculated closure velocity is 956,632 in/sec. The effects of the low tilt angle are seen in Figures V.96 through V.98 where the response of the forward three strain gages are nearly identical. The frequency of the oscillations about the plateau strain level is smaller for the gage 2 response than it is for the previous shots. For gages 1, 2, and 3 the rise times are 2.4, 2.0, and 4.4 μ sec, respectively, the durations are 43.0, 48.4, and 30.3 μ sec respectively, and the maximum strains are 1019, 1162, and 1160 μ in/in, respectively. In Figure V.98 for gage 3, after the strain drops off from a large magnitude, it goes through zero and then comes back up to a smaller plateau of strain than the original pulse. If this small plateau portion is included in the length of the primary pulse, then the duration is 44.5 μ sec, which agrees with the duration of the other two gages.

The axial strain versus time measurements for the rear triad of gages for shot 38 are shown in Figures V.99 through V.101. The complete duration of the primary pulse was not obtained on the oscilloscope for gages 4 and 5. The duration of the pulse on gage 6 is 35.5 μsec . If the additional small level of strain at the tail of the primary pulse of gage 6 is included in the duration calculation, just as was done for the gage at the corresponding circumferential location at the front of the bar, then the pulse duration is 43.0 μsec . For gages 4, 5, and 6 the rise times are 18.1, 17.5, and 17.8 μsec , respectively and the maximum strains are 807, 898, and 935 $\mu\text{in/in}$, respectively. Unlike the responses of the front triad of gages, these rear gage responses are not all similar. The response of gage number 4 for shot 38 is lower than the responses of gages 5 and 6. One explanation is a possible problem in the recording oscilloscope, perhaps in balancing the amplifier before the shot, or in the calibration procedure. The same general conclusions can be drawn as to the change in strain pulse with axial location, as is done for shot 37. As the wave moves down the bar, the axial strain pulse is slightly attenuated in magnitude, and has a longer rise time and slightly longer duration.

The calculated axial stress for a 156 ft/sec impact is 9618 psi which corresponds to a one dimensional strain state of 922 $\mu\text{in/in}$. The average 'plateau level of the front three gages is below this level, although the superposed peaks are well above it. Again the rear gages are below the 922 $\mu\text{in/in}$ level.

The velocity for shot 39 was 145.5 ft/sec. Data was obtained from all strain gages except gage 1 (Figures V.102 through V.106). Without gage 1 data, a tilt angle cannot be obtained. Nominally the tilt angle is nonzero because the beginning of the response of gage 2 occurs 0.5 μsec later than the beginning of the gage 3 response. The initial rise in the gage 2 response (Figure V.102) seems to have been clipped. The response of this gage is somewhat different for this shot than in previous shots. Three distinct oscillations occur about the plateau just as in the response of gage 3 (Figure V.103). In previous shots, gage number 2 demonstrated more oscillations than the other two front gages. For gages 2 and 3, the rise times are 4.4 and 4.9 μsec , respectively, the durations are 29.8 and 44.5 μsec , respectively, and the maximum strains are 1031 and 979 $\mu\text{in/in}$, respectively. The difference in duration times is due again to the trailing, low amplitude strain pulse behind the primary pulse.

The axial strains from the rear triad of gages are shown in Figures V.104 through V.106. Gages 4, 5, and 6 have rise times of 19.8, 21.4, and 25.3 μ sec, respectively, durations of 38.6, 38.5, and 39.3 μ sec, respectively, and maximum strains of 765, 804, and 705, respectively. The response of gage number 5 is generally larger than the other two gages.

The calculated axial stress from a 145.5 ft/sec impact is 8932 psi and this corresponds to a one dimensional axial strain of 856 μ in/in. The shot 39 front gage data oscillates around approximately this level whereas the rear gage data are well below it.

3. Mitigated Shot Data

A 2.5 inch diameter by 1.25 inch long nose made of rigid polyurethane foam was taped onto the front end of the 2.5 inch diameter semiconductor gage model to obtain experimental data on the mitigating effect of a crushable nose. Two different densities were used in these shots, 5 and 15 pounds per cubic feet (pcf). Data was obtained on similar foam material by Hinckley (Reference 22). The stress-strain response of this material basically consists of a linear elastic region, a small region of nonlinear elastic response up to a yield stress, and then a decrease to a plateau stress. The plateau stress remains essentially

constant out to a large strain (approximately 50%) at which point the pores in the material collapse and locking occurs. For the locked material, the elastic modulus is much higher than for the foam material. Equations were derived in Reference 23 for the modulus E , yield stress σ_y , and plateau stress σ_p as a function of the rigid polyurethane foam density. Using these equations, the following values are obtained for the two foam densities used in this experimental work:

$$\left. \begin{aligned} E &= 3548 \text{ psi} \\ \sigma_y &= 152.7 + 5.4 \ln \dot{\epsilon} \text{ psi} \\ \sigma_p &= 131.9 + 4.6 \ln \dot{\epsilon} \text{ psi} \end{aligned} \right\} \text{ for } \rho = 5 \text{ pcf (V-1)}$$

$$\left. \begin{aligned} E &= 22,966 \text{ psi} \\ \sigma_y &= 925.2 + 32.7 \ln \dot{\epsilon} \text{ psi} \\ \sigma_p &= 844.5 + 29.7 \ln \dot{\epsilon} \text{ psi} \end{aligned} \right\} \text{ for } \rho = 15 \text{ pcf (V-2)}$$

where $\dot{\epsilon}$ is the strain rate in in/in/sec.

Eight shots (40 through 47) were made with foam mitigators at the end of the program. Data were not obtained on shots 41 and 46. Shot 40 had a 15 pcf foam nose on the model that was shot through the thin mylar diaphragm at the muzzle of the gun barrel. A photograph of the model just prior to impact showed that the foam nose sheared the mylar diaphragm without sustaining any damage. On shot 41, a 5 pcf foam nose was used, so to avoid any damage to the nose prior to water impact, a diaphragm was

not placed on the gun barrel. Therefore, the air in the gun barrel ahead of the model prior to launch was at the vacuum chamber pressure. All subsequent shots were made without the gun barrel diaphragm. Shots 42, 43, and 44 were made with a 5 pcf foam nose and shots 40, 45, and 47 were made with a 15 pcf foam nose. Only the first 200 μ sec of the recorded pulses for all of these shots represent valid water impact data. After this time, reflections from the vacuum chamber diaphragm shown in Figure IV.4 reach the impact face and interfere with the loading pulse. The tensile strain data shown in the plotted data from the foam shots which comes from waves reflecting off the rear end of the model is only approximate since the compressive calibration data was applied to the negative voltage values that were recorded. No tensile calibration was made.

The impact velocity for shot number 40 was 146 ft/sec. The voltage sensitivity settings on the transient recorders were set too low for this shot, so gage 1 and 3 recordings were saturated. Part of the pulse for gage 2, shown in Figure V.107, has been clipped. The response of gages 4, 5, and 6 are shown in Figures V.108 through V.110. The oscilloscopes trigger delay was set for too long a time so the rise in the pulses at the rear triad of gages was not obtained. The recorded maximum strain for gage 2

is 245 $\mu\text{in/in}$. The actual maximum might have been larger. The rise time to this peak strain is 45.9 μsec and nothing can be stated about the duration since it is longer than the 200 μsec of valid recording time. The three strain plots of the rear gage data for shot 40 exhibit very erratic behavior, with gage 5 having a maximum strain twice as large as the maximum strain for gage 4. The reason for this behavior is probably due to the recording and does not actually exist in the bar. The maximum strains for gages 4, 5, and 6 are 84, 173, and 126 $\mu\text{in/in}$, respectively. Comparing the results of this shot with the unmitigated shot 39 at essentially the same velocity shows that a reduction in strain of approximately 76 percent is achieved at one diameter from the impact face with the 15 pcf foam at 146 ft/sec. Comparing corresponding axial strain response for the rear triad of gages, a reduction of 78 percent is achieved for this velocity.

Shot 45 had a 15 pcf foam nose and the impact velocity was 132.2 ft/sec. The only recorded data was from gage 4 but the magnitude was extremely low. Examination of the shot photograph showed disturbance of the water surface prior to impact, so the data were discarded. Shot 47 was a shot at 103.3 ft/sec with a 15 pcf foam nose. The data on gage 2 saturated the transient recorder channel. The

response of gages 1 and 3, shown in Figures V.111 and V.112, has been partially clipped and only 133 μ sec of the data pulse was obtained because the trigger pulse for recording these data occurred slightly late. The shot photograph, Figure V.113, indicates no disturbance of the water surface prior to impact. The maximum strains for gages 1 and 3 are 157 and 151 μ in/in, respectively. The rise times of these pulses are 15.6 and 17.6 μ sec, respectively, and are much smaller than the corresponding rise times of the axial strain pulses from shot 40 at a higher velocity. The reason is probably that the 15 pcf foam is responding elastically or with little plastic deformation at an impact velocity of 103.3 ft/sec but at 146 ft/sec, it undergoes large plastic strains. Neglecting the tangential stress component in the axial strain response at the front gages, the maximum transmitted axial stress at the axial location of the front triad of gages may be calculated. For shot 40, it is 1593 psi and for shot 47 it is 1021 psi. From the formulas (V.2) for yield and plateau stress, it is seen that only under astronomically large strain rates would the stresses in shot 40 not exceed the yield and plateau stresses. For shot 47, the stresses are approximately the same as the yield and plateau stresses. It is difficult to estimate the strain in the foam nose due to impact and the magnitudes due to the interactions that occur at the interface between the foam and the magnesium. An analysis of this problem would require a

treatise on two dimensional elastic-plastic, strain-rate dependent wave propagation with a study on the interaction at the water-foam and foam-bar interfaces. This is beyond the scope of this study.

The axial strain response at the rear triad of gages on the magnesium bar for shot 47 are shown in Figures V.114 through V.116. The comparative response among the three gages is erratic. The maximum strain from each gage ranges from 118 to 185 $\mu\text{in/in}$. The rise times are consistent-- 32.8, 32.4, and 34.4 μsec for gages 4, 5, and 6, respectively. The response of gage 5 appears unreasonable since it is larger in magnitude than the response at the front gages. The magnitudes are the same if not larger than the magnitudes of the corresponding gages in the shot 40 data. The difference is due to either experimental error or possibly the response of the foam is in different regimes of the stress-strain curve. In shot 47 the stress in the foam is around the yield stress whereas in shot 40 the stress is at the lower plateau value.

Shots 42, 43, and 44 were made with 5 pcf foam noses. No photographic data of the water surface condition prior to impact were obtained in any of these shots so caution should be exercised in interpretation of the following data. The magnitudes might represent the response

from impact on a disturbed water surface since no diaphragm was used on the gun barrel. Of the shots without a barrel diaphragm in which photographic data was obtained (shots 45, 46, and 47), only one showed any water disturbance and since the magnitudes of the strains from shots 42, 43, and 44 are consistent, it is believed that the impact conditions of these latter shots are acceptable. The impact velocities of shots 42, 43, and 44 were 103, 105, and 133 ft/sec, respectively. The axial strain gage data for these shots are shown in Figures V.117 through V.128. The maximum strain values and rise times for each one of these plots are given in Table V.3. There is not a statistically significant variation in magnitude from shot to shot except for the strain response of gage 6 in shot 44, which is small. The magnitudes of the strains at the rear gages appears to be larger (except for gage 6, shot 44). There is evidence of the pulse spreading out in duration as it moves down the bar. The differences in rise times of gages 5 and 6 between shots 42 and 43 are due to a slightly different wave shape at the peak of the rise of the pulse. It appears that at the velocities of these three shots, 103 to 133 ft/sec, the 5 pcf foam nose is undergoing deformation at the plateau stress. The flat-topped pulses in these data indicate that a constant stress

NSWC/WOL TR 77-128

Shot 42 Shot 43 Shot 44
(103 ft/sec) (105 ft/sec) (133 ft/sec)

<u>Gage</u>	<u>Maximum strain (μin/in)</u>		
#1	--	29	34
#2	--	25	28
#3	--	28	28
#4	--	--	--
#5	32	36	34
#6	30	26	16
<u>Gage</u>	<u>Rise time (μsec)</u>		
#1	--	19.6	17.6
#2	--	18.6	16.6
#3	--	26.4	16.6
#4	--	--	--
#5	27.1	39.2	--
#6	29.2	46.2	--

TABLE V.3 - MAXIMUM STRAINS AND PULSE RISE TIMES FOR 5 PCF
FOAM NOSE SHOTS

is being transmitted to the bar. In the magnesium bar 30 $\mu\text{in/in}$ of strain translates to an axial stress of 195 psi if the circumferential stress component is neglected in the axial strain. From the equations (V.1), this is slightly larger than the value of the plateau stress.

The maximum strain amplitudes of the response of the semiconductor gages at the mid-length of the 2.5 inch diameter magnesium bar are plotted in Figure V.129 for all data shots. The strain ranges shown represent the bounds on the maximum values for each gage at this axial location. Also shown on this plot is the calculated one dimensional axial strain developed at the impact face of an unmitigated bar. The effect of the rigid polyurethane foam noses can clearly be seen. The difference from using different foam densities can also be seen. The mitigating effect of the foam noses is only valid over the range of velocities shown. At higher velocities, locking will occur in the foam and transmitted stresses to the bar will increase. No attempt was made to plot the results from the three gages at one diameter from the impact face. The somewhat erratic maximum values due to the oscillations on the high level plateau of the strain pulse would produce a misleading plot.

C. Comparison of Analytical and Experimental Results

The computed axial strain histories at the forward location of the strain gages on each model have been plotted along with the experimental data from the unmitigated bar shots. For experimental impact velocities that are much different than the impact velocities for the computer runs, the calculated results are scaled by the ratio of the theoretical impact pressures. The comparison of computer cases 1 and 2, which is discussed in section A of this chapter, indicates that scaling of the analytical results may be done with good accuracy over the limited velocity range considered in this study.

1. The 2.75 Inch Diameter Bar

The experimental data from the unmitigated 2.75 inch diameter bar shots are plotted in Figures V.130 through V.132 along with the differences of the computed axial and circumferential stresses at 2.475 inches from the impact face. The gage location was 2.5 inches from the impact face. The agreement is generally good. The maximum value of stress for each shot agrees very well with the computed maximum stress. However, the initial peak in the experimental data pulse is not present in the computed stress response. The experimental pulses display

three predominant oscillations about the plateau stress, but these oscillations are not present in the computed pulse. The unloading portion of the computed stress pulse is more gradual than the abrupt drop in the experimental data. The smooth calculated response is probably due to the very coarse discretization grid used to represent the functional variation of variables in the bar. Only eleven grid lines were used between the axis and the radial boundary. With too coarse a grid, sharp stress wave fronts are smeared over a large distance.

2. The 2.5 Inch Diameter Bar

The comparisons of the analytical and experimental axial strain histories at one diameter from the impact face on the radial surface of the 2.5 inch diameter bar are given in Figures V.133 through V.140. The experimental data are from the three individually monitored strain gages located 120 circumferential degrees apart. Since the theoretical analysis is axisymmetric, the computed strain pulses at all locations for each shot are the same. The time from impact to the time of arrival of the initial disturbance at the gages was not measured. Only relative arrival times at the three gages was measured. Therefore, an arbitrary time on the experimental data was taken to coincide with the computed arrival time of the initial disturbance and all succeeding data is plotted relative to this time.

In Figures V.133 through V.135, the experimental data for shot 37 with an impact velocity of 91.7 ft/sec are plotted with the calculated axial strain response from a 96 ft/sec impact velocity. The calculated axial strain response exhibits three low amplitude oscillations at the top of the pulse, which the 2.75 inch diameter bar response did not exhibit. The discretization mesh for this run is half as coarse as the mesh for the 2.75 inch diameter bar. The finer mesh is providing more definition of wave fronts. A mesh finer than 21 radial grid lines might provide even more amplitude to the oscillations and yield a much closer agreement with the experimental data. The agreement in magnitude is good for mean plateau strain but the large amplitude oscillations present in the experimental data that contribute to maximum strain values have much smaller amplitudes in the computed data.

The calculated tilt angle for shot 37 is relatively large; that is, the closure velocity of the impact face is approximately equal to the dilatational wave speed in the bar. The effect of the large tilt angle can be seen in the rise times of the response of the three strain gages. The rise in the strain pulse of gage 1 agrees exactly with the calculated pulse in Figure V.133.

Gage 2 has a smaller rise time than the computed response (Figure V.134) and gage 3 has a larger rise time than the computed response (Figure V.135). Associated with this order of rise times is a relationship between comparison of initial peaks. Gage 2 has a much faster response than the calculated pulse and also has a much larger first peak in the experimental pulse. Gage 3 responds slower and has a lower-amplitude first peak. Gage 1 response agrees reasonably well with the computed response up to the first peak in the experimental data. The dropoff in the computed strain from the higher level is not in exact agreement with the experimental data and this could also be effected by the tilt angle.

The comparisons for shot 38 are shown in Figures V.136 through V.138. The calculated tilt angle for this shot is small. The rate of the initial rise in strain and the first peak amplitude of gage 2 are larger than the corresponding values of the computed strain pulse. The rise times of gages 1 and 3 are nearly the same as the computed rise time. The comparisons for shot 39 are shown in Figures V.139 and V.140. The first peak in the response of gage 2 appears to have been clipped by the transient recorder digitizing circuitry so the agreement in magnitudes is not as good as shown.

The computer runs discussed in section A of this chapter were not run long enough in simulated real time to obtain the maximum axial strain at the mid-length of the bar. Therefore, a direct comparison of the computed response and the experimental strain gage data at this location is not possible. The trends in the maximum amplitude (Figure V.141) and rise time (Figure V.142) of the computed axial strain pulse at various locations away from the impact face may be examined and compared to the experimental data at 7.2 diameters from the impact face of the 2.5 inch diameter bar. The data from the rear gages in shots 37, 38, and 39 are characterized by slightly lower amplitudes and longer rise times than the front gages. The recorded rise times at the rear gages range from 17.5 to 25.3 μ sec. The rise times of the computed strain pulses as plotted in Figure V.142 refer to the time from the initial disturbance to the time of the maximum strain. The strain pulse near the impact face has a fast rise to a maximum strain and then a gradual dropoff in strain. Between .75 and .90 of a diameter from the impact face the pulse is essentially flat-topped and at one diameter the maximum strain occurs late in the pulse as seen in Figures V.133 through V.139. Farther down the bar,

the pulse shape becomes more like the experimental data pulse from the rear gages. In Figure V.142, the rise time appears to be approaching an asymptote. The actual values of the rise times of the calculated pulses for the 2.5 inch diameter bar are lower than those for the 2.75 inch diameter bar at a corresponding location. The differences are due to either the diameter difference or the discretization mesh sizes used in the computer runs. The difference in radii of the two bars is very small and the coarser mesh of the 2.75 inch diameter bar contributes to smearing of waves so the actual values from the 2.5 inch diameter run are probably more accurate. At two diameters from the impact face, the rise time of the strain pulse is 18.3 μ sec and appears to be leveling off. The calculated maximum strain at 2 and 2.5 diameters from the impact face is much higher than the value at one diameter as seen in Figure V.141. However, the computed value for the 2.75 inch diameter bar at 2.5 diameters from the impact face is lower than the value at 2 diameters away. Even though, the exact values may be in error because of the coarse discretization mesh, the trend is probably valid. Computer runs should be made in follow-up studies to obtain the strain response at later simulated real times and with different discretization mesh sizes to investigate the numerical sensitivities of the method.

D. Comparison with Waser's Data

In Reference 10, a 2.75 inch diameter magnesium rod was launched with a vented gun barrel into an open tank at normal impact. Foil gages were mounted in a four active-arm Wheatstone bridge configuration, as shown in Figure V.7a, at 12 inches (4.4 diameters) from the impact face. At this axial location the analytical results indicate that a circumferential component of stress exists at the time of maximum stress so the data represent the measured maximum difference of axial and circumferential stresses. These data are plotted in Figure V.143 along with the data from the present study. Also plotted in this Figure is the theoretical axial impact stress and the theoretical stress difference ($\sigma_z - \sigma_\theta$) at impact. The stress difference is just $\left(\frac{1 - 2\nu}{1 - \nu}\right)$ times the axial impact stress. The difference between the Reference 10 data and the theoretical axial impact stress curve is the cause for concern in one dimensional stress analyses of the water impact problem. However, the computer results in section A of this chapter substantiated by the reasonably good agreement with experimental data indicate that two dimensional effects cause a reduction in the equivalent stress measured at points on the radial boundary with a Wheatstone bridge configuration.

The data from the present study and reference 10 agree quite well even though the axial locations of the

gage arrays are different. The maximum stress at 12 inches from the impact face of the 2.75 inch diameter bar was not obtained but the trends of the computer results may be used to explain the data agreement. The maximum axial stress at 2.75 inches from the impact face (Figure V.67) is lower than the maximum stress at points farther down the bar (Figure V.69). However, the circumferential stress at the times of maximum axial stress is a larger compressive value at 2.75 inches than at points farther down the bar. Thus the maximum difference of axial and compressive stresses at the two locations of measurement in Figure V.143 are nearly the same for a given impact velocity.

CHAPTER VI

CONCLUSIONS AND RECOMMENDATIONS FOR FURTHER WORK

The analytical and experimental results of Chapter V demonstrate the complicated two dimensional stress wave interactions that occur in an elastic bar from normal impact on water. It is the radial relief waves in the bar that decrease the magnitude of the axial stress at locations away from the impact face and not the cushion of air between the bar and water at impact. Comparison of the calculated axial strain response on the radial boundary of the bar near the impact face and the experimental data from strain gages at the same location indicates the analytical model, in general, adequately predicts the impact phenomenon and the subsequent wave propagation in the impact bar. There are discrepancies between the computed and experimental strain response in the unloading portion of the pulse and in the amplitude of the oscillations that occur about the average plateau strain level of the pulse. These discrepancies are believed to be caused by the numerical approximations in the computer calculations and the non-normal experimental water impacts. Computer results for the two slightly different diameter bars and for discretization mesh sizes that differed by a factor of two, show that the finer mesh yields a strain pulse with

three oscillations about an average strain level. Although the amplitude of these oscillations is not in agreement with the experimental data, further mesh refinement could produce better agreement. The number of oscillations in the experimental data pulses varies from gage to gage for most shots but generally there are three oscillations with peaks separated by the period of radial relief waves in the bar. Additional oscillations in the strain gage data could be caused from non-normal impact or strain gage errors.

Experimental data at two axial locations on the unmitigated 2.5 inch diameter bar demonstrate the change in character of the axial strain pulse as it travels down the rod. From 1.0 diameter to 7.2 diameters from the impact face, the rise time of the pulse increases, the duration remains constant, and the magnitude decreases. The computed results show the increase in rise time of the pulse with increasing axial distance from the impact face, but data for late times after impact are not available for a full comparison.

Computer results indicate that large axial compressive stresses develop in a region just behind the impact face about $17 \mu\text{sec}$ after impact. The cause of this high stress region is the reflection of tensile radial relief

waves from the bar-water interface as compressive waves which augment the existing compressive state from the impact. The larger wave propagation velocity in the bar, the decoupling of shear displacements at the interface, and the lower mechanical impedance of water contribute to this effect. The previously used method of a uniformly loaded impact face and one dimensional stress wave propagation in the bar does not predict the amplification of stress near the impact face and over-predicts the magnitude of the one dimensional stress wave that is formed farther down the bar. Furthermore, the capability of predicting multi-axial stress states and determining the location of onset of yielding in a solid bar from normal water impact is now available.

Scaling of the calculated results for a given bar material and diameter by the ratio of impact pressures is possible for velocities in the range covered in this study. The reason is that the wave propagation velocities in the bar are constant because the response is elastic and the sound propagation in water does not change very much over the velocity range. Higher velocity response will require further studies and the addition of shock wave modeling in the water response.

Experimental data from water impacts with two densities of rigid polyurethane foam noses on the elastic bar show a substantial stress reduction in the bar. The transmitted

stress from the 5 pound per cubic foot (pcf) foam is much lower than that from the 15 pcf foam. Over the velocity range of the shots, the response indicates that the pore collapse mechanism of foam behavior is taking place, whereby straining of the foam occurs at a fairly constant level of stress, called the plateau stress. Plateau stress is a function of foam density to the 1.69 power so the lower density foam transmits the lower stress to the elastic bar. Higher velocities would cause foam locking and associated substantial increases in transmitted stress.

The problem of the normal impact of a solid elastic bar on water has just begun to be understood with the results of this two dimensional wave propagation study. Much more work needs to be done to extend this knowledge. With the present FLEBOW computer program, numerical studies must be conducted to ascertain the optimum modeling parameters for the problem. In particular, one or more computer runs must be made for a 2.5 inch diameter magnesium bar with a more refined mesh than is used in the present study. By comparing results with computer case number 1 of this study, some statement about the convergence of the numerical scheme may be made. Another numerical study should be conducted on the stability criterion for elastic wave propagation in the bar and on the iteration control parameter for the calculations at the water grid points.

The response at higher velocities should be investigated analytically and experimentally. Experimentally, at higher velocities there is a problem in obtaining strain gage data with a trailing wire because of breakage. Telemetry could possibly be used for data acquisition. Instead of monitoring strain at three circumferential locations at the mid-length of the bar, these three gages should be placed, one each at various axial locations, to obtain the change in the strain pulse as a function of distance from the impact face. Analytically, obtaining the response at higher impact velocities requires the modeling of the shock wave propagation in water which is formed at impact. If this feature is added to the computer code, it would be interesting to compare the difference in response of a given impact bar at a given impact velocity, with and without the inclusion of the shock wave.

Some attempt should be made to obtain analytical results for impacts very close, but not equal to 90 degrees to the impact surface. The non-normal impact of a circular bar is a fully three dimensional problem and is impractical to solve numerically with the present generation of computers. Mark Wilkens of Lawrence Livermore Laboratory has developed a three dimensional version of the HEMP computer code (Reference 23), which requires the new generation computer

CDC STAR and is not available to the general public at this time. However, the two dimensional HEMP code (Reference 4) may be used to gain insight into the tilt problem by modeling the impact of an "infinitely deep" bar of finite width. Even though the Lagrangian zoning scheme used in this code poses problems in the water impact problem, early time response should be attainable and comparisons of response near the impact face for various small tilt angles might explain the differences between strain gage data and calculated data from this study.

A final recommendation for further analytical work is the modeling of the water impact of a bar with a rigid polyurethane foam nose. This problem is extremely difficult because the behavior of the foam is elastic-plastic-locking with finite strains and strain rate dependent properties. Not only does the modeling of the phenomenon require a large developmental effort, but a material characterization program is required. Some data is available in the literature on quasi-static and dynamic uniaxial stress response and on quasi-static multi-axial stress loading. However, multi-axial dynamic material response data in various tension-compression combination states including strain rate variations, and dynamic unloading data are required for a detailed analysis.

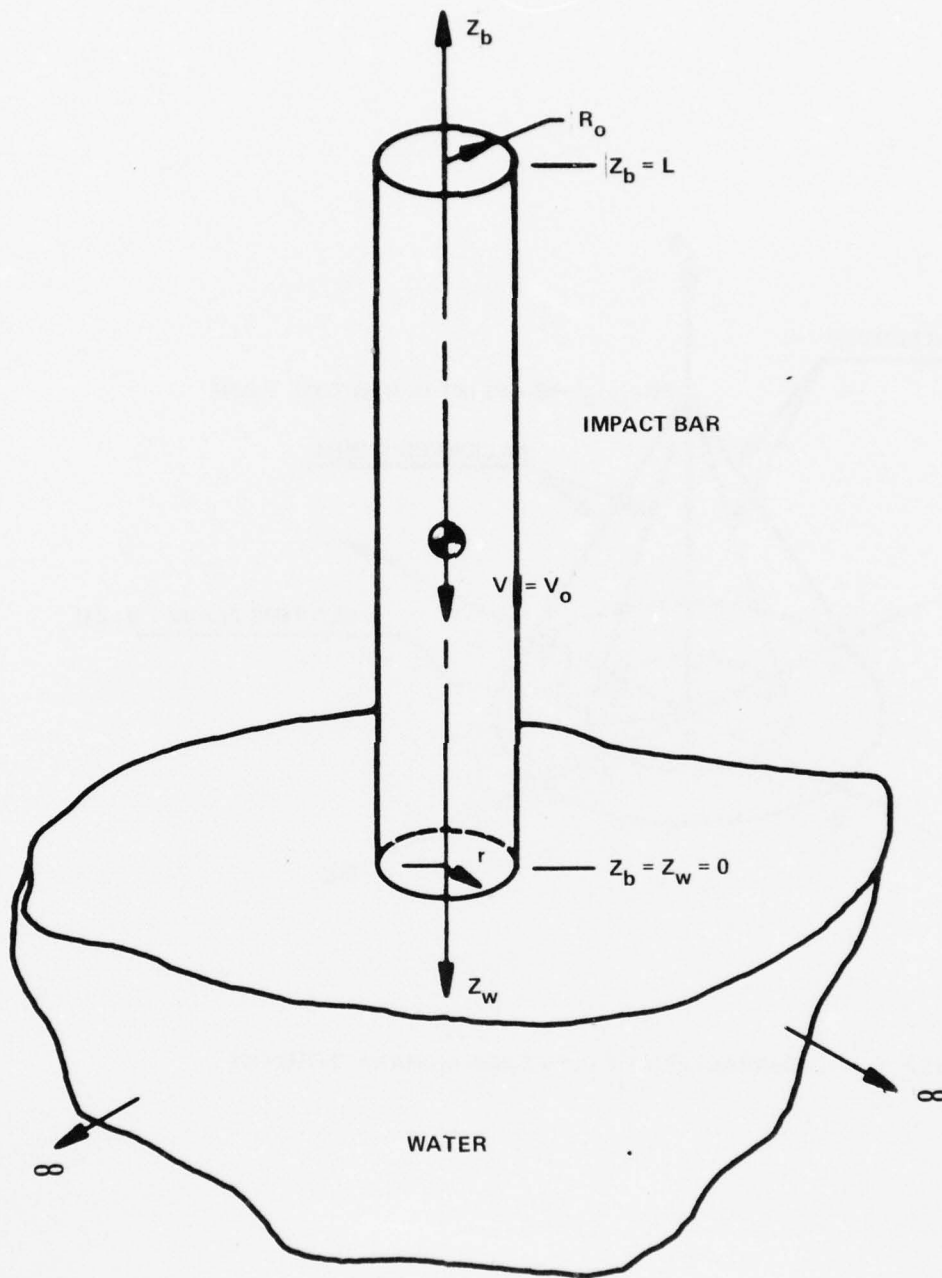


FIGURE II.1 NORMAL IMPACT OF A FINITE LENGTH ELASTIC BAR ON A SEMI-INFINITE SMOOTH SURFACE

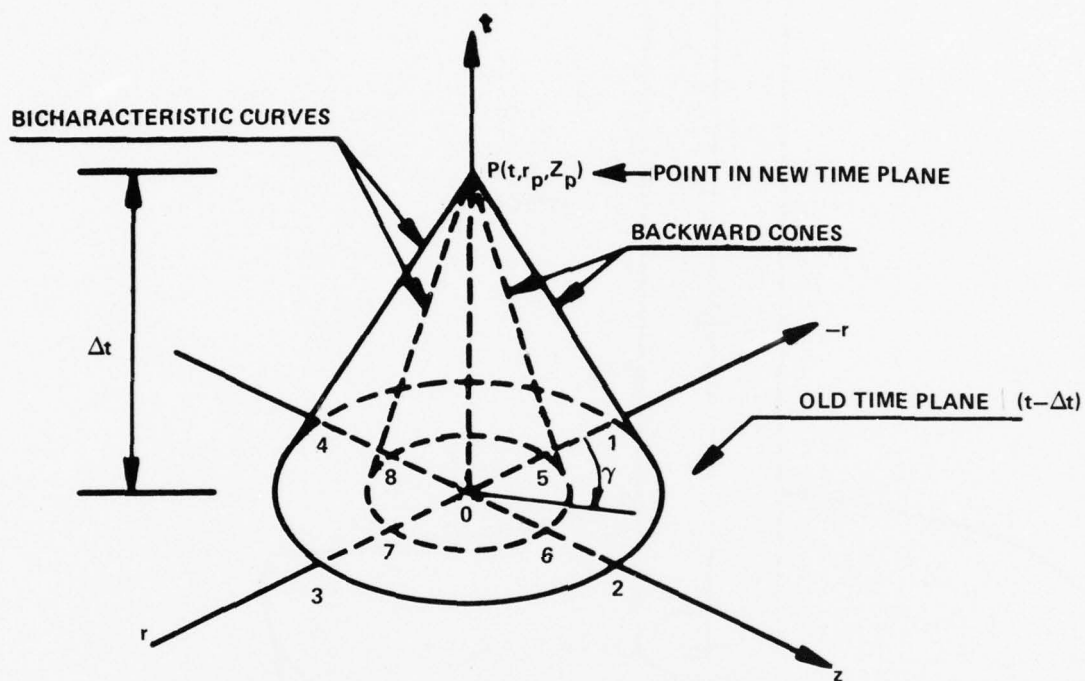
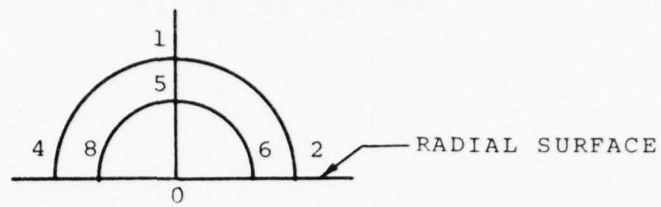
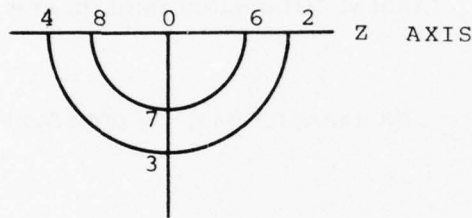


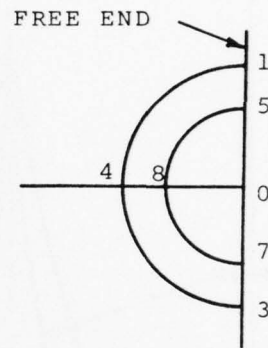
FIGURE II.2 CHARACTERISTIC CONES AND BICHARACTERISTICS



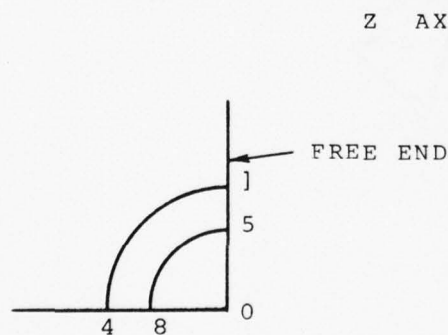
A.) AT THE RADIAL SURFACE



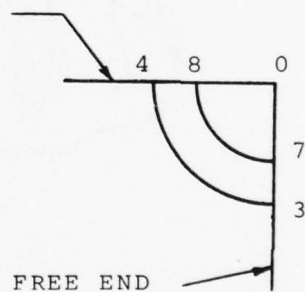
B.) ALONG THE Z AXIS



C.) AT THE FREE END



D.) AT THE CORNER OF THE
FREE END



E.) AT THE CENTER OF THE
FREE END

FIGURE II.3 - CHARACTERISTIC CONES AT THE BOUNDARIES
OF THE IMPACT BAR

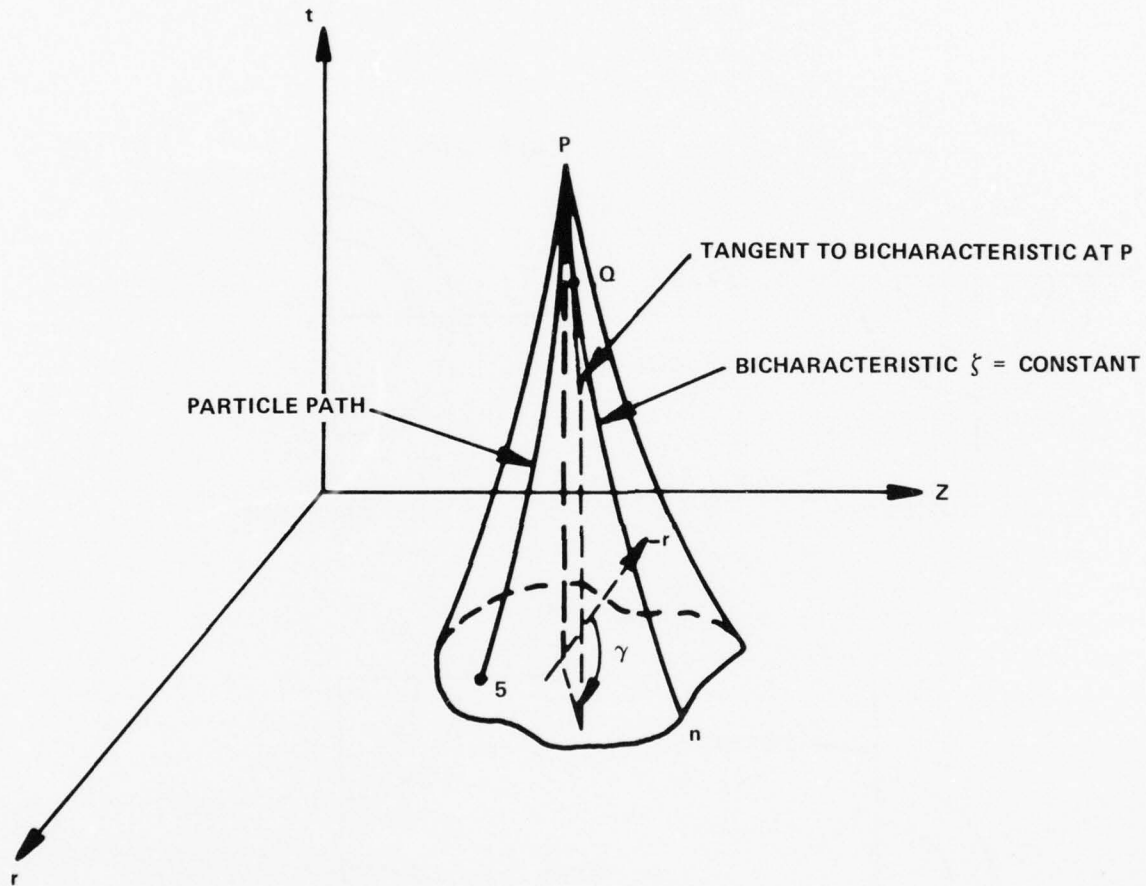
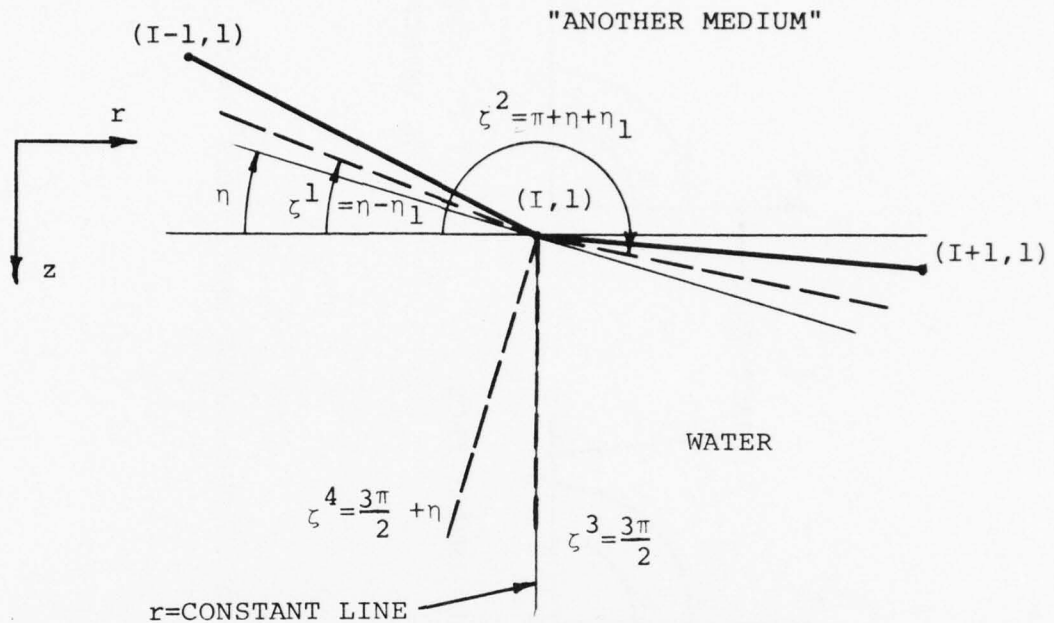


FIGURE II.4 CHARACTERISTIC CONOID FOR HYDRODYNAMIC
NONLINEAR WAVE PROPAGATION



LEGEND: $---$ rz PLANE PROJECTION OF TANGENT TO
BICHARACTERISTIC AT THE POINT $(I, 1)$
IN THE NEW TIME PLANE

$\bullet---$ FREE SURFACE LINE ELEMENT IN THE
OLD TIME PLANE

FIGURE II.5 - PLANVIEW OF RZ PLANE SHOWING BICHARACTERISTIC SCHEME AT WATER BOUNDARY

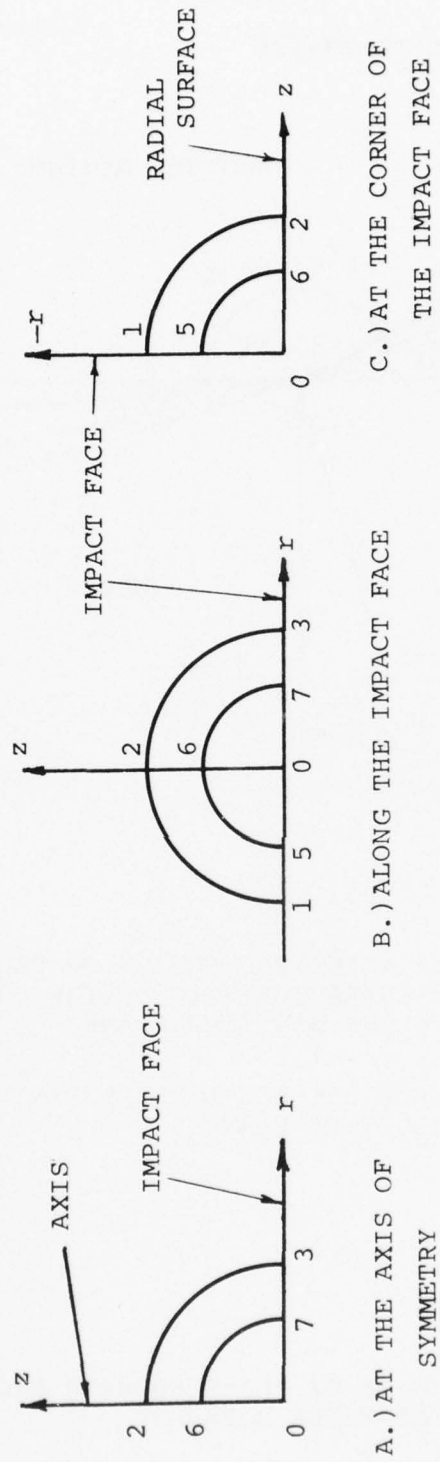


FIGURE II.6 - CHARACTERISTIC CONES IN THE IMPACT BAR AT THE IMPACT FACE

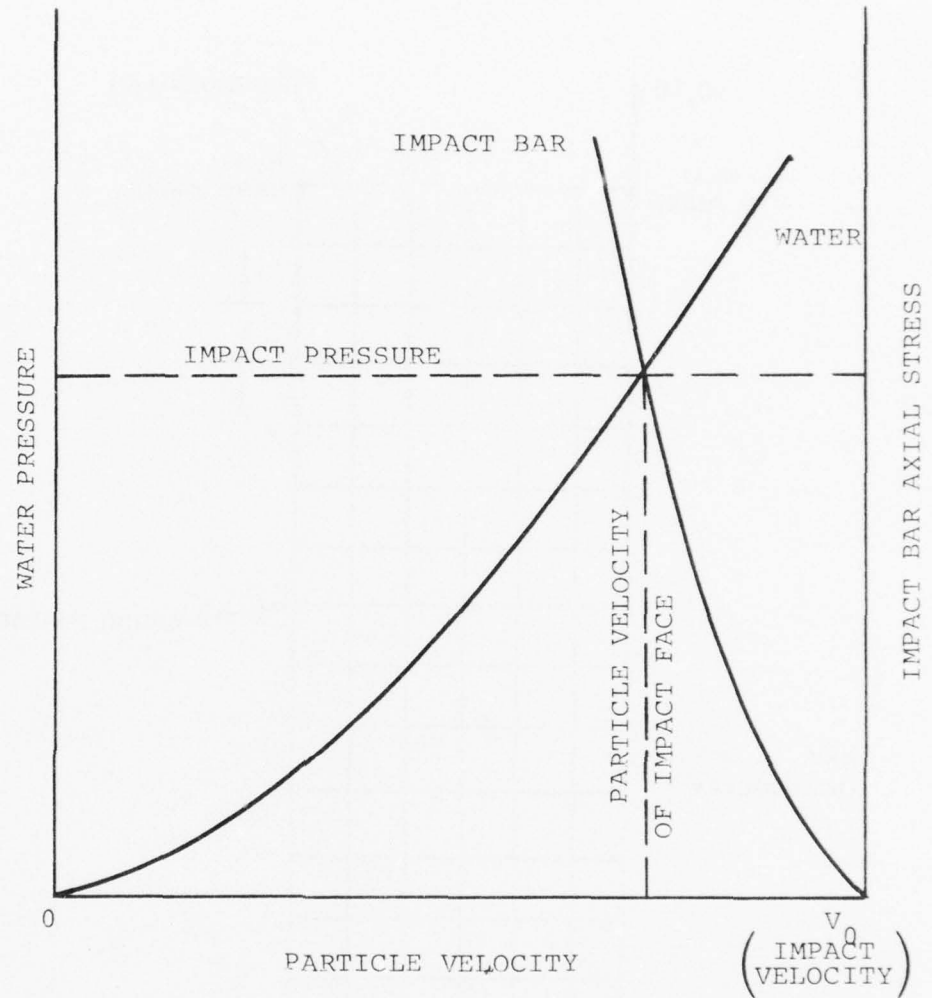


FIGURE II.7 - HUGONIOT MATCHING FOR OBTAINING IMPACT PRESSURE AND PARTICLE VELOCITY

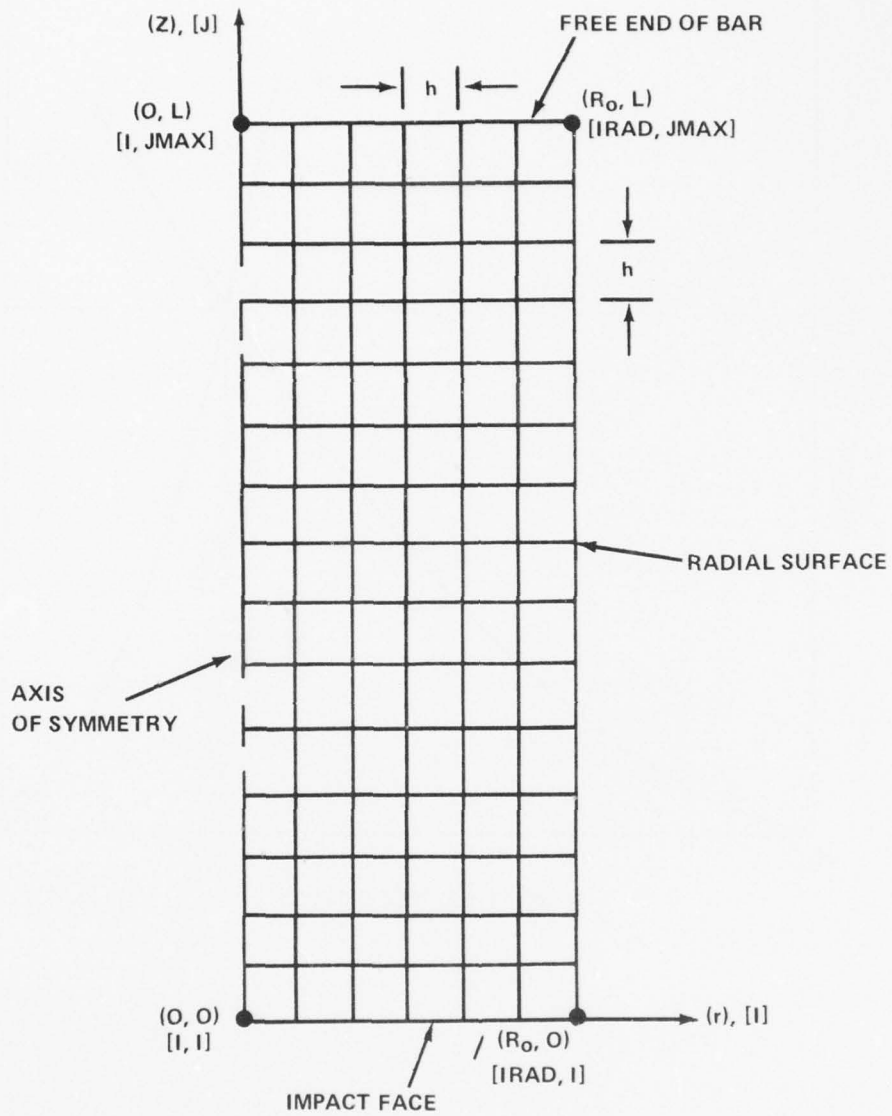


FIG. III.1 DISCRETIZED CONTINUUM OF THE IMPACT BAR

AD-A052 051

NAVAL SURFACE WEAPONS CENTER WHITE OAK LAB SILVER SP--ETC F/G 19/4
STRESS WAVE PROPAGATION IN BARS DUE TO NORMAL IMPACT ON WATER.(U)
AUG 77 W T MESSICK, J M MARSHALL

UNCLASSIFIED

NSWC/WOL/TR-77-128

NL

3 OF 5

AD
A052 051



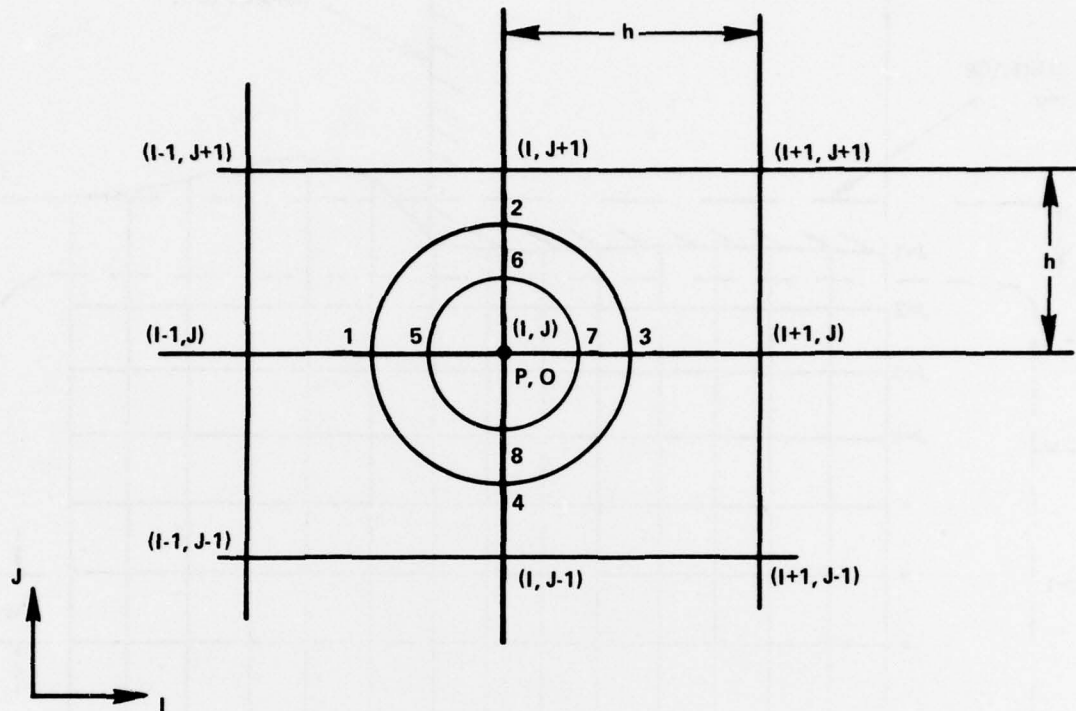


FIG. III. 2 INTERPOLATION IN IJ GRID

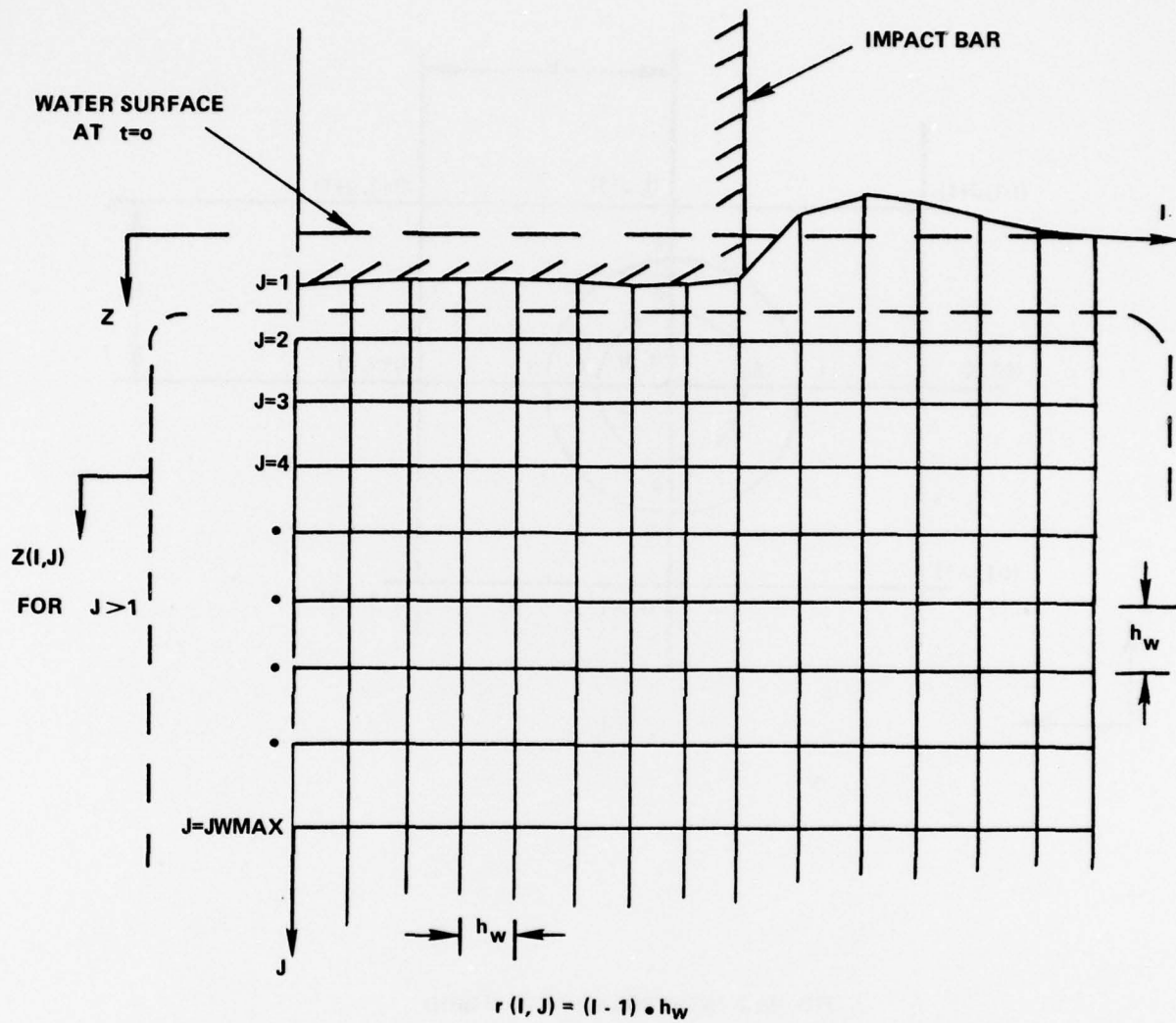


FIG. III.3 IJ GRID FOR WATER POINTS

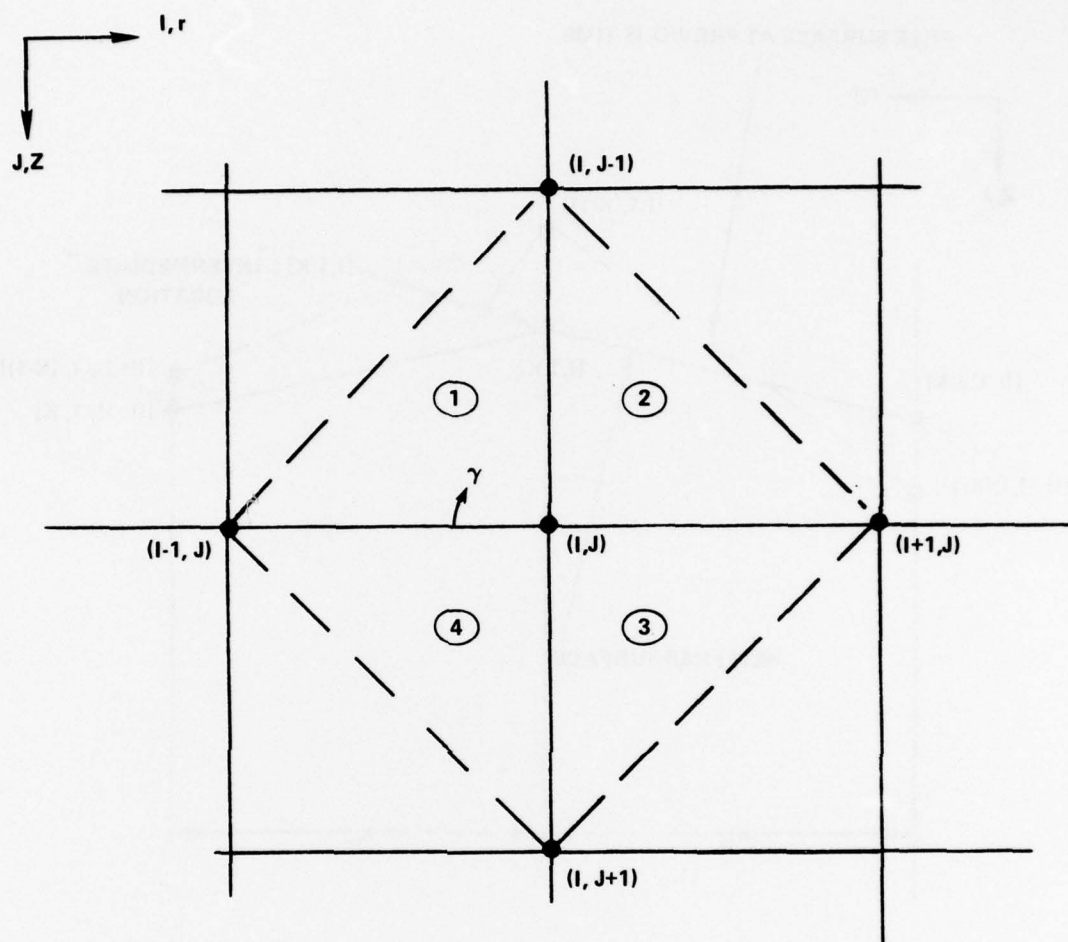


FIG. III.4 INTERPOLATING TRIANGLES FOR WATER I-J GRID

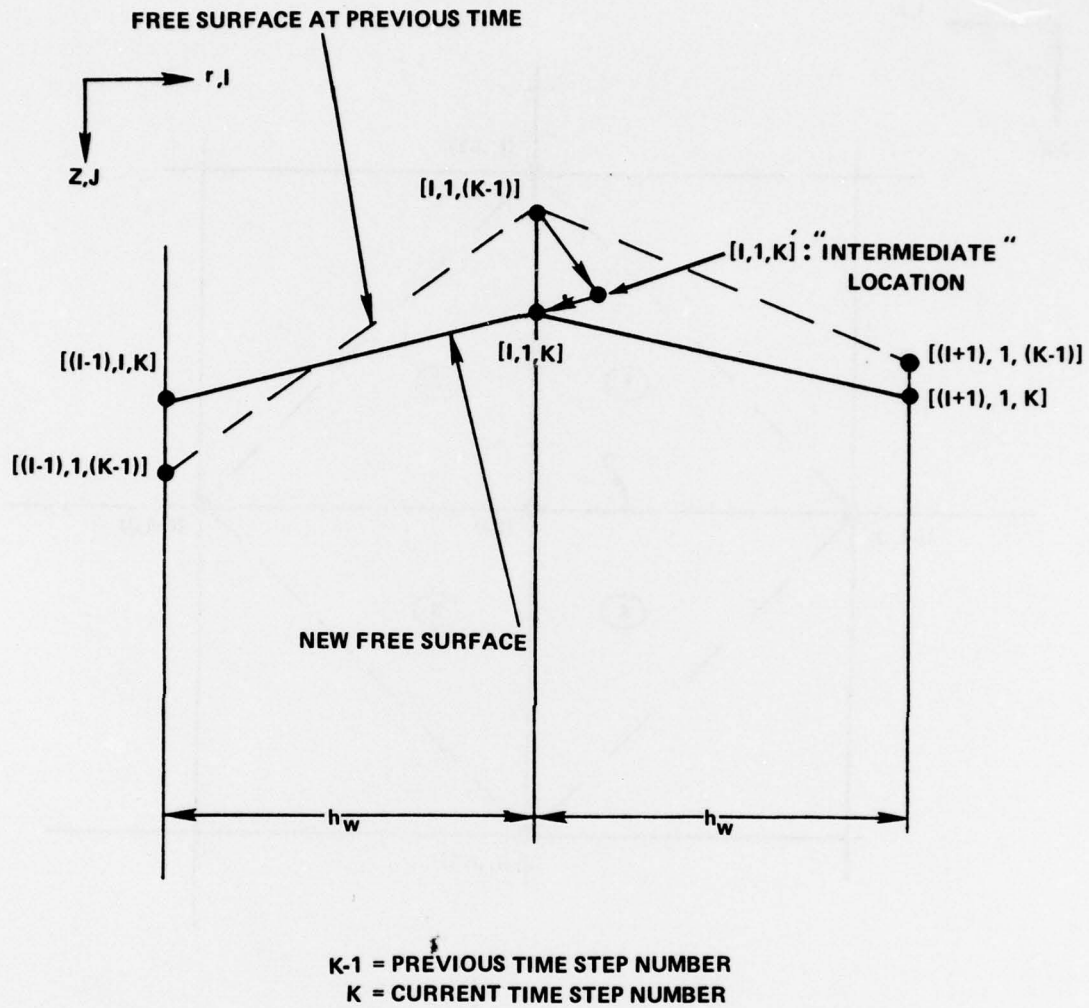


FIG. III. 5 WATER FREE SURFACE TRACING TECHNIQUE

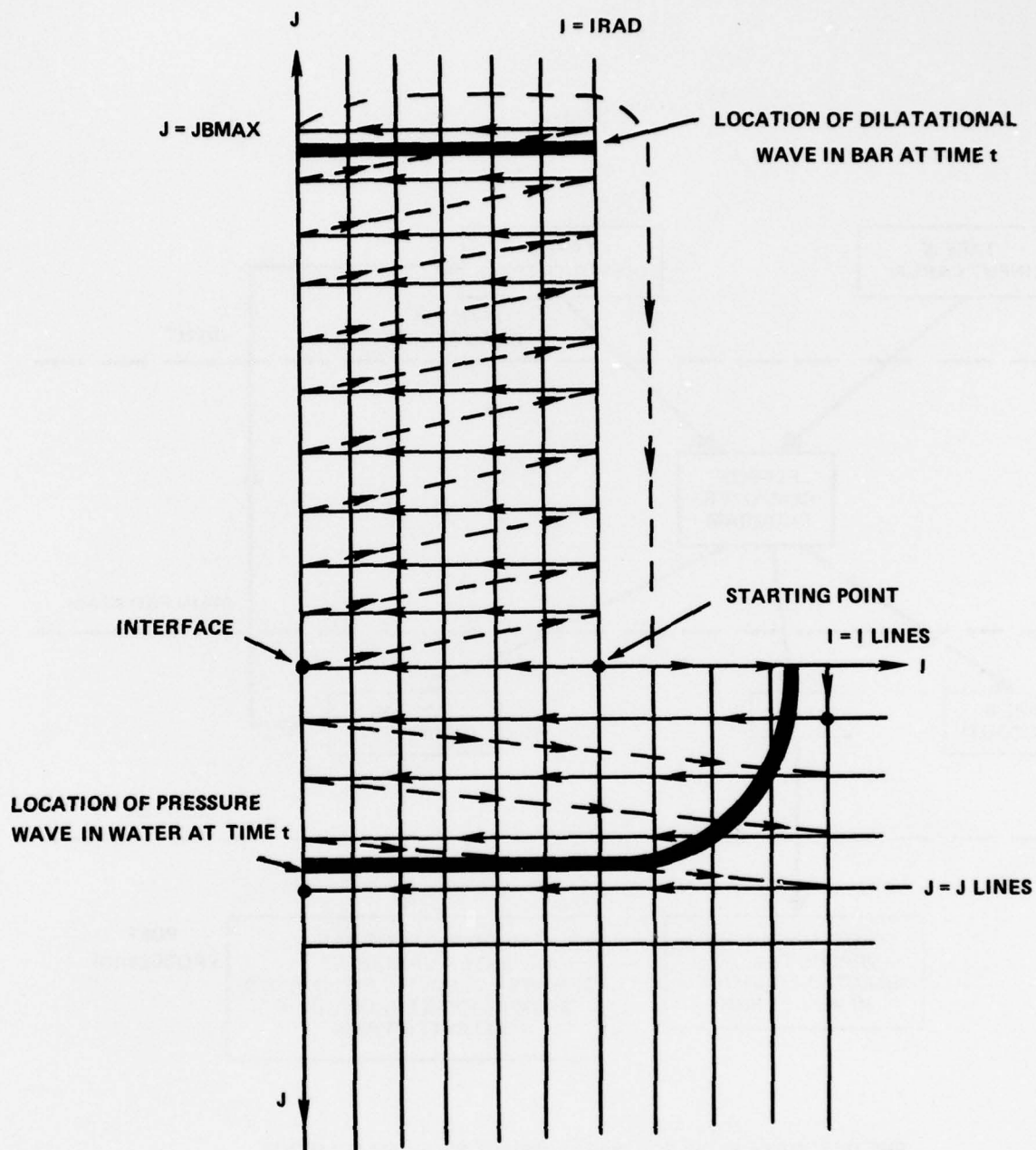


FIG. III.6 POINT BY POINT SOLUTION SEQUENCE ON IJ GRID

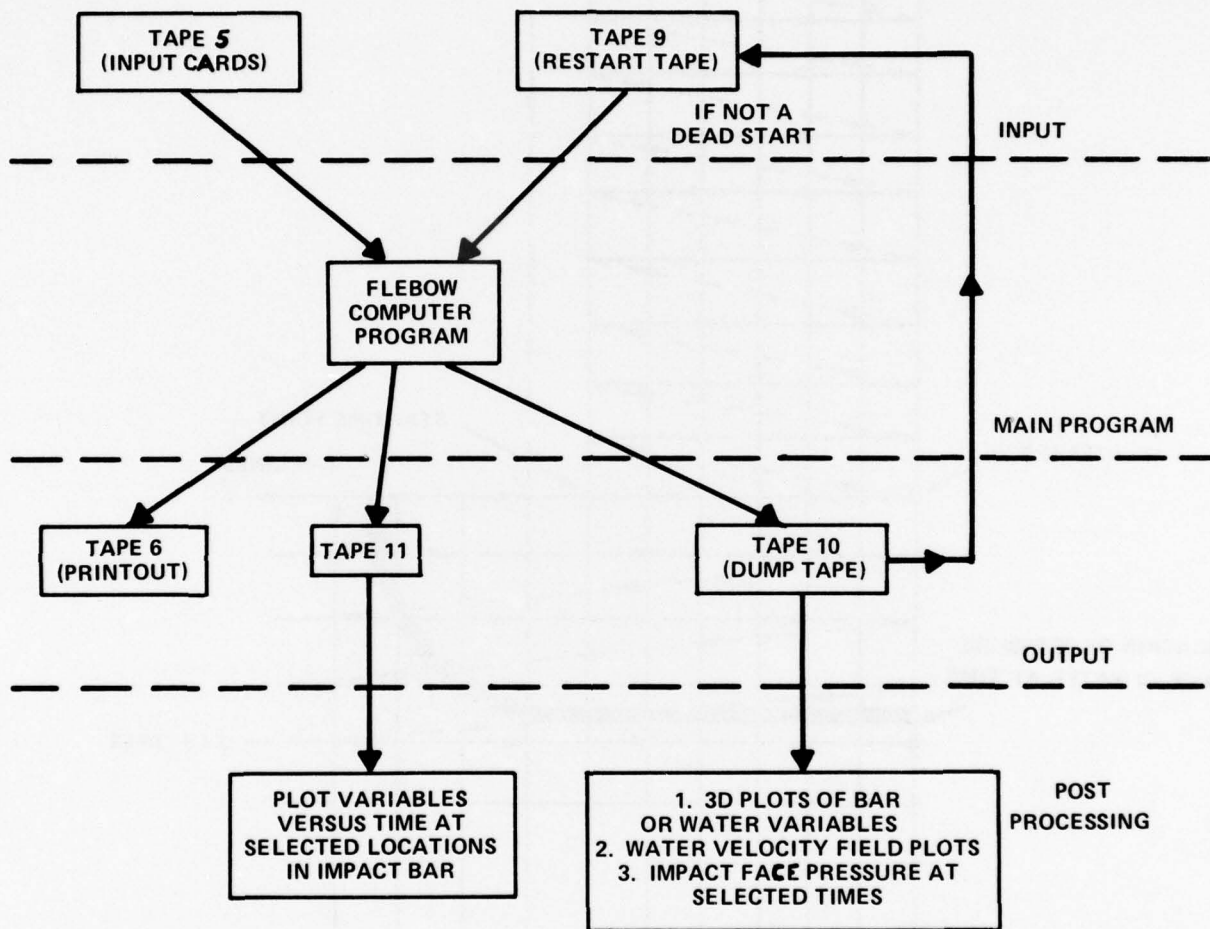


FIG. III.7 - DATA FLOW FOR WATER IMPACT PROBLEM SOLUTION

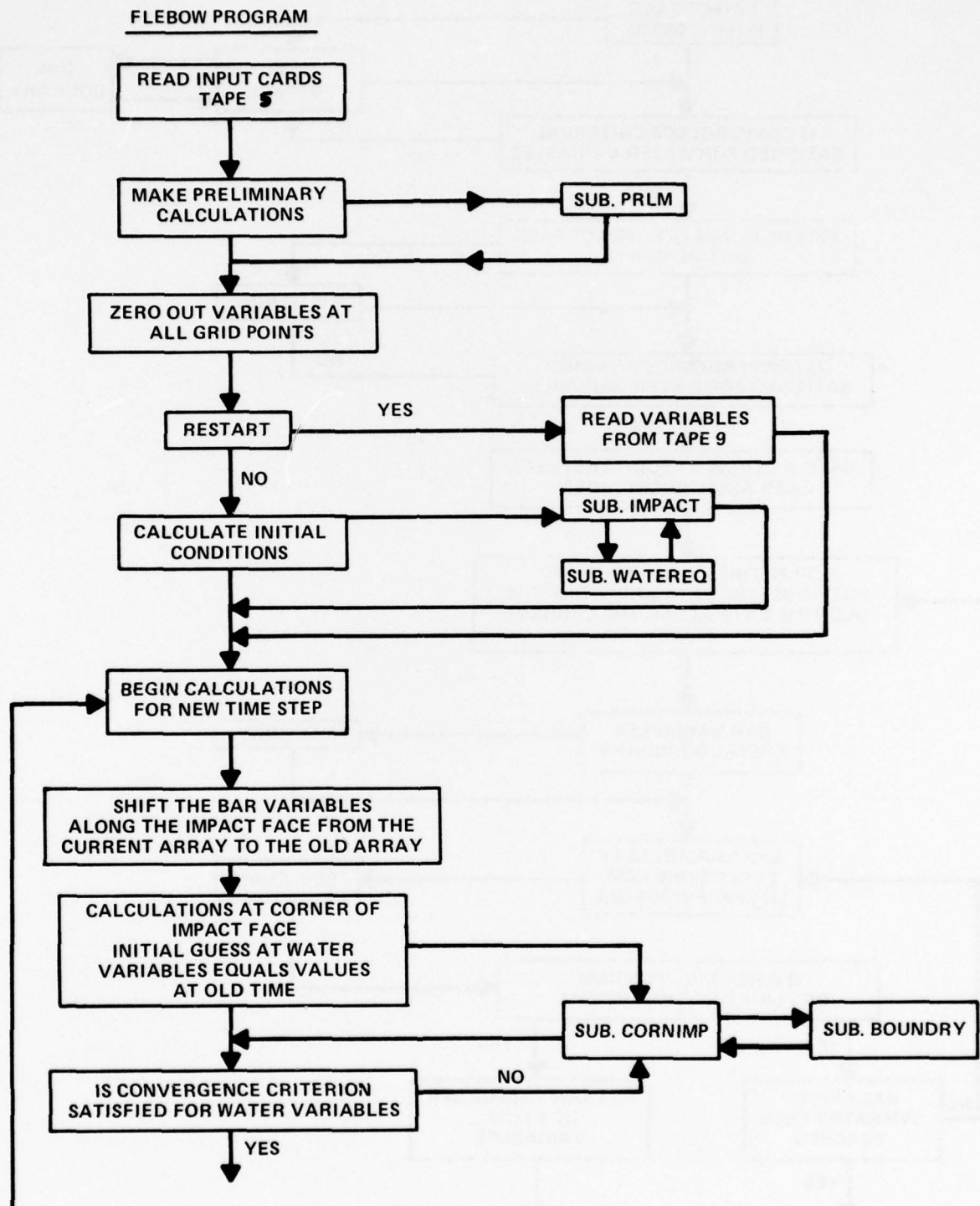


FIG. III.8 - FLOW CHART FOR FLEBOW PROGRAM

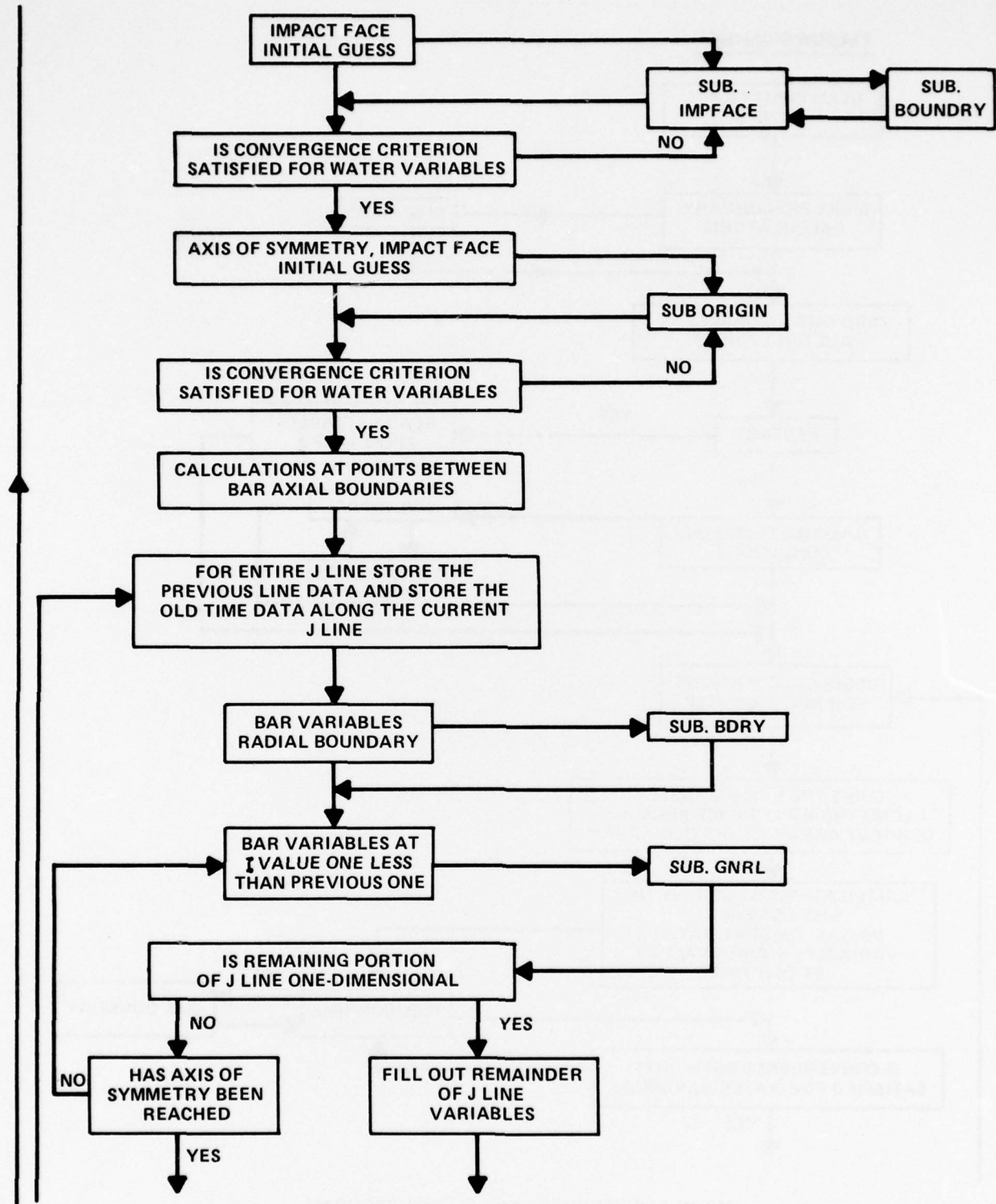


FIG. III.8 (CONT'D)

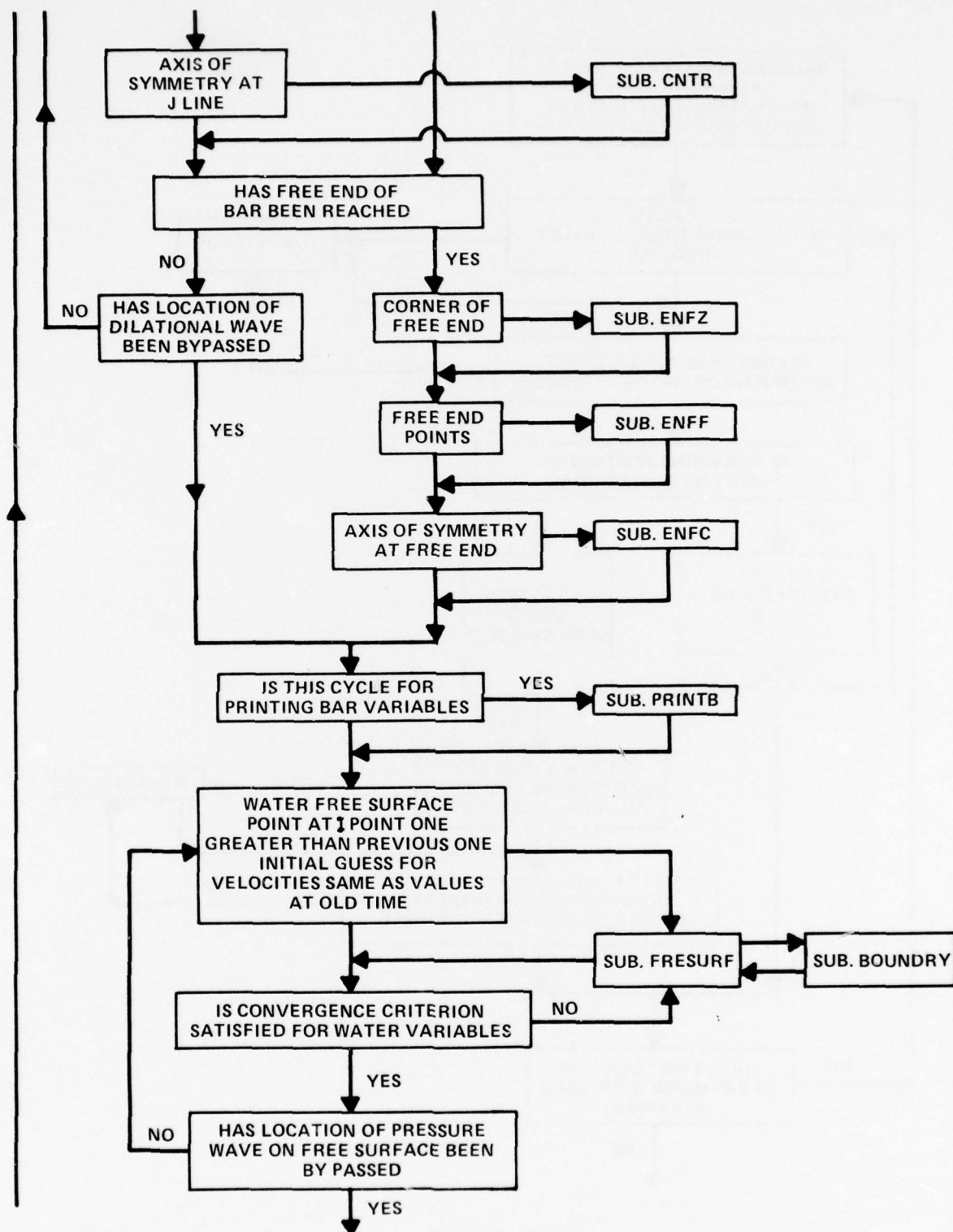


FIG. III.8 (CONT'D)

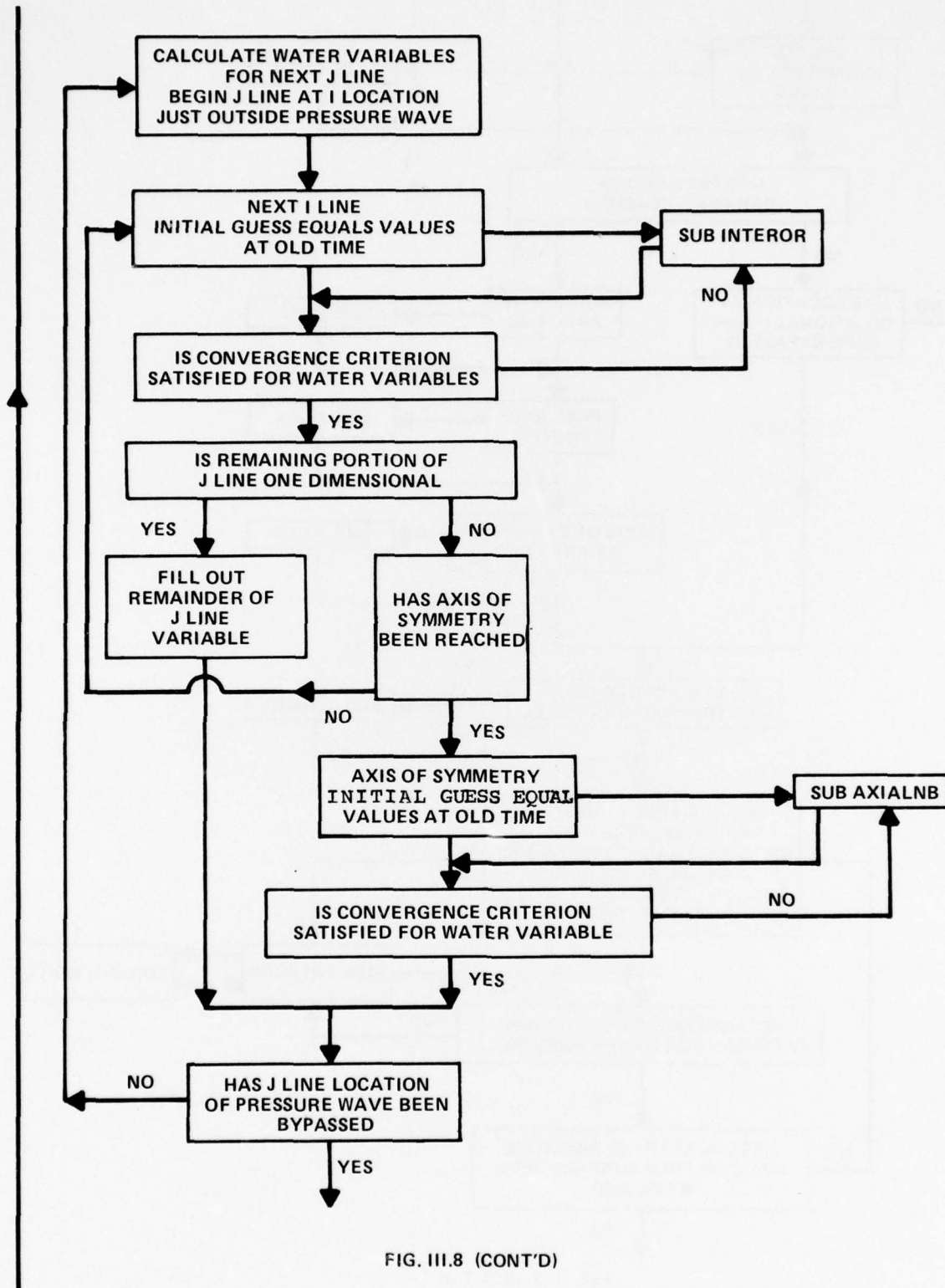


FIG. III.8 (CONT'D)

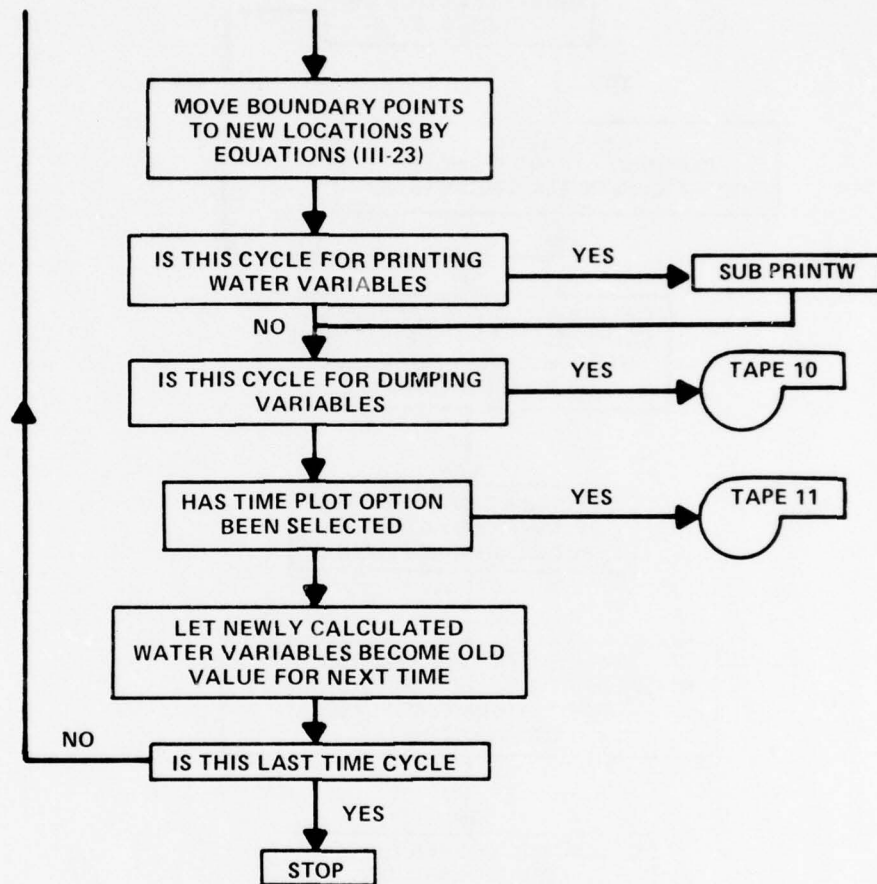


FIG. III.8 (CONT'D)

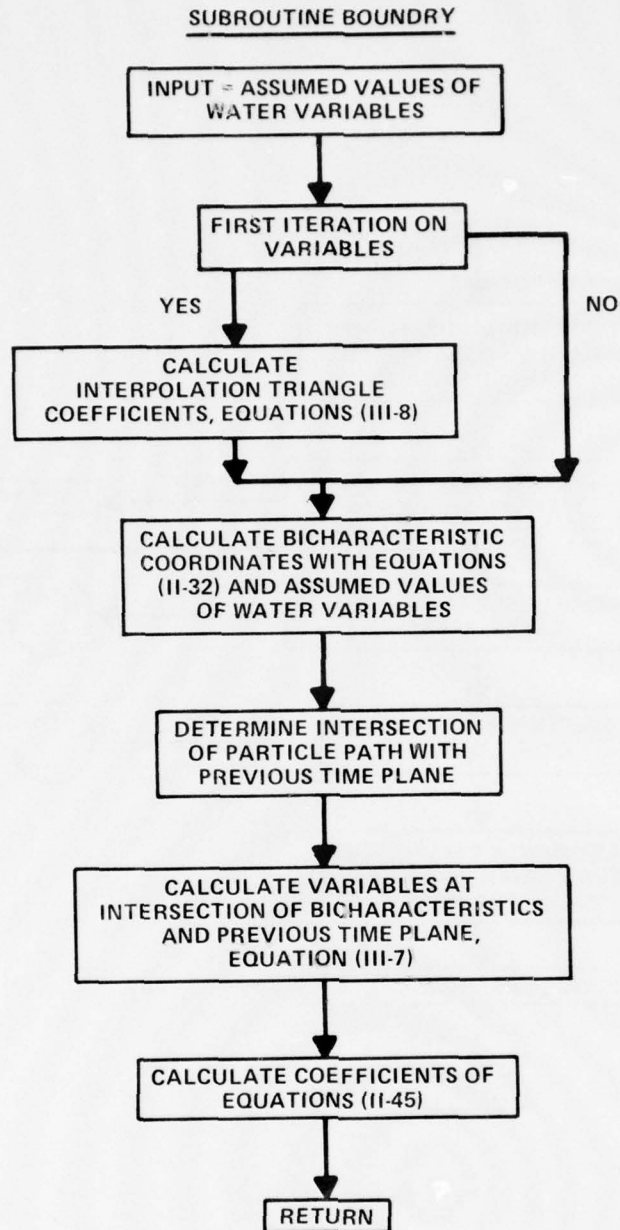


FIG. III.9 - SUBROUTINE BOUNDARY FOR WATER EQUATIONS NEAR BOUNDARY

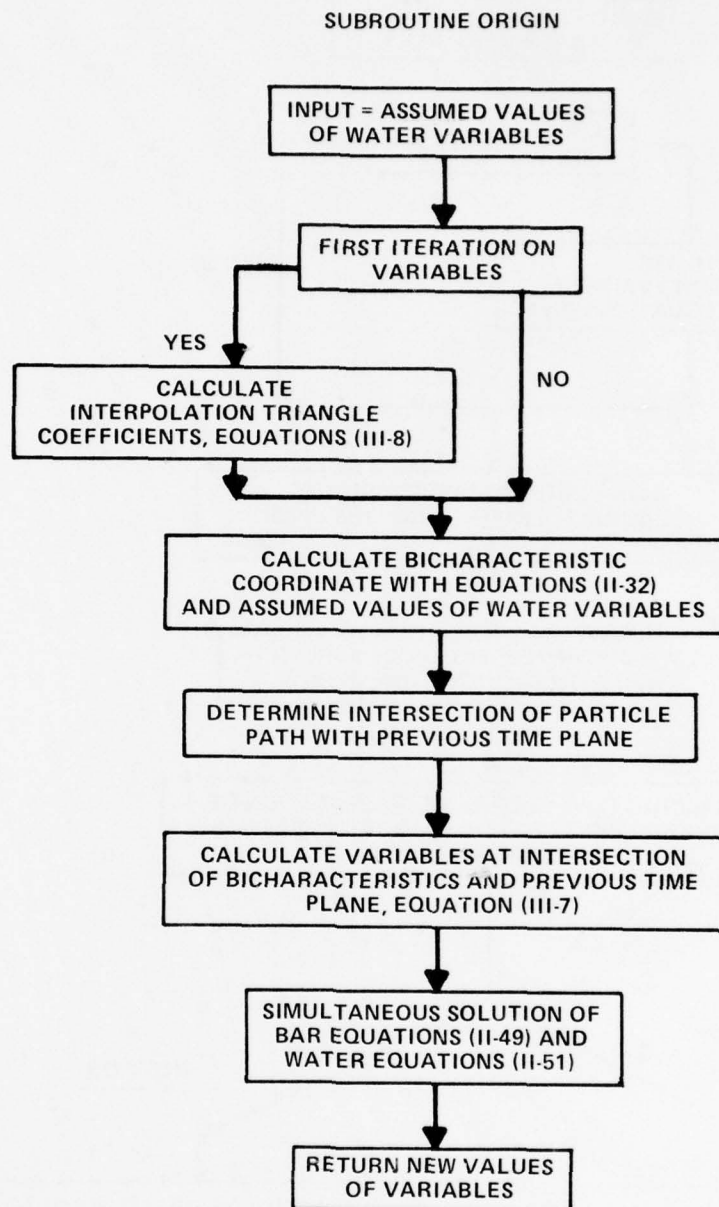


FIG. III.10 - SUBROUTINE ORIGIN FOR AXIS OF SYMMETRY ON IMPACT FACE

SUBROUTINES INTEROR AND AXIALNB

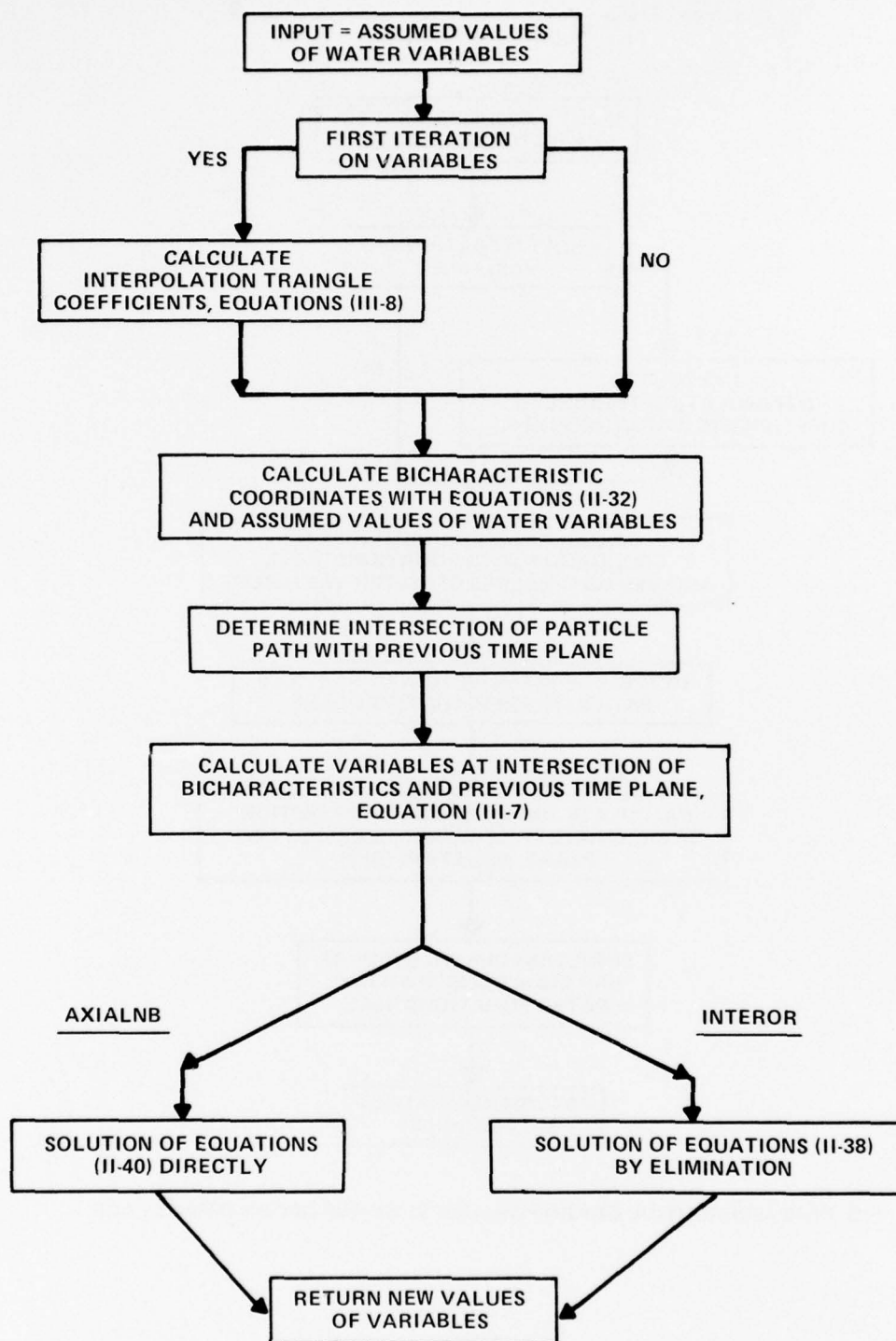


FIG. III.11 - SUBROUTINES INTEROR AND AXIALNB FOR WATER INTERIOR POINTS AND AXIS OF SYMMETRY POINTS, RESPECTIVELY

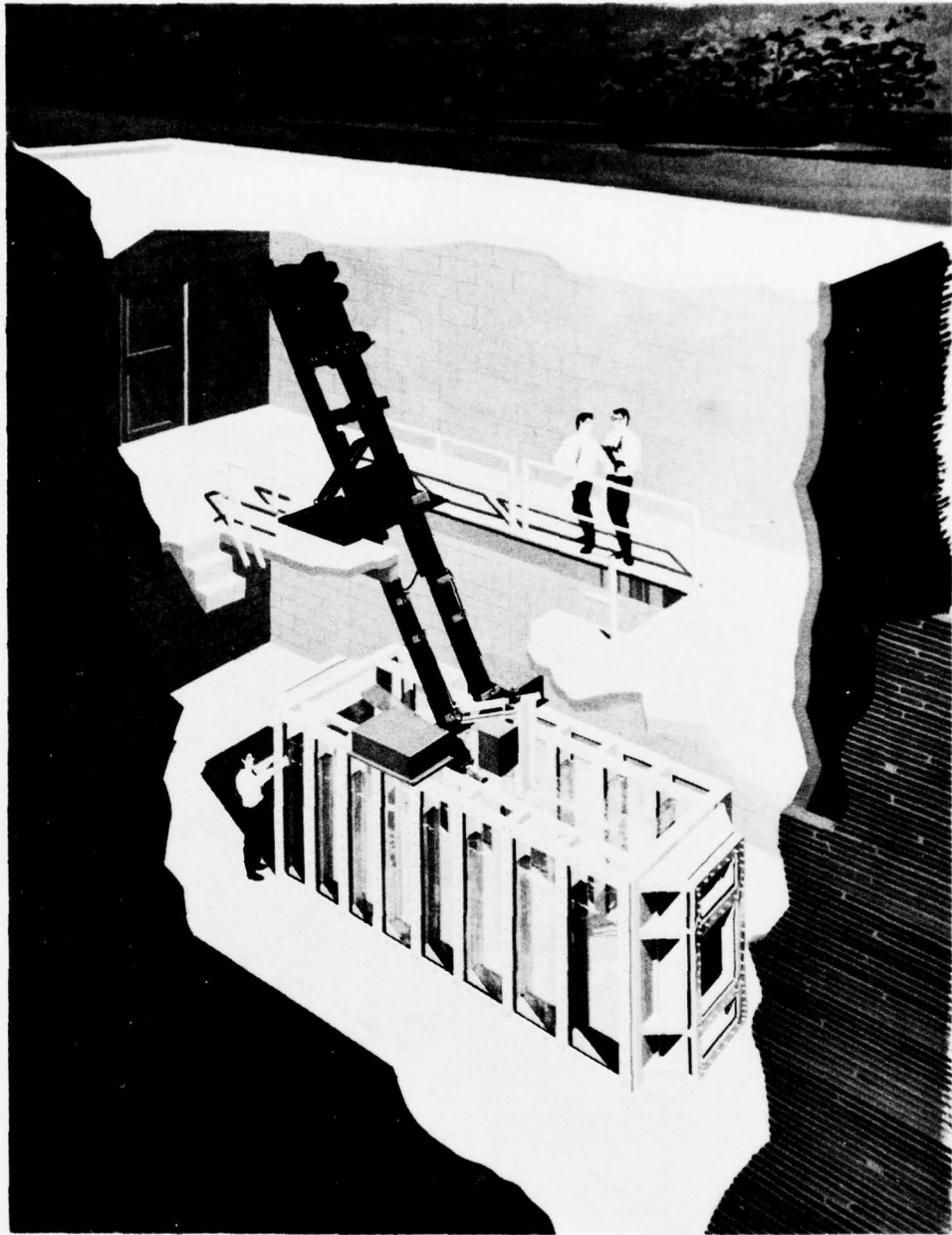
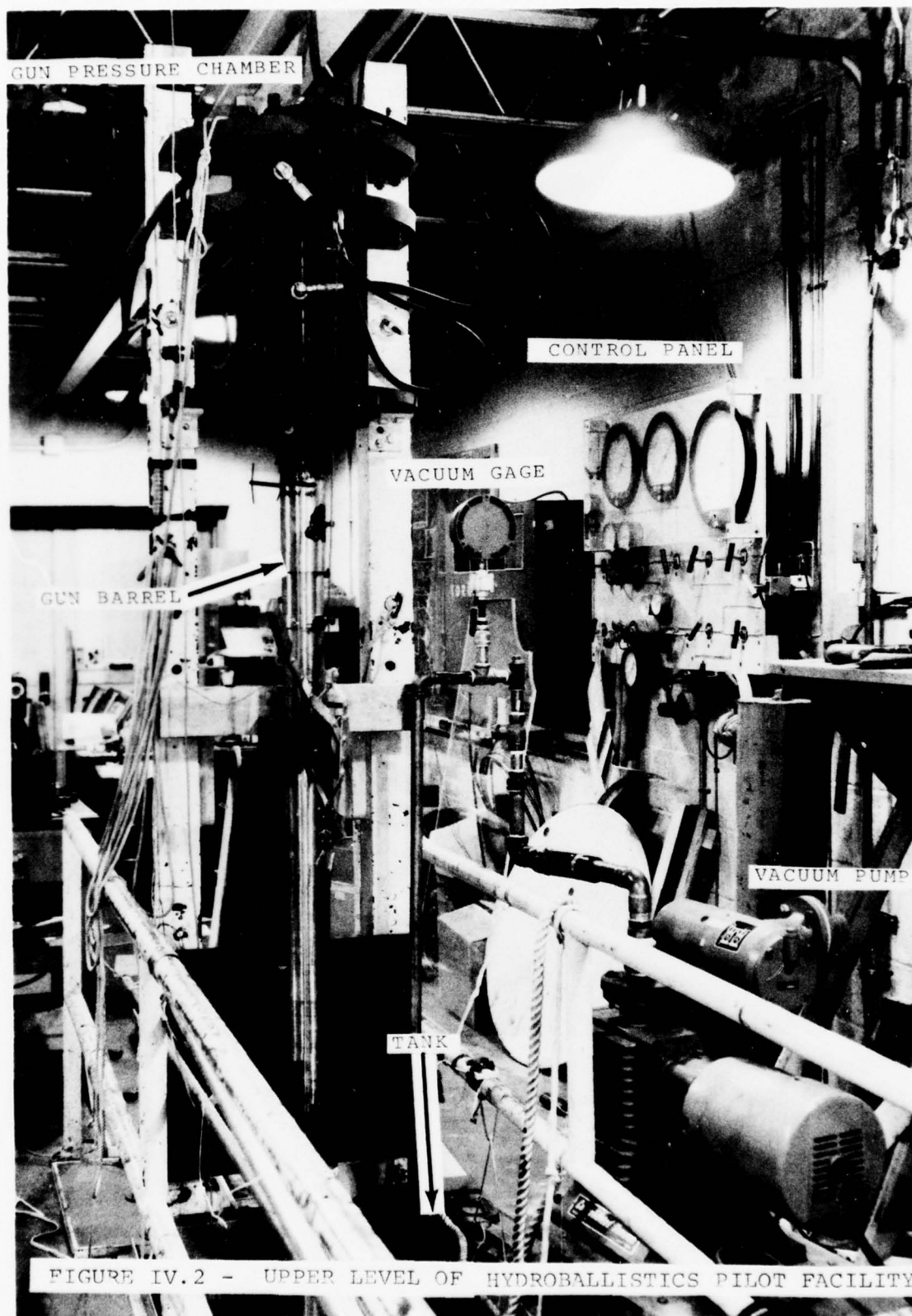


FIGURE IV.1 - HYDROBALLISTICS PILOT TANK



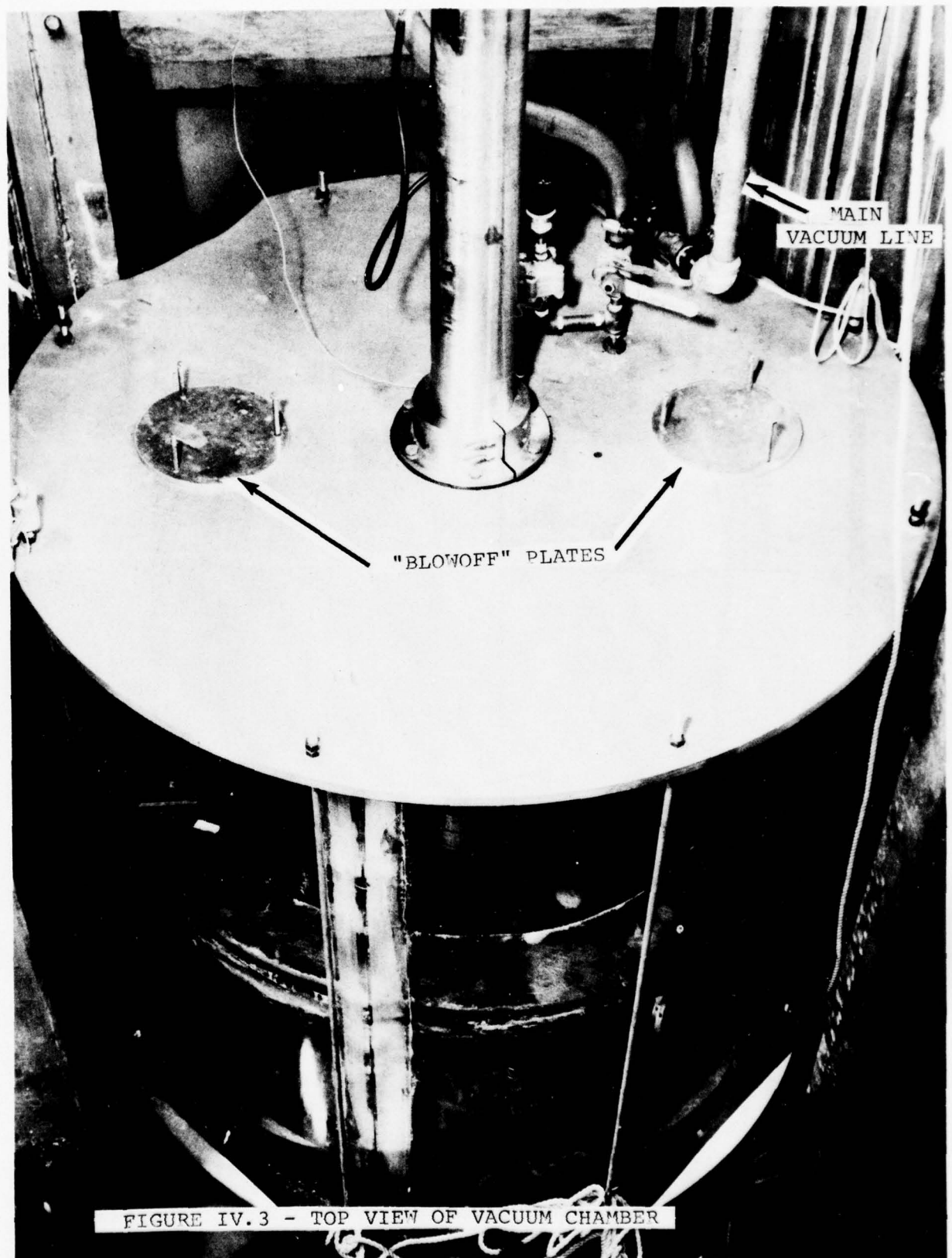
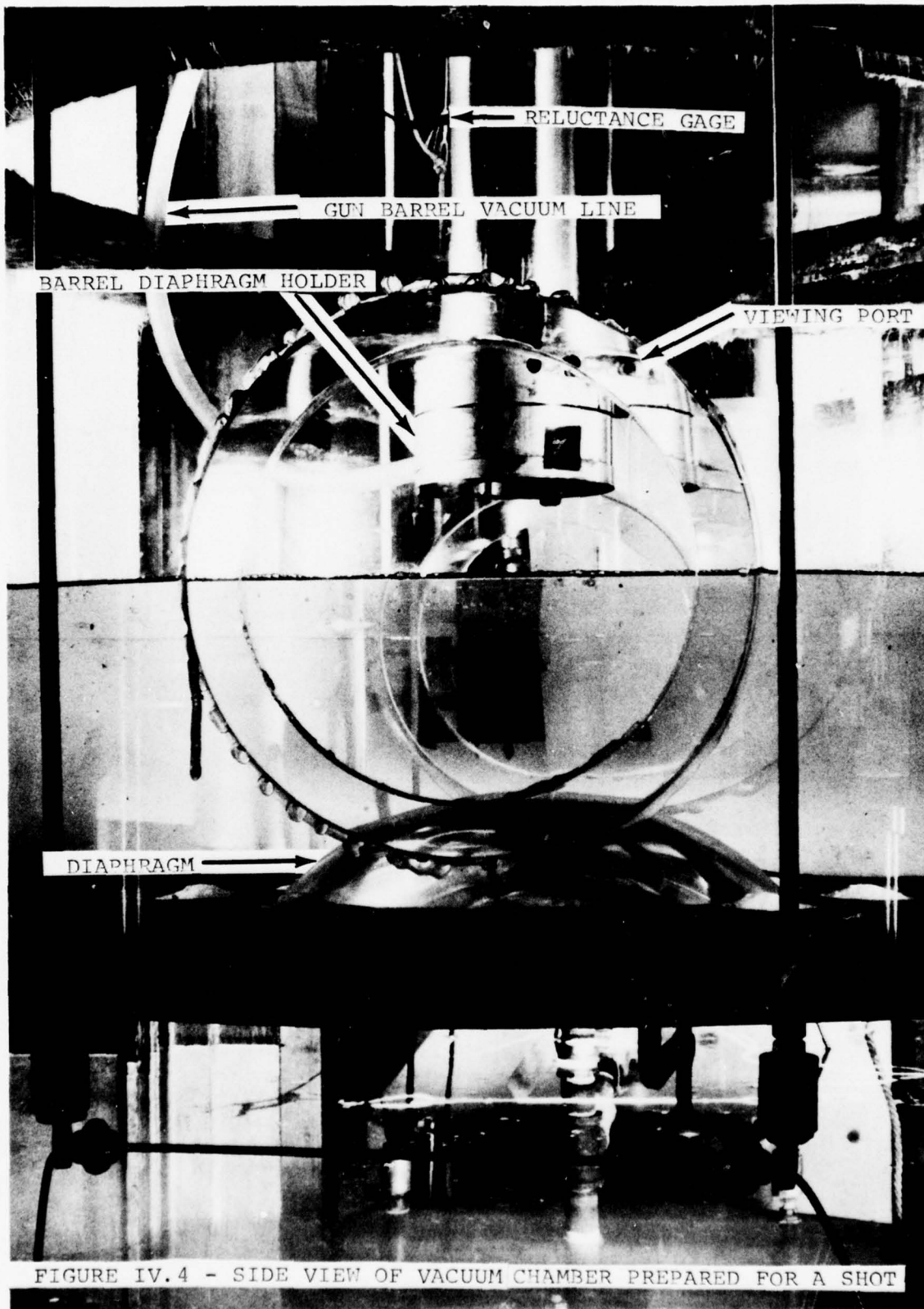


FIGURE IV.3 - TOP VIEW OF VACUUM CHAMBER



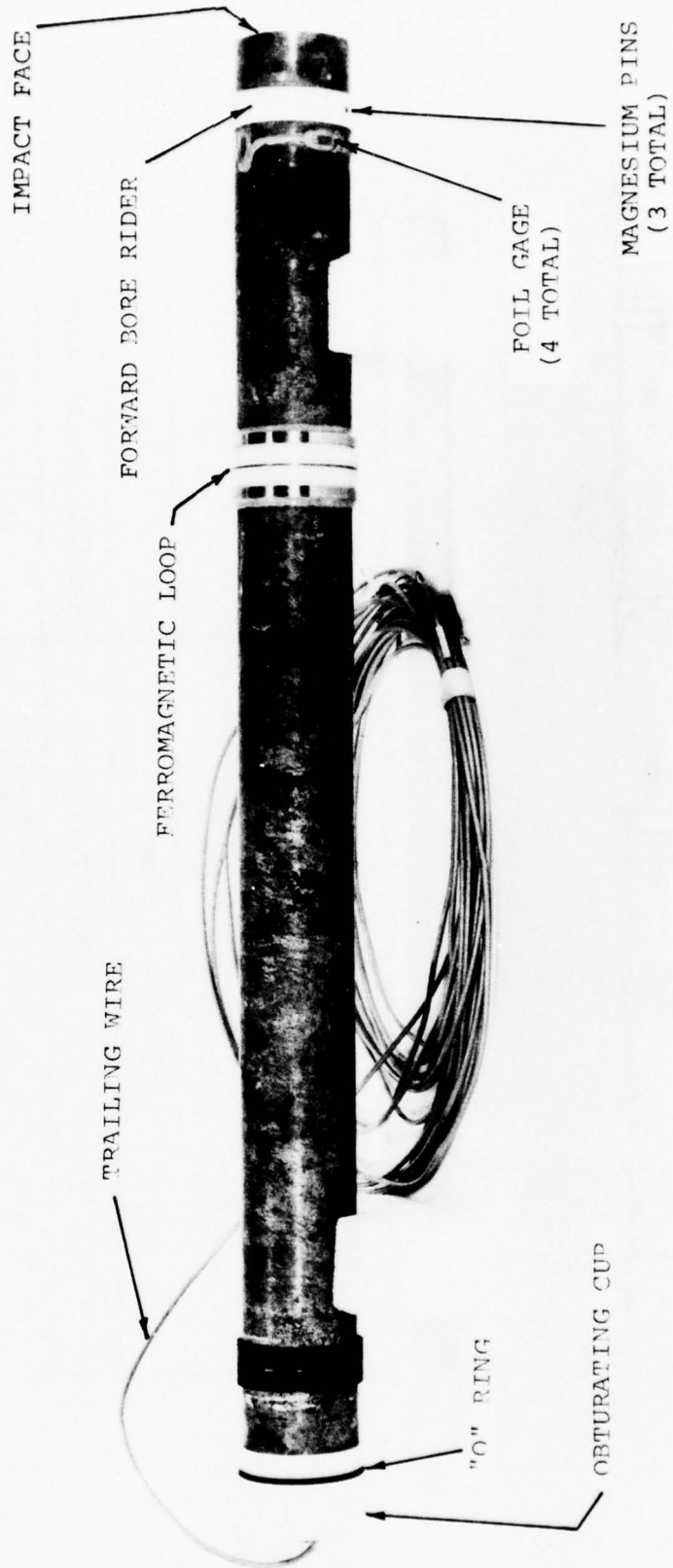
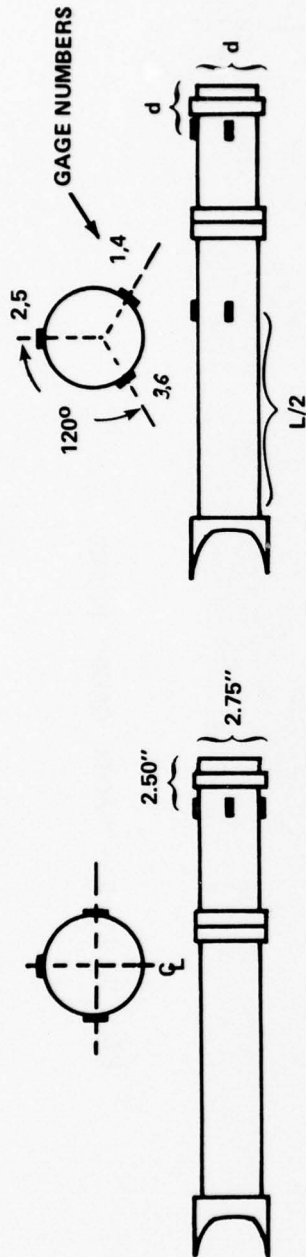
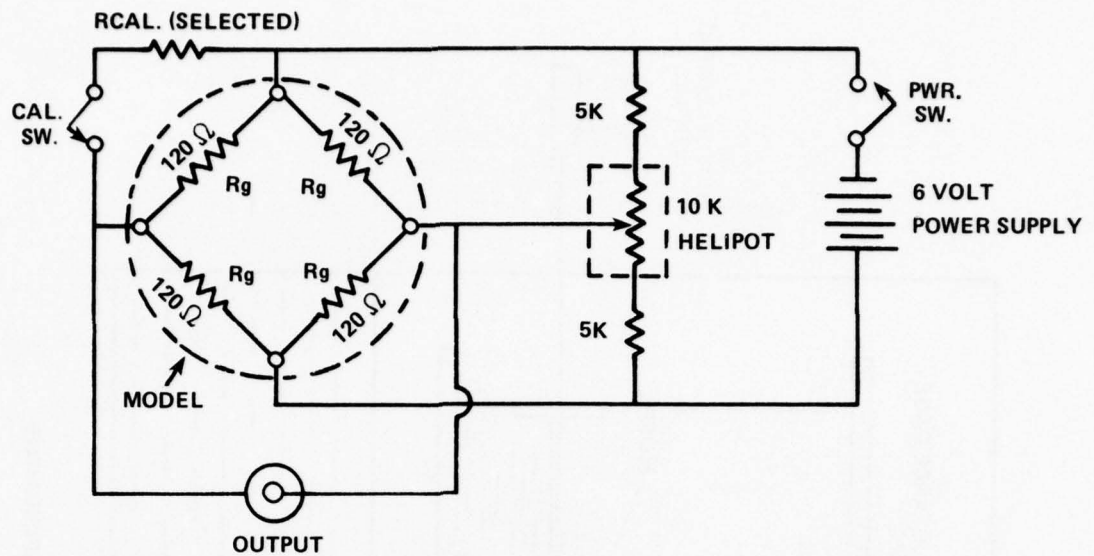


FIGURE IV.5 - "FOIL GAGE" MODEL

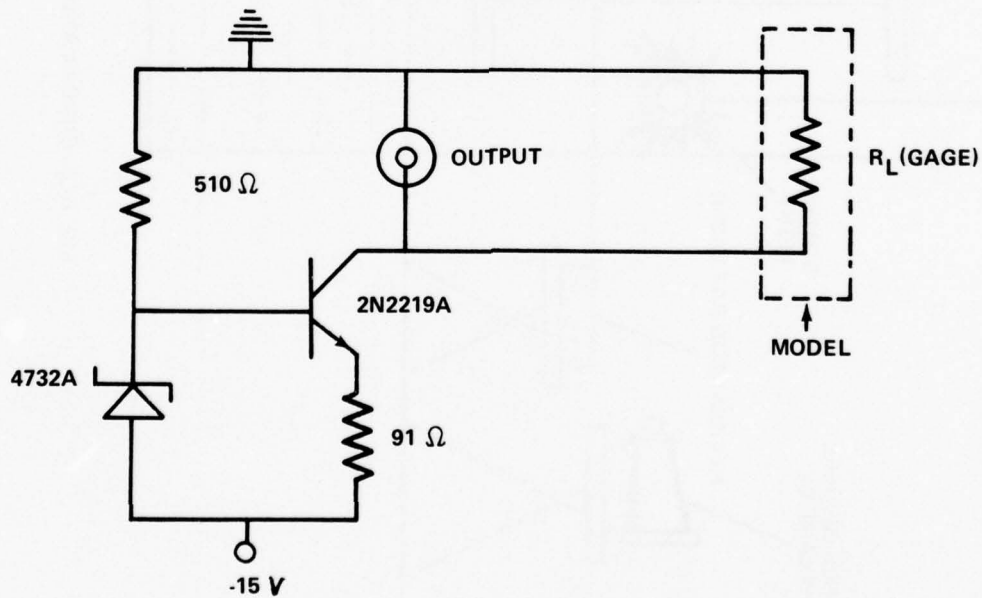


	FOIL GAGE MODEL	SEMICONDUCTOR GAGE MODEL
MATERIAL	MG. ZK60A-T5	MG. ZK60A-T5
MODULUS	6.5 (10 ⁶) psi	6.5 (10 ⁶) psi
DIAMETER	2.75"	2.50
LENGTH	33"	36"
INSTRUMENTATION	FOIL STRAIN GAGES	SEMI-CONDUCTOR STRAIN GAGES
TYPE	MICRO-MEASUREMENTS # EA-13-125BB-120	SR-4 TYPE SPB2-06-12
CIRCUIT	FULL BRIDGE (4 GAGES)	POTENTIOMETRIC (CONSTANT CURRENT)
LOCATION	2.50" FROM MODEL FRONT	6 LOCATIONS @ 120°

FIG. IV.6 TEST MODELS



a. $120\ \Omega$ FOIL STRAIN GAGE BRIDGE



b. SEMICONDUCTOR CONSTANT CURRENT CIRCUIT

FIGURE IV.7 - STRAIN GAGE CIRCUITS FOR THE TWO TEST MODELS

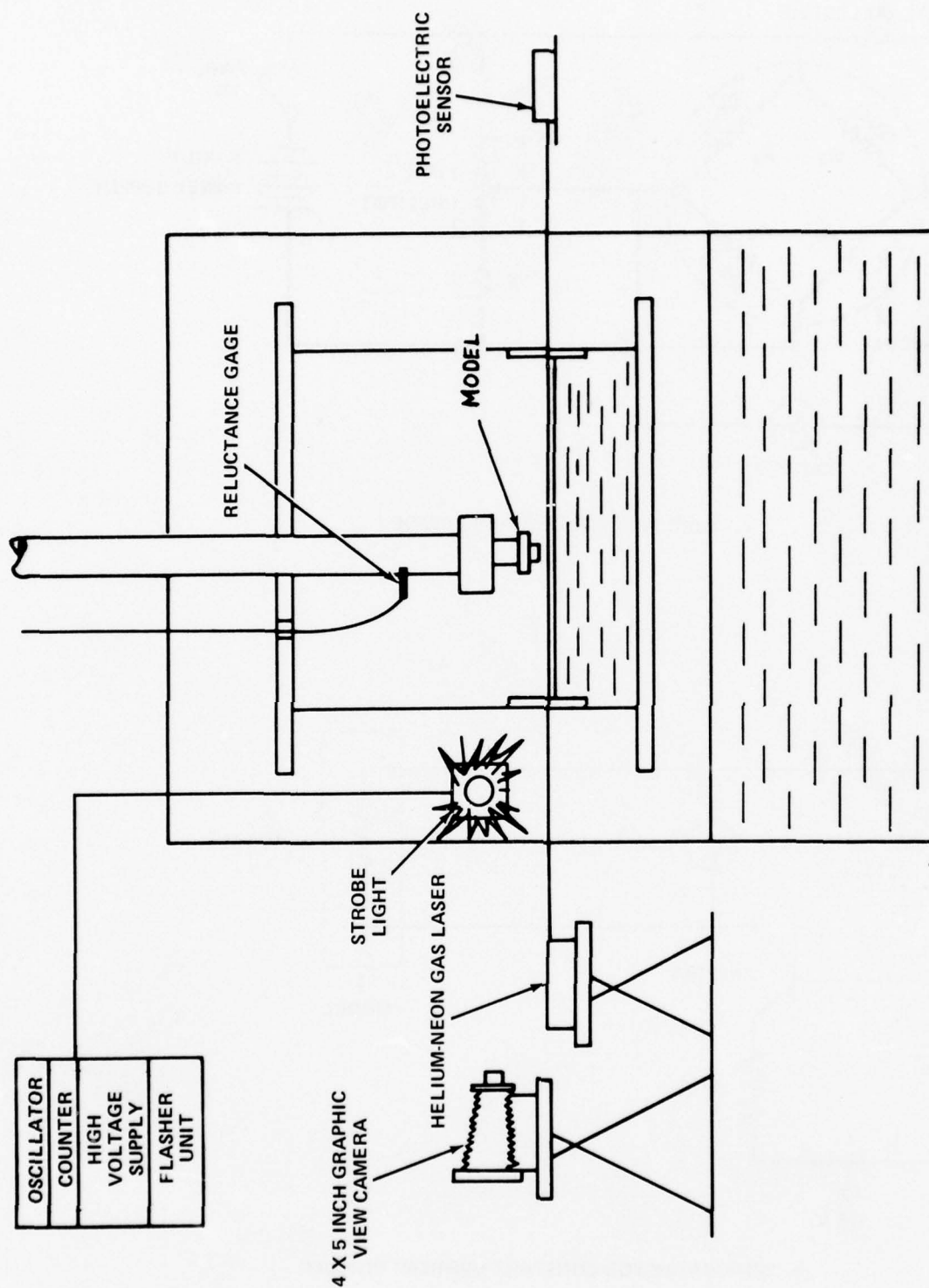


FIG. IV.8 - CAMERA AND LASER SETUPS FOR EXPERIMENTS

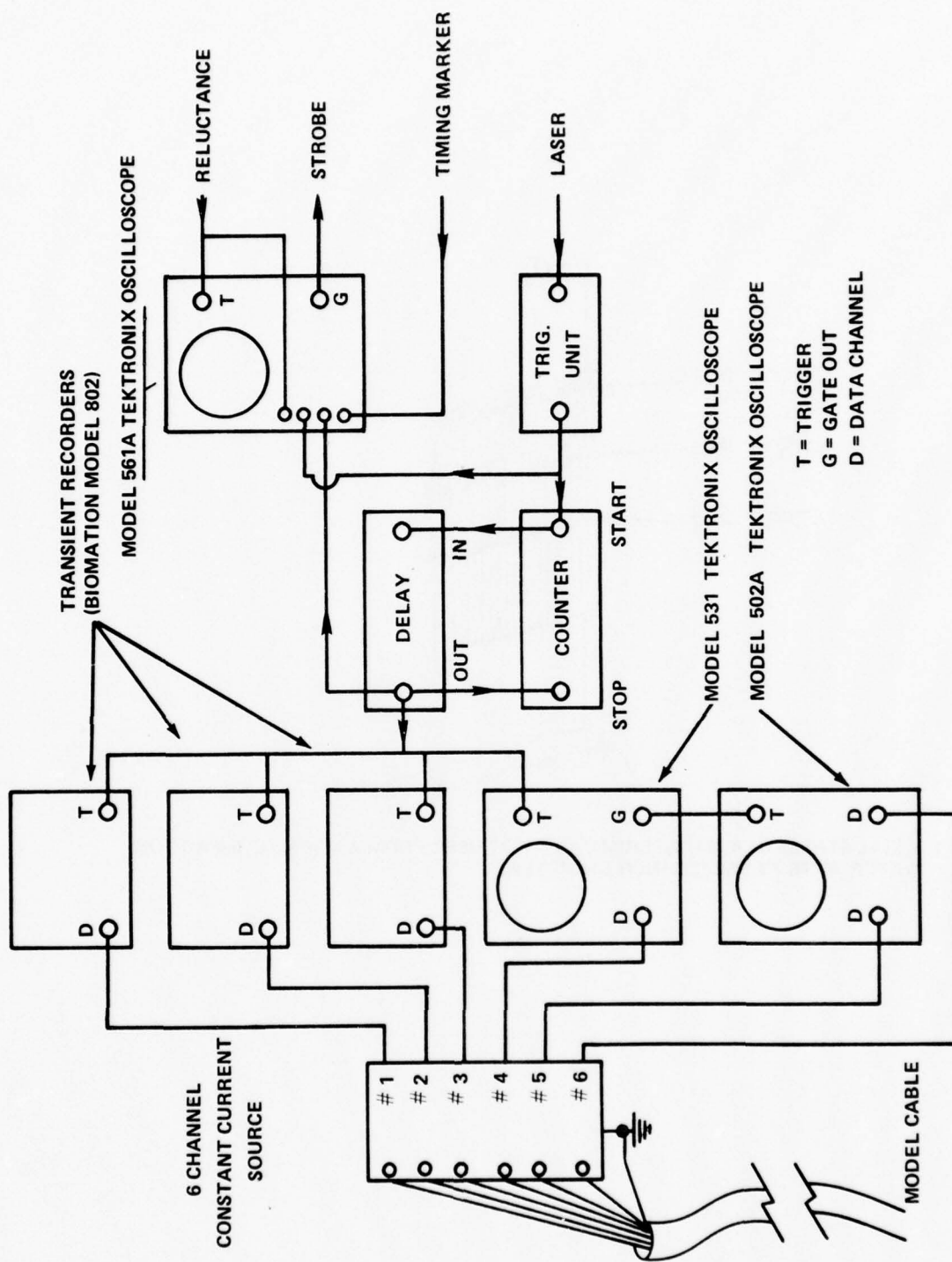


FIG. IV. 9 SCHEMATIC OF DATA RECORDING CIRCUIT FOR SEMICONDUCTOR GAGE MODEL

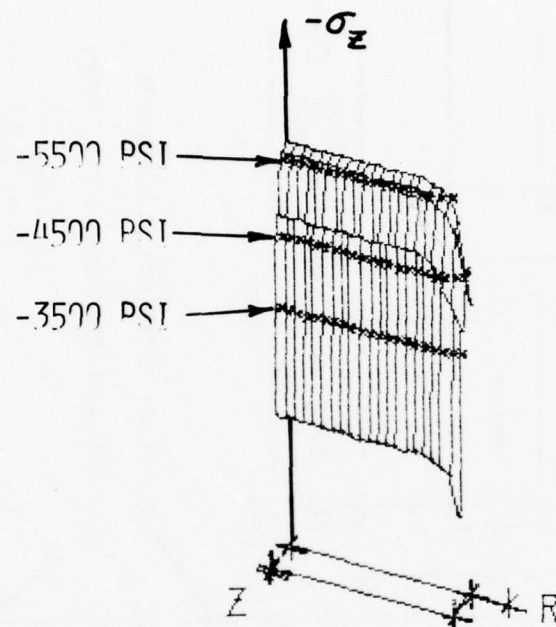


FIG. V.1 AXIAL STRESS IN A MAGNESIUM BAR AT .77 USEC FROM A NORMAL IMPACT ON WATER AT 96 FT/SEC (2.5 INCH DIAMETER)

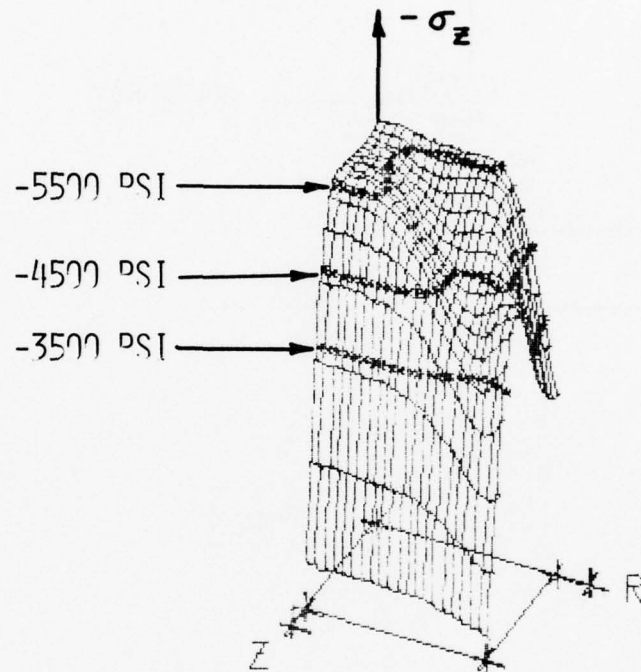


FIG. V.2 AXIAL STRESS IN A MAGNESIUM BAR AT 3.99 FROM A NORMAL IMPACT ON WATER AT 96 FT/SEC (2.5 INCH DIAMETER)

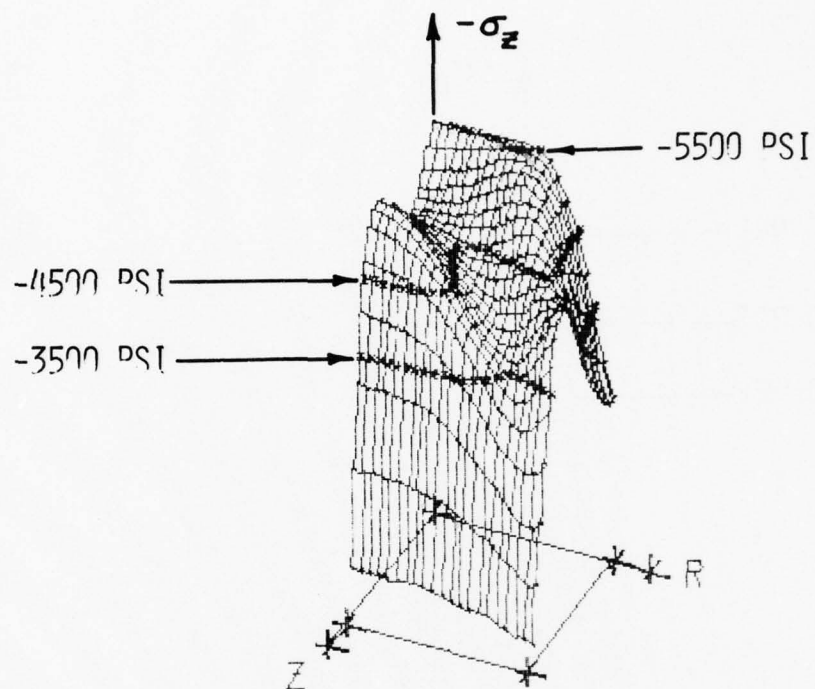


FIG. V.3 AXIAL STRESS IN A MAGNESIUM BAR AT 5.28 USEC FROM A NORMAL IMPACT ON WATER AT 96 FT/SEC (2.5 INCH DIAMETER)

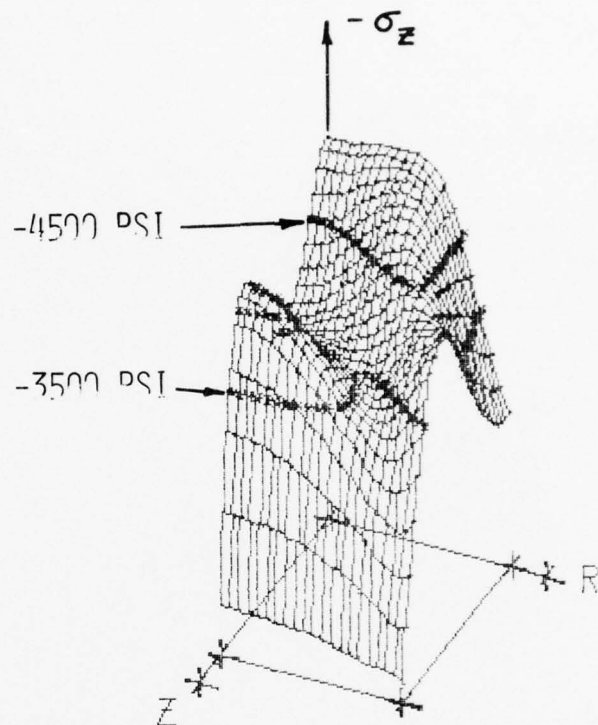


FIG. V.4 AXIAL STRESS IN A MAGNESIUM BAR AT 6.57 USEC FROM A NORMAL IMPACT ON WATER AT 96 FT/SEC (2.5 INCH DIAMETER)

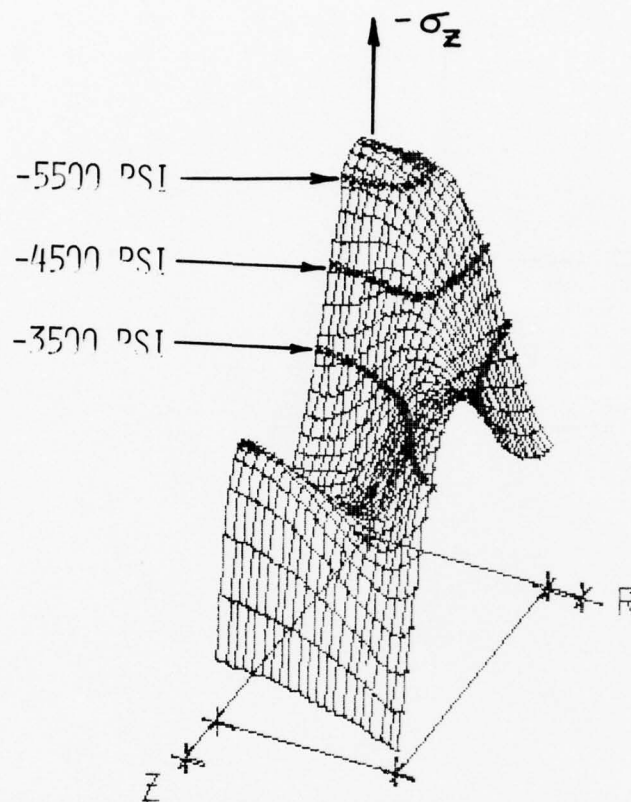


FIG. V.5 AXIAL STRESS IN A MAGNESIUM BAR AT 9.15 USEC FROM A NORMAL IMPACT ON WATER AT 96 FT/SEC (2.5 INCH DIAMETER)

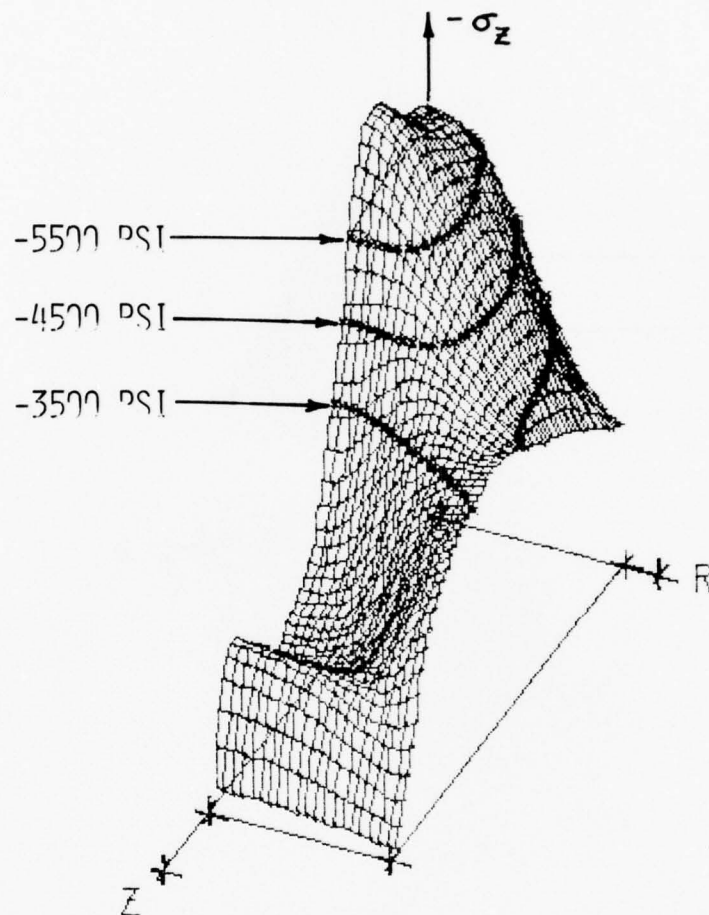


FIG. V.6 AXIAL STRESS IN A MAGNESIUM BAR AT 14.31 USEC FROM A NORMAL IMPACT ON WATER AT 96 FT/SEC (2.5 INCH DIAMETER)

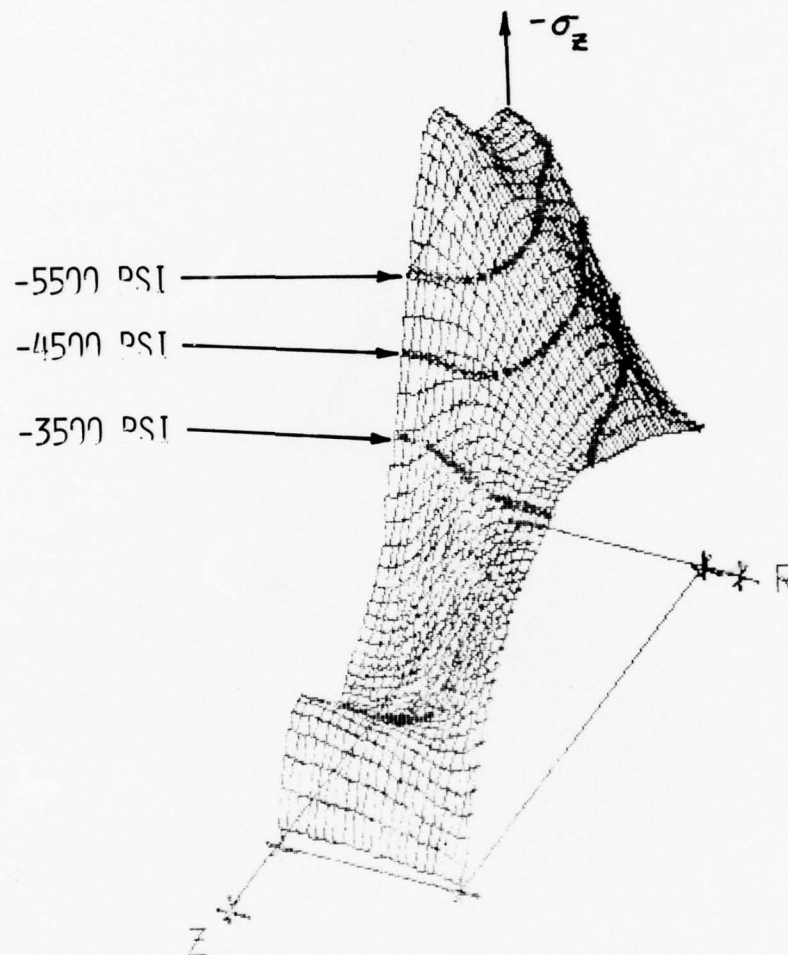


FIG. V.7 AXIAL STRESS IN A MAGNESIUM BAR AT 15.60 USEC FROM A NORMAL IMPACT ON WATER AT 96 FT/SEC (2.5 INCH DIAMETER)

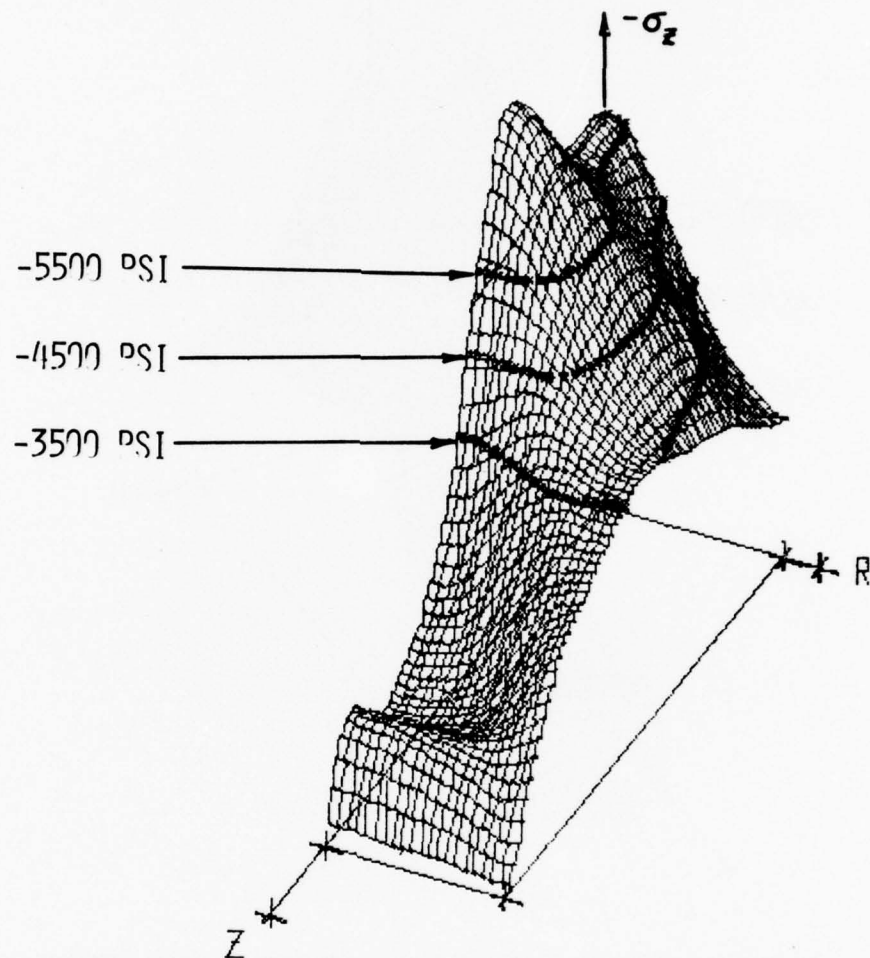


FIG. V.8 AXIAL STRESS IN A MAGNESIUM BAR AT 16.89 USEC FROM A NORMAL IMPACT ON WATER AT 96 FT/SEC (2.5 INCH DIAMETER)

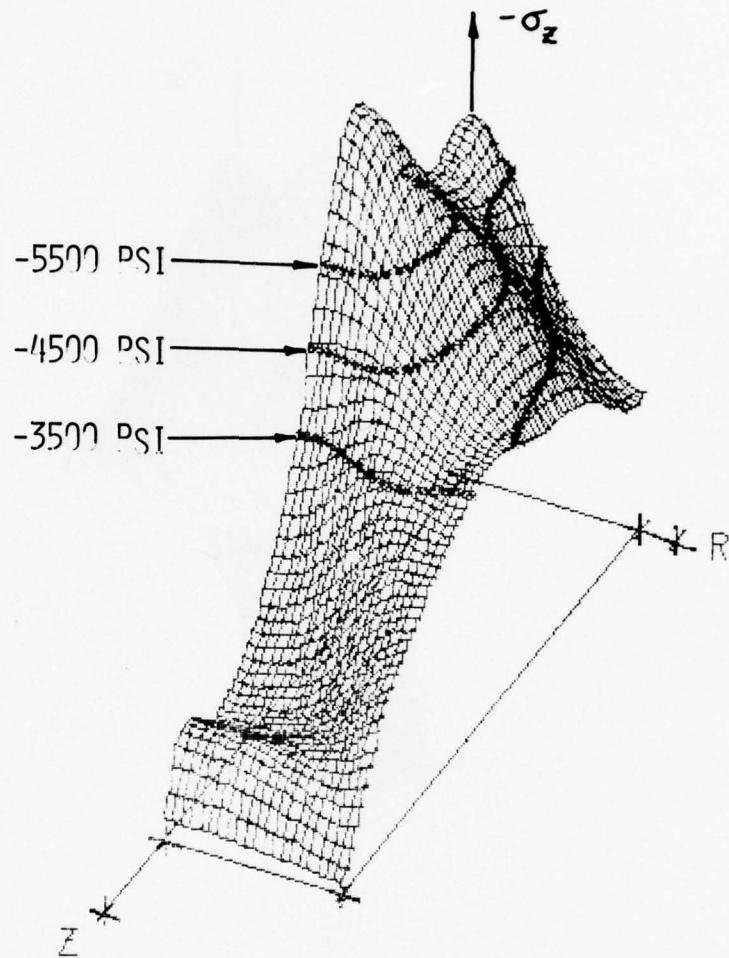


FIG. V.9 AXIAL STRESS IN A MAGNESIUM BAR AT 18.18 USEC FROM A NORMAL IMPACT ON WATER AT 96 FT/SEC (2.5 INCH DIAMETER)

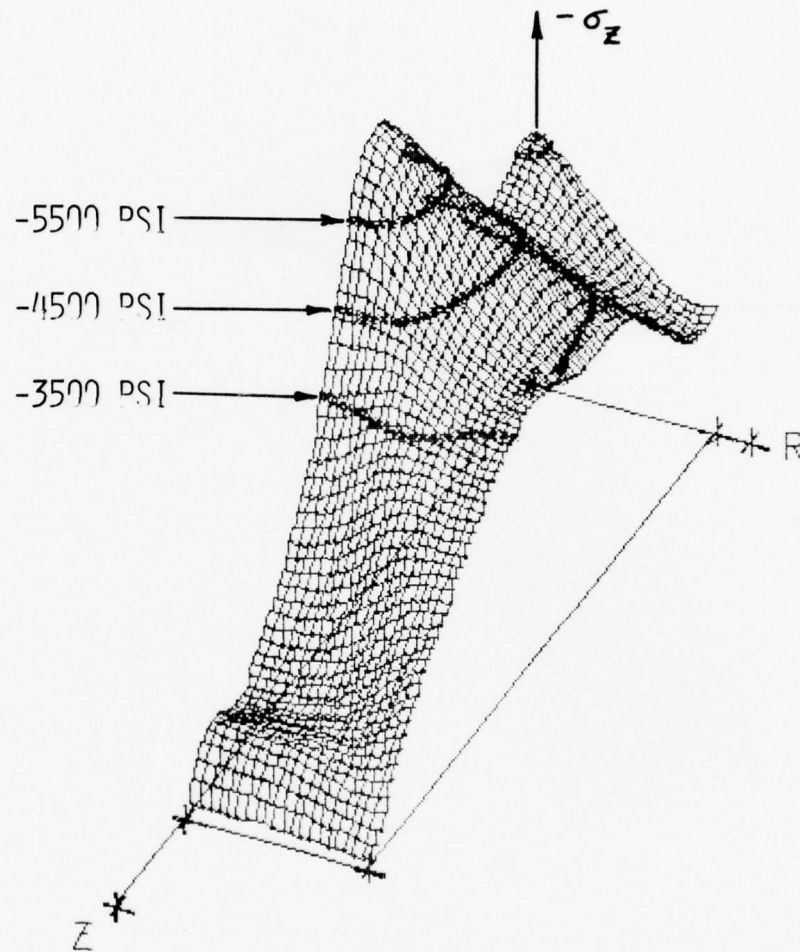


FIG. V.10 AXIAL STRESS IN A MAGNESIUM BAR AT 21.41 USEC FROM A NORMAL IMPACT ON WATER AT 96 FT/SEC (2.5 INCH DIAMETER)

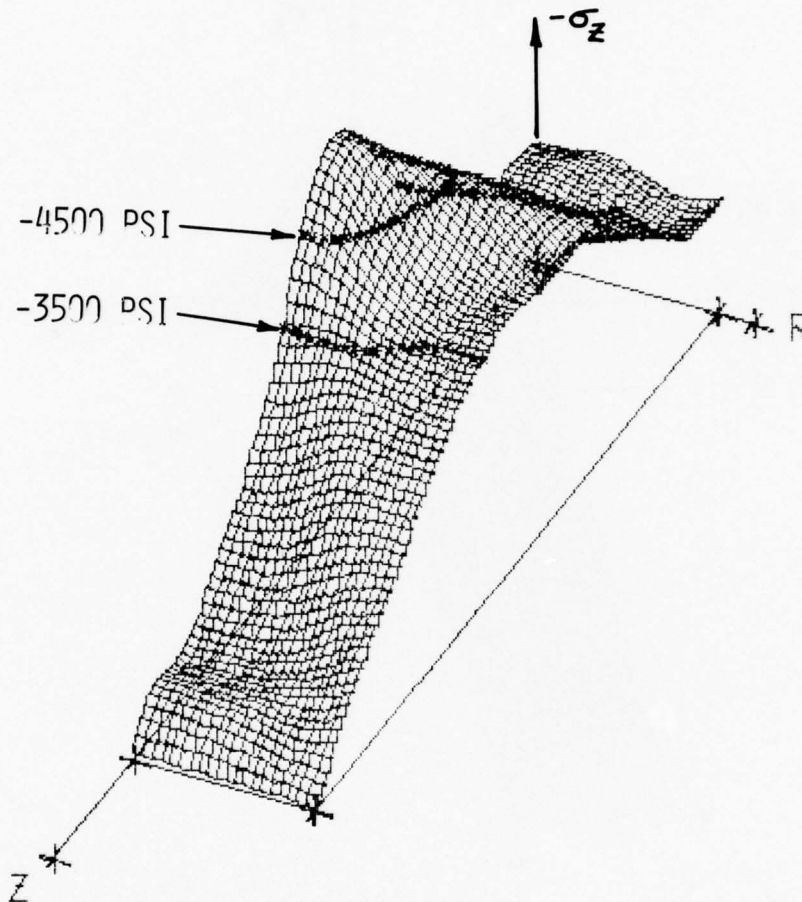


FIG. V.11 AXIAL STRESS IN A MAGNESIUM BAR AT 24.63 USEC FROM A NORMAL IMPACT ON WATER AT 96 FT/SEC (2.5 INCH DIAMETER)

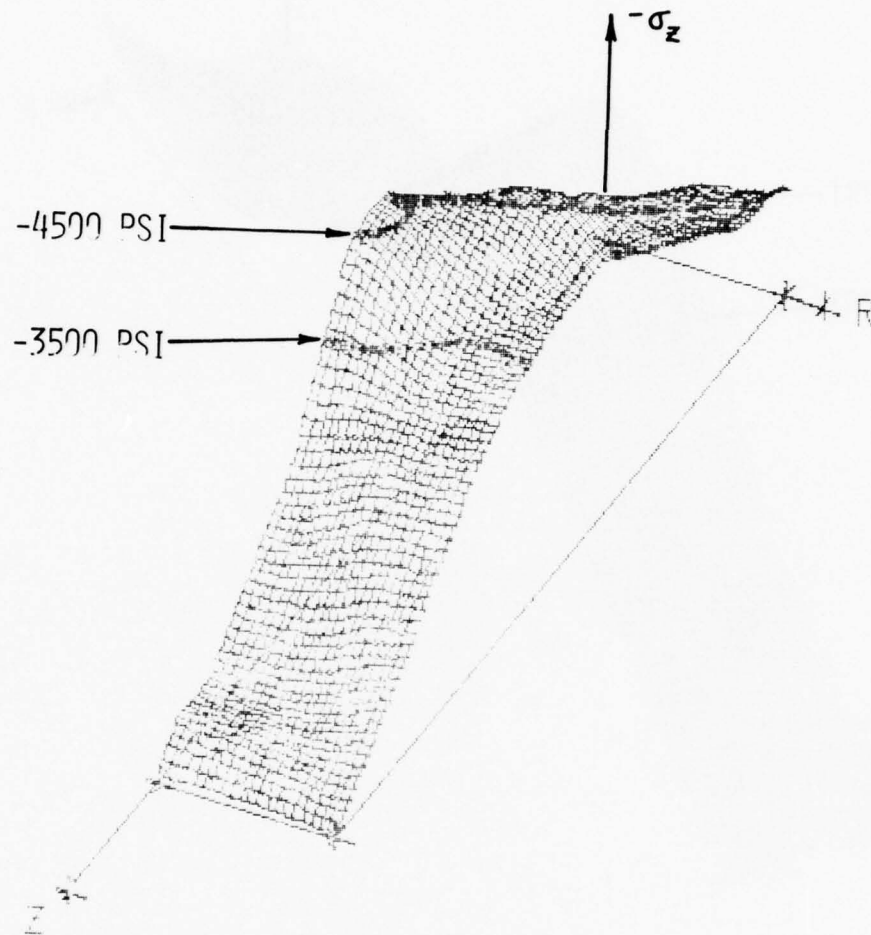


FIG. V.12 AXIAL STRESS IN A MAGNESIUM BAR AT 27.21 USEC FROM A NORMAL IMPACT ON WATER AT 96 FT/SEC (2.5 INCH DIAMETER)

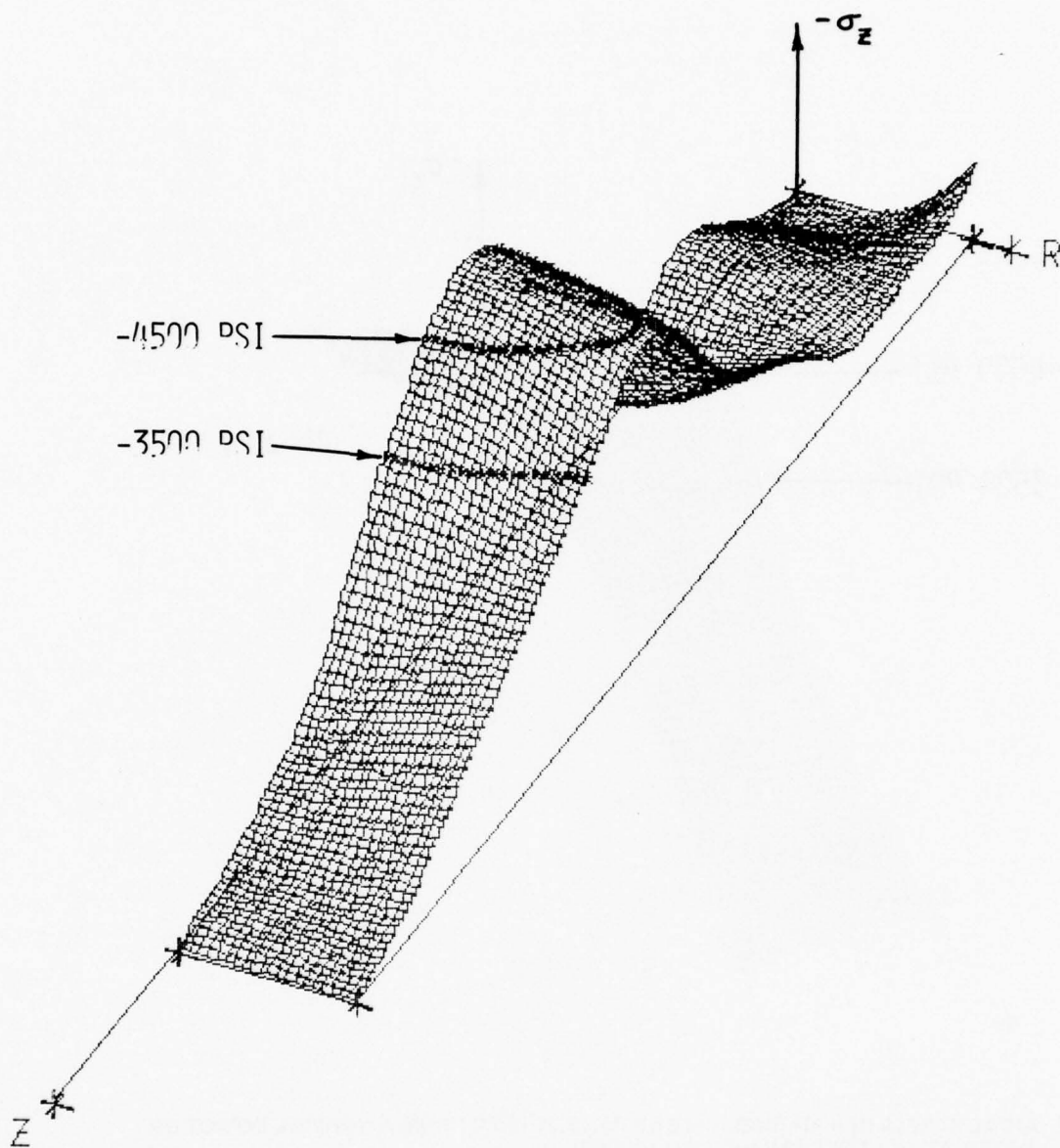


FIG. V.13 AXIAL STRESS IN A MAGNESIUM BAR AT 38.82 USEC FROM A NORMAL IMPACT ON WATER AT 96 FT/SEC (2.5 INCH DIAMETER)

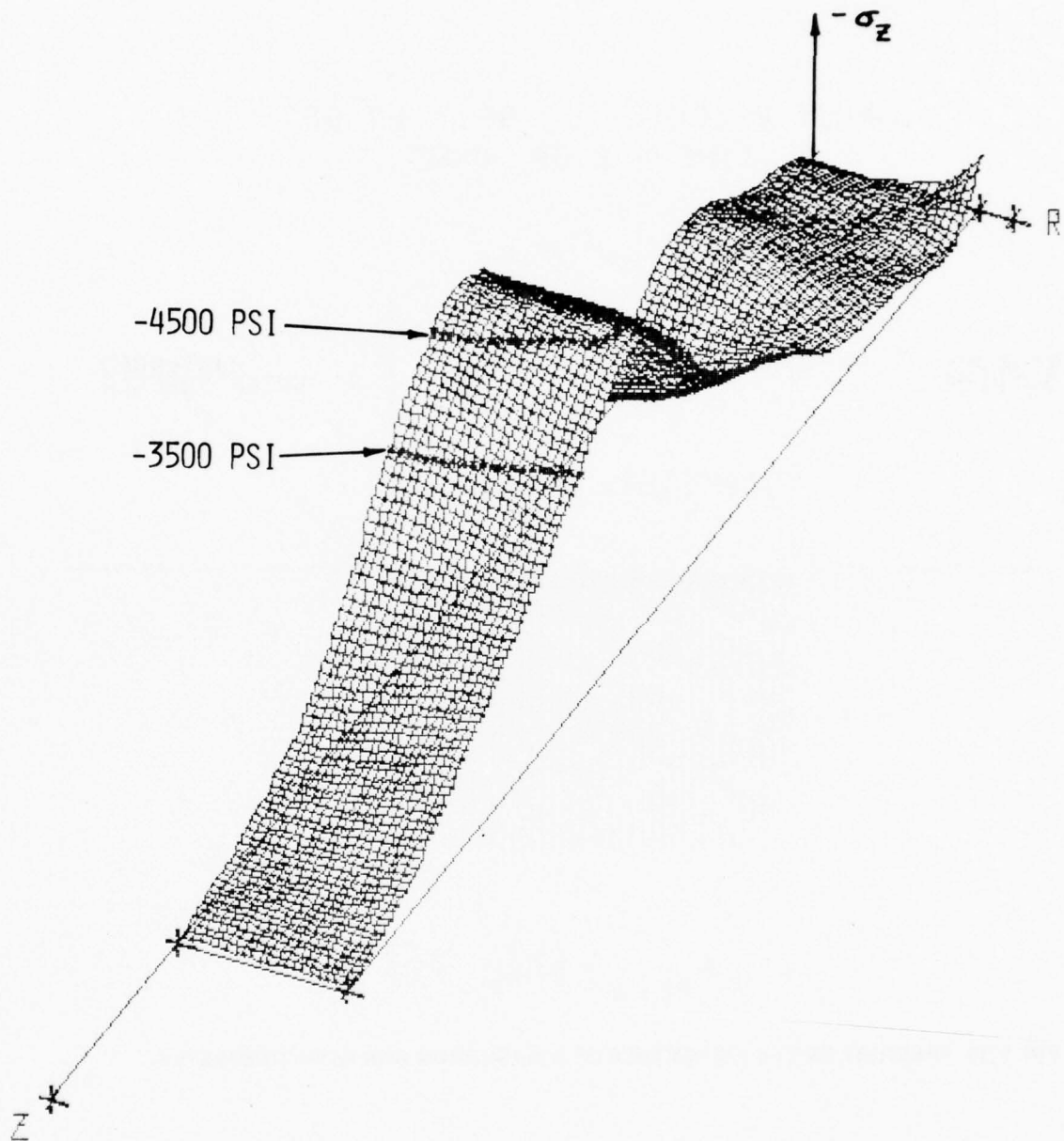


FIG. V.14 AXIAL STRESS IN A MAGNESIUM BAR AT 41.40 USEC FROM A NORMAL IMPACT ON WATER AT 96 FT/SEC (2.5 INCH DIAMETER)

IMPACT VELOCITY = 96 FT/SEC
TIME = 2.06 USEC

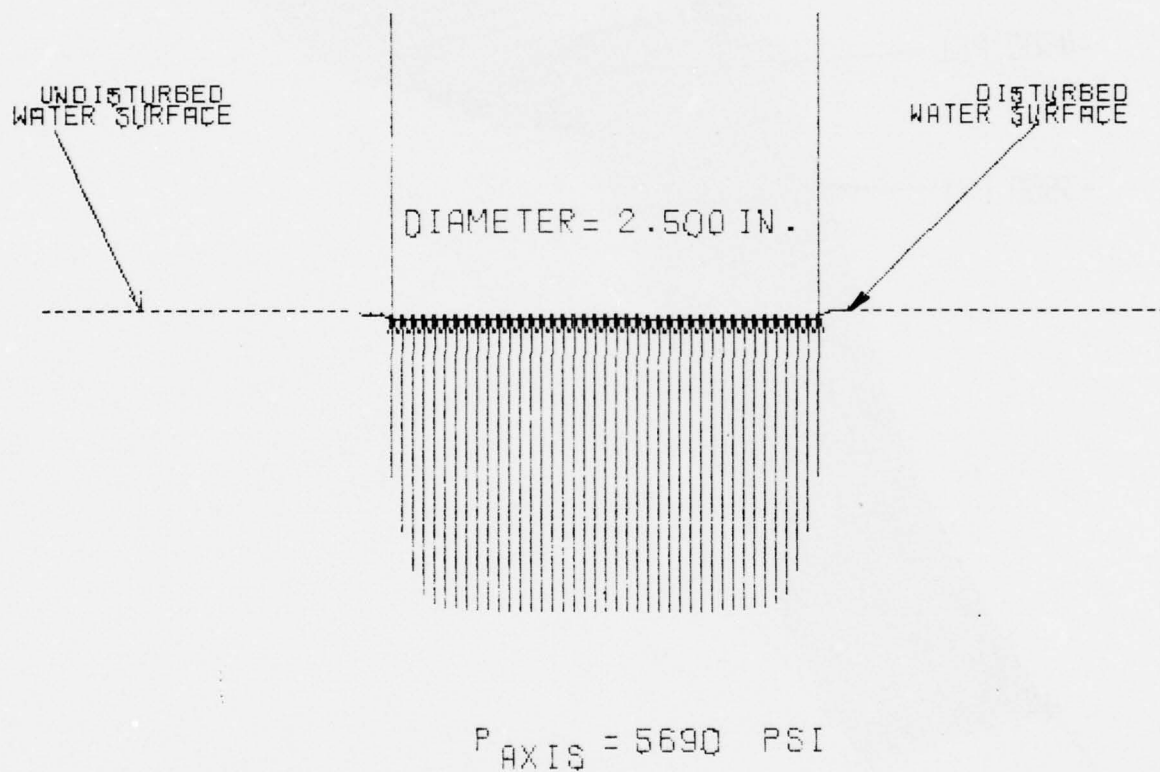
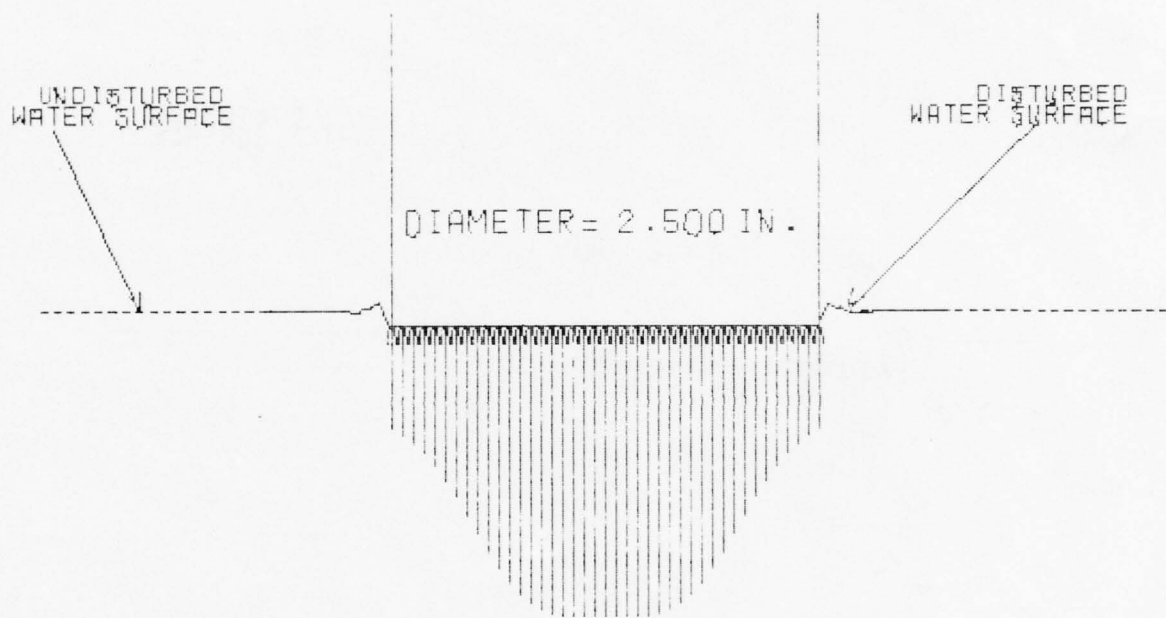


FIG. V.15 PRESSURE ON THE IMPACT FACE OF A MAGNESIUM BAR IMPACTING WATER

IMPACT VELOCITY = 96 FT/SEC
TIME = 11.73 USEC



$P_{\text{AXIS}} = 5549 \text{ PSI}$

FIG. V.16 PRESSURE ON THE IMPACT FACE OF A MAGNESIUM BAR IMPACTING WATER

IMPACT VELOCITY = 96 FT/SEC
TIME = 15.60 USEC

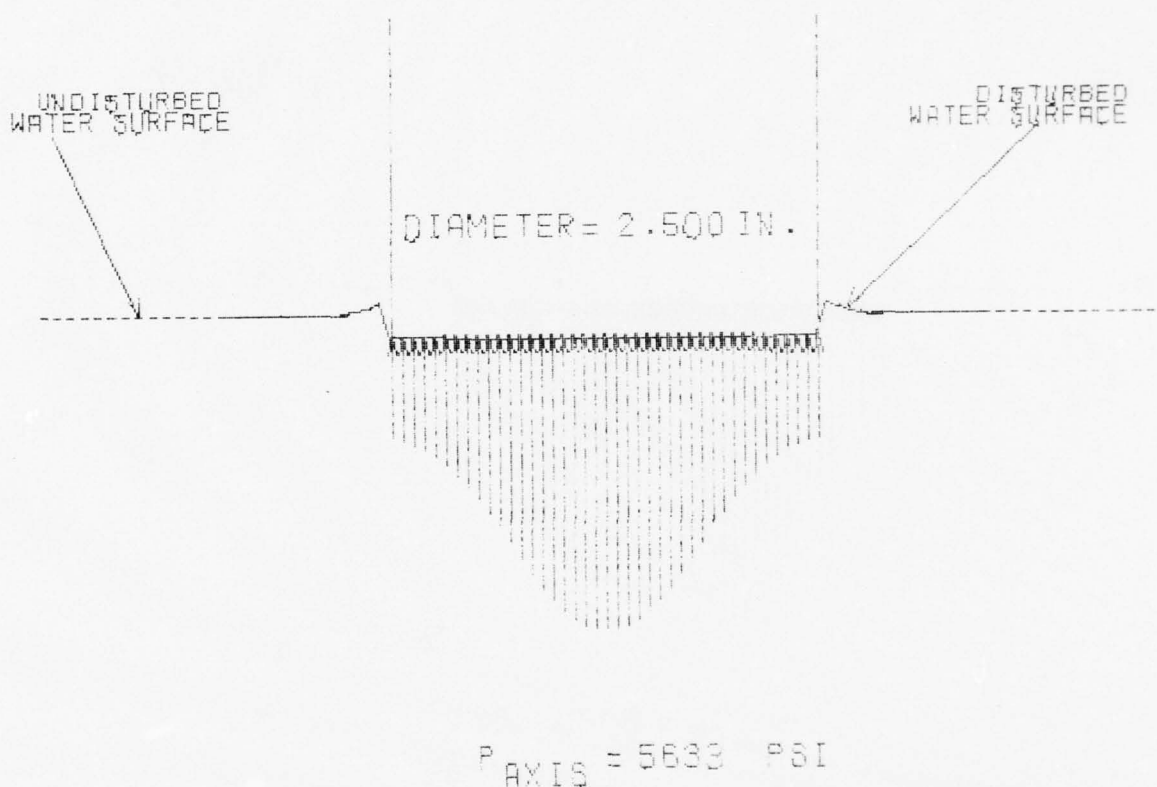
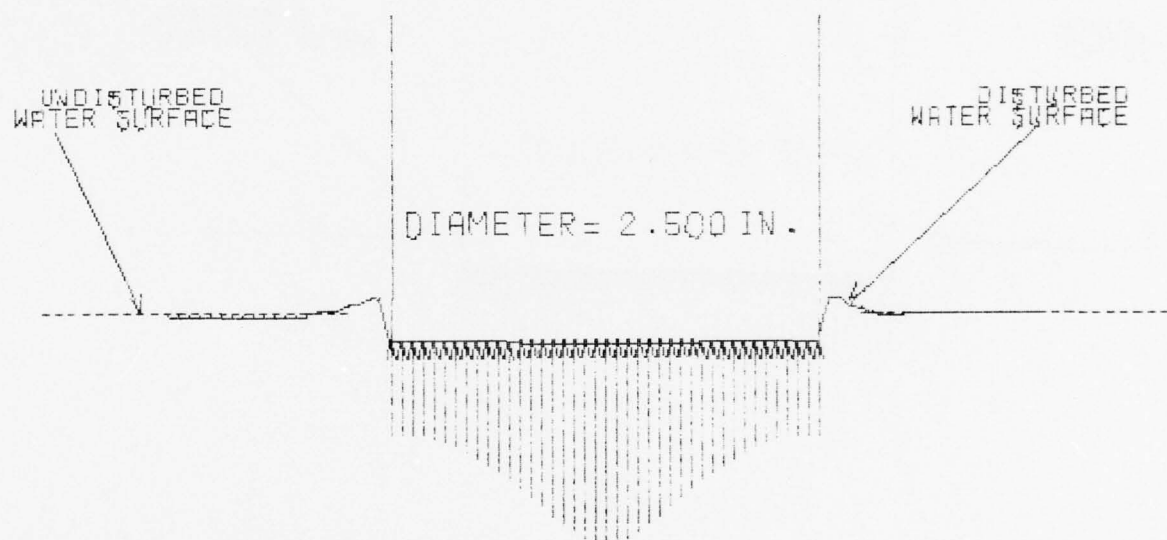


FIG. V.17 PRESSURE ON THE IMPACT FACE OF A MAGNESIUM BAR IMPACTING WATER

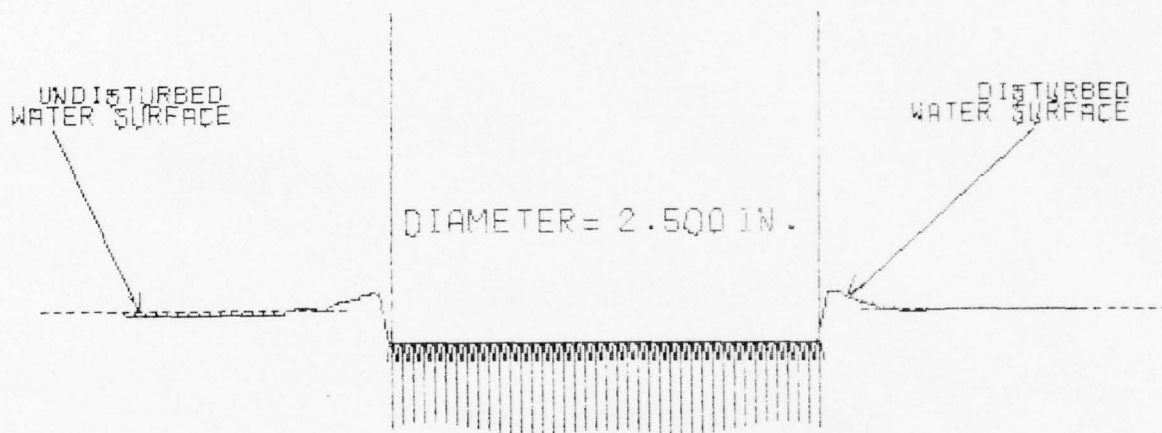
IMPACT VELOCITY = 96 FT/SEC
TIME = 20.76 USEC



$P_{\text{AXIS}} = 3858 \text{ PSI}$

FIG. V.18 PRESSURE ON THE IMPACT FACE OF A MAGNESIUM BAR IMPACTING WATER

IMPACT VELOCITY = 96 FT/SEC
TIME = 24.63 USEC



P_{AXIS} = 1675 PSI

FIG. V.19 PRESSURE ON THE IMPACT FACE OF A MAGNESIUM BAR IMPACTING WATER

IMPACT VELOCITY = 96 FT/SEC
TIME = 27.21 USEC

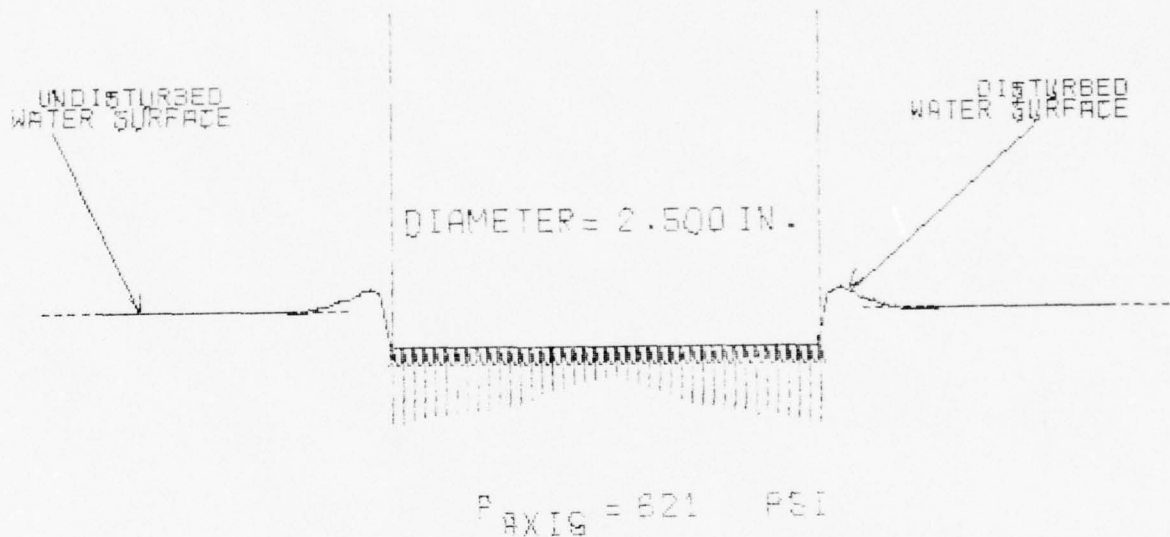


FIG. V.20 PRESSURE ON THE IMPACT FACE OF A MAGNESIUM BAR IMPACTING WATER

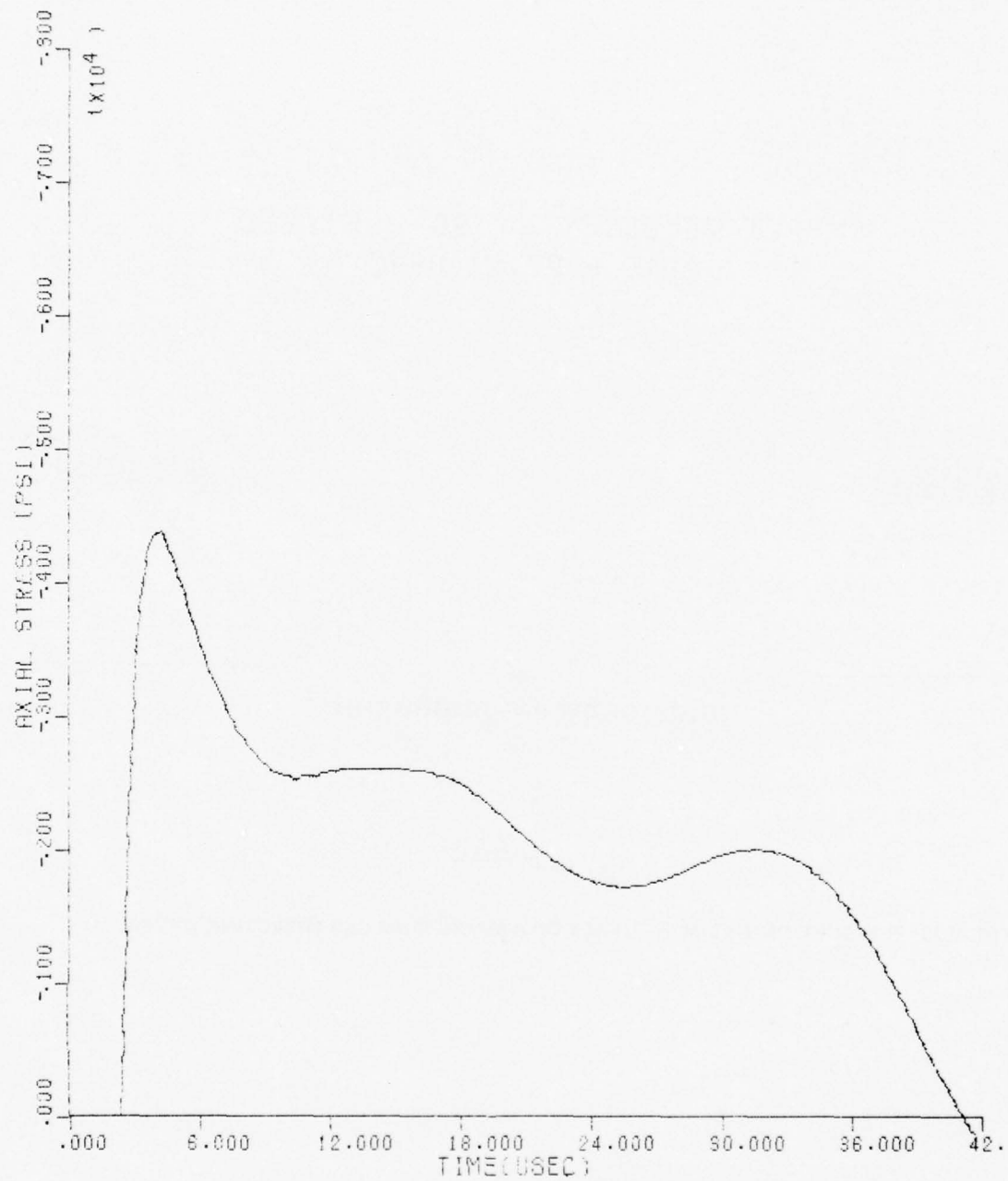


FIG. V.21 AXIAL STRESS VS TIME (2.500 INCH DIAMETER MAGNESIUM BAR IMPACT
VELOCITY = 96.0 FT/SEC R = 1.250 INCHES Z = .625 INCHES)

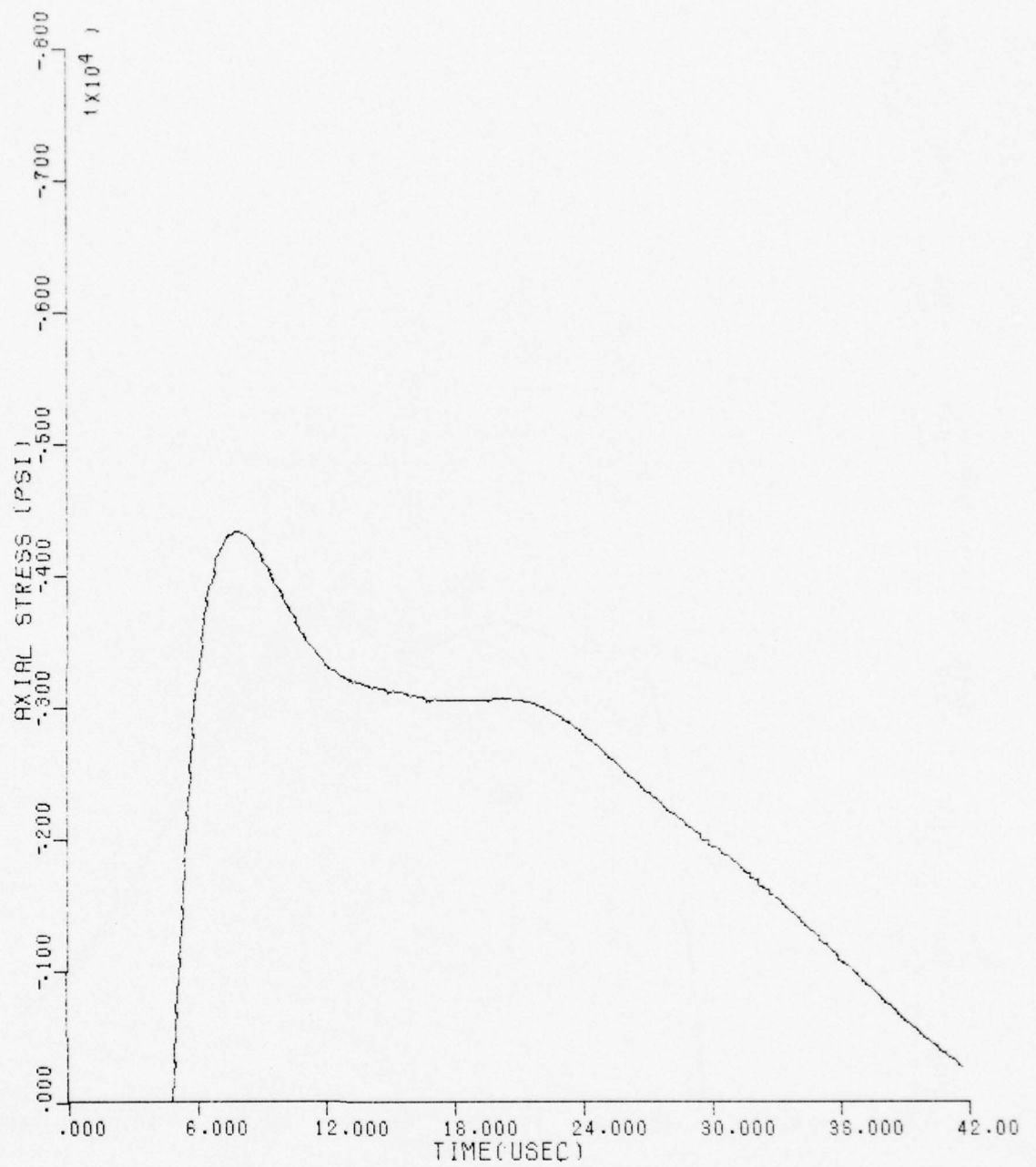


FIG. V.22 AXIAL STRESS VS TIME (2.500 INCH DIAMETER MAGNESIUM BAR IMPACT
VELOCITY = 96.0 FT/SEC R = 1.250 INCHES Z = 1.250 INCHES)

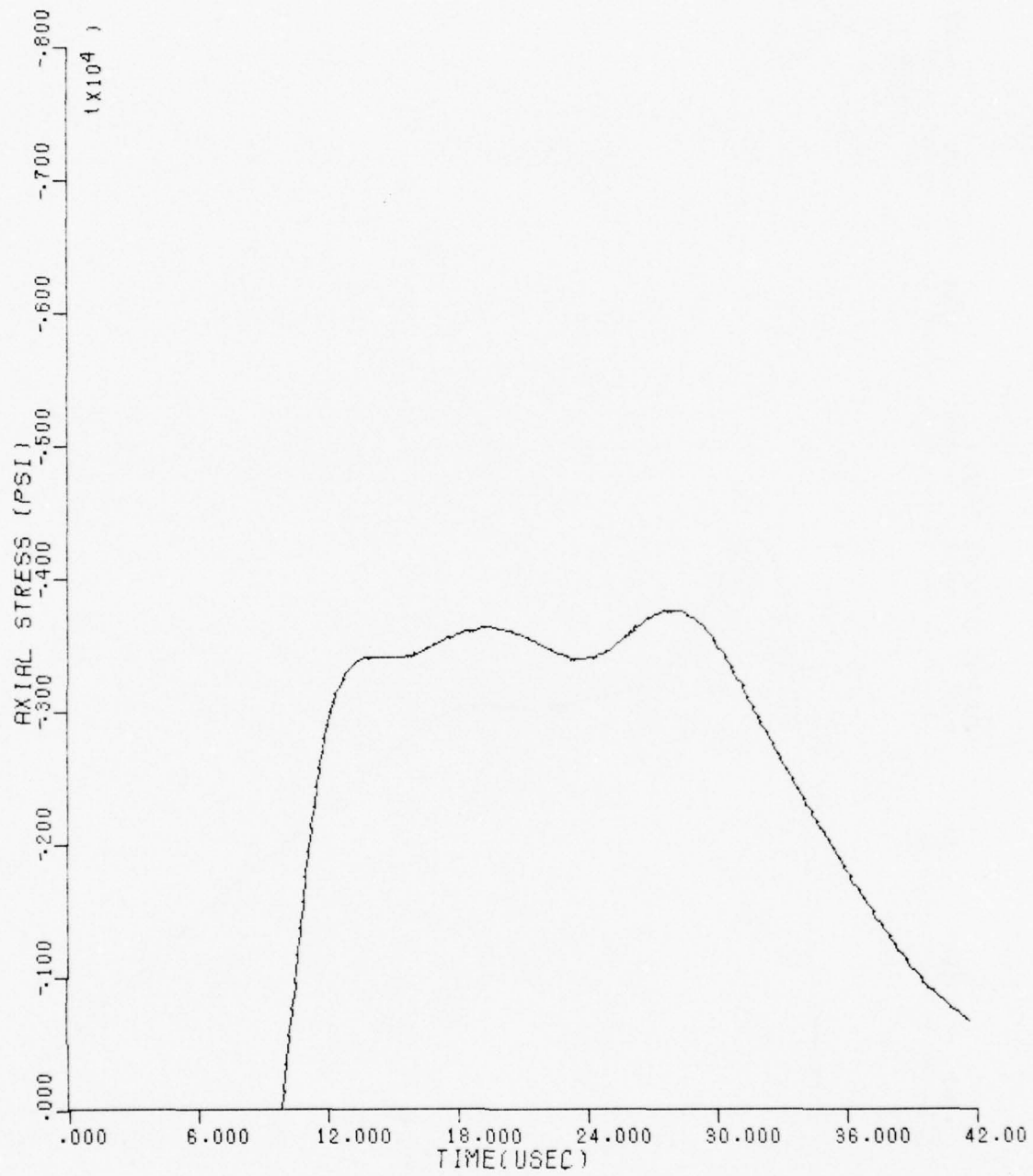


FIG. V.23 AXIAL STRESS VS TIME (2.500 INCH DIAMETER MAGNESIUM BAR IMPACT
VELOCITY = 96.0 FT/SEC R = 1.250 INCHES Z = 2.500 INCHES)

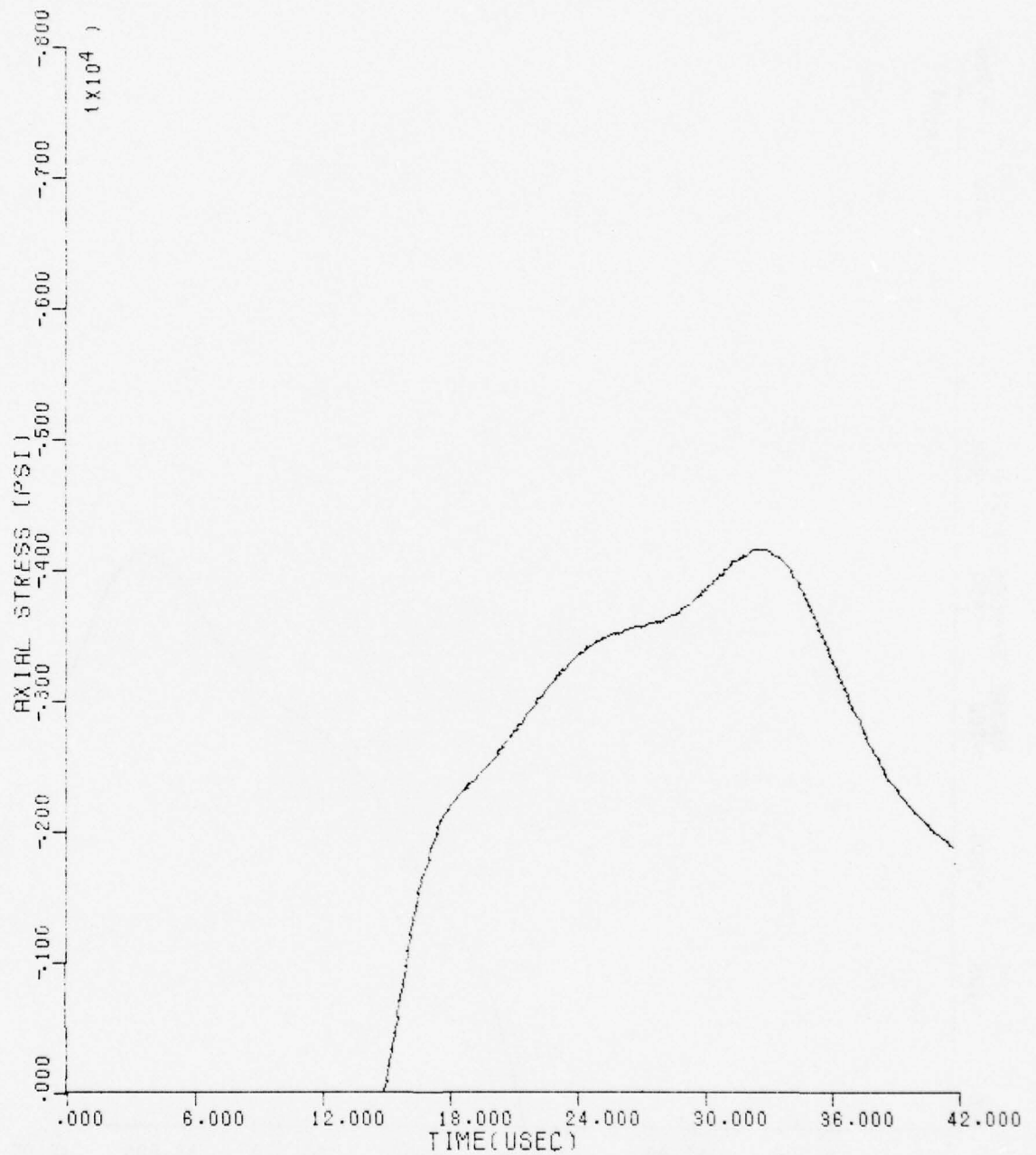


FIG. V.24 AXIAL STRESS VS TIME (2.500 INCH DIAMETER MAGNESIUM BAR IMPACT
VELOCITY = 96.0 FT/SEC R = 1.250 INCHES Z = 3.750 INCHES)

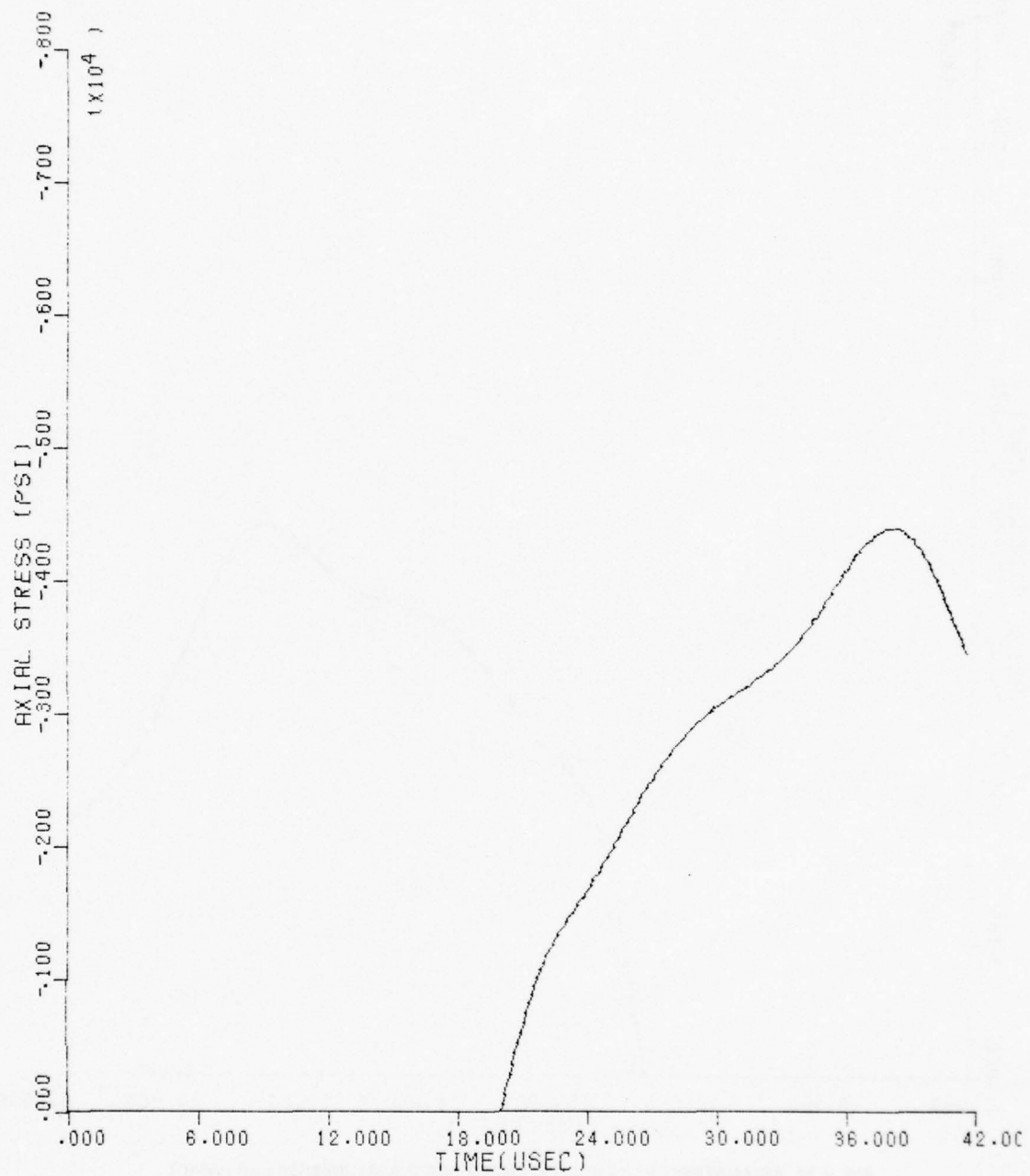


FIG. V.25 AXIAL STRESS VS TIME (2.500 INCH DIAMETER MAGNESIUM BAR IMPACT
VELOCITY = 96.0 FT/SEC R = 1.250 INCHES Z = 5.0 INCHES)

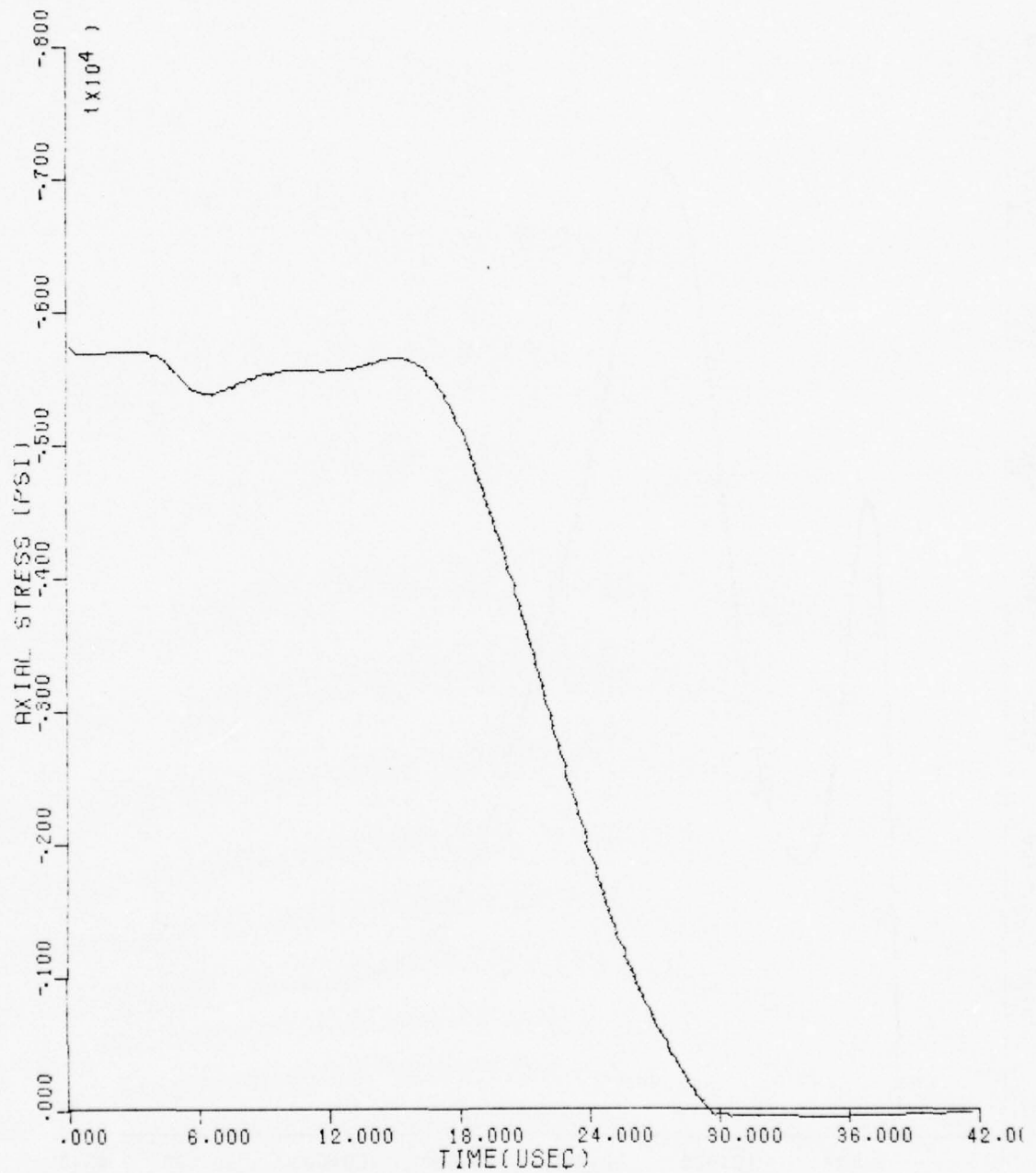


FIG. V.26 AXIAL STRESS VS TIME (2.500 INCH DIAMETER MAGNESIUM BAR IMPACT
VELOCITY = 96.0 FT/SEC R = 0.000 INCHES Z = 0.000 INCHES)

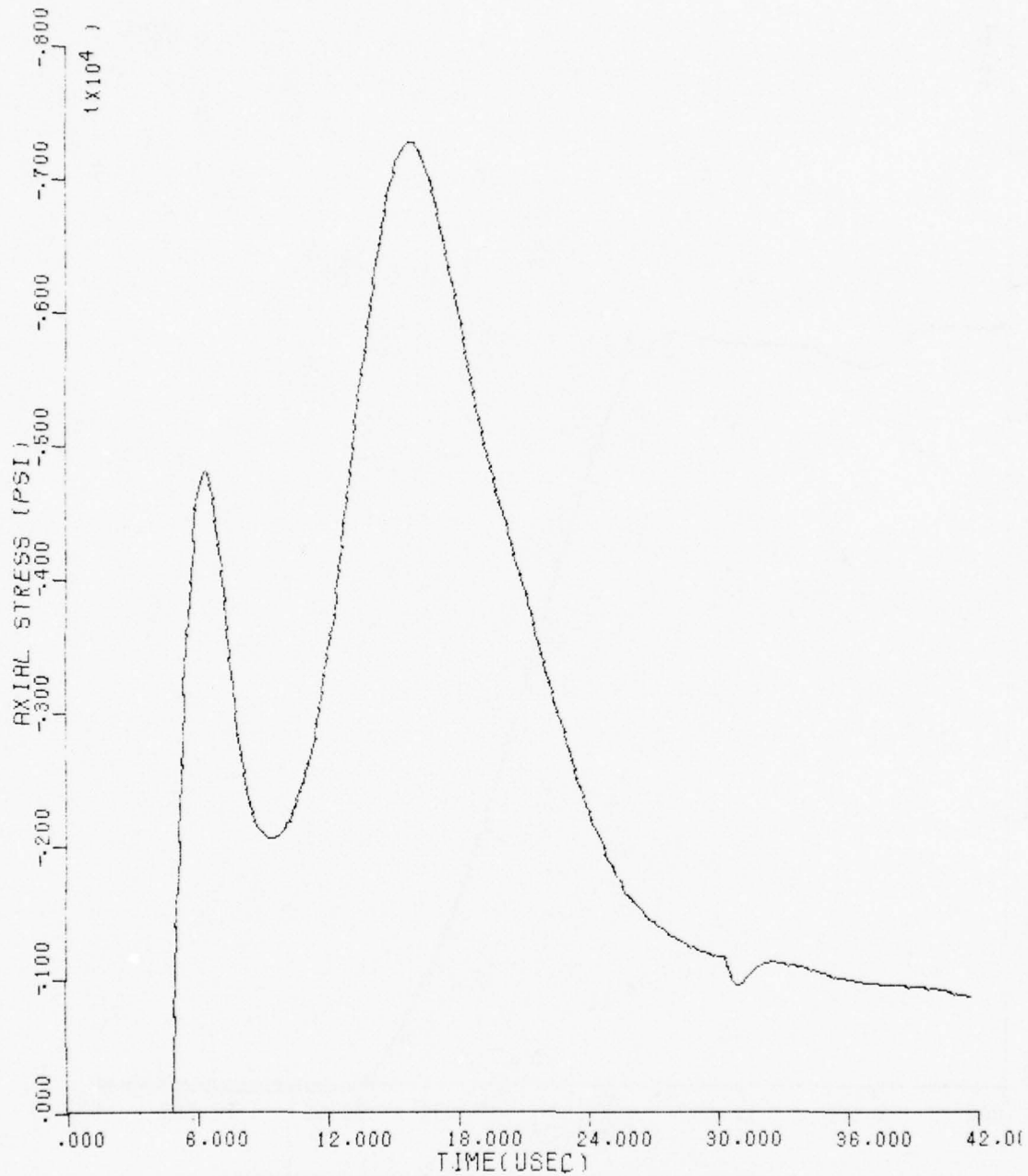


FIG. V.27 AXIAL STRESS VS TIME (2.500 INCH DIAMETER MAGNESIUM BAR IMPACT
VELOCITY = 96.0 FT/SEC R = 0.000 INCHES Z = 1.250 INCHES)

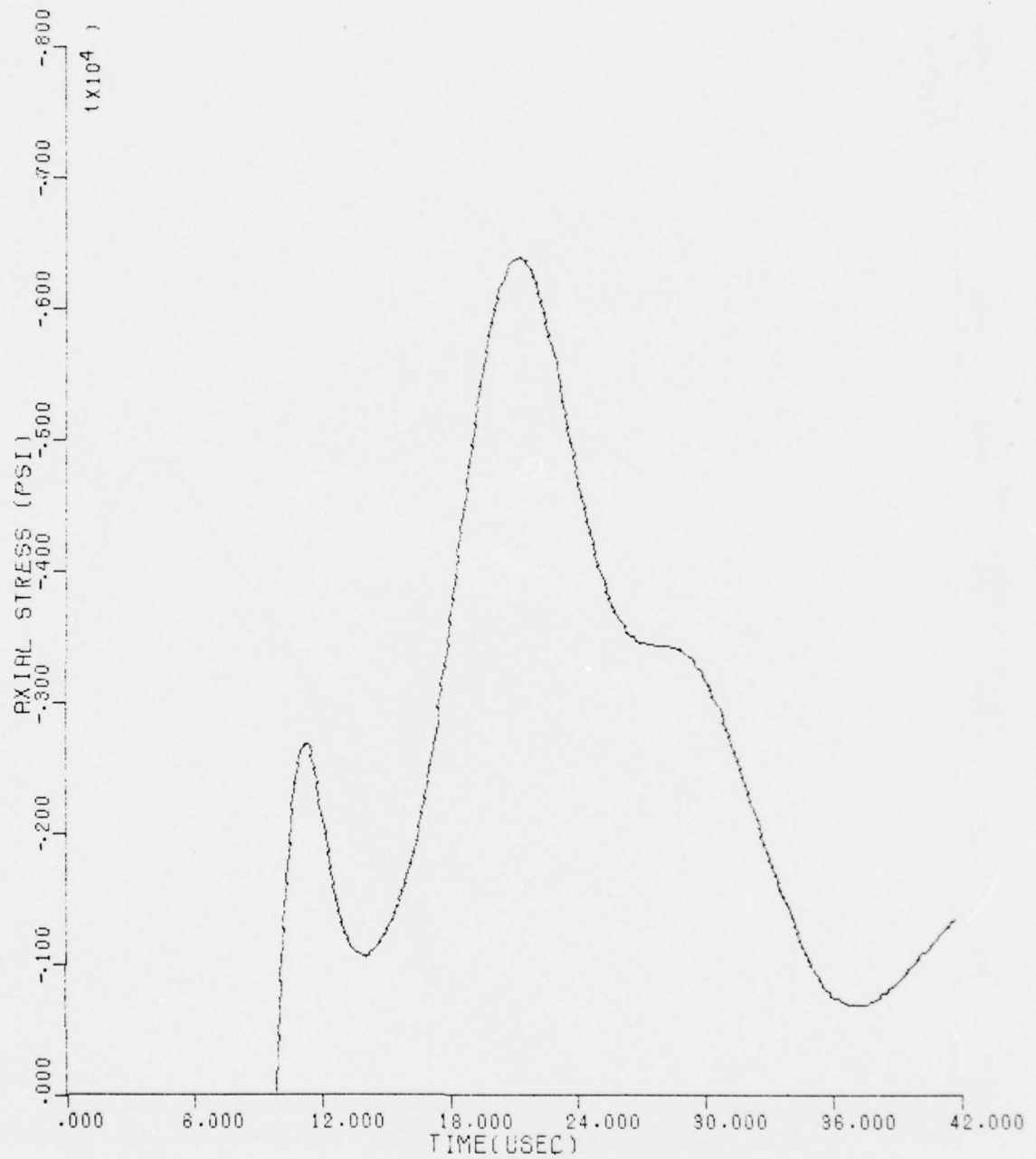


FIG. V.28 AXIAL STRESS VS TIME (2.500 INCH DIAMETER MAGNESIUM BAR IMPACT
VELOCITY = 96.0 FT/SEC R = 0.000 INCHES Z = 2.500 INCHES)

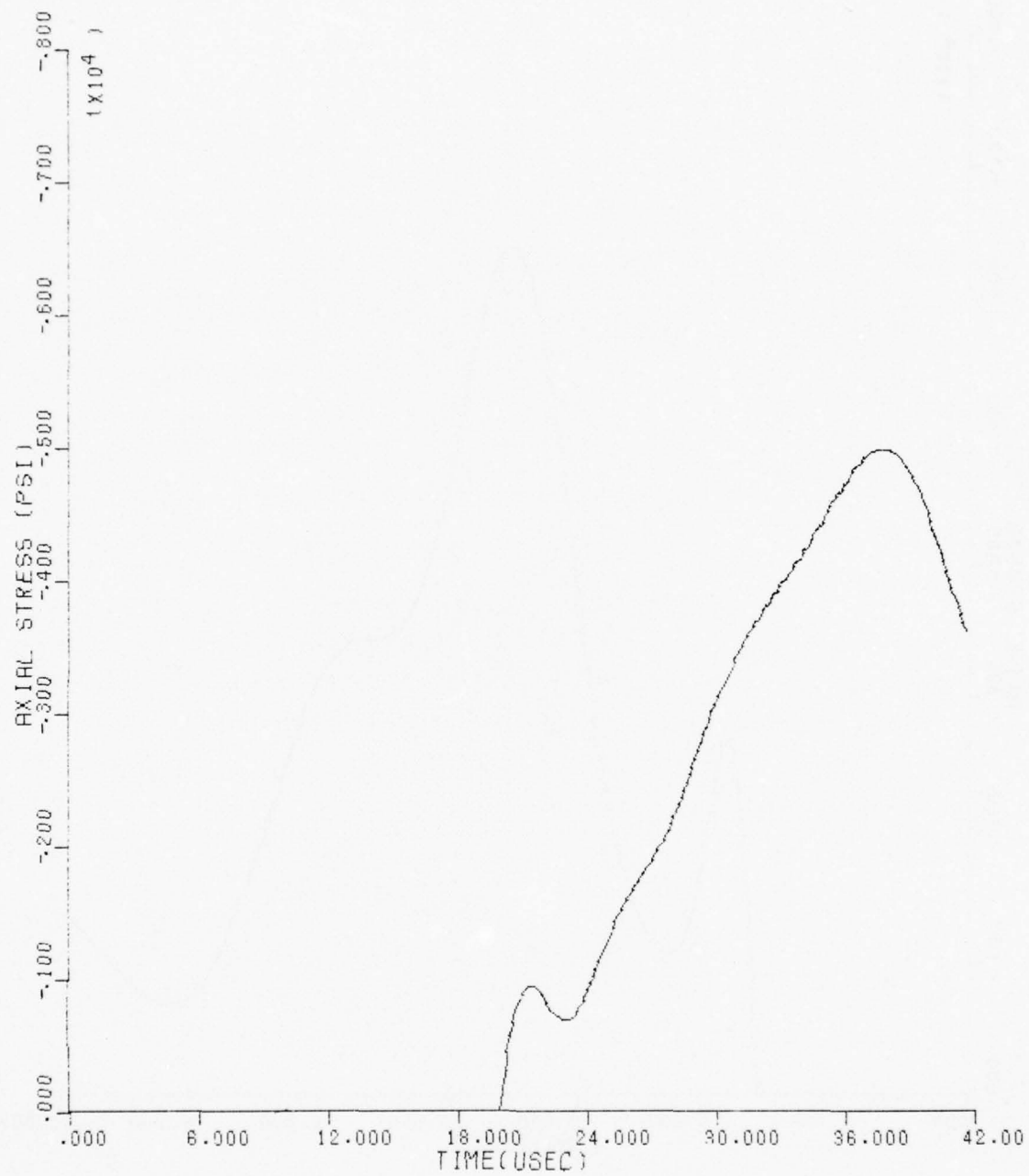


FIG. V.29 AXIAL STRESS VS TIME (2.500 INCH DIAMETER MAGNESIUM BAR IMPACT
VELOCITY = 96.0 FT/SEC R = 0.000 INCHES Z = 5.000 INCHES)

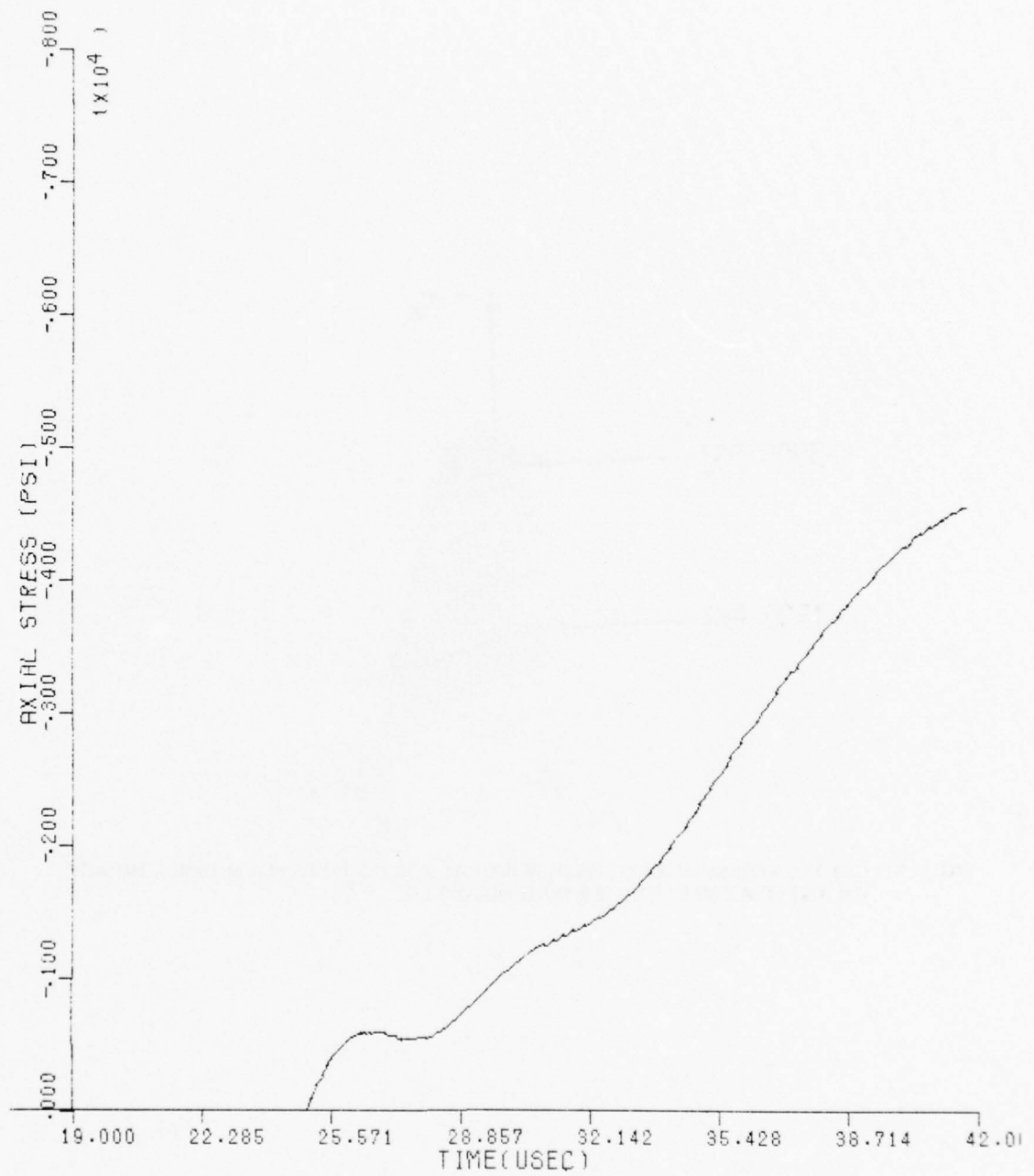


FIG. V.30 AXIAL STRESS VS TIME (2.500 INCH DIAMETER MAGNESIUM BAR IMPACT
VELOCITY = 96.0 FT/SEC R = 0.000 INCHES Z = 6.250 INCHES)

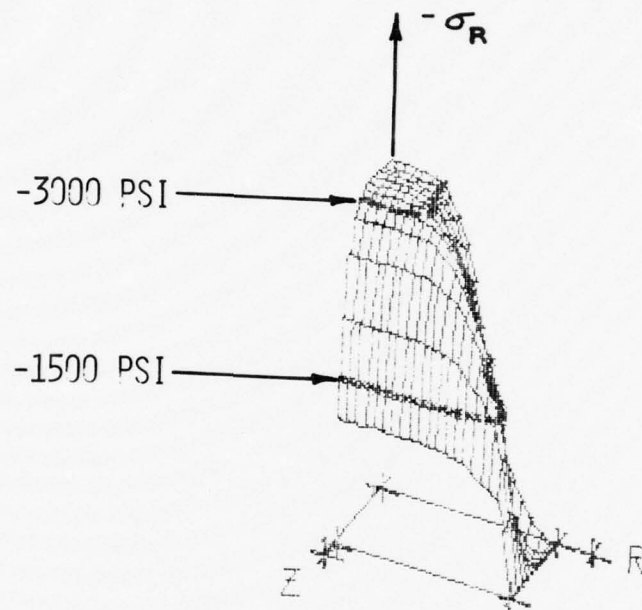


FIG. V.31 RADIAL STRESS IN A MAGNESIUM BAR AT 2.70 USEC FROM A NORMAL IMPACT ON WATER AT 96 FT/SEC (2.5 INCH DIAMETER)

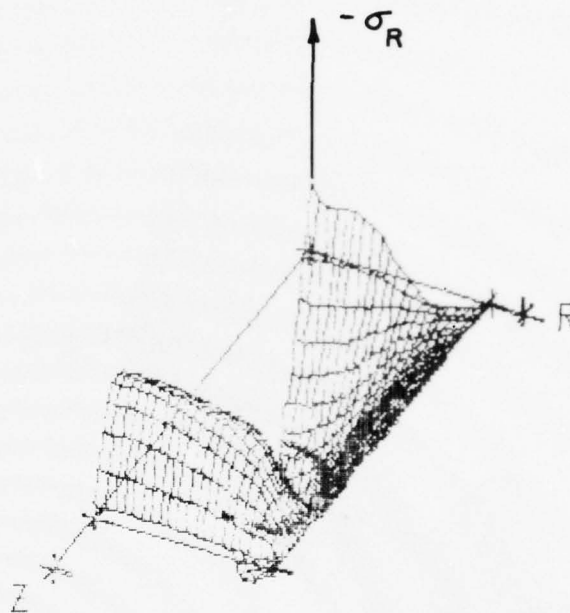


FIG. V.32 RADIAL STRESS IN A MAGNESIUM BAR AT 13.02 USEC FROM A NORMAL IMPACT ON WATER AT 96 FT/SEC (2.5 INCH DIAMETER)

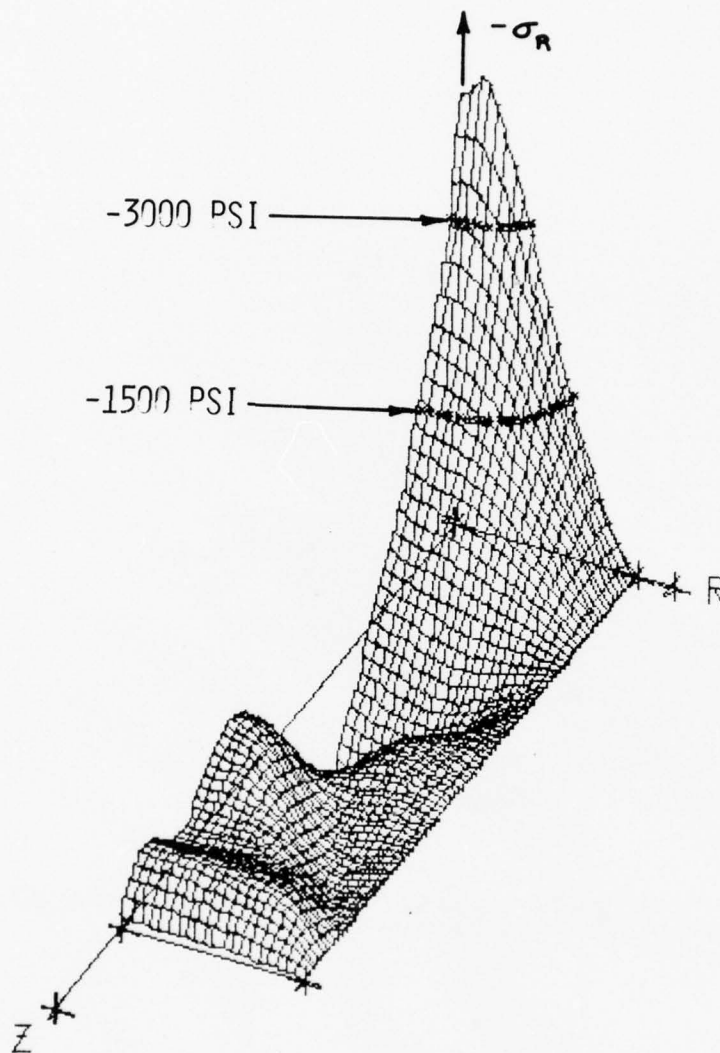


FIG. V.33 RADIAL STRESS IN A MAGNESIUM BAR AT 20.12 USEC FROM A NORMAL IMPACT ON WATER AT 96 FT/SEC (2.5 INCH DIAMETER)

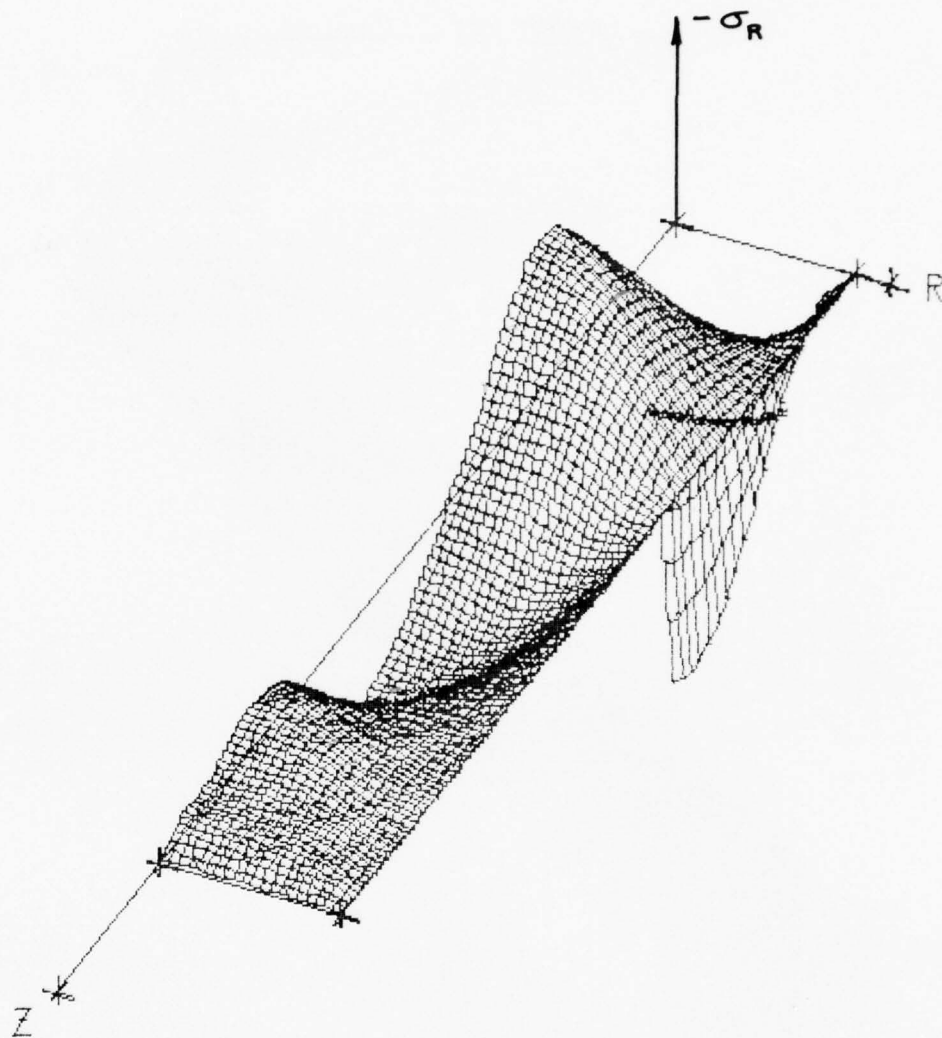


FIG. V.34 RADIAL STRESS IN A MAGNESIUM BAR AT 31.72 USEC FROM A NORMAL IMPACT ON WATER AT 96 FT/SEC (2.5 INCH DIAMETER)

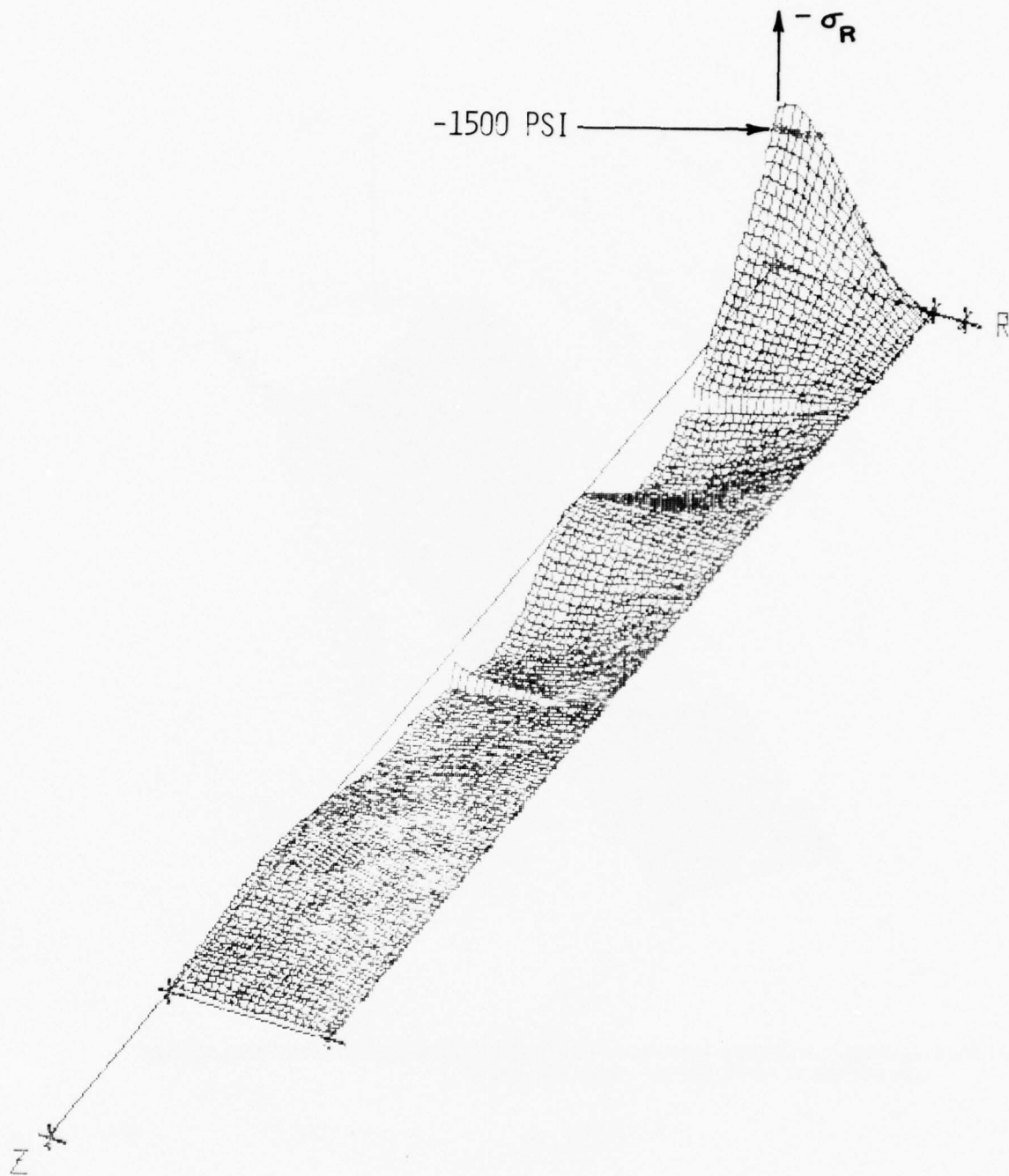


FIG. V.35 RADIAL STRESS IN A MAGNESIUM BAR AT 41.40 USEC FROM A NORMAL IMPACT ON WATER AT 96 FT/SEC (2.5 INCH DIAMETER)

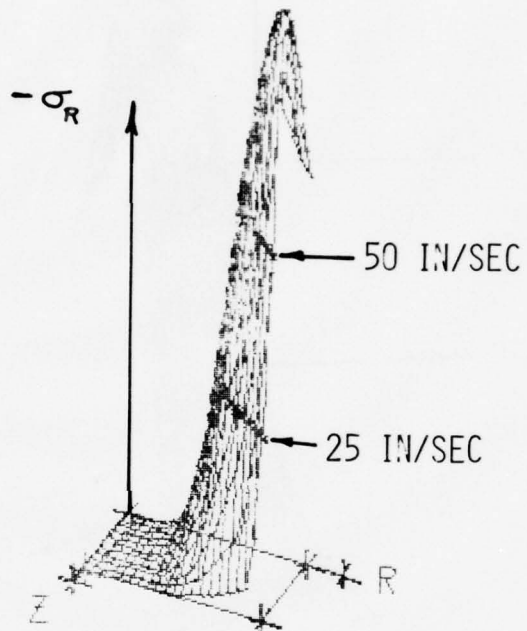


FIG. V.36 RADIAL VEL. IN A MAGNESIUM BAR AT 2.70 USEC FROM A NORMAL IMPACT ON WATER AT 96 FT/SEC (2.5 INCH DIAMETER)

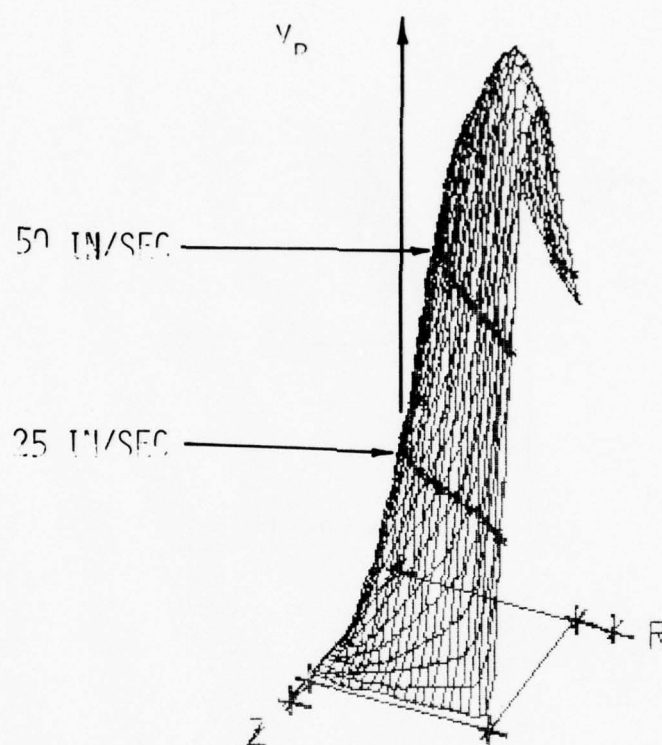


FIG. V.37 RADIAL VEL. IN A MAGNESIUM BAR AT 5.28 USEC FROM A NORMAL IMPACT ON WATER AT 96 FT/SEC (2.5 INCH DIAMETER)

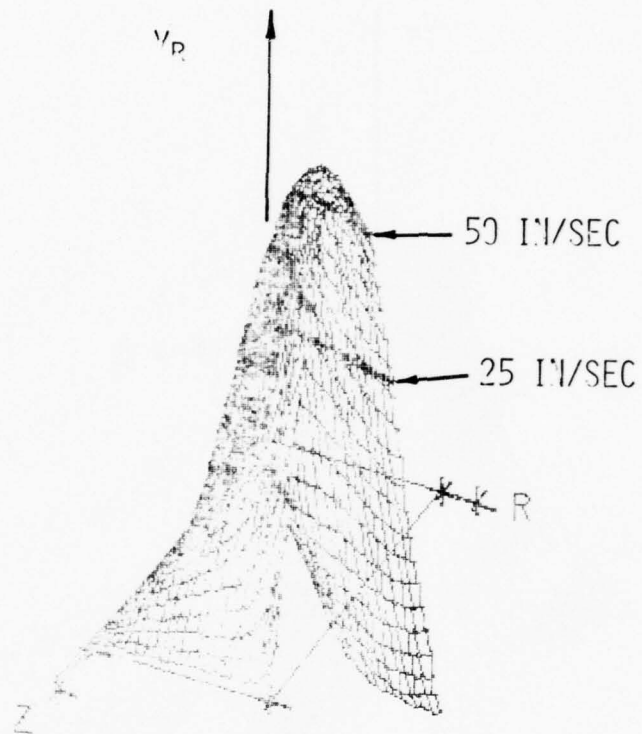


FIG. V. 38 RADIAL VEL. IN A MAGNESIUM BAR AT 10.44 USEC FROM A NORMAL IMPACT ON WATER AT 96 FT/SEC (2.5 INCH DIAMETER)

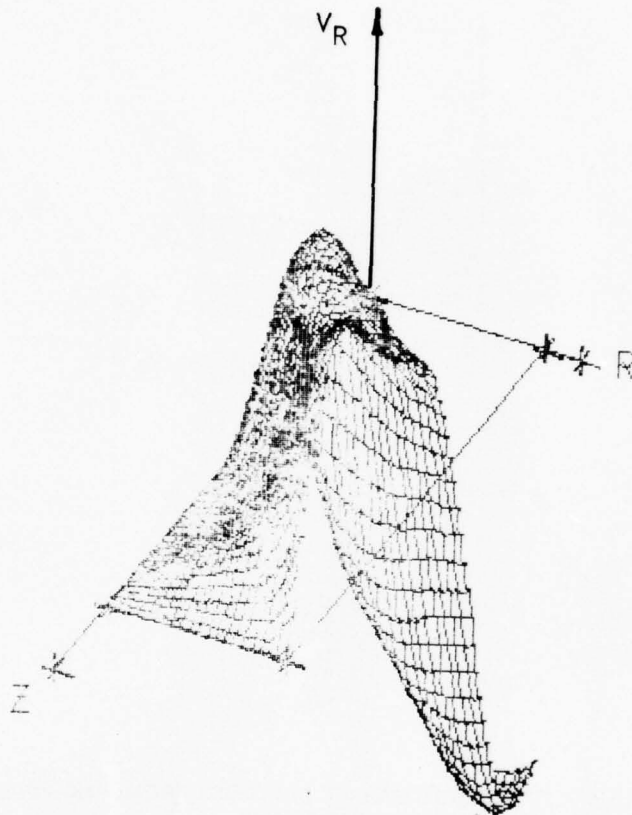


FIG. V.39 RADIAL VEL. IN A MAGNESIUM BAR AT 15.60 USEC FROM A NORMAL IMPACT ON WATER AT 96 FT/SEC (2.5 INCH DIAMETER)

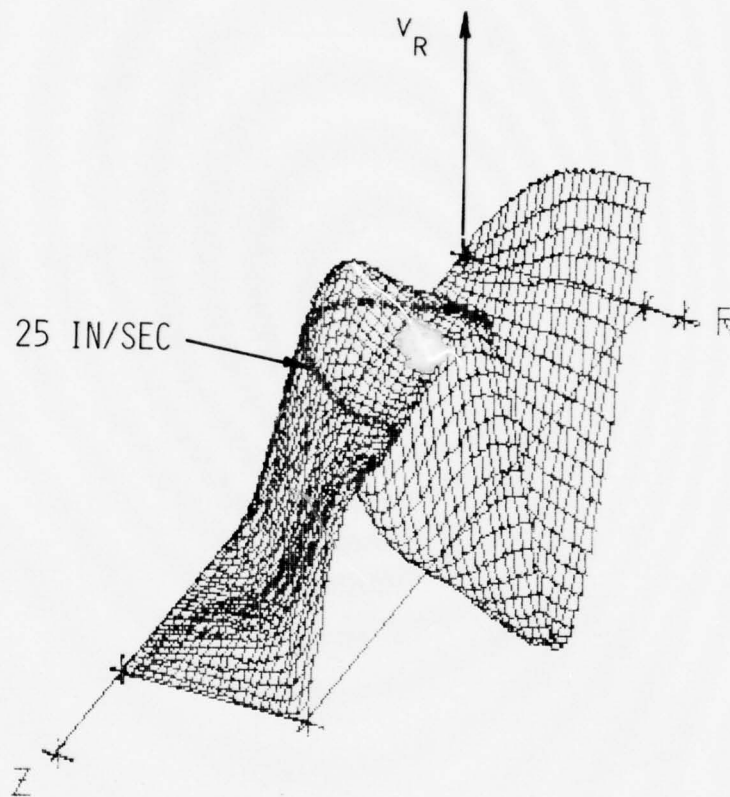


FIG. V.40 RADIAL VEL. IN A MAGNESIUM BAR AT 20.76 USEC FROM A NORMAL IMPACT ON WATER AT 96 FT/SEC (2.5 INCH DIAMETER)

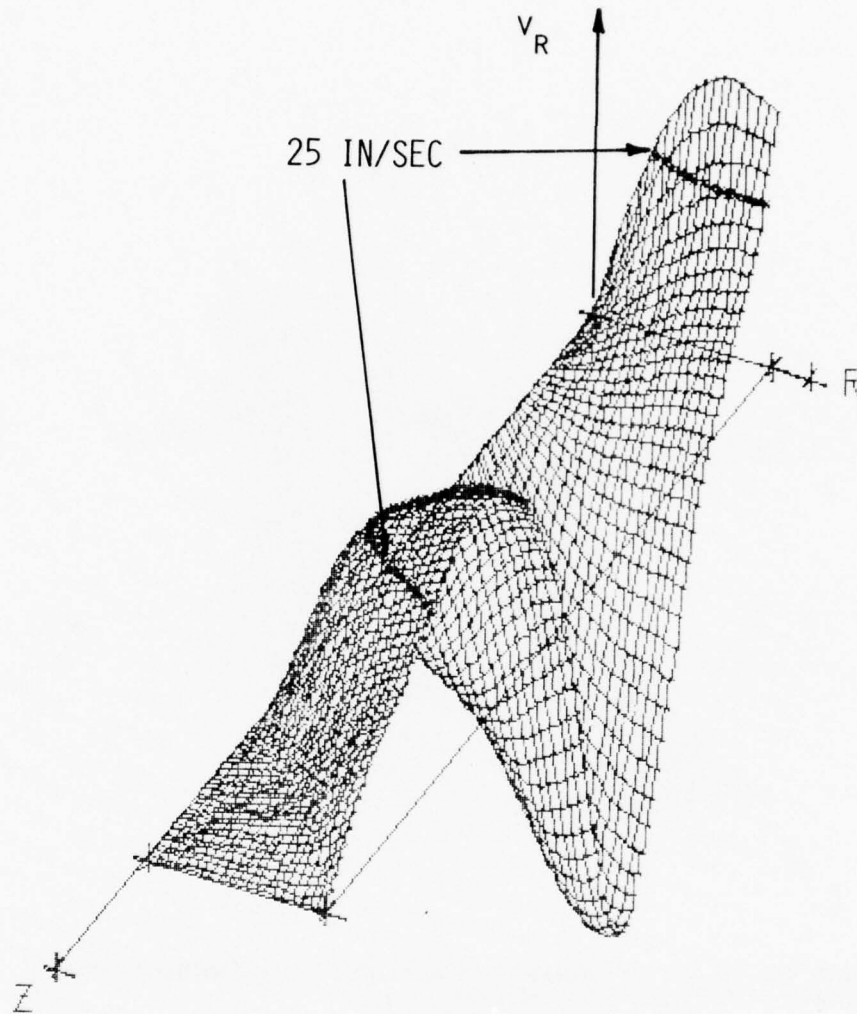


FIG. V.41 RADIAL VEL. IN A MAGNESIUM BAR AT 27.21 USEC FROM A NORMAL IMPACT ON WATER AT 96 FT/SEC (2.5 INCH DIAMETER)

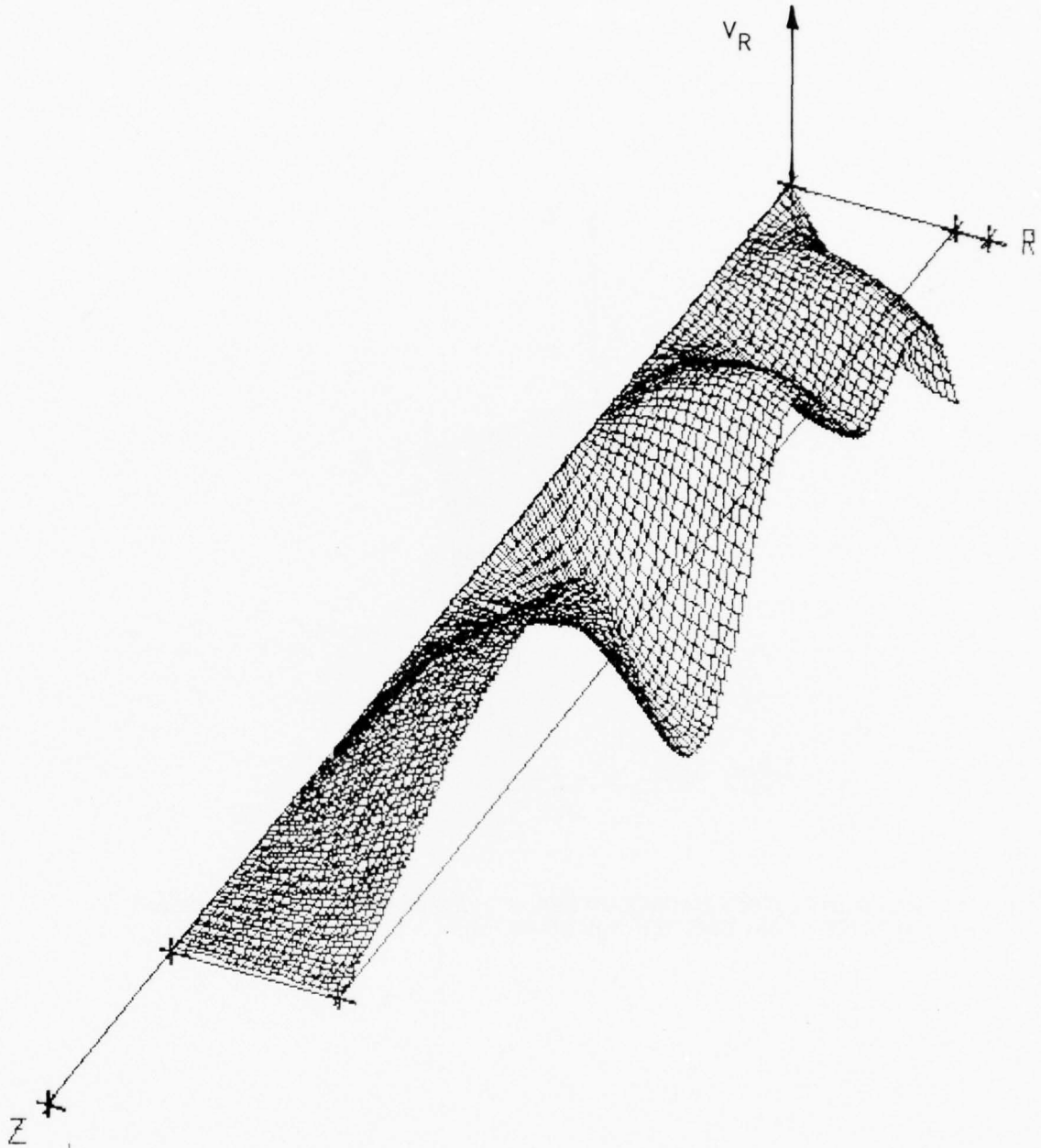


FIG. V.42 RADIAL VEL. IN A MAGNESIUM BAR AT 41.40 USEC FROM A NORMAL IMPACT ON WATER AT 96 FT/SEC (2.5 INCH DIAMETER)

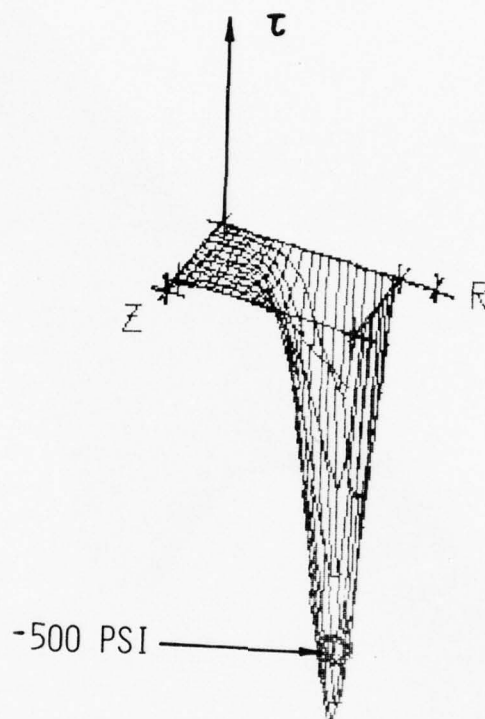


FIG. V.43 SHEAR STRESS IN A MAGNESIUM BAR AT 2.70 USEC FROM A NORMAL IMPACT ON WATER AT 96 FT/SEC (2.5 INCH DIAMETER)

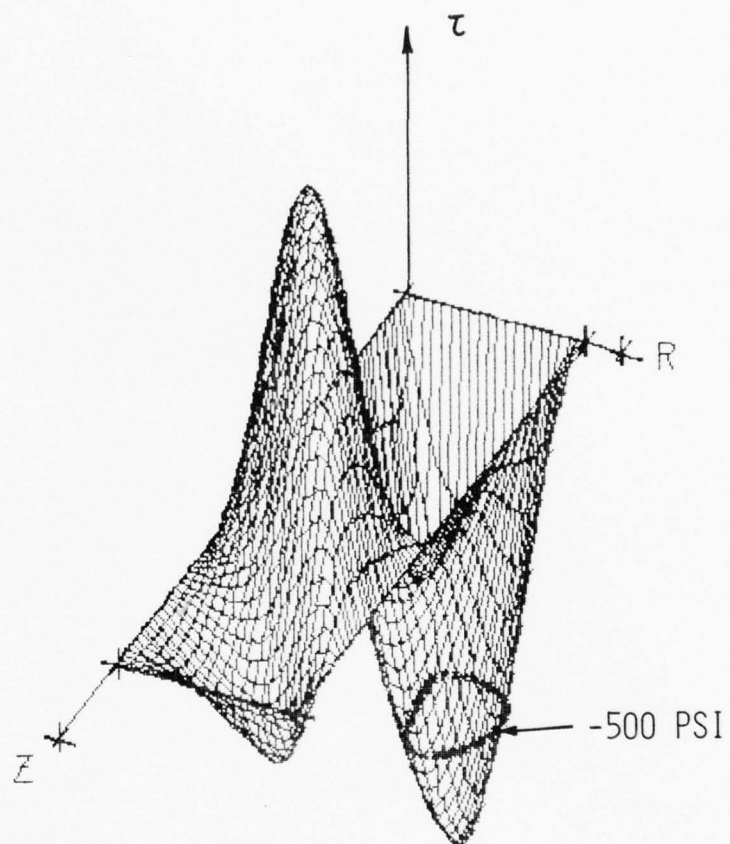


FIG. V.44 SHEAR STRESS IN A MAGNESIUM BAR AT 18.18 USEC FROM A NORMAL IMPACT ON WATER AT 96 FT/SEC (2.5 INCH DIAMETER)

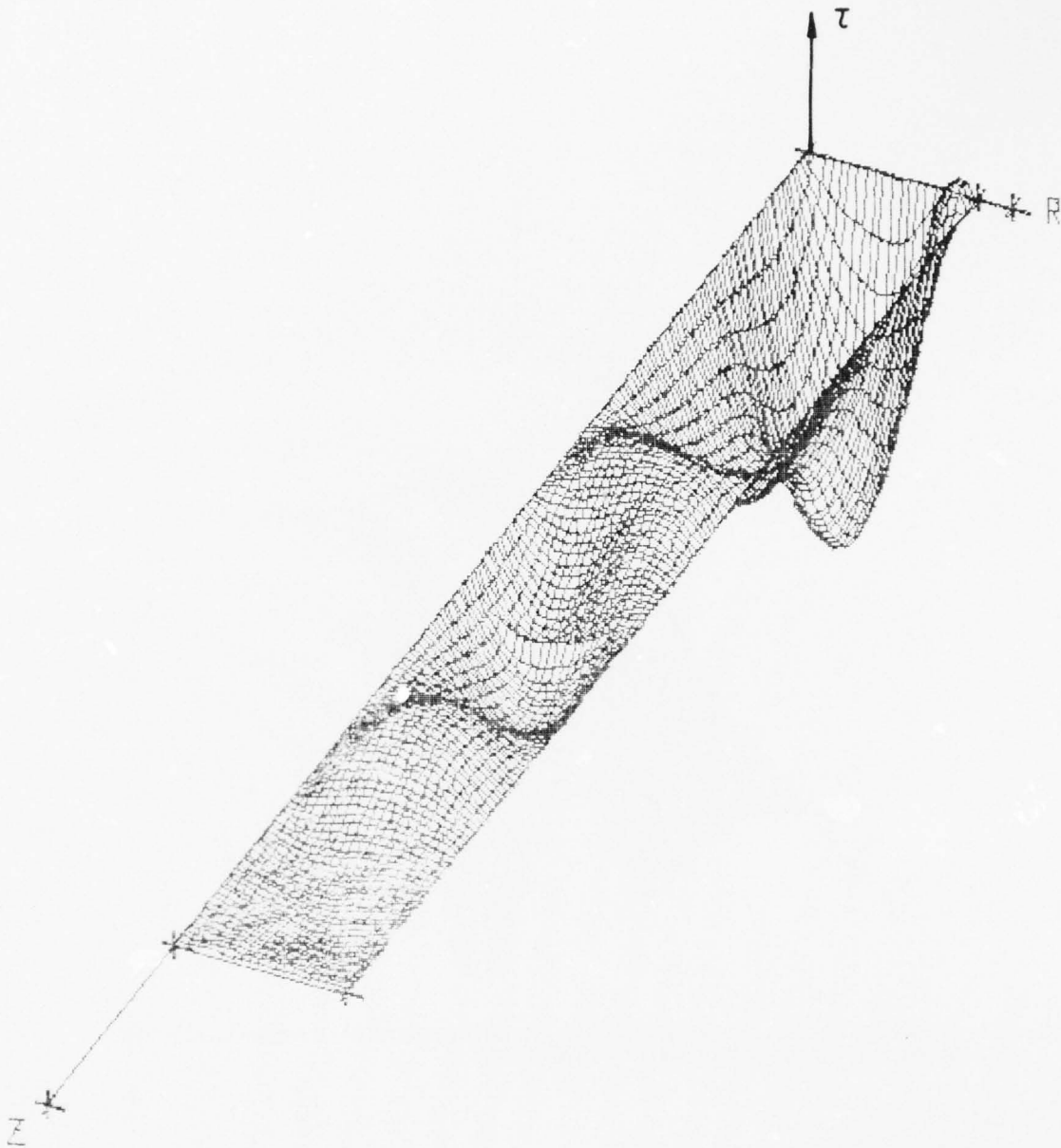


FIG. V.45 SHEAR STRESS IN A MAGNESIUM BAR AT 41.40 USEC FROM A NORMAL IMPACT ON WATER AT 96 FT/SEC (2.5 INCH DIAMETER)

SCALE FACTOR = .00012

UNDISTURBED
WATER SURFACE

DISTURBED
WATER SURFACE

DIAMETER = 2.500 IN.

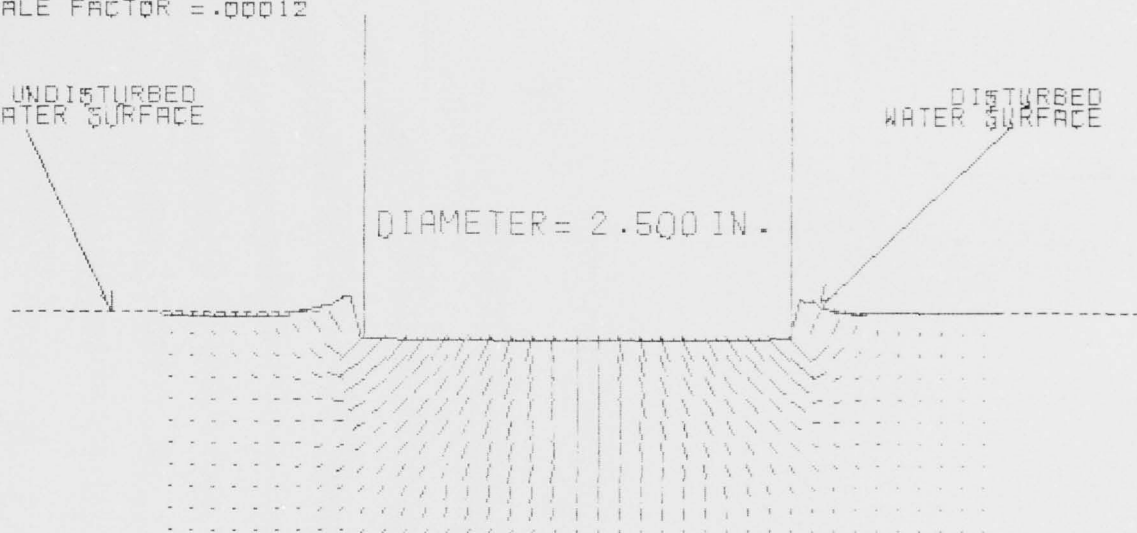


FIG. V.46 VELOCITY FIELD IN WATER

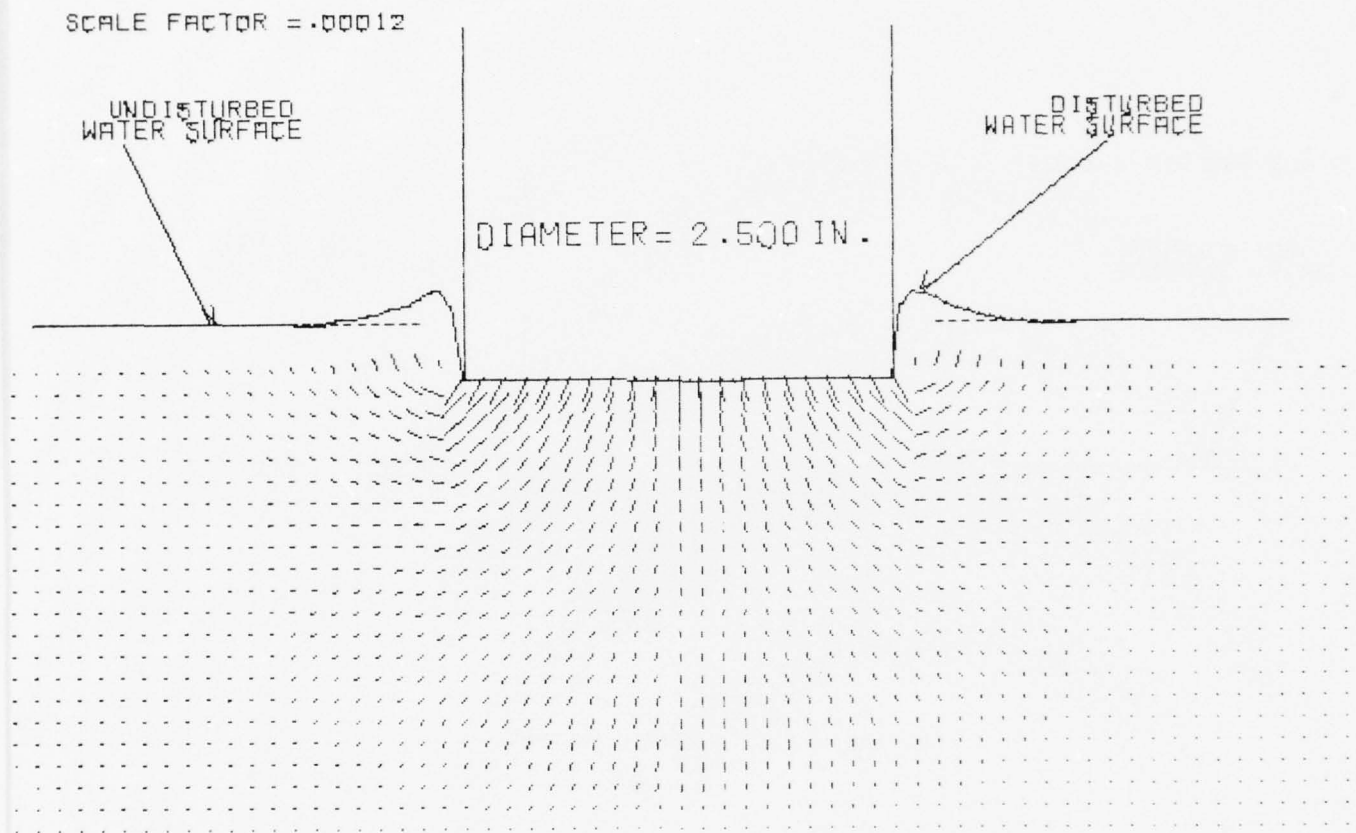


FIG. V.47 VELOCITY FIELD IN WATER

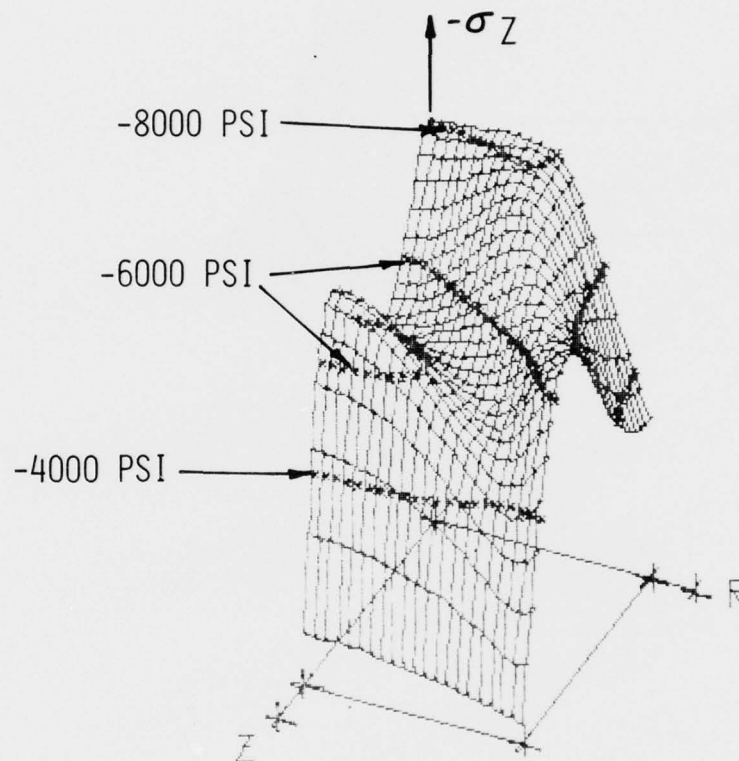


FIG. V.48 AXIAL STRESS IN A MAGNESIUM BAR AT 6.57 USEC FROM A NORMAL IMPACT ON WATER AT 142 FT/SEC (2.5 INCH DIAMETER)

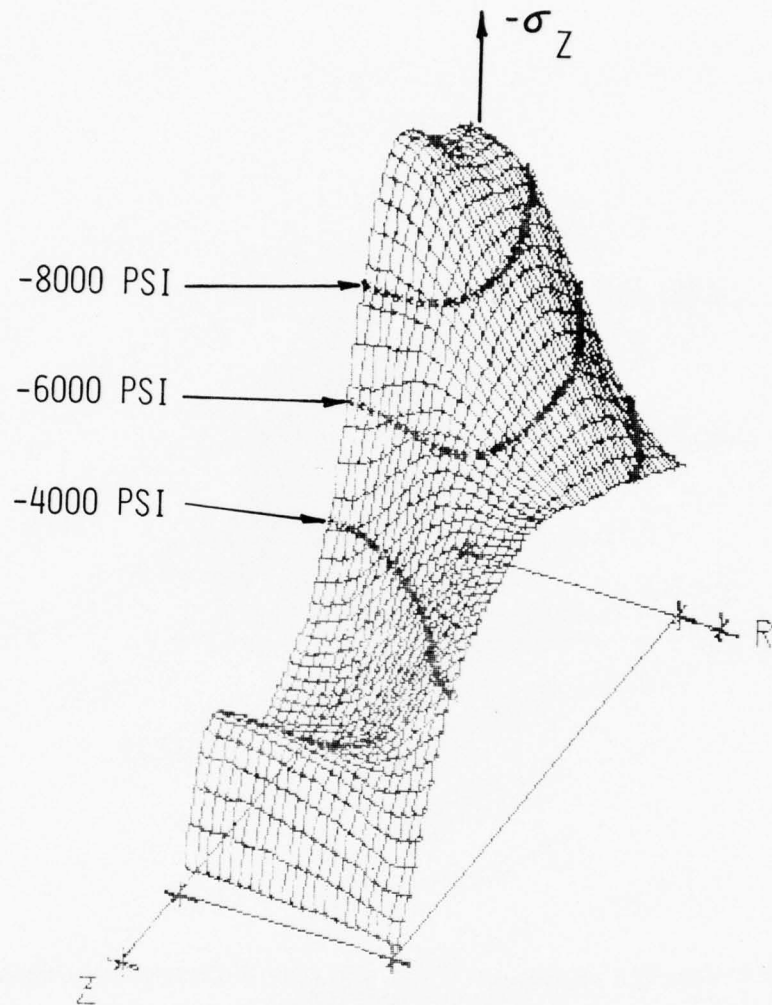
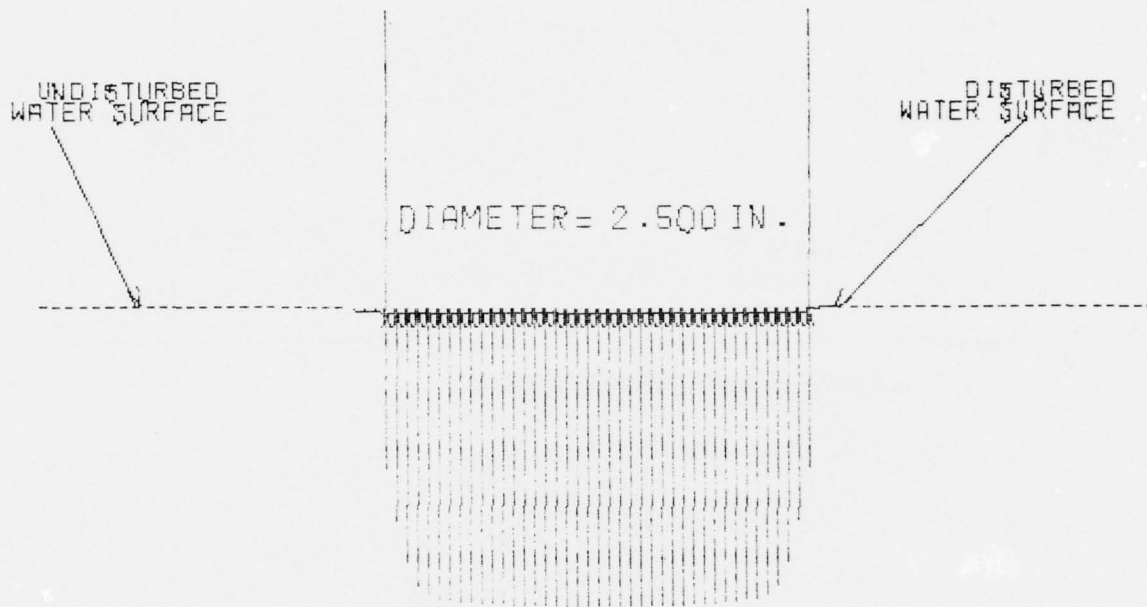


FIG. V.49 AXIAL STRESS IN A MAGNESIUM BAR AT 14.31 USEC FROM A NORMAL IMPACT ON WATER AT 142 FT/SEC (2.5 INCH DIAMETER)

IMPACT VELOCITY = 142 FT/SEC
TIME = 2.06 USEC



$P_{\text{AXIS}} = 8507 \text{ PSI}$

FIG. V.50 PRESSURE ON THE IMPACT FACE OF A MAGNESIUM BAR IMPACTING WATER

IMPACT VELOCITY = 142 FT/SEC
TIME = 11.73 USEC

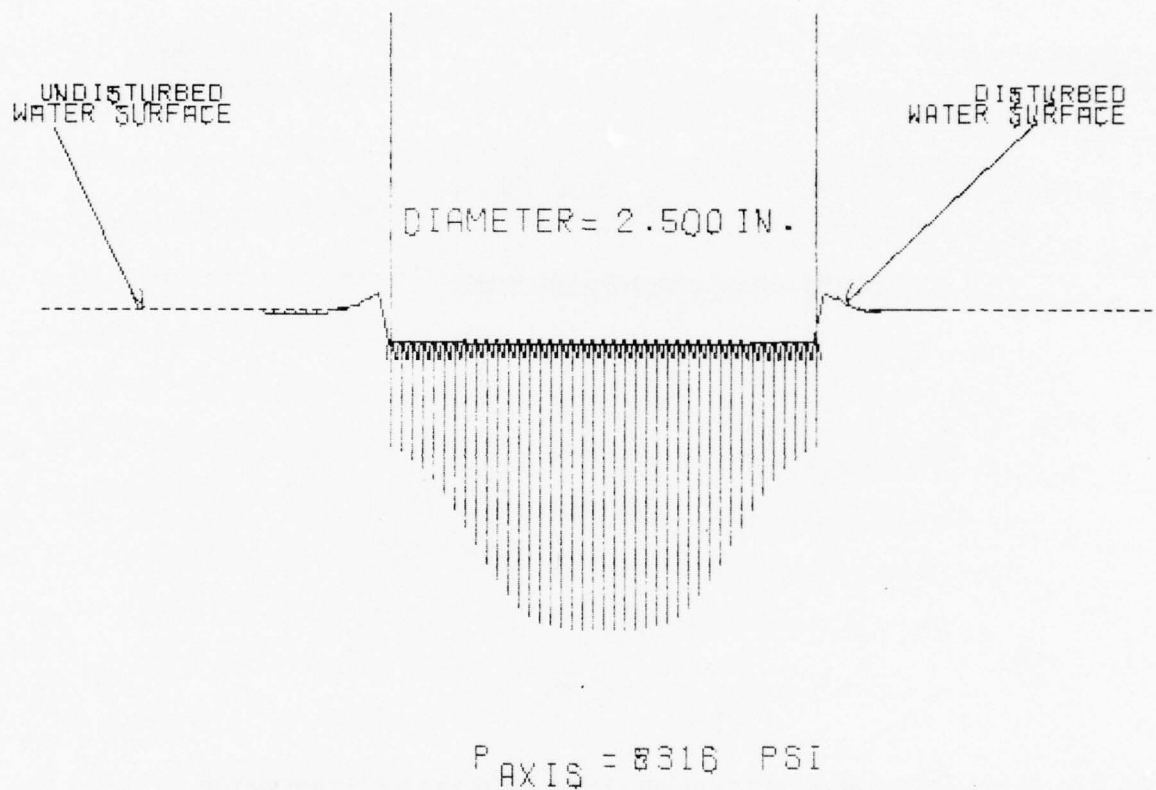


FIG. V.51 PRESSURE ON THE IMPACT FACE OF A MAGNESIUM BAR IMPACTING WATER

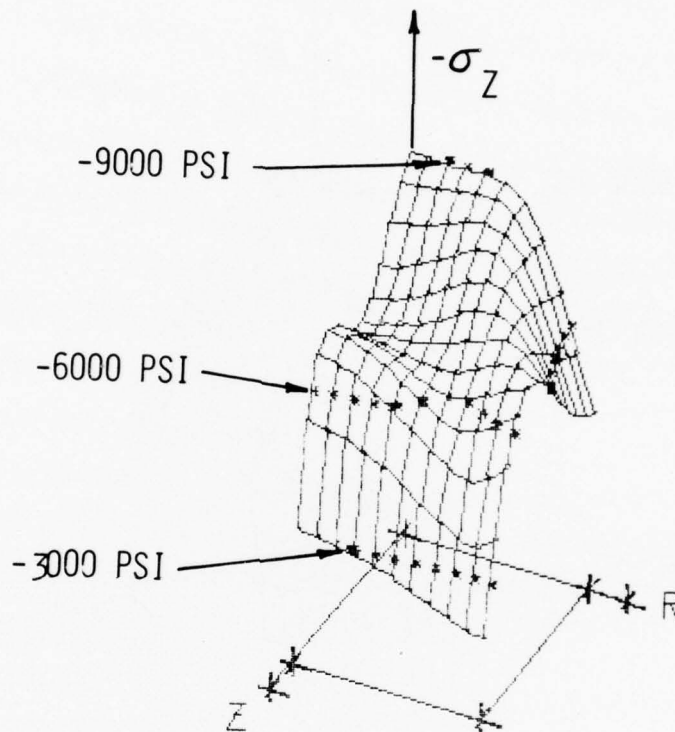


FIG. V.52 AXIAL STRESS IN A MAGNESIUM BAR AT 7.09 USEC FROM A NORMAL IMPACT ON WATER AT 157 FT/SEC (2.75 INCH DIAMETER)

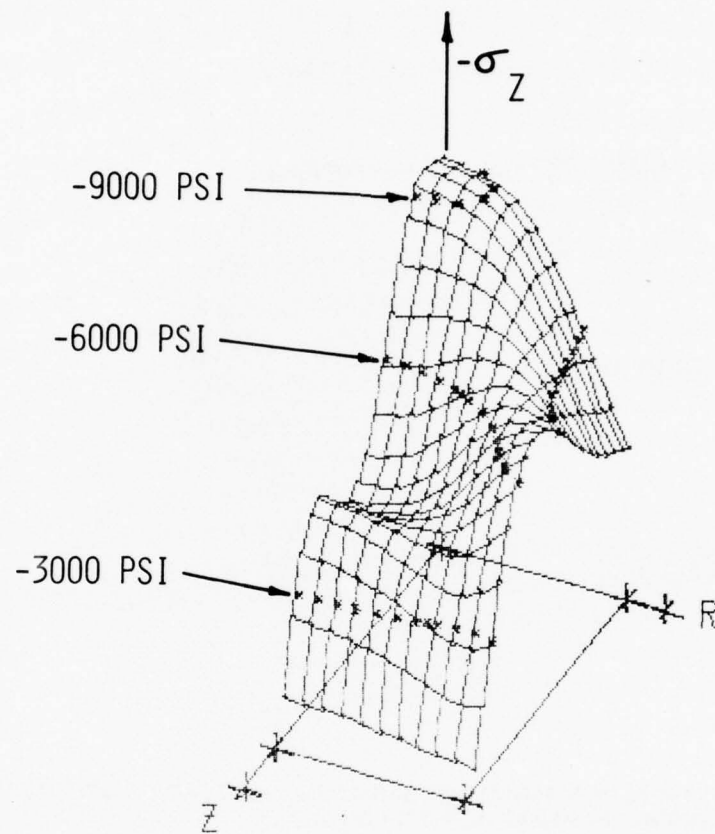


FIG. V.53 AXIAL STRESS IN A MAGNESIUM BAR AT 10.49 USEC FROM A NORMAL IMPACT ON WATER AT 157 FT/SEC (2.75 INCH DIAMETER)

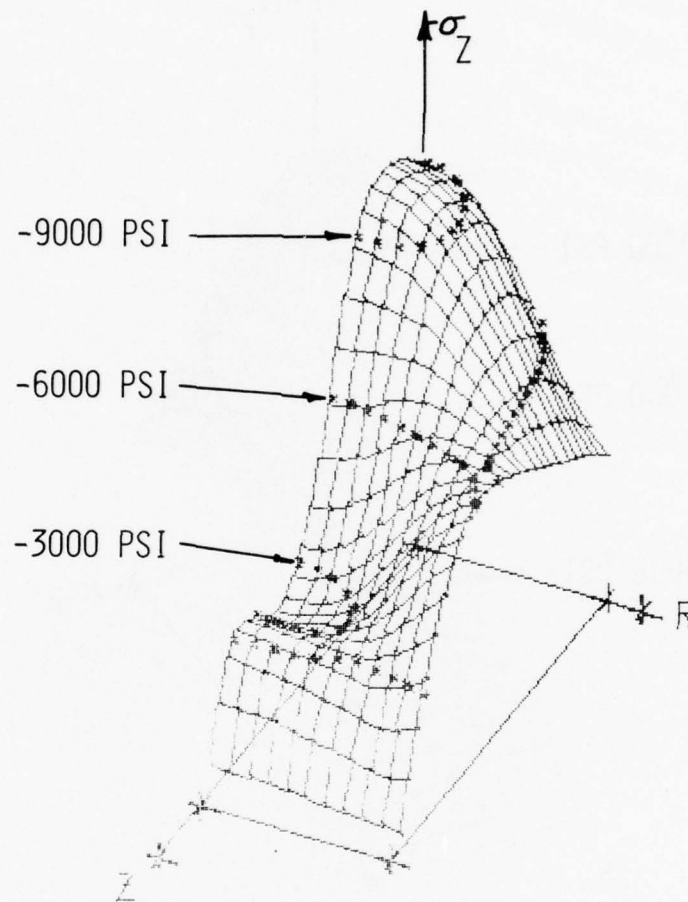


FIG. V.54 AXIAL STRESS IN A MAGNESIUM BAR AT 13.90 USEC FROM A NORMAL IMPACT ON WATER AT 157 FT/SEC (2.75 INCH DIAMETER)

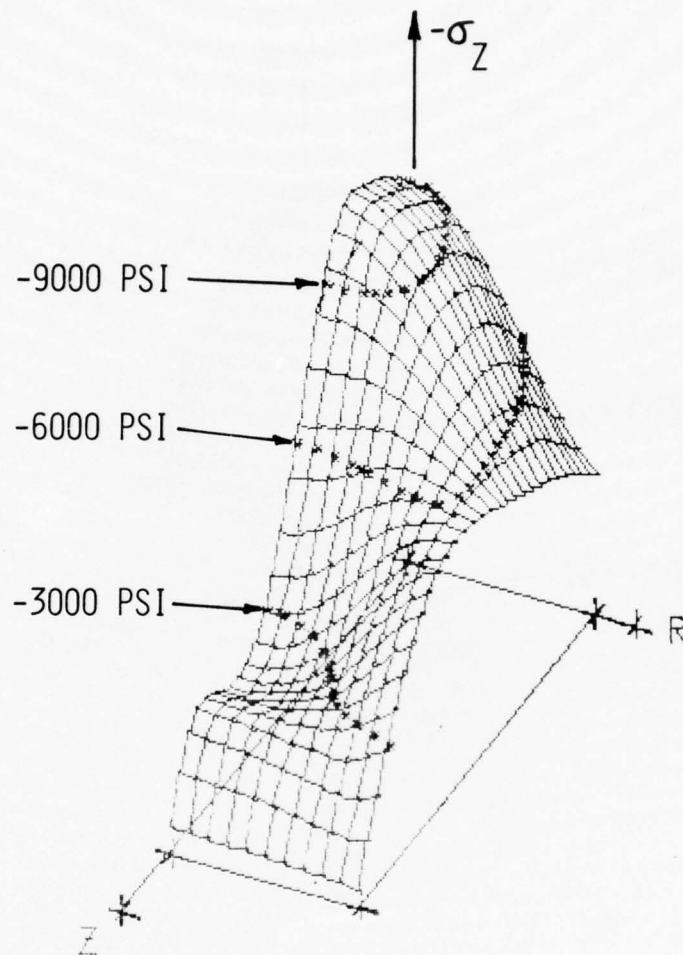


FIG. V.55 AXIAL STRESS IN A MAGNESIUM BAR AT 15.60 USEC FROM A NORMAL IMPACT ON WATER AT 157 FT/SEC (2.75 INCH DIAMETER)

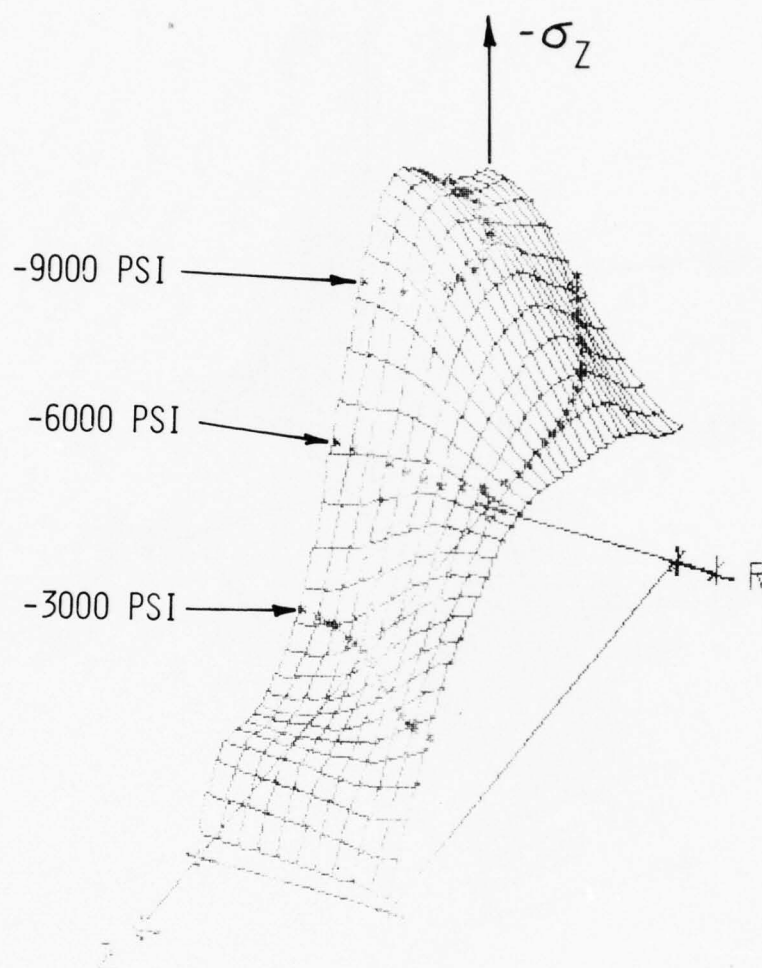


FIG. V.56 AXIAL STRESS IN A MAGNESIUM BAR AT 19.01 USEC FROM A NORMAL IMPACT ON WATER AT 157 FT/SEC (2.75 INCH DIAMETER)

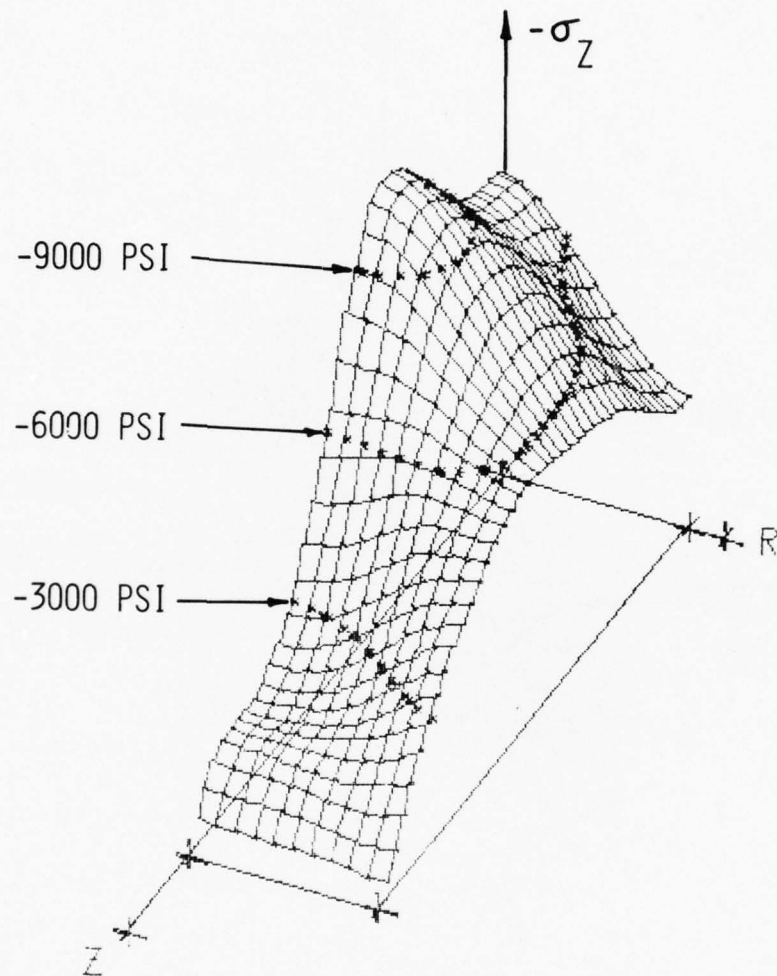


FIG. V.57 AXIAL STRESS IN A MAGNESIUM BAR AT 20.71 USEC FROM A NORMAL IMPACT ON WATER AT 157 FT/SEC (2.75 INCH DIAMETER)

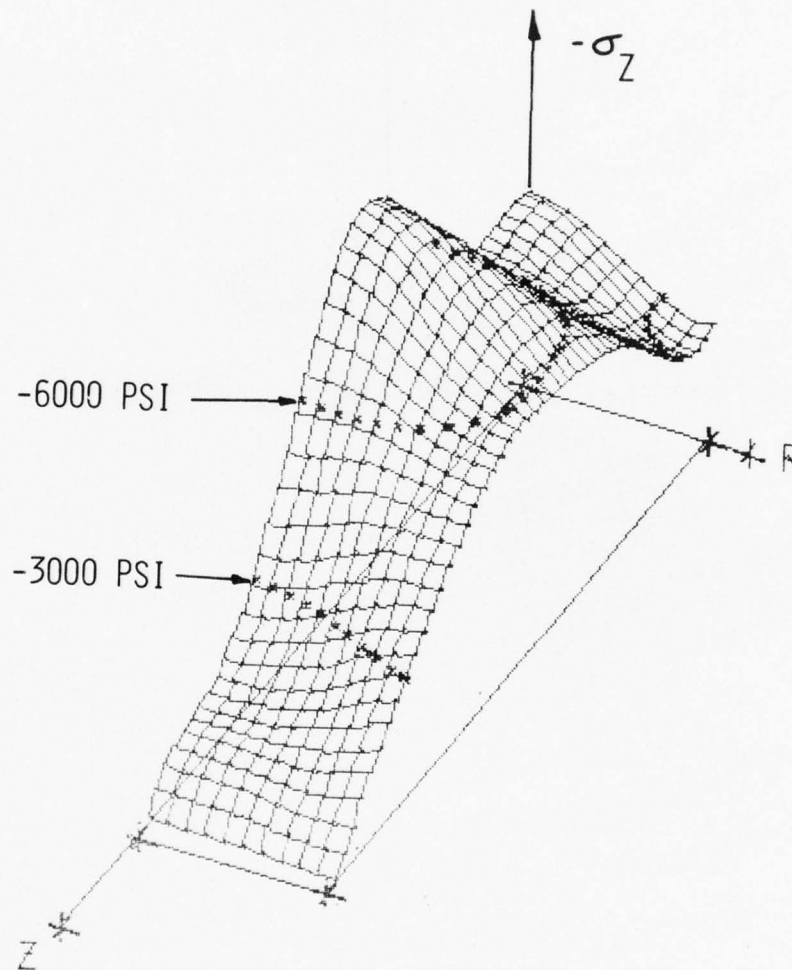


FIG. V.58 AXIAL STRESS IN A MAGNESIUM BAR AT 24.97 USEC FROM A NORMAL IMPACT ON WATER AT 157 FT/SEC (2.75 INCH DIAMETER)

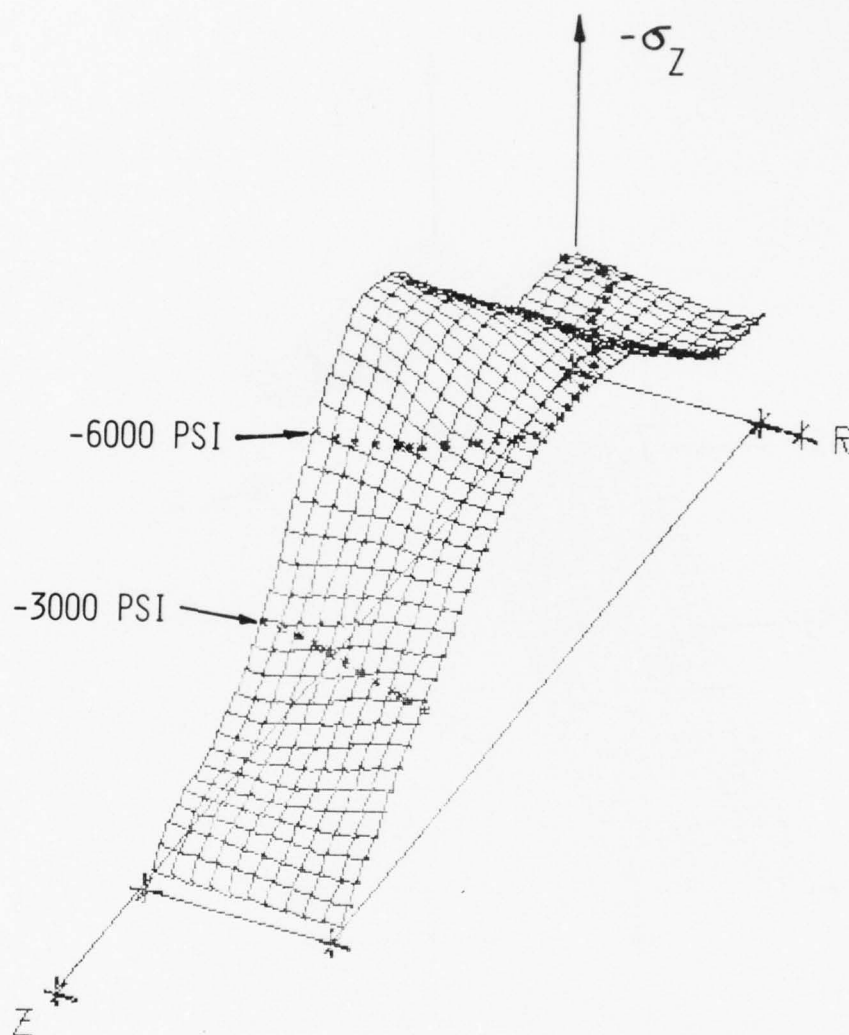


FIG. V.59 AXIAL STRESS IN A MAGNESIUM BAR AT 28.37 USEC FROM A NORMAL IMPACT ON WATER AT 157 FT/SEC (2.75 INCH DIAMETER)

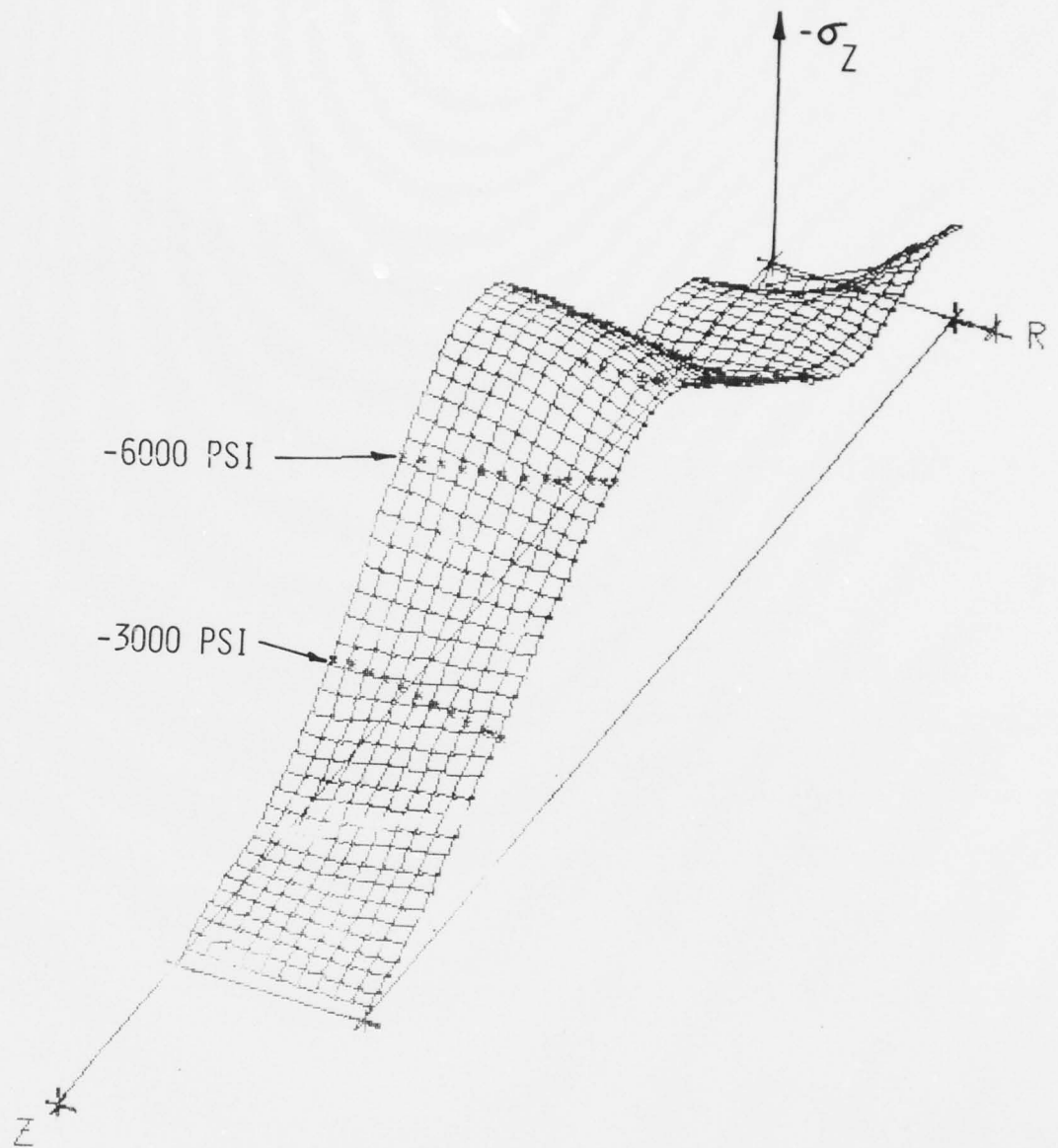


FIG. V.60 AXIAL STRESS IN A MAGNESIUM BAR AT 39.44 USEC FROM A NORMAL IMPACT ON WATER AT 157 FT/SEC (2.75 INCH DIAMETER)

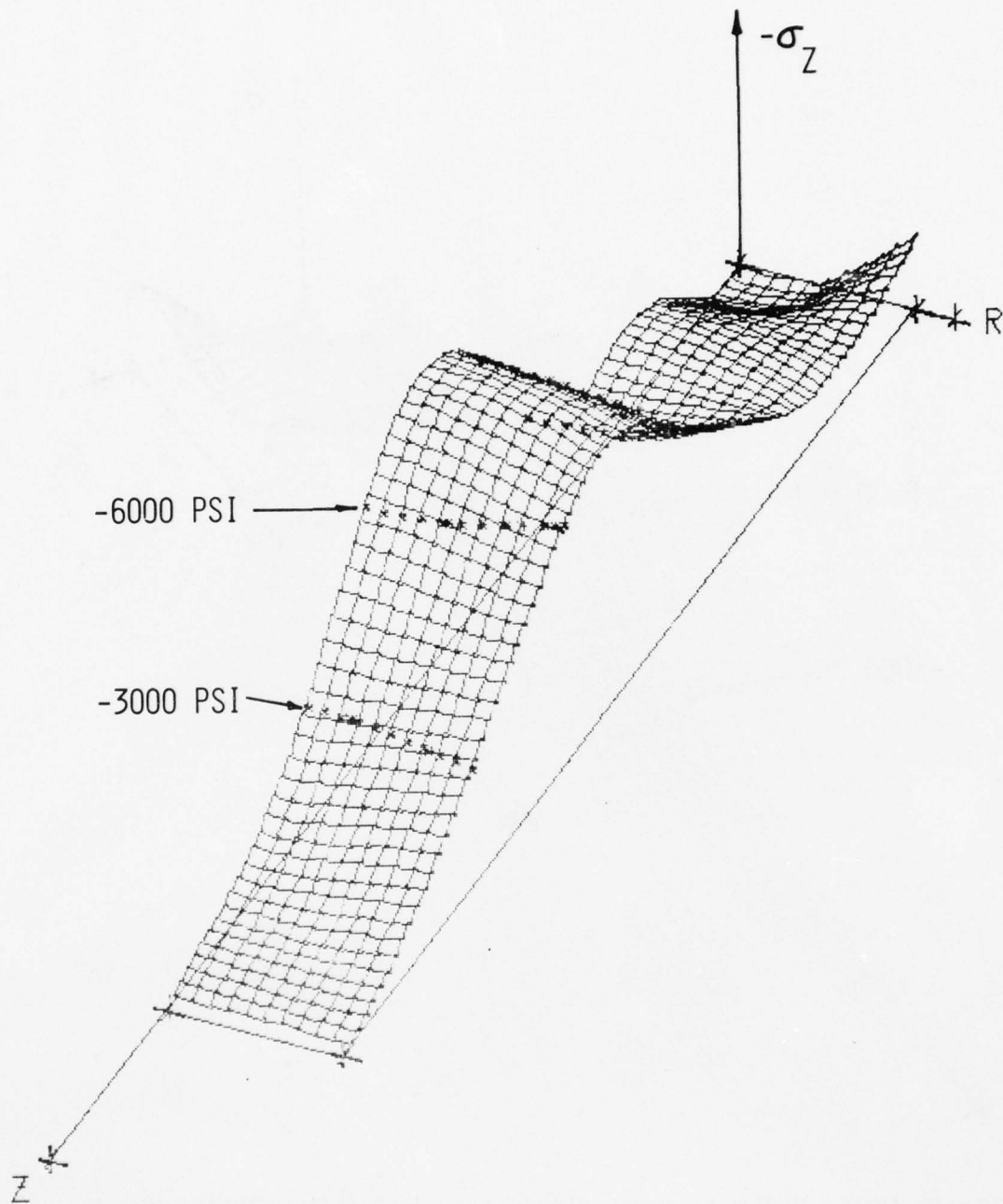


FIG. V.61 AXIAL STRESS IN A MAGNESIUM BAR AT 42.84 USEC FROM A NORMAL IMPACT ON WATER AT 157 FT/SEC (2.75 INCH DIAMETER)

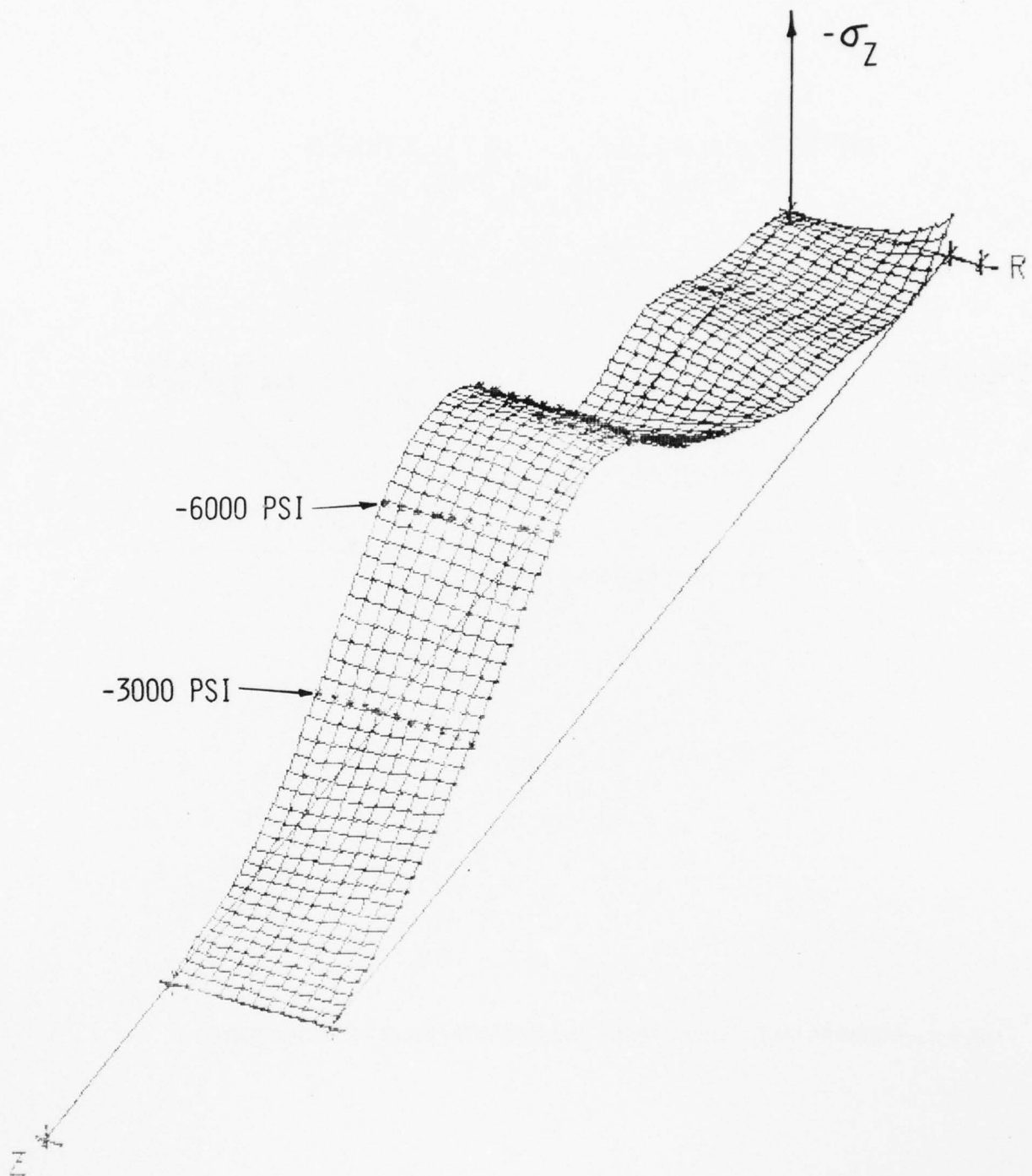


FIG. V.62 AXIAL STRESS IN A MAGNESIUM BAR AT 49.65 USEC FROM A NORMAL IMPACT ON WATER AT 157 FT/SEC (2.75 INCH DIAMETER)

IMPACT VELOCITY = 157 FT/SEC
TIME = 16.45 USEC

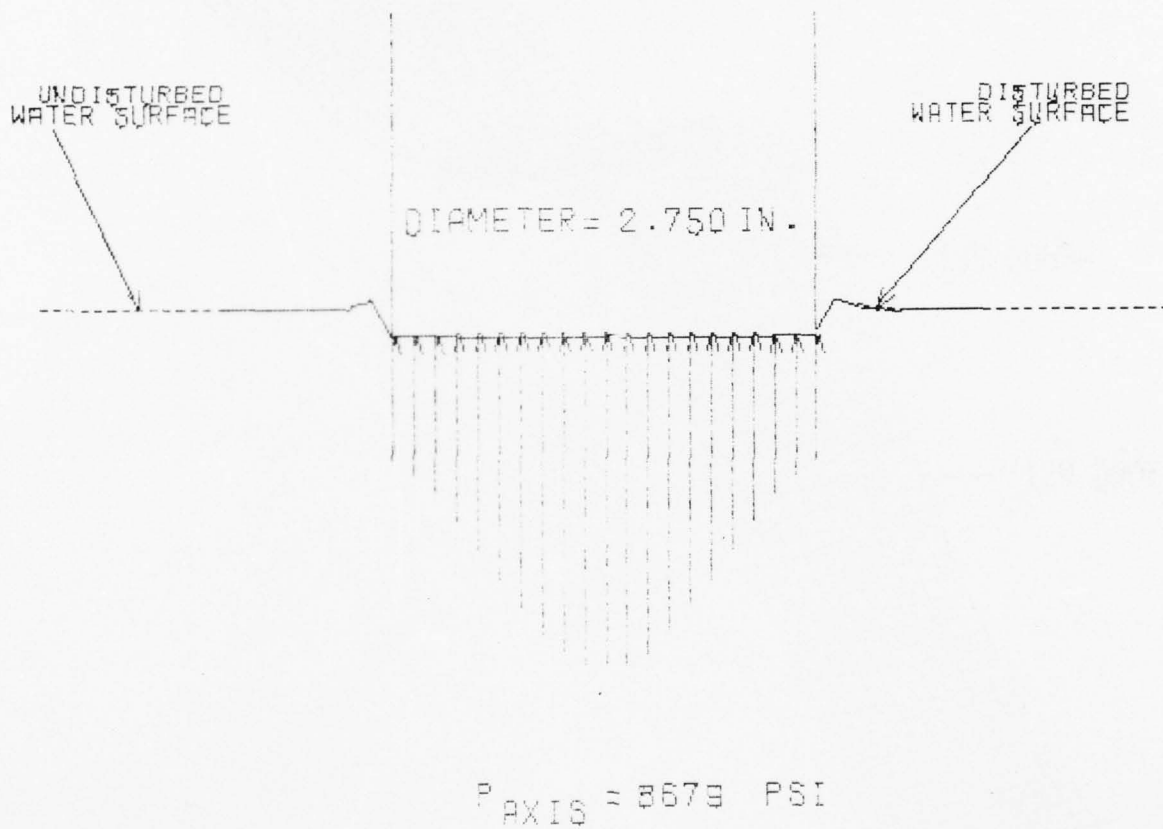
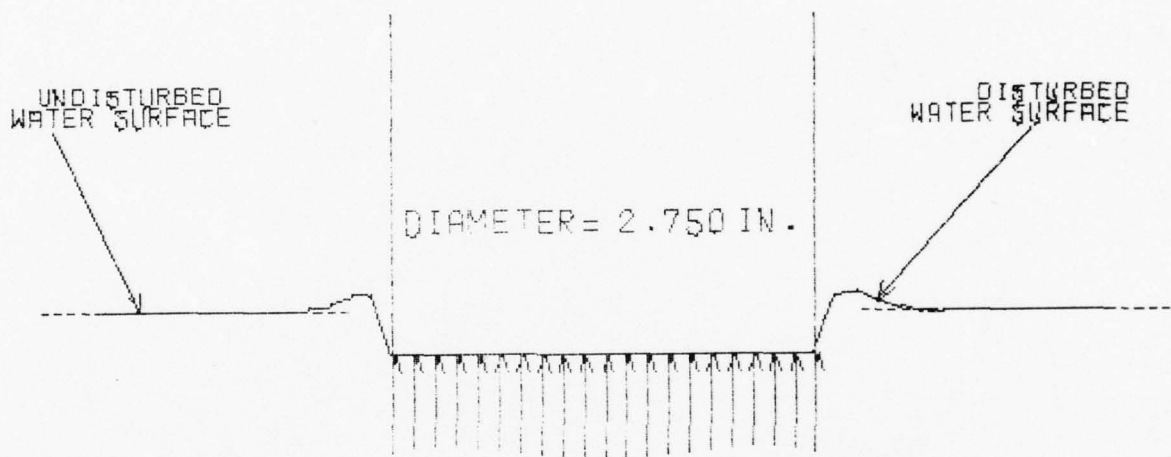


FIG. V.63 PRESSURE ON THE IMPACT FACE OF A MAGNESIUM BAR IMPACTING WATER

IMPACT VELOCITY = 157 FT/SEC
TIME = 28.37 USEC



$P_{\text{AXIS}} = 2721 \text{ PSI}$

FIG. V.64 PRESSURE ON THE IMPACT FACE OF A MAGNESIUM BAR IMPACTING WATER

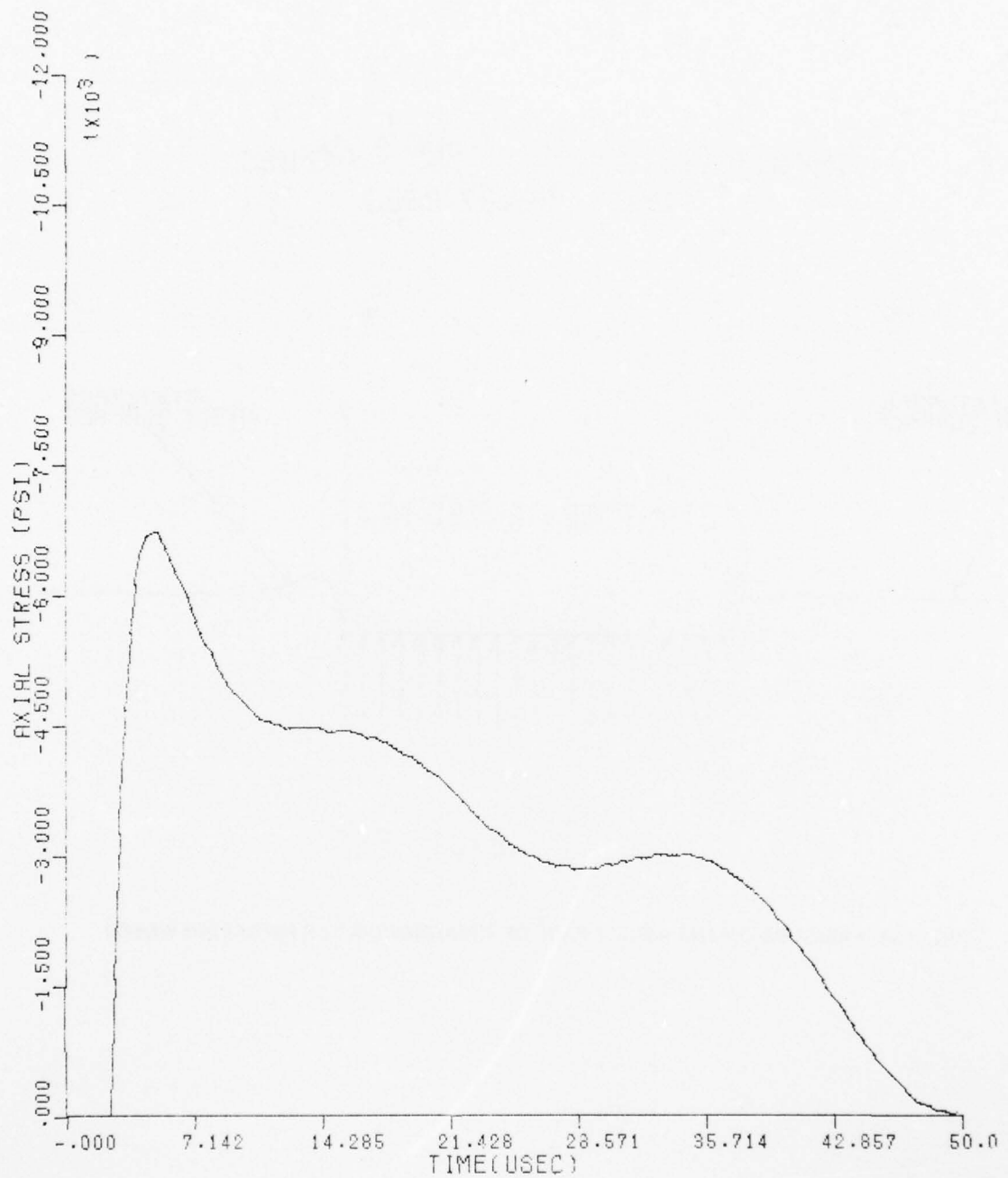


FIG. V.65 AXIAL STRESS VS TIME (2.750 INCH DIAMETER MAGNESIUM BAR IMPACT
VELOCITY = 157.0 FT/SEC R = 1.375 INCHES Z = .687 INCHES)

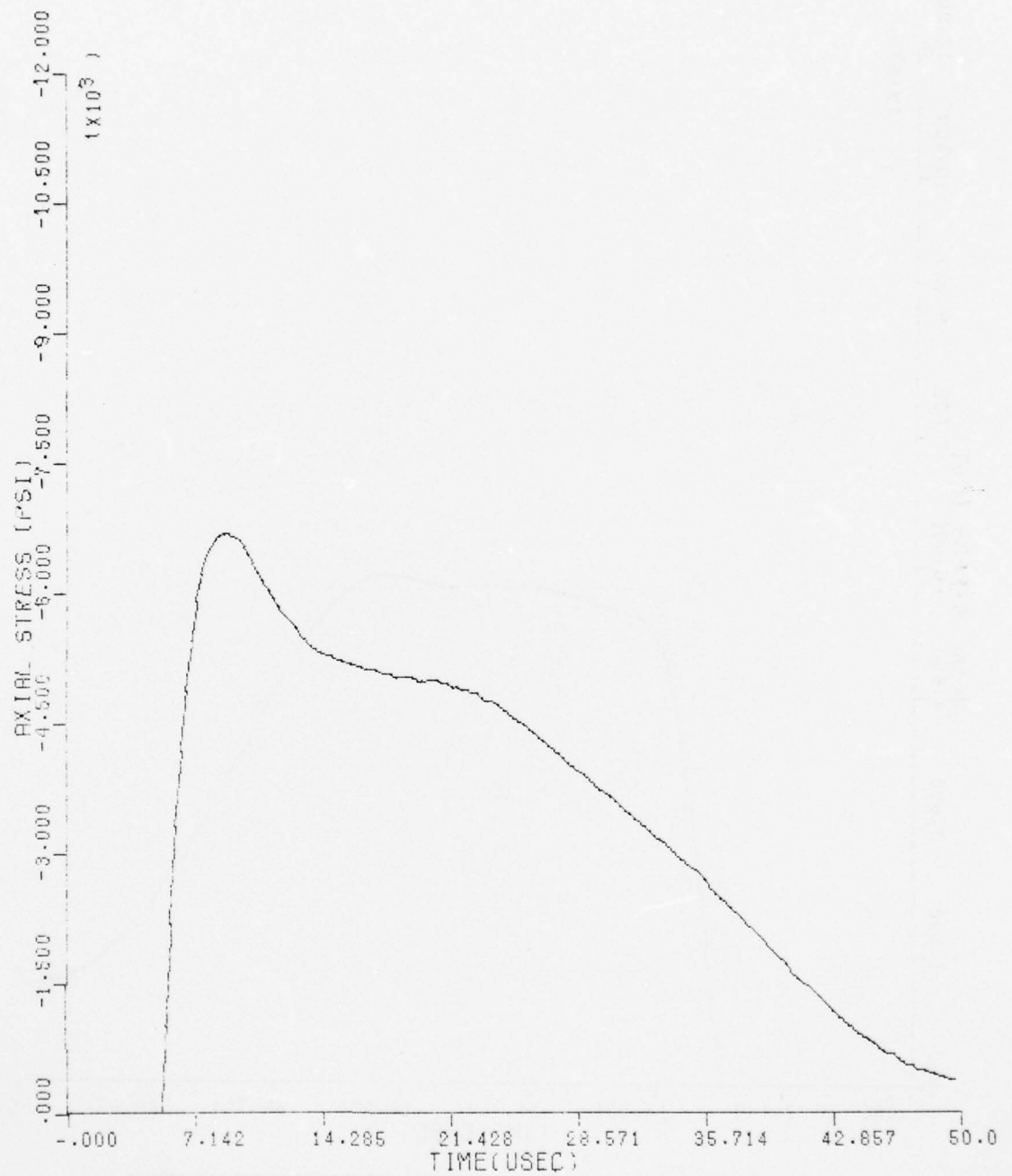


FIG. V.66 AXIAL STRESS VS TIME (2.750 INCH DIAMETER MAGNESIUM BAR IMPACT
VELOCITY = 157.0 FT/SEC R = 1.375 INCHES Z = 1.375 INCHES)

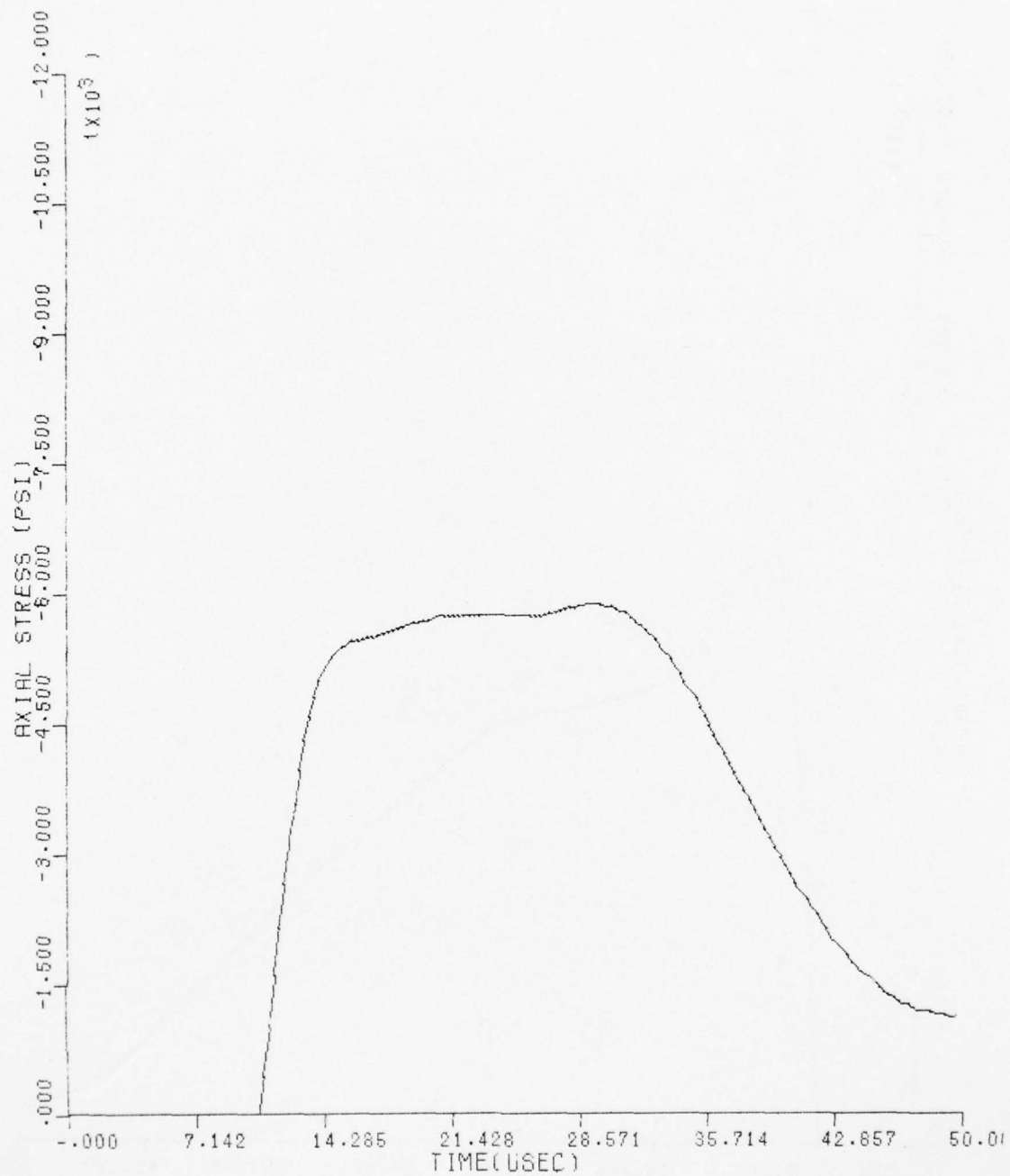


FIG. V.67 AXIAL STRESS VS TIME (2.750 INCH DIAMETER MAGNESIUM BAR IMPACT
VELOCITY = 157.0 FT/SEC R = 1.375 INCHES Z = 2.750 INCHES)

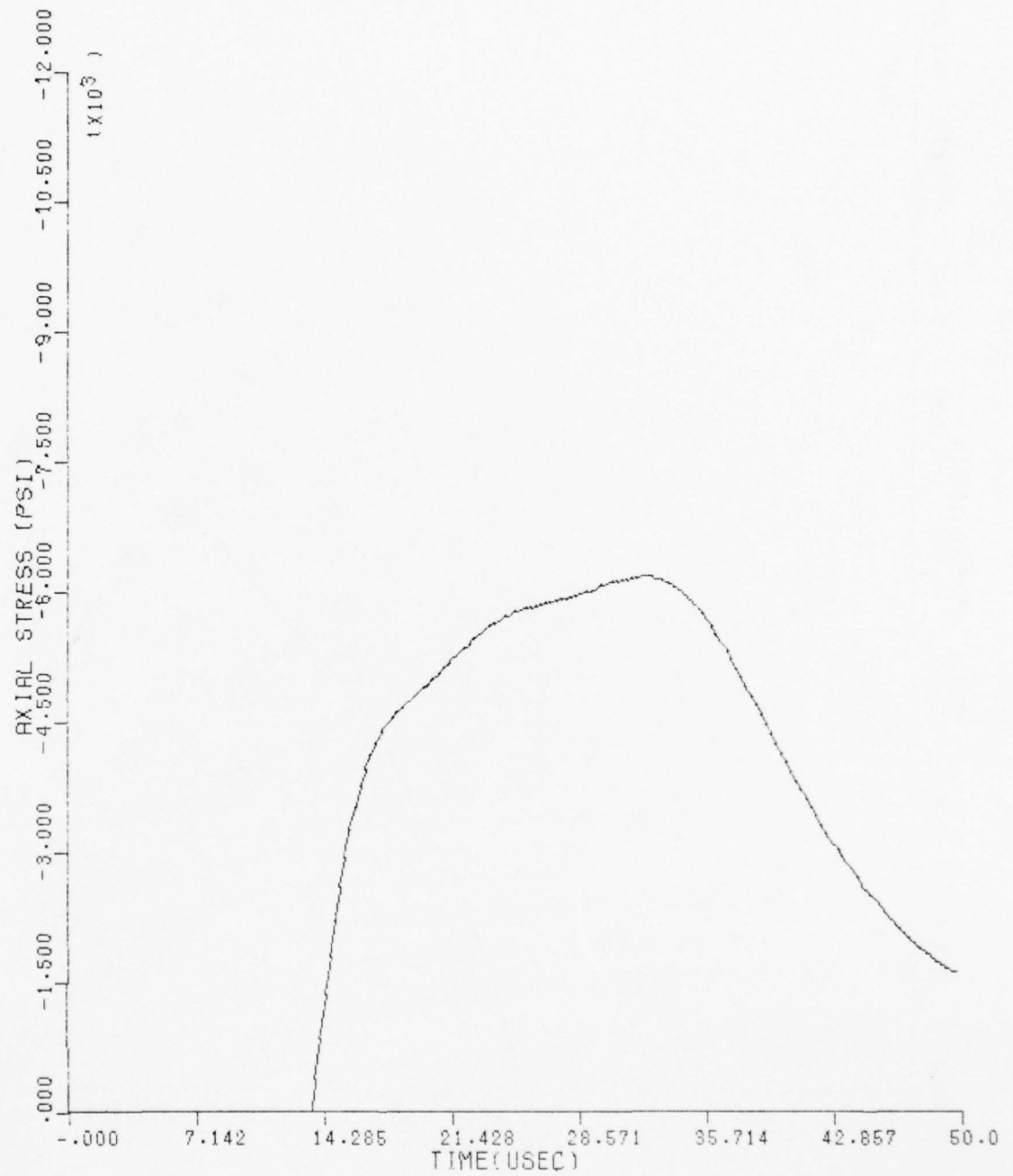


FIG. V.68 AXIAL STRESS VS TIME (2.750 INCH DIAMETER MAGNESIUM BAR IMPACT
VELOCITY = 157.0 FT/SEC R = 1.375 INCHES Z = 3.437 INCHES)

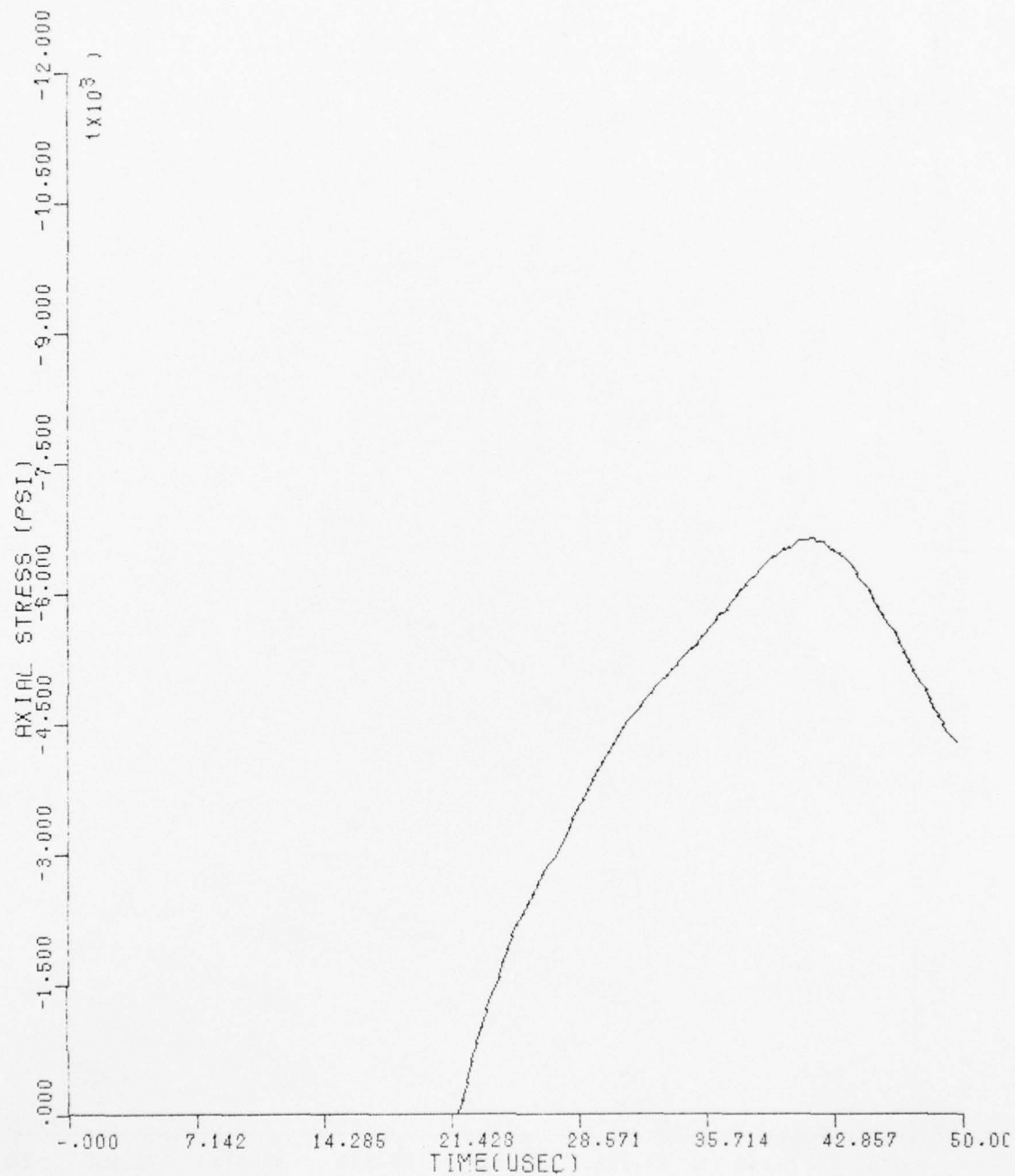


FIG. V.69 AXIAL STRESS VS TIME (2.750 INCH DIAMETER MAGNESIUM BAR IMPACT
VELOCITY = 157.0 FT/SEC R = 1.375 INCHES Z = 5.500 INCHES)

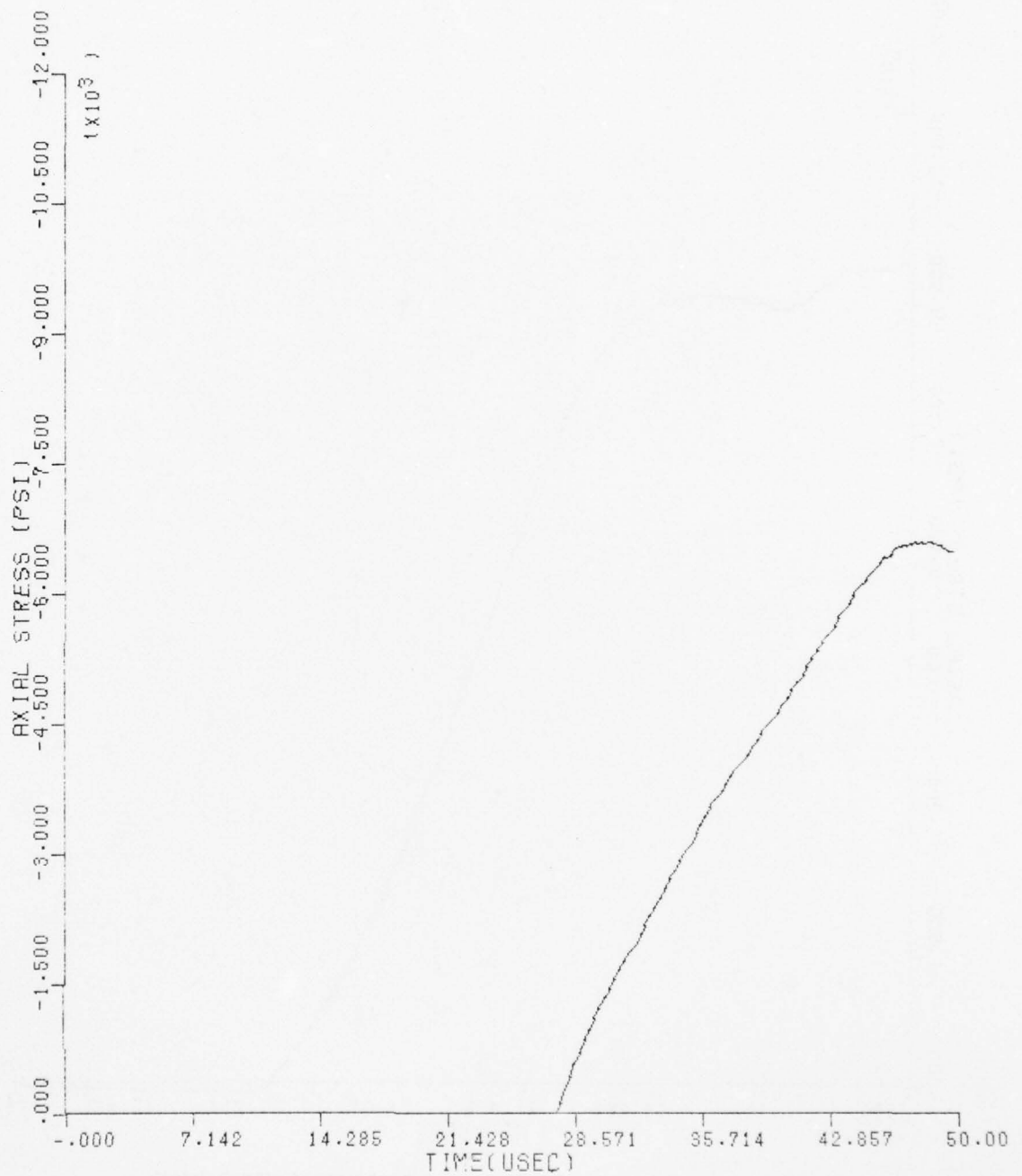


FIG. V.70 AXIAL STRESS VS TIME (2.750 INCH DIAMETER MAGNESIUM BAR IMPACT
VELOCITY = 157.0 FT/SEC R = 1.375 INCHES Z = 6.875 INCHES)



FIG. V.71 AXIAL STRESS VS TIME (2.750 INCH DIAMETER MAGNESIUM BAR IMPACT
VELOCITY = 157.0 FT/SEC R = 0.000 INCHES Z = 0.000 INCHES)

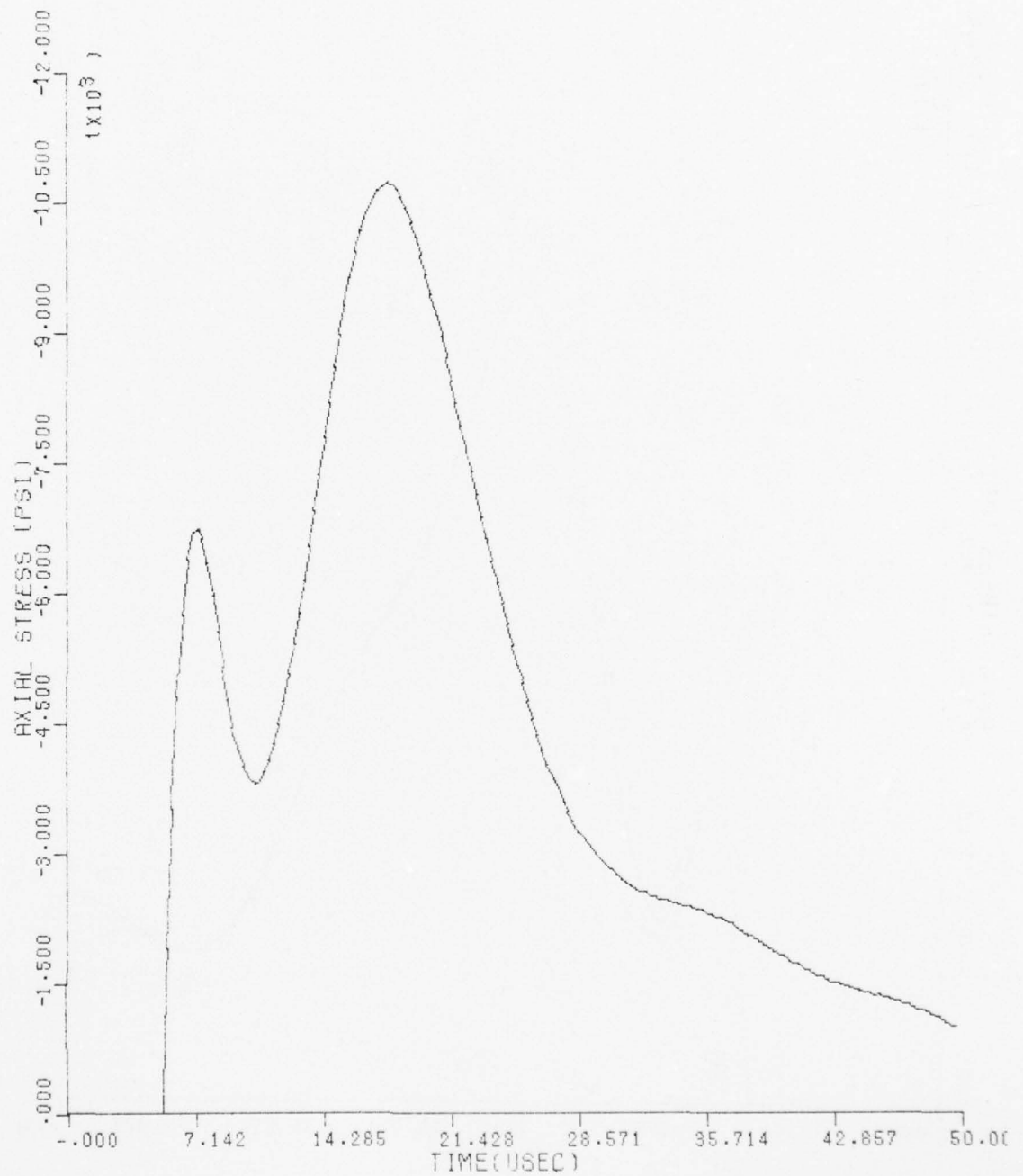


FIG. V.72 AXIAL STRESS VS TIME (2.750 INCH DIAMETER MAGNESIUM BAR IMPACT
VELOCITY = 157.0 FT/SEC R = 0.000 INCHES Z = 1.375 INCHES)

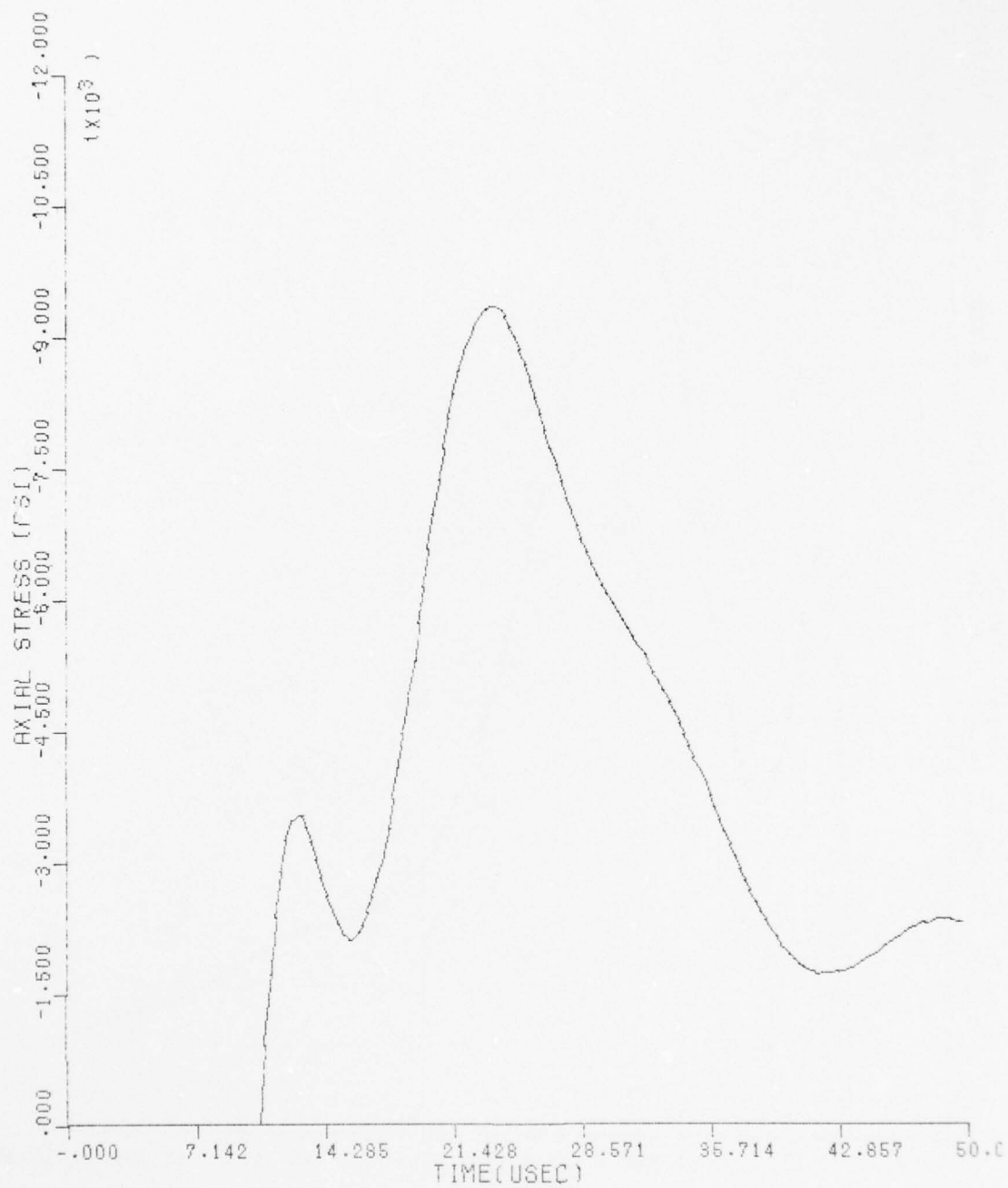


FIG. V.73 AXIAL STRESS VS TIME (2.750 INCH DIAMETER MAGNESIUM BAR IMPACT
VELOCITY = 157.0 FT/SEC R = 0.000 INCHES Z = 2.750 INCHES)

AD-A052 051

NAVAL SURFACE WEAPONS CENTER WHITE OAK LAB SILVER SP--ETC F/G 19/4
STRESS WAVE PROPAGATION IN BARS DUE TO NORMAL IMPACT ON WATER. (U)
AUG 77 W T MESSICK, J M MARSHALL

UNCLASSIFIED

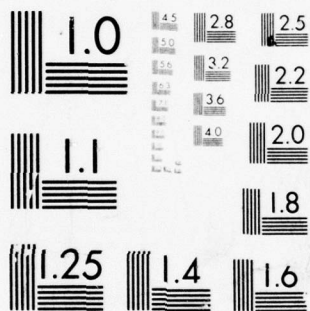
NSWC/WOL/TR-77-128

NL

4 OF 5

AD
A052 051





MICROCOPY RESOLUTION TEST CHART
NATIONAL BUREAU OF STANDARDS-1963-A

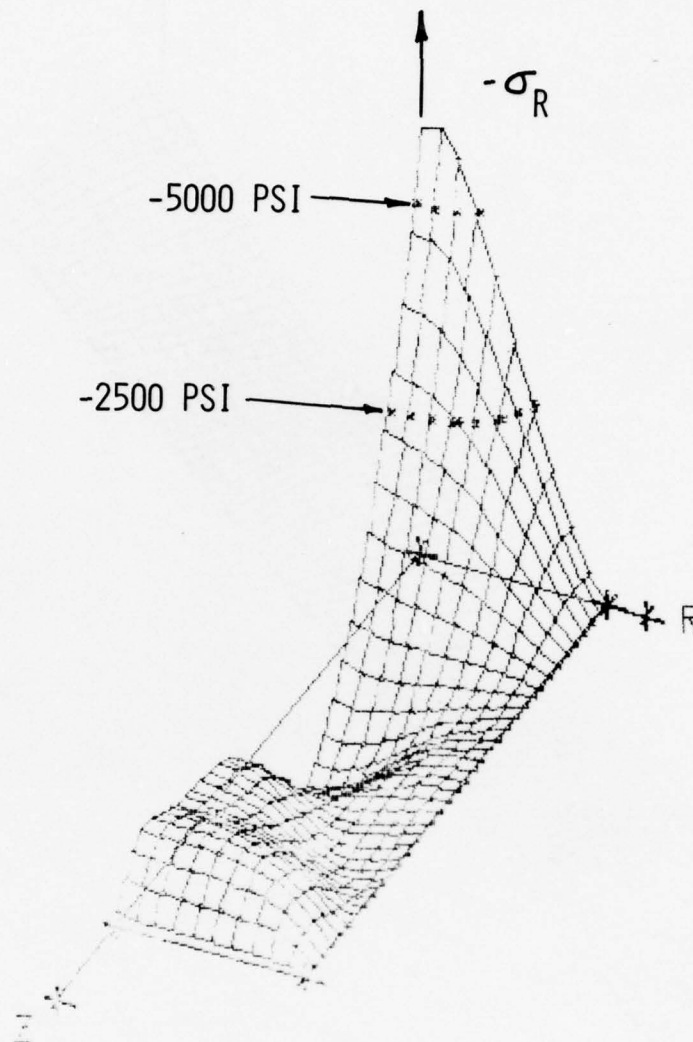


FIG. V.74 RADIAL STRESS IN A MAGNESIUM BAR AT 19.86 USEC FROM A NORMAL IMPACT ON WATER AT 157 FT/SEC (2.75 INCH DIAMETER)

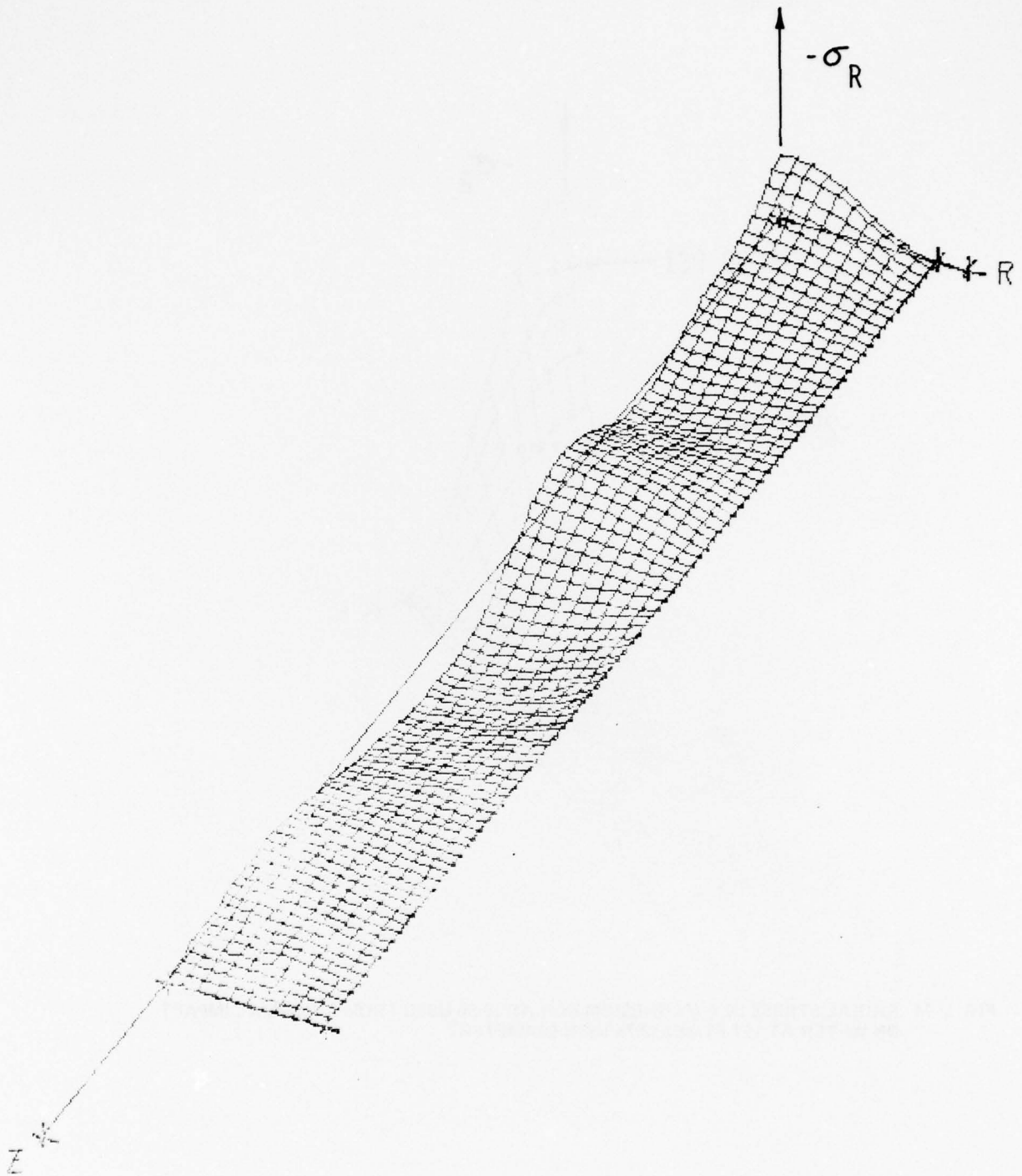


FIG. V.75 RADIAL STRESS IN A MAGNESIUM BAR AT 49.65 USEC FROM A NORMAL IMPACT ON WATER AT 157 FT/SEC (2.75 INCH DIAMETER)

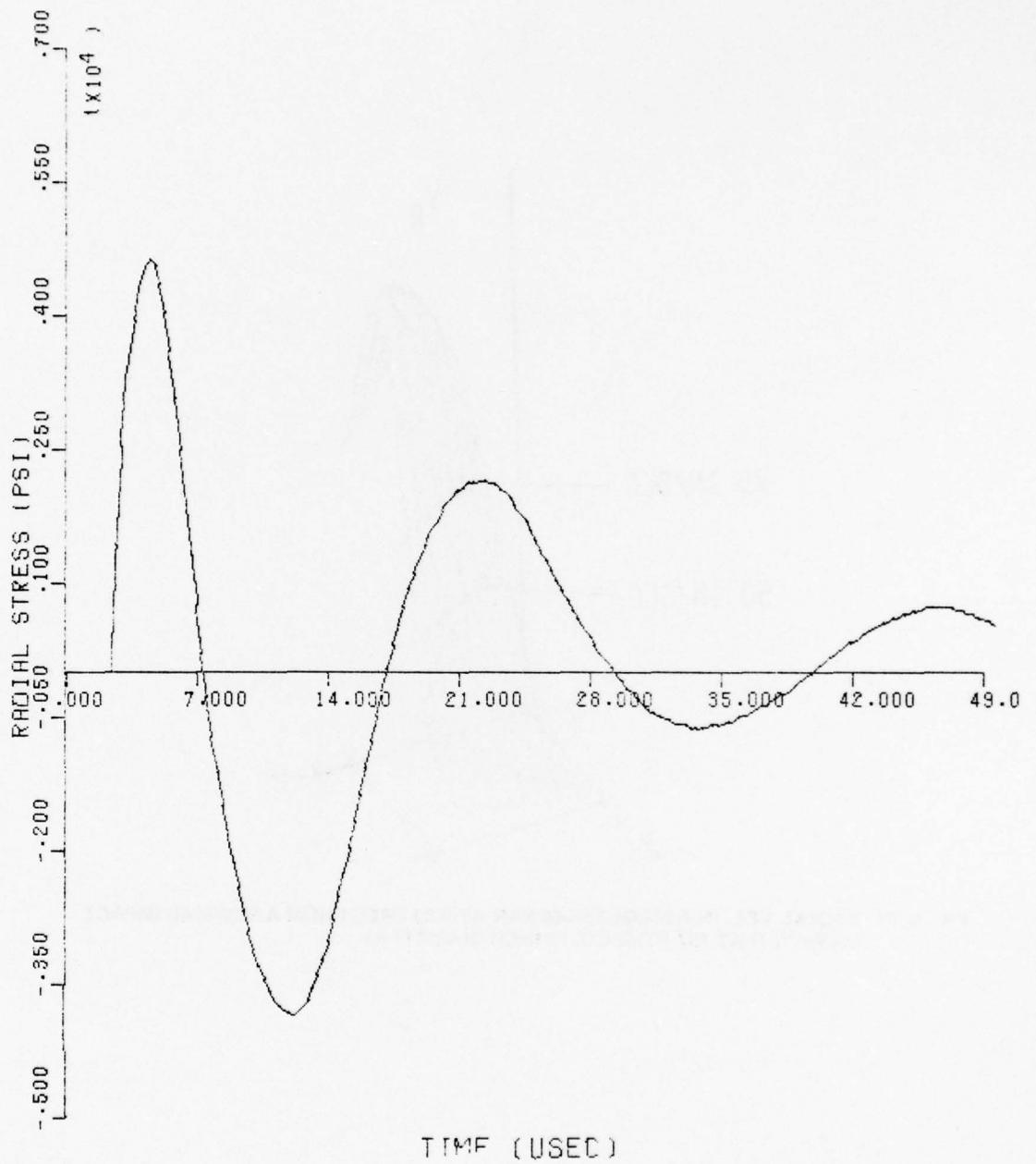


FIG. V.76 RADIAL STRESS VS TIME (2.750 INCH DIAMETER MAGNESIUM BAR
IMPACT VELOCITY = 157.0 FT/SEC R = 0.000 INCHES Z = .687 INCHES)

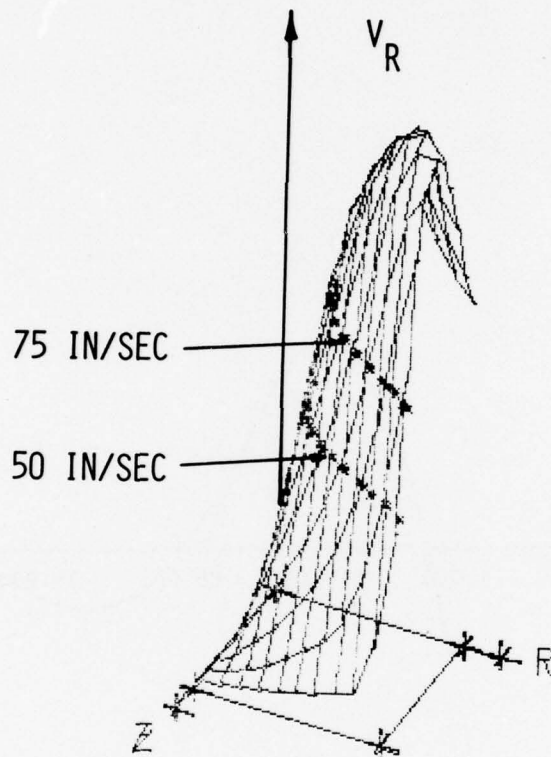


FIG. V.77 RADIAL VEL. IN A MAGNESIUM BAR AT 5.39 USEC FROM A NORMAL IMPACT ON WATER AT 157 FT/SEC (2.75 INCH DIAMETER)

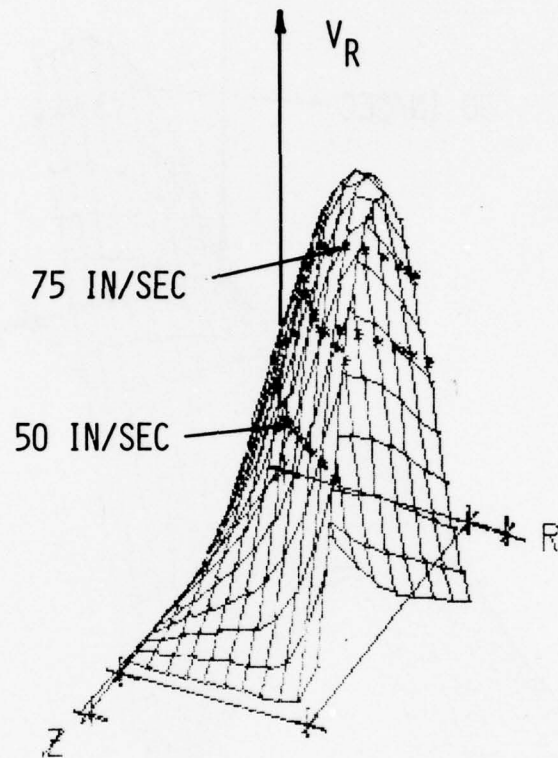


FIG. V.78 RADIAL VEL. IN A MAGNESIUM BAR AT 10.49 USEC FROM A NORMAL IMPACT ON WATER AT 157 FT/SEC (2.75 INCH DIAMETER)

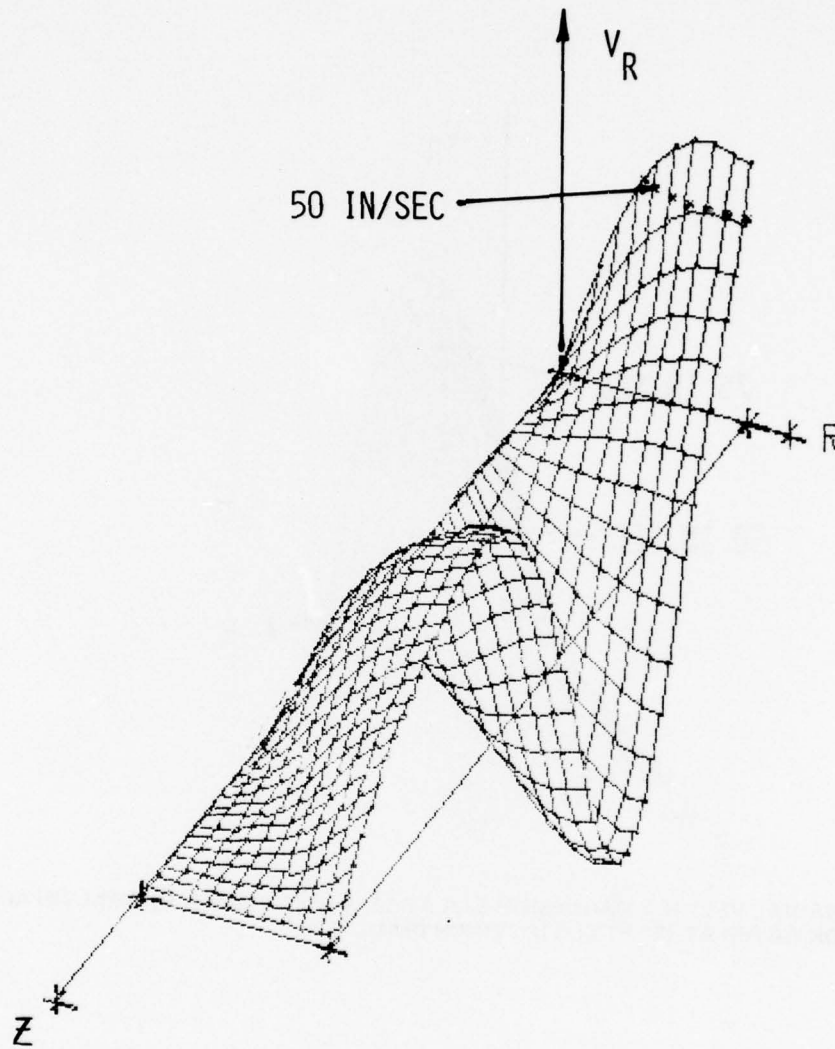


FIG. V.79 RADIAL VEL. IN A MAGNESIUM BAR AT 28.37 USEC FROM A NORMAL IMPACT ON WATER AT 157 FT/SEC (2.75 INCH DIAMETER)

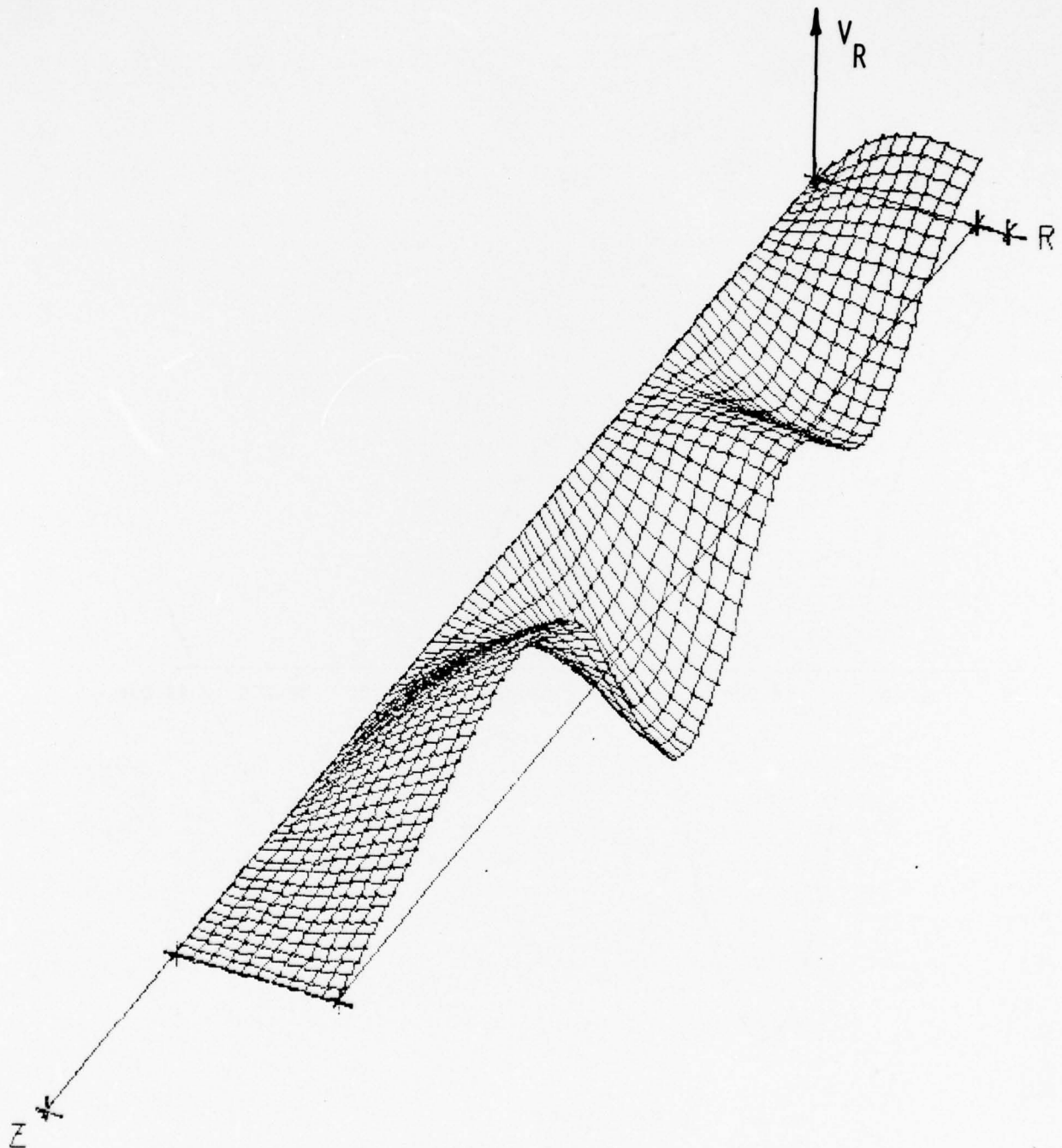


FIG. V.80 RADIAL VEL. IN A MAGNESIUM BAR AT 49.65 USEC FROM A NORMAL IMPACT ON WATER AT 157 FT/SEC (2.75 INCH DIAMETER)

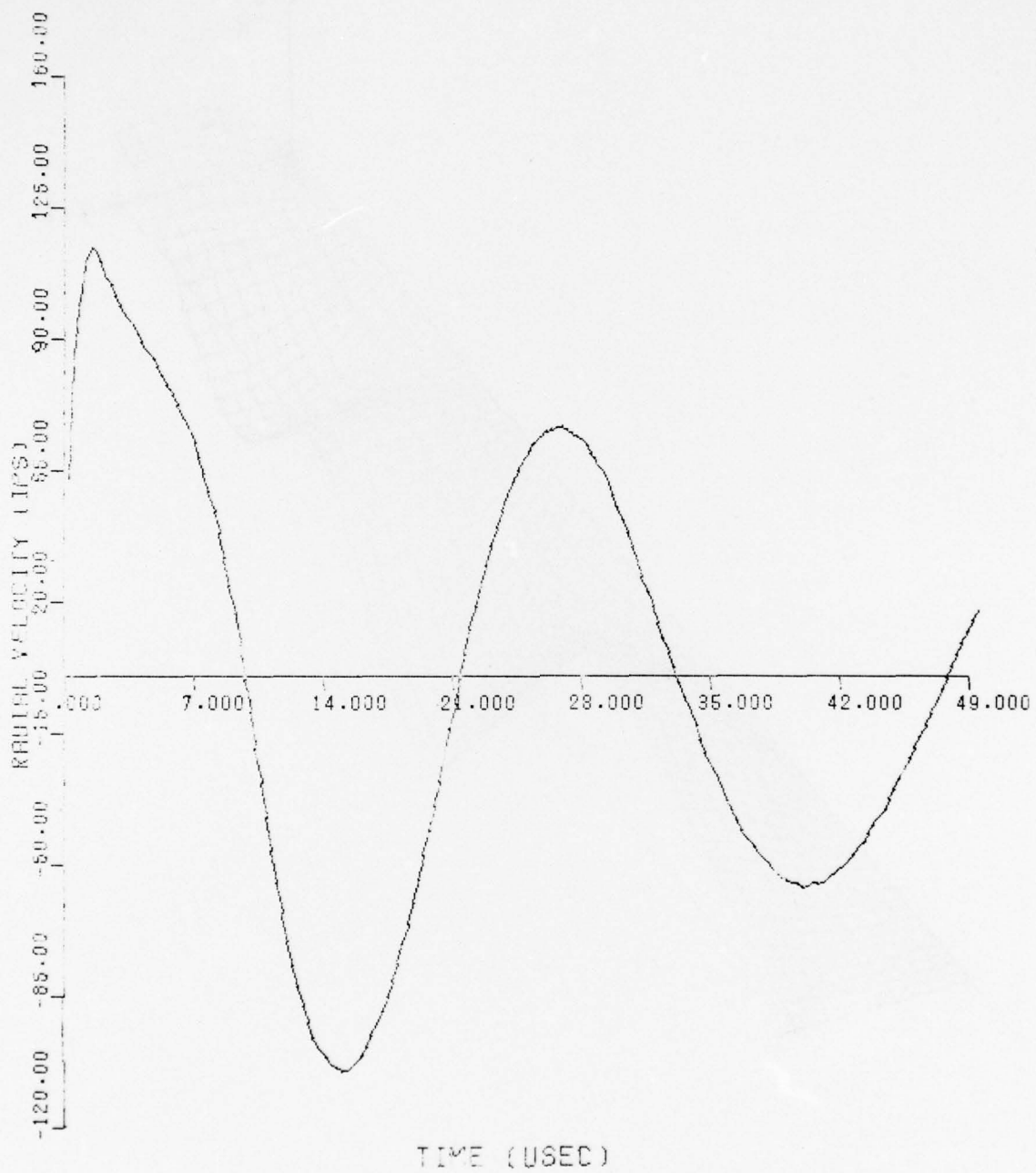


FIG. V.81 RADIAL VELOCITY VS TIME (2.750 INCH DIAMETER MAGNESIUM BAR
IMPACT VELOCITY = 157.0 FT/SEC R = 1.375 INCHES Z = 0.000 INCHES)

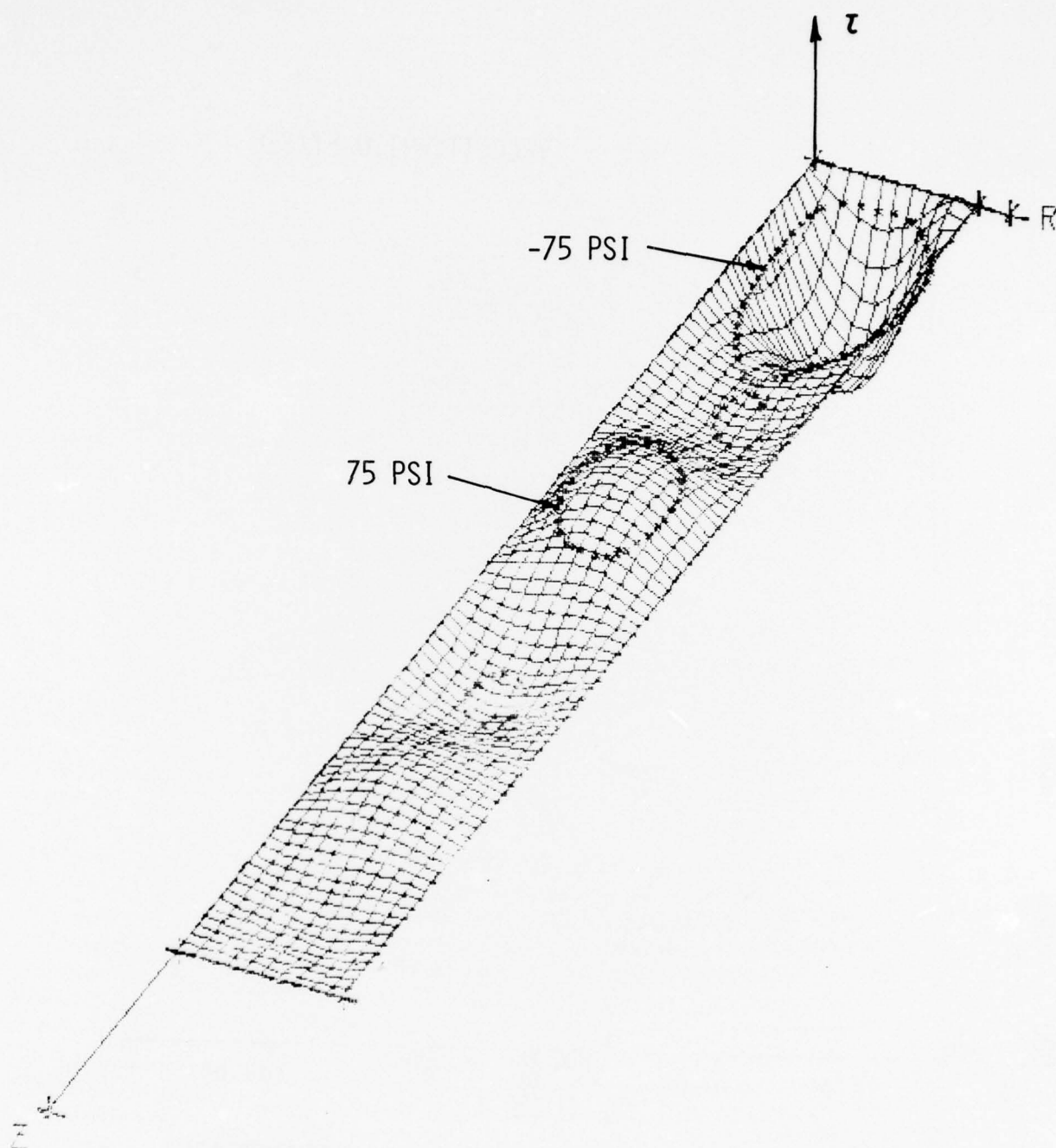


FIG. V.82 SHEAR STRESS IN A MAGNESIUM BAR AT 49.65 USEC FROM A NORMAL IMPACT ON WATER AT 157 FT/SEC (2.75 INCH DIAMETER)

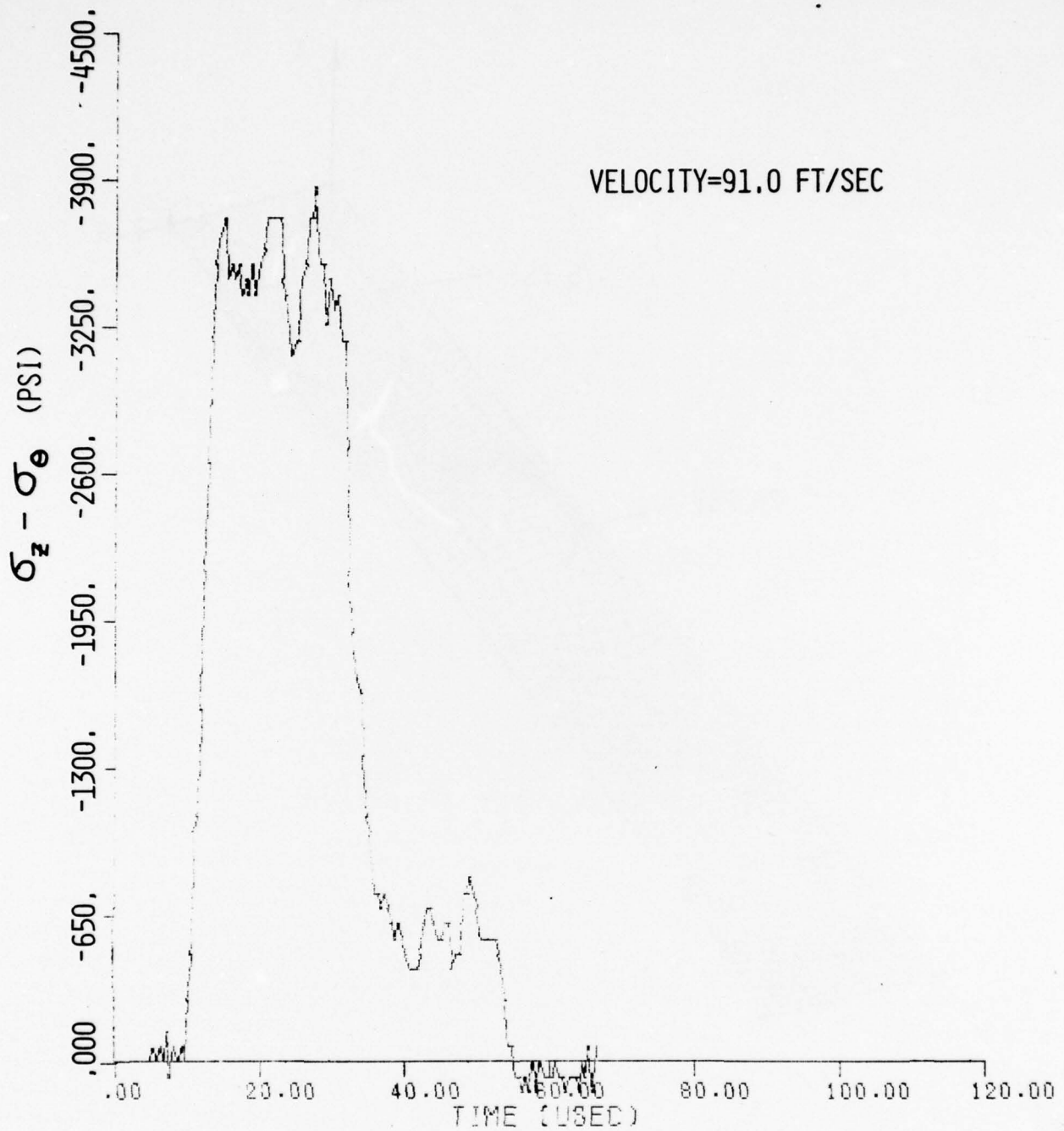


FIG. V.83 STRESS VERSUS TIME FOR 2.75 INCH DIAMETER BAR (SHOT NUMBER 31)

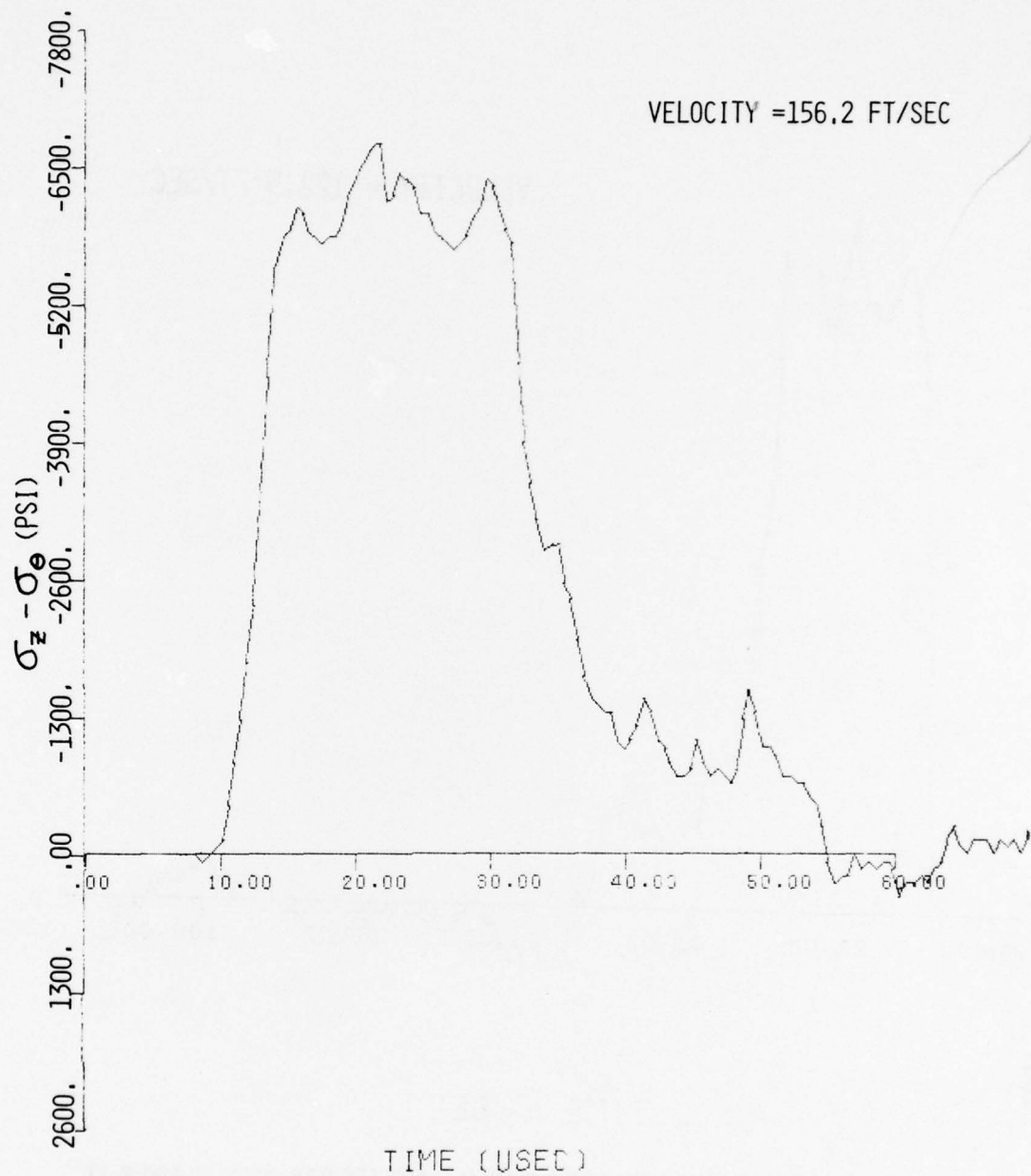


FIG. V.84 STRESS VERSUS TIME FOR 2.75 INCH DIAMETER BAR (SHOT NUMBER 32)

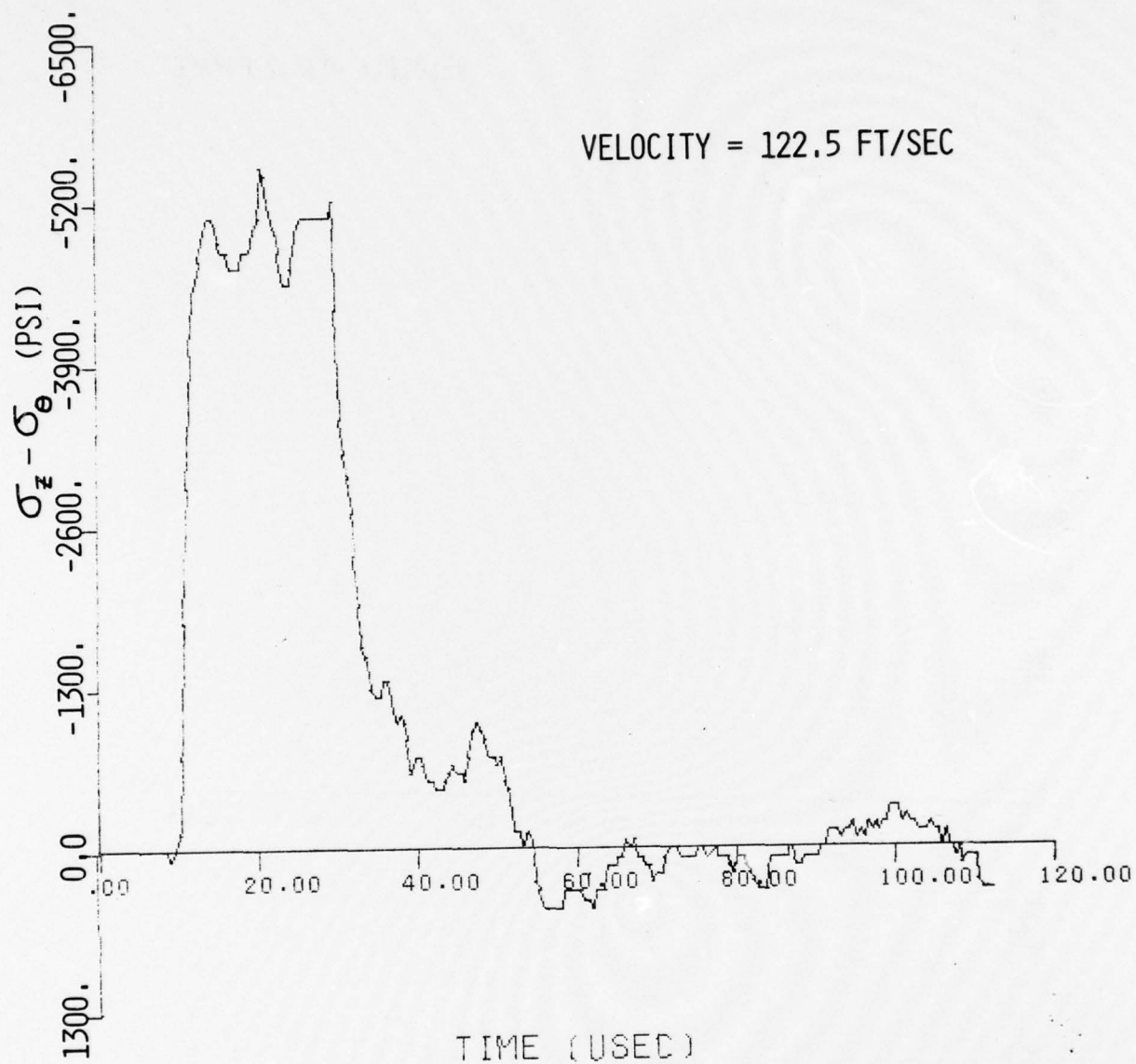


FIG. V.85 STRESS VERSUS TIME FOR 2.75 INCH DIAMETER BAR (SHOT NUMBER 33)

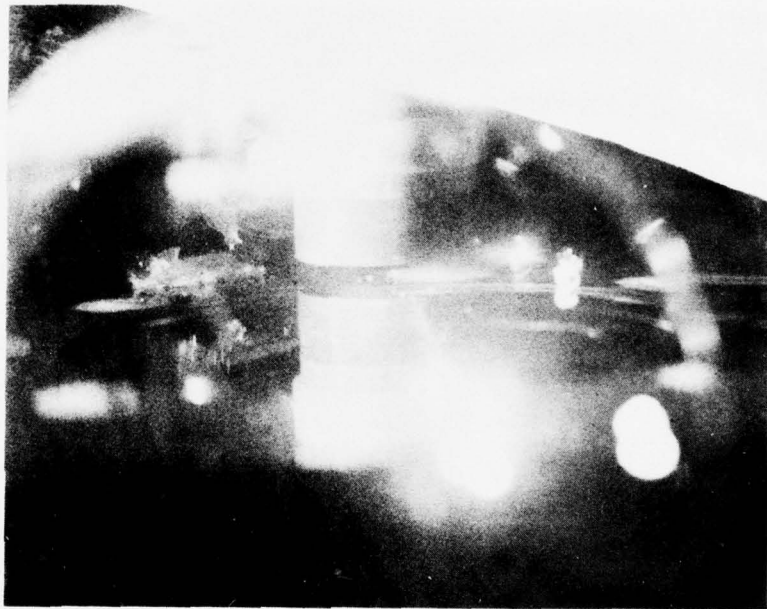


FIG. V.86 SHOT NO. 32 PHOTOGRAPH OF MODEL AND WATER SURFACE PRIOR TO IMPACT

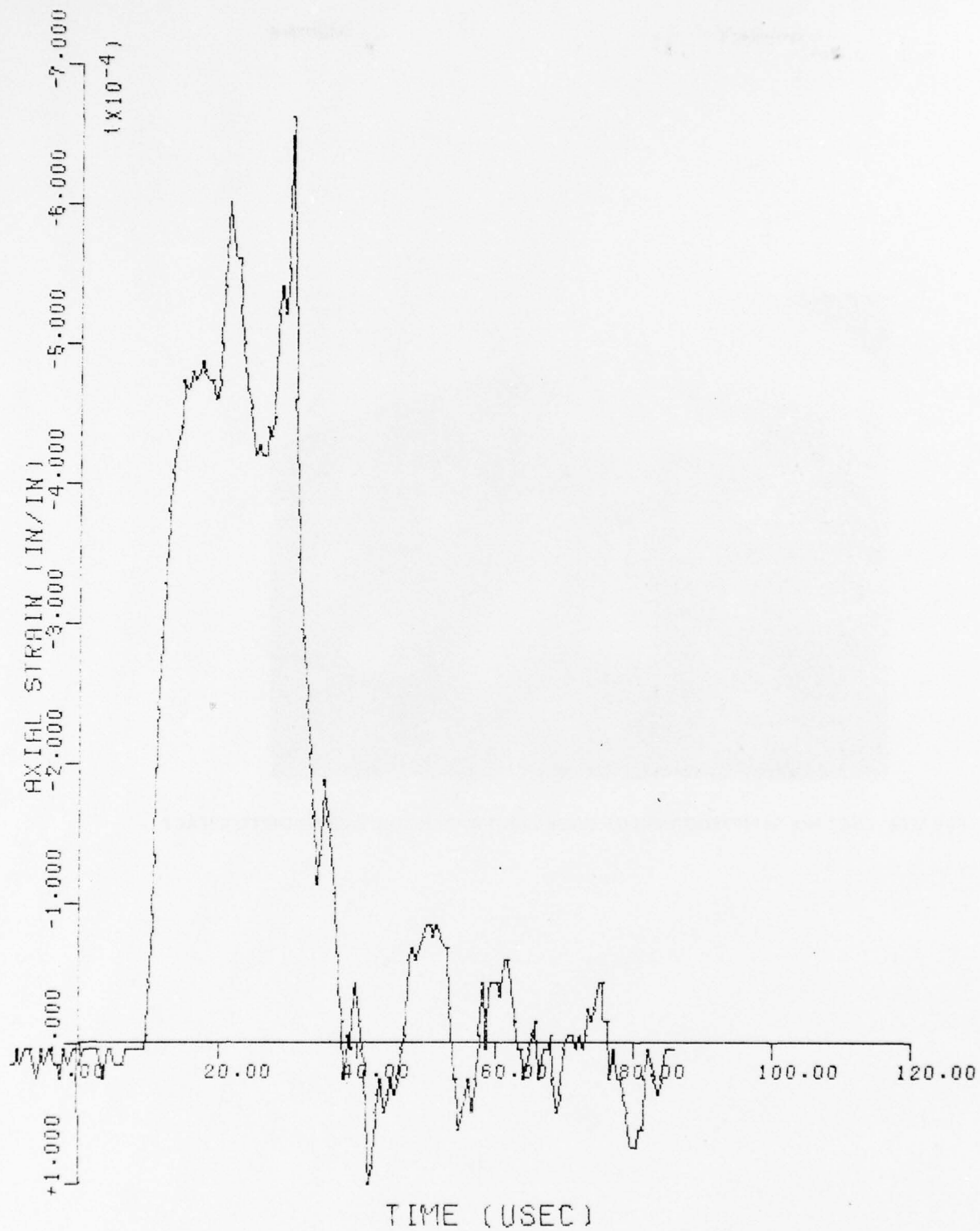


FIG. V.87 AXIAL STRAIN VERSUS TIME FOR GAGE NUMBER 1,
SHOT NUMBER 35

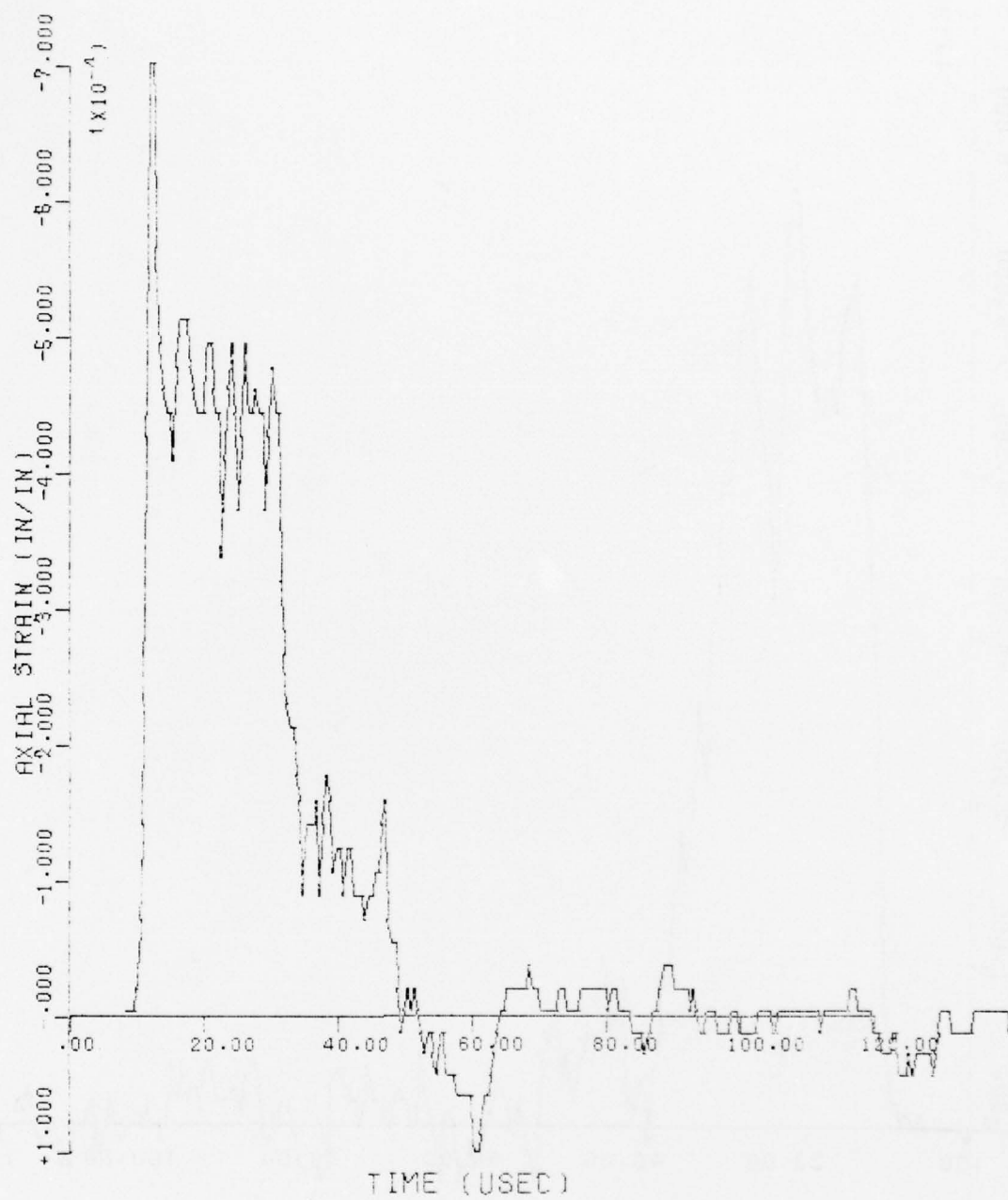


FIG. V.88 AXIAL STRAIN VERSUS TIME FOR GAGE NUMBER 2,
SHOT NUMBER 35

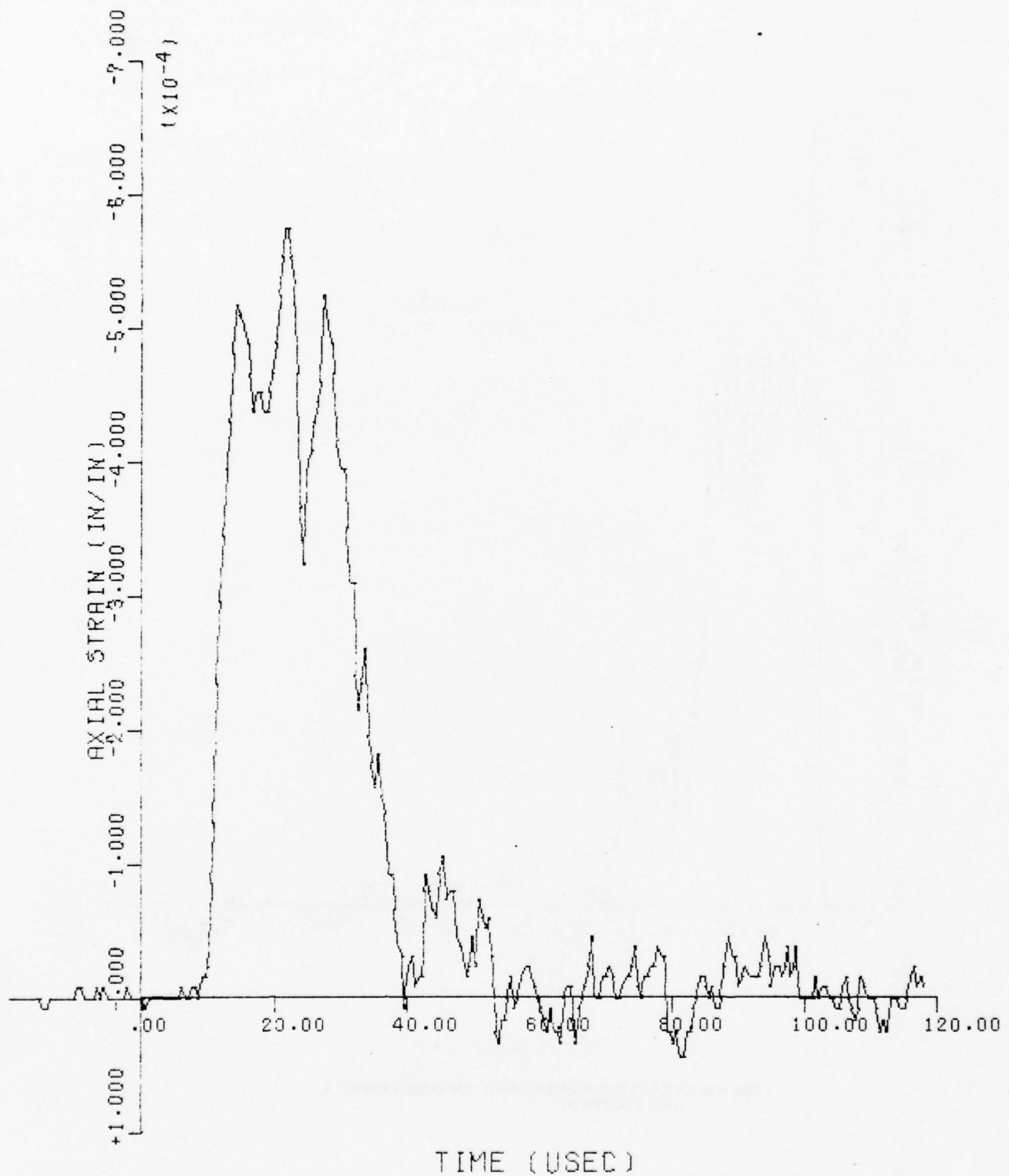


FIG. V.89 AXIAL STRAIN VERSUS TIME FOR GAGE NUMBER 3,
SHOT NUMBER 35

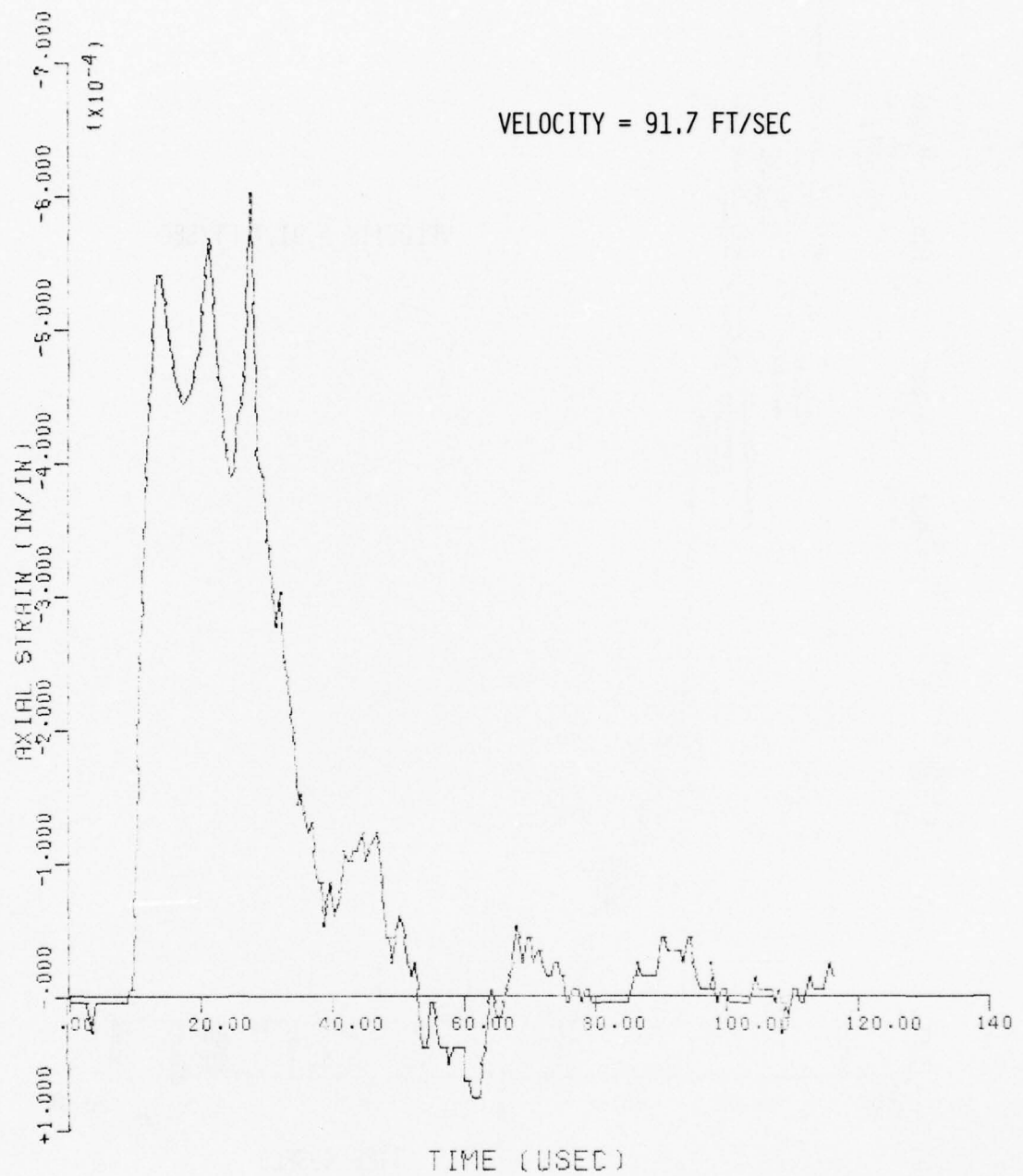


FIG. V.90 AXIAL STRAIN VERSUS TIME FOR GAGE NUMBER 1,
SHOT NUMBER 37

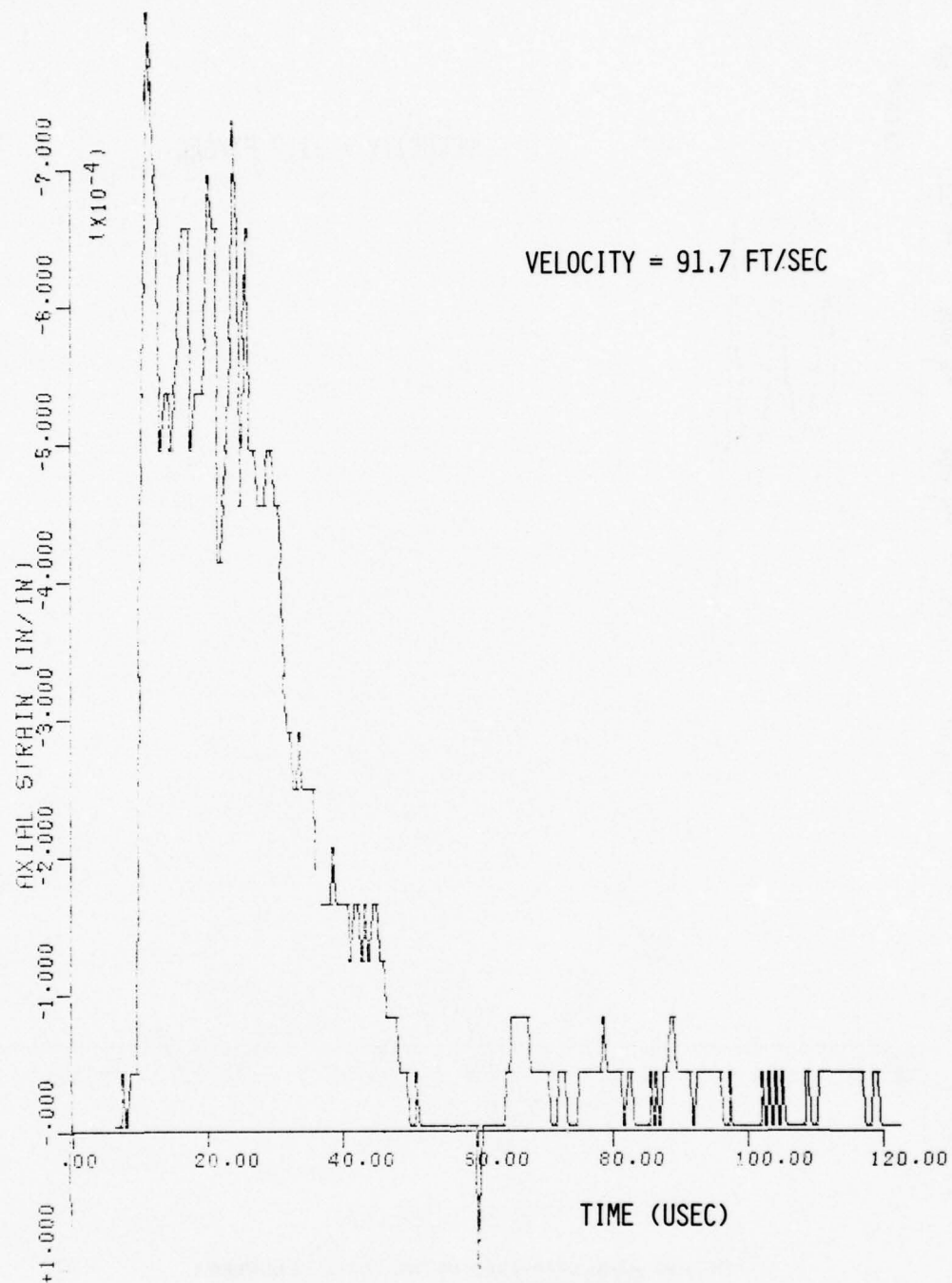


FIG. V.91 AXIAL STRAIN VERSUS TIME FOR GAGE NUMBER 2,
SHOT NUMBER 37

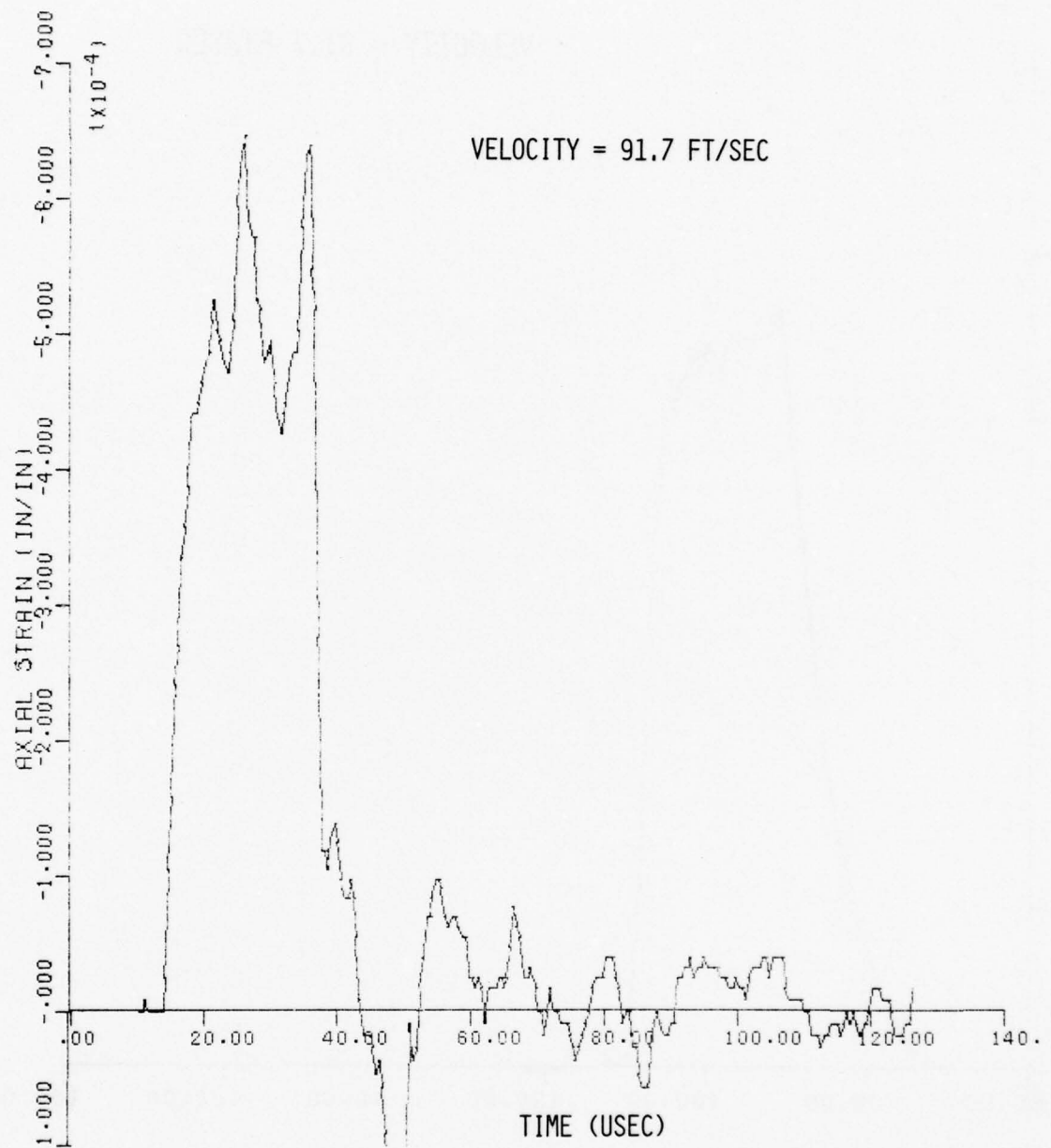


FIG. V.92 AXIAL STRAIN VERSUS TIME FOR GAGE NUMBER 3,
SHOT NUMBER 37

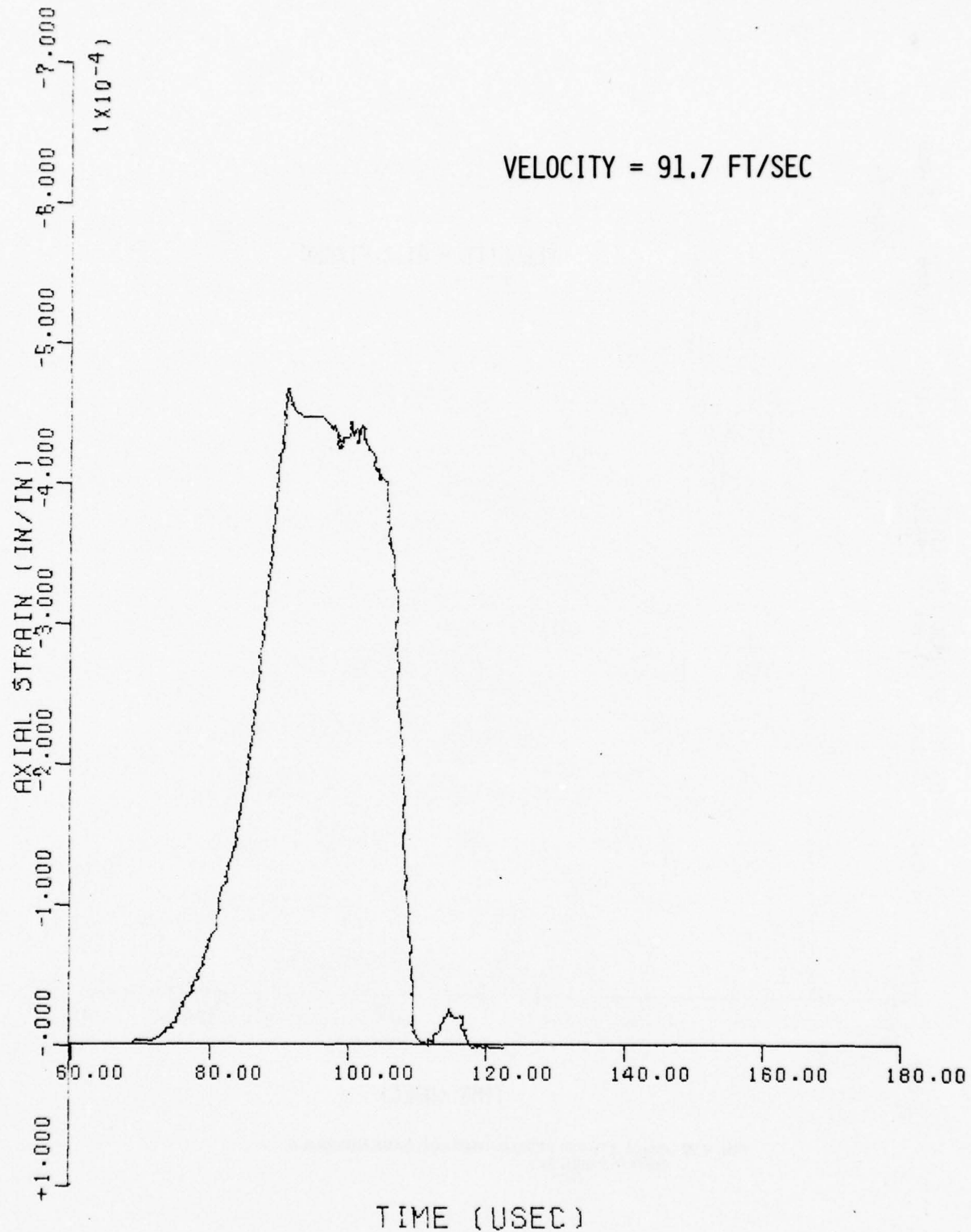


FIG. V.93 AXIAL STRAIN VERSUS TIME FOR GAGE NUMBER 4,
SHOT NUMBER 37

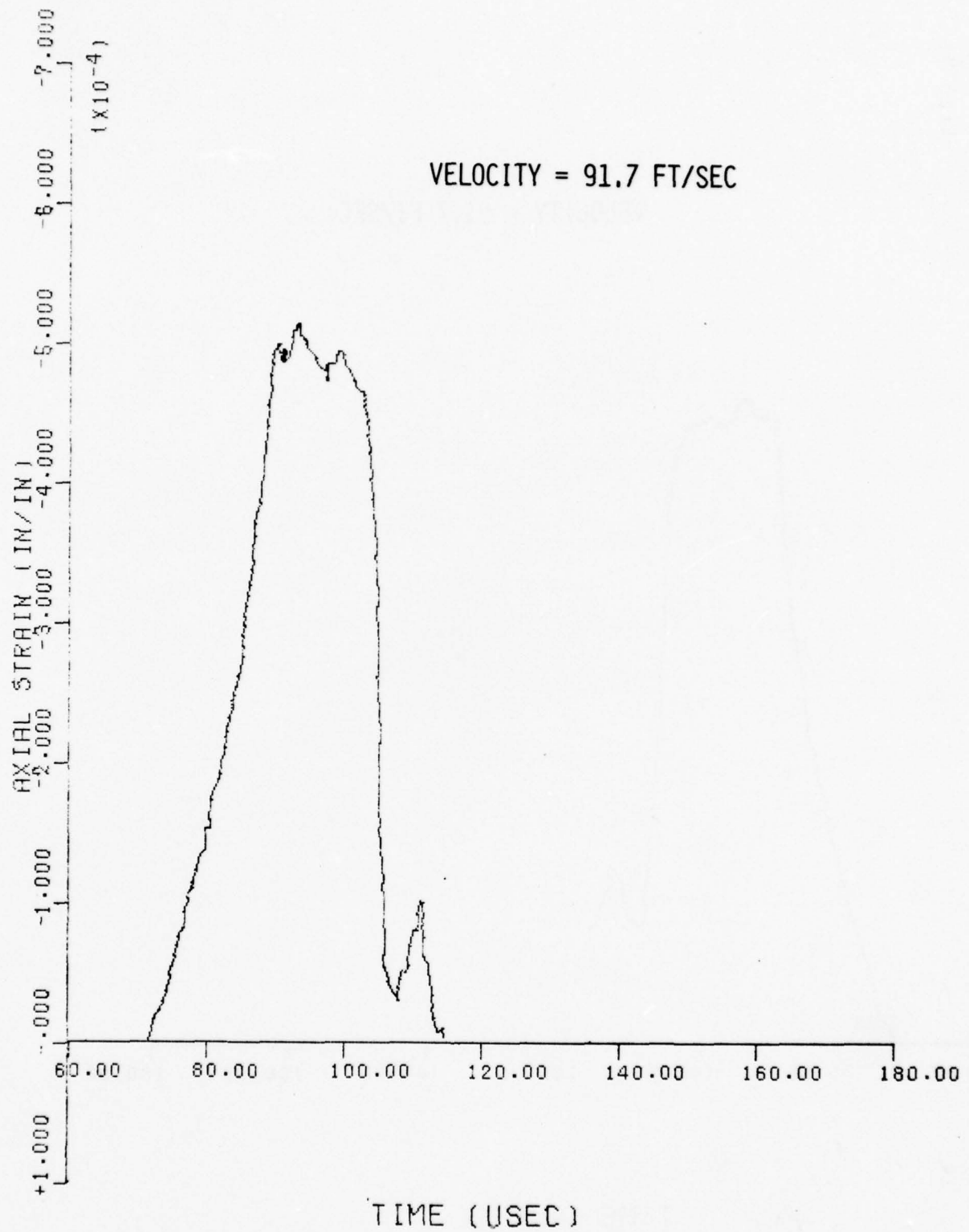


FIG. V.94 AXIAL STRAIN VERSUS TIME FOR GAGE NUMBER 5,
SHOT NUMBER 37

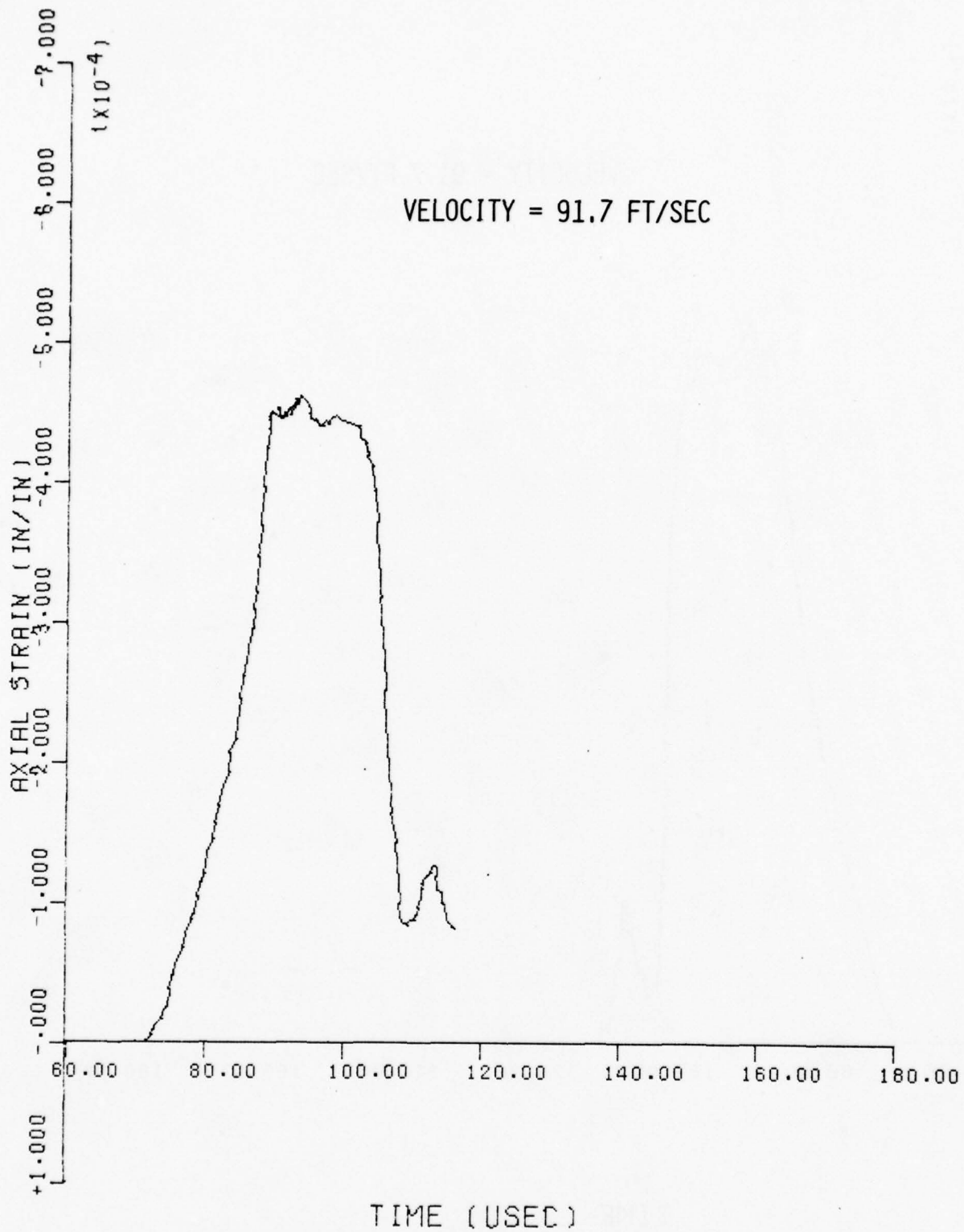


FIG. V.95 AXIAL STRAIN VERSUS TIME FOR GAGE NUMBER 6,
SHOT NUMBER 37

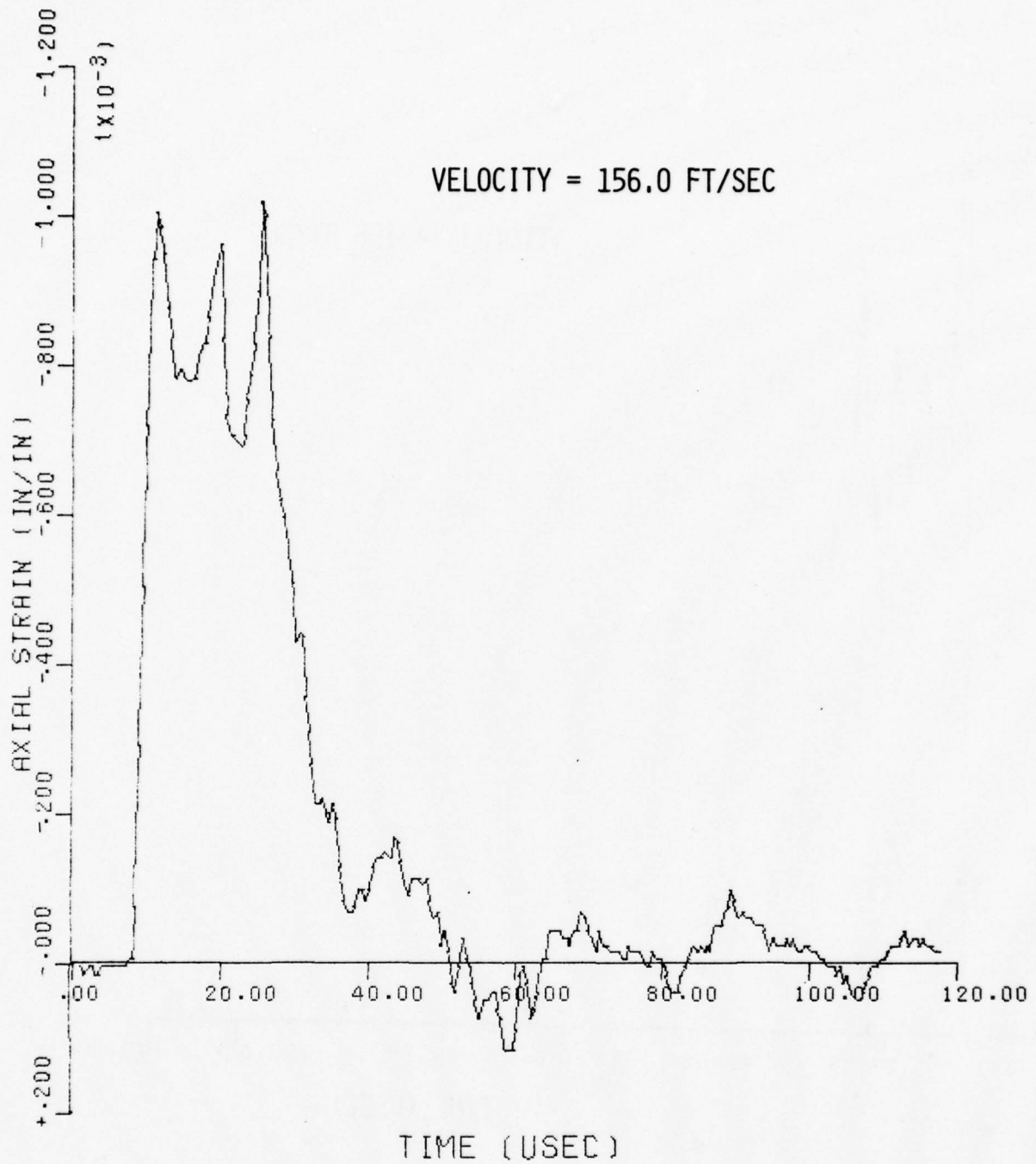


FIG. V.96 AXIAL STRAIN VERSUS TIME FOR GAGE NUMBER 1,
SHOT NUMBER 38

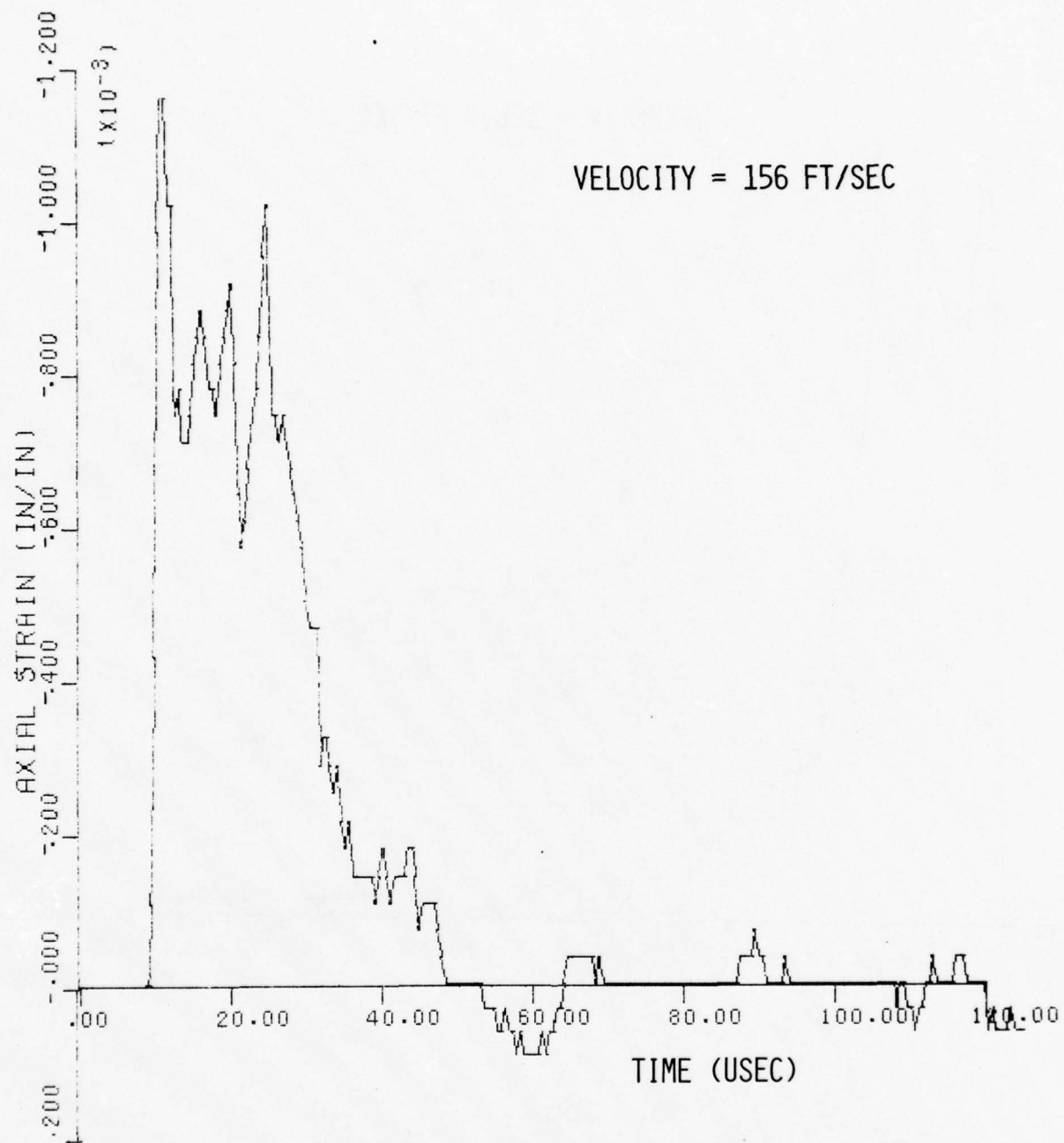


FIG. V.97 AXIAL STRAIN VERSUS TIME FOR GAGE NUMBER 2,
SHOT NUMBER 38

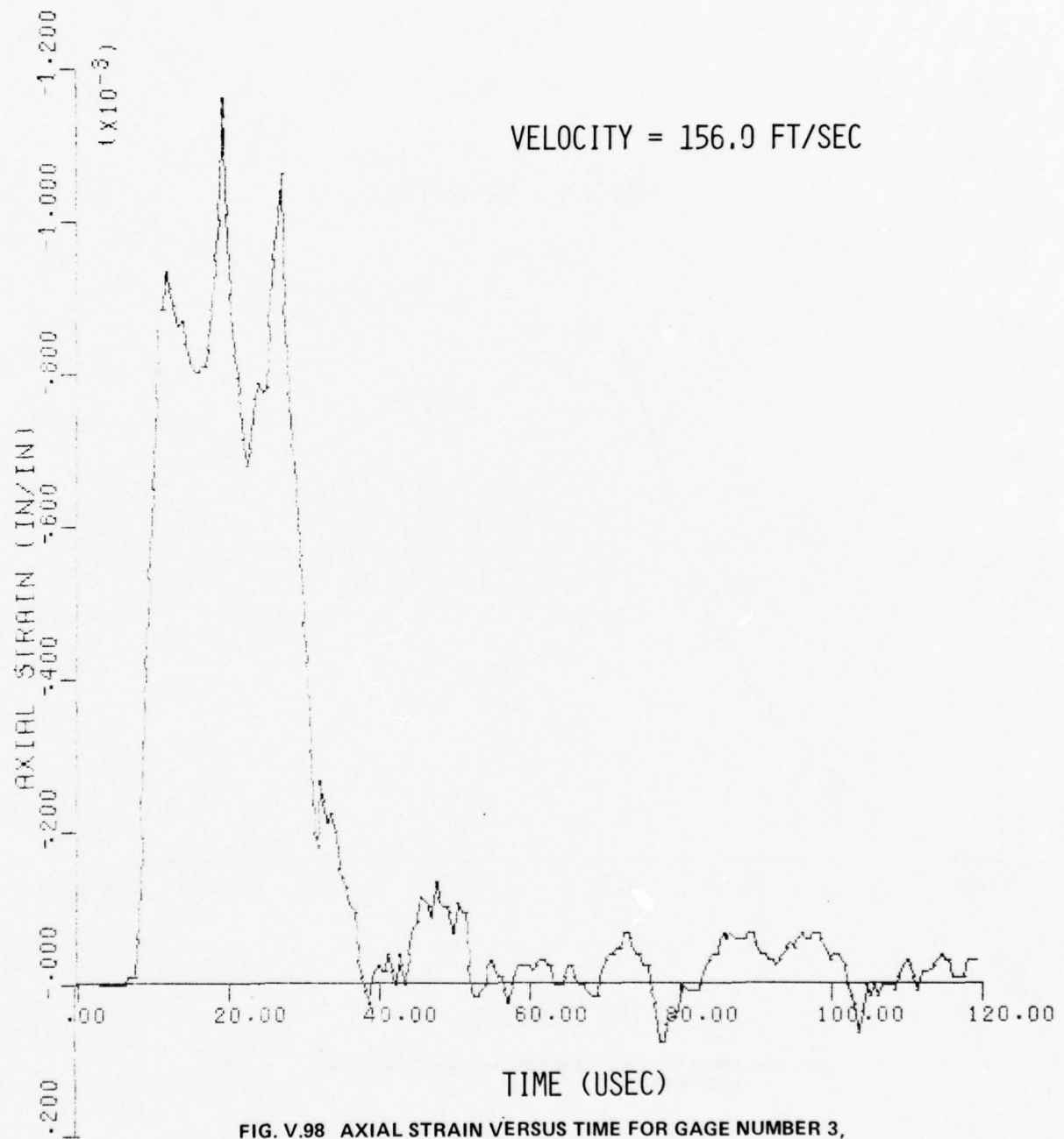


FIG. V.98 AXIAL STRAIN VERSUS TIME FOR GAGE NUMBER 3,
SHOT NUMBER 38

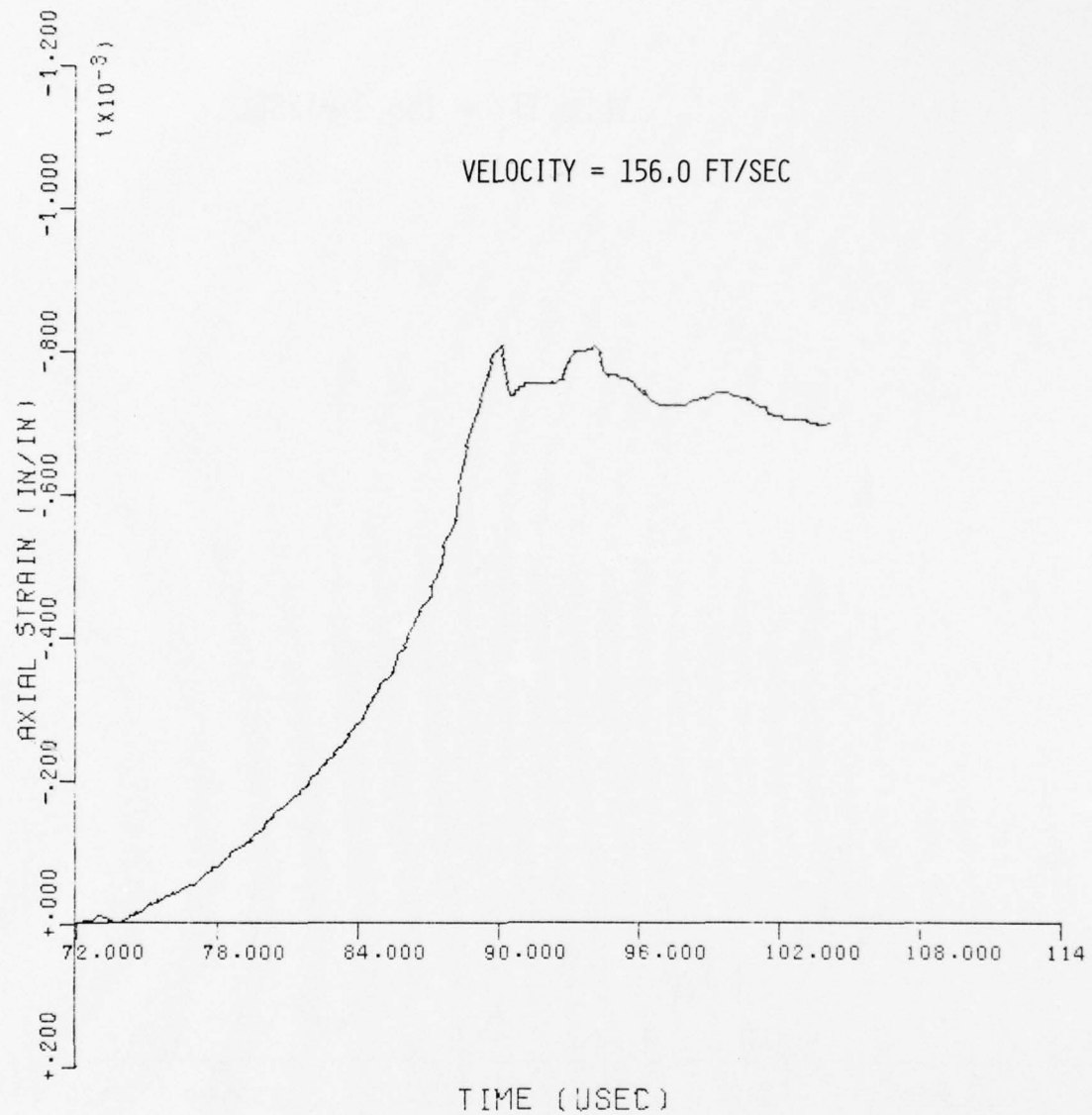


FIG. V.99 AXIAL STRAIN VERSUS TIME FOR GAGE NUMBER 4,
SHOT NUMBER 38

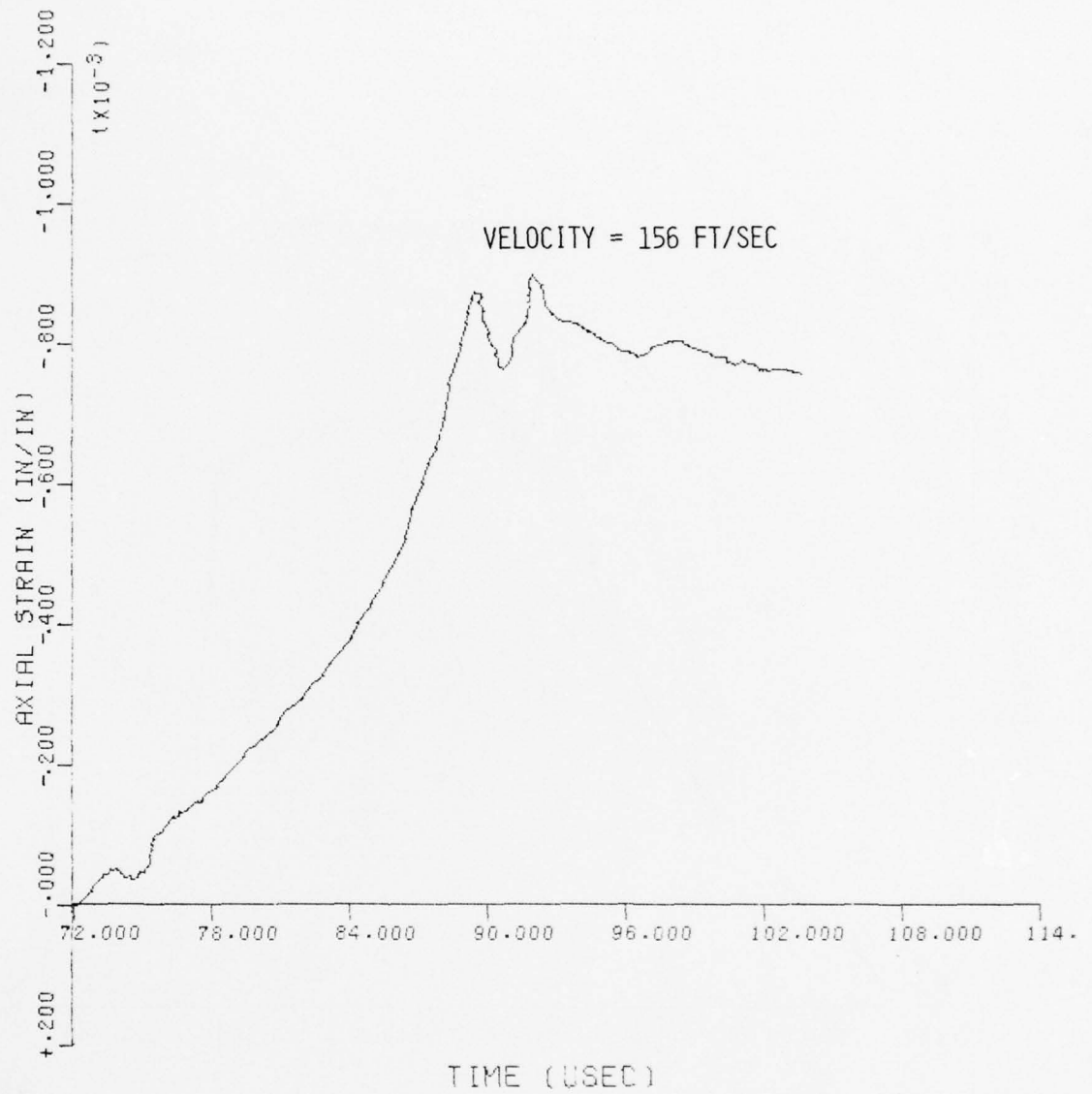


FIG. V.100 AXIAL STRAIN VERSUS TIME FOR GAGE NUMBER 5,
SHOT NUMBER 38

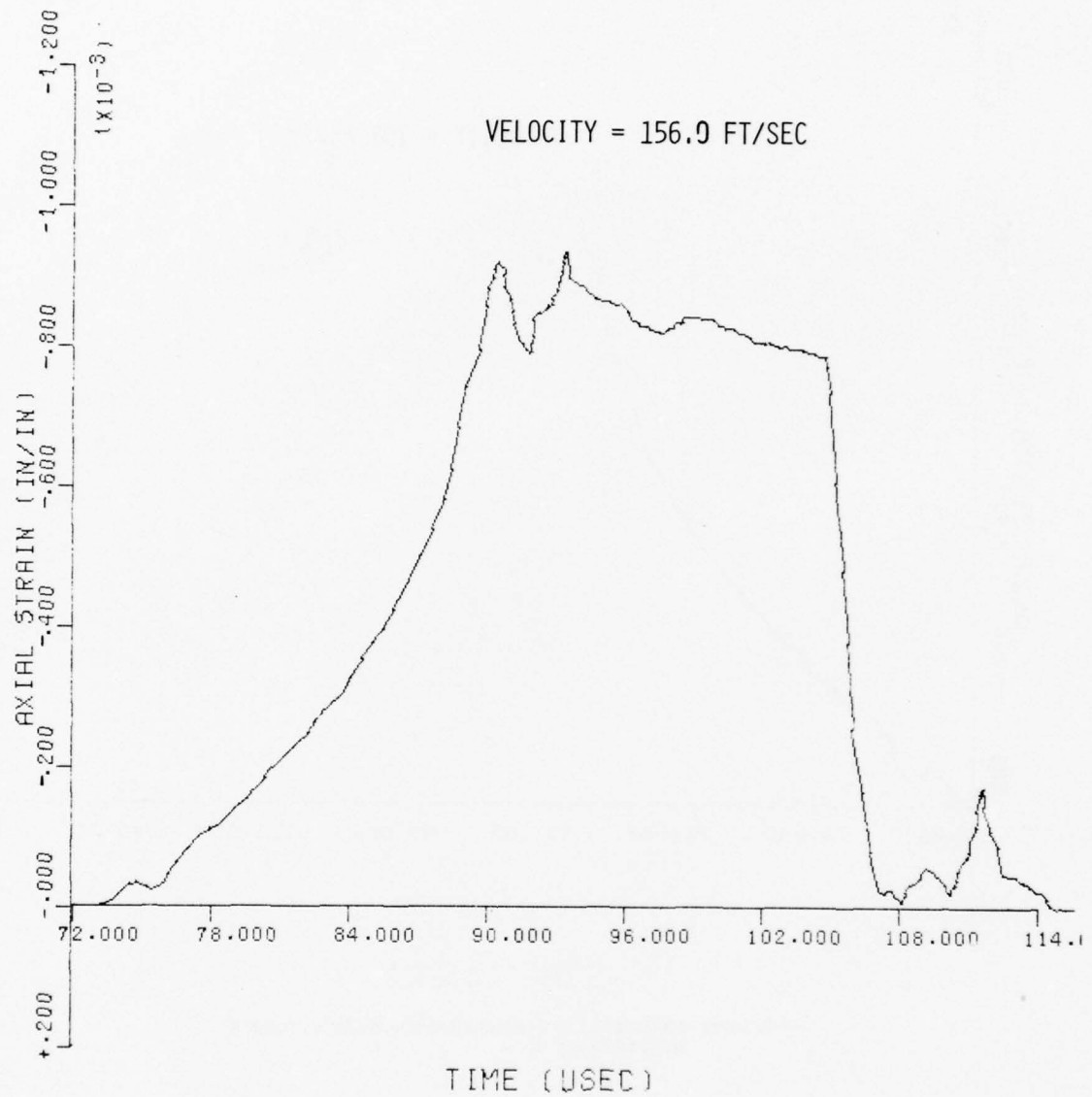


FIG. V.101 AXIAL STRAIN VERSUS TIME FOR GAGE NUMBER 6,
SHOT NUMBER 38

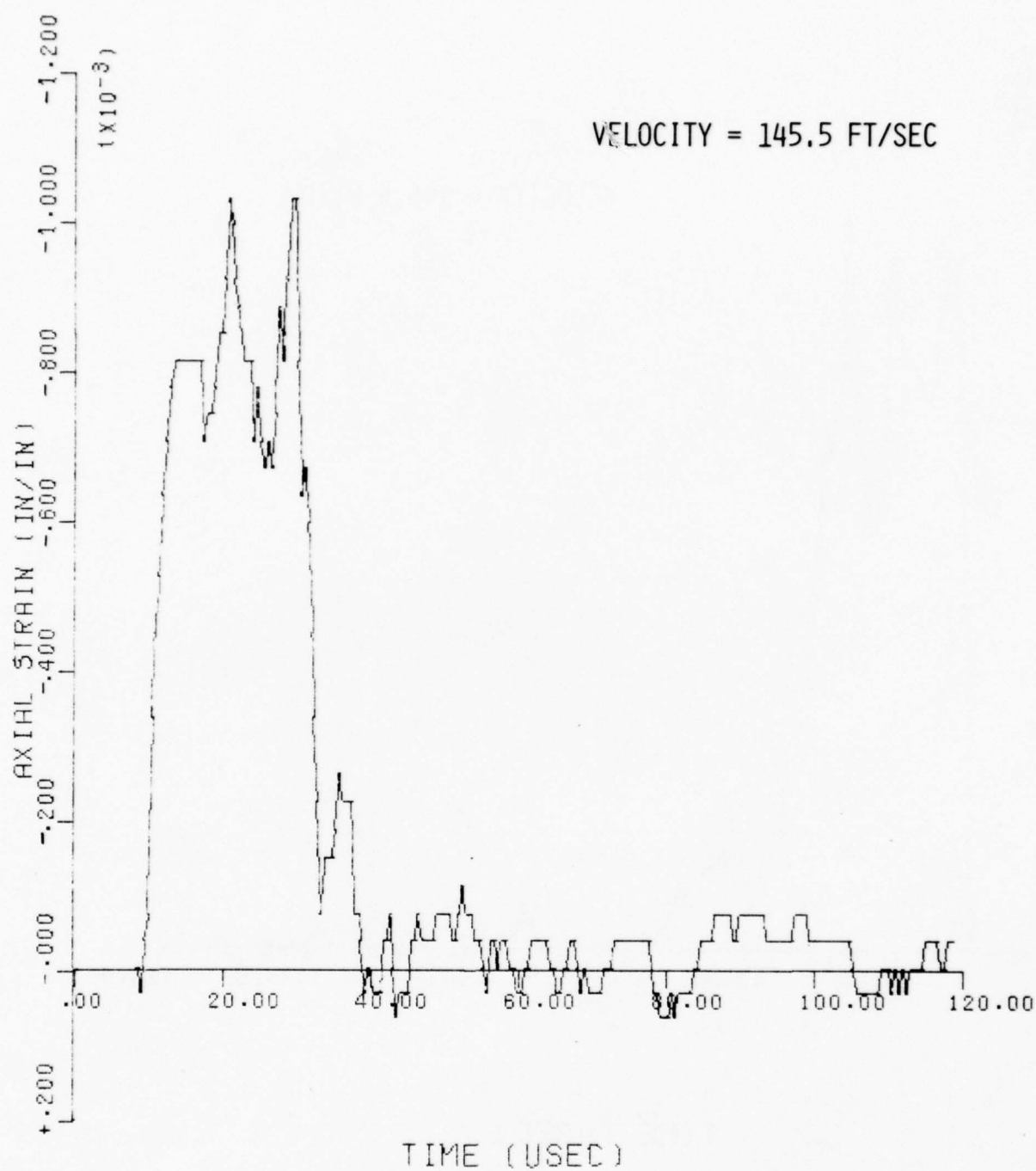


FIG. V.102 AXIAL STRAIN VERSUS TIME FOR GAGE NUMBER 2,
SHOT NUMBER 39

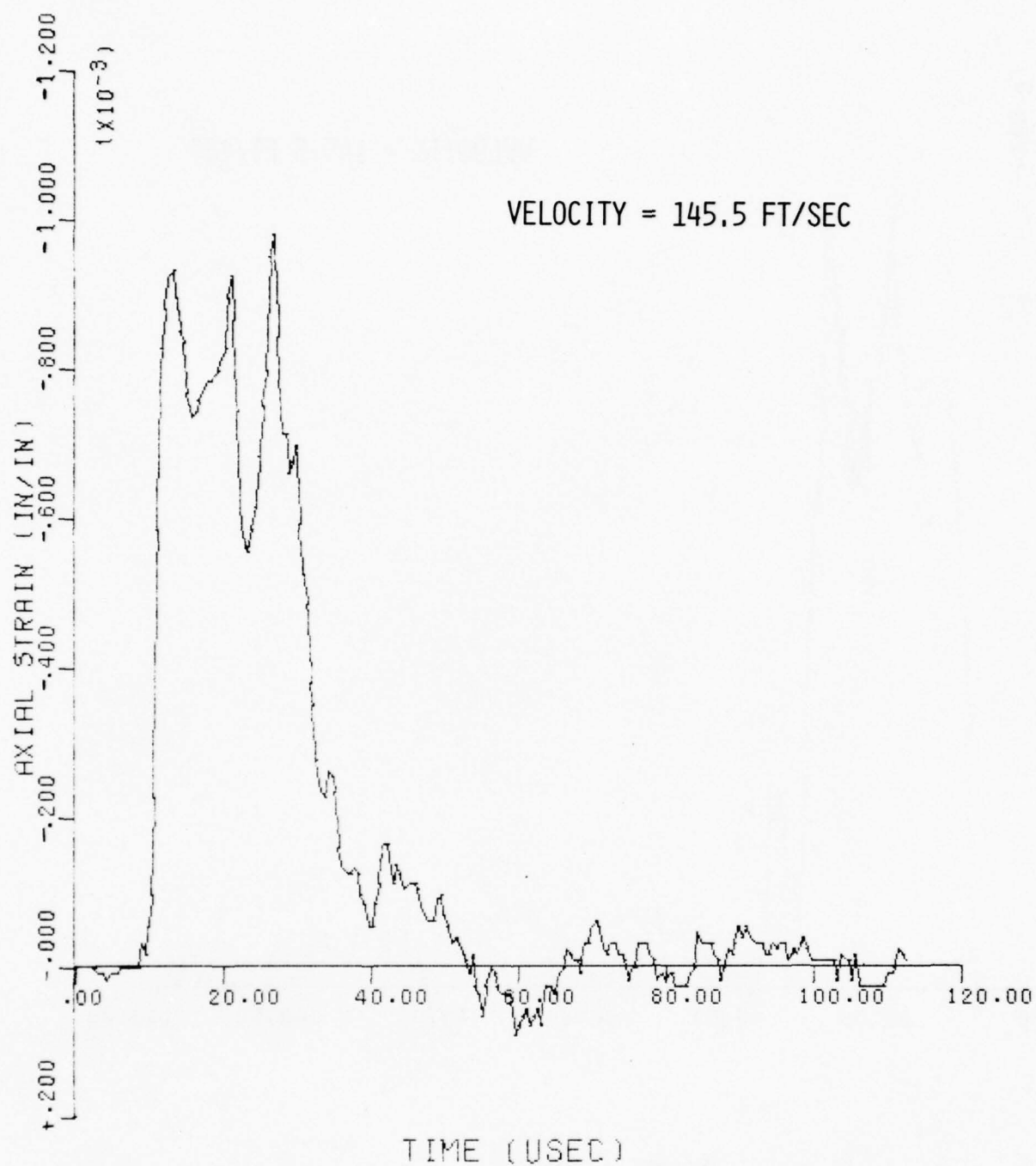


FIG. V.103 AXIAL STRAIN VERSUS TIME FOR GAGE NUMBER 3,
SHOT NUMBER 39

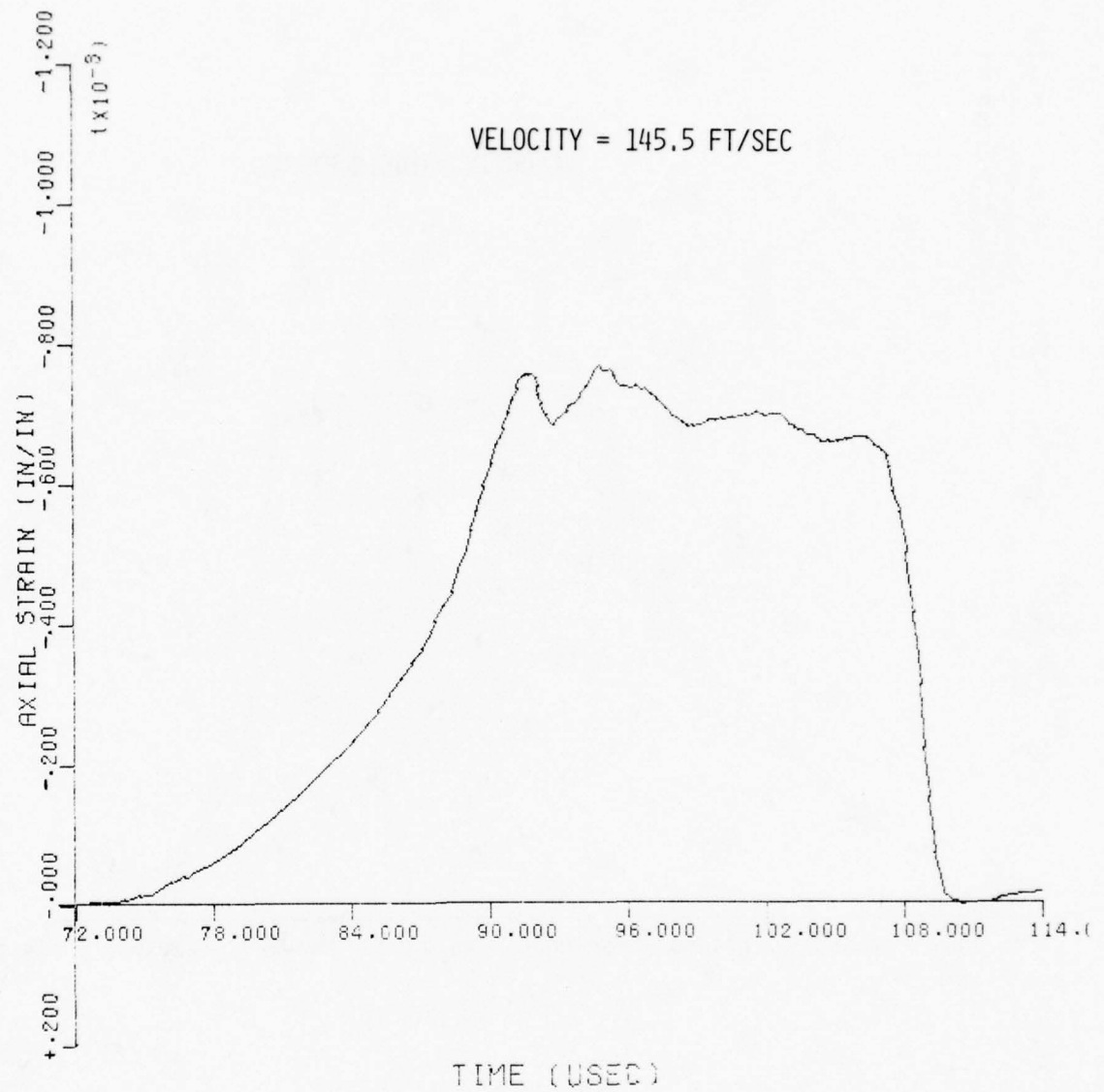


FIG. V.104 AXIAL STRAIN VERSUS TIME FOR GAGE NUMBER 4,
SHOT NUMBER 39

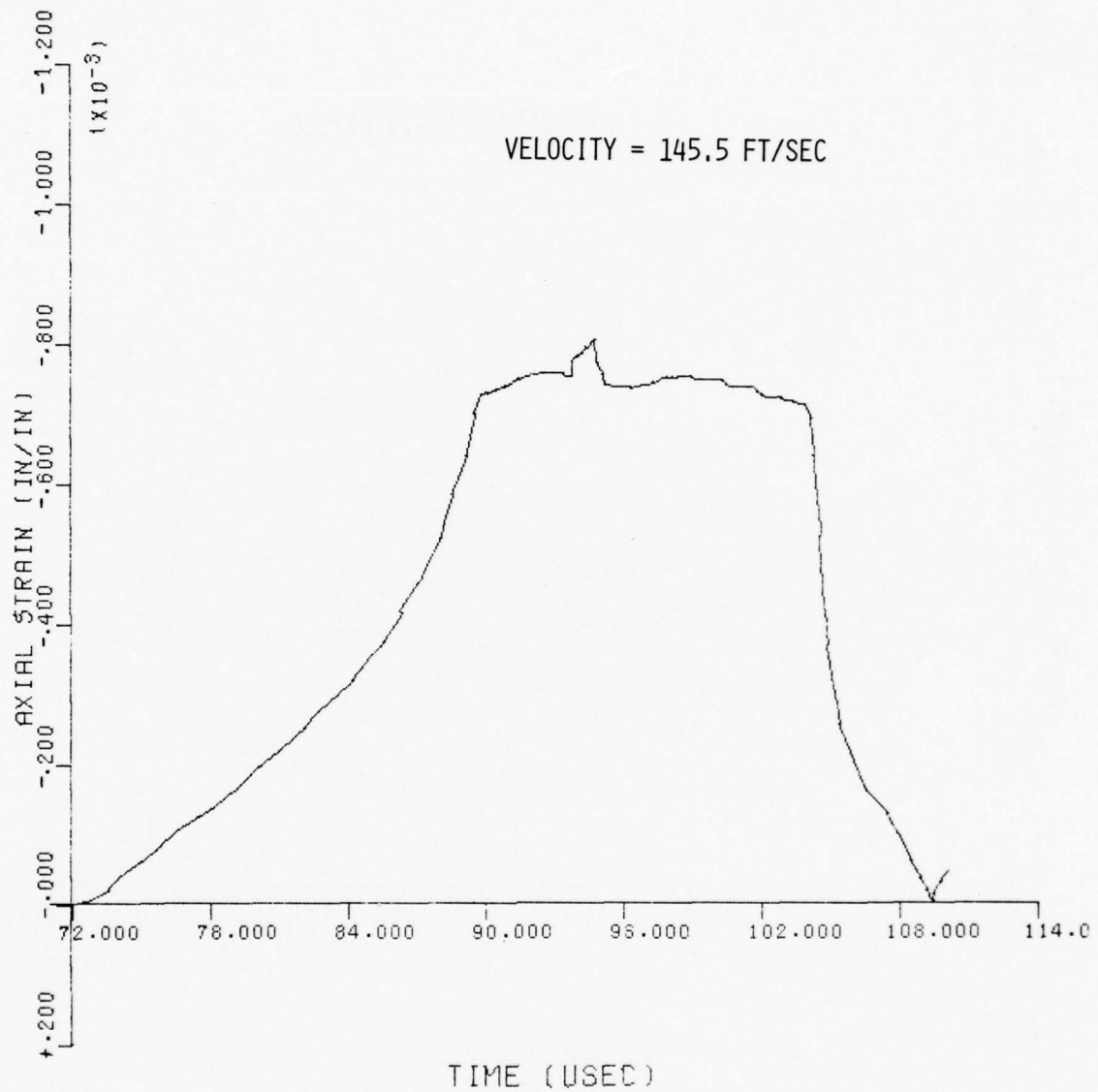


FIG. V.105 AXIAL STRAIN VERSUS TIME FOR GAGE NUMBER 5,
SHOT NUMBER 39

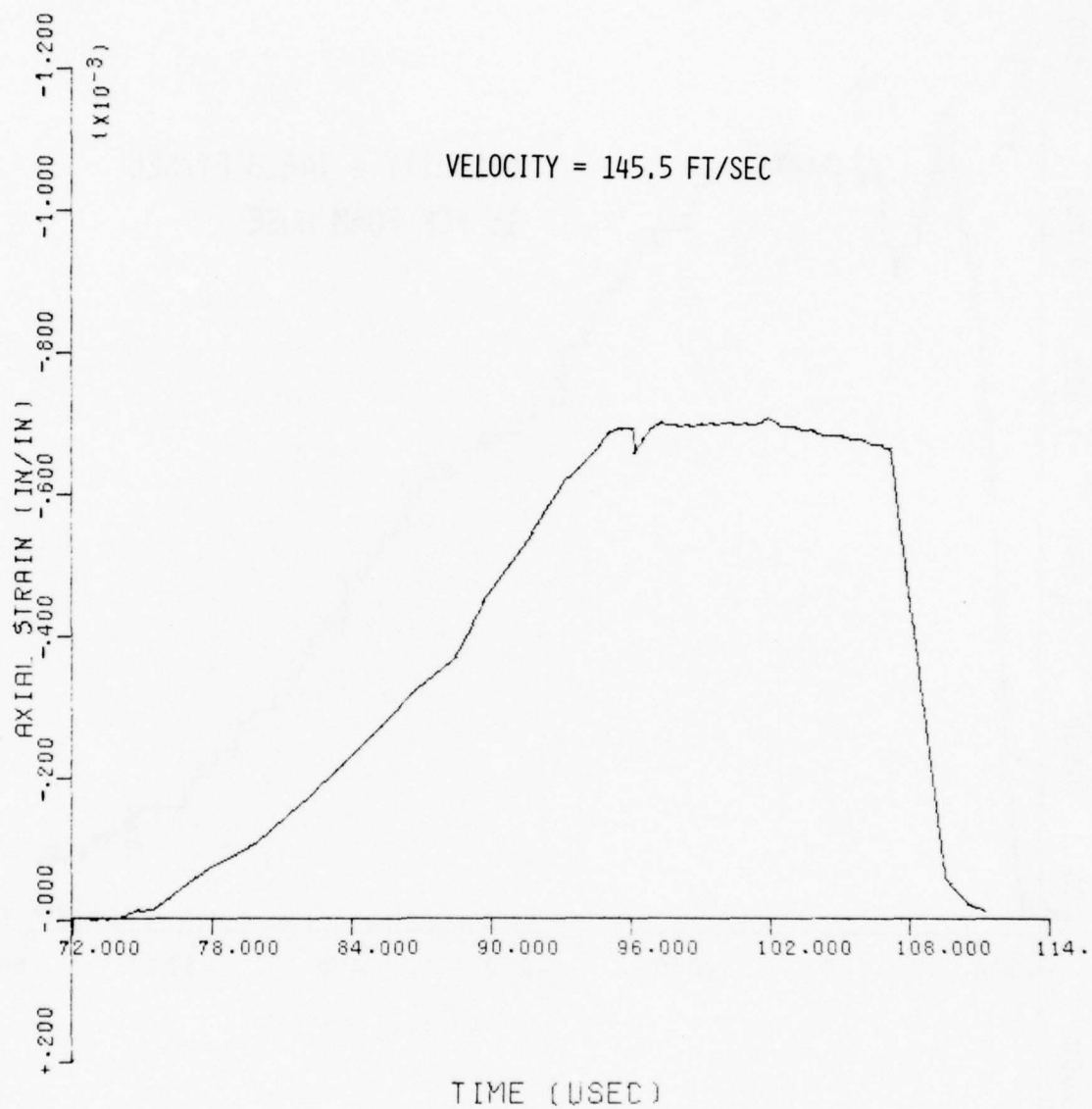


FIG. V.106 AXIAL STRAIN VERSUS TIME FOR GAGE NUMBER 6,
SHOT NUMBER 39

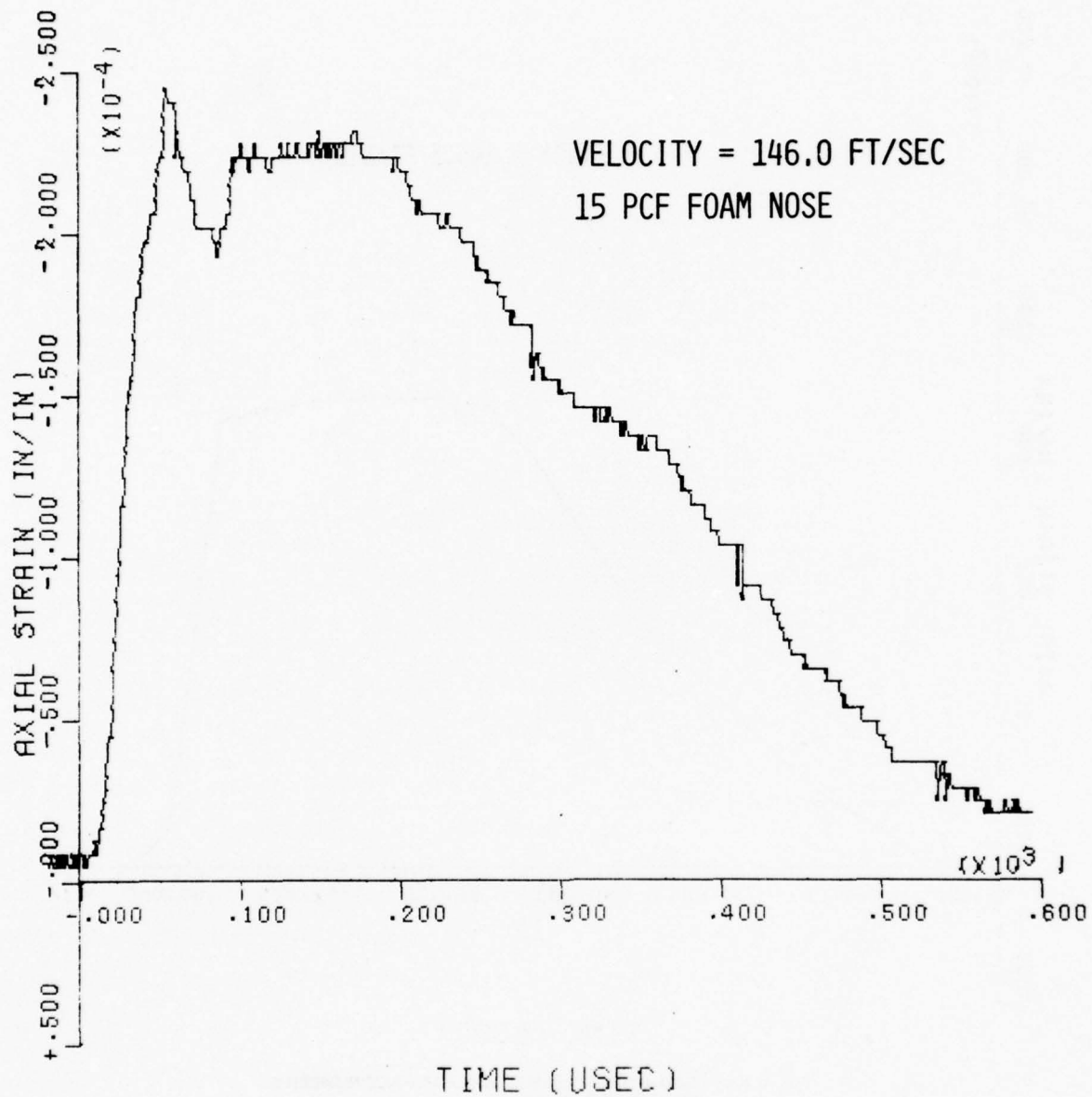


FIG. V.107 AXIAL STRAIN VERSUS TIME FOR GAGE NUMBER 2,
SHOT NUMBER 40

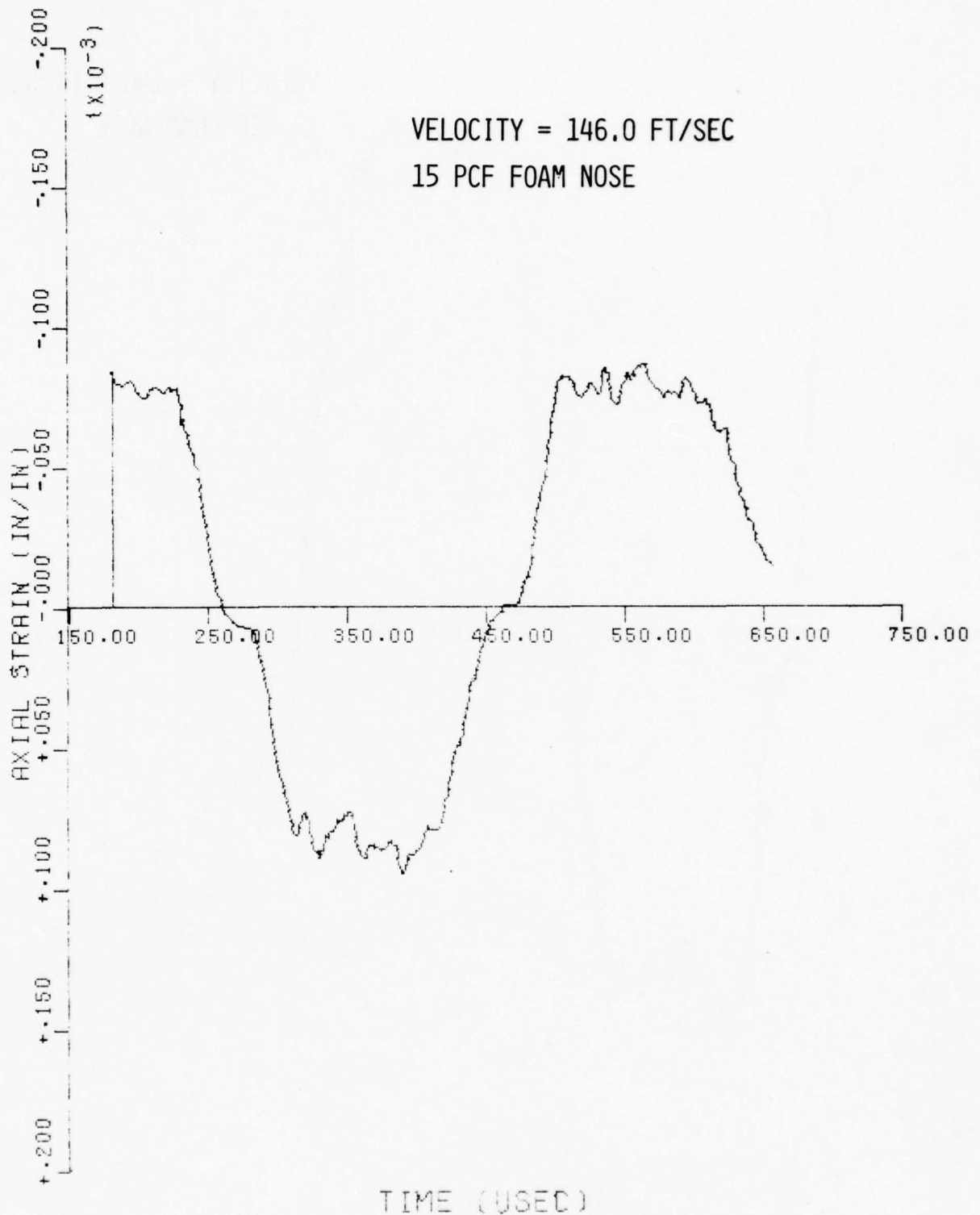


FIG. V.108 AXIAL STRAIN VERSUS TIME FOR GAGE NUMBER 4,
SHOT NUMBER 40

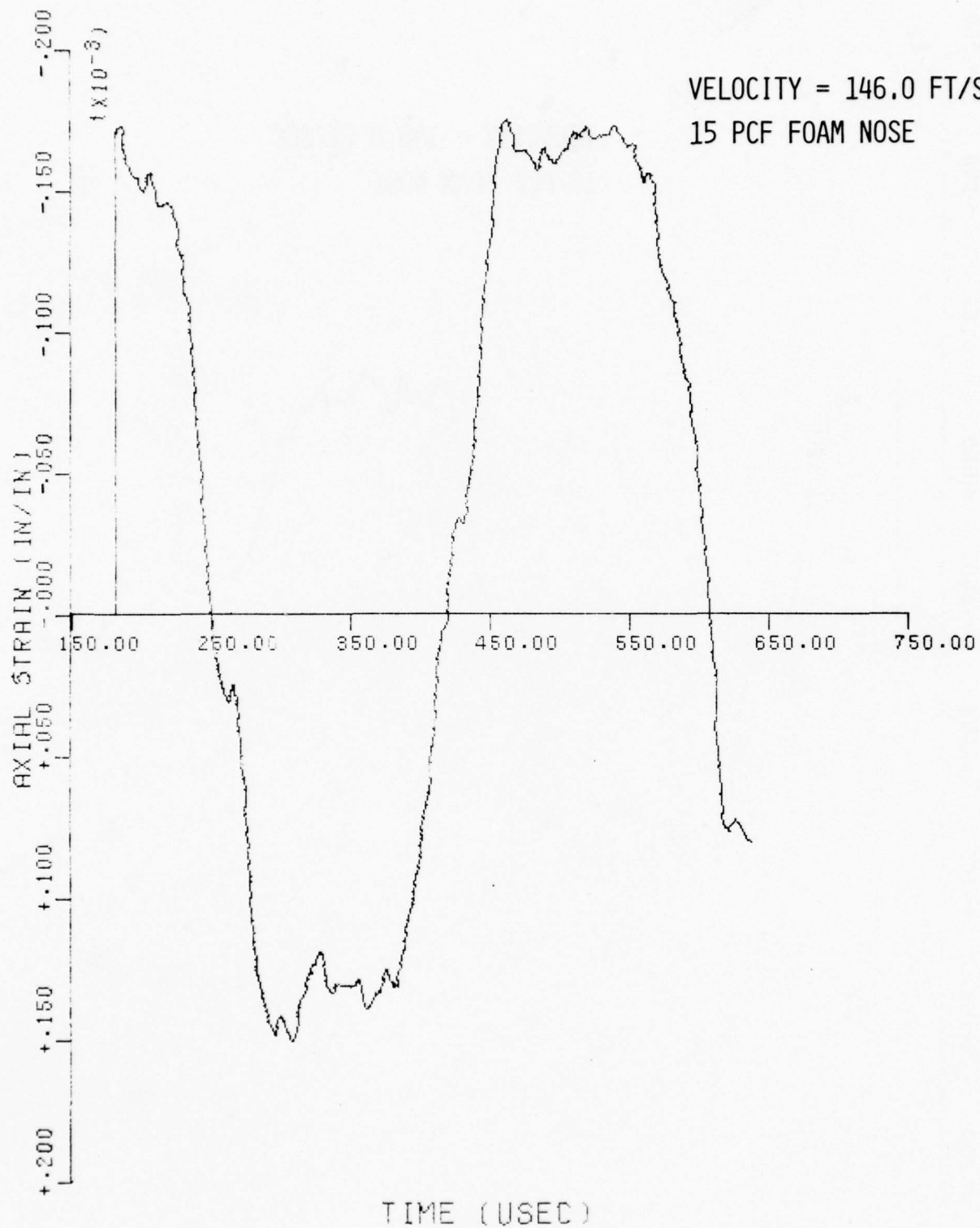


FIG. V.109 AXIAL STRAIN VERSUS TIME FOR GAGE NUMBER 5,
SHOT NUMBER 40

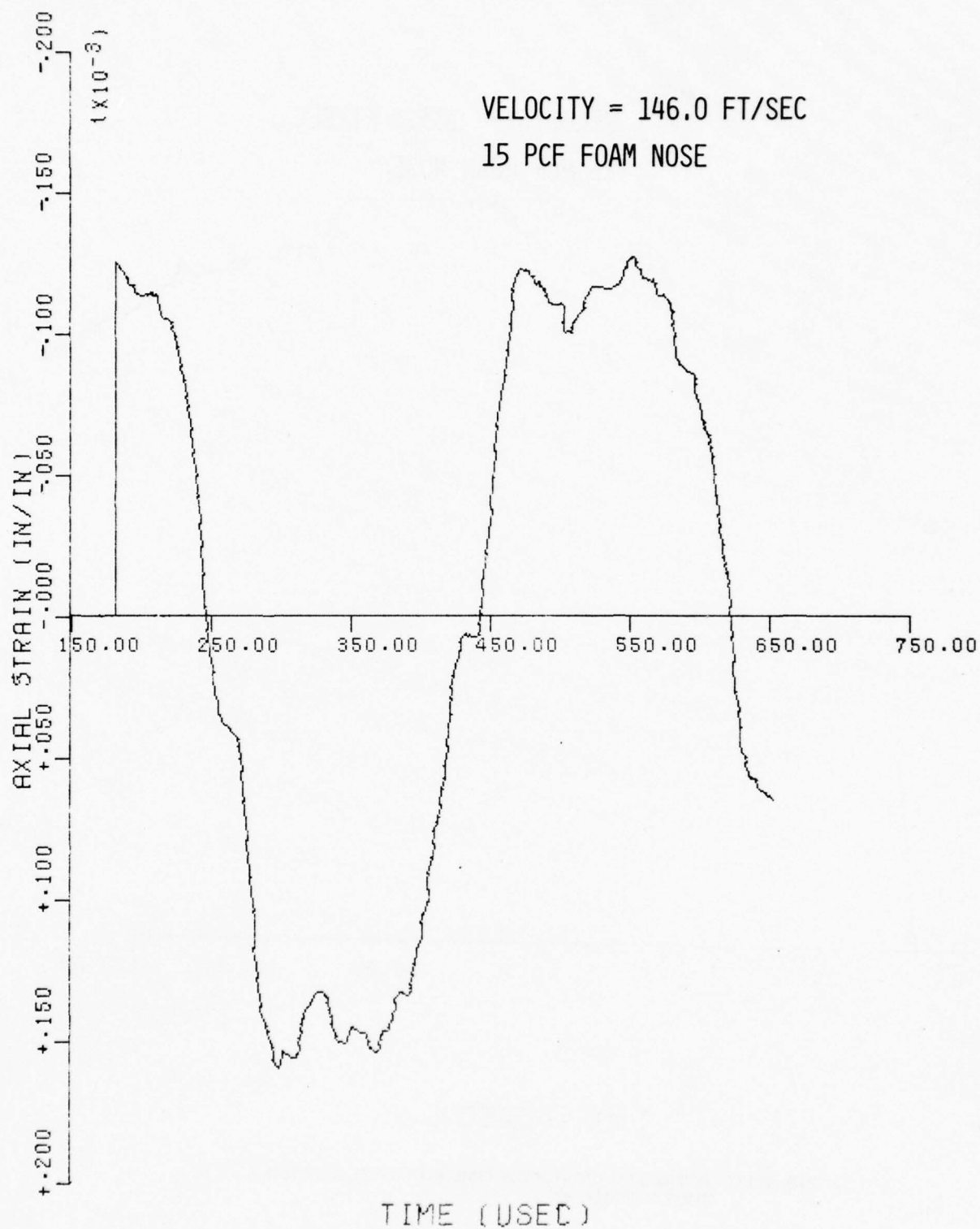


FIG. V.110 AXIAL STRAIN VERSUS TIME FOR GAGE NUMBER 6,
SHOT NUMBER 40

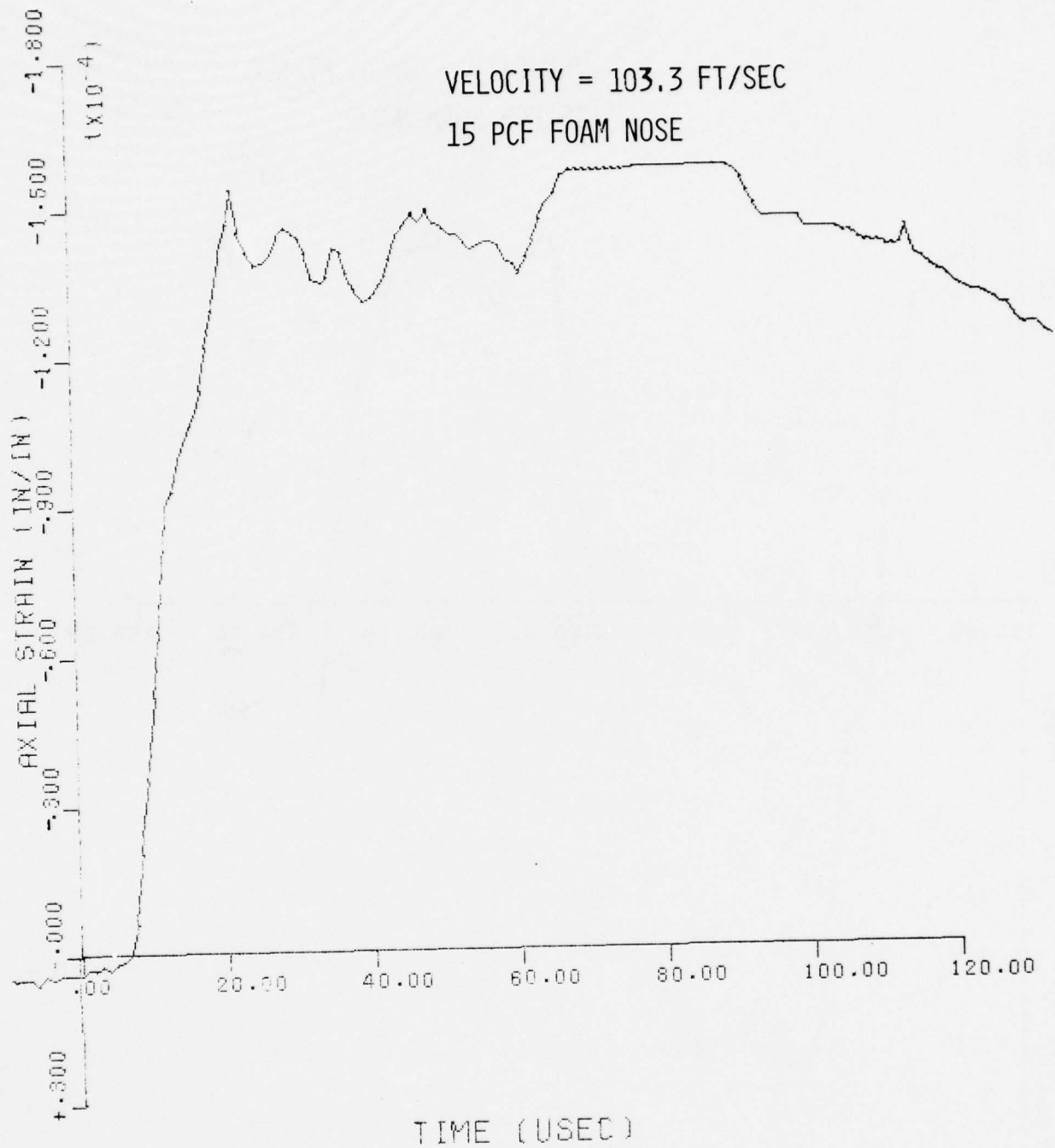


FIG. V.111 AXIAL STRAIN VERSUS TIME FOR GAGE NUMBER 1,
SHOT NUMBER 47

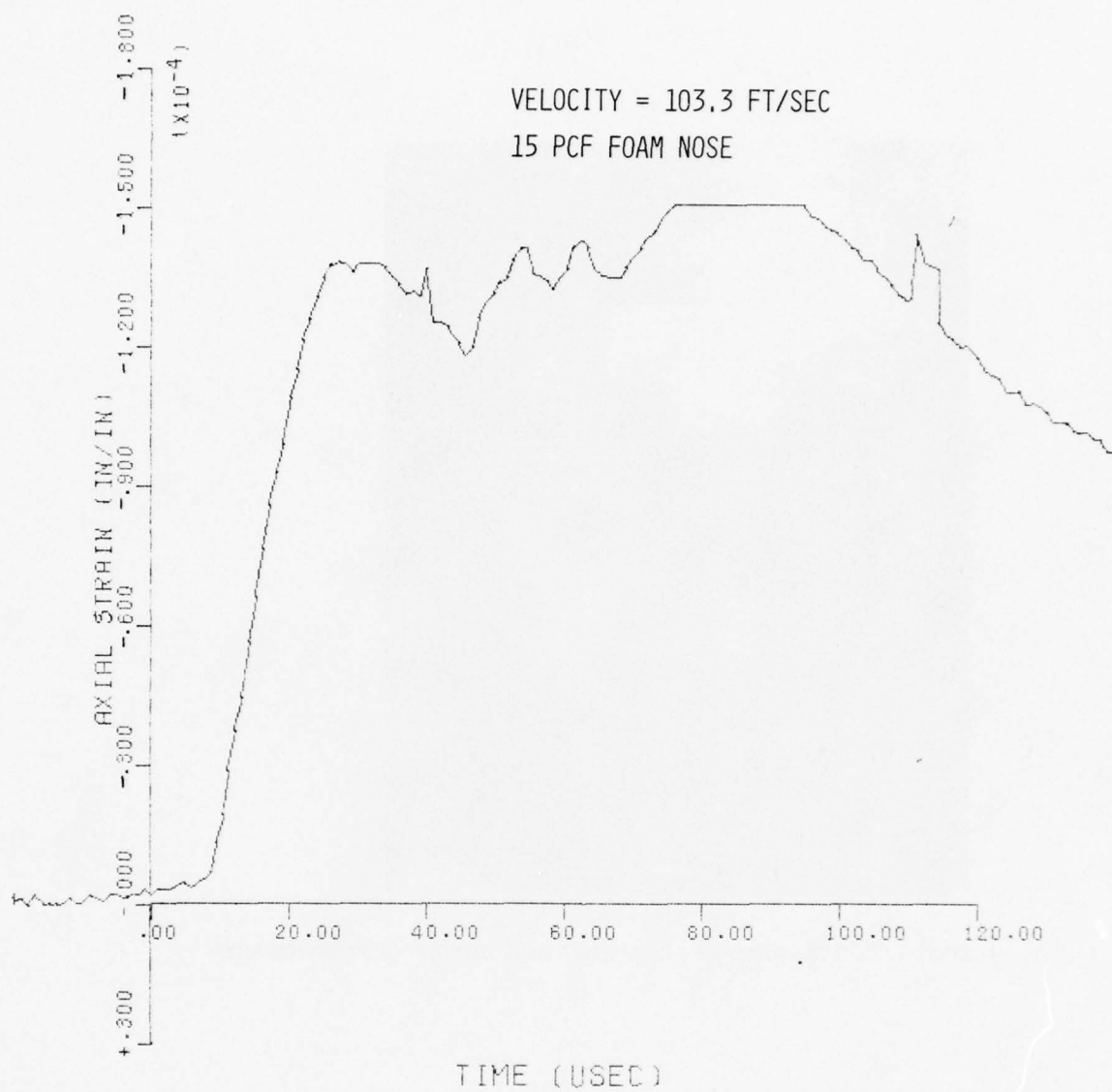


FIG. V.112 AXIAL STRAIN VERSUS TIME FOR GAGE NUMBER 3,
SHOT NUMBER 47

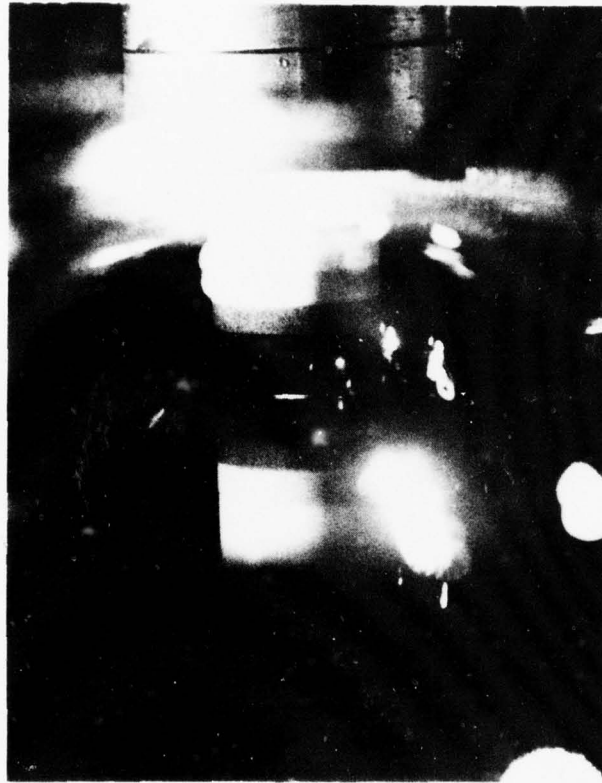


FIG. V.113 SHOT 47 PHOTOGRAPH OF FOAM NOSE AND WATER PRIOR TO IMPACT

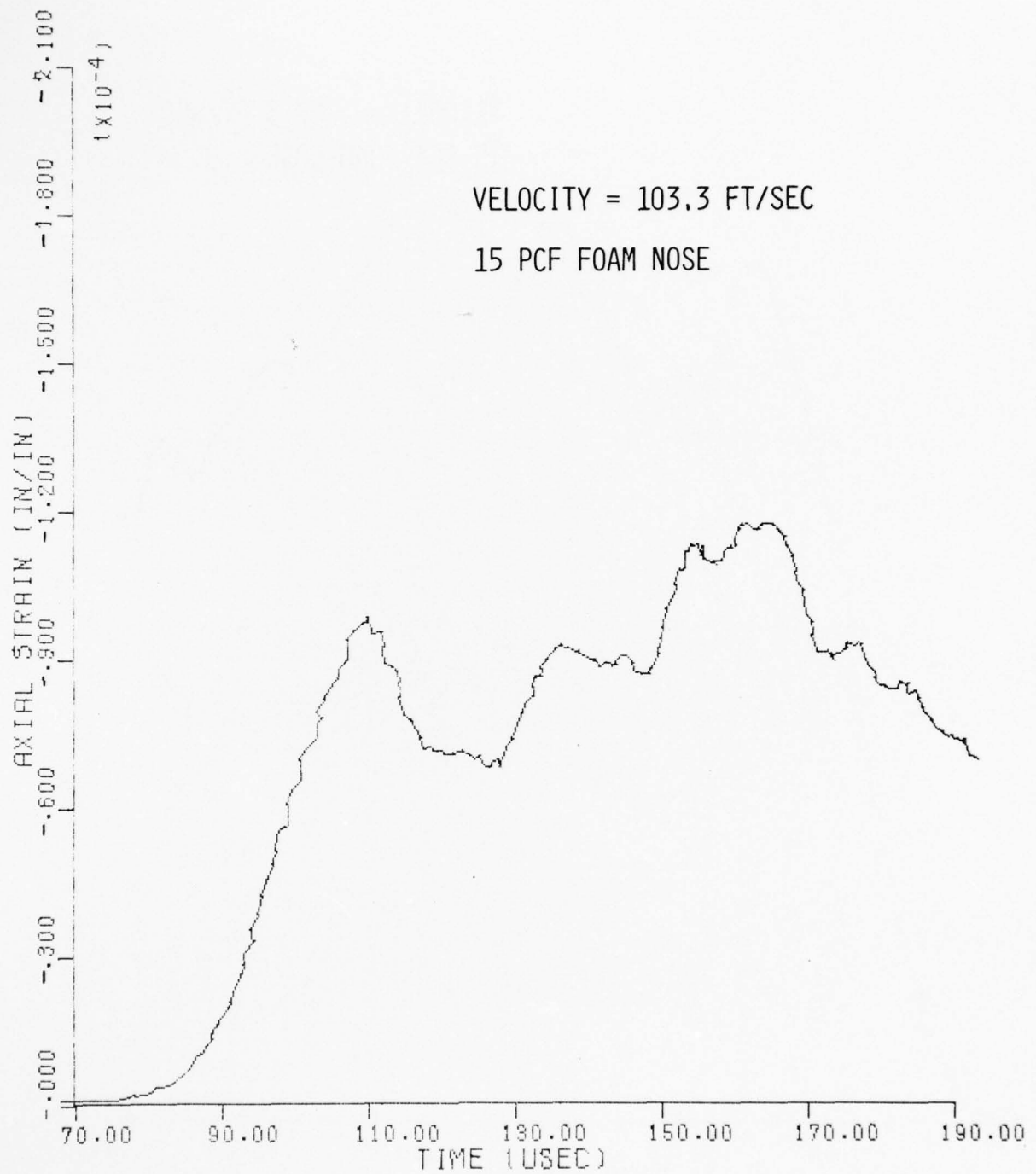


FIG. V.114 AXIAL STRAIN VERSUS TIME FOR GAGE NUMBER 4,
SHOT NUMBER 47

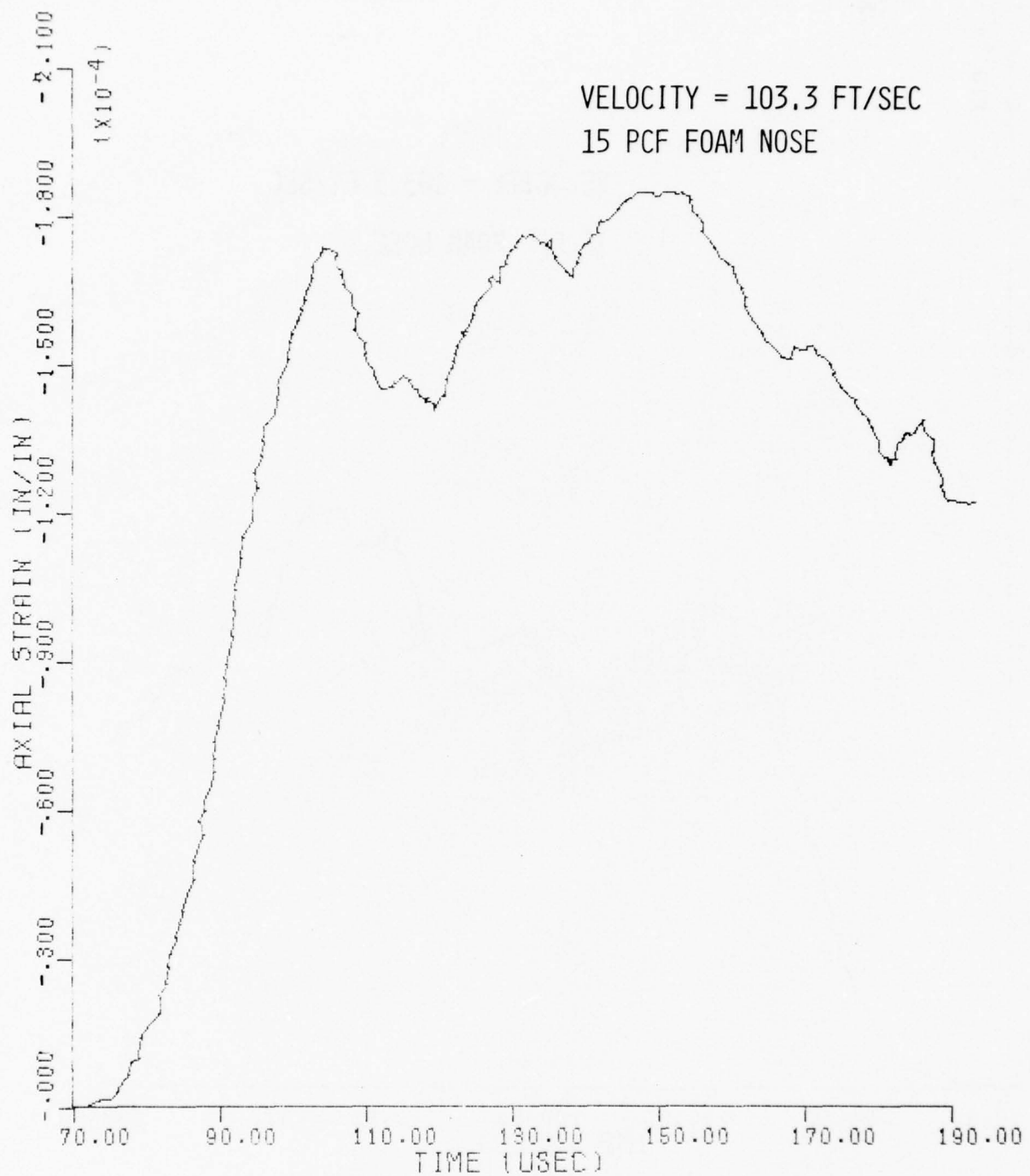


FIG. V.115 AXIAL STRAIN VERSUS TIME FOR GAGE NUMBER 5,
SHOT NUMBER 47

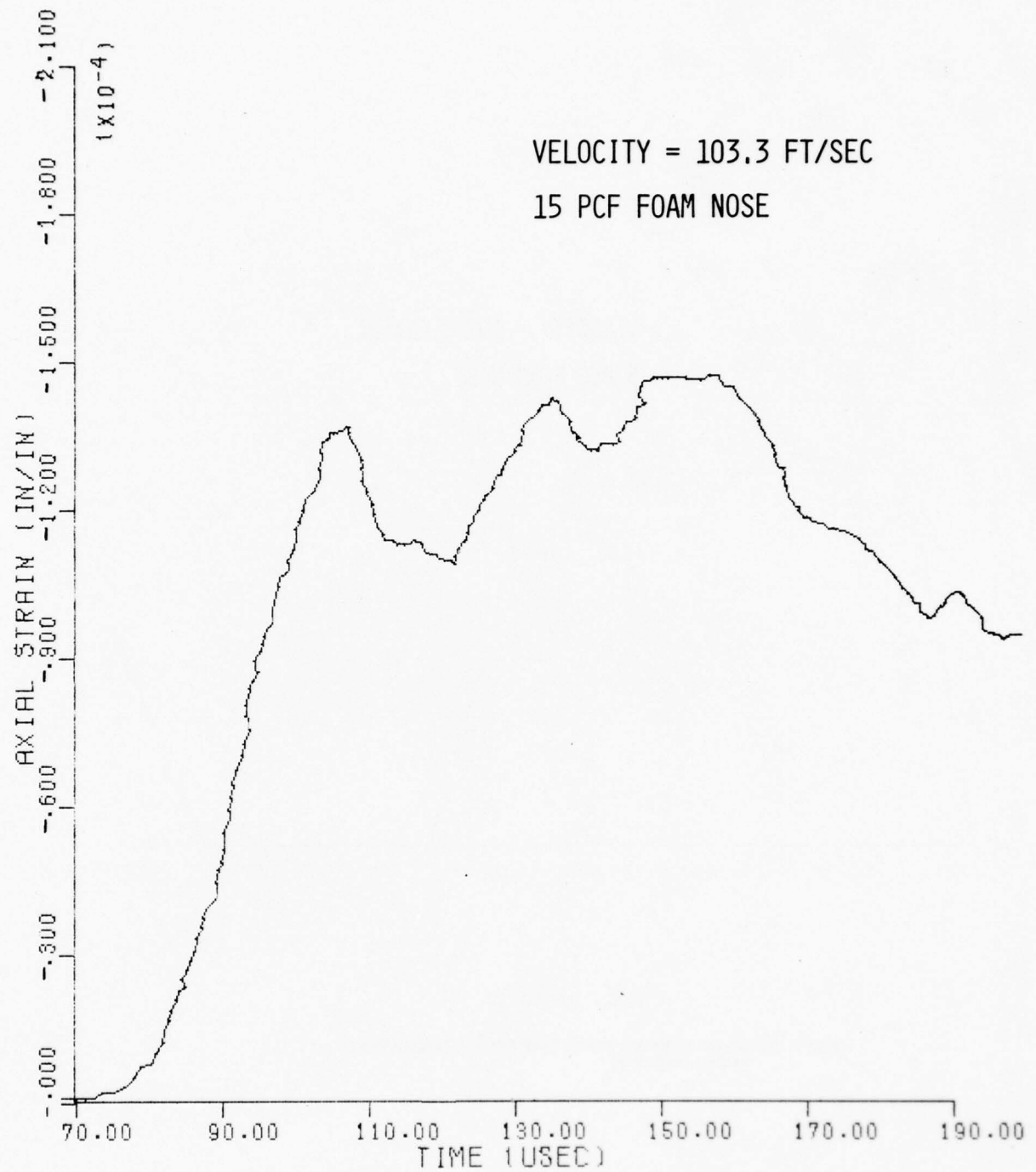


FIG. V.116 AXIAL STRAIN VERSUS TIME FOR GAGE NUMBER 6,
SHOT NUMBER 47

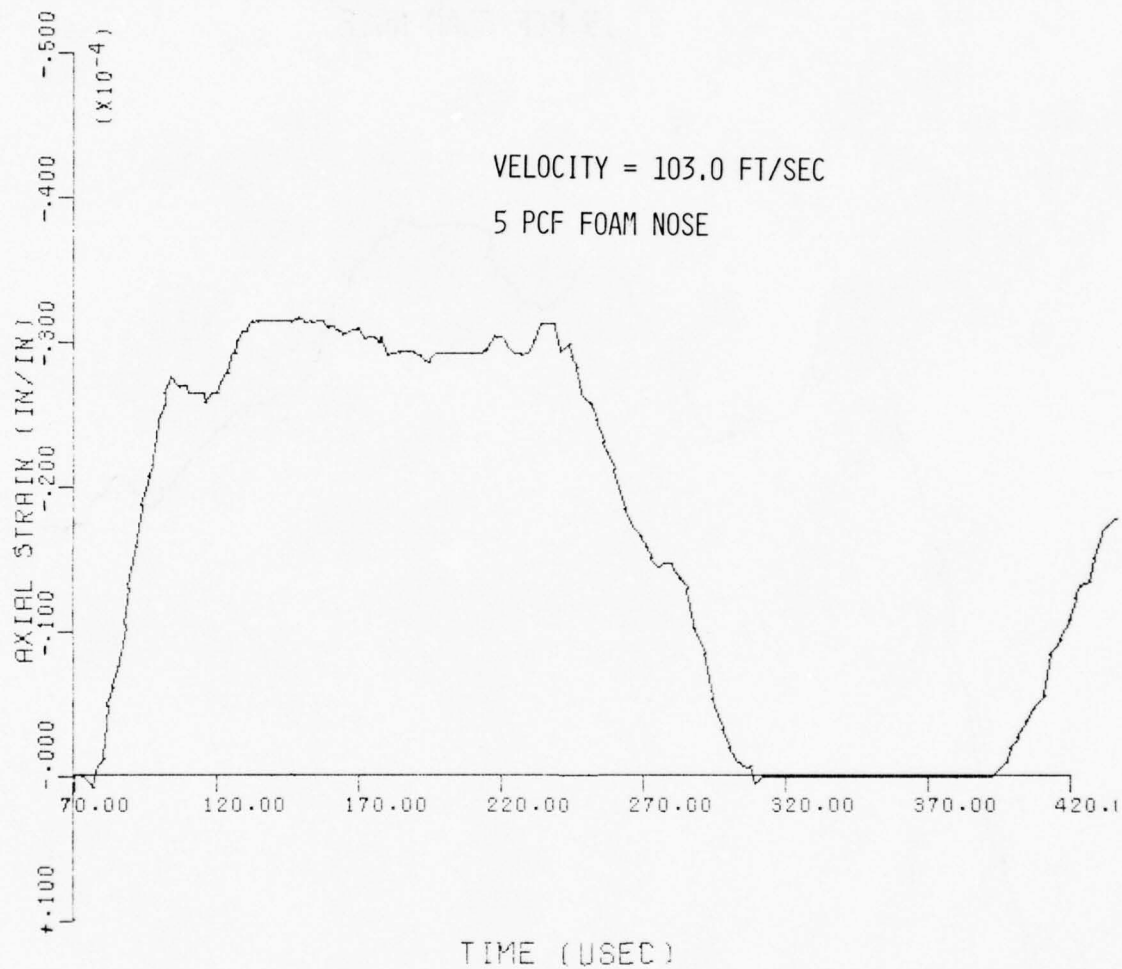


FIG. V.117 AXIAL STRAIN VERSUS TIME FOR GAGE NUMBER 5,
SHOT NUMBER 42

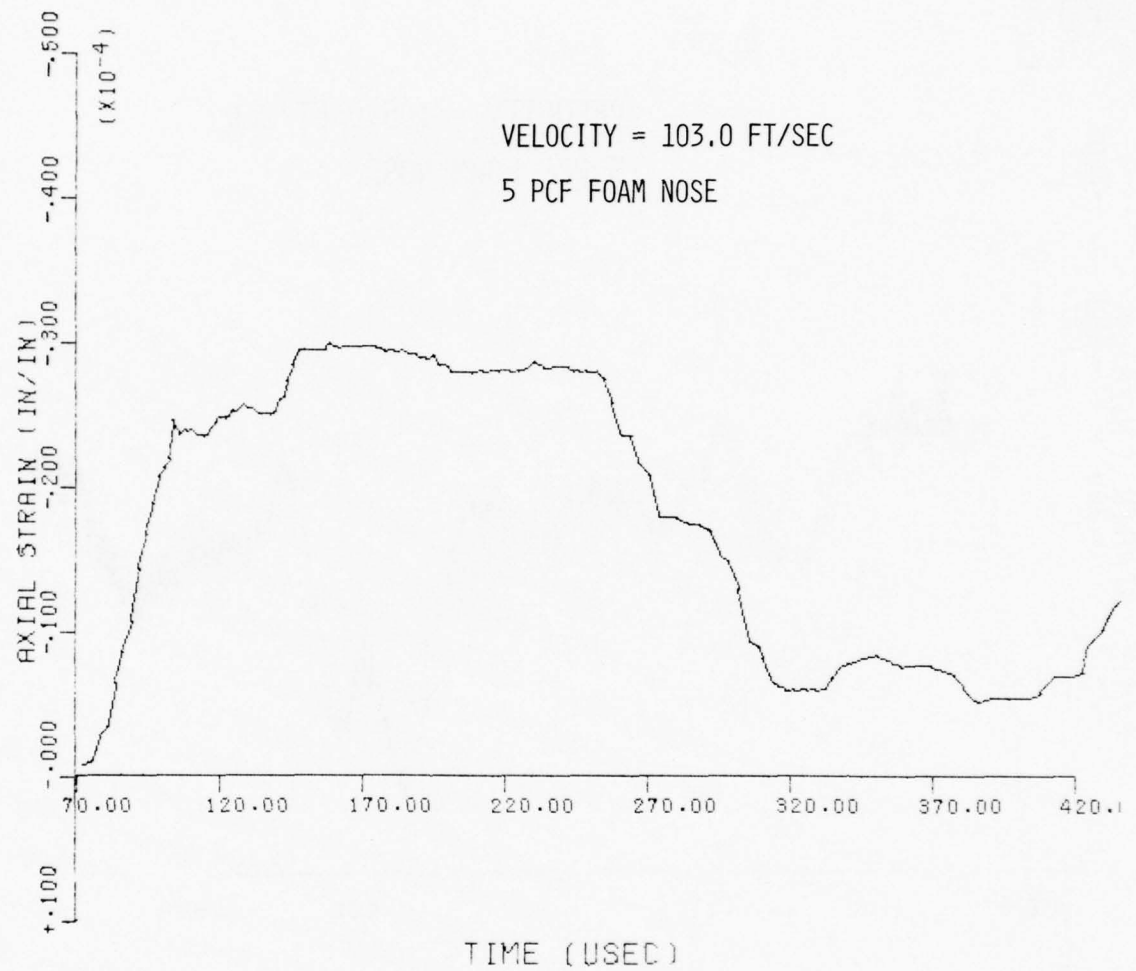


FIG. V.118 AXIAL STRAIN VERSUS TIME FOR GAGE NUMBER 6,
SHOT NUMBER 42

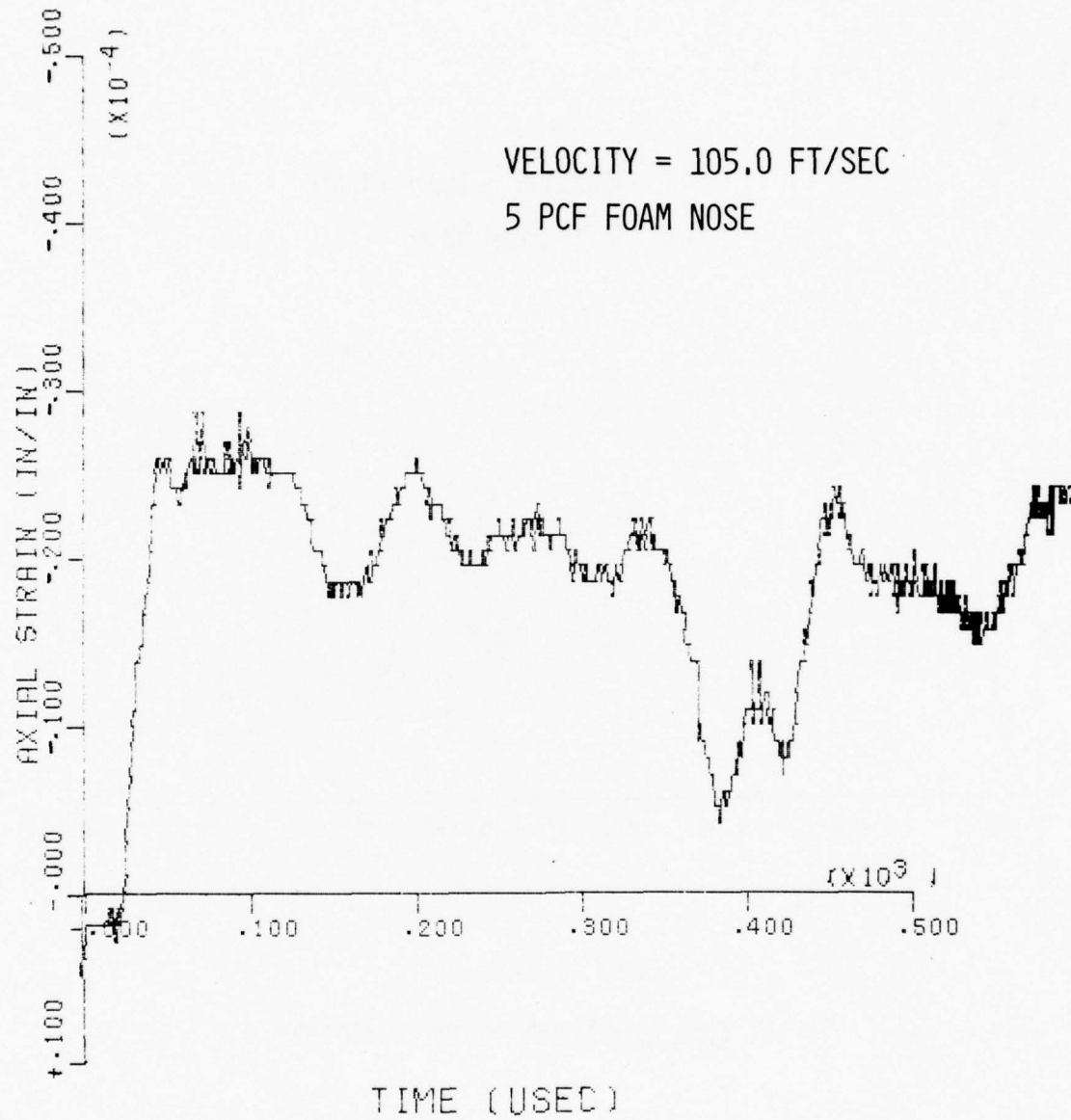


FIG. V.119 AXIAL STRAIN VERSUS TIME FOR GAGE NUMBER 1,
SHOT NUMBER 43

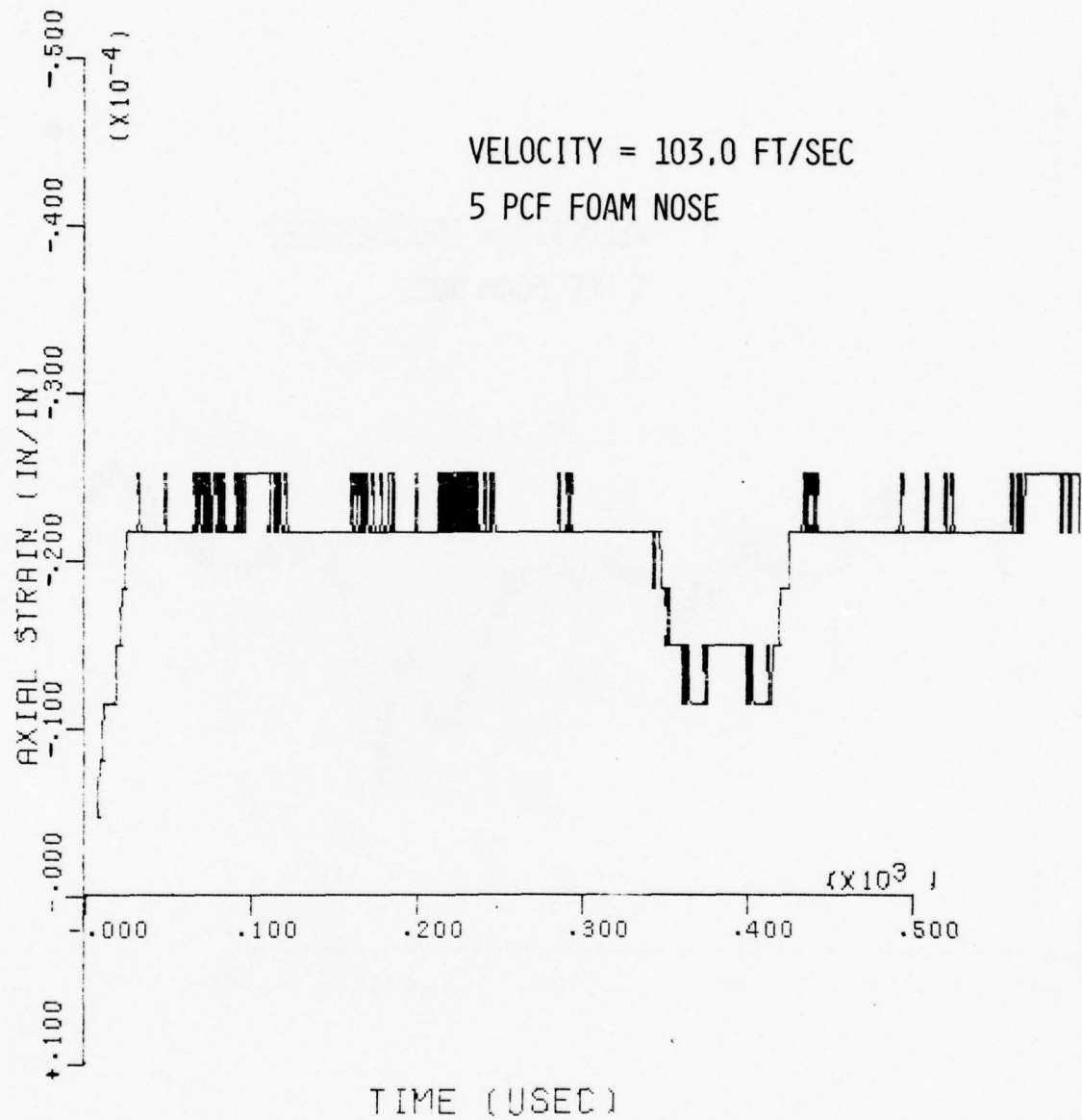


FIG. V.120 AXIAL STRAIN VERSUS TIME FOR GAGE NUMBER 2,
SHOT NUMBER 43

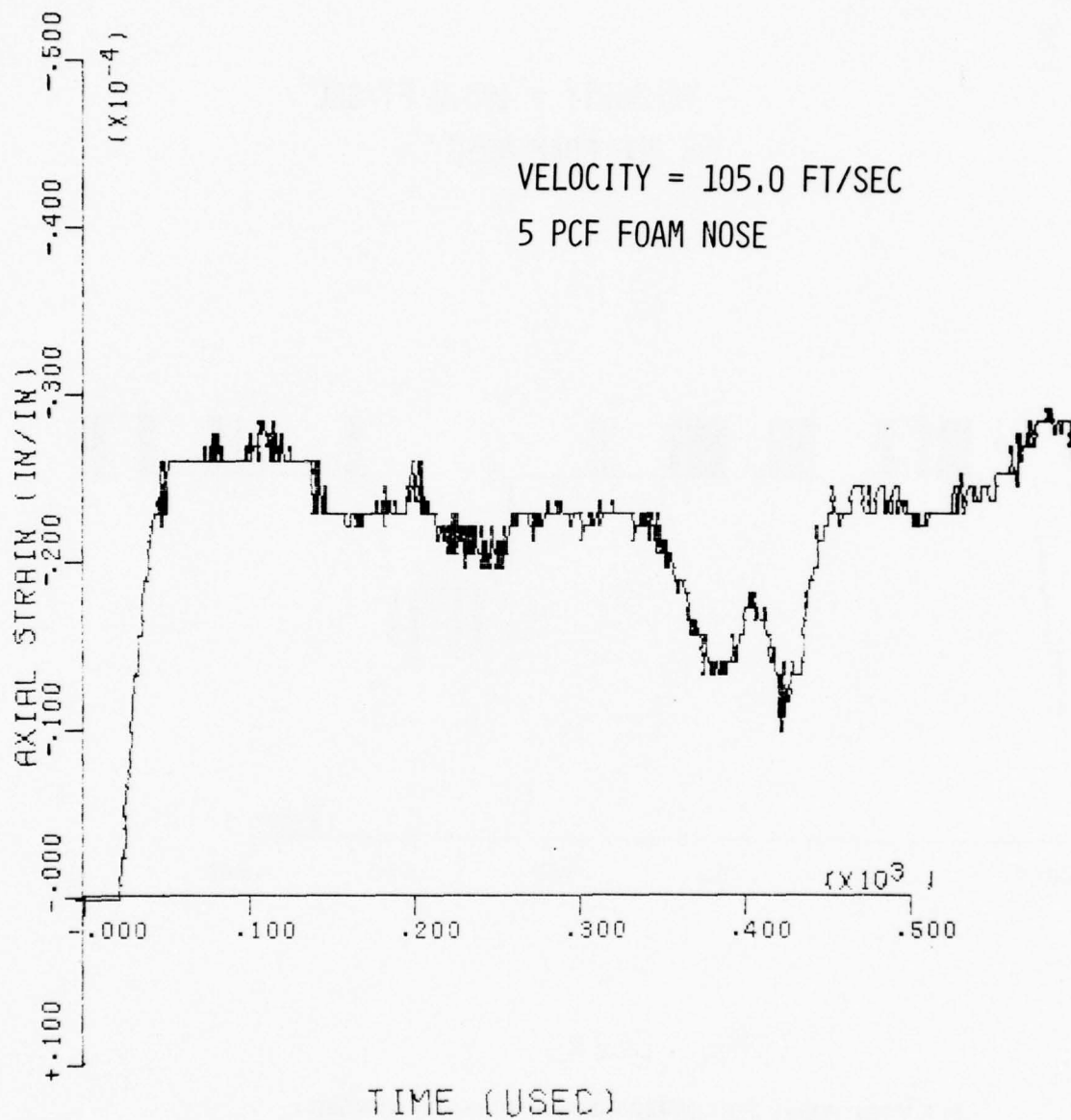


FIG. V.121 AXIAL STRAIN VERSUS TIME FOR GAGE NUMBER 3,
SHOT NUMBER 43

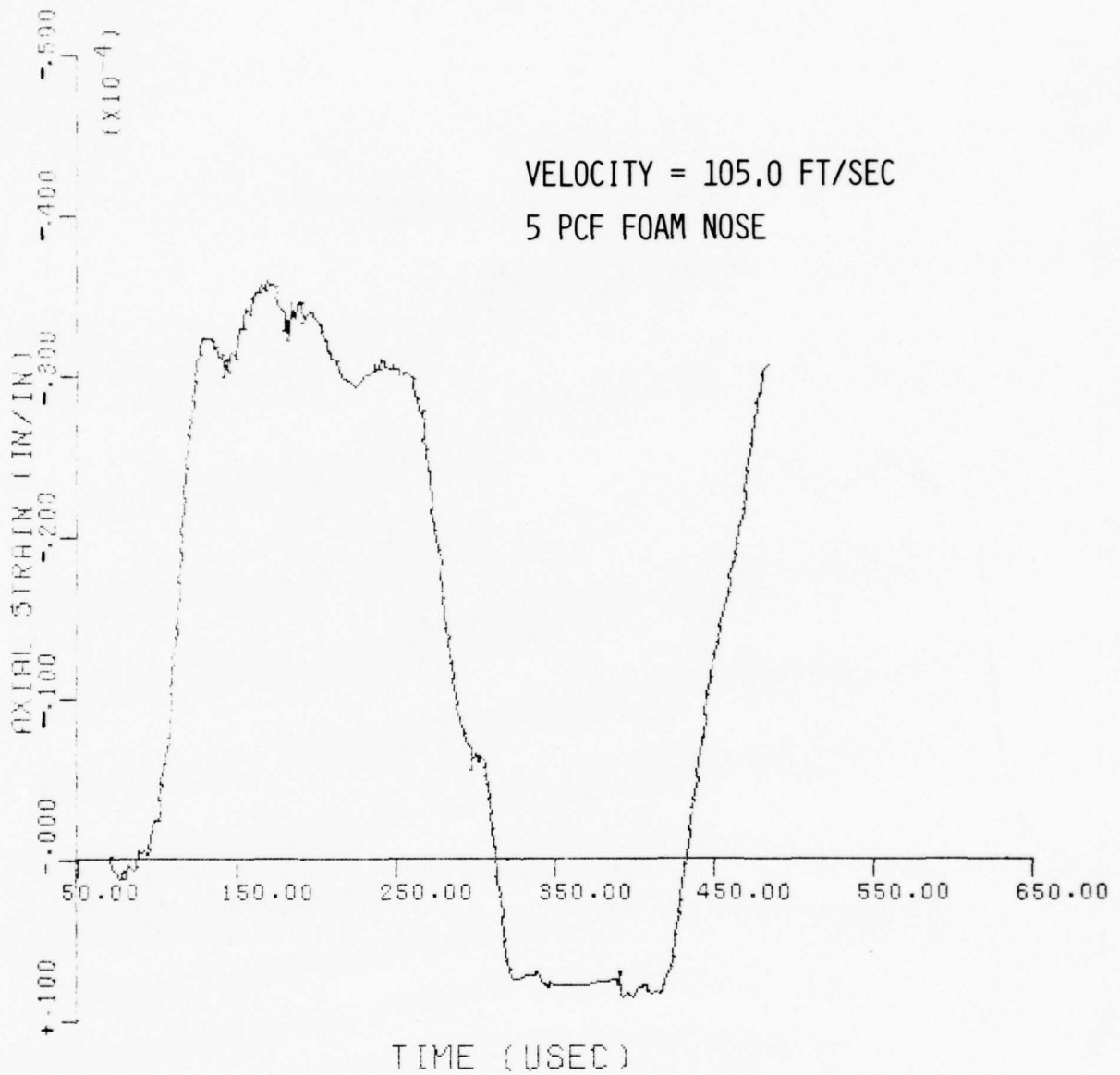


FIG. V.122 AXIAL STRAIN VERSUS TIME FOR GAGE NUMBER 5,
SHOT NUMBER 43

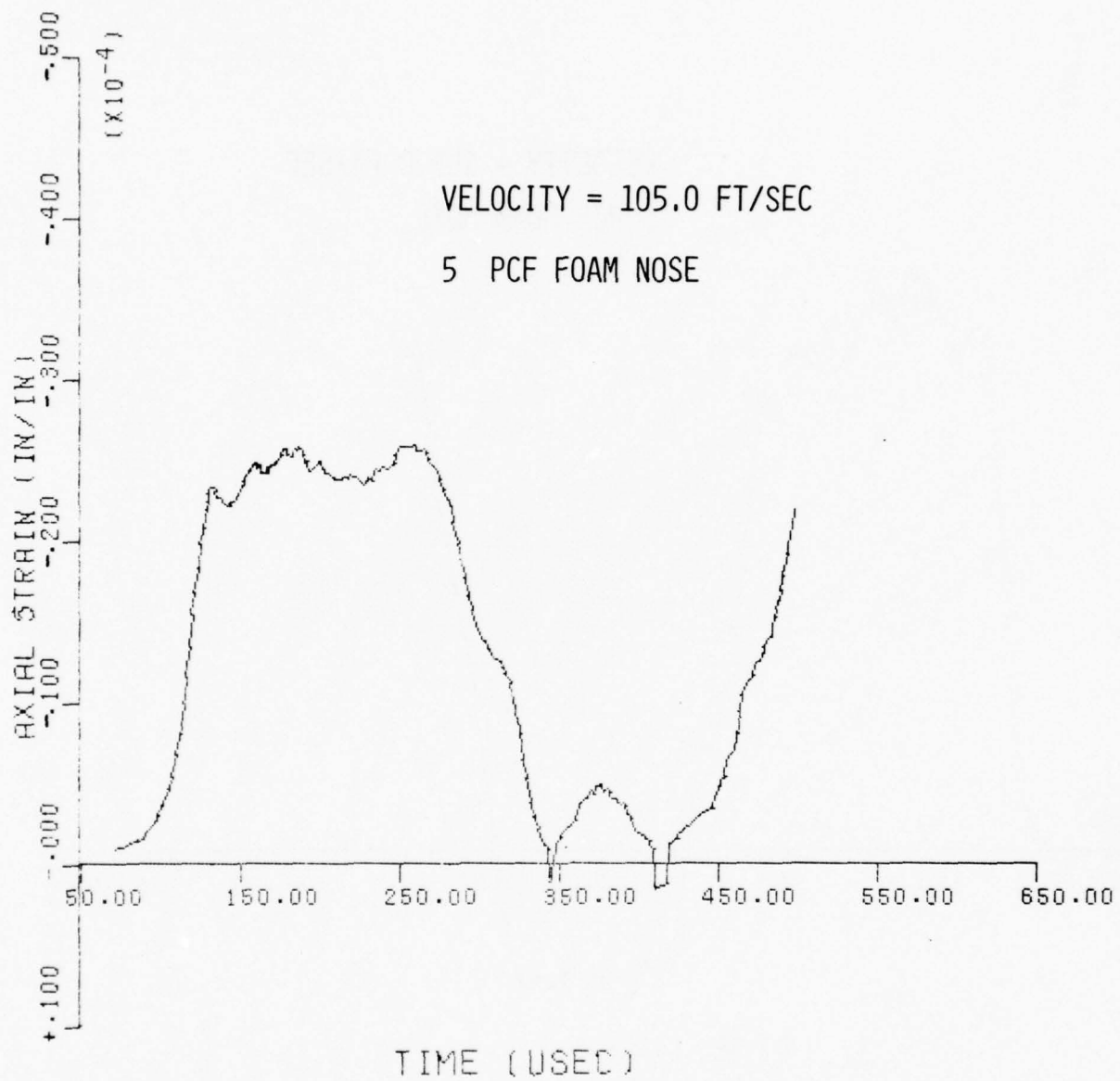


FIG. V.123 AXIAL STRAIN VERSUS TIME FOR GAGE NUMBER 6,
SHOT NUMBER 43

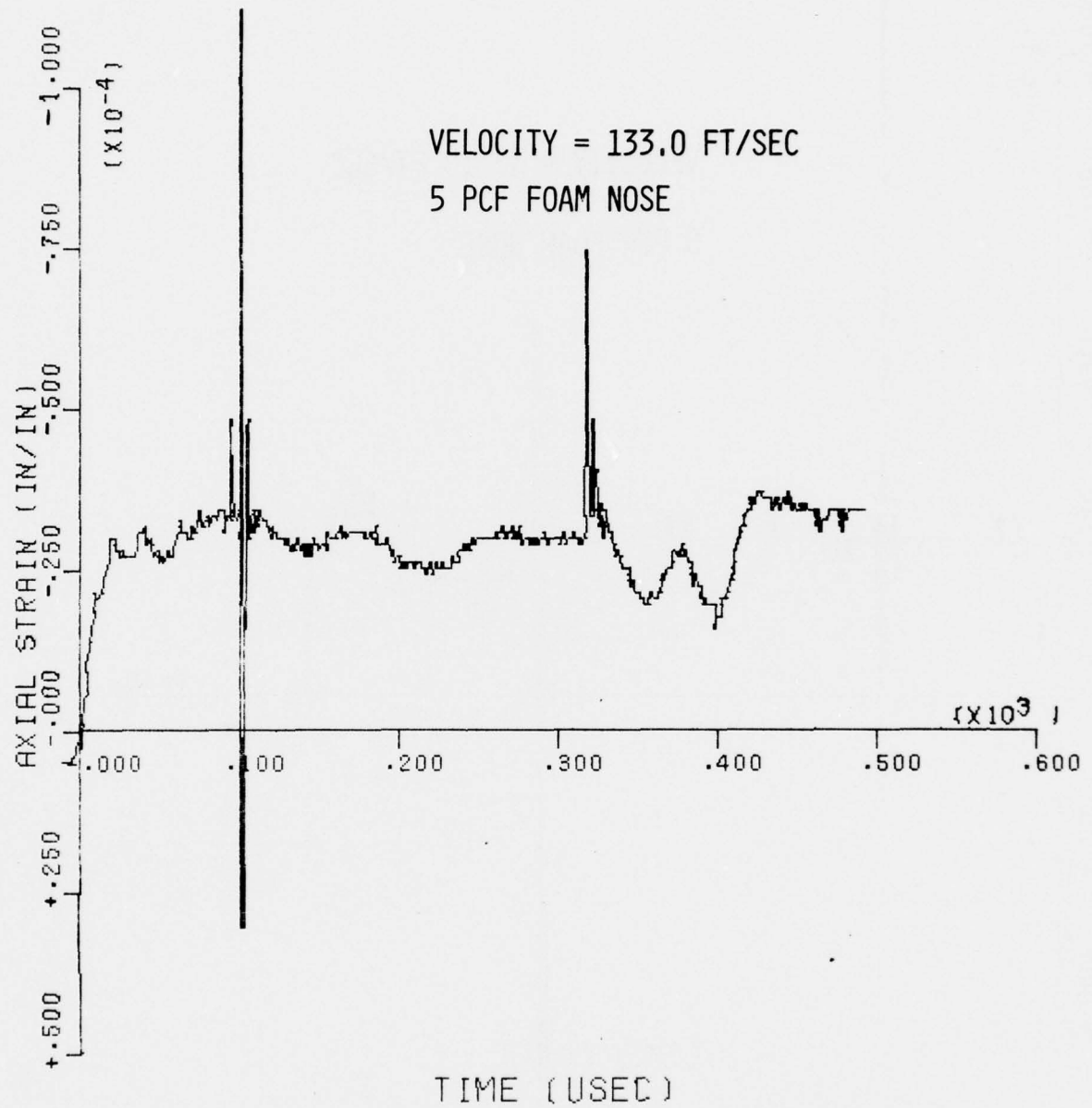


FIG. V.124 AXIAL STRAIN VERSUS TIME FOR GAGE NUMBER 1,
SHOT NUMBER 44

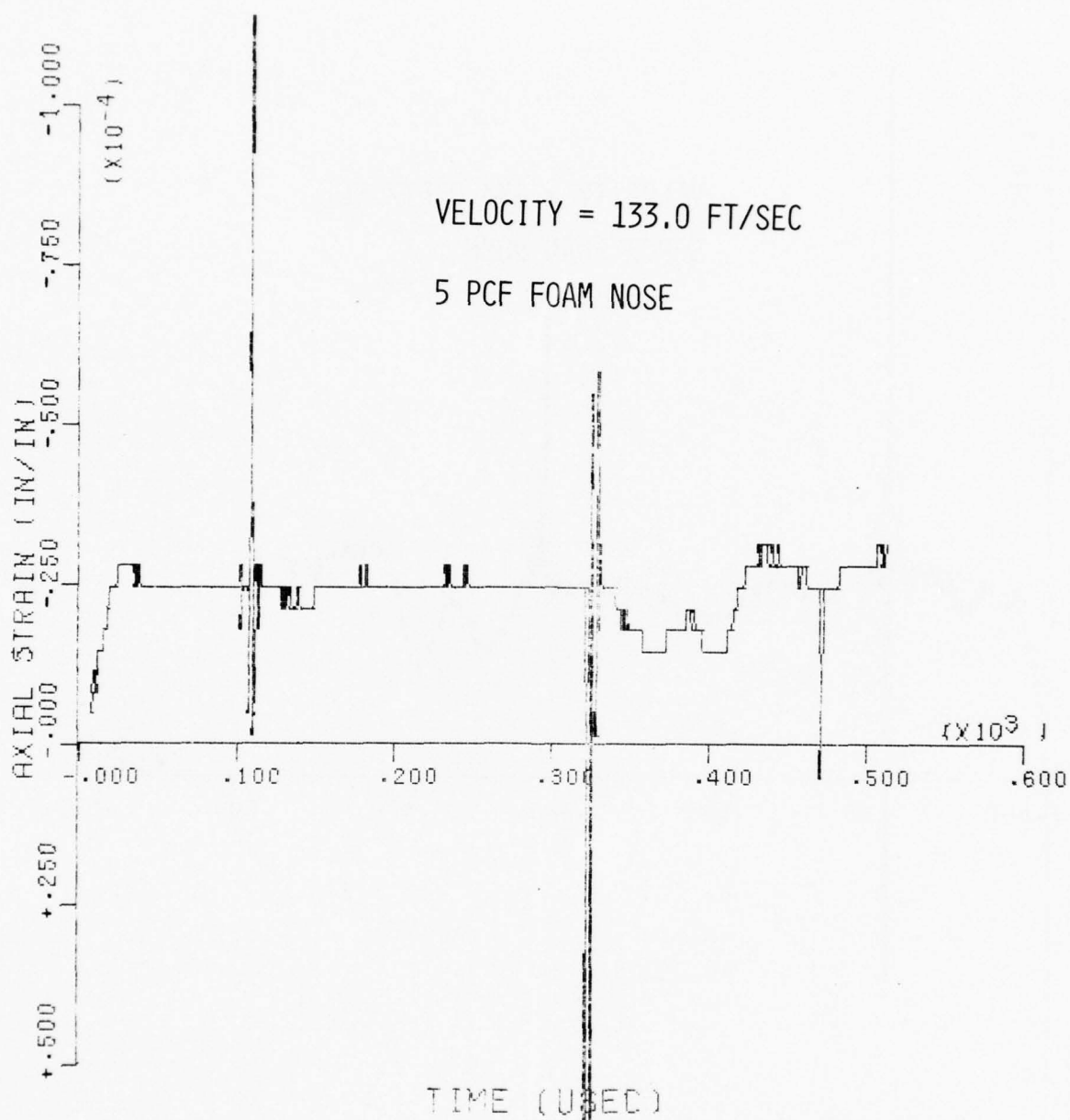


FIG. V.125 AXIAL STRAIN VERSUS TIME FOR GAGE NUMBER 2,
SHOT NUMBER 44

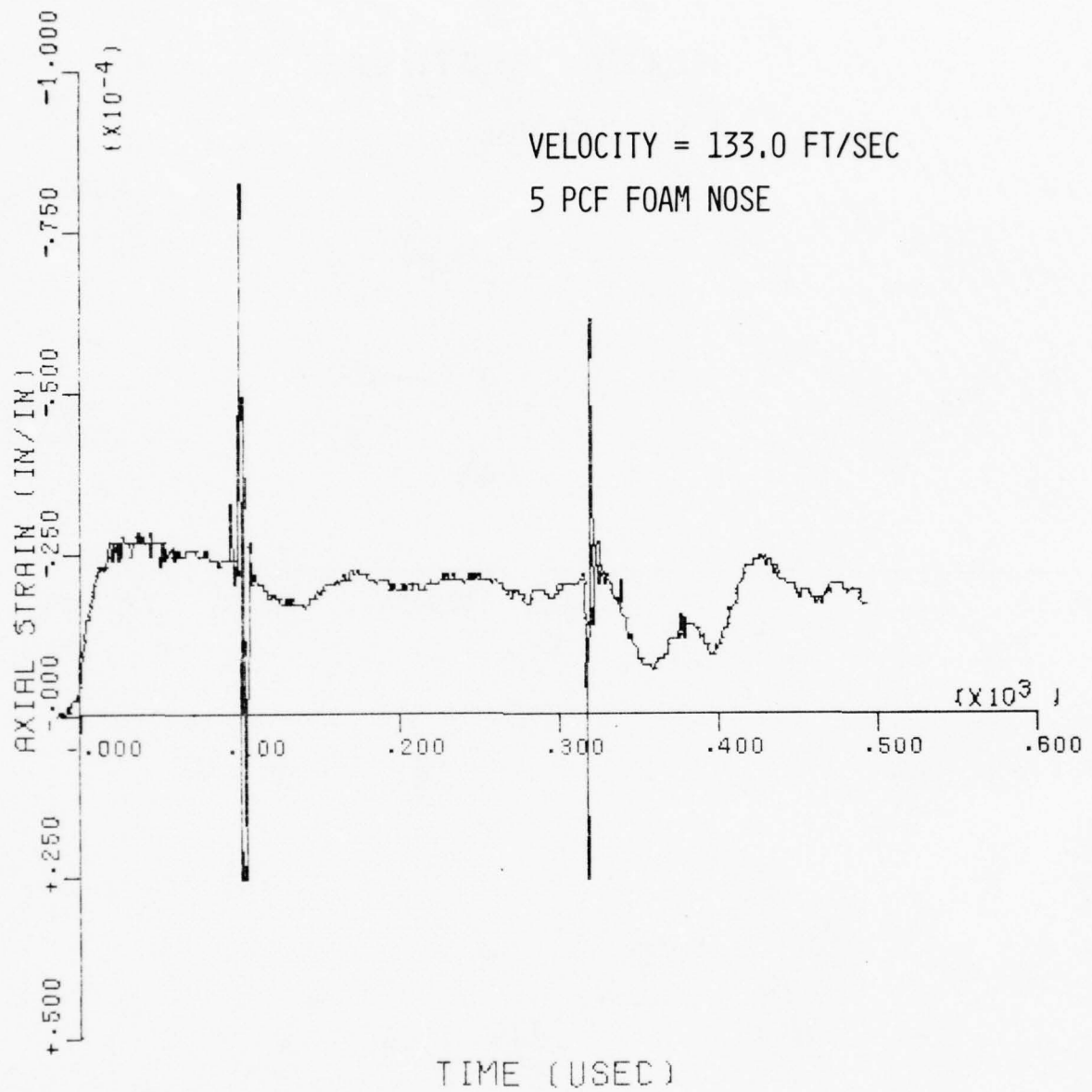


FIG. V.126 AXIAL STRAIN VERSUS TIME FOR GAGE NUMBER 3,
SHOT NUMBER 44

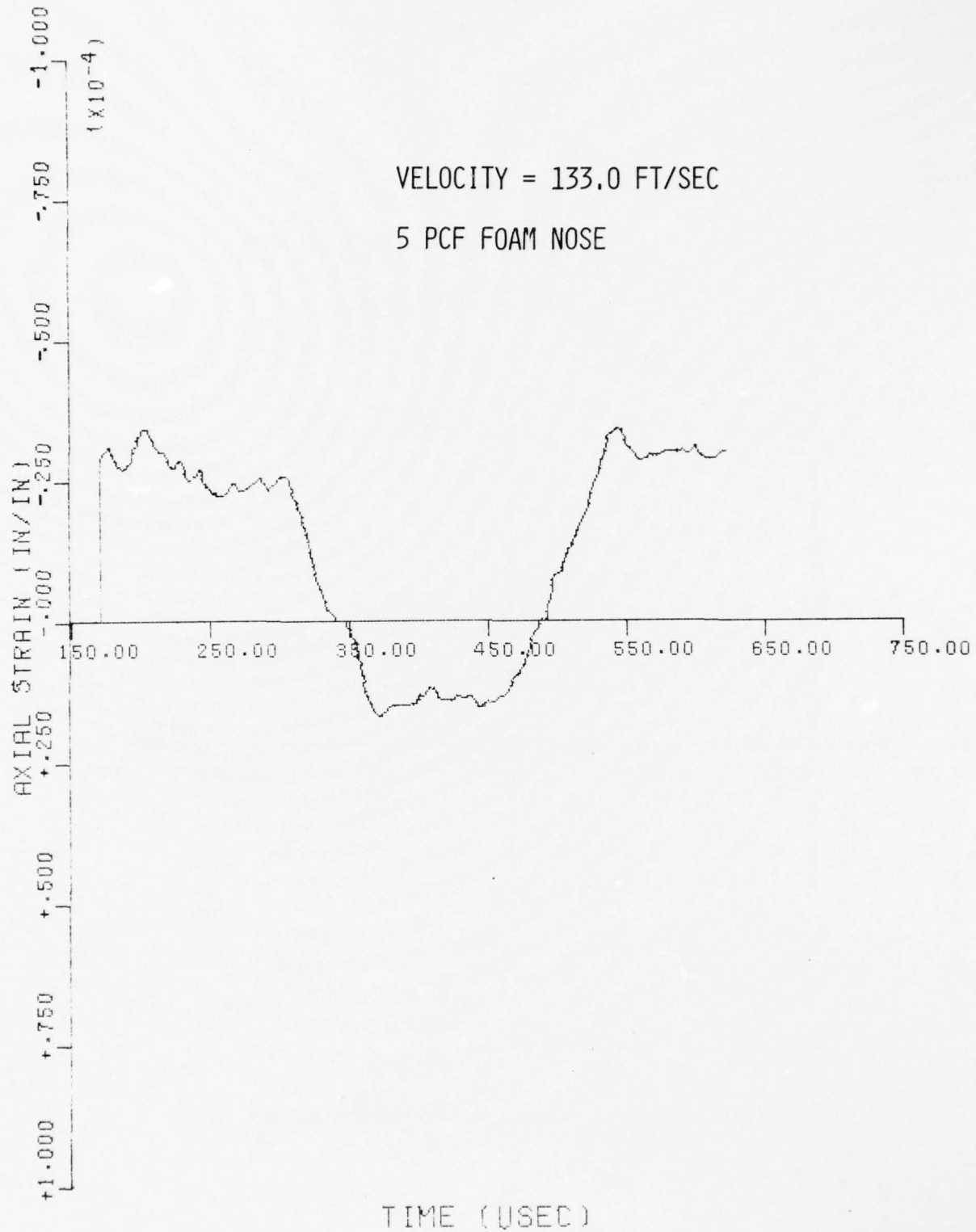


FIG. V.127 AXIAL STRAIN VERSUS TIME FOR GAGE NUMBER 5,
SHOT NUMBER 44

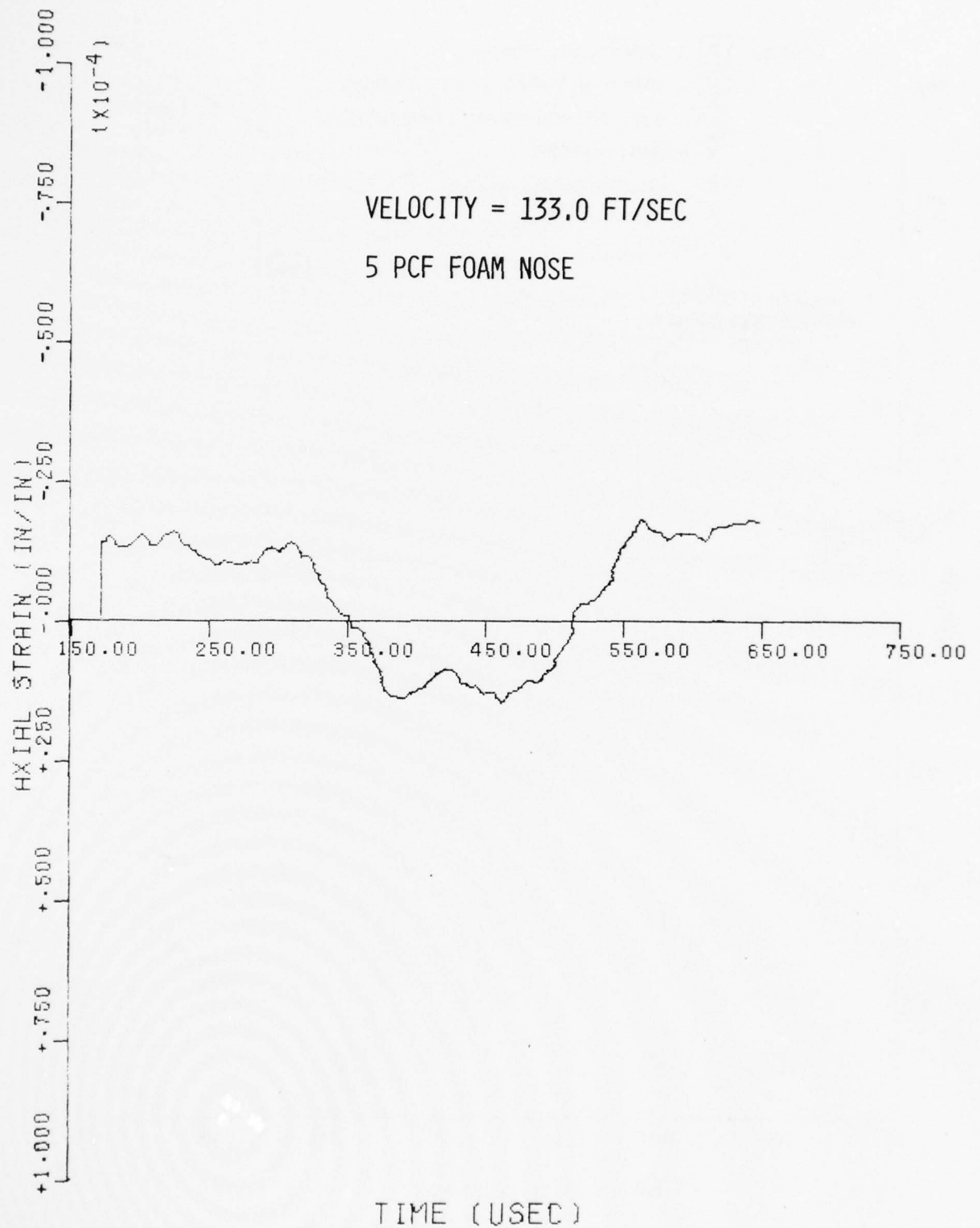


FIG. V.128 AXIAL STRAIN VERSUS TIME FOR GAGE NUMBER 6,
SHOT NUMBER 44

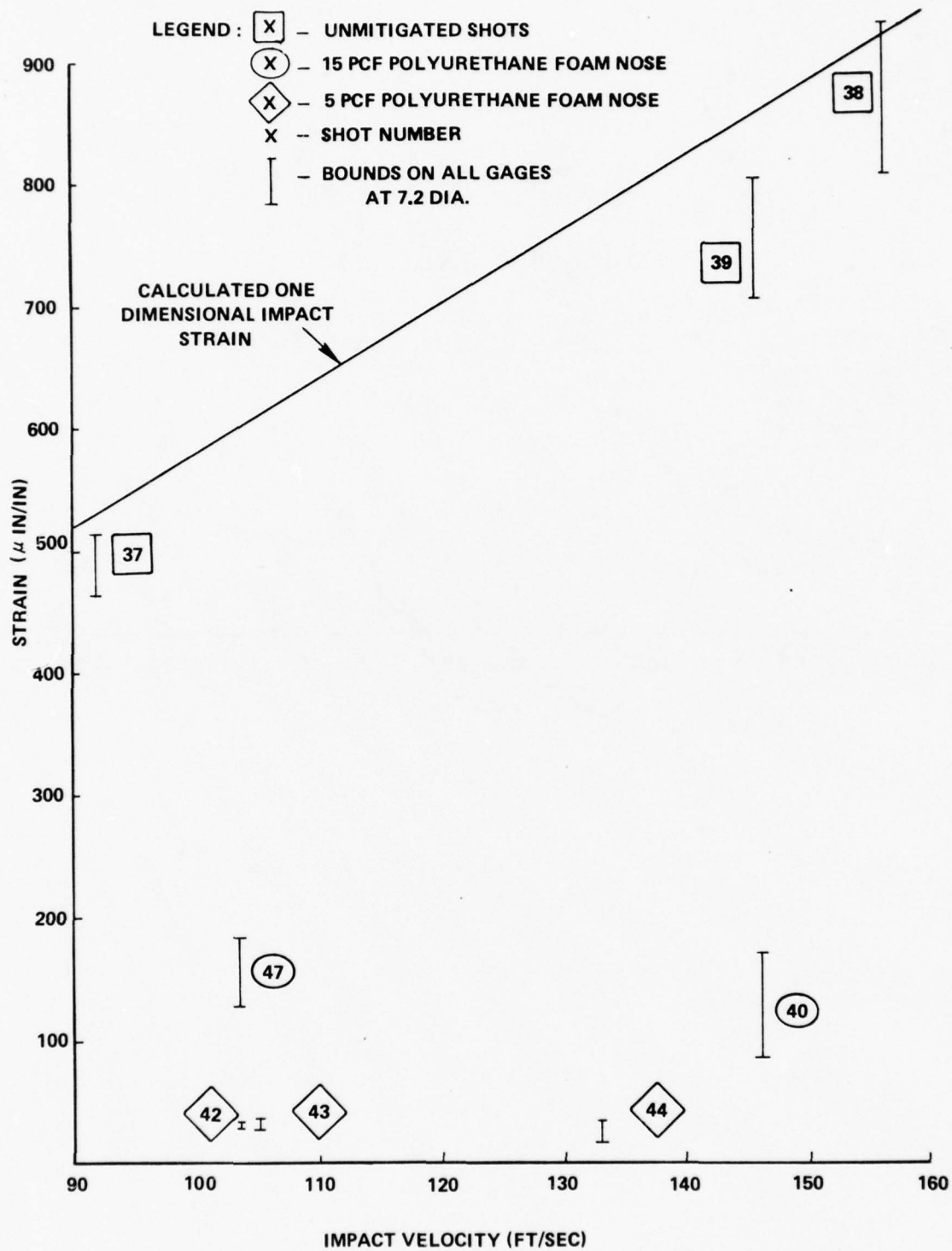


FIG. V. 129 EXPERIMENTAL MAXIMUM AXIAL STRAIN VALUES AT 7.2 DIAMETERS FROM FRONT FACE OF BAR

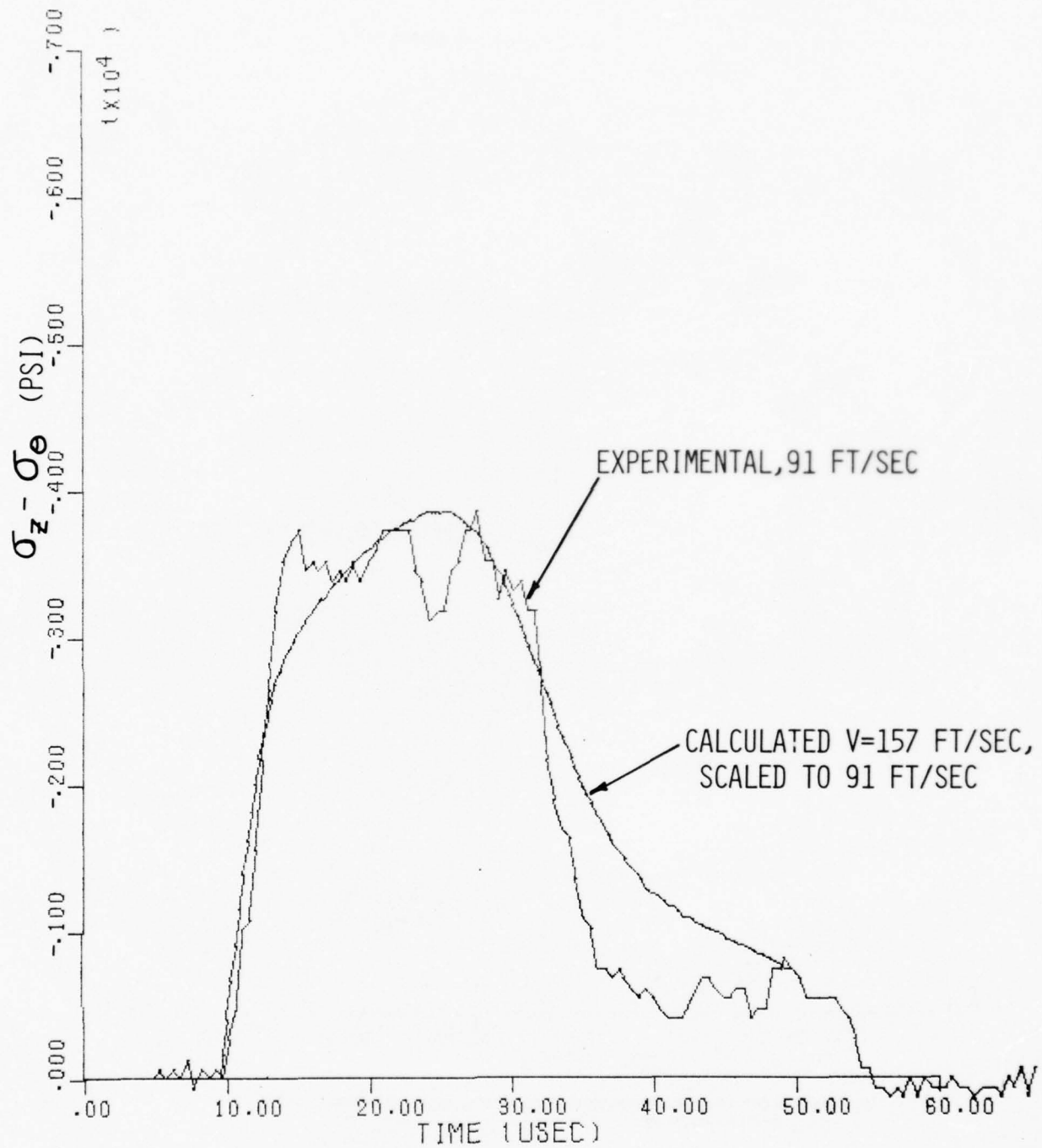


FIG. V.130 COMPARISON OF EXPERIMENTAL AND ANALYTICAL RESULTS FOR SHOT NUMBER 31

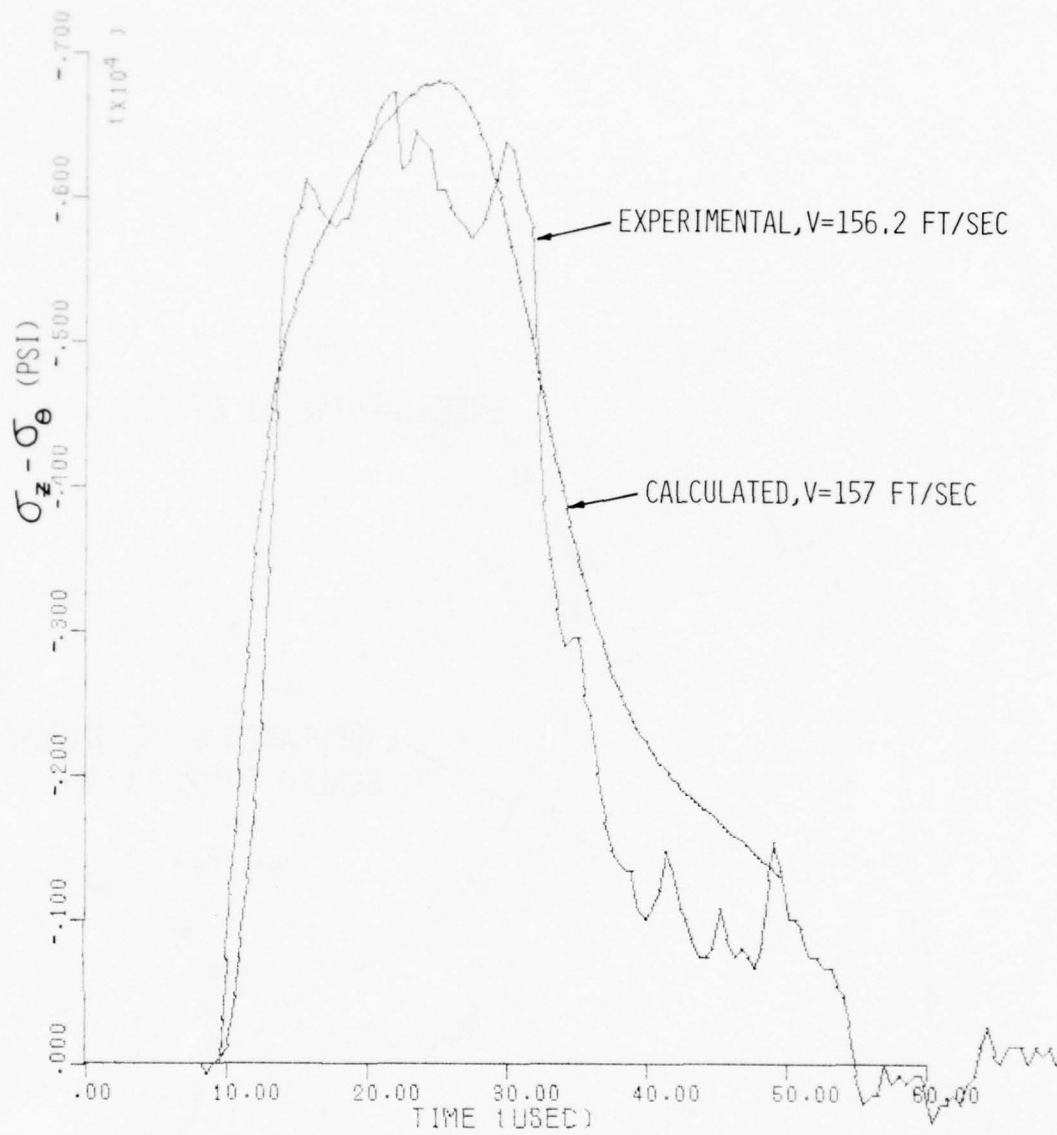


FIG. V.131 COMPARISON OF EXPERIMENTAL AND ANALYTICAL RESULTS FOR SHOT NUMBER 32

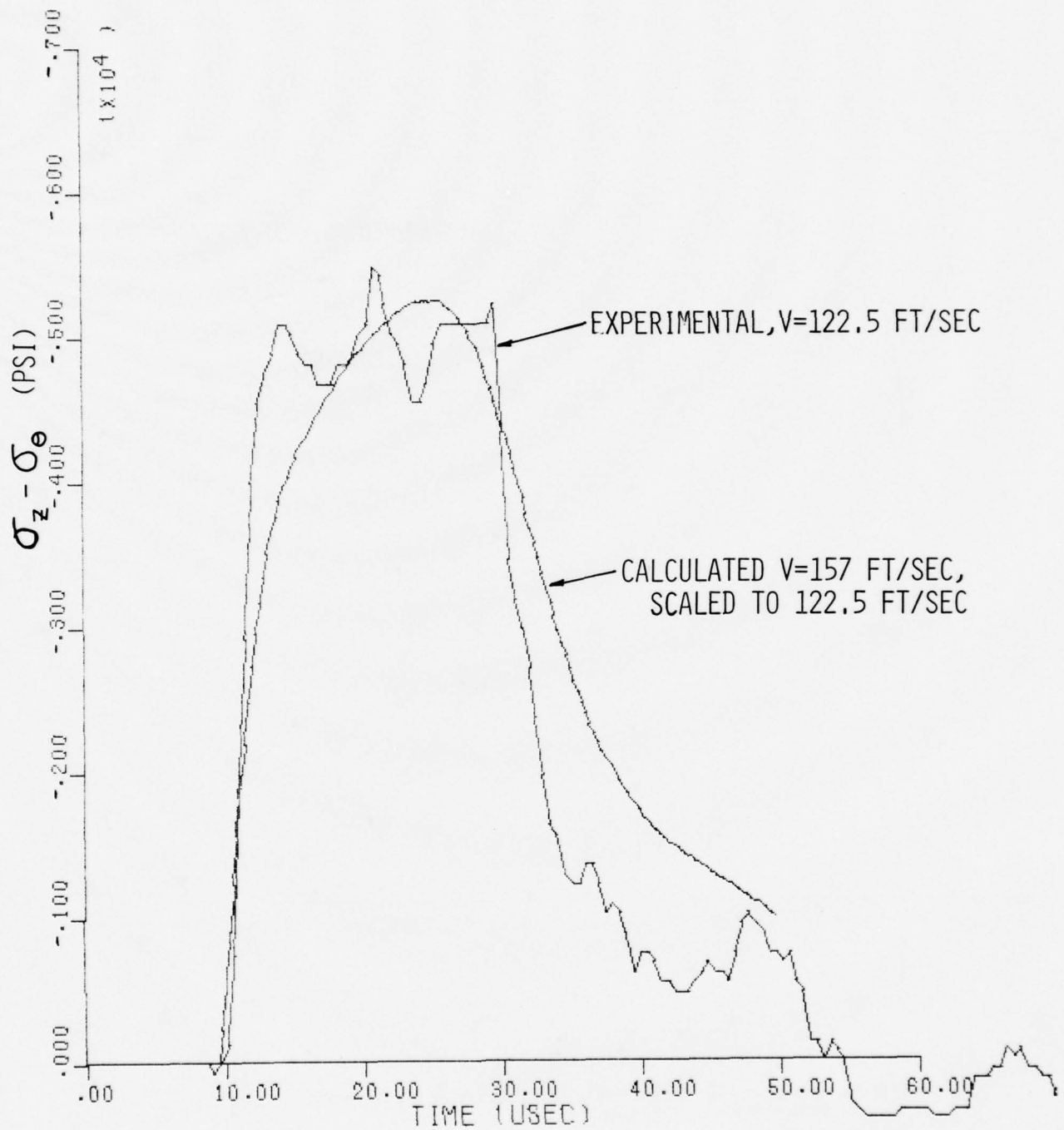


FIG. V.132 COMPARISON OF EXPERIMENTAL AND ANALYTICAL RESULTS FOR SHOT NUMBER 33

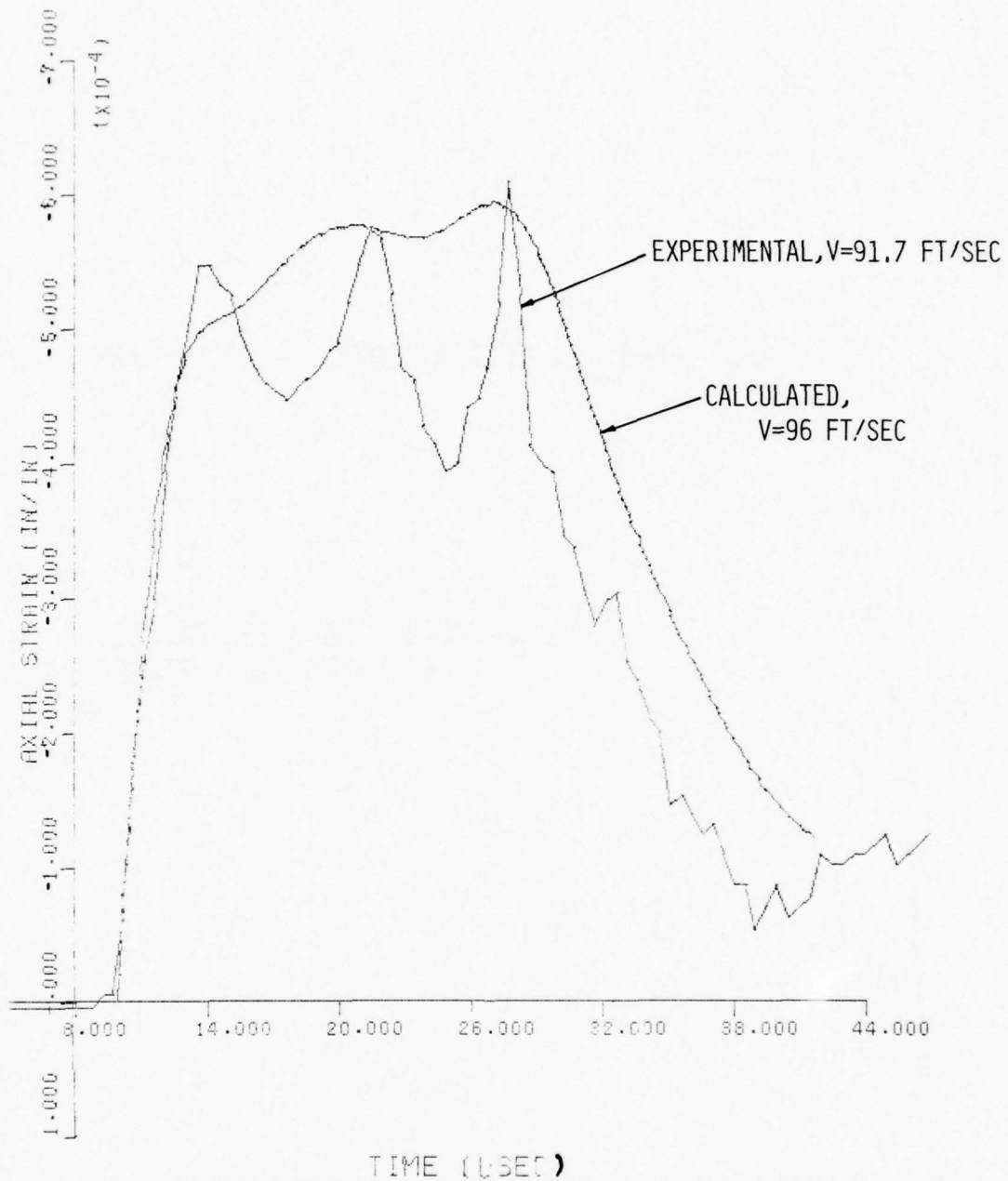


FIG. V.133 COMPARISON OF EXPERIMENTAL AND ANALYTICAL RESULTS FOR GAGE NUMBER 1, SHOT NUMBER 37

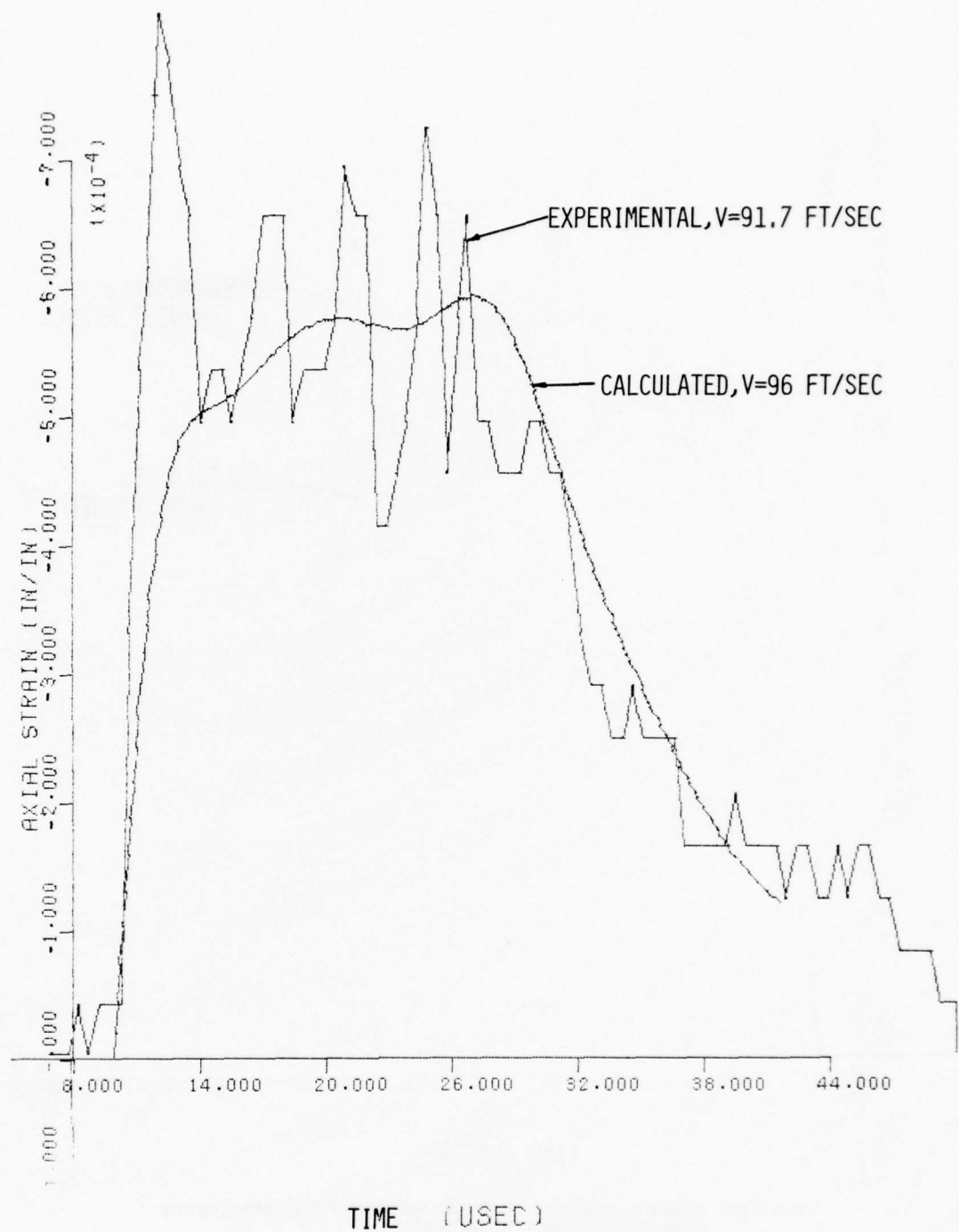


FIG. V.134 COMPARISON OF EXPERIMENTAL AND ANALYTICAL RESULTS FOR GAGE NUMBER 2, SHOT NUMBER 37

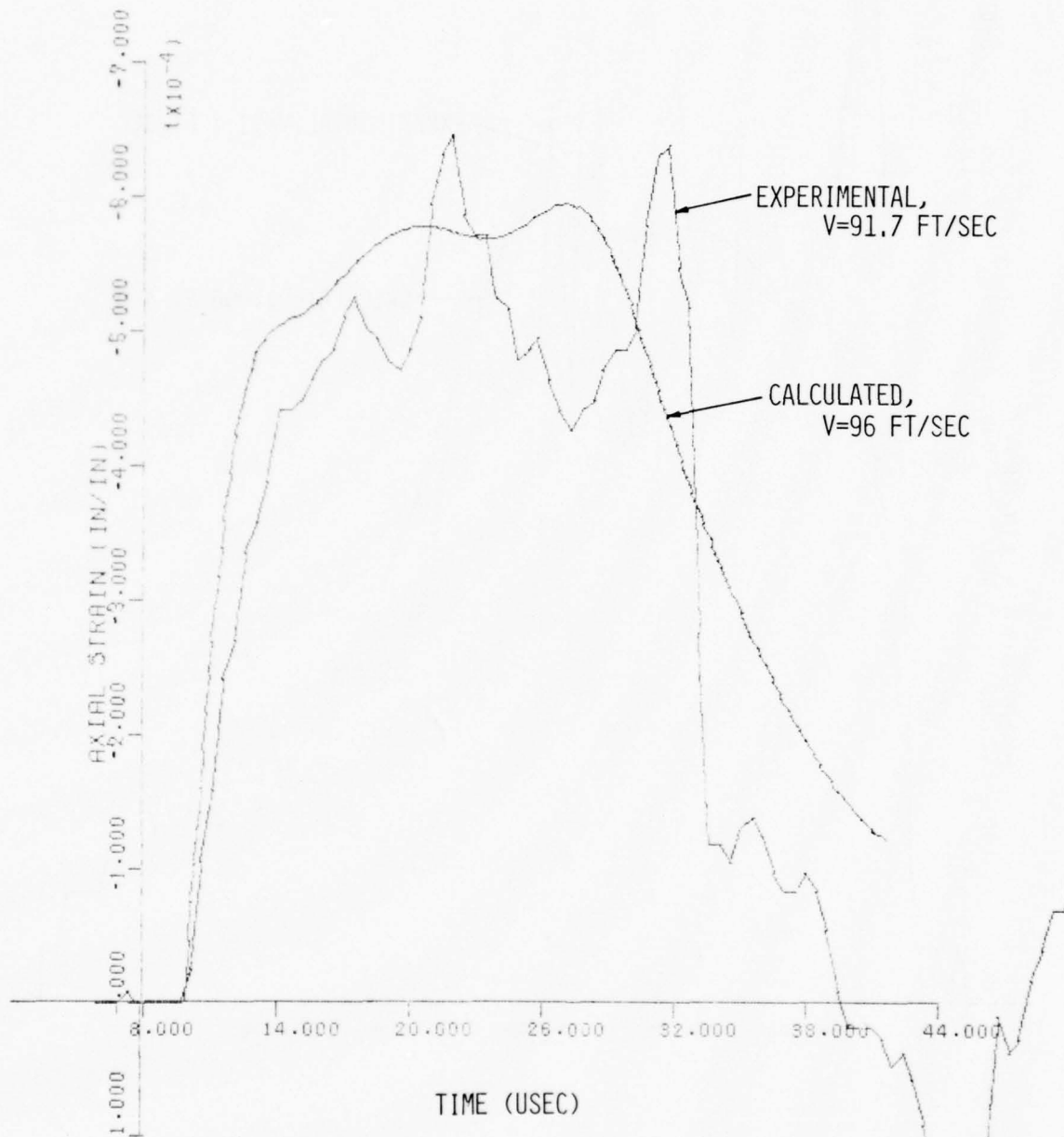


FIG. V.135 COMPARISON OF EXPERIMENTAL AND ANALYTICAL RESULTS FOR GAGE NUMBER 3, SHOT NUMBER 37

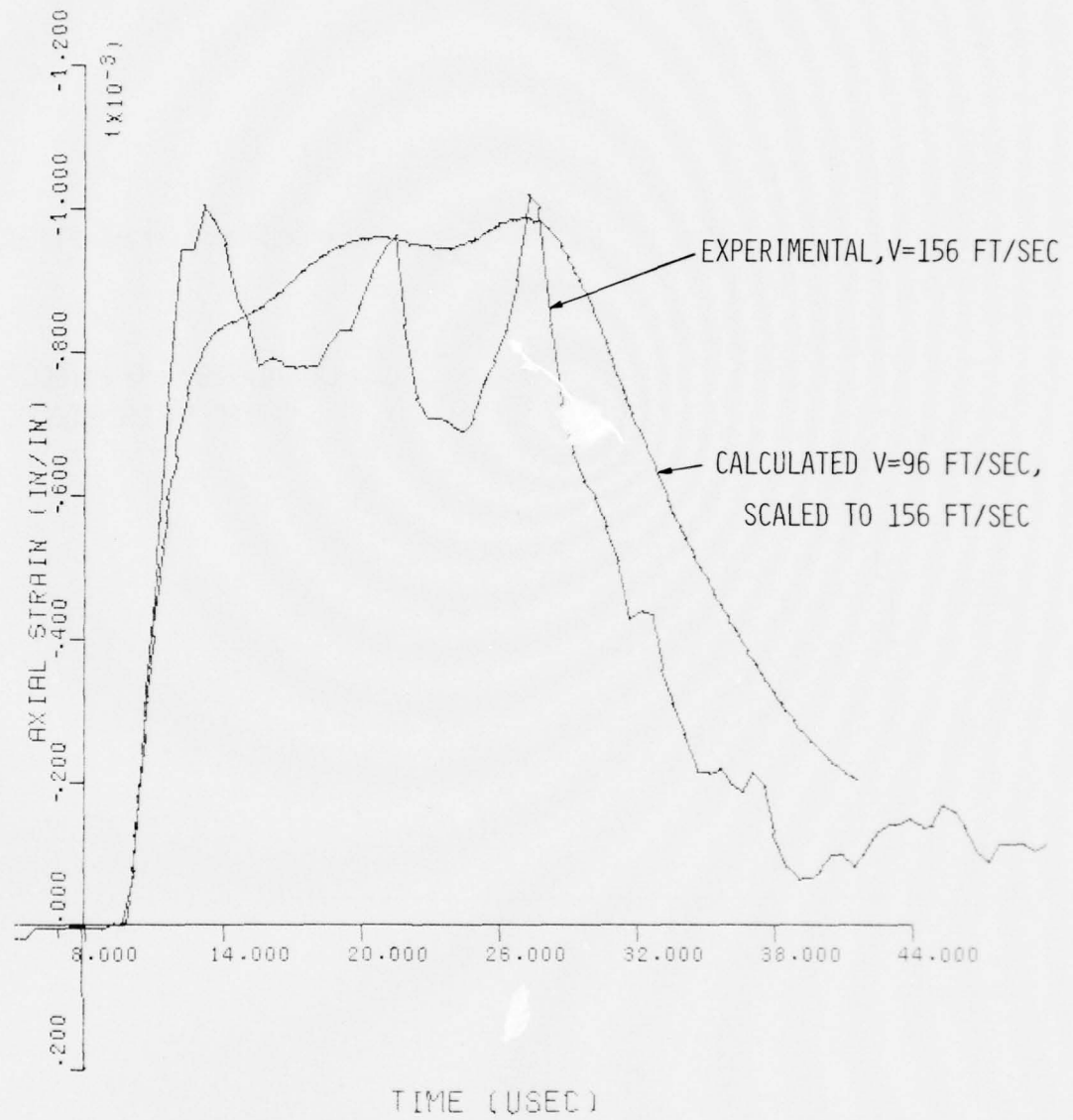


FIG. V.136 COMPARISON OF EXPERIMENTAL AND ANALYTICAL RESULTS FOR GAGE NUMBER 1, SHOT NUMBER 38

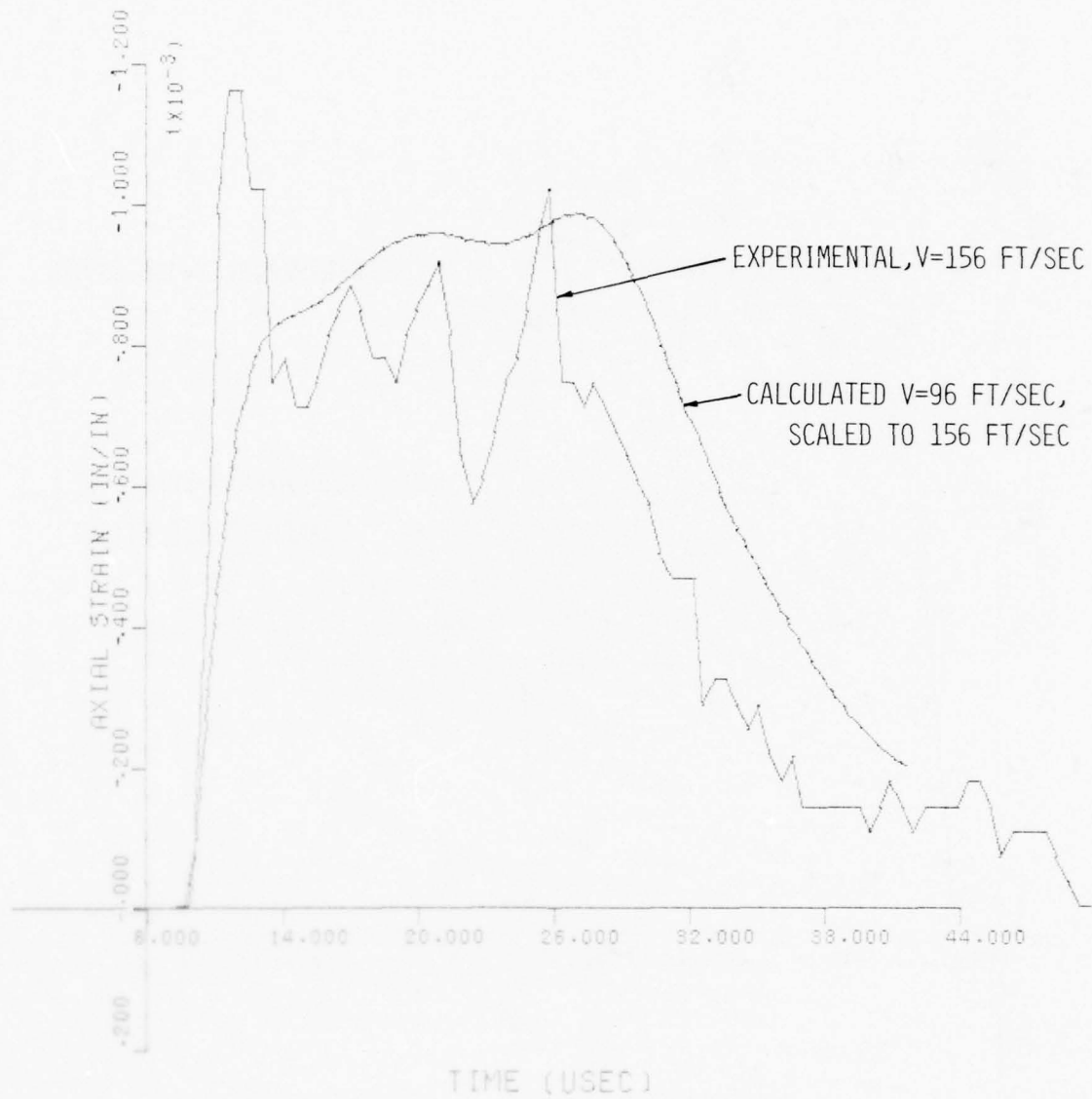


FIG. V.137 COMPARISON OF EXPERIMENTAL AND ANALYTICAL RESULTS FOR GAGE NUMBER 2, SHOT NUMBER 38

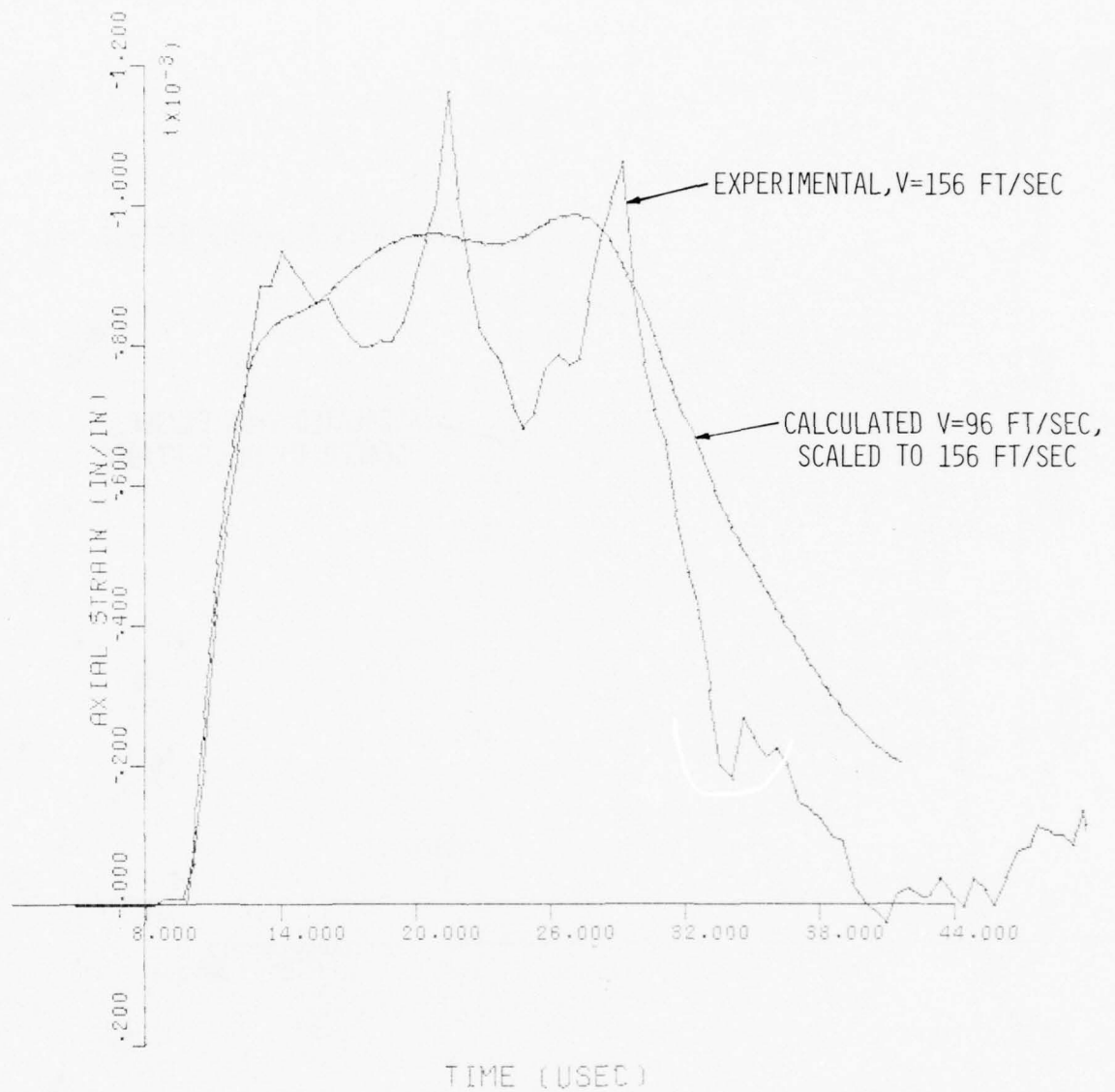


FIG. V.138 COMPARISON OF EXPERIMENTAL AND ANALYTICAL RESULTS FOR GAGE NUMBER 3, SHOT NUMBER 38

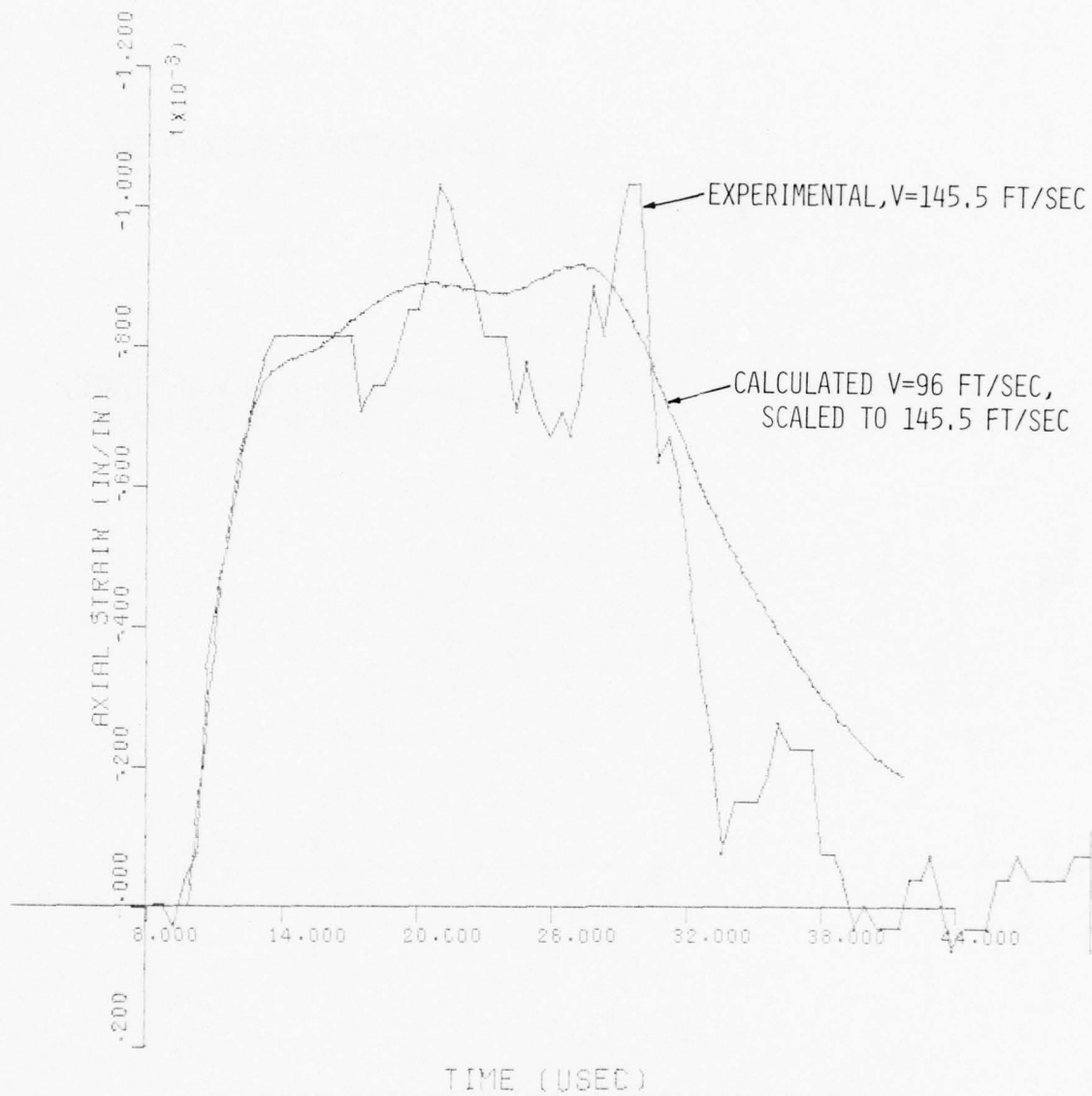


FIG. V.139 COMPARISON OF EXPERIMENTAL AND ANALYTICAL RESULTS FOR
GAGE NUMBER 2, SHOT NUMBER 39

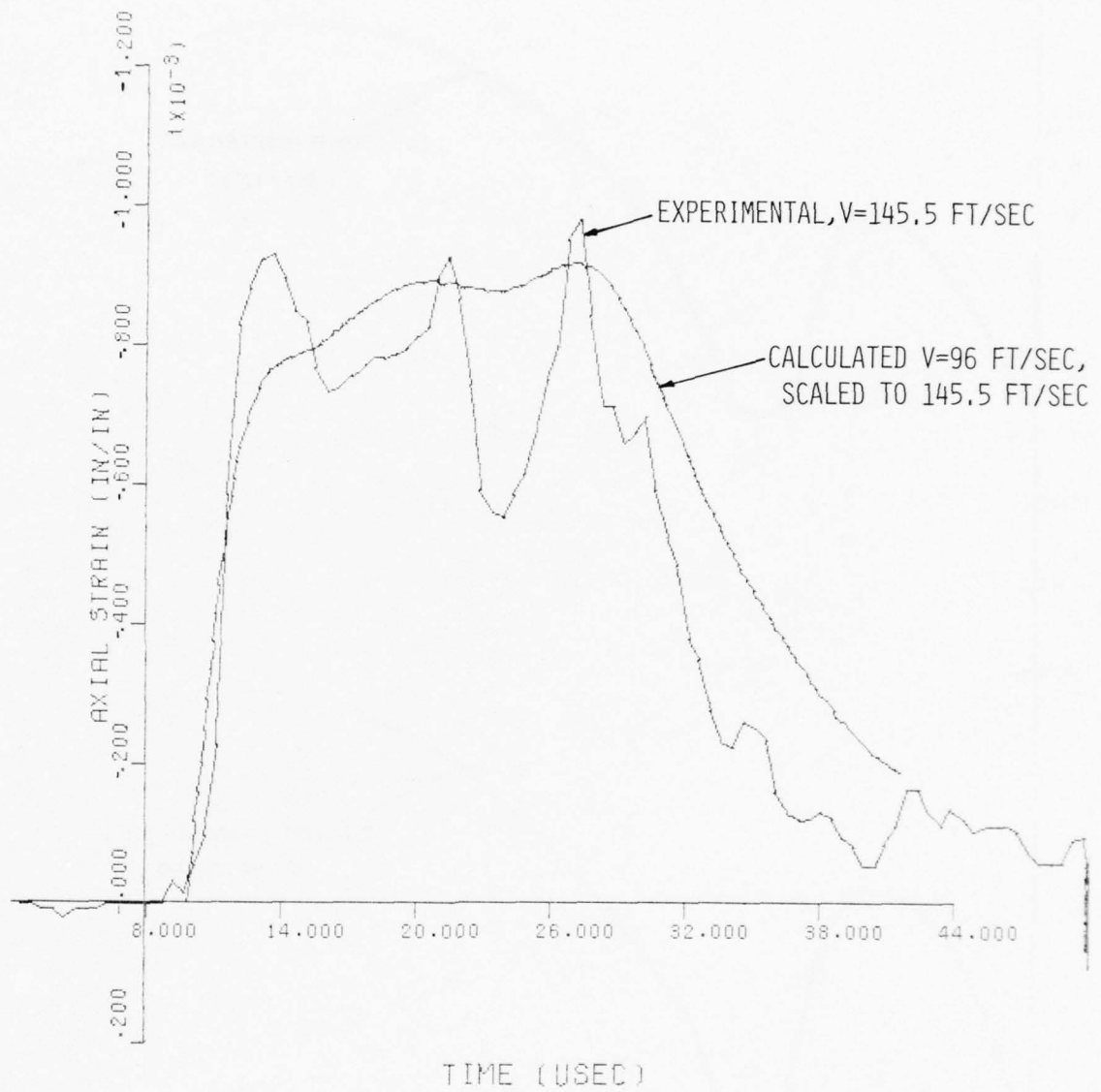


FIG. V.140 COMPARISON OF EXPERIMENTAL AND ANALYTICAL RESULTS FOR GAGE NUMBER 3, SHOT NUMBER 39

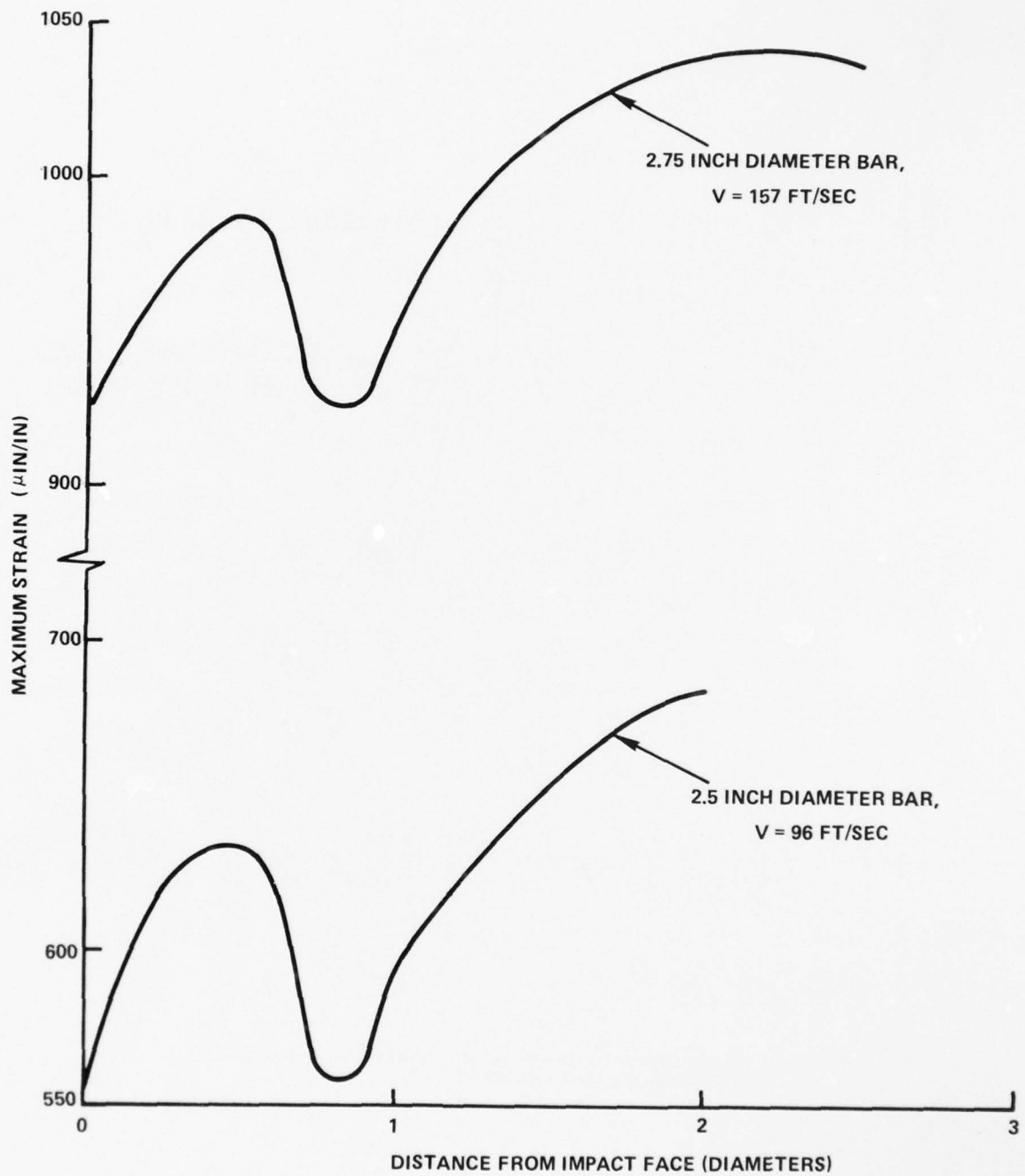


FIG. V. 141 MAXIMUM STRAIN ON RADIAL SURFACE OF BAR VERSUS DISTANCE FROM IMPACT FACE

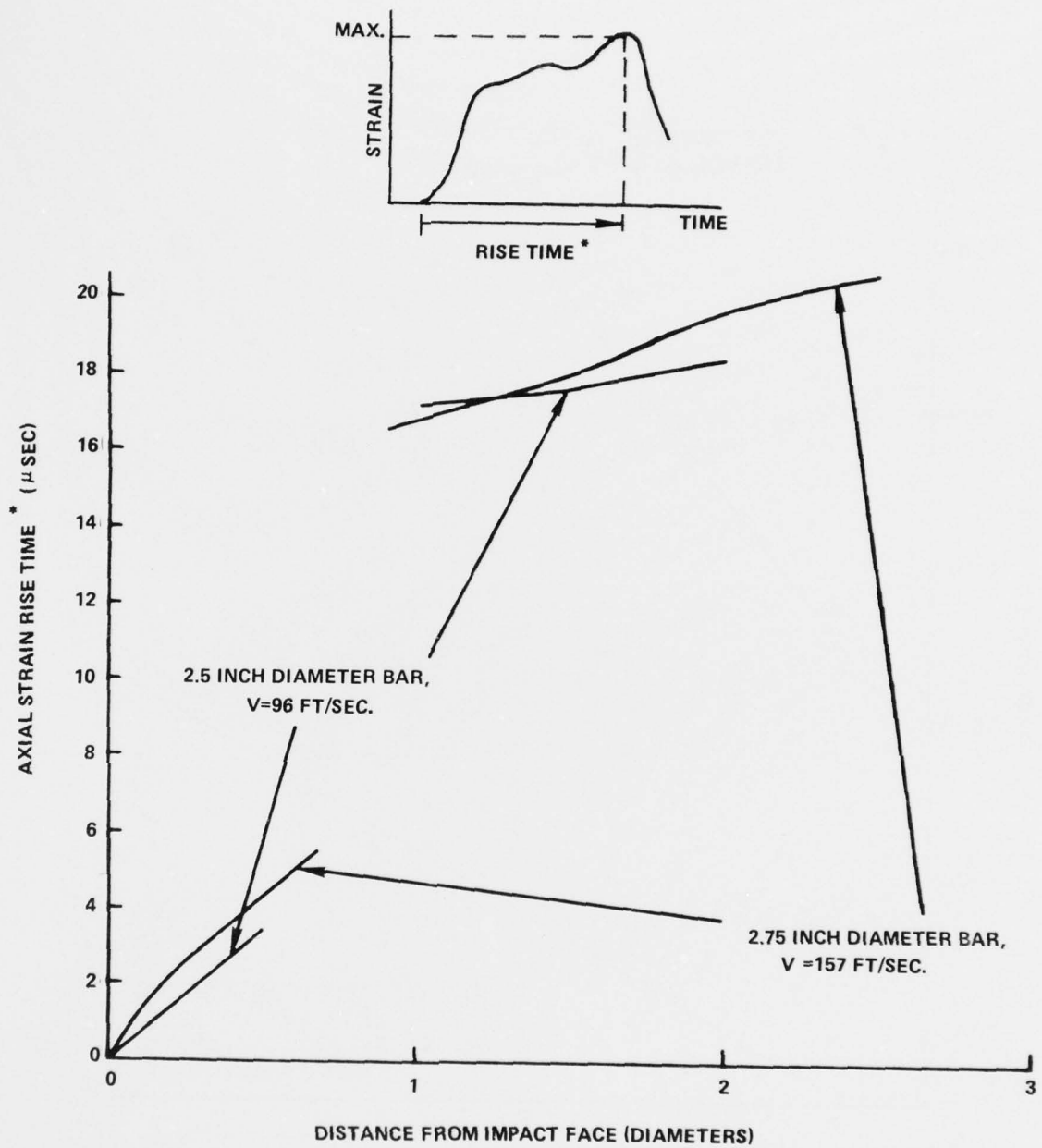


FIG. V. 142 RISE TIME OF AXIAL STRAIN PULSE ON RADIAL SURFACE OF BAR VERSUS DISTANCE FROM IMPACT FACE

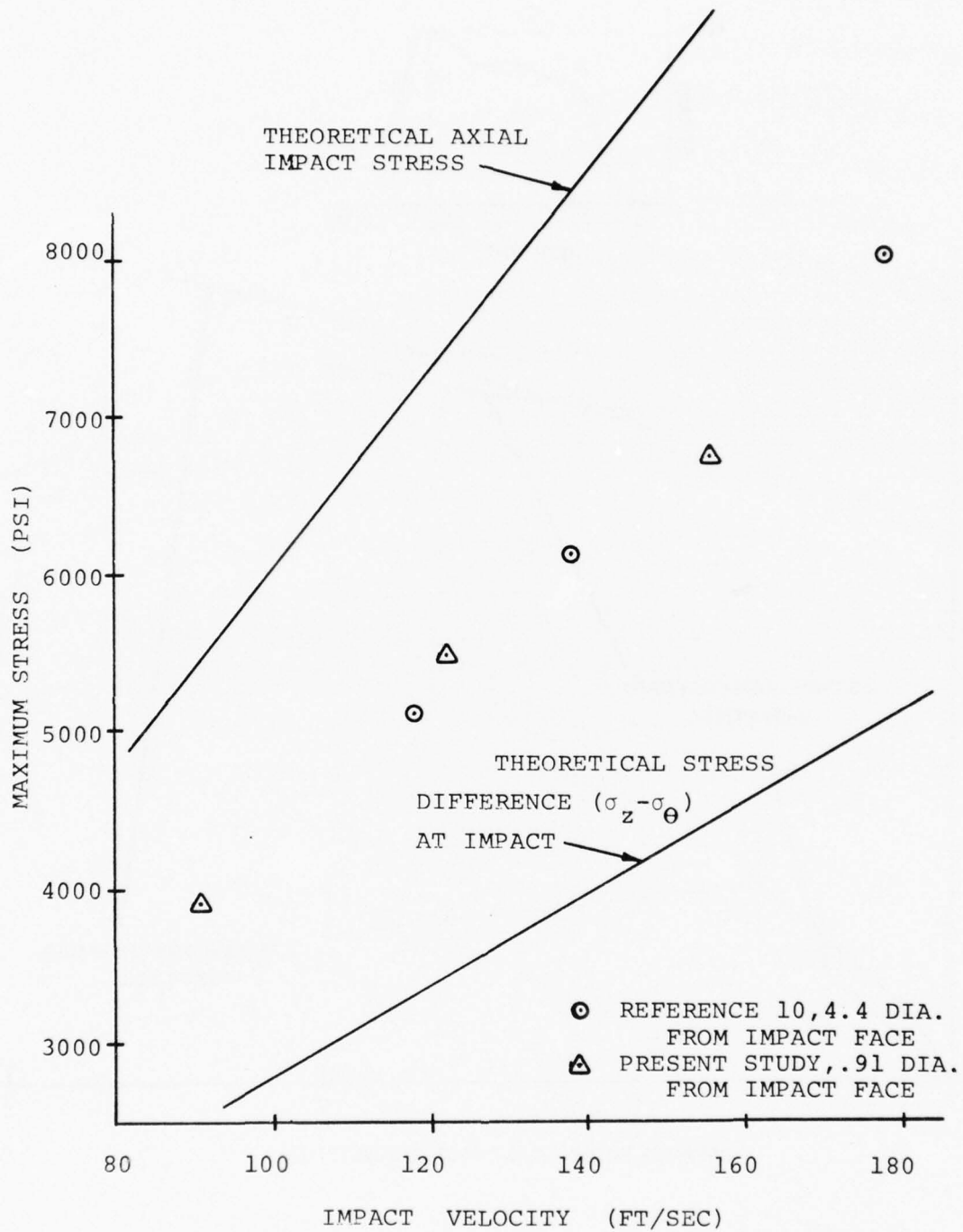


FIG. V. 143 COMPARISON OF 2.75 INCH DIAMETER BAR DATA AND REFERENCE 10 DATA

REFERENCES

1. Von Karman, T., "The Impact of Seaplane Floats During Landing", NACA TN 321, 1929.
2. "Proceedings of the NOL Water Entry Symposium", M. B. Tate (ed.), NavOrd Report 4180, U. S. Naval Ordnance Laboratory, White Oak, Maryland, 24 January 1956, pages 1-5.
3. Laumbach, D. D., "Impact Shock on a Blunt-Nosed Missile Striking Water with Its Axis Normal to the Water Surface", SC-TM-64-987, Sandia Corporation, Albuquerque, New Mexico, September 1964.
4. Wilkens, M. L., "Calculation of Elastic-Plastic Flow", UCRL-7322, Lawrence Radiation Laboratory, University of California Livermore, January 24, 1969.
5. Madden, R., and Chang, T. S., "Stress Waves Resulting from Hypervelocity Impact", AIAA Paper No. 69-355, presented at AIAA Hypervelocity Impact Conference, Cincinnati, Ohio, April 30 - May 2, 1969.
6. Madden, R., "Hypervelocity Impact Analysis by the Method of Characteristics", NASA TR-R-298, January 1969.
7. Bertholf, L. D., "Numerical Solution for Two-Dimensional Elastic Wave Propagation in Finite Bars", Journal of Applied Mechanics, Vol. 34, Trans. ASME, Vol. 89, Series E, 1969, pp 725-734.
8. Miklowitz, J., and Nisewanger, C. R., "The Propagation of Compressional Waves in a Dispersive Elastic Rod, Part II - Experimental Results and Comparison with Theory", Journal of Applied Mechanics, Vol. 24, Trans. ASME, Vol. 79, 1957, pp. 240-244.
9. Chang, H. L., and Horie, Y., "Two-Dimensional Stress Waves Resulting from the Axisymmetric Impact of Finite-Length Rods", Technical Report 73-1, North Carolina State University, Raleigh, North Carolina, January 1973.
10. Waser, R., "The Effect of Water Entry Angle on Impact Stress for Near-Normal Impacts", unpublished, Naval Ordnance Laboratory, 1972.

11. Lax, P. D., and Wendroff, B., "Difference Schemes with High-Order of Accuracy for Solving Hyperbolic Equations", Communications of Pure and Applied Math, Vol. 17, 1964, pp. 381-398.
12. Butler, D. S., "The Numerical Solution of Hyperbolic Systems of Partial Differential Equations in Three Independent Variables", Proc. Royal Soc. London (A) 255, 1960, pp. 232-252.
13. Clifton, R. J., "A Difference Method for Plane Problems in Dynamic Elasticity", Quarterly of Applied Math, Vol. 25, No. 1, 1967, pp. 97-116.
14. Recker, W. W., "A Numerical Solution of Axisymmetric Problems in Elastodynamics", International Journal for Numerical Methods in Engineering, Vol. 3, pp 361-377, 1971.
15. Richardson, D. J., "The Solution of Two-Dimensional Hydrodynamic Equations by the Method of Characteristics", Methods in Computational Physics, Vol. 3, Academic Press, New York, 1964, pp. 295-318.
16. Elliott, L. A., "Shock Fronts in Two-Dimensional Flow", Proc. Royal Soc. London (A) 262, pp. 558-565, 1962.
17. "SR-4 Semiconductor Strain Gages", Bulletin 102-2 Baldwin-Lima-Hamilton Corporation, Waltham, Massachusetts, May 1970.
18. Dorsey, J., Semiconductor Strain Gage Handbook Section I Theory, Baldwin-Lima-Hamilton Corporation, Waltham, Massachusetts, October 1964.
19. Dorsey, J., Semiconductor Strain Gage Handbook, Section VII Strain Measurement, Baldwin-Lima-Hamilton Corporation, Waltham, Massachusetts.
20. Murray, W., and Stein, P., Strain Gage Techniques, Massachusetts Institute of Technology, Cambridge, Massachusetts, 1960.
21. van Thiel, M., "Compendium of Shock Wave Data", UCRL-50108 (Vol. 1), Lawrence Radiation Laboratory, University of California, Livermore, California, June 1966.

22. Hinckley, W. M., "Analysis of Rigid Polyurethane Foam as a Shock Mitigator", Thesis, University of Maryland, College Park, MD., 1973.
23. Wilkens, M. L., Blum, R. E., Cronshagen, E., and Grantham, P., "A Method for Computer Simulation of Problems in Solid Mechanics and Gas Dynamics in Three Dimensions and Time", UCRL-51574, Lawrence Livermore Laboratory, University of California Livermore, April 24, 1974.

APPENDIX A

BICHARACTERISTIC EQUATIONS FOR THE LAGRANGIAN
FORMULATION OF LINEAR ELASTIC WAVE PROPAGATION

A.1 Governing Equations

The equations which describe the axisymmetric response of a right circular cylindrical bar to linear elastic wave propagation contain six independent variables: four stresses σ_r , σ_θ , σ_z , and τ_{rz} , and two velocities v_r and v_z . The equations of motion in Lagrangian coordinates with no body forces are given by

$$\begin{aligned}\sigma_{r,r} + \tau_{rz,z} + \frac{\sigma_r - \sigma_\theta}{r} &= \rho b v_{r,t} \\ \tau_{rz,r} + \sigma_{z,z} + \frac{\tau_{rz}}{r} &= \rho b v_{z,t}\end{aligned}\tag{A-1}$$

The strain rates $\epsilon_{r,t}$, $\epsilon_{z,t}$, $\epsilon_{\theta,t}$, $\gamma_{rz,t}$ are related to the velocities in linear elasticity by:

$$\begin{aligned}\epsilon_{r,t} &= v_{r,r} \\ \epsilon_{\theta,t} &= \frac{v_r}{r} \\ \epsilon_{z,t} &= v_{z,z} \\ \gamma_{rz,t} &= v_{r,z} + v_{z,r}\end{aligned}\tag{A-2}$$

The constitutive relations for an isotropic elastic material in strain rate form are

$$\begin{aligned}\epsilon_{r,t} &= C_1 \sigma_{r,t} - C_2 (\sigma_{\theta,t} + \sigma_{z,t}) \\ \epsilon_{\theta,t} &= C_1 \sigma_{\theta,t} - C_2 (\sigma_{r,t} + \sigma_{z,t})\end{aligned}\tag{A-3}$$

$$\begin{aligned}\epsilon_{z,t} &= C_1 \sigma_{z,t} - C_2 (\sigma_{r,t} + \sigma_{\theta,t}) \\ \gamma_{rz,t} &= C_3 \tau_{rz,t}\end{aligned}\tag{A-3}$$

The constants C_i are given by

$$C_1 = \frac{1}{E}, \quad C_2 = \frac{\nu}{E}, \quad C_3 = \frac{1}{G}\tag{A-4}$$

Eliminating strain rates from equations (A-2) and (A-3) yields the constitutive equations in terms of stresses and velocities

$$\begin{aligned}C_1 \sigma_{r,t} - C_2 \sigma_{\theta,t} - C_2 \sigma_{z,t} - v_{r,r} &= 0 \\ -C_2 \sigma_{r,t} + C_1 \sigma_{\theta,t} - C_2 \sigma_{z,t} - \frac{v_r}{r} &= 0 \\ -C_2 \sigma_{r,t} - C_2 \sigma_{\theta,t} + C_1 \sigma_{z,t} - v_{z,z} &= 0 \\ C_3 \tau_{rz,t} - v_{r,z} - v_{z,r} &= 0\end{aligned}\tag{A-5}$$

The four equations (A-5) together with the two equations of motion (A-1) represent a system of six first order partial differential equations in six dependent variables, which must be solved with the proper initial and boundary conditions.

A.2 Method of Characteristics Solution

The problem has now been formulated as a system of six first order partial differential equations in two spatial dimensions and time, subject to the proper initial and boundary conditions. The objective of using the method of characteristics on the partial differential

equations is to find a proper transformation of coordinates such that the number of independent variables decreases by at least one. In one dimensional wave propagation, this transformation results in a system of ordinary differential equations which are easily amenable to an accurate numerical solution. For two spatial dimensions, in general, the equations remain partial differential equations after the transformation. However, a system of partial differential equations in two independent variables is easier to solve than a system in three independent variables.

Consider a system of partial differential equations

$$A_{ij}U_{j,t} + B_{ij}U_{j,r} + C_{ij}U_{j,z} + D_i = 0; i, j = 1, 6 \quad (A-6)$$

A repeated index denotes summation over the range of that index. For the equations of axisymmetric, linear, elastic wave propagation, the terms in equation (A-6) are given by

$$U_i = \{U\} = \begin{pmatrix} \sigma_r \\ \sigma_\theta \\ \sigma_z \\ \tau_{rz} \\ v_r \\ v_z \end{pmatrix} = \text{dependent variable vector}$$

$$A_{ij} = [A] = \begin{bmatrix} C_1 & -C_2 & -C_2 & 0 & 0 & 0 \\ -C_2 & C_1 & -C_2 & 0 & 0 & 0 \\ -C_2 & -C_2 & C_1 & 0 & 0 & 0 \\ 0 & 0 & 0 & C_3 & 0 & 0 \\ 0 & 0 & 0 & 0 & \rho_b & 0 \\ 0 & 0 & 0 & 0 & 0 & \rho_b \end{bmatrix}$$

$$B_{15} = B_{46} = B_{51} = B_{64} = -1; \quad B_{ij} = 0 \text{ for the remaining components} \quad (A-7)$$

$$C_{36} = C_{45} = C_{54} = C_{63} = -1; \quad C_{ij} = 0 \text{ for the remaining components}$$

$$D_i = [D] = \begin{pmatrix} 0 \\ -\frac{v_r}{r} \\ 0 \\ 0 \\ -\frac{(\sigma_r - \sigma_\theta)}{r} \\ -\frac{\tau_{rz}}{r} \end{pmatrix}$$

It is desired to reduce the number of partial derivative terms in equation (A-6) by one and therefore, a transformation of equations (A-6) will be performed such that at a point in r, z, t space, differentiation occurs parallel to planes, called characteristic planes, and this differentiation occurs along two directions in the plane. First, the governing equations are premultiplied by a transformation matrix T_{ki} .

$$T_{ki}A_{ij}U_{j,t} + T_{ki}B_{ij}U_{j,r} + T_{ki}C_{ij}U_{j,z} + T_{ki}D_i = 0 \quad (A-8)$$

The transformation is chosen so that two linear combinations of partial derivative terms result; that is, it is required that the transformed equations be:

$$B'_{ij}(\alpha_{\underline{i}}U_{j,t} + U_{j,r}) + C'_{ij}(\beta_{\underline{i}}U_{j,t} + U_{j,z}) + D'_i = 0 \quad (A-9)$$

where the underlined index denotes no sum over that index. In order to obtain (A-9) from (A-8) it is necessary that:

$$T_{ki}A_{ij} = \alpha_{\underline{k}}T_{ki}B_{ij} + \beta_{\underline{k}}T_{ki}C_{ij} \quad (A-10)$$

and the tensor coefficients in (A-9) must be:

$$\begin{aligned} B'_{ij} &= T_{il}B_{lj} \\ C'_{ij} &= T_{il}C_{lj} \\ D'_i &= T_{il}D_l \end{aligned} \quad (A-11)$$

By finding two directions S_i^1 and S_i^2 such that

$$\begin{aligned} U_{j, s_i^1} &= \alpha_{\underline{i}}U_{j,t} + U_{j,r} \\ U_{j, s_i^2} &= \beta_{\underline{i}}U_{j,t} + U_{j,z} \end{aligned} \quad (A-12)$$

then the desired set of transformed partial differential equations will be obtained

$$B_{ij}' U_{j, s_i^1} + C_{ij}' U_{j, s_i^2} + D_i' = 0 \quad (A-13)$$

Consider the solution surface U_j and the derivatives in the directions of S_k^1 and S_k^2 :

$$\begin{aligned} U_{j,S_k^1} &= S_{k,t}^1 U_{j,t} + S_{k,r}^1 U_{j,r} + S_{k,z}^1 U_{j,z} \\ U_{j,S_k^2} &= S_{k,t}^2 U_{j,t} + S_{k,r}^2 U_{j,r} + S_{k,z}^2 U_{j,z} \end{aligned} \quad (A-14)$$

Then if the directions S_k are chosen such that

$$\begin{pmatrix} S_{k,t}^1 \\ S_{k,r}^1 \\ S_{k,z}^1 \end{pmatrix} = \begin{pmatrix} \alpha_k \\ 1 \\ 0 \end{pmatrix} \quad \text{and} \quad \begin{pmatrix} S_{k,t}^2 \\ S_{k,r}^2 \\ S_{k,z}^2 \end{pmatrix} = \begin{pmatrix} \beta_k \\ 0 \\ 1 \end{pmatrix} \quad (A-15)$$

equations (A-12) will be satisfied.

The curves S_k^1 and S_k^2 form a surface which will be called $S_k^3 = \text{constant}$, which is the characteristic surface. Since the direction vectors of S_k^1 and S_k^2 in (A-15) are both orthogonal to the vector $(-1, \alpha_k, \beta_k)$, that is,

$$\begin{aligned} (\alpha_k, 1, 0) \cdot (-1, \alpha_k, \beta_k) &= 0 \\ (\beta_k, 0, 1) \cdot (-1, \alpha_k, \beta_k) &= 0 \end{aligned} \quad (A-16)$$

then the vectors $(-1, \alpha_k, \beta_k)$ must be in the direction normal to the characteristic surface. Letting $S_k^3 = \phi$ then

$$\frac{\phi_{,t}}{-1} = \frac{\phi_{,r}}{\alpha_k} = \frac{\phi_{,z}}{\beta_k} = \text{constant} \quad (A-17)$$

Using α_k and β_k from equation (A-17) in the equation defining the transformation matrix, (A-10), yields:

$$T_{ki}(\phi, t A_{ij} + \phi, r B_{ij} + \phi, z C_{ij}) = 0 \quad (A-18)$$

Now k is a free index in the above equation so that (A-18) represents a system of equations which has non-trivial solutions if the determinant of the coefficient matrix is zero, or:

$$\det (\phi, t A_{ij} + \phi, r B_{ij} + \phi, z C_{ij}) = 0 \quad (A-19)$$

This yields an algebraic equation of sixth degree in the derivatives of the characteristic surface. Since the system of equations describing linear elastic wave propagation are hyperbolic, six real roots and therefore six characteristic surfaces will result. Substituting matrices A_{ij} , B_{ij} , and C_{ij} from equations (A-7) into (A-19) yields:

$$\det \begin{bmatrix} C_1 \phi, t & -C_2 \phi, t & -C_2 \phi, t & 0 & -\phi, r & 0 \\ -C_2 \phi, t & C_1 \phi, t & -C_2 \phi, t & 0 & 0 & 0 \\ -C_2 \phi, t & -C_2 \phi, t & C_1 \phi, t & 0 & 0 & -\phi, z \\ 0 & 0 & 0 & C_3 \phi, t & -\phi, z & -\phi, r \\ -\phi, r & 0 & 0 & -\phi, z & \rho_b \phi, t & 0 \\ 0 & 0 & -\phi, z & -\phi, r & 0 & \rho_b \phi, t \end{bmatrix} = 0 \quad (A-20)$$

Expanding the determinant yields the sixth order algebraic equation.

$$\frac{\rho_b^3 (1-2\nu)}{8G^3 (1+\nu)} [\phi_{,t}^2 - c_1^2 (\phi_{,r}^2 + \phi_{,z}^2)] [\phi_{,t}^2 - c_2^2 (\phi_{,r}^2 + \phi_{,z}^2)] \phi_{,t}^2 = 0$$

(A-21)

where

$$c_1 = \sqrt{\frac{\lambda+2G}{\rho_b}} = \text{dilatational wave speed}$$

$$c_2 = \sqrt{\frac{G}{\rho_b}} = \text{distortional wave speed}$$

and

$$\lambda = \frac{E}{(1+\nu)(1-2\nu)} = \text{Lame's constant}$$

The six roots of equation (A-21) are

$$\begin{aligned} \phi_{,t}^{(1),(2)} &= \pm c_1 \sqrt{\phi_{,r}^2 + \phi_{,z}^2} \\ \phi_{,t}^{(3),(4)} &= \pm c_2 \sqrt{\phi_{,r}^2 + \phi_{,z}^2} \\ \phi_{,t}^{(5),(6)} &= 0, 0 \end{aligned} \quad (\text{A-22})$$

The superscript on $\phi^{(k)}$ denotes the k^{th} characteristic root.

Now to find the equations of the characteristic surfaces $\phi^{(k)}$, let the factors of equation (A-21) be represented by

$$S_{ij} \phi_{,x_i} \phi_{,x_j} = 0 \quad (\text{A-23})$$

where

$$x_1 = t$$

$$x_2 = r$$

$$x_3 = z$$

and for example, the coefficient matrix of the first factor in (A-21) would be

$$S_{ij} = \begin{bmatrix} 1 & 0 & 0 \\ 0 & -c_1^2 & 0 \\ 0 & 0 & -c_1^2 \end{bmatrix}$$

The terms $\phi_{,xi}$ are proportional to the normal to the surfaces $\phi = \text{constant}$. Let the direction cosines of the normals at a point P be L_i . Then the equation

$$S_{ij}L_iL_j = 0 \quad (\text{A-24})$$

describes a quadratic cone in r, z, t space. Applying equation (A-24) to the normals and imposing some arbitrary normalization, yields a one parameter description of the surface. Let the parameter be γ which is the angle of the projection of the generator of the cone of normals onto the rz plane as shown in Figure A.1. The plane which is perpendicular to the normal at P is the tangent plane to the characteristic surface and the envelope of the tangent planes formed by varying γ is a conoid. The curves of intersection of the tangent planes and the enveloping conoid are called the bicharacteristic curves, and these are curves of constant γ . Now the points on the envelope are identified by two parameters. Let γ be one of these parameters and τ the other. Then these points on the envelope are represented by:

$$x_i = x_i(\gamma, \tau) \quad (A-25)$$

Directions dx_i lie within the tangent plane at P so

$$L_i dx_i = 0 \quad (A-26)$$

Since the conoid is the envelope of the tangent planes with respect to γ :

$$\frac{\partial L_i}{\partial \gamma} dx_i = 0 \quad (A-27)$$

Now since

$$L_i \frac{\partial L_i}{\partial \gamma} = 0 \quad (A-28)$$

the three vectors L_i , dx_i , and $\frac{\partial L_i}{\partial \gamma}$ are mutually orthogonal with two directions lying on the conoid surface for each γ

Take the vector $S_{ij}L_j$ and express it as a linear combination of the three orthogonal vectors.

$$S_{ij}L_j = a_1 L_i + a_2 dx_i + a_3 \frac{\partial L_i}{\partial \gamma} \quad (A-29)$$

Form the dot product with L_i :

$$S_{ij}L_j L_i = a_1 L_i L_i + a_2 L_i dx_i + a_3 L_i \frac{\partial L_i}{\partial \gamma} \quad (A-30)$$

Equations (A-24), (A-26), and (A-28) yield $a_1 = 0$. Forming the dot product of equation (A-29) with $\frac{\partial L_i}{\partial \gamma}$ and using equations (A-27) and (A-24) yields $a_3 = 0$. Therefore,

$$S_{ij}L_j = a_2 dx_i \quad (A-31)$$

If S_{ij} possesses an inverse, the normal to the characteristic surface is

$$L_j = a_2 S_{ij}^{-1} dx_i \quad (A-32)$$

Using equation (A-26) we obtain the equation of the conoid

$$S_{ij}^{-1} dx_i dx_j = 0 \quad (A-33)$$

The characteristic surface for linear elastic wave propagation in an isotropic homogeneous medium is found by taking the factors of the characteristic equation (A-21) and applying (A-33). The inverse of S_{ij}^{-1} for the first two factors is:

$$S_{ij}^{-1} = \begin{bmatrix} c_\alpha^{-4} & 0 & 0 \\ 0 & -c_\alpha^{-6} & 0 \\ 0 & 0 & -c_\alpha^{-6} \end{bmatrix}, \quad \alpha = 1, 2 \quad (A-34)$$

S_{ij}^{-1} for ϕ, t^2 does not exist. Two characteristic conoids are:

$$(dt)^2 - \frac{(dr)^2 + (dz)^2}{c_\alpha^2} = 0; \quad \alpha = 1, 2 \quad (A-35)$$

For $\phi, t^2 = 0$, this implies a cylindrical surface with axes parallel to the t axis.

Thus the characteristic surfaces (A-35) are cones and may be parameterized as

$$\begin{aligned} dt &= d\tau \\ dr &= c_\alpha \cos \gamma d\tau \\ dz &= c_\alpha \sin \gamma d\tau \end{aligned} \quad (A-36)$$

where γ is the angle in the rz plane. The cones extend in both the positive and negative t directions from P corresponding to the positive and negative roots of equation (A-35) and are shown in Figure A.2. On the forward cone, the bicharacteristic location γ is measured positive clockwise from the positive r axis and on the backward cone it is measured from the negative r axis in a counterclockwise sense.

Now that the directions for simplifying the governing partial differential equations (A-6) have been identified, the relations along these directions may be derived. Returning to the transformed equation (A-18), according to matrix theory, if the determinant of the coefficient is zero, equation (A-19), then the transformation matrix is a set of eigenvectors ξ_i^k such that

$$\xi_i^k (\phi_{,t} A_{ij} + \phi_{,r} B_{ij} + \phi_{,z} C_{ij}) = 0 \quad (A-37)$$

These eigenvectors are needed to solve for the relations on the transformed equations

$$\xi_i^k (A_{ij} U_{j,t} + B_{ij} U_{j,r} + C_{ij} U_{j,z} + D_i) = 0 \quad (A-38)$$

For the k^{th} eigenvector ξ_i^k corresponding to the k^{th} characteristic surface (equations (A-22)), equation (A-37) may be solved for ξ_i^k to within a proportionality factor. For this analysis the first component of the k^{th} eigenvector will be chosen as the factor. Expanding (A-37) for the k^{th} eigenvector corresponding to the k^{th} characteristic surface $\phi^{(k)}$ where

$$\phi_{,t}^{(1)} = +c_1 \sqrt{\phi_{,r}^{(1)2} + \phi_{,z}^{(1)2}}$$

$$\phi_{,t}^{(2)} = -c_1 \sqrt{\phi_{,r}^{(2)2} + \phi_{,z}^{(2)2}}$$

$$\phi_{,t}^{(3)} = +c_2 \sqrt{\phi_{,r}^{(3)2} + \phi_{,z}^{(3)2}}$$

(A-39)

$$\phi_{,t}^{(4)} = -c_2 \sqrt{\phi_{,r}^{(4)2} + \phi_{,z}^{(4)2}}$$

$$\phi_{,t}^{(5)} = \phi_{,t}^{(6)} = 0$$

a set of six equations in the six unknown components of the k^{th} eigenvector are obtained. Before carrying out the algebra, the equations of the characteristic surfaces (A-35) will be used.

Along a direction in the k^{th} characteristic surface

$$d\phi^{(k)} = \phi_{,t}^{(k)} dt + \phi_{,r}^{(k)} dr + \phi_{,z}^{(k)} dz = 0 \quad (\text{A-40})$$

Substituting the parametric equations (A-36) for the first four eigenvectors into equation (A-40) yields

$$\phi_{,t}^{(k)} d\tau + \phi_{,r}^{(k)} c_\alpha \cos \gamma d\tau + \phi_{,z}^{(k)} c_\alpha \sin \gamma d\tau = 0; \quad (\text{A-41})$$

$$k = 1, 2, 3, 4$$

or

$$c_{\alpha} \cos \gamma \frac{\phi_{,r}^{(k)}}{\phi_{,t}^{(k)}} + c_{\alpha} \sin \gamma \frac{\phi_{,z}^{(k)}}{\phi_{,t}^{(k)}} = -1; \quad (A-42)$$

$k = 1, 2, 3, 4$

The first four equations of (A-39) are

$$c_{\alpha}^2 \left(\frac{\phi_{,r}^{(k)}}{\phi_{,t}^{(k)}} \right)^2 + c_{\alpha}^2 \left(\frac{\phi_{,z}^{(k)}}{\phi_{,t}^{(k)}} \right)^2 = 1; \quad k = 1, 2, 3, 4 \quad (A-43)$$

Solving (A-42) and (A-43) yields:

$$\frac{\phi_{,r}^{(k)}}{\phi_{,t}^{(k)}} = - \frac{\cos \gamma}{c_{\alpha}} \quad ; k = 1, 2, 3, 4 \quad (A-44)$$

$$\frac{\phi_{,z}^{(k)}}{\phi_{,t}^{(k)}} = - \frac{\sin \gamma}{c_{\alpha}}$$

Now for the fifth and sixth characteristic surfaces, equation (A-40) with $\phi_{,t}^{(k)} = 0$ yields

$$\frac{\phi_{,r}^{(k)}}{\phi_{,t}^{(k)}} = - \frac{dz}{dr} ; \quad k = 5, 6 \quad (A-45)$$

Thus solving (A-37) with equations (A-44) and (A-45), after Gaussian elimination and algebraic manipulation yields the following equations:

For

$$\phi_{,t}^{(k)} = \pm c_1 \sqrt{\phi_{,r}^{(k)2} + \phi_{,z}^{(k)2}}$$

$$\left\{ \xi^{(1),(2)} \right\} = \frac{\xi_1^{(1),(2)}}{\lambda + 2G\cos^2\gamma} \begin{pmatrix} \lambda + 2G\cos^2\gamma \\ \lambda \\ \lambda + 2G\sin^2\gamma \\ G\sin 2\gamma \\ \mp c_1 \cos \gamma \\ \pm c_1 \sin \gamma \end{pmatrix} \quad (\text{A-46})$$

$$\text{For } \phi_{,t}^{(k)} = \pm c_2 \sqrt{\phi_{,r}^{(k)2} + \phi_{,z}^{(k)2}}$$

$$\left\{ \xi^{(3),(4)} \right\} = \xi_1^{(3),(4)} \begin{pmatrix} 1 \\ 0 \\ -1 \\ -\cot 2\gamma \\ \mp \frac{c_2}{2G\cos\gamma} \\ \pm \frac{c_2}{2G\sin\gamma} \end{pmatrix} \quad (\text{A-47})$$

$$\text{For } \phi_{,t}^{(k)} = 0, 0$$

$$\left\{ \xi^{(5)} \right\} = \frac{1}{\sqrt{1 + \frac{dr}{dz}^2 + \frac{dz}{dr}^2}} \begin{pmatrix} \frac{dr}{dz} \\ 0 \\ \frac{dz}{dr} \\ 1 \\ 0 \\ 0 \end{pmatrix} \quad (\text{A-48})$$

$$\left\{ \xi^{(6)} \right\} = \begin{pmatrix} 0 \\ 1 \\ 0 \\ 0 \\ 0 \\ 0 \end{pmatrix} \quad (\text{A-49})$$

Multiply equation (A-6) by $\phi_{,t}^{(k)}$ and then add to it the term $U_{j,t}(\phi_{,r}^{(k)} B_{ij} + \phi_{,z}^{(k)} C_{ij})$ and its negative.

$$\begin{aligned} & \phi_{,t}^{(k)} A_{ij} U_{j,t} + \phi_{,t}^{(k)} B_{ij} U_{j,r} + \phi_{,t}^{(k)} C_{ij} U_{j,t} + \phi_{,t}^{(k)} D_i \\ & + (\phi_{,r}^{(k)} B_{ij} U_{j,t} + \phi_{,z}^{(k)} C_{ij} U_{j,t}) \\ & - (\phi_{,r}^{(k)} B_{ij} U_{j,t} + \phi_{,z}^{(k)} C_{ij} U_{j,t}) = 0 \end{aligned} \quad (\text{A-50})$$

Multiplying by ξ_i^k , dividing by $\phi_{,t}^{(k)}$ and rearranging terms yields:

$$\begin{aligned} \frac{1}{\phi_{,t}^{(k)}} \xi_i^k (\phi_{,t}^{(k)} A_{ij} + \phi_{,r}^{(k)} B_{ij} + \phi_{,z}^{(k)} C_{ij}) U_{j,t} \\ + \xi_i^k (C_{ij} U_{j,z} - \frac{\phi_{,z}}{\phi_{,t}^{(k)}} C_{ij} U_{j,t}) + \xi_i^k D_i = 0 \end{aligned} \quad (A-51)$$

From equation (A-37), the first term is zero. Using the characteristic relations (A-44), equation (A-51) becomes:

$$\begin{aligned} \xi_i^k B_{ij} (U_{j,r} + \frac{\cos \gamma}{c_\alpha} U_{j,t}) + \xi_i^k C_{ij} (U_{j,z} + \frac{\sin \gamma}{c_\alpha} U_{j,t}) \\ + \xi_i^k D_i = 0 \end{aligned} \quad (A-52)$$

Now consider the derivative of the dependent variable vector with respect to the bicharacteristic parameter τ .

$$U_{i,\tau} = U_{i,t} t_{,\tau} + U_{i,r} r_{,\tau} + U_{i,z} z_{,\tau} \quad (A-53)$$

which becomes from equation (A-36)

$$U_{i,\tau} = U_{i,t} + c_\alpha \cos \gamma U_{i,r} + c_\alpha \sin \gamma U_{i,z} \quad (A-54)$$

Now along a bicharacteristic, $\gamma = \text{constant}$, so a total differential occurs:

$$U_{i,\tau} \bigg|_{\gamma=\text{constant}} = \frac{dU_i}{d\tau} \bigg|_{\gamma=\text{constant}} \quad (A-55)$$

Substituting for $U_{i,t}$ from equation (A-54) into (A-52),

$$\xi_i^k \left\{ B_{ij} \left[\frac{\cos \gamma}{c_\alpha} \frac{dU_j}{d\tau} + \sin^2 \gamma U_{j,r} - \sin \gamma \cos \gamma U_{j,z} \right] \right. \quad (A-56)$$

$$\left. + C_{ij} \left[\frac{\sin \gamma}{c_\alpha} \frac{dU_j}{d\tau} - \sin \gamma \cos \gamma U_{j,r} + \cos^2 \gamma U_{j,z} \right] + D_i \right\} = 0$$

Equations (A-56) give the relations among the dependent variables along the bicharacteristics on the characteristic cones. Substituting the eigenvectors from equations (A-46) and (A-47) into (A-56) yields the bicharacteristic relations. Along the characteristic cones $c_\alpha = \pm c_1$:

$$\rho_b c_1 [\cos \gamma dv_r + \sin \gamma dv_z] \mp \cos^2 \gamma d\sigma_r \mp \sin 2\gamma d\tau_{rz} + \sin^2 \gamma d\sigma_z$$

$$+ \left\{ \lambda \sin^2 \gamma v_{r,r} + \lambda \cos^2 \gamma v_{z,z} - \frac{\lambda}{2} \sin 2\gamma (v_{z,r} + v_{r,z}) \right.$$

$$+ c_1 \sin^2 \gamma \cos \gamma (\sigma_{z,r} - \sigma_{r,r}) \pm c_1 \cos^2 \gamma \sin \gamma (\sigma_{r,z} - \sigma_{z,z})$$

$$\left. \pm c_1 \cos 2\gamma (\sin \gamma \tau_{rz,r} - \cos \gamma \tau_{rz,z}) \right\} dt = \quad (A-57)$$

$$\left\{ \frac{c_1}{r} [(\sigma_r - \sigma_\theta) \cos \gamma + \sin \gamma \tau_{rz}] - \frac{\lambda v_r}{r} \right\} dt$$

Along the characteristic cones $\pm c_2$:

$$\rho_b c_2 (\sin \gamma dv_r - \cos \gamma dv_z) + \frac{1}{2} \sin 2\gamma (d\sigma_z - d\sigma_r) + \cos 2\gamma d\tau_{rz}$$

$$+ \left\{ G \sin \gamma \cos \gamma (v_{r,r} - v_{z,z}) + G (\sin^2 \gamma v_{z,r} - \cos^2 \gamma v_{r,z}) \right.$$

$$+ c_2 \sin \gamma \cos \gamma (\sin \gamma \sigma_{r,z} - \cos \gamma \sigma_{z,r}) + c_2 (\cos^3 \gamma \sigma_{z,z} - \sin^3 \gamma \sigma_{r,r})$$

$$\left. + c_2 \sin 2\gamma (\sin \gamma \tau_{rz,r} - \cos \gamma \tau_{rz,z}) \right\} dt = \quad (A-58)$$

$$\frac{c_2}{r} [\sin \gamma (\sigma_r - \sigma_\theta) - \cos \gamma \tau_{rz}] dt$$

For the repeated roots $\phi_{,t}^{(k)} = 0$, multiply equation (A-6) by ξ_i^k and then add to it the term $\frac{\xi_i^k}{\phi_{,z}^{(k)}} [(\phi_{,t}^{(k)} A_{ij} + \phi_{,r}^{(k)} B_{ij}) U_{j,z}]$ and its negative.

$$\begin{aligned} & \xi_i^k A_{ij} U_{j,t} + \xi_i^k B_{ij} U_{j,r} + \xi_i^k C_{ij} U_{j,z} + \xi_i^k D_i + \left(\xi_i^k \frac{\phi_{,t}^{(k)}}{\phi_{,z}^{(k)}} A_{ij} U_{j,z} \right. \\ & \quad \left. + \xi_i^k \frac{\phi_{,r}^{(k)}}{\phi_{,z}^{(k)}} B_{ij} U_{j,z} \right) - \left(\xi_i^k \frac{\phi_{,t}^{(k)}}{\phi_{,z}^{(k)}} A_{ij} U_{j,z} \right. \\ & \quad \left. + \xi_i^k \frac{\phi_{,r}^{(k)}}{\phi_{,z}^{(k)}} B_{ij} U_{j,z} \right) = 0 \end{aligned} \quad (A-59)$$

Rearranging terms:

$$\begin{aligned} & \frac{\xi_i^k}{\phi_{,z}^{(k)}} (\phi_{,t}^{(k)} A_{ij} + \phi_{,r}^{(k)} B_{ij} + \phi_{,z}^{(k)} C_{ij}) U_{j,z} + \xi_i^k \left[B_{ij} \left(U_{j,r} - \frac{\phi_{,r}^{(k)}}{\phi_{,z}^{(k)}} U_{j,z} \right) \right. \\ & \quad \left. + A_{ij} \left(U_{j,t} - \frac{\phi_{,t}^{(k)}}{\phi_{,z}^{(k)}} U_{j,z} \right) \right] + \xi_i^k D_i = 0 \end{aligned} \quad (A-60)$$

From equation (A-37), the first term is zero and using equation (A-45) and the fact that $\phi_{,t}^{(k)} = 0$ yields the following equation.

$$\xi_i^k \left[B_{ij} \left(U_{j,r} + \frac{dz}{dr} U_{j,z} \right) + A_{ij} U_{j,t} \right] + \xi_i^k D_i = 0 \quad (A-61)$$

Substituting for $\xi_i^{(5)}$ from (A-48) yields

$$\begin{aligned} & -v_{r,r} dr^2 - v_{r,z} dr dz + dr^2 C_{1\sigma r,t} - dr^2 C_{2\sigma\theta,t} - dr^2 C_{2\sigma z,t} \\ & - dz^2 C_{2\sigma r,t} - dz^2 C_{2\sigma\theta,t} + dz^2 C_{1\sigma z,t} - v_{z,r} dr dz - dz^2 v_{z,z} \\ & + dr dz C_{3\tau rz,t} = 0 \end{aligned} \quad (A-62)$$

Examining (A-62) it can be seen that when $dz = 0$

$$C_1^{\sigma}{}_{r,t} - C_2^{\sigma}{}_{\theta,t} - C_2^{\sigma}{}_{z,t} - v_{r,r} = 0 \quad (A-63)$$

When $dr = 0$

$$-C_2^{\sigma}{}_{r,t} - C_2^{\sigma}{}_{\theta,t} + C_1^{\sigma}{}_{z,t} - v_{z,z} = 0 \quad (A-64)$$

and when $dr = dz$

$$C_3^{\tau}{}_{rz,t} - (v_{r,z} + v_{z,r}) = 0 \quad (A-65)$$

Equations (A-63) through (A-65) are just three of the four constitutive equations (A-5). Substituting $\xi^{(6)}$ into equation (A-61) yields the fourth constitutive equation

$$-C_2^{\sigma}{}_{r,t} + C_1^{\sigma}{}_{\theta,t} - C_2^{\sigma}{}_{z,t} - \frac{v_r}{r} = 0 \quad (A-66)$$

Thus the constitutive equations and relations along the two bicharacteristic cones describe the wave propagation in a linear elastic axisymmetric bar.

As can be seen from the bicharacteristic compatability equations (A-57) and (A-58), there still remain partial derivatives. However, because of the sines and cosines of γ in these equations, bicharacteristics may be chosen to selectively eliminate some of these partial derivatives. The scheme to be used herein consists of evaluating the compatability relations along bicharacteristics at $\gamma = 0, 90^\circ, 180^\circ$, and 270° on each of the two backward characteristic

surfaces as shown in Figure II.2. Disturbances from the previous time plane at these γ locations are propagated to point P along these directions. Along the dilatational surface c_1 :

$$\gamma = 0:$$

$$\rho_b c_1 dv_r - d\sigma_r + \left[\lambda v_{z,z} - c_1 \tau_{rz,z} - \frac{c_1}{r} (\sigma_r - \sigma_\theta) + \frac{\lambda v_r}{r} \right] dt = 0$$

$$\gamma = \frac{\pi}{2}:$$

$$\rho_b c_1 dv_z - d\sigma_z + \left[\lambda v_{r,r} - c_1 \tau_{rz,r} - \frac{c_1}{r} \tau_{rz} + \frac{\lambda v_r}{r} \right] dt = 0$$

$$\gamma = \pi:$$

$$-\rho_b c_1 dv_r - d\sigma_r + \left[\lambda v_{z,z} + c_1 \tau_{rz,z} + \frac{c_1}{r} (\sigma_r - \sigma_\theta) + \frac{\lambda v_r}{r} \right] dt = 0 \quad (A-67)$$

$$\gamma = \frac{3\pi}{2}:$$

$$-\rho_b c_1 dv_z - d\sigma_z + \left[\lambda v_{r,r} + c_1 \tau_{rz,r} + \frac{c_1}{r} + \frac{\lambda v_r}{r} \right] dt = 0$$

Along the distortional surface c_2 :

$$\gamma = 0:$$

$$-\rho_b c_2 dv_z + dv_z + d\tau_{rz} + \left[-G v_{r,z} + c_2 \sigma_{z,z} + \frac{c_2}{r} \tau_{rz} \right] dt = 0$$

$$\gamma = \frac{\pi}{2}:$$

$$\rho_b c_2 dv_r - d\tau_{rz} + \left[G v_{z,r} - c_2 \sigma_{r,r} - \frac{c_2}{r} (\sigma_r - \sigma_\theta) \right] dt = 0$$

$$\gamma = \pi:$$

$$\rho_b c_2 dv_z + d\tau_{rz} + \left[-G v_{r,z} - c_2 \sigma_{z,z} - \frac{c_2}{r} \tau_{rz} \right] dt = 0 \quad (A-68)$$

$$\gamma = \frac{3\pi}{2}:$$

$$-\rho_b c_2 dv_r - d\tau_{rz} + \left[G v_{z,r} + c_2 \sigma_{r,r} + \frac{c_2}{r} (\sigma_r - \sigma_\theta) \right] dt = 0$$

To insure that this scheme is feasible for obtaining a solution, the number of variables and equations are checked. In equations (A-63) through (A-68) there are fourteen unknowns and twelve equations. Two more equations may be obtained without introducing additional variables by using the equations of motion (A-1). In these equations, the partial derivative with respect to "t" becomes the total derivative because of the Lagrangian formulation. Since the system of fourteen equations is a coupled first order partial differential equation system there is no straightforward solution technique, so numerical methods must be applied to obtain a solution. The particular numerical technique used is a simple central difference method with second order difference methods applied at the radial and axial boundaries and at the centerline of the bar.

The bicharacteristic equations (A-67) and (A-68) are integrated along the bicharacteristic from the old time plane to the new time. If P_i denotes the i^{th} bicharacteristic extending from the point P in the new time plane to the intersection of this i^{th} bicharacteristic in the old time plane (Figure II.2), then the integrated terms in the bicharacteristic equations are approximated by

$$\int_{P_i} d\omega = \Delta\omega^i = \omega - \omega^i$$

$$\int_{P_i} \omega dt = (\delta\omega^i) \frac{\Delta t}{2} = (\omega + \omega^i) \frac{\Delta t}{2} \quad (A-69)$$

$$\int_{P_i} \frac{\omega}{r} dt = \frac{\delta\omega^i}{r^i} \frac{\Delta t}{2} \text{ where } r^i = \frac{r|_t + r|_{t-\Delta t}}{2}$$

Integrating the equations (A-67) yields

$$\begin{aligned} \rho_b c_1 \Delta v_r^1 - \Delta\sigma_r^1 + \frac{\Delta t}{2} \left[\lambda \delta v_{z,z}^1 - c_1 \delta \tau_{rz,z}^1 - \frac{c_1}{r^1} (\delta\sigma_r^1 - \delta\sigma_\theta^1) \right. \\ \left. + \frac{\lambda}{r^1} \delta v_r^1 \right] = 0 \\ \rho_b c_1 \Delta v_z^4 - \Delta\sigma_z^4 + \frac{\Delta t}{2} \left[\lambda \delta v_{r,r}^4 - c_1 \delta \tau_{rz,r}^4 - \frac{c_1}{r^4} \delta \tau_{rz}^4 + \frac{\lambda}{r^4} \delta v_r^4 \right] = 0 \\ -\rho_b c_1 \Delta v_r^3 - \Delta\sigma_r^3 + \frac{\Delta t}{2} \left[\lambda v_{z,z}^3 + c_1 \delta \tau_{rz,z}^3 + \frac{c_1}{r^3} (\delta\sigma_r^3 - \delta\sigma_\theta^3) \right. \\ \left. + \frac{\lambda}{r^3} \delta v_r^3 \right] = 0 \\ -\rho_b c_1 \Delta v_z^2 - \Delta\sigma_z^2 + \frac{\Delta t}{2} \left[\lambda \delta v_{r,r}^2 + c_1 \delta \tau_{rz,r}^2 + \frac{c_1}{r^2} \delta \tau_{rz}^2 + \frac{\lambda}{r^2} \delta v_r^2 \right] = 0 \end{aligned} \quad (A-70)$$

Integrating equations (A-74) yields

$$\begin{aligned} -\rho_b c_2 \Delta v_z^5 + \Delta \tau_{rz}^5 + \frac{\Delta t}{2} \left[-G \delta v_{r,z}^5 + c_2 \delta \sigma_{z,z}^5 + \frac{c_2}{r^5} \delta \tau_{rz}^5 \right] = 0 \\ \rho_b c_2 \Delta v_r^8 - \Delta \tau_{rz}^8 + \frac{\Delta t}{2} \left[G \delta v_{z,r}^8 - c_2 \delta \sigma_{r,r}^8 - \frac{c_2}{r^8} (\delta\sigma_r^8 - \delta\sigma_\theta^8) \right] = 0 \\ \rho_b c_2 \Delta v_z^7 + \Delta \tau_{rz}^7 + \frac{\Delta t}{2} \left[-G \delta v_{r,z}^7 - c_2 \delta \sigma_{z,z}^7 - \frac{c_2}{r^7} \delta \tau_{rz}^7 \right] = 0 \\ -\rho_b c_2 \Delta v_r^6 - \Delta \tau_{rz}^6 + \frac{\Delta t}{2} \left[G \delta v_{z,r}^6 + c_2 \delta \sigma_{r,r}^6 + \frac{c_2}{r^6} (\delta\sigma_r^6 - \delta\sigma_\theta^6) \right] = 0 \end{aligned} \quad (A-71)$$

Integrating the constitutive equations (A-63) through (A-67) yields

$$\begin{aligned}
 C_1 \Delta \sigma_r^0 - C_2 \Delta \sigma_\theta^0 - C_2 \Delta \sigma_z^0 - \frac{\Delta t}{2} \delta v_{r,r}^0 &= 0 \\
 -C_2 \Delta \sigma_r^0 - C_2 \Delta \sigma_\theta^0 + C_1 \Delta \sigma_z^0 - \frac{\Delta t}{2} \delta v_{z,z}^0 &= 0 \\
 C_3 \Delta \tau_{rz}^0 - \frac{\Delta t}{2} (\delta v_{r,z}^0 + \delta v_{z,r}^0) &= 0 \\
 -C_2 \Delta \sigma_r^0 + C_1 \Delta \sigma_\theta^0 - C_2 \Delta \sigma_z^0 - \frac{\Delta t}{2r^0} \delta v_r^0 &= 0
 \end{aligned} \tag{A-72}$$

Integrating the equation of motion (A-1) yields

$$\begin{aligned}
 \rho_b \Delta v_r^0 - \frac{\Delta t}{2} \left[\delta \sigma_{r,r}^0 + \delta \tau_{rz,z}^0 + \frac{(\delta \sigma_r^0 - \delta \sigma_\theta^0)}{r^0} \right] &= 0 \\
 \rho_b \Delta v_z^0 - \frac{\Delta t}{2} \left[\delta \sigma_{z,z}^0 + \delta \tau_{rz,r}^0 + \frac{\delta \tau_{rz}}{r^0} \right] &= 0
 \end{aligned} \tag{A-73}$$

Equations (A-70) through (A-73) are then used to obtain solutions within the bar.

AD-A052 051

NAVAL SURFACE WEAPONS CENTER WHITE OAK LAB SILVER SP--ETC F/G 19/4
STRESS WAVE PROPAGATION IN BARS DUE TO NORMAL IMPACT ON WATER.(U)
AUG 77 W T MESSICK, J M MARSHALL

UNCLASSIFIED

NSWC/WOL/TR-77-128

NL

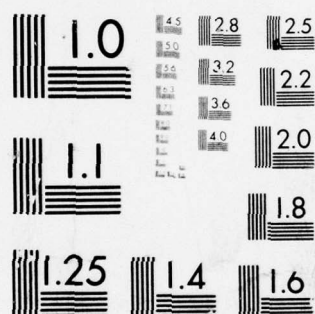
5 OF 5

AD
A052 051



END
DATE
FILMED
5-78

DDC



MICROCOPY RESOLUTION TEST CHART
NATIONAL BUREAU OF STANDARDS-1963-A

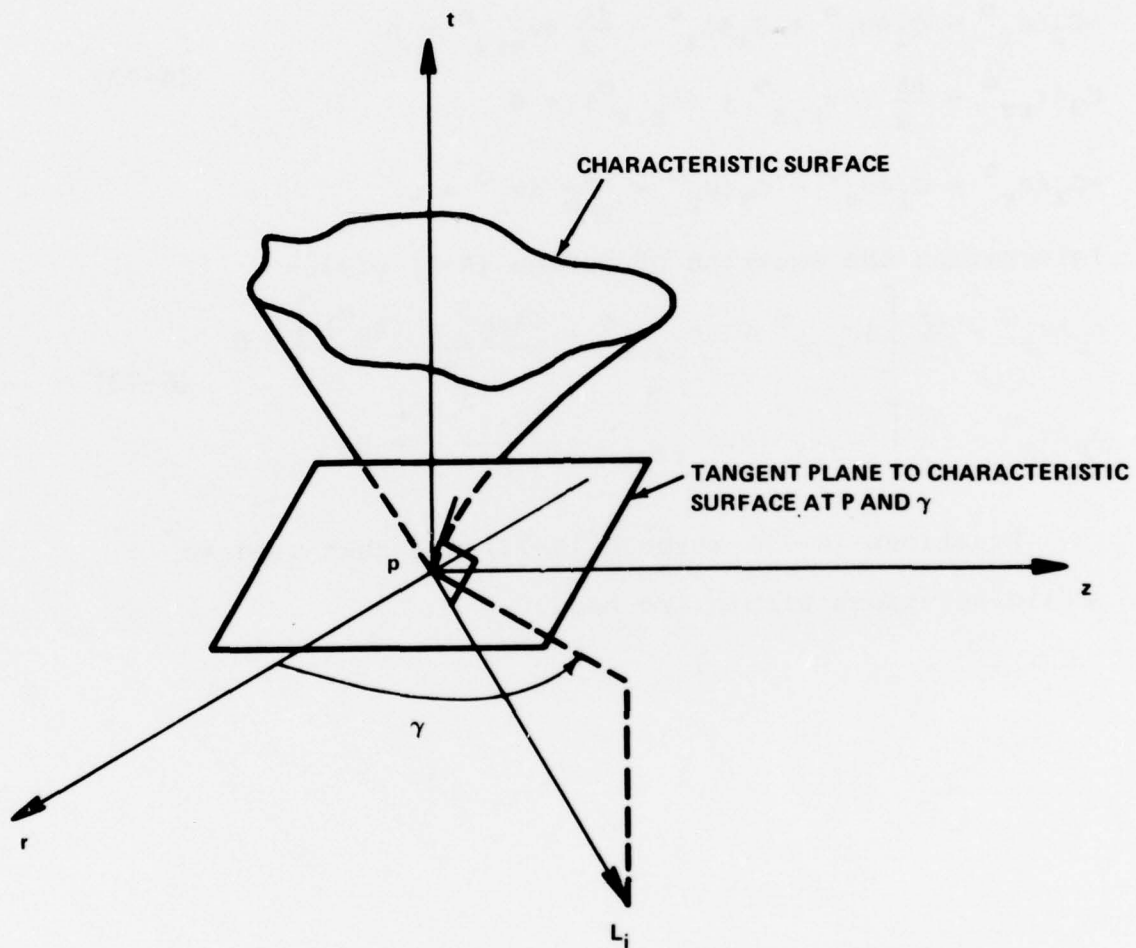


FIGURE A.1 CHARACTERISTIC SURFACE AND ASSOCIATED GEOMETRY

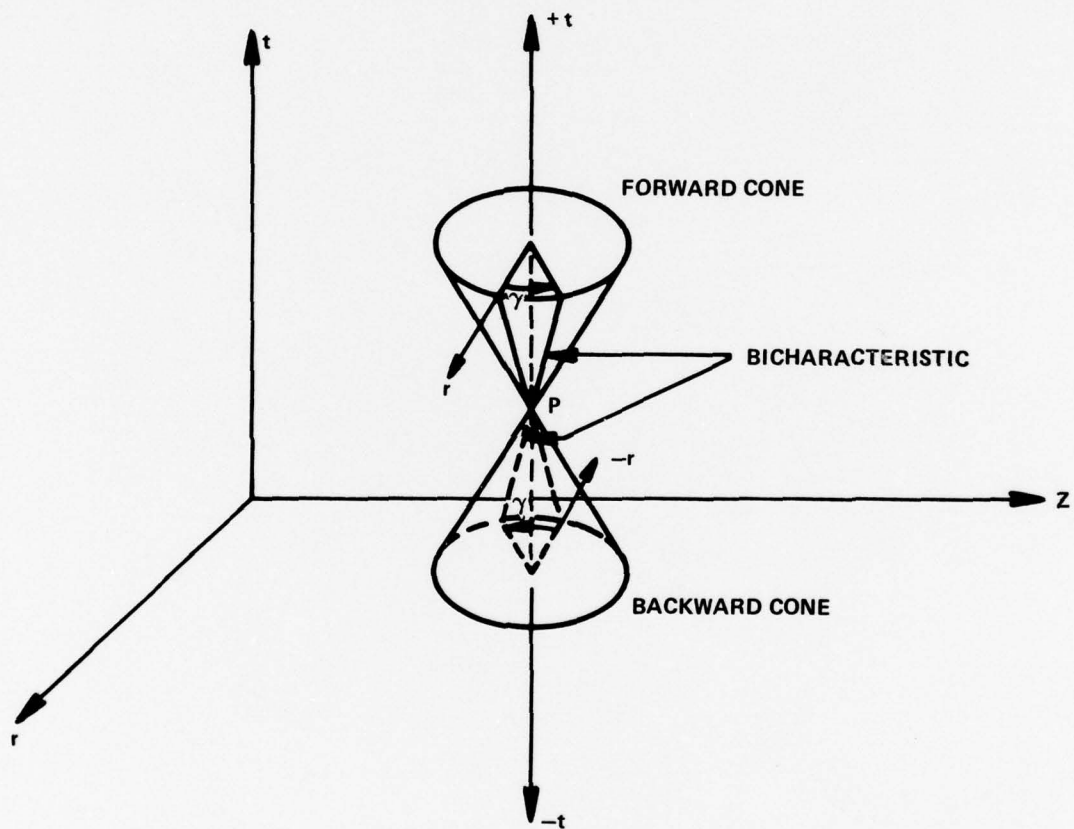


FIGURE A.2 CHARACTERISTIC CONES AND BICHARACTERISTICS FOR WAVE PROPAGATION IN LINEAR ELASTIC BAR

APPENDIX B

BICHARACTERISTIC EQUATIONS FOR THE EULERIAN
FORMULATION OF NONLINEAR WAVE PROPAGATION IN WATER

B.1 Governing Equations

If the disturbances on a body of water are symmetric about some axis, then a cylindrical coordinate system may be used to describe the wave propagation into the water space. The hydrodynamic momentum equations in Eulerian coordinates are given by:

$$\rho_w u_{,t} + \rho_w uu_{,r} + \rho_w vu_{,z} + p_{,r} = 0 \quad (B-1)$$

$$\rho_w v_{,t} + \rho_w uv_{,r} + \rho_w vv_{,z} + p_{,z} = 0$$

where ρ_w is the density of water, u and v are the velocity components in the r and z directions, respectively, p is the pressure, and the comma denotes partial differentiation. The continuity equation is given by

$$\frac{d\rho_w}{dt} + \rho_w \left(u_{,r} + v_{,z} + \frac{u}{r} \right) = 0 \quad (B-2)$$

The total derivative of a variable ω for this Eulerian formulation is:

$$\frac{d\omega}{dt} = \omega_{,t} + u\omega_{,r} + v\omega_{,z} \quad (B-3)$$

From conservation of entropy along a particle path in compressible flow

$$\frac{dp}{dt} - a^2 \frac{d\rho_w}{dt} = 0 \quad (B-4)$$

where a is the local sound velocity. Using equations (B-3) and (B-4) in the continuity equation (B-2)

$$p_{,t} + up_{,r} + vp_{,z} + \rho_w a^2 u_{,r} + \rho_w a^2 v_{,z} + \rho_w a^2 \frac{u}{r} = 0 \quad (B-5)$$

Equations (B-1) and (B-5) are cast into matrix form as

$$A_{ij} U_{j,t} + B_{ij} U_{j,r} + C_{ij} U_{j,z} + D_i = 0 \quad (B-6)$$

where

$$U_i = \left\{ U \right\} = \begin{Bmatrix} u \\ v \\ p \end{Bmatrix} = \text{dependent variable vector}$$

$$A_{ij} = [A] = \begin{bmatrix} \rho_w & 0 & 0 \\ 0 & \rho_w & 0 \\ 0 & 0 & 1 \end{bmatrix}$$

$$B_{ij} = [B] = \begin{bmatrix} \rho_w u & 0 & 1 \\ 0 & \rho_w u & 0 \\ \rho_w a^2 & 0 & u \end{bmatrix} \quad (B-7)$$

$$C_{ij} = [C] = \begin{bmatrix} \rho_w v & 0 & 0 \\ 0 & \rho_w v & 1 \\ 0 & \rho_w a^2 & v \end{bmatrix}$$

$$D_i = \left\{ D \right\} = \begin{Bmatrix} 0 \\ 0 \\ \rho_w a^2 \frac{u}{r} \end{Bmatrix}$$

B.2 Equations of Bicharacteristic Curves

The system of equations (B-6) may be transformed so that differentiation occurs in only two directions within a surface called the characteristic surface. The derivation of the characteristic equation is outlined in Appendix A. Given the system of equations (B-6), the characteristic equation (A-19) is

$$\det(\phi_{,t} A_{ij} + \phi_{,r} B_{ij} + \phi_{,z} C_{ij}) = 0 \quad (B-8)$$

where $\phi = \text{constant}$ is the characteristic surface. Substituting the coefficients from (B-7) into equation (B-8) and expanding yields:

$$\rho_w^2 (\phi_{,t} + u\phi_{,r} + v\phi_{,z}) \left\{ \phi_{,t}^2 + (u^2 - a^2)\phi_{,r}^2 + (v^2 - a^2)\phi_{,z}^2 + 2u\phi_{,r}\phi_{,t} + 2v\phi_{,z}\phi_{,t} + 2uv\phi_{,r}\phi_{,z} \right\} = 0 \quad (B-9)$$

Casting equation (B-9) into a quadratic form yields:

$$\rho_w^2 (\phi_{,x_1} + u\phi_{,x_2} + v\phi_{,x_3}) S_{ij} \phi_{,x_i} \phi_{,x_j} = 0 \quad (B-10)$$

where

$$S_{ij} = \begin{bmatrix} 1 & u & v \\ u & u^2 - a^2 & uv \\ v & uv & v^2 - a^2 \end{bmatrix}$$

$$x_1 = t$$

$$x_2 = r$$

$$x_3 = z$$

From equation (A-33) of Appendix A, the equation of the characteristic surface is

$$S_{ij}^{-1} dx_i dx_j \quad (B-11)$$

The inverse of S_{ij} is given by

$$S_{ij}^{-1} = \frac{1}{a^2} \begin{bmatrix} a^2 - u^2 - v^2 & u & v \\ u & -1 & 0 \\ v & 0 & -1 \end{bmatrix} \quad (B-12)$$

Substituting for S_{ij} yields the characteristic conoid for axisymmetric hydrodynamic flow:

$$(dr - udt)^2 + (dz - vdt)^2 = a^2 dt^2 \quad (B-13)$$

The variable terms udt and vdt in the conoid equation are convective terms which result from the Eulerian formulation. Since the flow field is changing with time, the conoid shape is also changing with time and is dependent on the actual flow field. The "sound speed" a also changes because of the compressibility formulation.

Because of the variable terms (variable with time) in the characteristic conoid equation, a bicharacteristic curve $\zeta = \text{constant}$ will not remain at a fixed angle in the rz plane as it does in linear elastic wave propagation in Lagrangian coordinates. Let the angle between the negative r axis and

the projection of the tangent to the bicharacteristic onto the rz plane be γ as shown in Figure II.4. γ is measured positive clockwise from the negative r axis when looking in the negative t direction. Choosing the two parameters γ and τ to describe the characteristic conoid (B-13), a parametric description of the surface is:

$$\begin{aligned} dr &= (u + a \cos \gamma) d\tau \\ dz &= (v + a \sin \gamma) d\tau \\ dt &= d\tau \end{aligned} \tag{B-14}$$

The bicharacteristics are the intersections of the characteristic surfaces (B-10) with their envelope which is the characteristic conoid (B-13) or (B-14). In the general case of nonlinear wave propagation, the bicharacteristics are curves, the coordinates of which depend on time t and the flow field u , v , and the sound velocity a . In order to describe the propagation of disturbances from the old time plane to the point P along a particular bicharacteristic ζ^P , the coordinates of the intersection of the ζ^P characteristic with the old time plane must be known as a function of the angle γ^P . Let

$$dx_i = (\lambda_i + \mu_i \cos \gamma + \nu_i \sin \gamma) d\tau \tag{B-15}$$

be the differential change in coordinates of the characteristic conoid as a function of γ and τ . Equation (B-15) also

describes the bicharacteristic at the apex P of the conoid. Now consider a point Q near P, also on the conoid. Since it lies on the characteristic conoid defined by $x_i = x_i(\zeta, \tau)$,

$$dx_i = x_{i,\tau} d\tau + x_{i,\zeta} d\zeta \quad (\text{B-16})$$

Now the direction given by (B-16) will lie on the conoid and go through P only if equation (B-11) is satisfied in the form of

$$(\lambda_i + \mu_i \cos \gamma + v_i \sin \gamma) S_{ij}^{-1} (x_{j,\tau} d\tau + x_{j,\zeta} d\zeta) = 0 \quad (\text{B-17})$$

But for a point to be on the conoid and go through the apex P it must be a bicharacteristic which is a curve of constant ζ . Thus at Q

$$(\lambda_i + \mu_i \cos \gamma + v_i \sin \gamma) S_{ij}^{-1} x_{j,\tau} = 0 \quad (\text{B-18})$$

and the bicharacteristic relationship at P is given by

$$(\lambda_i + \mu_i \cos \gamma + v_i \sin \gamma) S_{ij}^{-1} x_{j,\zeta} = 0 \quad (\text{B-19})$$

From equation (B-14), the vectors λ_i , μ_i , v_i in equation (B-19) are given by

$$\lambda_i = \begin{Bmatrix} 1 \\ u \\ v \end{Bmatrix}, \quad \mu_i = \begin{Bmatrix} 0 \\ a \\ 0 \end{Bmatrix}, \quad v_i = \begin{Bmatrix} 0 \\ 0 \\ a \end{Bmatrix} \quad (\text{B-19})$$

Using equations (B-12), (B-15), and (B-19), the equations for each bicharacteristic through the apex P of the conoid are

$$dt = d\tau$$

$$dr = (u + a \cos \gamma) d\tau$$

(B-20)

$$dz = (v + a \sin \gamma) d\tau$$

$$z_{,\zeta} \sin \gamma + r_{,\zeta} \cos \gamma = 0$$

τ is chosen to be zero at the apex P and the initial condition for equations (B-20) is

$$\gamma = \zeta \text{ at } \tau = 0$$

On the characteristic conoid, equation (B-16) applies, and on a bicharacteristic curve, ζ is constant so

$$dx_i = x_{i,\tau} d\tau \text{ on a bicharacteristic} \quad (\text{B-21})$$

Equations (B-20) become:

$$t = \tau + \text{constant}$$

$$r(\zeta, \tau)_{,\tau} = u + a \cos \gamma$$

$$z(\zeta, \tau)_{,\tau} = v + a \sin \gamma \quad (\text{B-22})$$

$$r(\zeta, \tau)_{,\zeta} \cos \gamma + z(\zeta, \tau)_{,\zeta} \sin \gamma = 0$$

with initial conditions from the apex of

$$t = t^P, r = r^P, z = z^P \text{ at } \gamma = \zeta = \zeta^P \text{ and } \tau = 0 \quad (\text{B-23})$$

In order to obtain a solution to equations (B-22), the variables u , v , a , and γ will be expanded with a linear variation about the values at the apex. If u^P , v^P , a^P , and γ^P are the values at the apex independent of ζ , then let

$$\begin{aligned}
u &= u^P + \bar{u}(\zeta)\tau + 0(\tau^2) \\
v &= v^P + \bar{v}(\zeta)\tau + 0(\tau^2) \\
a &= a^P + \bar{a}(\zeta)\tau + 0(\tau^2) \\
\gamma &= \zeta + \bar{\gamma}(\zeta)\tau + 0(\tau^2)
\end{aligned}
\tag{B-24}$$

The terms $0(\tau^2)$ denote second order terms in τ and $\bar{u}(\zeta)$, $\bar{v}(\zeta)$, $\bar{a}(\zeta)$, $\bar{\gamma}(\zeta)$ depend on the particular bi-characteristic ζ . Substituting equations (B-24) into the second and third of equations (B-22) yields

$$\begin{aligned}
r(\zeta, \tau)_{,\tau} &= [u^P + \bar{u}(\zeta)\tau] + [a^P + \bar{a}(\zeta)\tau]\cos(\zeta + \bar{\gamma}(\zeta)\tau) + 0(\tau^2) \\
z(\zeta, \tau)_{,\tau} &= [v^P + \bar{v}(\zeta)\tau] + [a^P + \bar{a}(\zeta)\tau]\sin(\zeta + \bar{\gamma}(\zeta)\tau) + 0(\tau^2)
\end{aligned}
\tag{B-25}$$

Integrating these equations with respect to τ and using the initial conditions (B-23) yields:

$$\begin{aligned}
r(\zeta, \tau) &= r^P + (u^P + a^P \cos \zeta)\tau + \frac{1}{2}[\bar{u}(\zeta) + \bar{a}(\zeta)\cos \zeta - a^P \bar{\gamma}(\zeta)\sin \zeta]\tau^2 \\
&\quad + 0(\tau^3) \\
z(\zeta, \tau) &= z^P + (v^P + a^P \sin \zeta)\tau + \frac{1}{2}[\bar{v}(\zeta) + a^P \bar{\gamma}(\zeta)\cos \zeta \\
&\quad + \bar{a}(\zeta)\sin \zeta]\tau^2 + 0(\tau^3)
\end{aligned}
\tag{B-26}$$

In arriving at equations (B-26), small angle approximations were used

$$\begin{aligned}
\cos \gamma &= \cos(\zeta + \bar{\gamma}(\zeta)\tau) = \cos \zeta - \bar{\gamma}(\zeta)\tau \sin \zeta \\
\sin \gamma &= \sin(\zeta + \bar{\gamma}(\zeta)\tau) = \sin \zeta + \bar{\gamma}(\zeta)\tau \cos \zeta
\end{aligned}
\tag{B-27}$$

Now differentiate equations (B-26) with respect to ζ :

$$\begin{aligned} r(\zeta, \tau)_{,\zeta} &= -a^P \tau \sin \zeta + \frac{1}{2} \tau^2 [\bar{u}'(\zeta) + \bar{a}'(\zeta) \cos \zeta - \bar{a}(\zeta) \sin \zeta \\ &\quad - a^P \bar{\gamma}'(\zeta) \sin \zeta - a^P \bar{\gamma}(\zeta) \cos \zeta] + 0(\tau^3) \\ z(\zeta, \tau)_{,\zeta} &= a^P \tau \cos \zeta + \frac{1}{2} \tau^2 [\bar{v}'(\zeta) + a^P \bar{\gamma}'(\zeta) \cos \zeta - a^P \bar{\gamma}(\zeta) \sin \zeta \\ &\quad + \bar{a}'(\zeta) \sin \zeta + \bar{a}(\zeta) \cos \zeta] + 0(\tau^3) \end{aligned} \quad (B-28)$$

where the prime denotes differentiation with respect to the independent variable. Substituting these equations into the fourth of equations (B-22) and using the small angle approximations yields the following equation after simplification.

$$\tau^2 [\bar{u}'(\zeta) \cos \zeta + \bar{v}'(\zeta) \sin \zeta + \bar{a}'(\zeta) + a^P \bar{\gamma}(\zeta)] + 0(\tau^3) = 0 \quad (B-29)$$

For equation (B-29) to be true for any τ the coefficients of each of the τ terms must be zero. Thus

$$\bar{u}'(\zeta) \cos \zeta + \bar{v}'(\zeta) \sin \zeta + \bar{a}'(\zeta) + a^P \bar{\gamma}(\zeta) = 0 \quad (B-30)$$

From the definition of the bar terms in equations (B-24), equation (B-30) to the first order in τ becomes:

$$\cos \zeta u_{,\zeta} + \sin \zeta v_{,\zeta} + a_{,\zeta} + a^P \bar{\gamma}(\zeta) \tau = 0 \quad (B-31)$$

For any flow variable ω

$$\omega_{,\zeta} = \omega_{,t} \tau_{,\zeta} + \omega_{,r} r_{,\zeta} + \omega_{,z} z_{,\zeta} \quad (B-32)$$

which from equations (B-22) and (B-28) become

$$\omega_{,\zeta} = -a^P \tau \sin \zeta \omega_{,r} + a^P \tau \cos \zeta \omega_{,z} + 0(\tau^2) \quad (B-33)$$

Making use of equation (B-33) in equation (B-31) yields an expression for $\bar{\gamma}(\zeta)$ which when substituted into the fourth of equations (B-24) becomes

$$\begin{aligned} \gamma - \zeta = \tau [\sin \zeta \cos \zeta u_{,r} - \cos^2 \zeta u_{,z} + \sin^2 \zeta v_{,r} - \sin \zeta \cos \zeta v_{,z} \\ + \sin \zeta a_{,r} - \cos \zeta a_{,z}] + O(\tau^2) \end{aligned} \quad (B-34)$$

Using the equations (B-24), the coordinates of the bicharacteristics may finally be written as

$$\begin{aligned} r &= r^P + \frac{1}{2} \tau \left\{ u^P + u + a^P \cos \zeta + a \cos \gamma \right\} + O(\tau^3) \\ z &= z^P + \frac{1}{2} \tau \left\{ v^P + v + a^P \sin \zeta + a \sin \gamma \right\} + O(\tau^3) \end{aligned} \quad (B-35)$$

where γ is given by equation (B-34).

Since u , v , and a are functions of r , z , and t the bicharacteristic coordinates in equations (B-35) must be solved by an iteration procedure.

B.3 Compatability Equations Along Bicharacteristics

The relationships between the spatial coordinates (r , z) and the characteristic conoid coordinates (ζ , τ) have now been derived. With these equations, the terms in the governing equations of hydrodynamic flow may now be transformed. For a variable ω , along the bicharacteristic curves $\zeta = \text{constant}$:

$$\omega_{,\tau} = \omega_{,t} t_{,\tau} + \omega_{,r} r_{,\tau} + \omega_{,z} z_{,\tau} \quad (B-36)$$

Using the bicharacteristic relations (B-22), equation (B-36) becomes

$$\omega_{,\tau} = \omega_{,t} + (u + a\cos\gamma)\omega_{,r} + (v + a\sin\gamma)\omega_{,z} \quad (\text{B-37})$$

The governing equations (B-1) and (B-5) rewritten in a form to utilize equation (B-37) are:

$$\begin{aligned} \rho_w u_{,\tau} + \rho_w (u + a\cos\gamma)u_{,r} + \rho_w (v + a\sin\gamma)u_{,z} \\ + (p_{,r} - \rho_w a\cos\gamma u_{,r} - \rho_w a\sin\gamma u_{,z}) &= 0 \\ \rho_w v_{,\tau} + \rho_w (u + a\cos\gamma)v_{,r} + \rho_w (v + a\sin\gamma)v_{,z} \\ + (p_{,z} - \rho_w a\cos\gamma v_{,r} - \rho_w a\sin\gamma v_{,z}) &= 0 \\ p_{,\tau} + (u + a\cos\gamma)p_{,r} + (v + a\sin\gamma)p_{,z} \\ + \rho_w a^2 (u_{,r} + v_{,z} + \frac{u}{r}) - (a\cos\gamma p_{,r} + a\sin\gamma p_{,z}) &= 0 \end{aligned} \quad (\text{B-38})$$

Multiplying the first equation in (B-38) by $a\cos\gamma$, adding it to $a\sin\gamma$ times the second equation and adding this sum to the third equation yields

$$\begin{aligned} p_{,\tau} + \rho_w a\cos\gamma u_{,\tau} + \rho_w a\sin\gamma v_{,\tau} + \rho_w a^2 \left[\sin^2\gamma u_{,r} \right. \\ \left. - \sin\gamma\cos\gamma (u_{,z} + v_{,r}) + \cos^2\gamma v_{,z} + \frac{u}{r} \right] &= 0 \end{aligned} \quad (\text{B-39})$$

where the relation (B-37) has been used. Since (B-39) has been derived along a bicharacteristic where (B-21) holds, equation (B-39) can be written as:

$$dp + \rho_w a \cos \gamma du + \rho_w a \sin \gamma dv = -\rho_w a^2 J d\tau \quad (B-40)$$

$$\text{where } J = \sin^2 \gamma u_{,r} - \sin \gamma \cos \gamma (u_{,z} + v_{,r}) + \cos^2 \gamma v_{,z} + \frac{u}{r}.$$

Now along a particle path equation (B-5) yields

$$dp = -\rho_w a^2 (u_{,r} + v_{,z} + \frac{u}{r}) dt \quad (B-41)$$

It is desired to determine the variables u , v , and p at a point P in the new time plane t . By using the bicharacteristic curves, relations between the known variables in the old time plane ($t - \Delta t$) and those at P may be found. Equation (B-40) yields these relations but the unknown partial derivative terms in J at the point P must be eliminated. This can be done by forming combinations of relations along different bicharacteristic curves ζ^P . The scheme to be used for determining the unknown variables is to use four bicharacteristics emanating from P . For a variable ω , the value of ω at P will be denoted by ω^P and the value at the point where the n^{th} bicharacteristic intersects the old time plane will be denoted by ω^n . Integrating equation (B-40) along the n^{th} bicharacteristic and using a trapezoidal integration rule where necessary yields

$$\begin{aligned} p - p^n + \frac{1}{2} (\rho a \cos \zeta^n + \rho^n a^n \cos \gamma^n) (u - u^n) + \frac{1}{2} (\rho a \sin \zeta^n \\ + \rho^n a^n \sin \gamma^n) (v - v^n) = -\frac{1}{2} \rho(a) [\sin^2 \zeta^n u_{,r} \\ - \sin \zeta^n \cos \zeta^n (u_{,z} + v_{,r}) + \cos^2 \zeta^n v_{,z} + \frac{u}{r}] (t - t^n) \\ - \frac{1}{2} \rho^n (a^n)^2 J^n (t - t^n) \end{aligned} \quad (B-42)$$

where

$$J^n = \sin^2 \gamma^n u_{,r}^n - \sin \gamma^n \cos \gamma^n (u_{,z}^n + v_{,r}^n) + \cos^2 \gamma^n v_{,z}^n + \frac{u^n}{r^n} \text{ and } \gamma^n \text{ at } P = \zeta^n \quad (B-43)$$

The nonsuperscripted variables in the above equation refer to the unknown variables at P in the new time plane (time = t).

An additional equation is obtained by integrating the particle path equation from P to its intersection with the previous time plane, which will be point 5:

$$p - p^5 = -\frac{1}{2} \rho(a)^2 [u_{,r} + v_{,z} + \frac{u}{r}] (t - t^5) - \frac{1}{2} \rho^5 (a^5)^2 [u_{,r}^5 + v_{,z}^5 + \frac{u^5}{r^5}] (t - t^5) \quad (B-44)$$

Equations (B-42) and (B-44) are simplified by letting

$$\begin{aligned} U_{Pn} &= \frac{1}{2} (\rho a \cos \zeta^n + \rho^n a^n \cos \gamma^n) \\ V_{Pn} &= \frac{1}{2} (\rho a \sin \zeta^n + \rho^n a^n \sin \gamma^n) \\ P_{Pn} &= p^n + U_{Pn} u^n + V_{Pn} v^n + \frac{1}{2} \rho^n (a^n)^2 (t - t^n) J^n \\ \Delta t &= t - t^n \end{aligned} \quad (B-45)$$

Using the (B-45) relationships, equations (B-42) become

$$p + U_{Pn} u + V_{Pn} v + \frac{1}{2} \rho(a)^2 \Delta t [\sin^2 \zeta^n u_{,r} - \sin \zeta^n \cos \zeta^n (u_{,z} + v_{,r}) + \cos^2 \zeta^n v_{,z} + \frac{u}{r}] = P_{Pn} \quad (B-46)$$

; n = 1, 2, 3, 4

Equation (B-44) becomes

$$p + \frac{1}{2} \rho(a)^2 \Delta t [u_{,r} + v_{,z} + \frac{u}{r}] = P_5 \quad (B-47)$$

$$\text{where } P_5 = p_5 + \frac{1}{2} \tau_5 \rho_5 a_5^2 [u_{,r}^5 + v_{,z}^5 + \frac{u_5}{r_5}].$$

The location of the intersection of the n^{th} bi-characteristic with the previous time plane (t^n, r^n, z^n) is given by equations (B-35) and (B-34)

$$\begin{aligned} r^n &= r - \frac{1}{2} \Delta t [u + u^n + a \cos \zeta^n + a^n \cos \gamma^n] \\ z^n &= z - \frac{1}{2} \Delta t [v + v^n + a \sin \zeta^n + a^n \sin \gamma^n] \end{aligned} \quad (B-48)$$

$$\cos \gamma^n = \cos \zeta^n - \delta \gamma^n \sin \zeta^n$$

$$\sin \gamma^n = \sin \zeta^n + \delta \gamma^n \cos \zeta^n$$

$$\begin{aligned} \delta \gamma^n = \gamma^n - \zeta^n &= -\Delta t [\sin \zeta^n \cos \zeta^n u_{,r}^n - \cos^2 \zeta^n u_{,z}^n + \sin^2 \zeta^n v_{,r}^n \\ &\quad - \sin \zeta^n \cos \zeta^n v_{,z}^n + \sin \zeta^n a_{,r}^n - \cos \zeta^n a_{,z}^n] \end{aligned}$$

for $n = 1, 2, 3, 4$

Along the particle path

$$\begin{aligned} r^5 &= r - \frac{1}{2} \Delta t (u + u^5) \\ z^5 &= z - \frac{1}{2} \Delta t (v + v^5) \end{aligned} \quad (B-49)$$

The four bicharacteristics are chosen so that they are separated by a quadrant and biased by an angle η relative to the negative r axis.

$$\zeta^n = \eta + \frac{(n-1)}{2} \pi ; \quad n = 1, 2, 3, 4 \quad (\text{B-50})$$

Substituting these values of ζ_n into the equations (B-46) yields:

$$p + U_{P_1} u + V_{P_1} v + \frac{1}{2} \Delta t \rho (a)^2 [\sin^2 \eta u_{,r} - \sin \eta \cos \eta (u_{,z} + v_{,r}) + \cos^2 \eta v_{,z} + \frac{u}{r}] = P_{P1}$$

$$p + U_{P_2} u + V_{P_2} v + \frac{1}{2} \Delta t \rho (a)^2 [\cos^2 \eta u_{,r} + \sin \eta \cos \eta (u_{,z} + v_{,r}) + \sin^2 \eta v_{,z} + \frac{u}{r}] = P_{P2}$$

$$p + U_{P_3} u + V_{P_3} v + \frac{1}{2} \Delta t \rho (a)^2 [\sin^2 \eta u_{,r} - \sin \eta \cos \eta (u_{,z} + v_{,r}) + \cos^2 \eta v_{,z} + \frac{u}{r}] = P_{P3}$$

$$p + U_{P_4} u + V_{P_4} v + \frac{1}{2} \Delta t \rho (a)^2 [\cos^2 \eta u_{,r} + \sin \eta \cos \eta (u_{,z} + v_{,r}) + \sin^2 \eta v_{,z} + \frac{u}{r}] = P_{P4}$$

(B-51)

By proper combinations of the above equations for particular boundary conditions, the derivatives of the variables at P may be eliminated. However, the terms U_{P_n} , V_{P_n} , and P_{P_n} are functions of ρ and a which depend upon the pressure at P, p . Thus an iterative technique must be used to obtain a solution. Furthermore, an iterative solution must be used to obtain the intersections of the bicharacteristics with the previous time plane because of the implicit relations for r^n and z^n (equation (B-48)).

DISTRIBUTION

Office of the Secretary of Defense
Director of Defense Research and Engineering
Washington, D. C. 20301
Mr. J. Persh (CAD/ET)

Office of the Chief of Naval Operations
Department of the Navy
Washington, D. C. 20350
Mr. R. Blaise (OP-620E)

Office of the Chief of Naval Material
Department of the Navy
Washington, D. C. 20360
Mr. Ralph W. Judy (MAT-0342)

Commander
Naval Sea Systems Command
Naval Sea Systems Command Headquarters
Washington, D. C. 20360
SEA-03B
Mr. M. A. Kinna (SEA-0352)
Mr. L. Pasiuk (SEA-03513)
Mr. G. Sorkin (SEA-035)
SEA-09G32

2

Commander
Naval Air Systems Command
Department of the Navy
Washington, D. C. 20361
Mr. W. Volz (AIR-320C)

Director
Naval Research Laboratory
Washington, D.C. 20375
Dr. P. Mast

Office of the Chief of Naval Research
800 North Quincy Street
Arlington, VA 22217
Dr. N. Perrone (Code 439)

2

Office of the Chief of Research and Development
Department of the Army
Washington, D. C. 20310
Dr. J. Bryant (DARS-ARS-PM)

Defense Documentation Center
Cameron Station
Alexandria, VA 22314

12

Director
Defense Nuclear Agency
Washington, D.C. 20305
Mr. J. Moulton

Naval Postgraduate School
Monterey, CA 93940
Dr. R. Ball

Commander
Naval Weapons Center
China Lake, CA 93557
Mr. E. L. Jeter

Commander
Naval Air Development Center
Warminster, PA 18974
Dr. R. K. Lobb

Commander
Naval Underwater Systems Center
New London, CT 06320
Mr. A. Carlson

Army Ballistic Research Laboratories
Aberdeen Proving Ground, MD 21005
Dr. Robert Karp
Dr. N. J. Huffington, Jr.
Dr. Frederick Grace

Army Materials and Mechanics Research Center
Watertown, MA 92172
Mr. J. S. Mescal

Air Force Office of Scientific Research
Building 410
Bolling Air Force Base
Washington, D. C. 20332
Mr. W. J. Walker

National Aeronautics and Space Administration
Scientific and Technical Information Facility
P.O. Box 33
College Park, MD 20740

Sandia Laboratories
P.O. Box 5800
Albuquerque, NM 87115
Dr. S. Key
Dr. L. Bertholf

University of Maryland
College Park, MD 20740
Dr. H. G. Schaeffer
Dr. J. Yang

3

Drexel University
32nd and Chestnut Streets
Philadelphia, PA 19104
Dr. P. C. Chow
Dr. J. Rose
Dr. R. Mortimer

Lawrence Livermore Laboratory
University of California
P.O. Box 808
Livermore, CA 94550
Mr. M. L. Wilkens
Mr. E. D. Giroux

Stanford Research Institute
333 Ravenswood Avenue
Menlo Park, CA 94025
Dr. Y. Horie

Babcock and Wilcox
Power Generation Division
P.O. Box 1260
Lynchburg, VA 24505
Dr. H. L. Chang

Terra Tek Company
815 E. 4th Street
Salt Lake City, UT 84102
Sidney Green

Systems, Sciences, and Software
P.O. Box 1620
LaJolla, CA 92037
Dr. G. A. Gurtman